



Cellular and extracellular aspects of  
posterior eye microstructure and biomechanics

Petar Petrov Markov

Thesis submitted to Cardiff University for the degree of Doctor of Philosophy

School of Optometry and Vision Sciences

School of Biosciences

School of Engineering

January 2020

## Abstract

A quarter of the entire human population is affected by vision disorders, with extensive efforts directed towards developing new and improved treatments. The peripapillary sclera (PPS) has a large influence on the forces exerted on the optic nerve under fluctuating intraocular pressure (IOP), implying a role in the mechanics of glaucoma. To better comprehend these processes, physiologically relevant data were collected on both the scleral extracellular matrix (ECM) and cell cytoskeletal components. The cytoskeletal architecture was reconstructed using a novel approach for generating geometrically accurate models for finite element (FE) analysis.

Wide-angle X-ray scattering (WAXS) was used to map the scleral collagen orientation and distribution in humans and 11 mammalian species. The bovine sclera was selected as a suitable animal model, with further clarity on the ECM depth profile provided by second harmonic generation microscopy. To accomplish this analysis, a bespoke MATLAB script was developed and implemented. Cultured bovine scleral fibroblasts were subjected to simulated IOP, with the organisation of major cytoskeletal elements visualised using immuno-confocal microscopy and quantified using several image analysis packages. Finally, the collected stacks of images were reconstructed to 3D isosurfaces.

WAXS revealed alterations in the PPS collagen architecture in highly myopic human eyes, as well as that the bovine PPS closely resembles that of humans. Applied strain caused reorganisation to the scleral fibroblast cytoskeleton, specifically to the F-actin stress fibres. The reconstructed surfaces allowed for greater accuracy in comparison to current models, with further possibilities for simplification and optimisation.

Scleral ECM structural analysis confirms the bovine eye as an appropriate human analogue for biomechanical studies. Mechanical loading of scleral fibroblasts leads to alterations in cytoskeletal microstructure, with a tendency for the rearrangements to revert with time. The collected cell and ECM physiological data will be used to create integrated FE models of the eye.

## Acknowledgements

It has been an interesting, arduous and yet enlightening experience that allowed me to improve myself immensely and reach the end of the path I have been following until now. The culmination of a journey, if you wish to be even more dramatic. I was able to become a much more proactive and confident person, whilst retaining my acerbic wit and still fulfil my promise. Working on this project has been the most worthwhile thing I have accomplished yet and I sincerely hope that it will be of scientific use. The experiences I received from three different fields developed my knowledge and skills, broadening my perspectives on the world as a whole. And I must acknowledge the people who in one shape or another helped me along the way.

First, I would like to express my profound gratitude to my supervisors for providing me with the opportunity to do this interdisciplinary PhD and the time they have given me. I truly appreciate their patience in dealing with my enthusiastic ideas, enormous emails and encouraging my growth as a researcher. In order of direct supervision: *Craig Boote*, for the constant support, trust and quick feedback. *Emma Blain*, for the productive meetings, friendly advice and ideas. *Hanxing Zhu*, for the freedom to conduct my research at my own pace.

I am happy that I was able to become close friends with people with whom I have had many fun times and who accepted my disillusioned workaholicism and supported me through it. Amongst them, three people stand out: *Jacek Pijanka*, with whom I was able to work together in a great close-knit team. *Laura Paletto*, with whom we shared numerous academic and teaching discussions. *Aleksandar Živković*, for being the best friendly rival I have ever had.

Everyday life would not be the same without the colleagues from both the Schools of Optometry and Vision Sciences and the School of Biosciences, with whom I have shared an amusing and distracting work environment, which was honestly for the best. Special gratitude to *Alfred Požarickij*, *Greg Hammond*, *Sean Ashworth*, *Benjamin Rumney*, *Alina Akhbanbetova*, *Eleanor Feneck*, *Mukhit Kulmaganbetov*, *James Bell*, *Sally Hayes*, *Siân Morgan*, *Philip Lewis*, *Robert Young* and the rest of the Structural Biophysics Group from OPTOM; *Cleo Bonnet*, *Carole Elford*, *Sophie Gilbert*, *Paul White*, *Victor Duance*, *Benjamin Egan*, *Cindy Ikie*, *Joel Alves* from BIOSI.

I would also like to thank *Ahmed Elsheikh* and *Ashkan Eliasy* from the Biomechanical Engineering Group (University of Liverpool) for access to their laboratory and help in performing the eye reconstruction work and for collaborating in general. *Anthony Hayes* from the Bioimaging Hub for access to their facilities and insight into making the best use of them. *Neil Patterson* from the Diamond Light Source for his help in conducting the eye tunic X-ray scattering. *Hla Myint Htoon* from the Singapore Eye Research Institute for the collaborative linear mixed-model statistical analysis. This work would have not been possible without the awarded Doctoral Training Grant funded by the Engineering and Physical Sciences Research Council.

I was also fortunate to be able to develop leadership capabilities through a variety of roles. I wish to express my gratitude to *Julie Albon* and *Malgorzata Rozanowska*, for whose modules in OPTOM I acted as a Laboratory Demonstrator for the last three years. The Fencing club at Cardiff University for spending my Monday and Friday evenings stabbing and slashing at people with swords when I was not preoccupied organising things as Vice-President or looking out for everyone as Welfare Officer. Special thanks to *Thomas Knight*, *Robin Elliott*, *Toby Brann*, *Benjamin Hibbert*, *Ania Krzyżanowska*, *Adam Cobbold*, *Ellie Paul*, *Alexander Stewart*, *Elsa Merrett*, *Xuan Lim*, *Weronika Kozuch*, *Michael Farebrother*, *Razvan Timis* and everyone else whom I have faced off against. And whilst on the topic of safety, *George Jukes* and *Hannah Tayler* for sharing cold and rainy Wednesday and Saturday evenings, from 22:00 to 03:00, looking after students and making sure they made it home safely and to Cardiff Volunteering for running the Safety Walk Scheme itself.

Additional people I would like to thank include *Barbara Farkaš* and *Petra Kovačević* for the interesting conversations, as well as the housemates I have had throughout the years who made the little time I actually spent indoors entertaining. Also, all the students that I have taught the last three years and who hopefully paid attention and will use what they learned in some form as professionals. Special gratitude goes to *Vasilij Goltsev*, *Marc-André Delsuc* and *Radka Vladkova*, my MSc and BSc supervisors, for promoting my scientific development, along with everyone from the Department of Biophysics and Radiobiology at Sofia University.

I am also grateful to my friends back home for not forgetting me even when I was busy with all of the different responsibilities I was involved with: *Alexander Kostadinov, Filip Zaikov, Krasimir Grozev, Martin Ninov, Georgi Popov, Milena Petkova, Viktoria Nikolova, Petya Petrova-Grozeva, Alexander Stoykov, Radoslava Pavlova, Miroslava Dermendzhieva, Desislava Mantovska, Tihomira Stoyanova, Maria Davidova, Antonio Stefanov, Gergana Savova, Dobromir Karev.*

Finally, I would like to dedicate this work to my loving family who have been putting up with me my entire life and I certainly have not made that task easy. They have always encouraged my studies and development and gave me reason to push forward. My late grandmother, *Todorka Mineva*, who I know would have been proud to see me now. My father, *Petar Markov*, who passed away before I could complete this PhD, to whom I promised to finish this, becoming my drive – I fulfilled my promise. My mother, *Vesselina Markova*, for always supporting me, based on whom I became an improved version of. And my sister, *Teodora Markova*, for being the best sister I could have and for dealing with my endless ideas. I love you all very much and I would not be the same sarcastic, goal-driven, idealistic fool without you.

# Table of Content

Abstract .....	II
Acknowledgements .....	III
List of Figures .....	XII
List of Tables.....	XVII
List of Abbreviations.....	XVIII
<b>1 Chapter I General introduction .....</b>	<b>001</b>
1.1 Structure of the eye .....	002
1.1.1 Eye globe.....	002
1.1.2 Sclera.....	003
1.1.3 Optic nerve head.....	004
1.1.4 Lamina cribrosa.....	005
1.1.5 Collagen extracellular matrix .....	006
1.2 Scleral cells .....	009
1.2.1 Fibroblasts .....	009
1.2.1.1 Myofibroblasts .....	010
1.2.2 Cytoskeleton.....	011
1.2.3 Actin microfilaments.....	013
1.2.3.1 F-actin stress fibres.....	015
1.2.4 Intermediate filaments.....	015
1.2.5 Microtubules.....	016
1.2.6 Mechanotransduction .....	017
1.3 Scleral biomechanics.....	019
1.3.1 Intraocular pressure .....	023
1.4 Glaucoma .....	023
1.4.1 Disease biomechanics .....	024
1.4.2 Risk factors.....	026
1.4.3 New treatments.....	027
1.5 Myopia .....	027

1.5.1 Development .....	028
1.5.2 High myopia.....	029
1.6 Technical approaches .....	031
1.6.1 X-ray scattering.....	031
1.6.2 Laser scanning microscopy .....	035
1.6.3 Finite element modelling.....	037
1.6.3.1 Eye modelling .....	038
1.6.3.2 Cell modelling.....	038
1.7 Aims and objectives .....	039
<b>2 Chapter II Materials and methods .....</b>	<b>040</b>
2.1 Ethical statement .....	041
2.2 Wide-angle X-ray scattering procedures.....	041
2.2.1 Specimen details and preparation.....	041
2.2.1.1 Human samples .....	041
2.2.1.2 Bovine samples .....	043
2.2.1.3 Other samples .....	044
2.2.2 Wide-angle X-ray scattering data collection.....	044
2.2.3 Wide-angle X-ray scattering data analysis.....	046
2.2.3.1 Assessment of collagen fibre angular displacement in myopic sclerae .....	048
2.3 Second harmonic generation imaging procedures .....	049
2.3.1 Bovine peripapillary sclera specimen preparation .....	049
2.3.2 Collagen fibre visualisation using second harmonic generation microscopy .....	050
2.4 Filum Trace – bespoke image analysis approach development .....	050
2.4.1 Image partitioning .....	051
2.4.2 Fast Fourier transform.....	051
2.4.2.1 Apodization .....	054
2.4.2.2 Periodic plus smooth image decomposition.....	055
2.4.3 Fibre orientation distribution analysis.....	059
2.4.4 Polar vector plot mapping .....	062
2.5 Image data analysis .....	063
2.5.1 ImageJ and FibrilTool .....	063

2.5.2 OrientationJ .....	064
2.5.3 CT-FIRE and CurveAlign .....	064
2.5.4 CytoSpectre .....	065
2.5.5 Chromatin condensation parameter.....	065
2.6 Cell mechanical loading procedures .....	066
2.6.1 Bovine scleral fibroblast experiments .....	066
2.6.1.1 Bovine scleral fibroblast isolation: explant crawl-out.....	066
2.6.1.2 Bovine scleral fibroblast cultivation .....	067
2.6.1.3 Bovine scleral fibroblast mechanical loading .....	067
2.6.2 Cytoskeletal visualisation using confocal microscopy.....	070
2.7 Specimen specific surface reconstruction .....	071
2.7.1 Recording eye globe topology.....	072
2.7.2 Measurements of eye tunic thickness.....	073
2.7.3 Finite element and isosurface reconstructions .....	074
2.8 Statistical analysis .....	075
<b>3 Chapter III Collagen microstructure in human normal and highly myopic sclera.....</b>	<b>076</b>
3.1 Introduction .....	077
3.2 Results and Discussion.....	078
3.2.1 Non-myopic control group.....	078
3.2.2 High myopia case 1 .....	085
3.2.3 High myopia case 2 .....	088
3.2.4 High myopia case 3 .....	091
3.2.5 Regional differences in anisotropy between normal and myopic eyes .....	093
3.2.6 Peripapillary scleral fibre angle displacement in high myopia .....	094
3.2.7 Observations and limitations.....	098
3.3 Summary, conclusions and future work.....	100
<b>4 Chapter IV Collagen microstructure in mammalian sclera.....</b>	<b>103</b>
4.1 Introduction .....	104
4.2 Results and Discussion.....	105
4.2.1 Wide-angle X-ray scattering analysis .....	105

4.2.1.1 Laboratory mouse.....	106
4.2.1.2 Northern tree shrew.....	108
4.2.1.3 Guinea pig.....	110
4.2.1.4 Black lion tamarin.....	112
4.2.1.5 Azara’s agouti.....	114
4.2.1.6 Lesser mouse-deer.....	116
4.2.1.7 Red panda.....	118
4.2.1.8 North American river otter.....	120
4.2.1.9 Domestic pig.....	122
4.2.1.10 Brazilian tapir.....	124
4.2.1.11 Domestic cattle.....	126
4.2.1.12 Mammalian posterior scleral comparison.....	129
4.2.1.12.1 Ventral groove.....	134
4.2.2 Second harmonic generation microscopy analysis.....	134
4.2.2.1 Regional polar vector plots.....	134
4.2.2.2 Peripapillary scleral fibre angular displacement from circumferential.....	141
4.3 Summary, conclusions and future work.....	146
<b>5 Chapter V Effects of mechanical loading on bovine scleral fibroblasts.....</b>	<b>148</b>
5.1 Introduction.....	149
5.2 Results and Discussion.....	150
5.2.1 Scleral fibroblast shape response to physiological and pathological strain.....	150
5.2.1.1 Fibroblast area.....	150
5.2.1.2 Fibroblast length.....	151
5.2.1.3 Fibroblast width.....	152
5.2.1.4 Fibroblast eccentricity.....	152
5.2.1.5 Summary of tensile strain-induced effects on scleral fibroblast shape.....	153
5.2.2 F-Actin stress fibre response to physiological and pathological strain.....	154
5.2.2.1 Differential effect of strain on F-actin stress fibre rearrangement.....	154
5.2.2.2 ImageJ analysis.....	159
5.2.2.2.1 Anisotropy.....	159
5.2.2.2.2 Coherency.....	160

5.2.2.3 Summary of tensile strain-induced effects on F-actin stress fibres.....	161
5.2.3 Vimentin intermediate filament response to physiological and pathological strain .....	163
5.2.3.1 Differential effect of strain on vimentin intermediate filament rearrangement .....	163
5.2.3.2 ImageJ analysis .....	167
5.2.3.2.1 Anisotropy .....	167
5.2.3.2.2 Coherency.....	167
5.2.3.3 Summary of tensile strain-induced effects on vimentin intermediate filaments.....	168
5.2.4 $\beta$ -Tubulin microtubule response to physiological and pathological strain .....	170
5.2.4.1 Differential effect of strain on $\beta$ -tubulin microtubule rearrangement.....	170
5.2.4.2 ImageJ analysis .....	174
5.2.4.2.1 Anisotropy .....	174
5.2.4.2.2 Coherency.....	174
5.2.4.3 Summary of tensile strain-induced effects on $\beta$ -tubulin microtubules .....	175
5.2.5 Nuclear response to physiological and pathological strain .....	176
5.2.5.1 Differential effect of strain on nuclear rearrangement .....	176
5.2.5.2 Nuclear area.....	180
5.2.5.3 Nuclear roundness .....	180
5.2.5.4 Chromatin condensation.....	181
5.2.5.5 Summary of tensile strain-induced effects on nuclei .....	183
5.2.6 Pathological strain inhibits proper cytoskeletal orientation in scleral fibroblasts.....	184
5.2.7 Advantages and limitations of experimental system.....	186
5.3 Summary, conclusion and future work .....	188
<b>6 Chapter VI Finite element reconstruction of eye globe and cellular components .....</b>	<b>191</b>
6.1 Introduction .....	192
6.2 Results and Discussion.....	193
6.2.1 Eye globe reconstruction .....	193
6.2.1.1 Ocular globe geometric modelling .....	193
6.2.1.2 Ocular globe tunic thickness assessment .....	195
6.2.1.3 Advantages and limitations of the experimental system.....	198
6.2.2 Cellular component reconstruction .....	199
6.2.2.1 Imaris.....	202

6.2.2.2 MeshLab.....	206
6.2.2.3 Instant Meshes.....	211
6.2.2.4 Geometry repair and smoothing.....	213
6.2.2.4.1 Netfabb geometry repair.....	213
6.2.2.4.2 MeshLab post-simplification.....	213
6.2.2.5 Gmsh.....	217
6.2.2.5.1 Volume construction.....	217
6.2.2.5.2 Quality assessment.....	218
6.2.2.6 ABAQUS.....	219
6.2.2.7 Mesh quality comparison.....	221
6.2.2.7.1 Vertices and elements.....	222
6.2.2.7.2 Area and volume.....	225
6.2.2.7.3 Aspect ratio.....	226
6.2.2.7.4 Gamma.....	229
6.2.2.8 ImageJ.....	231
6.2.2.9 Advantages and limitations of the reconstruction procedures.....	233
6.2.2.9.1 Procedural steps.....	234
6.3 Summary, conclusion and future work.....	237
<b>7 Chapter VII General discussion.....</b>	<b>241</b>
<b>Bibliography.....</b>	<b>248</b>
<b>Appendix.....</b>	<b>A01</b>
A.1 Wide-angle X-ray scattering analysis.....	A02
A.2 Confocal image analysis.....	A16
A.3 Publications, conference presentations and achievements.....	A22

## List of Figures

1.01 – Sagittal section of a human eye.....	003
1.02 – Bovine peripapillary sclera and lamina cribrosa.....	005
1.03 – Collagen molecule organisation.....	007
1.04 – Collagen structural hierarchy.....	008
1.05 – Primary bovine scleral fibroblast.....	010
1.06 – Primary components of the cytoskeleton.....	012
1.07 – Actin microfilament treadmilling as part of an actin stress fibre.....	014
1.08 – Fibroblast embedded in collagenous extracellular matrix.....	018
1.09 – Polar vector plots distribution in peripapillary and mid-posterior sclera.....	021
1.10 – Normal and glaucomatous field of vision.....	024
1.11 – Posterior eye deformation in glaucoma.....	025
1.12 – Normal and myopic visual perception.....	028
1.13 – Electromagnetic spectrum.....	031
1.14 – Bragg's law for X-ray diffraction.....	032
1.15 – Wide-angle X-ray scattering pattern generation.....	033
1.16 – Primary components of a synchrotron facility.....	034
1.15 – Comparison of fluorescent and second harmonic generation emission.....	036
1.18 – Finite element cube model.....	037
2.01 – Flat-mounted human posterior eye cup.....	043
2.02 – Diamond Light Source Beamline I03 custom setup.....	045
2.03 – Wide-angle X-ray scattering polar vector plot creation.....	047
2.04 – Idealised mathematical distribution of polar vector plots.....	049
2.05 – Input images with corresponding frequency spectra.....	053
2.06 – Input and apodized images with corresponding frequency spectra.....	055
2.07 – Input, periodic and smooth component images with corresponding frequency spectra.....	057
2.08 – Image correction signal intensity alterations.....	058
2.09 – Angular signal distribution amplitudes after image correction.....	060
2.10 – Input and corrected images with corresponding frequency spectra and polar plots.....	061
2.11 – Polar vector plots overlaid on top of interwoven scleral collagen fibres.....	062

2.12 – In-wall hoop stress in bovine eye globes .....	068
2.13 – Application of equibiaxial strain on bovine scleral fibroblasts.....	069
2.14 – Eye globe topology imaging setup .....	072
2.15 – Eye tunic thickness measurement setup .....	073
2.16 – Utilised finite element types.....	074
3.01 – Polar vector plots overlaid on top of human non-myopic specimen N3.....	079
3.02 – Distance measurements between the optic nerve and inferior oblique muscle.....	081
3.03 – Polar vector plot map of human non-myopic specimen N4.....	083
3.04 – Anisotropic proportion contour map of human non-myopic specimen N4 .....	084
3.05 – Polar vector plot map of human highly myopic specimen HM1 .....	086
3.06 – Anisotropic proportion contour map of human highly myopic specimen HM1 .....	087
3.07 – Polar vector plot map of human highly myopic specimen HM2 .....	089
3.08 – Anisotropic proportion contour map of human highly myopic specimen HM2 .....	090
3.09 – Polar plot and anisotropic proportion map of human highly myopic specimen HM3 .....	092
3.10 – Mean collagen anisotropic proportion in human peripapillary sclera by quadrant .....	094
3.11 – Heat map of human peripapillary scleral collagen fibril displacement angles.....	095
3.12 – Mean collagen fibril displacement angle in human peripapillary sclera by quadrant.....	096
3.13 – Bar charts of mean collagen anisotropic proportion and fibril displacement angles .....	097
4.01 – Wide-angle X-ray scattering maps of a laboratory mouse posterior sclera .....	107
4.02 – Wide-angle X-ray scattering maps of a northern tree shrew posterior sclera .....	109
4.03 – Wide-angle X-ray scattering maps of a guinea pig posterior sclera .....	111
4.04 – Wide-angle X-ray scattering maps of a black lion tamarin posterior sclera .....	113
4.05 – Wide-angle X-ray scattering maps of an Azara’s agouti posterior sclera.....	115
4.06 – Wide-angle X-ray scattering maps of a lesser mouse-deer posterior sclera .....	117
4.07 – Wide-angle X-ray scattering maps of a red panda posterior sclera.....	119
4.08 – Wide-angle X-ray scattering maps of a North American river otter posterior sclera .....	121
4.09 – Wide-angle X-ray scattering maps of a domestic pig posterior sclera.....	123
4.10 – Wide-angle X-ray scattering maps of a Brazilian tapir posterior sclera .....	125
4.11 – Wide-angle X-ray scattering maps of domestic cattle posterior sclera B1 .....	127
4.12 – Wide-angle X-ray scattering maps of domestic cattle posterior sclera B2 .....	128

4.13 – Scaled mammalian posterior sclerae polar vector plot maps .....	131
4.14 – Scaled mammalian posterior sclerae anisotropic proportion contour maps.....	132
4.15 – Human and domestic cattle polar vector plot maps .....	133
4.16 – Second harmonic generation of inner, middle and outer bovine peripapillary sclera.....	137
4.17 – Depth-dependent collagen fibre orientation in a left bovine peripapillary sclera .....	139
4.18 – Depth-dependent collagen fibre orientation in a right bovine peripapillary sclera.....	140
4.19 – Image analysis software outputs overlaid on top of scleral collagen fibres.....	142
4.20 – Heat map of bovine peripapillary sclera sectional displacement angles .....	143
4.20 – Heat map of bovine peripapillary sclera sectional displacement angles .....	144
5.01 – Bovine scleral fibroblast area 1h, 6h and 24h after cyclic tensile strain.....	151
5.02 – Bovine scleral fibroblast length 1h, 6h and 24h after cyclic tensile strain.....	152
5.03 – Bovine scleral fibroblast eccentricity 1h, 6h and 24h after cyclic tensile strain .....	153
5.04 – F-actin stress fibres in bovine scleral fibroblasts 1h after cyclic tensile strain .....	156
5.05 – F-actin stress fibres in bovine scleral fibroblasts 6h after cyclic tensile strain .....	157
5.06 – F-actin stress fibres in bovine scleral fibroblasts 24h after cyclic tensile strain .....	158
5.07 – F-actin stress fibre anisotropy 1h, 6h and 24h after cyclic tensile strain .....	160
5.08 – F-actin stress fibre coherency 1h, 6h and 24h after cyclic tensile strain.....	161
5.09 – Vimentin filaments in bovine scleral fibroblasts 1h after cyclic tensile strain .....	164
5.10 – Vimentin filaments in bovine scleral fibroblasts 6h after cyclic tensile strain .....	165
5.11 – Vimentin filaments in bovine scleral fibroblasts 24h after cyclic tensile strain .....	166
5.12 – Vimentin filament anisotropy 1h, 6h and 24h after cyclic tensile strain.....	167
5.13 – Vimentin filament coherency 1h, 6h and 24h after cyclic tensile strain .....	168
5.14 – $\beta$ -tubulin microtubules in bovine scleral fibroblasts 1h after cyclic tensile strain.....	171
5.15 – $\beta$ -tubulin microtubules in bovine scleral fibroblasts 6h after cyclic tensile strain.....	172
5.16 – $\beta$ -tubulin microtubules in bovine scleral fibroblasts 24h after cyclic tensile strain.....	173
5.17 – $\beta$ -tubulin microtubule anisotropy 1h, 6h and 24h after cyclic tensile strain .....	174
5.18 – $\beta$ -tubulin microtubule coherency 1h, 6h and 24h after cyclic tensile strain .....	175
5.19 – Nuclei in bovine scleral fibroblasts 1h after cyclic tensile strain.....	177
5.20 – Nuclei in bovine scleral fibroblasts 6h after cyclic tensile strain.....	178
5.21 – Nuclei in bovine scleral fibroblasts 24h after cyclic tensile strain.....	179
5.22 – Nuclear area 1h, 6h and 24h after cyclic tensile strain.....	180

5.23 – Nuclear roundness 1h, 6h and 24h after cyclic tensile strain .....	181
5.24 – Chromatin condensation parameter 1h, 6h and 24h after cyclic tensile strain.....	182
5.25 – Proposed scleral fibroblast performance as a function of applied strain.....	185
6.01 – Bovine eye globe topology reconstruction.....	194
6.02 – Surface triangulation of a bovine eye globe.....	195
6.03 – Regional variation of bovine eye tunic thickness.....	196
6.04 – Transversal section of the bovine eye globe reconstruction .....	197
6.05 – Cellular component-specific 3D reconstruction.....	200
6.06 – Workflow for generation of cellular component-specific 3D reconstructions.....	201
6.07 – Imaris reconstruction of a bovine scleral fibroblast $\beta$ -tubulin cytoskeleton .....	203
6.08 – Input signal and 3D reconstruction of intracellular structures in Imaris.....	204
6.09 – FilamentTracer 3D reconstructed human peripapillary scleral collagen fibres .....	205
6.10 – FilamentTracer 3D reconstructed F-actin stress fibre .....	207
6.11 – Cellular component initial triangular surfaces .....	209
6.12 – Cellular component quadratically decimated triangular surfaces .....	210
6.13 – Cellular component uniform triangular surfaces.....	212
6.14 – Surface repair of a 3D reconstructed F-actin stress fibre .....	213
6.15 – Combined visualisation of 3D reconstructed cellular components .....	214
6.16 – Cellular component smoothed triangular surfaces .....	216
6.17 – Volume rendering of triangular geometry of an F-actin stress fibre.....	217
6.18 – Gamma value plot before and after volume construction .....	218
6.19 – Cellular component 3D reconstruction with respect to applied cyclic tensile strain .....	220
6.20 – Percentage change of number of vertices and elements of complex geometries .....	223
6.21 – Percentage change of number of vertices and elements of simple geometries .....	224
6.22 – Percentage change of area and volume of complex geometries.....	225
6.23 – Percentage change of area and volume of simple geometries.....	226
6.24 – Gamma values of complex and simple geometries .....	230
6.25 – Imaris and ImageJ triangular surfaces of nuclei and F-actin stress fibres .....	232

A.01 – Polar vector plot map of human non-myopic specimen N1 .....	A02
A.02 – Anisotropic proportion contour map of human non-myopic specimen N1.....	A03
A.03 – Polar vector plot map of human non-myopic specimen N2.....	A04
A.04 – Anisotropic proportion contour map of human non-myopic specimen N2.....	A05
A.05 – Polar vector plot map of human non-myopic specimen N3.....	A06
A.06 – Anisotropic proportion contour map of human non-myopic specimen N3.....	A07
A.07 – Polar vector plot map of human non-myopic specimen N5.....	A08
A.08 – Anisotropic proportion contour map of human non-myopic specimen N5.....	A09
A.09 – Polar vector plot map of human non-myopic specimen N6.....	A10
A.10 – Anisotropic proportion contour map of human non-myopic specimen N6.....	A11
A.11 – Polar vector plot map of human non-myopic specimen N7.....	A12
A.12 – Anisotropic proportion contour map of human non-myopic specimen N7.....	A13
A.13 – Wide-angle X-ray scattering maps of domestic cattle posterior sclera B3 .....	A14
A.14 – Wide-angle X-ray scattering maps of domestic cattle posterior sclera B4 .....	A15
A.15 – F-actin stress fibre alignment 1h, 6h and 24h after cyclic tensile strain .....	A16
A.16 – Vimentin filament alignment 1h, 6h and 24h after cyclic tensile strain.....	A17
A.17 – $\beta$ -tubulin microtubule alignment 1h, 6h and 24h after cyclic tensile strain.....	A17
A.18 – F-actin stress fibre circular variance 1h, 6h and 24h after cyclic tensile strain.....	A18
A.19 – Vimentin filament circular variance 1h, 6h and 24h after cyclic tensile strain.....	A19
A.20 – $\beta$ -tubulin microtubule circular variance 1h, 6h and 24h after cyclic tensile strain .....	A19
A.21 – F-actin stress fibre angular deviation 1h, 6h and 24h after cyclic tensile strain .....	A20
A.22 – Vimentin filament angular deviation 1h, 6h and 24h after cyclic tensile strain.....	A21
A.23 – $\beta$ -tubulin microtubule angular deviation 1h, 6h and 24h after cyclic tensile strain .....	A21
A.24 – Poster for Speaking of Science 2018 (Cardiff, UK) .....	A23
A.25 – Poster for ARVO Annual Meeting 2019 (Vancouver, Canada) .....	A23

## List of Tables

2.1 – Specimen details of the utilised human eyes.....	042
2.2 – Specimen details of the utilised mammalian eyes.....	044
2.3 – Number of recorded bovine scleral fibroblasts and confocal Z-stacks .....	071
3.1 – Total collagen scatter in human peripapillary sclerae per quadrant .....	080
3.2 – Alterations in highly myopic posterior sclerae in comparison to normal sclerae .....	101
5.1 – Alterations in bovine scleral fibroblast shape after cyclic tensile strain .....	189
5.2 – Rearrangement of bovine scleral fibroblast cytoskeleton after cyclic tensile strain .....	189
5.3 – Alterations in bovine scleral fibroblast nuclei after cyclic tensile strain .....	190
6.1 – Mean element aspect ratio at different simplification stages .....	227
6.2 – Worse element aspect ratio at different simplification stages.....	228
6.3 – Percentages of element aspect ratio greater than 10 at different simplification stages .....	228
6.4 – Suggestions for possible procedural step software alternatives .....	237
6.5– Surface triangulation of complex geometries at different simplification steps.....	238
6.6 – Surface triangulation of simple geometries at different simplification steps.....	239
6.7 – Volume mesh simple geometries at different simplification steps .....	239

## List of Abbreviations

ADP	–	Adenosine diphosphate
ANOVA	–	Analysis of variance
AR	–	Aspect ratio
ARVO	–	Association for Research in Vision and Ophthalmology
ATP	–	Adenosine triphosphate
CAD	–	Computer-aided design
CCP	–	Chromatin condensation parameter
CSFP	–	Cerebrospinal fluid pressure
CITER	–	Cardiff Institute for Tissue Engineering and Repair
CT	–	Curvelet transform
CTS	–	Cyclic tensile strain
CZI	–	Zeiss file format
DAPI	–	4',6-diamidino-2-phenylindole
DIC	–	Digital image correlation
DLS	–	Diamond Light Source
DMEM	–	Dulbecco's modified Eagle's medium
ECM	–	Extracellular matrix
EDTA	–	Ethylenediaminetetraacetic acid
ELISA	–	Enzyme-linked immunosorbent assay
FCS	–	Foetal calf serum
FE	–	Finite element
FFT	–	Fast Fourier transform
FIRE	–	Fibre extraction
FITC	–	Fluorescein isothiocyanate
GAG	–	Glycosaminoglycan
GDP	–	Guanosine diphosphate
GLY	–	Glycine
GTP	–	Guanosine triphosphate
HBSS	–	Hank's balanced salt solution

HYP	–	Hydroxyproline
I	–	Inferior
I <sub>a</sub>	–	Anisotropic scatter
I <sub>i</sub>	–	Isotropic scatter
IN	–	Inferior nasal
INP	–	ABAQUS input file format
IOP	–	Intraocular pressure
IT	–	Inferior temporal
LC	–	Lamina cribrosa
LSM	–	Laser scanning microscope
LUT	–	Look-up-table
MTOC	–	Microtubule organising centre
N	–	Nasal
OBJ	–	Wavefront object geometry file format
ONH	–	Optic nerve head
ONH-IO	–	Optic nerve head to inferior oblique muscle distance
P+SID	–	Periodic plus smooth image decomposition
PBS	–	Phosphate buffered saline
PDB	–	Protein data bank
PFA	–	Paraformaldehyde
PG	–	Proteoglycan
POAG	–	Primary open-angle glaucoma
PPS	–	Peripapillary sclera
PRO	–	Proline
QECD	–	Quadric edge collapse decimation
qPCR	–	Real-time polymerase chain reaction
RGC	–	Retinal ganglion cell
ROCK	–	Rho-associated kinase
ROI	–	Region of interest
RVE	–	Representative volume element
S	–	Superior

SAXS	–	Small-angle X-ray scattering
SD	–	Standard deviation
SHG	–	Second harmonic generation
SN	–	Superior nasal
ST	–	Superior temporal
STL	–	Stereolithography file format
T	–	Temporal
TIF	–	Tagged image file
TGF $\beta$ 1	–	Transforming growth factor $\beta$ 1
TPEF	–	Two-photon-excited fluorescence
TUNEL	–	Terminal deoxynucleotidyl transferase-mediated dUTP nick end labelling
WAXS	–	Wide-angle X-ray scattering
WRL/VRML2	–	Virtual reality modelling language 2 file format

# **Chapter I**

## **General introduction**

Vision is the primary sense through which humans receive information on their surrounding world. Given that it is often thought as the most important out of all senses, losing the ability to see, by becoming blind or visually impaired, is considered amongst the most terrible losses that can beset a person. However, the trauma is not the only consequence – the quality of life for these people decreases concomitant with an increasingly large socio-economic burden worldwide. More than 217 million people live with a moderate or severe form of visual impairment, of which 36 million are blind, with the number affected constantly increasing (Holden et al., 2016; Bourne et al., 2017). All these factors make it imperative to both continue studying and searching for new treatments for vision disorders. Moreover, it is vital to comprehend both the cellular and extracellular contributions to the mechanisms of ocular pathologies.

### 1.1 Structure of the eye

#### 1.1.1 Eye globe

Vision is facilitated by the visual sensory system, with the main organ of perception being the eye. The human eye globe is approximately spherical (Figure 1.01), with a diameter of around 24mm, and consists of three tunic layers, the names of which reflect their location. *Tunica externa* is the outer layer, composed of the cornea and the sclera, sometimes referred to as corneosclera, whilst the limbus is the border that separates the two structures. The external tunic contains and protects the inner components of the eye globe. The middle layer of the eye is *tunica media*, which includes the choroid, ciliary body and the iris. The final layer is the internal one, the *tunica interna* – the retina.

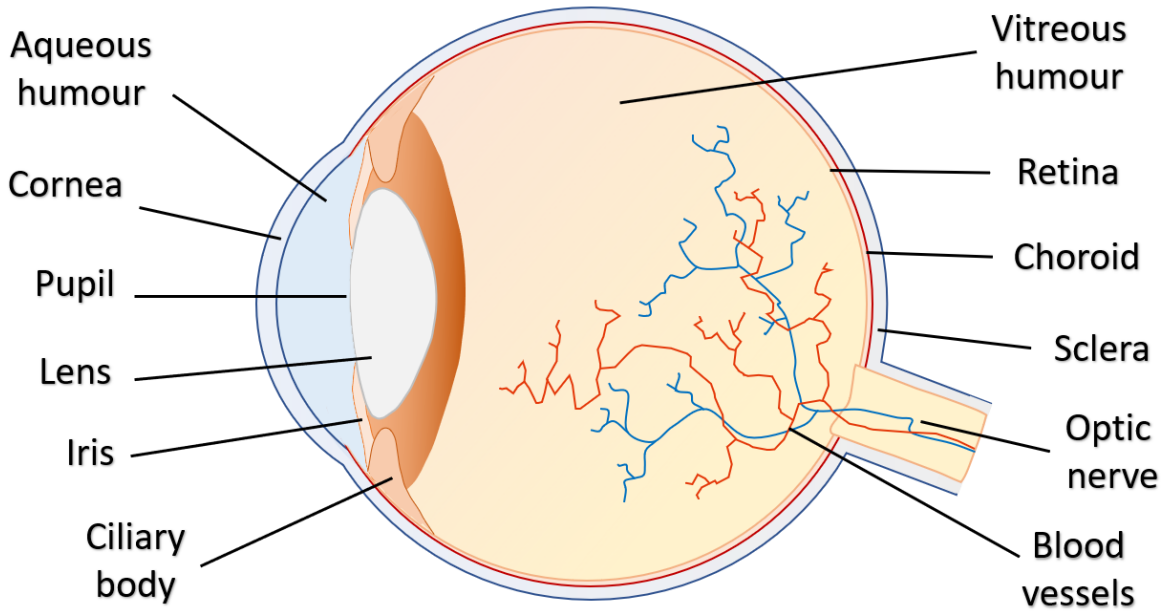


Figure 1.01 – Sagittal section of a human eye with indicated components.

When quanta of light, photons, hit the outer surface of the cornea they pass through the pupil. The lens contributes to refracting and concentrating the light on the back of the eye where the photoreceptive cells of the retina are situated. The resulting stimulus is converted into electrical impulses and then forwarded by the optic nerve, *Nervus opticus*, to the visual cortex of the brain. To accomplish this function correctly, the eye must have a precise and constant shape, which is supported by the corneoscleral tunic and the fluid pressure internally exerted on it – the intraocular pressure (IOP).

### 1.1.2 Sclera

Commonly referred to as the white of the eye, the sclera is the main load-bearing tissue of the ocular globe and comprises about 85% of the outer corneoscleral tunic in humans. It consists predominantly of densely woven fibres of the protein collagen, which give the sclera its opacity and mechanical rigidity and which, in turn, support maintaining the eye's structural integrity and shape (Watson and Young, 2004). The name stems from the Greek word for 'hard', *skleros*, indicating a key role in mechanical stability. The tissue's opacity also participates in visual perception by preventing scattered light from interfering with image registration on the retina (Boote et al., 2019).

The sclera consists of three layers, the first of which is the *episclera*, composed of loose vascularised connective tissue, which serves as a connection between the sclera and the overlying Tenon's capsule (*Fascia bulbi*). The capsule is a thin membrane of compact collagen fibres that envelops the eye globe from the limbus and continues into the sheaths of the extraocular muscles and the optic nerve. Between the capsule and the sclera is the episcleral space, which allows the eye to move freely, similarly to a ball-and-socket joint. The *episclera* merges with the scleral stroma, *substantia propria sclerae*, which forms the major tissue layer and is composed of interwoven collagen-rich lamellae (Boote et al., 2019). The deepest layer of the sclera is the *lamina fusca* and is contiguous with the *tunica media*.

The width of the sclera itself varies between regions (Vurgese et al., 2012). At the limbus border the scleral thickness is about 0.5mm, which declines to 0.4mm behind the equator of the eye. Afterwards, in the direction of the posterior pole, the sclera widens and reaches 1.0-1.3mm, whilst the *lamina cribrosa* (LC; Section 1.1.4) is the thinnest region with great variability due to its porous nature (Watson and Young, 2004). Even though there is a regional difference in the structure, the sclera remains largely stable during processes that induce mechanical loading on the eye globe, such as eye rotation and movement, ensuring that vision remains unperturbed (McBrien et al., 2009).

### 1.1.3 Optic nerve head

The LC and the surrounding peripapillary sclera (PPS) collectively form the connective tissue aspect of the optic disk, or optic nerve head (ONH), where the optic nerve enters the sclera (Figure 1.02) (Downs et al., 2008). The nutrition and innervation are provided by small arteries and nerves that traverse to the anterior portion of the ONH, whilst supportive function is provided by several cell populations, such as astrocytes, glial and endothelial cells (Hayreh, 2001; Burgoyne and Downs, 2008). The PPS is a particularly important load-bearing region of the sclera, where non-linear IOP increase deformations, governed by the collagen meshwork, are transmitted to the rest of the ONH (Girard et al., 2009a; Pijanka et al., 2012). As the microarchitecture of the LC makes it particularly susceptible to external forces, this area is of key mechanical interest,

exemplifying a discontinuity, or ‘weak spot’, in the eye tunic (Strouthidis and Girard, 2013; Kim et al., 2018; Ling et al., 2019).

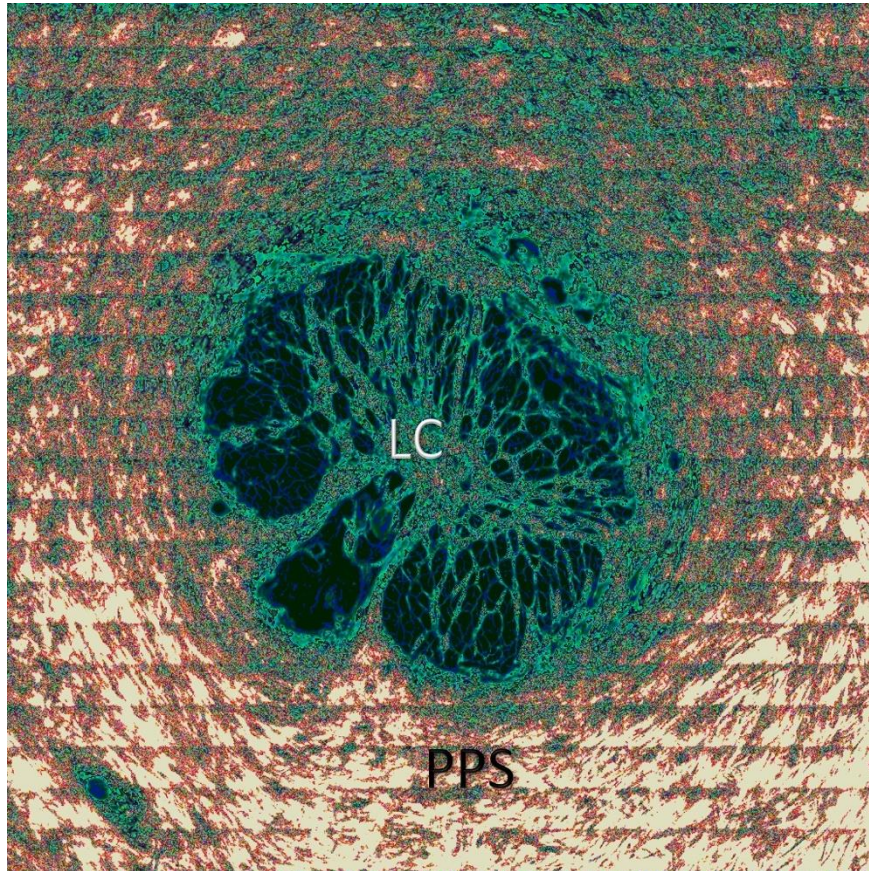


Figure 1.02 – Second harmonic generation (SHG) image of an intermediate depth section of a bovine optic nerve head (ONH), with indicated peripapillary sclera (PPS) and fenestrated *lamina cribrosa* (LC). ‘3-3-2 RGB’ look-up-table (LUT) selected in ImageJ for enhanced tissue contrast.

#### 1.1.4 Lamina cribrosa

The term *lamina cribrosa* is derived from the Latin *lamina*, meaning ‘thin plate’, whilst *cribrosa* comes from *cribrum*, ‘sieve’, indicative of its fenestrations. Composed of tightly packed collagen and elastin fibres, the LC mechanically supports and permits the passing of the optic nerve axons through it (Strouthidis and Girard, 2013). The LC can be divided into three regions: (I) the prelamina adjacent to the retina; (II) the proper lamina, composed of interconnected laminar beams; (III) and the postlamina, where the collagen and elastin fibres no longer horizontally

circumscribe the optic nerve axons but are rather vertically parallel to them. It is around this region that the axons of the optic nerve become myelinated as well. With ageing the LC becomes stiffer and more prone to permanent deformations, thus making it more vulnerable to IOP-driven glaucomatous damage (Section 1.4). This is of great importance given that glaucoma is the second leading cause of blindness worldwide (Albon et al., 2000; Campbell et al., 2014; Tun et al., 2019).

### 1.1.5 Collagen extracellular matrix

Similar to most connective tissues, the sclera is composed of an extracellular matrix (ECM), which facilitates the embedding of cells within the tissue environments (Rada et al., 2000b). The macromolecule components are secreted by a rather diffuse population of fibroblasts and include proteoglycans (PG), glycosaminoglycans (GAG), elastin and interwoven lamellae of collagen. Elastin is a highly elastic fibrous protein that is secreted in response to stretching, contributing to about 2% of the scleral dry weight (Watson and Young, 2004). Sulphated GAGs are negatively charged polysaccharides, due to the presence of a sulphate group on most of their sugars. As a result of osmosis, a large amount of water is imbibed into the ECM, resulting in a porous hydrated gel which helps withstand compressive forces. PGs are heavily glycosylated proteins containing up to hundreds of GAG chains, with the most common scleral PGs being decorin, biglycan and aggrecan, found throughout the full thickness of the tissue and contributing to 0.7-0.9% of its dry weight (Johnson et al., 2006; Summers Rada et al., 2006). They function in maintaining collagen orientation and spacing between the fibrils through their GAG chains, which in turn permits the transparent properties of the cornea (Lewis et al., 2010).

In vertebrates the primary load-bearing and most abundant macromolecule is the protein collagen, which in mammals can make up to 25% of their total body protein mass (Prockop and Kivirikko, 1995). In the human sclera, about 93% of the dry weight is due to collagen, which in its hydrated state, provides the sclera's white colouring and opaqueness (Boote et al., 2019). Collagen is a fibrous protein consisting of three polypeptide chains, referred to as  $\alpha$ -chains, that intertwine to form a long regular triple helix – tropocollagen (Figure 1.03A and B). The molecules are non-centrosymmetric and exhibit a complex structural hierarchy which permits their study with non-linear microscopy (Figure 1.03C; Section 1.6.2).

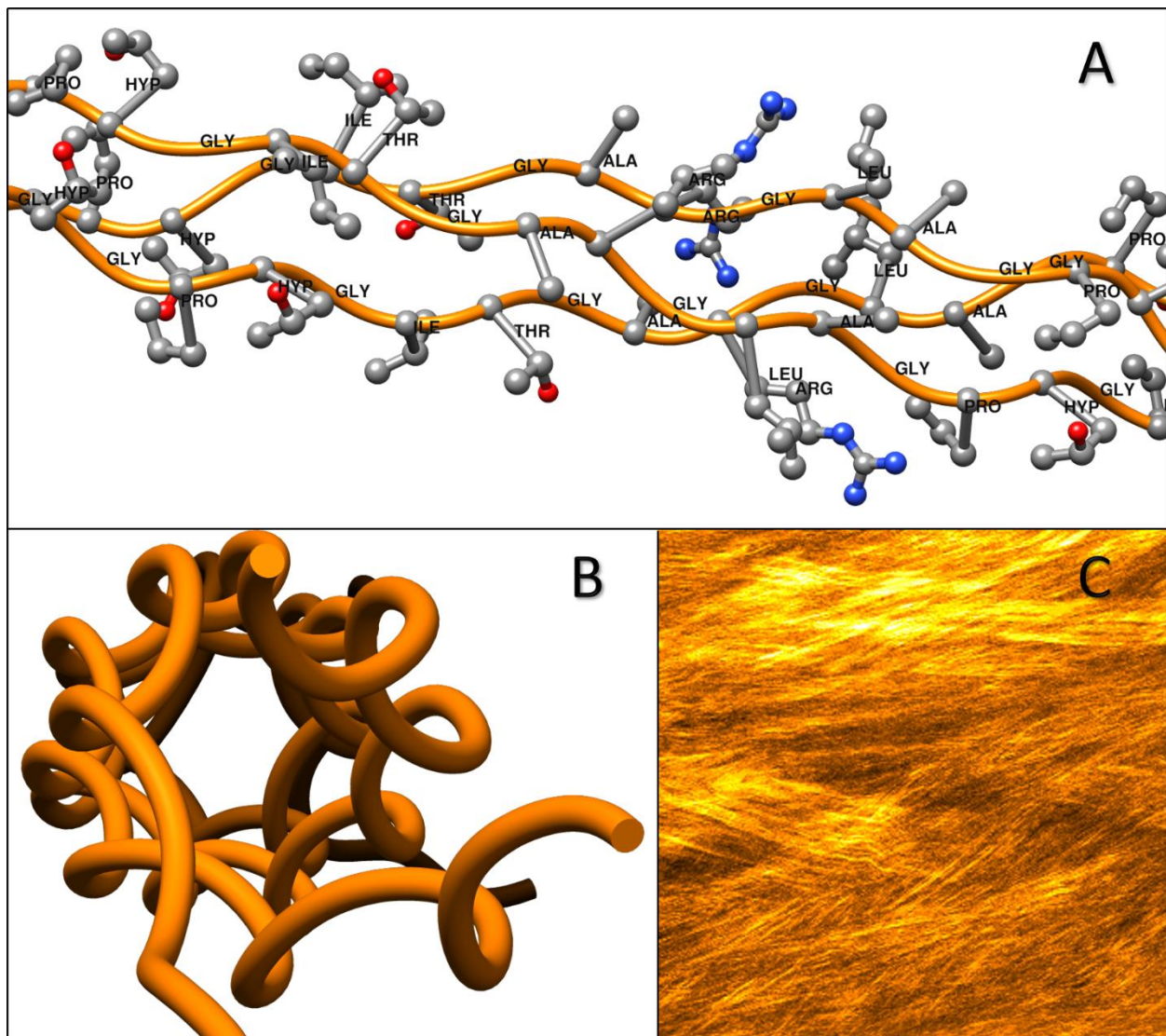


Figure 1.03 – Collagen molecule organisation. (A) Side view of a tropocollagen triple helix (orange) with amino acid R-groups indicated as ‘ball and stick’ models. Oxygen (red) and nitrogen (blue) atoms and methylene groups (grey) of the R-groups are visualised. Collagen triple helix protein data bank (PDB) file 1BKV visualised in Chimera (Kramer et al., 1999; Pettersen et al., 2004); (B) Cross-section view of the tropocollagen molecule in A without the sidechains. Each  $\alpha$ -chain is twisted in a left-handed helix, with three of them wrapped around in a right-handed spiral; (C) SHG image of interwoven collagen fibres from a bovine PPS.

A defining characteristic of the  $\alpha$ -chain is the GLY-PRO/HYP-X repeats, where GLY is the amino acid glycine, PRO is proline, HYP is hydroxyproline and X is one of the remaining 18 proteinogenic amino acids (Shoulders and Raines, 2009). GLY has the smallest functional (R) group out of any amino acid, which is a singular hydrogen atom. As every third amino acid is GLY this permits the  $\alpha$ -chains to turn and be packed closely together, thus forming the final collagen superhelix. The PRO side chain forms a ring, taking part in the stabilisation of the helical

conformation in each  $\alpha$ -chain. The HYP form hydrogen bonds between individual chains, providing structural integrity for the triple helix.

The tropocollagen molecules pack closely in parallel, thus forming collagen microfibrils (Figure 1.04). Each microfibril has a diameter of around 4nm, with adjacent tropocollagens displaced by 66.8nm, referred to as the collagen D period (Piez and Miller, 1974). In turn, the collagen microfibrils assemble into higher-order polymers, collagen fibrils, which have a wide range of diameters, from 25 to 230nm (Komai and Ushiki, 1991). In length, they span many hundreds of  $\mu\text{m}$  in mature tissue and are clearly visible under electron micrographs (Shoulders and Raines, 2009). The repeats of the collagens give a striped appearance of the fibrils, which provide the tensile strength of the sclera (Buehler, 2006). Whilst the cornea is composed of highly spatially aligned fibrils, in the majority of the sclera they are much more isotropically distributed, with a major exclusion being the PPS. Collagen fibrils often aggregate into larger, cable-like bundles, that are visible under a light microscope – collagen fibres. In the *episclera*, the collagen fibres form a rather thin tissue layer, whilst in the deeper regions, the fibre thickness increases becoming lamellae, which merge with the stromal collagen (Geroski and Edelhauser, 2001; Watson and Young, 2004; Boote et al., 2019).

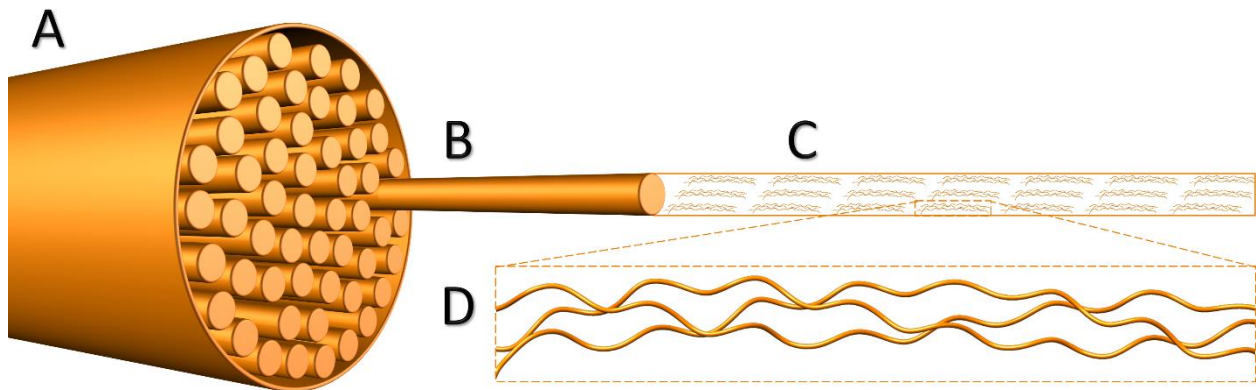


Figure 1.04 – Collagen structural hierarchy. (A) Collagen fibril; (B) Microfibril; (C) Tropocollagen molecules; (D) Tropocollagen  $\alpha$ -chains. Collagen triple helix PDB file 1BKV visualised in Chimera (Kramer et al., 1999; Pettersen et al., 2004).

In accordance with Ricard-Blum's systematisation, 28 different types of collagen and 46 types of  $\alpha$ -chains have been identified in humans (Ricard-Blum, 2011). The collagen composition of the sclera is predominately made from type I collagen (around 95%) and to a much lesser extent from

type III, V and VI (less than 5%) (Watson and Young, 2004; Boote et al., 2019). The LC, however, contains less type I collagen than either the sclera or cornea (Grytz et al., 2011). No significant differences have been reported in the collagen content in the sclera in adults and juveniles or between the anterior and posterior scleral regions. However, with age, there is an increase in the extent of glycosylation, as well as reduction of the number of elastin fibres and PG content, apart from aggrecan which remains relatively constant (Keeley et al., 1984; Rada et al., 2000a; Watson and Young, 2004).

## 1.2 Scleral cells

### 1.2.1 Fibroblasts

Connective tissue cells have a mesenchymal origin and include fibroblasts, chondrocytes, and osteocytes, all of which secrete the collagenous ECM that forms the architectural framework of the body. As with other cells, resident scleral fibroblasts (Figure 1.05) are constantly subjected to external forces, most notably the exerted pressure of the intraocular fluids (Tan et al., 2006). Research into application of mechanical loading to cultured scleral fibroblasts revealed alterations in division, programmed cell death and gene expression (Cui et al., 2004; Qiu et al., 2018). One notable finding was the tendency for trans-differentiation into a myofibroblastic phenotype (Qu et al., 2015). As fibroblasts have a key role of both synthesising and remodelling the ECM, they can have a profound effect on tissue architecture, relevant to ocular diseases involving biomechanical perturbations (Summers Rada et al., 2006; McBrien et al., 2009). Cellular impact on tissue level biomechanics can be accomplished either via the reorganisation of the ECM or in dynamic mechanotransduction processes, through which mechanical stimuli are transmitted to and from the cell through cytoskeletal fibre networks, regulated by associated signalling molecules (McBrien, 2013; Boote et al., 2019; Markov et al., 2019).



Figure 1.05 – Light microscopy photograph of a primary bovine scleral fibroblast cultured on a plastic plate.

#### 1.2.1.1 Myofibroblasts

The diffusely spread fibroblasts in the sclera also participate in tissue wound healing. They start to divide and migrate towards the injury, where they produce copious amounts of collagen fibrils, to fill in the gap left by the wound and to isolate and repair the damaged site. The resulting mechanical stress leads to some fibroblasts gaining contractile characteristics, similarly to those of smooth muscle cells (Tomasek et al., 2002). This subtype, the myofibroblast, participates in the wound healing process by contracting the edges of the wound. The progression into myofibroblasts can also be stimulated *in vitro* by the application of high frequency and magnitude strains, along with the presence of transforming growth factor  $\beta 1$  (TGF $\beta 1$ ) which is involved in the regulation of type I collagen and  $\alpha$ -smooth muscle actin transcription (Tomasek et al., 2002; Qu et al., 2015; Pitha et al., 2018). This actin subtype associates with non-muscle myosin and together play a role in the cell contractile capabilities which involve the remodelling and reinforcement of the surrounding

ECM (Tomasek et al., 2002; Hinz et al., 2003; Hinz et al., 2007). Several studies suggest that there is an age-dependent increase in the proportion of myofibroblasts and that they can be distributed across as much as 20% of the scleral thickness (Poukens et al., 1998; McBrien et al., 2009). These cells are in sparse numbers during the initial stages of ontogenesis when the eye is growing rapidly and become more commonly found after reaching its full size. It should be noted that there is a constant population of scleral myofibroblasts in non-pathological eyes, which is uncommon in most tissues (McBrien et al., 2009).

### 1.2.2 Cytoskeleton

Whilst fibroblasts are hypothesised to actively participate in scleral biomechanics, limited information has been reported on how the macroscopic stress and strain are transmitted in the cytoskeletal network. The cytoskeleton is a complex system of protein filaments that serves a plethora of roles, from participating in intracellular vesicle transport to pulling apart the chromosomes during mitosis. In terms of cellular mechanics, the cytoskeleton has a central role in keeping the cells correctly structured, supporting the plasma membrane and providing the mechanical linkages that enable the cell to bear environmental perturbations (Fletcher and Mullins, 2010). This is accomplished through three types of cytoskeletal filaments (Figure 1.06) which are organised in the form of a complex network within the cell cytoplasm: (I) the actin microfilaments determine cellular shape, participate in movements and are distributed throughout the cell volume, most notably as cortical actin around the edges underneath the plasma membrane; (II) the intermediate filaments provide the mechanical strength by acting as scaffolding around the nucleus; (III) the microtubules participate in intracellular transport and organelle positioning, spread throughout the cell (Tan et al., 2006; Barreto et al., 2014).

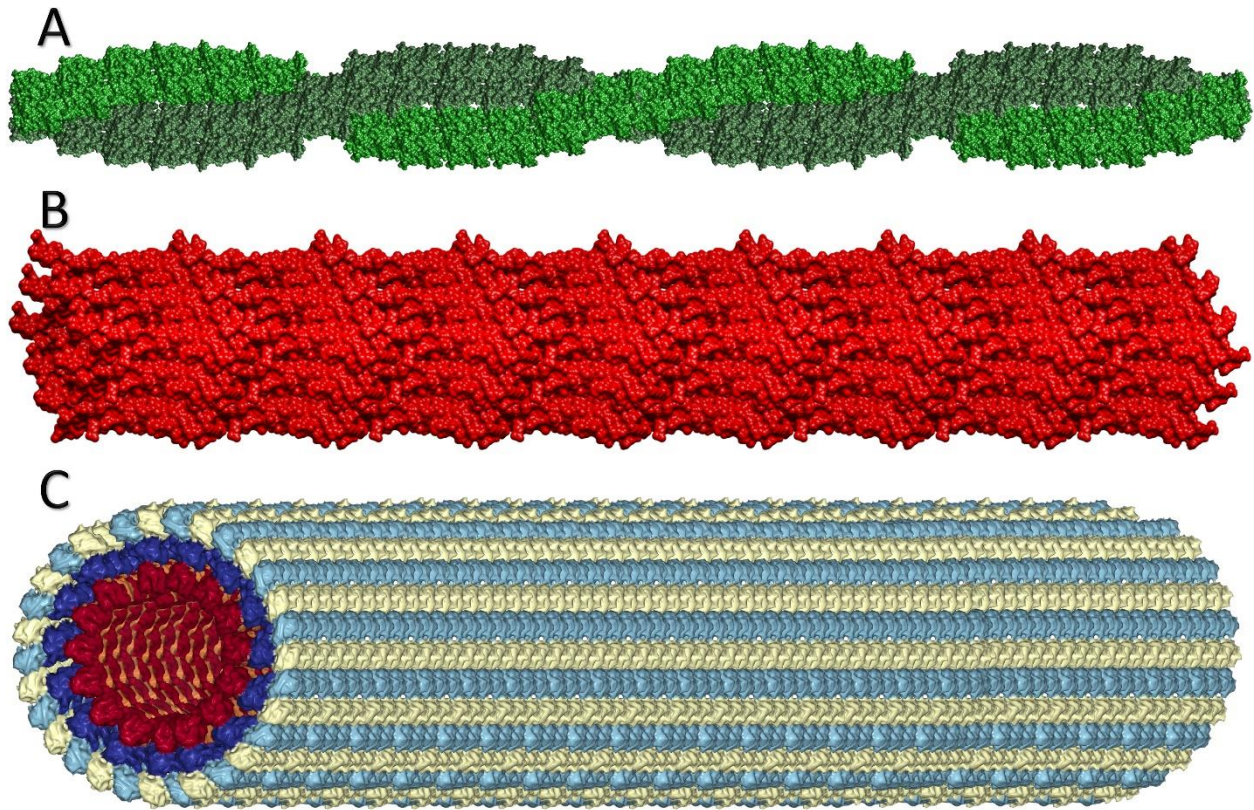


Figure 1.06 – Primary components of the cytoskeleton. (A) F-Actin microfilaments. G-actin PDB file 1J6Z visualised in Chimera (Otterbein et al., 2001; Pettersen et al., 2004); (B) Vimentin intermediate filaments. Vimentin coil PDB file 3SSU visualised in Chimera (Chernyatina et al., 2012); (C) Tubulin microtubules. Microtubule PDB file visualised in NGL viewer (Asenjo et al., 2013; Rose et al., 2018).

The cytoskeleton persists in a state of dynamic equilibrium with constant polymerisation and depolymerisation of the interconnected filamentous proteins (Fletcher and Mullins, 2010). This feature permits the cytoskeletal stiffness regulation and connectivity to the ECM through a range of accessory molecules. Fibroblast mechanosensitivity is accomplished by all three principal cytoskeletal elements, mediating external forces and communication with other cells and the ECM. Whilst microtubules are the largest components, they mainly govern intracellular compression, with tension being regulated through the intermediate filaments and notably the actin stress fibres (Alenghat and Ingber, 2002; Deguchi et al., 2006). Although the effect of mechanical loading on cellular structures has been widely reported, considerably less is known about how the same loads affect the proteins that organise the network of cytoskeletal filaments (Malone et al., 2007; Jackson et al., 2008). Therefore, an improved understanding of how the cytoskeletal components respond to mechanical loading in the eye could yield valuable insight into the mechanisms used by scleral

cells to adapt to their environment, specifically in pathological conditions such as glaucoma (Chapter V).

### 1.2.3 Actin microfilaments

The microfilaments (Figure 1.06A) are the smallest of the cytoskeletal components, with a diameter of 6-7nm (Fuchs and Cleveland, 1998). Actin exists as monomeric globular actin (G-actin) which provides subunits for filamentous actin (F-actin) assembly via a hydrolysis reaction. The subunits are bound either to adenosine triphosphate (ATP) or adenosine diphosphate (ADP) which is produced by the release of a free phosphate and energy. F-actin assembly is an active ‘treadmilling’ process, in which to one end of the filament, designated as positive (barbed end), ATP bound subunits are added, whilst from the negative end (pointed end) ADP-subunits are released (Figure 1.07A). The result is ‘movement’ of the filament as it is being constantly reconstructed (Pollard and Cooper, 2009; Stricker et al., 2010; Tojkander et al., 2012). The numerous functions of the actin microfilament cytoskeleton are dependent on its ability to undergo this rapid remodelling and reorganisation. This behaviour is governed by the action of various actin-binding proteins such as cofilin and  $\alpha$ -actinin, vinculin and talin at the focal adhesions (Alenghat and Ingber, 2002; Jackson et al., 2008). Mechanical loading has been noted to lead to both remodelling of the actin microfilaments, as well as alteration of those dynamics in bovine articular chondrocytes (Campbell et al., 2007). For example, in mouse osteoblasts after 2h of exposure to 2Pa of fluid shear, there was a significant increase in the amount of  $\alpha$ -actinin and filamin that was available to interact with and reorganise the cytoskeleton (Jackson et al., 2008). It is possible that the cells had upregulated the synthesis of these actin-binding proteins in response to the loading to account for the observed increase in the cytoskeletal fraction. Gene expression of actin-binding proteins was also shown to be mechanosensitive in bovine intervertebral disc cells (Li et al., 2011). In addition,  $\alpha$ -smooth muscle actin has been suggested to be involved in the contractile action of tree shrew myofibroblasts in regulating ocular globe axial lengthening (Phillips and McBrien, 2004). Actin microfilaments also regularly bind with myosin proteins to form highly contractile stress fibres.

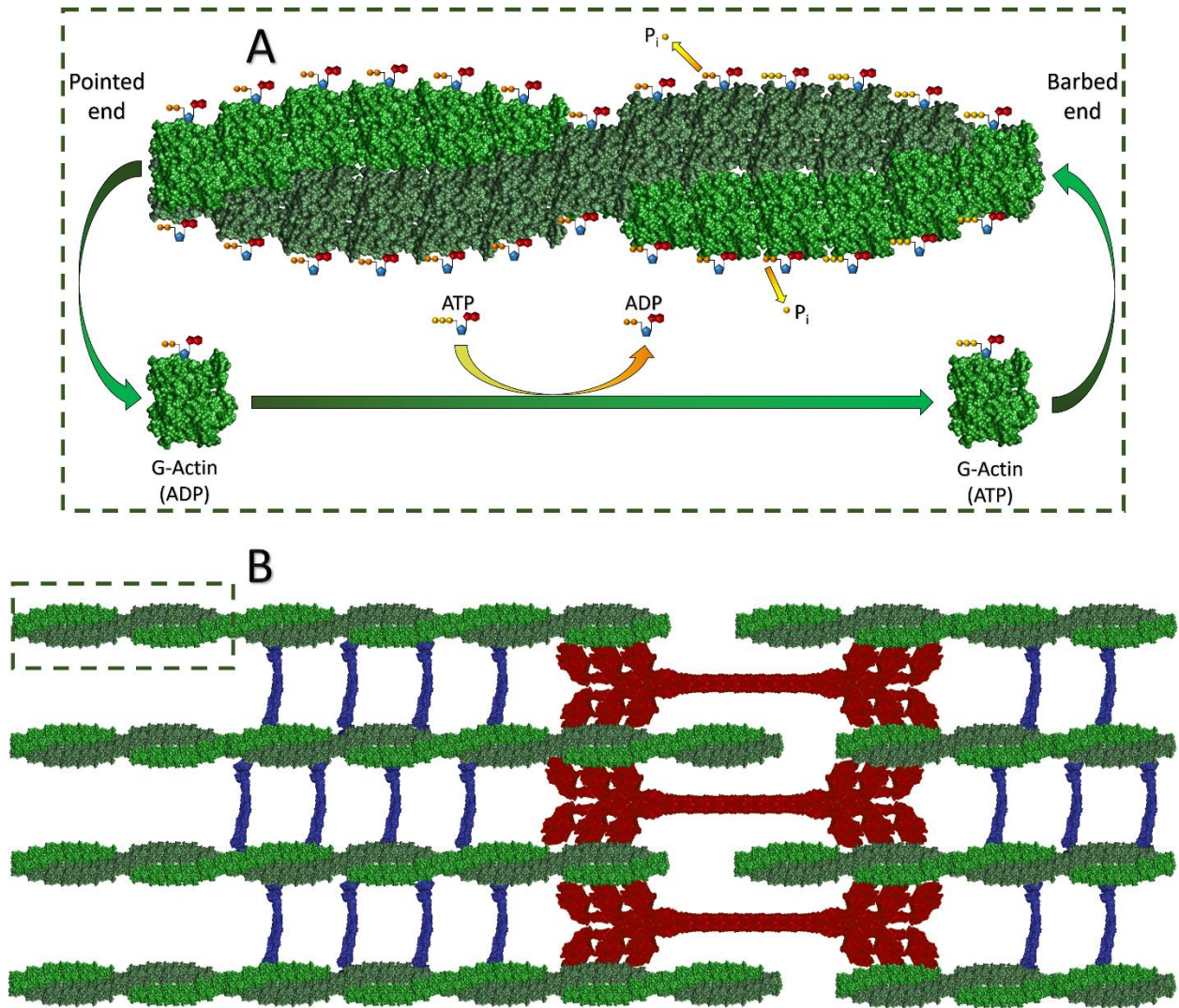


Figure 1.07 – Actin microfilament treadmilling (A) as part of an actin stress fibre (B). (A) F-actin assembles through adenosine triphosphate (ATP) hydrolysis, releasing energy and inorganic phosphate (P<sub>i</sub>). G-actin subunits bound to ATP are added to the barbed (positive) end of the microfilament, which as it develops hydrolyses ATP, producing adenosine diphosphate (ADP). The ADP bound subunits are released from the pointed (negative) end, which then undergo nucleotide exchange (ADP→ATP) and again are included at the barbed end, thus achieving ‘movement’ of the microfilament. G-actin PDB file 1J6Z visualised in Chimera (Otterbein et al., 2001; Pettersen et al., 2004); (B) Structural composition of an actin stress fibre. Microfilaments (green) bundle through crosslinking mediated by myosin II (crimson) and α-actinin (indigo). Myosin II PDB file 5I4E visualised in NGL viewer (Chinthalapudi et al., 2017; Rose et al., 2018). α-actinin PDB file 4D1E visualised in NGL viewer (Ribeiro et al., 2014).

### 1.2.3.1 F-actin stress fibres

Stress fibres are contractile bundles assembled from F-actin microfilaments, myosin II motor protein and additional actin-binding proteins, such as  $\alpha$ -actinin and filamin, making them reminiscent of muscle sarcomeres (Peterson et al., 2004). Formation of stress fibres is triggered by external mechanical, or internal biochemical, stimuli through several parallel signalling pathways, including  $\text{Ca}^{2+}$  and Rho proteins (Deshpande et al., 2006; Dowling et al., 2013). Influx of  $\text{Ca}^{2+}$  into the cytoplasm causes activation of proteinases that cleave actin microfilaments, with the free ends being rapidly elongated by G-actin, as well as myosin II phosphorylation, to form bipolar filaments (Deshpande et al., 2006). Through  $\alpha$ -actinin these filaments bind with the long F-actin microfilaments, thus forming stress fibres, which participate in a number of processes, including cell adhesion, movement and mechanotransduction (Figure 1.07B) (Pellegrin and Mellor, 2007). Cross-bridge cycling of the actin-myosin pairs generates the stress fibre tension needed for contraction, indicating that they are dynamic structures (Stricker et al., 2010). Stress fibres are widely grouped based on their function and composition as: (I) ventral, which are contractile, basally positioned and are the most commonly observed; (II) dorsal, which have been indicated to have a structural supportive role; (III) transverse arcs, with a motility function (Pellegrin and Mellor, 2007; Lu et al., 2008). Out of the three primary components of the cytoskeleton, it is thought that the actin stress fibres have the greatest contribution to the stiffness and tension of the cell and can also rearrange their organisation as a result of mechanical loading (Campbell et al., 2007; Na et al., 2007; Markov et al., 2019). This is accomplished through their ability to contract and form attachments to the underlying integrins at the focal adhesions, resulting in strong stress fibre interconnectivity (Hu et al., 2003). During wound healing stress fibres can also recruit  $\alpha$ -smooth muscle actin, providing greater contractility to the fibroblasts. This can also further activate  $\text{TGF}\beta 1$  to induce a myofibroblastic phenotype (Kassianidou and Kumar, 2015).

### 1.2.4 Intermediate filaments

Unlike the actin microfilaments, the intermediate filaments (Figure 1.06B) are not involved directly in cell movement, but instead provide structural stability to resist tensile and/or compressive forces. They are typically considered to be the most stable cytoskeletal components

and, unlike the other two, are not polarized (Fletcher and Mullins, 2010; Robert et al., 2016). They also exist in a state of dynamic equilibrium between the polymeric (dephosphorylated) and subunit (phosphorylated) form (Vikstrom et al., 1992; Herrmann and Aebi, 2000). Intermediate filament polypeptides align and form homodimers, further associating into tetramers, with eight tetramers assembling into unit-length filaments, which anneal into mature non-polar filaments (Blain, 2009; Lowery et al., 2015; Robert et al., 2016). This class of cytoskeletal element displays significant heterogeneity and exists as six distinct types encoded by multiple genes (Steinert et al., 1999; Hesse et al., 2001; Guérette et al., 2007). Vimentin (a type III intermediate filament) is present in scleral fibroblasts and has been noted to contribute to cell stiffness (Chen et al., 2004; Cui et al., 2008). Murine vimentin-deficient fibroblasts also have a reduction in stiffness, mechanical stability and motility (Henson and Vincent, 2008). Vimentin intermediate filaments and microtubules form a link between the plasma membrane and the nucleus, with vimentin also directly interacting with F-actin (Shah et al., 1998).

### 1.2.5 Microtubules

The largest of the cytoskeletal elements with a 23nm diameter, microtubules (Figure 1.06C) are also the stiffest and most complex (Fletcher and Mullins, 2010). The tubulin subunit is a heterodimer formed from two closely related globular proteins –  $\alpha$ - and  $\beta$ -tubulin, bound together by noncovalent bonds (Nogales et al., 1998). The microtubule itself is a hollow cylindrical structure built from 13 parallel protofilaments, each composed of alternating  $\alpha$ -tubulin and  $\beta$ -tubulin molecules. The assembly of the tubulin network is similar to the actin microfilaments, with a noticeable difference being the utilisation of guanosine triphosphate (GTP), and by extension guanosine diphosphate (GDP), instead of ATP and ADP (Erickson and O'Brien, 1992). GTP binds to both the  $\alpha$ - and  $\beta$ -tubulin, however, only the latter of the pair is able to be hydrolysed, which is necessary to add the dimer to the microtubule. As a result, the protofilaments are polarised, with the  $\beta$ -tubulin of each heterodimer being on the side of the faster-growing (plus) end and the  $\alpha$ -tubulin on the slower-growing (minus) one (Blain, 2009). Minus ends tend to cluster and form the microtubule organising centre (MTOC), such as the centrosome in animals, anchor to organelles, or remain free in the cytoplasm (Wu and Akhmanova, 2017). Microtubules are essential

for intracellular protein transport, formation of the mitotic spindle, synthesis and secretion of collagen and withstanding mechanical deformation (Blain, 2009; Li et al., 2011).

### 1.2.6 Mechanotransduction

The conversion of mechanical stimuli into intracellular biochemical signals is known as ‘mechanotransduction’. In cells exposed to external forces, it has been found that mechanical signals regulate many aspects of their functions, including differentiation, gene expression, protein synthesis and apoptosis (Malone et al., 2007; Jaalouk and Lammerding, 2009). Activation of signalling pathways is largely dependent on the interactions between the cytoskeleton and the sites of transduction of mechanical signals; the connection with the ECM (Figure 1.08) is accomplished through the transmembrane integrin receptors: (I) at focal adhesions for the actin microfilaments; (II) hemidesmosomes for the intermediate filaments; (III) focal adhesions and podosomes for the microtubules (Tan et al., 2006; Huang et al., 2012; Seetharaman and Etienne-Manneville, 2019). The transmitted stress through the ECM to fibroblasts can, in turn, stimulate them to produce new ECM components, as well as rearrange and stiffen the matrix (Alenghat and Ingber, 2002; Sapir and Tzliil, 2017).

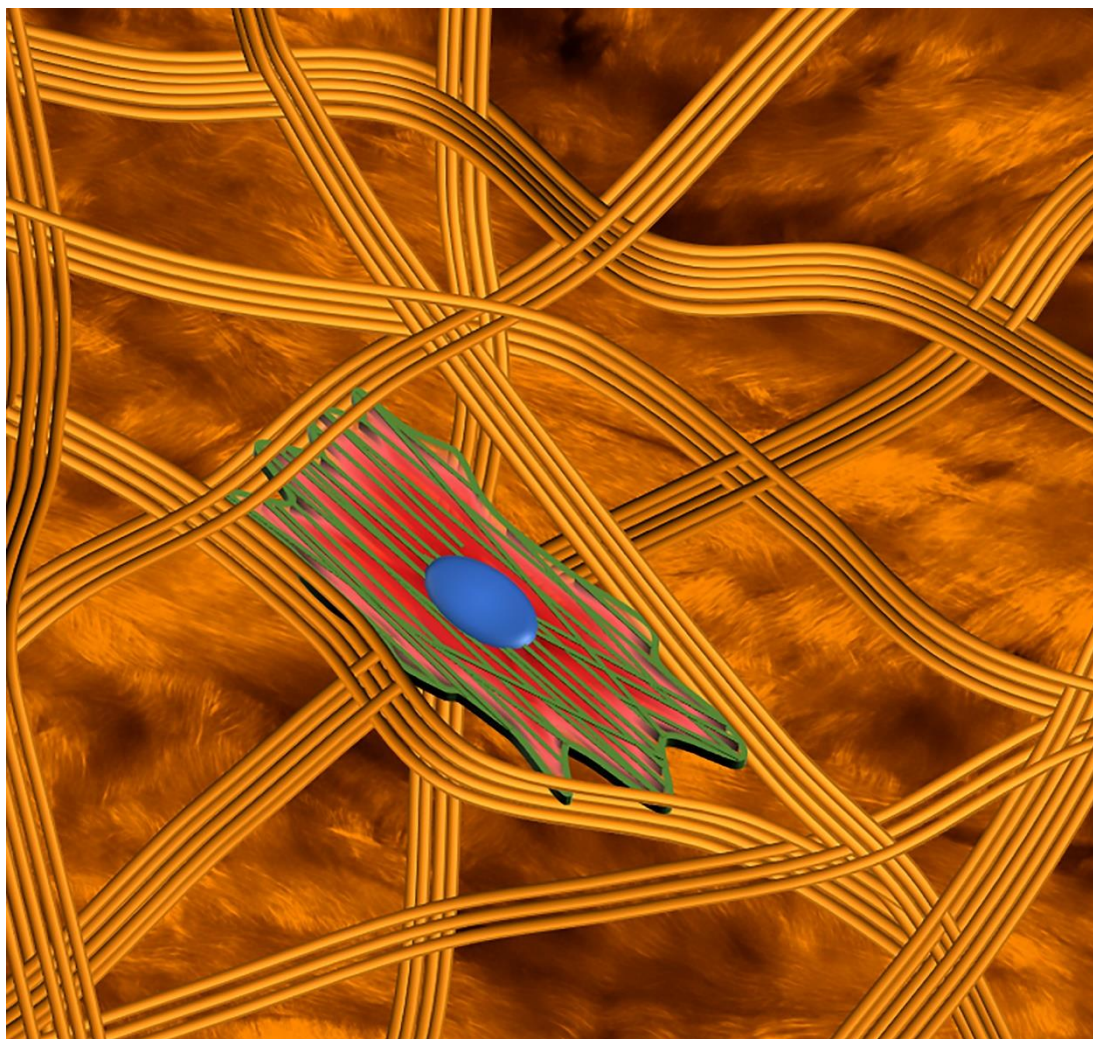


Figure 1.08 – Representation of a fibroblast embedded in collagenous (orange) extracellular matrix (ECM). The fibroblast cortical F-actin and stress fibres are indicated in green, whilst the nucleus in blue.

Many structural modifications have been observed as part of the cellular response to mechanical loading in a variety of cell types. For example, computational and experimental validations showed that under compression the occurring reorganisation of F-actin reinforces the cell's mechanical structure, with higher distribution around the cell edges (Barreto et al., 2013). Other structural modifications include shape change and alterations in the attachments to both substrates and adjacent cells. Proteins, such as the Rho GTPase family, are also involved in the signalling cascades (Tan et al., 2006). Collectively, these cellular responses protect the cell from the mechanical forces not only by reinforcing the plasma membrane, but also the cell adhesions, which is reliant on the contribution of all three cytoskeletal networks (Hu et al., 2003). There is also evidence that, as the cytoskeleton rearranges, it modulates the amount of force required to initiate

mechanical signals and the mechanotransduction pathways that transmit those signals to the nucleus, affecting both gene expression and cell differentiation processes (Chiquet et al., 2009). Further study of how the amounts of specific structural proteins in the cytoskeleton alter in response to mechanical loading would help to elucidate cellular mechanisms of functional adaptation to the applied mechanical forces (Jackson et al., 2008).

### 1.3 Scleral biomechanics

The sclera is a non-linear viscoelastic structure, having both an elastic and viscous component. To function properly the sclera must not only stretch under increasing load, but also be able to return to its native state, which has been noted to involve hysteresis (McBrien et al., 2009; Boote et al., 2019). Given the regional variations in the scleral biomechanical properties, the posterior exhibits different elasticity and creep properties compared to the rest of the sclera, even if it is noted to be nearly incompressible (Pavlatos et al., 2016). Studies of the PPS biomechanics present an interest not solely in terms of fundamental research but from a clinical viewpoint as well, since this is the region where the ONH must bear the large pressure differences between the IOP, the cerebrospinal fluid pressure (CSFP) and the eye's external environment. Understanding the biomechanics of the ONH links both the IOP-related and non-pressure risk factors for optic neuropathies, including glaucoma. To achieve this, one must combine the scleral and lamellar geometry with material properties (strength, stiffness, structural rigidity, compliance) to explain the physiology of normal ONH ageing, susceptibility to IOP, and the clinical manifestation of disease (Burgoyne and Downs, 2008).

The mechanical properties of the sclera are of particular importance for determining the deformation of the ONH in response to IOP elevation, with a key factor being the collagen fibre architecture (Pijanka et al., 2012). This is related to the pathophysiological changes that occur in glaucoma, which is linked with death of retinal ganglion cells (RGC). Contrary to expectations, the scleral thickness and stiffness do not balance each other out during a uniform IOP increase (Girard et al., 2009a). In fact, the relationship was inverse, even if not pronounced – a thin scleral region (the peripheral) tended to be associated with a larger stiffness, whilst a thick region (the peripapillary) was less stiff. It is thought that at small loads on the sclera the collagen fibres are

not fully stretched and retain a residual crimp (Jan et al., 2017; Gogola et al., 2018a; Jan et al., 2018). With the application of an external mechanical load the fibres progressively straighten, which causes them to exhibit non-linear, strain-stiffening behaviour. The collagen fibre stiffness treadmilling is influenced by several factors, including the diameter of the fibre and the density of the cross-links between the fibrils (Coudrillier et al., 2015a). GAG depletion in the PG population also causes significant effects on the stiffness and mechanical behaviour of the sclera, although it remains uncertain if PG composition is altered in ocular pathologies such as glaucoma (Murienne et al., 2015).

A decade ago Winkler and colleagues reported higher collagen fibril density around the LC in humans (Winkler et al., 2010). This collagen structure is not exclusive to humans, as presence of orientated collagen fibrils in the posterior sclera was also observed in cynomolgus monkeys, a year before Winkler's study (Roberts et al., 2009). Wide-angle X-ray scattering (WAXS) experiments first confirmed a clearly distinct circumferential ring of collagen fibres in humans and that the alignment can be quantified (Figure 1.09) (Pijanka et al., 2012). The PPS was the only region where such a highly aligned collagen organisation was found, whilst the mid-posterior region was observed to be mostly isotropic. Coudriller et al. determined that at the scale of WAXS measurements, the circumferential collagen fibres were twice as stiff as those in the meridional direction and that there were large differences in the degree of fibre alignment between different regions of the PPS (Coudrillier et al., 2013; Coudrillier et al., 2015a). Incorporation of the scleral WAXS data in finite element (FE) analysis indicated that altering the collagen fibre structure of the (mostly) isotropic mid-posterior sclera does not significantly affect the mechanical response of the ONH, whereas in contrast, changing the collagen anisotropy in the PPS region has immediate and large effects on scleral canal, expansion, as well as significant, but lesser, impact on the posterior bowing of the LC (Coudrillier et al., 2013; Coudrillier et al., 2015c). Multi-photon microscopy studies performed by the same research groups revealed that the circumferential fibre alignment in the PPS is limited to the mid-to-outer two-thirds of the depth of the sclera and does not extend through the full thickness of the scleral tissue (Pijanka et al., 2015).

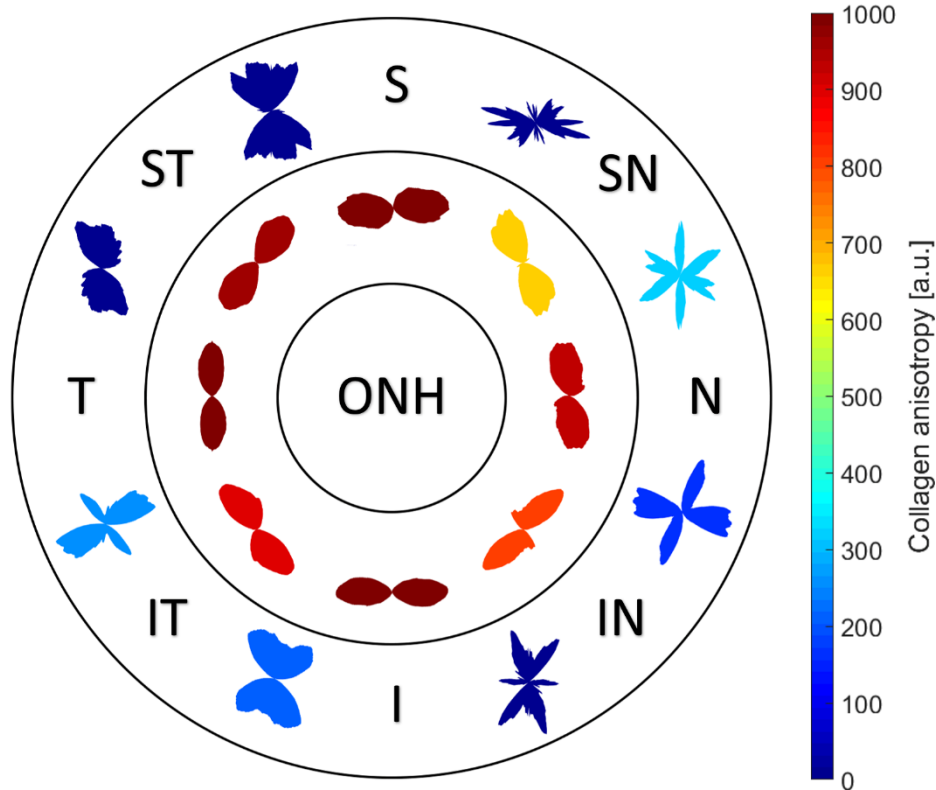


Figure 1.09 – Annulus of aligned collagen fibres around the ONH in the PPS (inner ring) and mid-posterior sclera collagen fibre organisation (outer ring) represented as polar vector plots. The orientation of the polar plots illustrates the average collagen fibre directional spread, whilst the colouring is indicative of the level of anisotropy, with hotter colours correlating to greater alignment. The posterior sclera was divided into eight sections, indicated clockwise: S (superior); SN (superior nasal); N (nasal); IN (inferior nasal); I (inferior); IT (inferior temporal); T (temporal); ST (superior temporal).

The above studies were significant in that they provided the first direct experimental support for the idea that circumferential collagen fibres in the PPS fulfil a neuroprotective role in providing mechanical stability to the optic nerve axons as they traverse the LC. Specifically, the PPS collagen structure limits the IOP-related expansion of the scleral canal and hence reduces the transverse strains in the LC (Pijanka et al., 2013) – a theoretical scheme which was earlier propounded by computational simulations (Grytz et al., 2011). It should be taken into account that it is not solely the circumferential fibre orientation that limits the scleral canal expansion, but the high fibre concentration in preferred directions as well (Girard et al., 2009a; Girard et al., 2009b). The level of collagen fibre interweaving should also have an effect, with suggestion towards an increase in scleral stiffness (Boote et al., 2019). Given the smaller amount of type I collagen in the LC, the mechanical response of the ONH is mostly determined by the elastic behaviour of the collagen

fibril network. Thus, it can be concluded that even local modifications to the collagen structure of the PPS can lead to significant influence on the mechanical response of the ONH. It is thought that these regional differences in the collagen orientation are an adaptive change to the IOP, promoting retention of biomechanical homeostasis within the ONH. A neuroprotective role for the PPS collagen structure is further supported by studies that showed significantly lower regional variations in posterior sclera affected by glaucoma and myopia and could partly explain individual-specific eye susceptibility to these conditions (Pijanka et al., 2012; Coudrillier et al., 2013; Markov et al., 2018).

There are also age and race-related differences in the scleral material properties, which can lead to a loss of scleral compliance. Several studies revealed that the PPS organisation also significantly vary with race and glaucoma, but not with age (Yan et al., 2011; Pijanka et al., 2012; Danford et al., 2013). However, older age does have an effect as it leads to scleral stiffening and a chronic elevation in the IOP, which could also likely explain the prevalence of age-related optic neuropathy (Burgoyne and Downs, 2008; Girard et al., 2009c; Coudrillier et al., 2012; Geraghty et al., 2012; Fazio et al., 2014). Loss of collagen crimp is also age-dependent and possibly related to the aforementioned scleral stiffening (Gogola et al., 2018a). In terms of ethnicity, people from African descent were shown to have a significantly lower in-plane strain when compared to European descent donors, as well as the existence of microstructural differences in the posterior sclera (Yan et al., 2011; Grytz et al., 2014). Similar to ageing, this was shown to be primarily due to a higher shear stiffness and the lower level of stretch at which the collagen fibrils uncrimp and stiffen. These age- and race-dependant changes could be the result of a higher density of collagen cross-linking, possibly in conjunction with loss of elastin-driven recoil, as it is known that the amount of elastin decreases with age (Watson and Young, 2004). The cross-links are a result of PGs binding collagen fibres with their core proteins, whilst the side GAG chains form connections with neighbouring fibres (Coudrillier et al., 2015a). In terms of other pathologies, it has been noted that older diabetic sclerae had a lower degree of collagen anisotropy than that of comparable nondiabetic sclerae (Coudrillier et al., 2015b). However, the mechanistic relationship between diabetes and ocular pathologies, such as glaucoma, remains poorly delineated beyond a basic epidemiological link.

### 1.3.1 Intraocular pressure

Along with the sclera and cornea, the exerted IOP also helps maintain the shape of the eye as it keeps it in an expanded globular form. It is measured in mmHg and for humans, the standard pressure varies between individuals, with a statistically normal range from 10 to 21mmHg, with 15.5mmHg taken as mean value (Klein et al., 1992). The main factors that regulate the IOP are the production and drainage of the aqueous humour, which when not in equilibrium can cause an increase or decrease in the pressure. There are also fluctuations during the day-night cycle, as the pressure tends to be higher in the morning, because of the prolonged time in a lying position (Downs et al., 2011). The cardiac cycle has also been indicated to alter the IOP and indirectly affects ONH deformations (Jin et al., 2018). Reducing the IOP remains the principal approach to prevent and delay the progression of damage from glaucoma (Jia et al., 2016).

### 1.4 Glaucoma

Glaucoma is a group of optic neuropathies, which cause loss of RGCs, along with atrophy and excavation of the optic nerve (Casson et al., 2012). It was first documented over 24 centuries ago in Ancient Greece, with the exact origin of the name remaining controversial, most likely from *glaukos*, which could have meant ‘owl’, ‘blue-green’ or ‘to shine’ (Tsatsos and Broadway, 2007; Laios et al., 2016). In addition, until around the early 18th century, cataract and glaucoma were not distinguished and were thought to be the same disease (Brisseau, 1709; Drews, 2006). The pathology presents itself initially as degradation in the peripheral visual field, which can progress centrally and lead to irreversible, functional blindness (Figure 1.10). In fact, glaucoma is the second most widespread reason for blindness after cataract and the leading global cause of currently non-treatable vision loss. The condition has a severe impact on the patient’s quality of life, with many exhibiting depression and social withdrawal (Quaranta et al., 2016). The number of people with glaucoma continues to increase at an alarming rate: 80 million people are expected to have primary open-angle glaucoma (POAG) by 2020 and 111.8 million by 2040, with the disease disproportionately affecting people in Africa and Asia (Quigley and Broman, 2006; Tham et al., 2014). As the disease is a neuropathy, most interventions target IOP reduction, as it is the only proven method for treating POAG (Boland et al., 2013). This includes laser eye surgery to increase

aqueous humour outflow or regular application of topical medication, which can have postoperative complications or can cause local adverse effects, respectively (Weinreb et al., 2014).



Figure 1.10 – Loss of peripheral sight in glaucoma. Normal (Left) and glaucomatous field of vision (Right).

#### 1.4.1 Disease biomechanics

As the LC is the primary site of glaucomatous damage, the PPS circumferential collagen fibre structure is of key interest in the glaucoma disease process. Whilst the bulk fibre directions in glaucomatous and non-glaucomatous PPS were similar, WAXS tissue studies showed that regional differences in peripapillary fibre anisotropy do exist (Pijanka et al., 2012). This may be the result of pathological changes or due to structural properties that are associated with predisposition to glaucomatous axonal damage. These differences were specific only to the PPS and were not observed in the mid-posterior region. It has been reported that damaged glaucomatous human sclera subjected to inflation tests have a different biomechanical response in the PPS than non-glaucomatous control eyes (Coudrillier et al., 2012). In addition, stress-strain behaviour in the mid-posterior region lacked significant differences, further underlying the importance of the peripapillary region for normal eye biomechanics. In terms of fibre anisotropy in the PPS, glaucoma specimens displayed a more homogeneous structure (Coudrillier et al., 2015c). It has also been shown that the choroidal thickness decreases with acute IOP, with further implication for the retina as well (Wang et al., 2016c; Muñoz-Sarmiento et al., 2019).

A typical glaucomatous change is the pathological enlargement of the optic disk, referred to as ‘cupping’ (Quigley, 2011). Burgoyne and Downs proposed that individual fibres in the anterior LC yield and then mechanically fail, thus transferring the force they were resisting to the adjacent collagen fibres, which increases their load at the same IOP (Figure 1.11) (Burgoyne and Downs, 2008). Thus, even if there is a constant level of IOP, the adjacent lamellar fibres progressively yield and/or fail as the IOP-induced load is spread over a continually decreasing volume of connective tissue. A recent study reported the existence of regional variations in the strain exerted on the LC, which might prove to be predictive of the progression of axonal damage in glaucoma (Midgett et al., 2017). It is possible that elevated IOP disrupts the nutrient supply in the axons, starting a reactional cascade which leads to a loss of proper function and apoptosis, which spreads to adjacent cells, all of which will eventually lead to axonal dysfunction and death (Strouthidis and Girard, 2013; Coudrillier et al., 2015c).

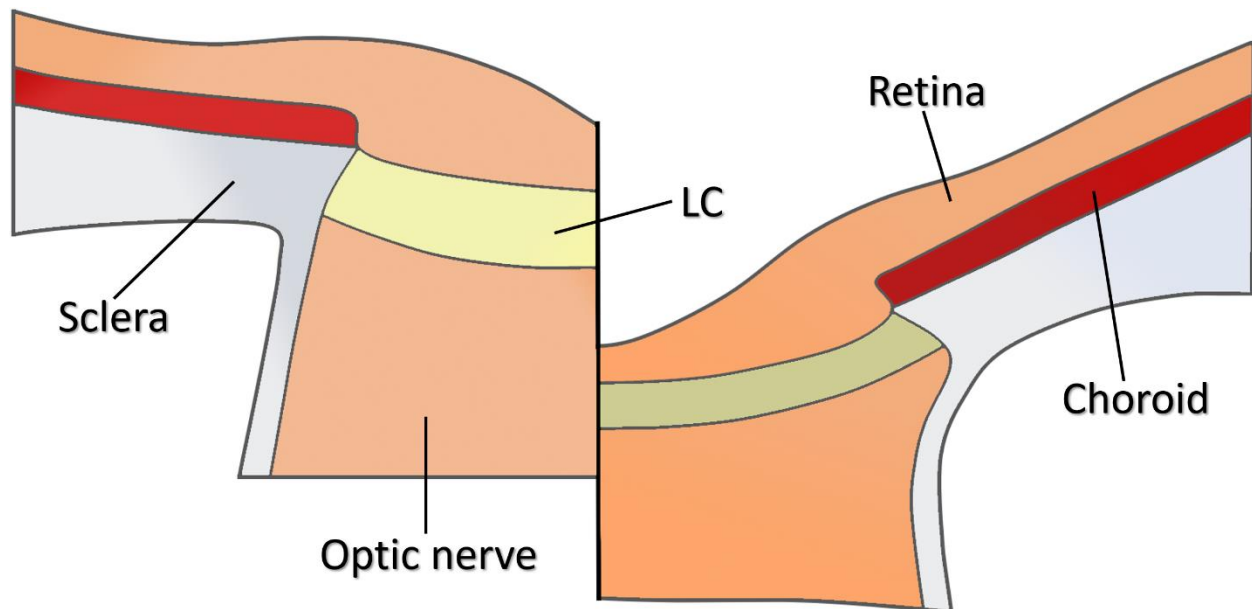


Figure 1.11 – Normal (Left) and deformed glaucomatous (Right) ONH with indicated components. Glaucomatous LC posteriorly displaces and thins, which also affects the structure of adjacent tissues. The mechanical yielding of the LC causes axonal transport disruption and apoptotic death in retinal ganglion cells (RGC).

### 1.4.2 Risk factors

In the majority of glaucoma cases, the principal pathological factor is elevated IOP, but it is far from the only risk for developing the disease. IOP fluctuates by as much as 10mmHg in the day-night cycle in rhesus macaques, with the ocular pulse amplitude increasing with IOP, which suggests that snapshot IOP measurements may be inadequate to capture the true dynamic character of the IOP (Downs et al., 2011). High-frequency IOP fluctuations become larger as IOP increases, presumably driven by stretching and stiffening of the ocular coats, which reduces elastic damping. Furthermore, the LC and scleral stiffness and microarchitecture would be key in resisting IOP-related damage (Grytz et al., 2012).

Other contributing factors associated with an increased incidence of glaucoma are advanced age and ethnicity, with both having differences in the scleral material properties, which might impact the mechanical loading conditions of the ONH, making it more susceptible to IOP-related injury (Tielsch et al., 1991; Grytz et al., 2014). A study by Girard and colleagues reported that the posterior sclera of aged rhesus monkeys is significantly stiffer than of younger ones, therefore subject to higher stresses but lower strains at all levels of IOP (Girard et al., 2009c). Advanced age stiffening of the sclera may significantly influence ONH biomechanics and potentially contribute to age-related susceptibility to glaucomatous vision loss, as it puts more strain on the LC (Zhou et al., 2019a). However, it is thought that for a range of IOP, the aged ONH should actually demonstrate less deformation due to the presence of stiffer LC and PPS, which is a result of age-related increases in lamellar beam thickness and ECM hardening (Burgoyne and Downs, 2008). Whilst age is a risk factor for the onset of glaucoma, congenital cases have also been documented (deLuise and Anderson, 1983).

Whether or not diabetes is a risk factor for developing glaucoma remains a topic of intense scientific and clinical research. Some research suggests that the age-related scleral stiffness is accelerated in the eyes of diabetic people (Coudrillier et al., 2015b). In addition, the elevated levels of sugar due to diabetes may confer neuroprotection for RGC from glaucomatous damage by providing an accessible energy source (Casson et al., 2014; Coudrillier et al., 2015b). In contrast, studies utilising animal models indicated that glaucoma is associated with an increased scleral

stiffness (Coudrillier et al., 2015c). Moreover, due to the axial elongation and thinning that occurs in myopic eyes, individuals with a prescription of  $>4D$  refractive error are considered to be at significantly greater risk of developing glaucoma.

### 1.4.3 New treatments

Reduction of IOP is not always an effective or advisable course for treating glaucoma. There are a large number of people with normal-tension glaucoma, and also a significant number who bear ostensibly higher pressures without any detrimental effect on vision. A study conducted in southwest Japan determined that 82% of patients with POAG had IOP levels under 22mmHg (Yamamoto et al., 2014). For these patients new treatments are needed that would allow the eye globe to retain the same pressure, without impairing proper vision. This could potentially be accomplished by altering the mechano-signal transduction of the scleral fibroblasts with drugs targeting a specific receptor/pathway, to make the eyes more resilient. For example, the result could be the cells secreting a more compliant collagen matrix, and thus protecting the retinal ganglion cells from damage (Morris et al., 2013; Strouthidis and Girard, 2013). This, in combination with present therapies, could lead to even better outcomes for patients. However, there is insufficient understanding of the specifics of cell mechanics in terms of glaucoma, making it necessary for further research to be conducted. Recent *in vivo* and *in vitro* experiments have indicated increases in actin reorganisation and integrin related signalling, alterations in proliferation and apoptosis and a possible transition into a scleral myofibroblastic phenotype (Oglesby et al., 2016; Pitha et al., 2018; Qiu et al., 2018; Markov et al., 2019).

## 1.5 Myopia

There are over a hundred types of visual impairment, of which near-sightedness, or myopia, is the most prevalent one. Myopia affects 23% of the world's population, with the number expected to reach 50% by 2050 (Holden et al., 2016). The term myopia stems from the Greek *myein* 'to shut' and *ops* 'eye'. This refractive error is defined by the inability to see at greater distances and is caused in major part by an abnormal axial lengthening of the globe, placing the eye's focal plane

in front of the retina. The incident parallel rays entering a myopic eye cross somewhere in the vitreous body, after which they diverge and reach the retina to form an unclear image (Figure 1.12). As a result of the elongation, the sclera is also markedly thinner than in normal emmetropic eyes (Vurgese et al., 2012). The occurrence of mild forms of myopia could be considered a reaction or adaptation to modern lifestyle, specifically in relation to time spent in education and indoors, further underpinning the global increase of myopia (Pan et al., 2012; Goldschmidt and Jacobsen, 2014; Holden et al., 2014; Williams and Hammond, 2014; Wu et al., 2015; Nickels et al., 2019).

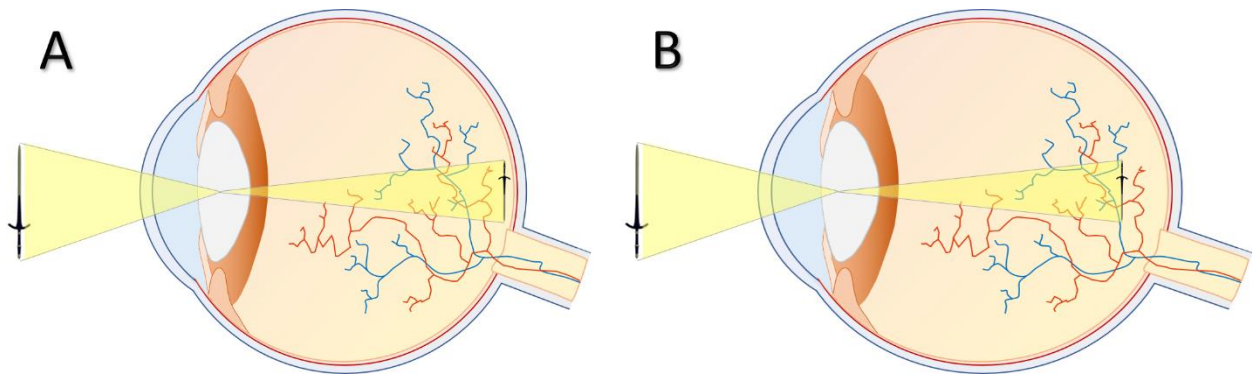


Figure 1.12 – Emmetropic (A) and myopic (B) visual perception. Axial lengthening of the eye globe in myopia results in a displacement of the focus in front of the retina (B), rather than directly on top of it (A).

### 1.5.1 Development

The axial elongation in the developing myopic eye is not solely due to tissue redistribution and thinning and is, in fact, a complex two-step process involving structural ECM alterations (Gentle et al., 2003; McBrien et al., 2009). The amount of collagen decreases due to a downregulation in type I collagen synthesis and increased stimulation of the expression of matrix metalloproteinase 2, which is known to degrade collagen fibrils (Guggenheim and McBrien, 1996; Jones et al., 1996; Schippert et al., 2006). The end result is both a reduction in the already existing collagen and prevention of *de novo* synthesis. In addition, a decrease in the diameter of collagen fibrils, particularly near the posterior pole, has also been noted (McBrien et al., 2001). These observations are further confirmed by studies in other mammalian species, where the changes during myopic development are the result of active tissue remodelling rather than just passive stretching of the sclera (Guggenheim and McBrien, 1996; McBrien et al., 2006).

The elasticity of the sclera is increased in eyes developing myopia, along with the creep rate, which, however, is reduced in eyes recovering from myopia and can occur within 24h of the initial development (McBrien et al., 2009). However, computational simulations reveal that this greater scleral elasticity could account for only 20% of the elongation of the eye, suggesting the importance of other factors for myopic progression (McBrien et al., 2009). Alterations in creep properties were also observed, which remained a factor in the progression of myopia, regardless of changes in the scleral thickness. Apart from collagen, *de novo* synthesis of other ECM components also declines, such as PGs and integrin receptors, which could have implications in impairing cell-matrix interactions under mechanical stress (Tomasek et al., 2002; McBrien et al., 2006; Siegwart and Strang, 2007).

As previously noted, scleral myofibroblasts have the capacity to contract the matrix and are regulated by tissue stress and growth factors such as TGF $\beta$ 1 (Section 1.2.1.1). Changes in these regulatory components have been observed during myopia development, implicating cellular factors in the scleral weakening process. Specifically, proper cellular functioning could prove protective against myopic onset (Phillips and McBrien, 2004). Other pathologies have also been reported to cause myopia; for example, Marfan syndrome is a genetic connective tissue disorder attributed to mutations in the ECM protein fibrillin-1, with most patients being myopic and having a greater glaucoma predisposition (Mauumenee, 1981; Hayward and Brock, 1997; Nemet et al., 2006). Myopic tree shrew eyes exhibited an evident reduction in both scleral thickness and dry weight as well (Norton and Rada, 1995; McBrien et al., 2001). It is hypothesized that the eye controls the scleral matrix based on the image quality falling on the retina, which in turn signals the sclera to weaken, or strengthen, to accelerate or slow eye growth. For example, in mammals with high myopia, this signal leads to biochemical remodelling of the scleral matrix, producing a thinner, weaker tissue (Summers Rada et al., 2006).

### 1.5.2 High myopia

In humans, high myopia, or *myopia gravis*, refers to patients having >6D of myopic refractive error (Verkicharla et al., 2015). Whilst for the mild and moderate forms of myopia the eyes appear normal in terms of shape, highly myopic ones are slightly elongated in the axial dimension, the

pupil is dilated, and the anterior chamber is deeper. The sclera becomes weaker and more extensible, which results in its inability to withstand the expansion that occurs with elevating IOP (McBrien et al., 2009). Due to the alterations in the globular structure of the eye, this form of near-sightedness is linked to a heightened risk of retinal detachment, cataract and especially glaucoma (Xu et al., 2007). Myopic cases have been noted to have lower of the ocular globe rigidity, suggesting that glaucoma may enhance the myopic changes to tissue biomechanics (Chansangpetch et al., 2017). Recent findings in the bulk collagen fibre orientation in human sclerae supports the idea that pathological structural remodelling takes place with high myopia leading to a greater susceptibility to mechanical damage and deformation of the scleral tissue (Markov et al., 2018).

The development of high myopia is associated with a decreased amount of scleral collagen, thinning and loss of scleral tissue, in both humans and animal models (Gentle et al., 2003; Vurgese et al., 2012). Like the other forms of myopia, the collagen fibril diameter is reduced which could be of importance for patients with pathological myopia for the subsequent development of posterior staphyloma (Curtin et al., 1979). The thinning of the sclera in the posterior pole logically results in changes to the LC, which, because of the axial elongation of the globe, becomes thinned and extended (Vurgese et al., 2012; Jonas and Xu, 2014). The stretching of the eye could also lead to expansion in the retina and reduce retinal function. Another possibility for the higher susceptibility to glaucoma could be the increase of the distance between the ONH and the Zinn-Haller arterial circle, which vascularizes it, resulting in distortion to the normal blood supply to the LC (Jonas et al., 2013). Furthermore, with high myopia, the choroid becomes very thin, a process that continues with age and myopic progression. The occurring abnormalities of the choroid could further play a role in the pathogenesis of myopic degeneration (Fujiwara et al., 2009). All of these alterations further exemplify the necessity for novel ways of studying ocular composition and biomechanics.

## 1.6 Technical approaches

### 1.6.1 X-ray scattering

X-rays are a high-frequency form of electromagnetic radiation, with a wavelength normally ranging from 0.1 to 10nm (Figure 1.13). Techniques using X-rays find a wide arrangement of scientific application, with 89% of the known protein structures determined by X-ray diffraction (Gore et al., 2017). The phenomenon arises when monochromatic X-rays are elastically scattered by periodically arranged atoms, such as those in a crystalline lattice. The scattered radiation is in phase, causing constructive interference between the wave component of the photons, with the direction of the scattered beams being depended on the material's intrinsic structure. As based on Bragg's law (Figure 1.14), the angle ( $\theta$ ) between the incident beam and the periodic lattice will be reflected with an angle of scattering of the same proportion ( $\theta$ ).

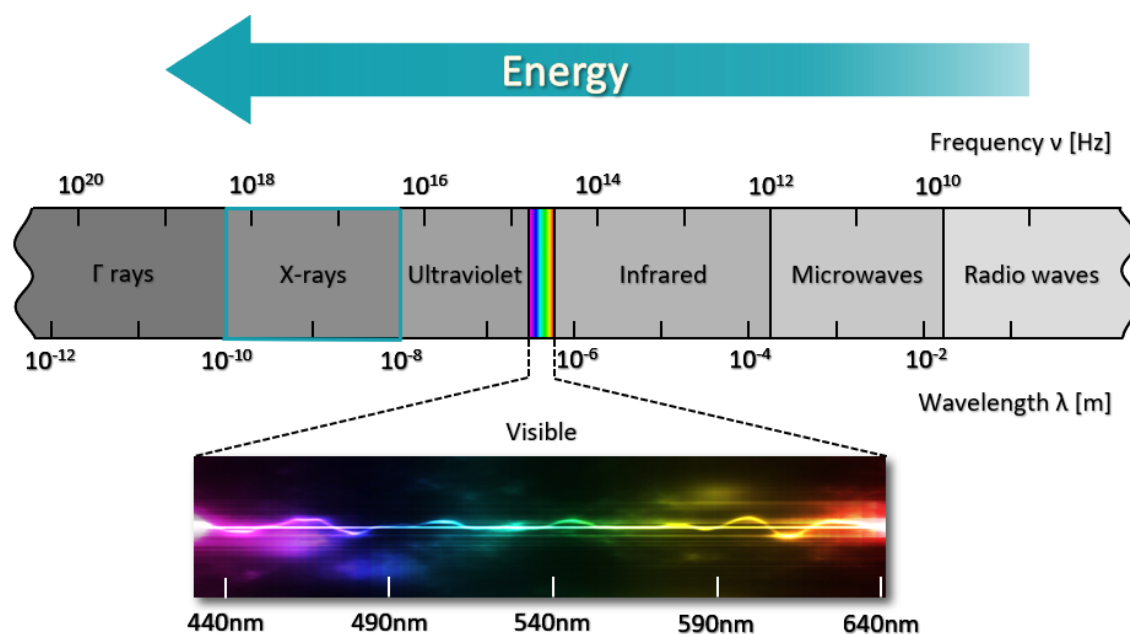


Figure 1.13 – Electromagnetic spectrum, with highlighted visible spectrum and X-ray range indicated in teal.

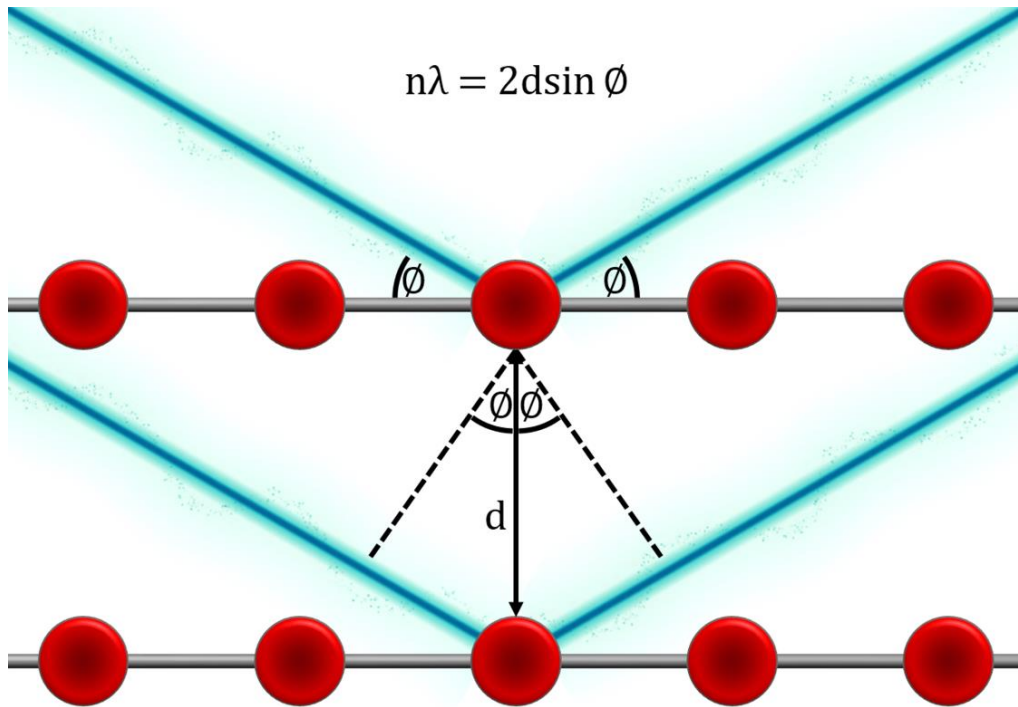


Figure 1.14 – Representation of Bragg's law for X-ray diffraction from atoms of a periodic crystal lattice. When two identical monochromatic X-rays beams with the same wavelength ( $\lambda$ ) hit two atoms from different crystal planes, with a characteristic spacing ( $d$ ) between them, the angle of incidence ( $\phi$ ) will be equal to the reflected angle of scattering ( $\phi$ ). Another parameter is the order of diffraction ( $n$ ), which is an integer. If the scattered beams are in phase, they will constructively interfere and by measuring the angle ( $\phi$ ) it is therefore possible to determine the interplanar spacing ( $d$ ) of different materials.

WAXS is an *ex vivo* approach, that permits the quantification of collagen fibril distribution and orientation in corneal and scleral tissues (Meek and Quantock, 2001; Meek and Boote, 2009; Pijanka et al., 2012; Coudrillier et al., 2013). As incident X-rays pass through tissue, a fraction is scattered from the constituent collagen molecules that form the fibrous ECM, producing a Fourier transform scatter pattern reflective of the intrinsic architecture. Instead of a direct image visualisation of the surface, like most forms of microscopy, X-ray scattering samples the full tissue thickness, from which both qualitative information and quantitative structural parameters can be indirectly extracted. As the tissue is not labelled, embedded or sectioned before the experimental procedures, artificial disruption of the tissue microstructure is largely avoided. Another advantage of WAXS is that the diameter of the collagen molecules is highly uniform, which gives rise to a sharp well-resolved signal (Meek and Quantock, 2001; Pijanka et al., 2012).

WAXS arises from X-ray beam scattering at angles larger than  $2^\circ$  and originates from the  $\sim 1.6\text{nm}$  lateral packing of collagen molecules within the fibrils (Meek and Boote, 2009). This scatter occurs perpendicularly to the collagen fibril axis and is referred to as the equatorial WAXS pattern. As the scleral collagen fibrils are distributed in multiple orientations, the diffraction pattern recorded on an X-ray detector will form arcs (Figure 1.15), from whose angular intensity distribution the angular fibril distribution function within the tissue plane can be extracted. It should be noted that there will be artefactual angular smearing in the patterns due to the tilt of the molecules that form the intermediate microfibrillar structure of the fibrils. However, in the sclera this tilt is small, at around  $5^\circ$ , and thus its contribution will be minimal (Yamamoto et al., 2000).

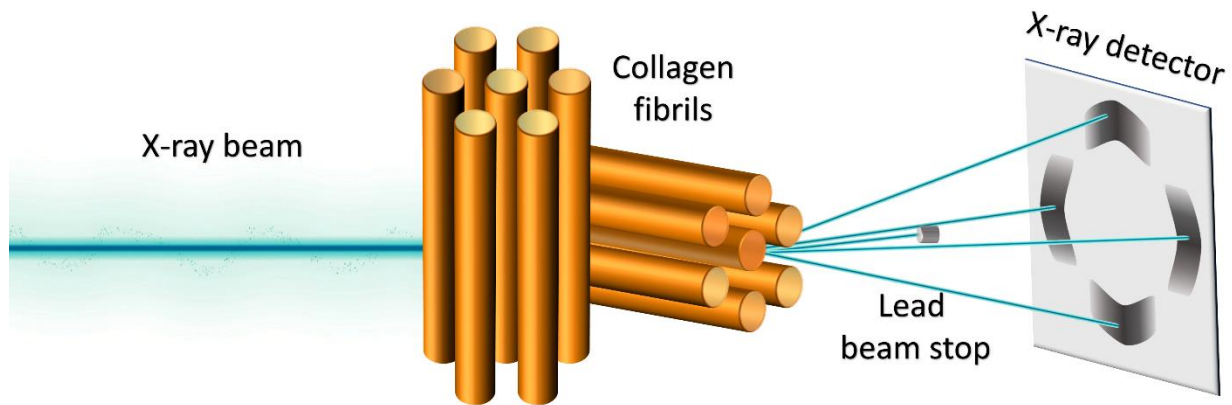


Figure 1.15 – WAXS intermolecular equatorial pattern from incident X-ray beam hitting orthogonally orientated groups of collagen fibrils.

X-ray beam scattering at angles smaller than  $2^\circ$  is referred to as small-angle X-ray scattering (SAXS). Unlike WAXS, where the X-ray detector was positioned several dozen cm away from the sample, this distance needs to be several metres to record the small-angle pattern. This technique has been utilised in multiple studies of the corneal architecture, with the signal being most pronounced in the meridional direction and stemming from the collagen fibril organisation (Meek and Quantock, 2001; Meek and Boote, 2009). The SAXS meridional signal depends on several factors, such as tissue hydration, the lateral separation of the collagen fibrils and their diameter, which in the cornea is much more uniform,  $\sim 35\text{nm}$ , whilst in the sclera varies between 25 to 230nm, thus making the WAXS equatorial signal from the intermolecular collagen spacing to be a more suitable choice in investigating the scleral collagen organisation (Komai and Ushiki, 1991; Meek and Boote, 2009).

Due to the destructive nature of X-ray radiation, most data collection require sufficiently high signal-to-noise ratio in the shortest possible time frame, necessitating the use of an ultra-high intensity synchrotron X-ray source (Figure 1.16) (Bilderback et al., 2005).

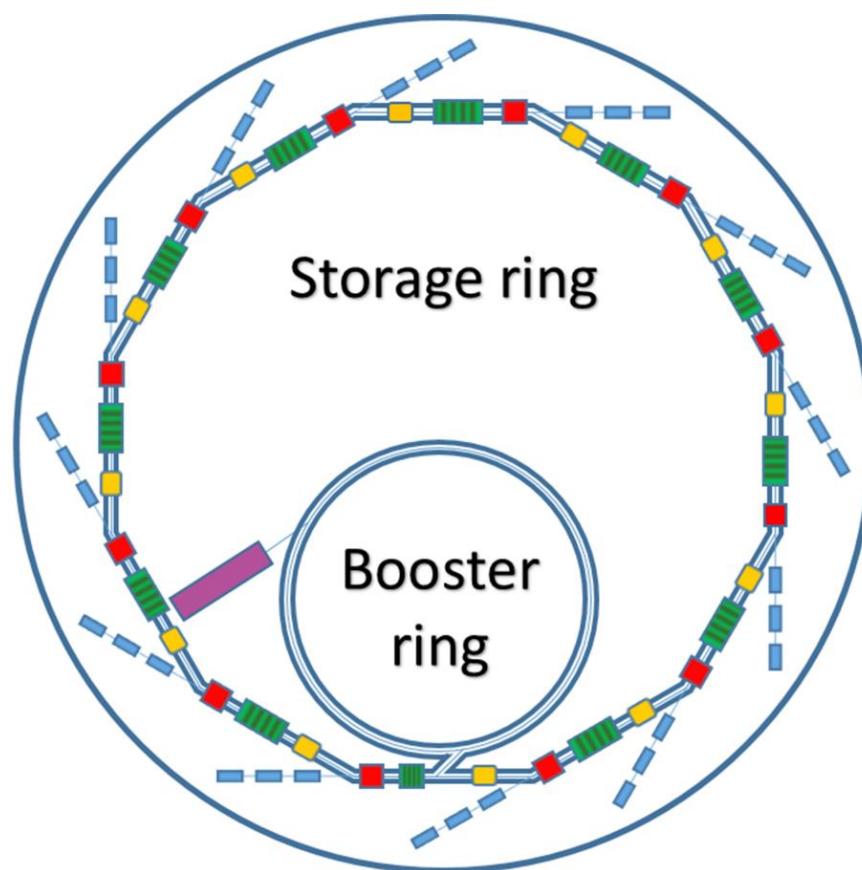


Figure 1.16 – Primary components of a synchrotron facility. Once fired from an electron gun (purple), the electrons are accelerated in a booster ring, following which the electron beam starts moving along a storage ring in a vacuum tube, surrounded by bending magnets (red). Undulator magnets (green) cause the electrons to release energy in the form of X-rays which are directed to different beamlines (blue). Radiofrequency cavities (yellow) replenish the electrons with the energy that was lost in the form of X-rays.

First, a high voltage cathode, or highly heated element, produces free electrons that are fired as a stream of electrons from an electron gun. In a linear accelerator, or linac, high energy radio waves accelerate the electrons to near relativistic speed and energy of hundreds of MeV. Afterwards, the electrons are injected into a booster ring where bending dipole magnets force the electrons to travel in a circular path, which are further accelerated by radiofrequency cavities and achieve a few GeV energy. From the booster ring, the highly accelerated electrons are fed to the outer storage ring, where high vacuum is required so that there are very few gas molecules in the beam path, which

would otherwise scatter the near relativistic particles before they reach their target. In addition to bending magnets, there are constantly repeated magnets with opposite magnetic poles, with the alteration leading to small dipole fields to be generated, which causes the electrons to undulate and release energy in the form of brilliant electromagnetic radiation. The high-intensity X-rays travel to beamlines, which are designed to support a specific technique or type of sample. Whilst their design can vary a lot, they, in general, are composed of an optics hutch, where the radiation is focused and filtered, an experimental hutch housing the experimental equipment, such as the X-ray detector and sample holders, and a control station, where the procedures can be monitored (Winick, 1995). Synchrotron light sources have been used in studying structural organisation at tissue levels as well, including both the cornea and sclera (Chapter III and Chapter IV) (Meek and Quantock, 2001; Boote et al., 2005; Pijanka et al., 2012; Coudrillier et al., 2015a; Markov et al., 2018).

### 1.6.2 Laser scanning microscopy

Laser scanning microscopes (LSM) provide images with high contrast on the basis of excitation and emission of a fluorescent signal from a fluorophore (Lichtman and Conchello, 2005). The absorbed light causes an electron to transit to a higher energy level, resulting in an excited state. The following return to ground state is accomplished through emission of the excess energy as a photon with less energy (higher wavelength) than the absorbed one, causing a Stokes shift in the emission spectra (Figure 1.17). LSM are commonly used for optical sectioning, producing several consecutive image slices of the original specimen, allowing for a greater depth visualisation (Conchello and Lichtman, 2005). Amongst the different linear approaches, confocal microscopy permits optical sectioning by scanning the specimen with laser irradiation and focusing the emitted light through a filter, most commonly a pinhole (Paddock, 1999). By employing a pinhole the background noise is greatly reduced by eliminating out-of-focus fluorescence to generate high-quality optical sections. Fluorescent confocal LSM have been employed in a number of studies of microscopical structures, including the cytoskeleton (Chapter V) (Idowu et al., 2000; Campbell et al., 2007; Li et al., 2011; Kuboki et al., 2012; Jiu et al., 2017; Qiu et al., 2018).

Multiphoton microscopy is a non-linear imaging approach that achieves optical sectioning through thick biological tissue samples by using high frequency, pulsed laser-generated photons. Second harmonic generation (SHG) is a coherent form of multiphoton microscopy that emits a photon which has precisely half the wavelength, or twice the frequency, of two incident photons, most commonly in the infrared part of the electromagnetic spectrum (Figure 1.13) (Zipfel et al., 2003). A distinguishable feature of SHG is that emission stems from virtual states, unlike the standard Stokes shift emission fluorescence from a singlet excited state (Figure 1.17). Whilst initially utilised in birefringent crystals, SHG signal can be produced in non-centrosymmetric biological structures as well, such as microtubules and most notably collagen fibrils, allowing for their visualisation without the requirement of labelling (Dombeck et al., 2003; Williams et al., 2005; Chen et al., 2011; Chen et al., 2012b). Therefore, several research studies have applied SHG microscopy to the collagen architecture in the corneoscleral tunic (Chapter IV) (Han et al., 2005; Girard et al., 2011; Jones et al., 2015; Pijanka et al., 2019).

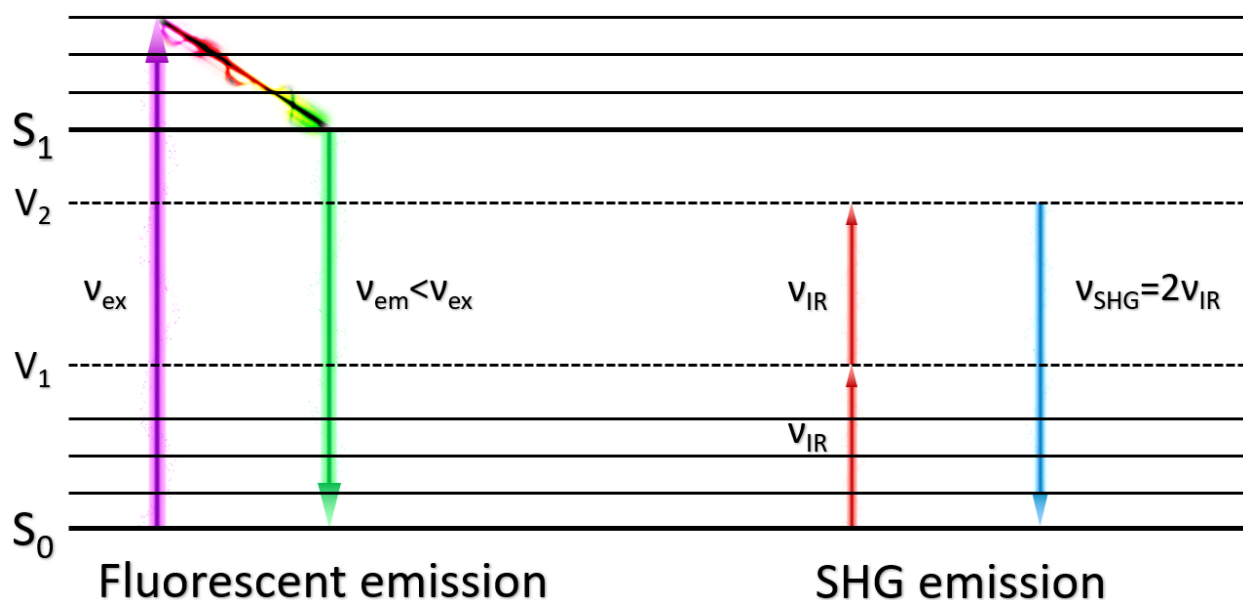


Figure 1.17 – Jablonski diagram of standard fluorescence and SHG emission. Initial photon excitation ( $v_{ex}$ ) from singlet ground state ( $S_0$ ) is to a higher vibrational level of the excited state ( $S_1$ ). This is followed by a rapid non-emission decay to the vibrational ground state of  $S_1$ , followed by emission of a photon with lower energy ( $v_{em}$ ; lower frequency, higher wavelength) than the absorbed one. This process is referred to as a Stokes shift in the fluorescence emission spectrum. In SHG, two photons with the same energy ( $v_{IR}$ ) are subsequently excited in a single quantum event, to intermediate virtual states ( $V_1$  and  $V_2$ ). The reemitted photon is half the wavelength ( $v_{SHG}$ ; twice the frequency) of the two incident ones.

### 1.6.3 Finite element modelling

Numerical modelling is an approach for representing real systems in a simplified manner. This permits a multitude of advantages, as it allows the determination of only relevant characteristics, often in conditions which cannot be replicated experimentally. Models can also interpolate and extrapolate results and predict behaviours. Amongst the commonly employed modelling methods, FE analysis is the most widely used. The approach is based on the assumption that any object can be represented as a large number of composing parts or ‘finite elements’. The nodes, or vertices, of each element can be connected by either straight lines (first-order) or curves (second-order), to create a simple (Figure 1.18) or complex structure. A major advantage of the FE models is that they are much more time and cost-efficient and in biological research can reduce the number of laboratory animals used, thus preventing ethically ambiguous situations. However, oversimplification and overapproximation pose persistent problems associated with the FE approach.

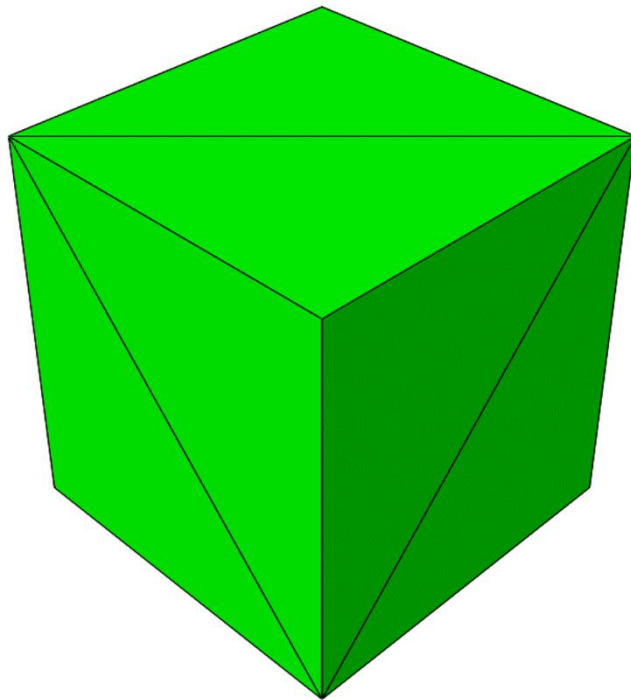


Figure 1.18 – Finite element (FE) cube model composed of 12 first-order triangular elements and 8 vertices.

### 1.6.3.1 Eye modelling

Over the last decade, numerous FE models of the eye have been created. FE models allow the handling of complex geometry, dynamic properties, loading and non-linear pressure changes, all of which applies to the sclera and its mechanics. Such computational studies have revealed that scleral stiffness, geometry and collagen fibre structure significantly influence the response of the ONH to changes in IOP and are important factors in the deformation of the LC (Sigal et al., 2005; Girard et al., 2009c; Grytz et al., 2011; Norman et al., 2011; Coudrillier et al., 2013; Campbell et al., 2015). Through FE analysis it was shown that the scleral canal size and shape and scleral thickness were the most important geometrical factors affecting the ONH stresses in human eyes (Bellezza et al., 2000). Models also predicted that posterior scleral deformations are non-linear after acute IOP elevations and are governed by the scleral collagen microstructure (Girard et al., 2009a). The FE approach also independently predicted the existence of the highly orientated ring of collagen fibrils around the ONH (Grytz et al., 2014). In conjunction with WAXS experiments on the collagen fibre structure, FE analysis was used to model the anisotropic stress response of the posterior sclera (Coudrillier et al., 2015a; Coudrillier et al., 2015c). Furthermore, recent research combined human corneal and scleral WAXS data with ocular globe surface reconstruction to more accurately represent the biomechanics of the whole eye tunic for further investigation (Zhou et al., 2019a; Zhou et al., 2019b).

### 1.6.3.2 Cell modelling

Whilst the scleral ECM has been previously investigated with FE analysis, this has not been performed for the cytoskeletal proteins in the context of cellular biomechanics. FE cellular models are notable for being oversimplified, with the cytoskeleton being absent or restricted to basic representation of a singular continuous network (Ronan et al., 2012; Dowling et al., 2013; Abhilash et al., 2014; Ronan et al., 2015). Whilst a few studies utilised cytoskeletal components they were all represented as simplified linear elements (Barreto et al., 2013; Barreto et al., 2014). Another approach is to create FE models on the basis of actual experimental imaging data (Dailey et al., 2009; Slomka and Gefen, 2010; Or-Tzadikario and Gefen, 2011). These cell-specific models permit the representation of actual cellular geometries, as well as the incorporation of several

intracellular components. Although they provide an improvement in accuracy there remains a necessity for standardised procedures for their creation and optimisation (Chapter VI). Furthermore, there is no model that takes into account the cellular component of the sclera as well, whilst none of the existing simulations has included experimental results that combine both the slow ECM and the fast fibroblast remodelling in response to varying levels of IOP over a range of different time-scales.

## 1.7 Aims and objectives

The objective of this interdisciplinary project was to provide further clarity on scleral fibroblast and ECM composition and biomechanical behaviour utilising multiple biophysical, biochemical and bespoke techniques. This will be instrumental in our understanding of the sclera and the associated differences with certain pathologies, such as myopia and glaucoma.

The following specific objectives were set:

1. To ascertain whether alterations in the ECM occur in the bulk collagen fibre level in human high myopia.
2. To evaluate the collagen microarchitecture surrounding the optic nerve in several mammalian species, in order to identify appropriate human analogues for scleral/ONH biomechanical studies.
3. To develop an algorithm for extracting and processing laser microscopy data to determine alterations in the bovine scleral collagen organisation.
4. To quantify the effect of physiological and pathological (glaucomatous-like) mechanical strain on scleral fibroblast cytoskeletal protein orientation.
5. To develop an approach for creating cell-specific FE models that retain physiological accuracy of the organisation of the cytoskeleton.

The overarching future goal is to incorporate the collected physiological tissue and cellular data into quantitative FE models, which are envisioned to be applied in the study of ocular pathologies and determining novel targets for future treatments.

# **Chapter II**

## **Materials and methods**

### 2.1 Ethical statement

All human tissues in this work were collected and handled in accordance with the World Medical Association Declaration of Helsinki on Ethical Principles for Medical Research involving Human Subjects and approved by the Human Science Ethical Committee (School of Optometry and Vision Sciences, Cardiff University, Cardiff, UK) and the South East Wales Research Ethics Committee (Cardiff, UK).

### 2.2 Wide-angle X-ray scattering procedures

#### 2.2.1 Specimen details and preparation

##### 2.2.1.1 Human samples

Nine eye globes from human donors, seven emmetropic and two highly myopic ( $>6D$  of refractive error), were obtained within 13-18h *post-mortem* (Fondazione Banca degli Occhi del Veneto, Venice, Italy), through a contract with the Biomechanical Engineering Group (University of Liverpool). A third highly myopic globe was acquired from the Department of Ophthalmology at the University of Hong Kong (Markov et al., 2018). Prior to donation, all eyes were previously assessed for refractive status by an ophthalmologist and confirmed to have no registered previous history of glaucoma, posterior scleral surgery or disease (apart from myopia). The average age of the non-myopic specimens was  $66.3 \pm 7.1$  years and  $66.7 \pm 8.3$  years for the highly myopic. The specimens were dissected and prepared in accordance with previously established protocols (Pijanka et al., 2012; Pijanka et al., 2013). External remaining adipose, muscle and connective tissues (muscle tendons, blood vessels and *episclera*) were carefully removed with scissors, whilst the optic nerve was excised with a razor blade flush to the sclera. An incision was made with a scalpel in the equatorial sclera, separating the anterior and posterior cups and the internal vitreous, lens, retina and choroid were subsequently removed. The implementation of four to eight relaxing incisions in the posterior eye cups prevented notable creasing and allowed for flat mounting of the specimens so that the whole tissue surface was perpendicular to the incident X-ray beam. Posterior cup specimens were then immediately fixed in 4% (w/v) paraformaldehyde (PFA; Sigma-Aldrich, Poole, UK) solution and stored at  $4^{\circ}C$  until time of wide-angle X-ray scattering (WAXS)

experiments. Table 2.1 provides details on the eyes used in the study, whilst Figure 2.01 exemplifies a flat-mounted posterior sclera (N3). In addition, specimen polar vector plot maps (Chapter III) were utilised to retrospectively determine relative myopic elongation of the posterior sclera by measuring the distance between the optic nerve canal edge and the insertions of the inferior oblique muscle, referred to as the ONH-IO distance.

Table 2.1 – Specimen details of the human eyes utilised in the wide-angle X-ray scattering (WAXS) experiments. Note: the optic nerve head to inferior oblique muscle (ONH-IO) distance was calculated using polar vector plot maps (Chapter III), representing a measure of axial globe length. The ONH-IO distance for the highly myopic eyes was noticeably larger than the non-myopic eyes, apart from HM1 which was not measurable (denoted as N.A.).

Specimen	N1	N2	N3	N4	N5	N6	N7	HM1	HM2	HM3
Age	75	75	64	65	53	63	69	60	64	76
Left/Right	Left	Right	Left	Right	Right	Right	Left	Left	Right	Left
Myopic Status	Normal	Myopic	Myopic	Myopic						
Anterior Cup	Yes	No	No							
Beamline	I02	I02	I02	I02	I02	I03	I03	I02	I03	I02
ONH-IO distance [mm]	9.49	9.41	9.29	9.14	9.78	8.66	9.59	N.A.	12.57	10.80

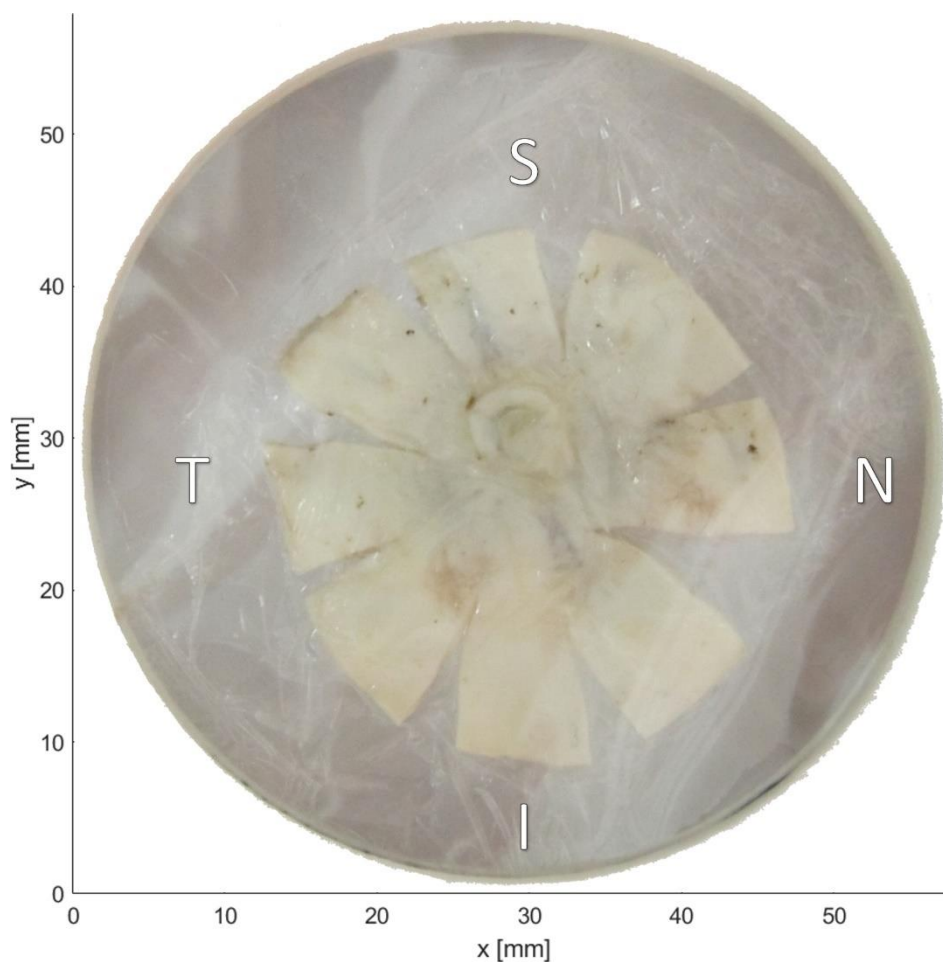


Figure 2.01 – Photograph of flat-mounted posterior eye cup of specimen N3 with distinguishable relaxation incisions. The specimen was covered with Mylar sheets and positioned in a WAXS sample holder (window only presented). Superior (S), nasal (N), inferior (I), temporal (T) directions are indicated.

### 2.2.1.2 Bovine samples

Four bovine eyes were obtained from a local abattoir (Maddock Kembrey Meats Lt, Maesteg, UK), with a mean age of  $23.4 \pm 4.4$  months, based on records from 118 animals. The globes were recovered within 12h *post-mortem* and were transported on ice and stored at  $4^{\circ}\text{C}$  until processing. Preparational procedures followed the ones presented in Section 2.2.1.1, with posterior cups further cut with scissors to a circular biopsy with a diameter of 20mm, encompassing the optic nerve head (ONH) and surrounding peripapillary sclera (PPS). All tissue manipulations were performed within 24h after death to minimise *post-mortem* changes in the tissue biomechanics (Girard et al., 2007). The excised scleral samples were then immediately fixed in 4% (w/v) PFA (Sigma-Aldrich, Poole, UK) and stored at  $4^{\circ}\text{C}$  until the WAXS experiments at Beamline I03 at the Diamond Light Source

(DLS) synchrotron facility (Harwell Science and Innovation Campus, Oxfordshire, UK). Specimens for the eye geometry experiments were frozen intact and stored at  $-80^{\circ}\text{C}$  until experimental analysis (Section 2.7).

### 2.2.1.3 Other samples

Sample preparation and WAXS data collection at Beamline I02 at the DLS on specimens from ten mammalian species were conducted by Dr Craig Boote and Dr Jacek Pijanka (Structural Biophysics Group, Cardiff University) (Table 2.2). All Bristol Zoo animals died of natural causes and all specimens were acquired up to 12h *post-mortem* and handled according to outlined procedures (Section 2.2.1.1 and 2.2.1.2).

Table 2.2 – Specimen details of the mammalian eyes utilised in the WAXS experiments. Animals are listed by increase in body size with both their common and scientific names provided. All specimens were scanned at different data acquisition steps at Beamline I02 at the Diamond Light Source (DLS) after collection from appropriate sources.

Name	Laboratory Mouse	Northern Tree Shrew	Guinea Pig	Black Lion Tamarin	Azara's Agouti	Lesser Mouse-deer	Red Panda	North American River Otter	Domestic Pig	Brazilian Tapir
Latin Name	<i>Mus musculus</i>	<i>Tupaia belangeri</i>	<i>Cavia porcellus</i>	<i>Leontopithecus chrysopygus</i>	<i>Dasyprocta azarae</i>	<i>Tragulus javanicus</i>	<i>Ailurus fulgens</i>	<i>Lontra canadensis</i>	<i>Sus scrofa domesticus</i>	<i>Tapirus terrestris</i>
Eye position on the head	Side	Side	Side	Front	Side	Side	Front	Front	Side	Side
WAXS step interval [mm]	0.15	0.25	0.3	0.25	0.3	0.3	0.3	0.3	0.5	0.5
Source	Charles River Laboratories	Colony at Cardiff University	Bristol Zoo	Bristol Zoo	Bristol Zoo	Bristol Zoo	Bristol Zoo	Bristol Zoo	Maddock Kembrey Abattoir	Bristol Zoo

### 2.2.2 Wide-angle X-ray scattering data collection

WAXS experiments were performed at the identical capability macromolecular crystallography Beamlines I02 and I03 at the DLS, the UK's national synchrotron. Beamline I02 measurements were conducted by Dr Craig Boote and Dr Jacek Pijanka, whilst the ones at Beamline I03 were carried out by the author (Table 2.1).

Specimens were recorded at regular intervals in a custom-modified fibre-diffraction setup, with 0.5mm spacing in the abscissa and ordinate directions for the human samples and selected intervals for the mammalian ones appropriate to the eye size (Table 2.2). Four scans on bovine posterior sclera were conducted, three with a step of 0.5mm and the final one at every 0.25mm. Specimens were mounted inside airtight Perspex (Lucite Group Ltd, Southampton, UK) chambers with Mylar (DuPont-Teijin, Middlesbrough, UK) windows, that magnetically attached to an integrated goniometer for directional translation between the 1s or 0.5s X-ray exposures (Figure 2.02). Each of the posterior sclerae was also wrapped in polyvinylidene chloride film to limit tissue dehydration during irradiation. The incident focused X-ray beam had a wavelength of 0.09795nm and 150x80µm cross-section dimensions, which was electronically recorded on a Pilatus-6MF silicon pixel detector (Dectris Ltd, Baden, Switzerland), situated 350mm behind the specimens (Pijanka et al., 2015; Markov et al., 2018). A final Mylar sheet with a lead beam stop was positioned to prevent undiffracted rays from reaching and damaging the detector. For pattern centration and camera length calibration, the X-ray reflection from powdered calcite ( $\text{CaCO}_3$ ) was used.

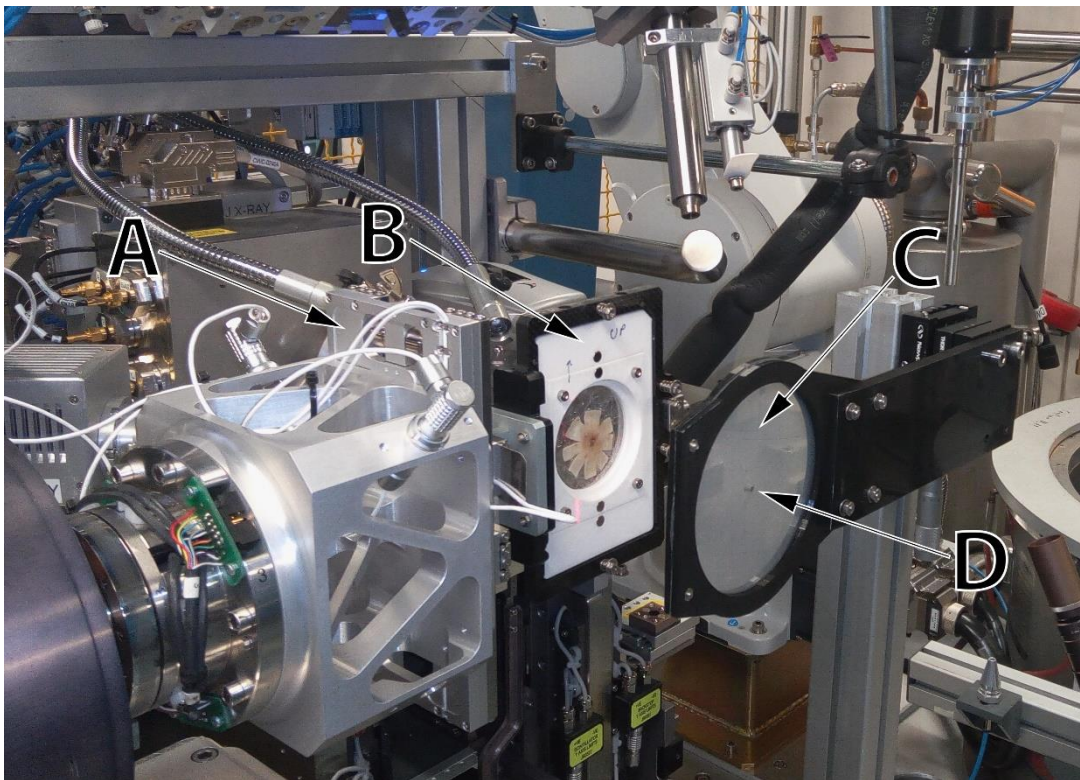


Figure 2.02 – Beamline I03 at the DLS operating in a custom fibre-diffraction setup and viewed from the detector side (detector out of shot). (A) Goniometer; (B) Sample holder with posterior human sclera; (C) Mylar sheet; (D) Lead beam stop.

### 2.2.3 Wide-angle X-ray scattering data analysis

The recorded pixel intensity patterns were stored and converted locally to tagged image files (TIF). The analytical procedures were performed via a bespoke MATLAB script (MATLAB 9.6; MathWorks, Natick, USA), composed by Dr Ahmed Abass and Mr Martin Sprang (Structural Biophysics Group, Cardiff University), adapting a previously used approach based on the use of Microsoft Excel macro procedures (Pijanka et al., 2012; Pijanka et al., 2014). The script was custom-modified by the author in the following ways: (I) combined several of the initial executable components; (II) superseded the necessity for conversion of the TIF images before processing them; (III) reduced the total and self-execution time; (IV) incorporated an option for exporting transparent background polar vector plot maps; (V) included further storage parameters, most notably for the collagen anisotropy.

The bulk collagen fibril angular orientation can be acquired from the ~1.6nm intermolecular signal in the WAXS diffraction patterns (Figure 2.03A). After fitting a unique radial power-law background scatter function and subsequently subtracting it (Figure 2.03B) for each scleral scanned point, the fibril content was calculated over 720 radial divisions, one at each 0.5° (Pijanka et al., 2012; Markov et al., 2018). Analysis of the resulting signal distribution and intensity can be used to assess: (I) the collagen fibril orientation distribution, represented as the preferential alignment over the azimuth angle  $\varnothing$  (between 0 and  $2\pi$ ); (II) the collagen anisotropic proportion, which is the ratio of the preferentially aligned collagen fibrils ( $I_a$ ) against the total collagen scatter ( $I_a+I_i$ ; where  $I_i$  is the isotropic collagen scatter) in Equation 1 (Figure 2.03C). The resulting signal peaks were normalised against the fluctuation of the X-ray beam current and exposure time, radially integrated and stored in angular bins. To accommodate for the equatorial X-ray scattering occurring at right angles to the fibril axis, a  $\pi/2$  rotation was performed in the total collagen scatter distribution (Meek and Boote, 2009). The anisotropic intensity distribution at each sampling point was represented as polar vector plots (Figure 2.03D). Subsequently, the individual plots were incorporated in a grid, with their position corresponding to their geometric coordinates on the scanned specimen. The degree of collagen anisotropy in the contour maps was represented with heatmap colour codes, with hotter colours denoting a greater alignment.

Equation 1: 
$$\text{Anisotropic proportion} = \frac{\int_0^{2\pi} I_a \partial\phi}{\int_0^{2\pi} (I_a + I_i) \partial\phi}$$

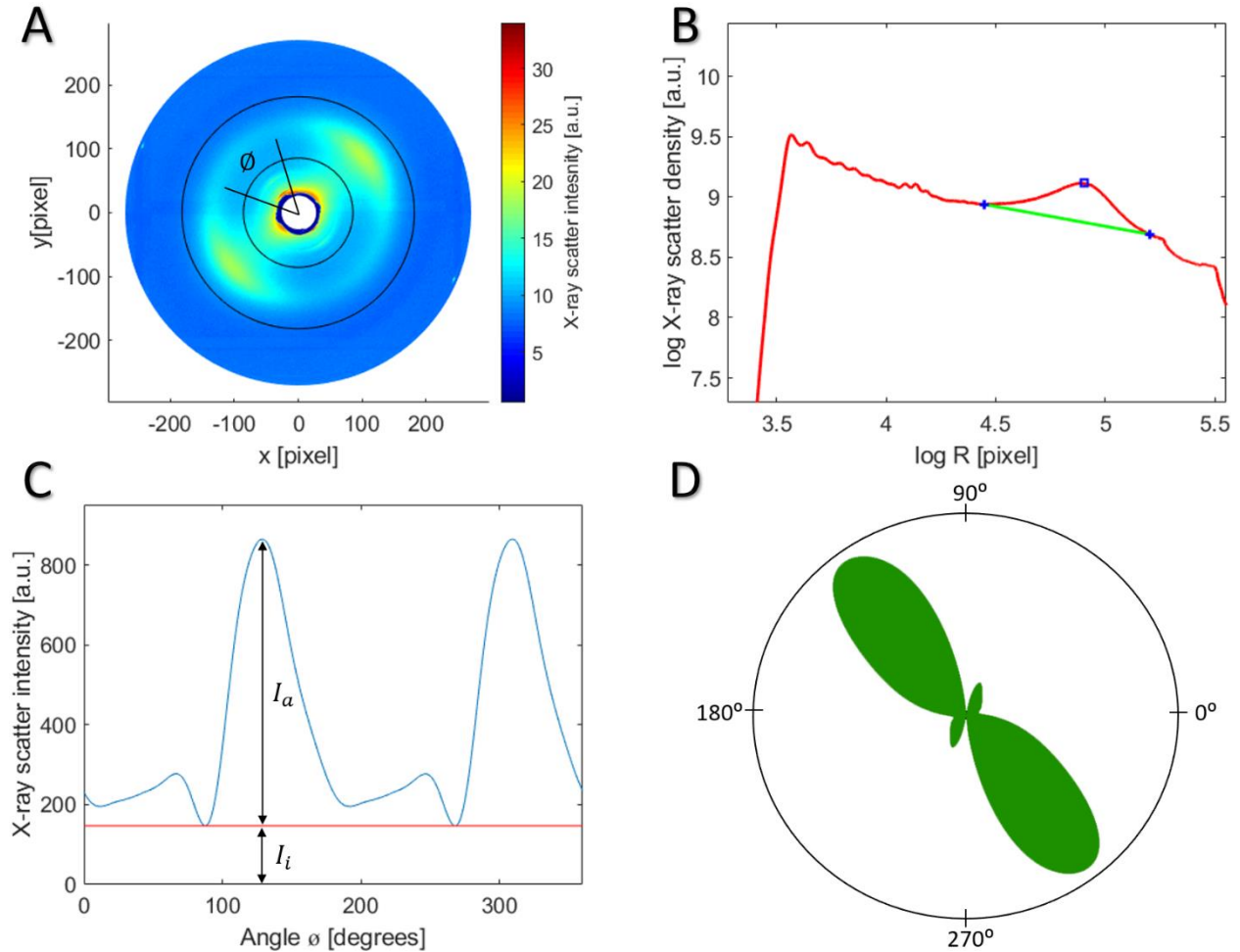


Figure 2.03 – Creation of polar vector plots from X-ray scattering experimental data from human peripapillary sclera (PPS) collagen fibrils. (A) WAXS angular intensity distribution, as a function of the azimuth angle  $\phi$  around the collagen peaks, from which the distribution of the fibril orientation can be extracted. The two-lobed characteristic pattern is indicative of uniaxial fibril distribution. (B) Radial intensity profile with a collagen signal peak (red line) with a fitted power-law background function (green line) through the pattern presented in A. The blue open circle marks the collagen intensity peak, whilst the blue crosses indicate the fitting points of the background function, which was fitted to each WAXS scatter pattern along 720 equally spaced radial directions. (C) Angular intensity profile of A represented as isotropic ( $I_i$ ) and anisotropic scatter component ( $I_a$ ), the latter arising from preferentially aligned collagen fibrils. (D) Polar vector plot of the collagen orientation distribution of A. The anisotropic collagen scatter is displayed in polar coordinates, with the length of each lobe proportional to the relative number of orientated collagen fibrils in that direction.

### 2.2.3.1 Assessment of collagen fibre angular displacement in myopic sclerae

For Chapter III analysis, the PPS was represented as a fixed region composed of 64 sampling points, circumferentially encompassing a 1.5mm wide ring around the optic nerve, whilst all others were considered part of the mid-posterior sclera (Pijanka et al., 2012). For further comparison between the individuals, the PPS was subdivided into four quadrants on the basis of the eye's anatomical directions: superior nasal (SN), superior temporal (ST), inferior temporal (IT), inferior nasal (IN). To assess possible myopic distortions in the normally predominantly circumferential collagen fibril alignment in the PPS, a comparison of the polar plot main angle direction of the individual myopic specimens and an average control of the non-myopic ones was conducted. For this purpose, an 'idealised' Gaussian polar vector plot angular distribution was created, representative of the size and orientation of the collagen fibril annulus in the PPS of an averaged control group. The idealised distribution closely followed the results of the emmetropic control group and was composed of three full inner and one partial outer ring, with a total angle range of 180° (Figure 2.04). The assigned angles in each quadrant were  $90/(n+1)$  for the angle step and  $n+2$  for the number of polar vector plots, where 'n' is the position of the concentric rings. To ascertain angular displacement, for all specimen the main angular direction of each of the 64 polar vector plots was compared point-for-point with the corresponding ones in the idealised distribution, with the mode of the difference positioned on a 0° to 90° scale.

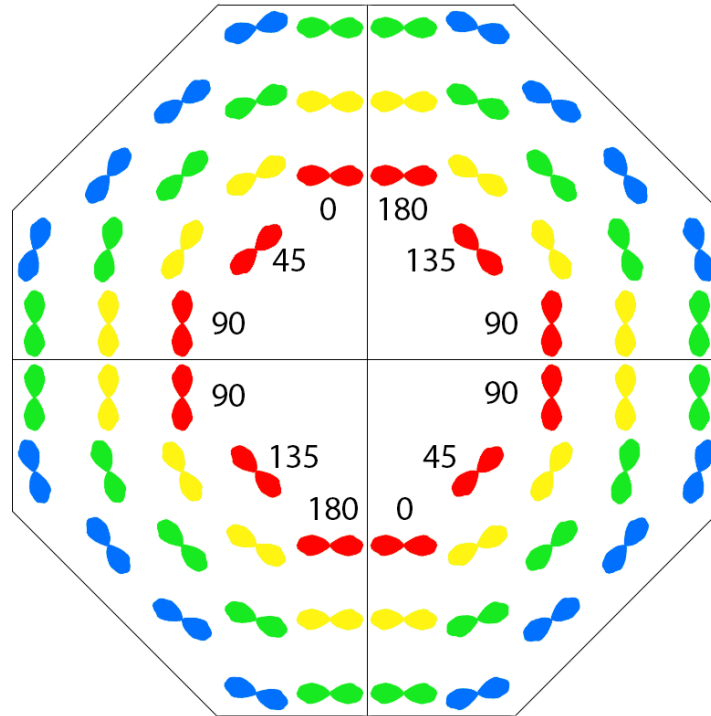


Figure 2.04 – Idealised mathematical distribution of polar vector plots circumferentially around the optic nerve. Numerical values from 0 to 180 denote the primary orientation angle in degrees. Per quadrant, the number of polar vector plots in each coloured ring is  $n+2$ , with an angular orientation step of  $90/(n+1)$ , with ‘n’ being the number of concentric rings going outwards. Note: Red ( $n=1$ ); Yellow ( $n=2$ ); Green ( $n=3$ ); Blue ( $n=4$ ).

## 2.3 Second harmonic generation imaging procedures

### 2.3.1 Bovine peripapillary sclera specimen preparation

Two bovine eyes (left and right; from two different animals) were obtained from a local abattoir and processed (Section 2.2.1.2). From each sclera, a 12mm diameter circular specimen, incorporating the ONH and surrounding PPS, was cut with fine dissection scissors. To retain proper orientation and curvature each of the two specimens was marked by an incision in the superior aspect, before immersion in 4% (w/v) PFA solution in 1x phosphate-buffered saline (PBS; Sigma-Aldrich, Poole, UK). Using a sledge cryo-microtome HM440E (Microm, Walldorf, Germany), 16 in-plane 160 $\mu$ m thick serial sections were cut from each specimen. Sections were mounted on polysine adhesion glass slides (Fisher Scientific, Loughborough, UK) in 1:1 solution of PBS and glycerol (Sigma-Aldrich, Poole, UK), helping retain hydration whilst minimising refractive index mismatching at the specimen/medium interface, and covered with 0.16-0.19mm thick rectangular

borosilicate glass coverslips (VWR International Ltd, Lutterworth, UK) (Girard et al., 2011; Pijanka et al., 2012). The anterior surface of the sections was positioned to face the incoming laser beam and indexed 1 to 16, going from the inner (closer to the choroid) to outer (proximal to the neural sheaths).

### 2.3.2 Collagen fibre visualisation using second harmonic generation microscopy

Non-linear second harmonic generation (SHG) microscopy was performed using a Zeiss laser scanning microscope (LSM) 880 META NLO (Carl Zeiss Ltd, Welwyn Garden City, UK) with an ultrafast Ti:sapphire tunable infrared (680-1080nm) Chameleon Vision II laser (Coherent Lasers, Ely, UK). The laser operated at 800nm with a pulse duration of 140fs and 80MHz repetition rate, whilst the signal was detected in the forward scatter direction after passing through a 400nm (6nm bandwidth) filter. The field of view of each tile before stitching was  $425 \times 425 \mu\text{m}$ , as a result of using a Plan-Apochromat 20x/0.8 M27 water immersion objective lens. The scan area was  $65.2 \text{mm}^2$  in 21x21 tiles, with a 10% tile overlap for stitching and collected on an integrated motorized x-y stage. Individual tiles were recorded at a 512x512 pixel resolution, averaging each line twice, with pixel grid element size of  $0.83 \times 0.83 \mu\text{m}$  and dwell time of  $1.03 \mu\text{s}$  per pixel. 8-bit images were recorded with non-de-scanned NDD2 detectors and saved as Zeiss file format (CZI). Tile stitching was performed post-image acquisition in Zen Blue 2.2 software package (Carl Zeiss Ltd, Jena, Germany).

## 2.4 Filum Trace – bespoke image analysis approach development

Over the last decade, a variety of quantitative imaging analysis approaches have been developed to measure orientation and other parameters of biological fibrillar structures (Section 2.5). One commonly employed approach evaluates image pixel intensity and distribution in their spatial frequencies by applying a discrete Fourier transform. This permits superior recognition of structural alignments, such as the one exhibited by the collagen and cytoskeletal networks (Sander and Barocas, 2009). In collaboration with Dr Jacek Pijanka, a bespoke automated imaging technique for assessment of fibrillar organisation was developed in MATLAB 9.6 (MathWorks,

Natick, USA). The algorithm ‘Filum Trace’ (Name subject to change) utilises the Fourier transform method to mimic the well-established WAXS analysis technique (Section 2.2.3) to create montages of polar vector plots. An individual image, or stack of images, is first divided into tiles of identical user-assigned size. This is followed by an image decomposition solution to avoid image edge discontinuation artefacts when applying subsequently a discrete Fourier transform. From the resulting power spectrum the angular distribution is extracted to create an integrated grid of preferential fibrillar orientation, with polygon colouring representative of the aligned fibre content, analogous to the X-ray orientation analysis presented in Section 2.2.3. The technique was validated using SHG results of the collagen circumferential fibrillar distribution in human PPS against corresponding measurements from WAXS (Pijanka et al., 2019).

### 2.4.1 Image partitioning

Collected laser microscopy images are first loaded into MATLAB in the form of a cell array, as a matrix composed of other matrices, which allows for fast handling of high-resolution image stacks. Following that, the image matrices are partitioned into individual tiles for the subsequent Fourier transform analysis. The tile sampling size is adjustable to accommodate different tissue types and image resolutions. For example, highly fenestrated and porous tissue, such as the LC, require smaller tiles to accurately represent the individual beam architecture, whilst the densely interwoven collagen fibres in the sclera can be better visualised and quantified by larger tiles. There is, however, an empirically based restriction in the smallest partition tile size that can be employed; application of Fourier transform to an image below 16x16 pixel results in inaccurate and false data. As the assessment of fibre parameters is on the basis of the tile grid and not single pixel intensity, this further underlines the necessity for higher-resolution input.

### 2.4.2 Fast Fourier transform

Fourier transform is a widely utilised mathematical approach in image processing, as it decomposes a signal’s original domain into the composing frequencies. This has many advantages, as for example, it is much easier and more effective to apply functions, such as filtering, to an

image's frequency domain. Instead of adjustments to the pixel intensities, high amplitude frequencies, which form background noise in the original time domain, can be discarded, making a significantly faster and more accurate solution. Discrete Fourier transform, such as the fast Fourier transform (FFT), is a faster variation of the standard approach, as it reduces the calculation complexity by only selecting discrete frequency values, working on signal lengths of  $2^N$  pixels. A 2D FFT of an image trigonometrically decomposes it to a superposition of the sine and cosine components, along the abscissa and ordinate, representative of the signal intensity changes in the original domain. Thus, in biological tissue images abrupt local extremums will be indicative of fibre boundaries, allowing the tracking of their orientation. The utilisation of 2D FFT has found wide application in the study of the collagenous extracellular matrix (ECM) through SHG microscopy images (Matteini et al., 2009; Cicchi et al., 2010; Mercatelli et al., 2017; Sugita and Matsumoto, 2017).

Before performing FFT to each partitioned tile, a notable, often overlooked, artefact from the processing needs to be addressed for optimal results. 2D FFT was performed on three photographs (Figure 2.05), with the corresponding Fourier power spectrums optimised for better visualisation (Pijanka et al., 2019). As digital images are not periodic at their boundaries the FFT function 'jumps' over the four borders of the image and never returns to zero, resulting in a noticeable cross pattern artefact known as the Gibbs phenomenon (Gottlieb and Shu, 1997). When the input has many well-resolved details the produced FFT power spectrum will be intense and the cross-shaped artefact will be overshadowed (Figure 2.05A and B). However, images relatively void of detailed structures exhibit a dominant cross artefact, which does not provide any image-relevant information (Figure 2.05C and D). Furthermore, images with highly aligned objects will have strong corresponding patterns and the Gibbs phenomenon can cause a mistaken interpretation and lead to false results (Figure 2.05E and F). Unfortunately, many biological studies employing image 2D FFT neglect to accommodate or correct for this artefact (Matteini et al., 2009; Cicchi et al., 2010).

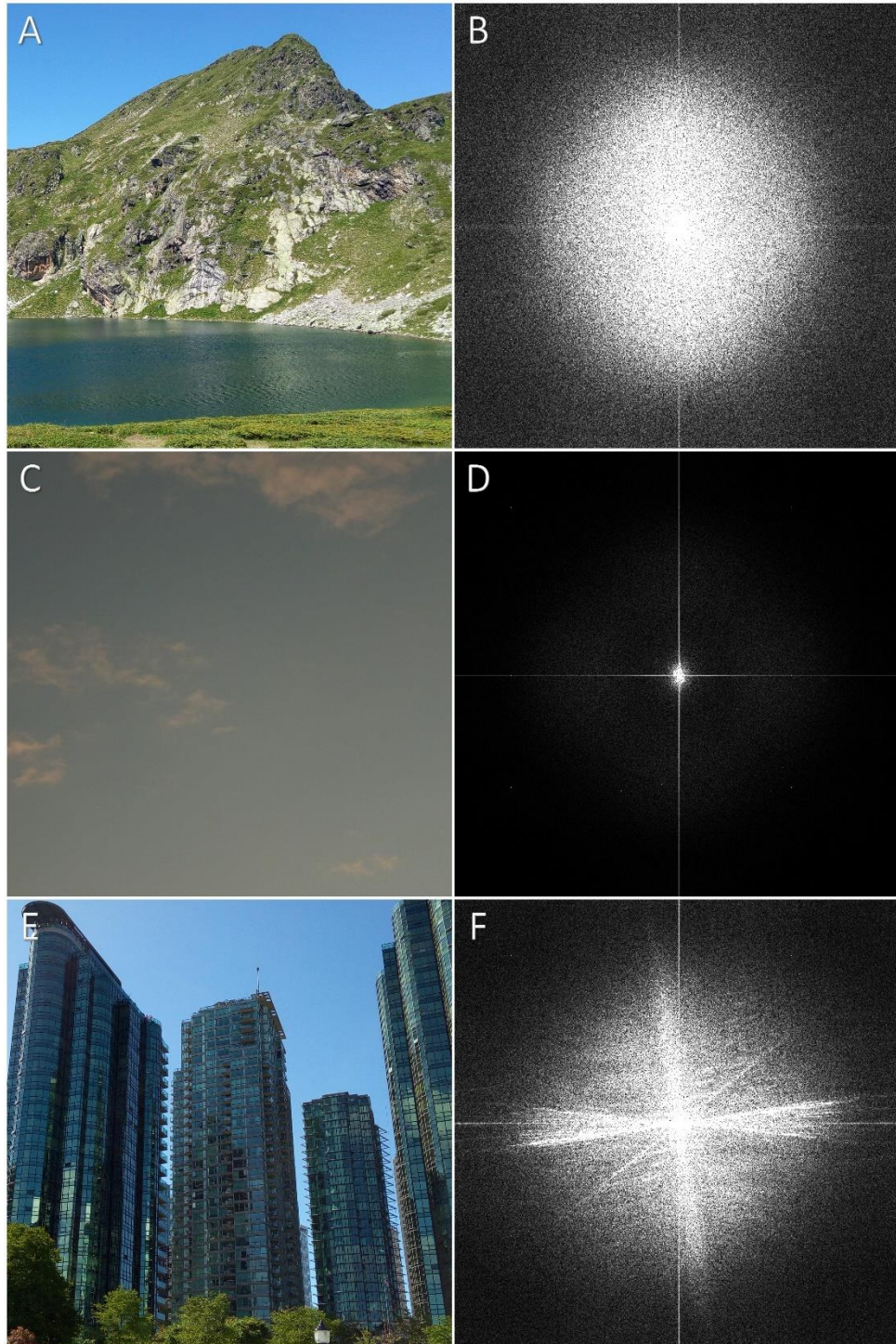


Figure 2.05 – Initial input images and corresponding 2D fast Fourier transform (FFT) frequency power spectra. Images with a spread of features (A) exhibit a strong signal in frequency space and less pronounced cross pattern artefact (B). Images mostly devoid of features (C) exhibit a strong cross pattern artefact in frequency space (D).

Images with distinguishable orientated features (E) exhibit multiple intensity spreads in frequency space, which can lead to a false inclusion of the cross pattern artefact as part of the actual signal (F).

Note: Frequency power spectra are set to an identical intensity range.

### 2.4.2.1 Apodization

The standard approach of resolving the Gibbs phenomenon is by applying an apodization damping window function to the input image. This enables a smoother transition at the image edges, ameliorating the inherent discontinuities. A commonly utilised function is the Hann window, which is a projection of a cosine function (Equation 2), having a maximum (1) at the centre of the window and decreasing to a minimum (0) at the borders (Bees and Hill, 1997; Hardy et al., 2013).

Equation 2: 
$$H(x) = \cos^2\left(\frac{\pi x}{2a}\right) = \frac{1}{2}\left[1 + \cos\left(\frac{\pi x}{a}\right)\right]$$

The input raster image is multiplied by a same-sized Hann window, which can be generated, for example, by the ImageJ macro ‘Hann Window’ and the resulting output matrix can be represented again as an image (Figure 2.06) (Burger and Burge, 2016). This, however, degrades the resolution in frequency space and also, unfortunately, can omit a large portion of the details in the peripheral image (Figure 2.06C). The notable loss of pixel intensity and structural formations is a significant issue when applied to multiple small tile partitions, which necessitates application of a less invasive solution to the Gibbs phenomenon.

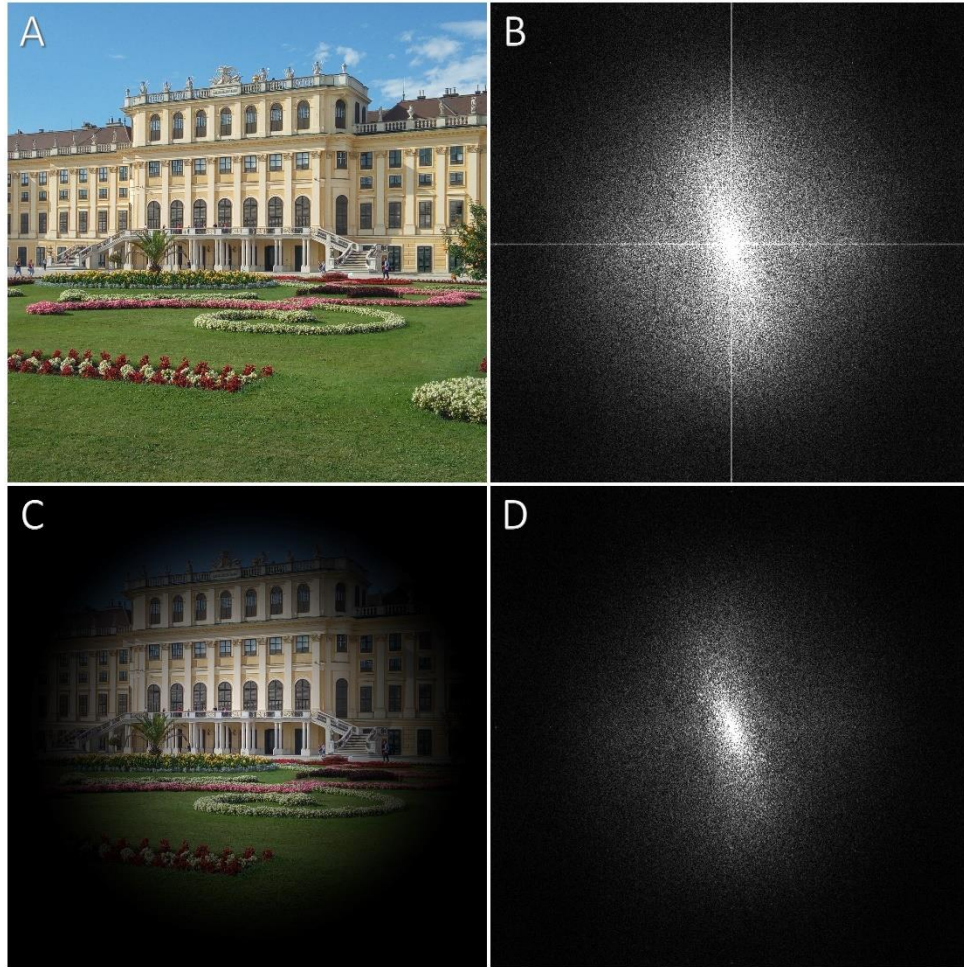


Figure 2.06 –Input (A) and apodized image (C) in the original and frequency space (B, D). (A) Original input image with a 2,048x2,048 pixel resolution; (B) Corresponding 2D FFT frequency power spectrum of A with a notable cross pattern artefact; (C) Resulting 2,048x2,048 pixel image after multiplication of A with a 2,048x2,048 pixel Hann window; (D) Corresponding 2D FFT frequency power spectrum of C with a decreased signal intensity in comparison to B and a lack of a cross pattern artefact.

#### 2.4.2.2 Periodic plus smooth image decomposition

A promising alternative solution to apodization is the periodic plus smooth image decomposition (P+SID), which removes the cross pattern artefact whilst much more effectively preserves the image composition (Moisan, 2011). The algorithm utilises Poisson's equation to separate the input image into two components: (I) the periodic component that contains almost the entire image information (Figure 2.07C), which after 2D FFT does not exhibit the Gibbs phenomenon (Figure 2.07D); (II) the smooth background component, which whilst presenting very slow variations inside the image domain (Figure 2.07E), however, gives rise to the cross pattern artefact

in the frequency domain (Figure 2.07F), as this component contains specifically the image edge discontinuities. By subtracting the smooth component from the original image, the periodic component can reliably be used for further image processing and extraction of relevant data.

The P+SID has been applied to several computational works and research studies (Hovden et al., 2015; Brisard et al., 2019). Incorporation of P+SID to laser microscopy image tiles resulted in negligible alterations in signal contrast and intensity. To evaluate the retention of input image information, a comparison of pixel signal intensity alteration with the raw image between the apodized and periodic component ones was carried out (Figure 2.08). A heatmap colour representation was performed, with none or very minimal changes represented in green, whilst decreases in signal were depicted with colder colours and increases with warmer colours. Apodization results in a loss of signal information for the majority of the image, with the centre being close to the original in terms of values. For Figure 2.08B the remaining pixel intensity corresponded to only 25.5% of the input, whilst concurrently P+SID retained 100.0% of the signal intensity (Figure 2.08C). However, this interpretation is partly misleading, as P+SID accommodates the contrast and background of the entire image; the algorithm decreases the intensity in brighter regions and increases the pixel values of darker areas by the same amount, therefore preserving the same integrated intensity sum as the raw image. As the photographic images in Figure 2.07 were 8-bit, the minimal pixel intensity was 0, visualised as black, making it not possible to have negative numbers. This was, however, possible for Figure 2.08, where the pixel values were directly handled in matrices and subtracted, exemplifying this characteristic progressive intensity change for the smooth P+SID component. Even if there is minimal alteration, P+SID permits the overall structure to be kept intact to a significantly higher level than the typically employed windowing functions. Therefore, P+SID was successfully integrated into the Filum Trace algorithm.

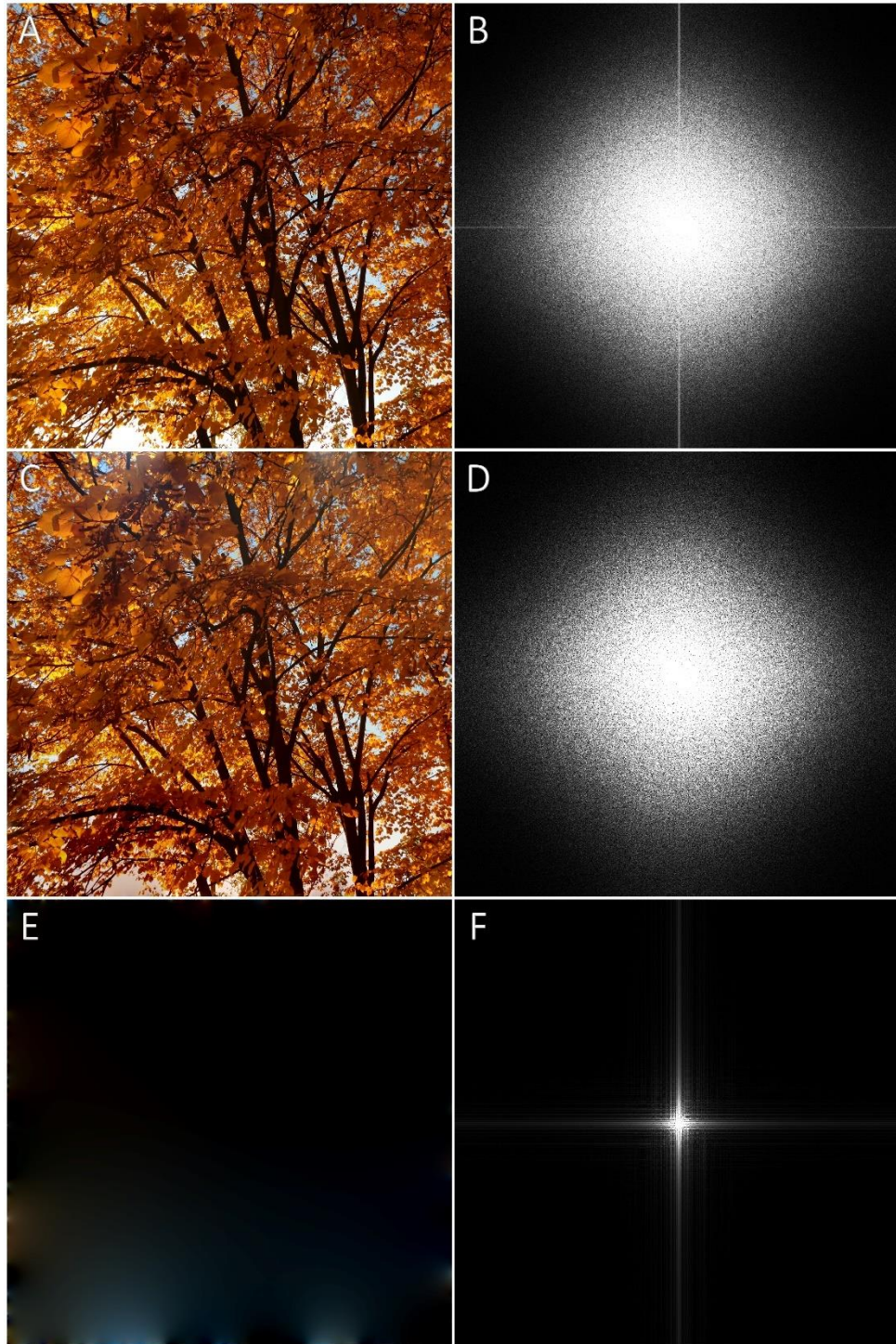


Figure 2.07 –Input (A, B), periodic plus smooth image decomposition (P+SID) periodic (C, D) and smooth (E, F) components in the original (A, C, E) and frequency (B, D, F) space. (A) Original input image with a 2,048x2,048 pixel resolution; (B) Corresponding 2D FFT frequency power spectrum of A with a notable cross pattern artefact; (C) Inverse FFT of the periodic component after application of P+SID; (D) Corresponding 2D FFT frequency power spectrum of the periodic component, revealing the same intensity spread as B but with a lack of cross pattern artefact; (E) Inverse FFT of the smooth component after application of P+SID; (F) Corresponding 2D FFT frequency power spectrum of the smooth component, revealing only the cross pattern artefact.

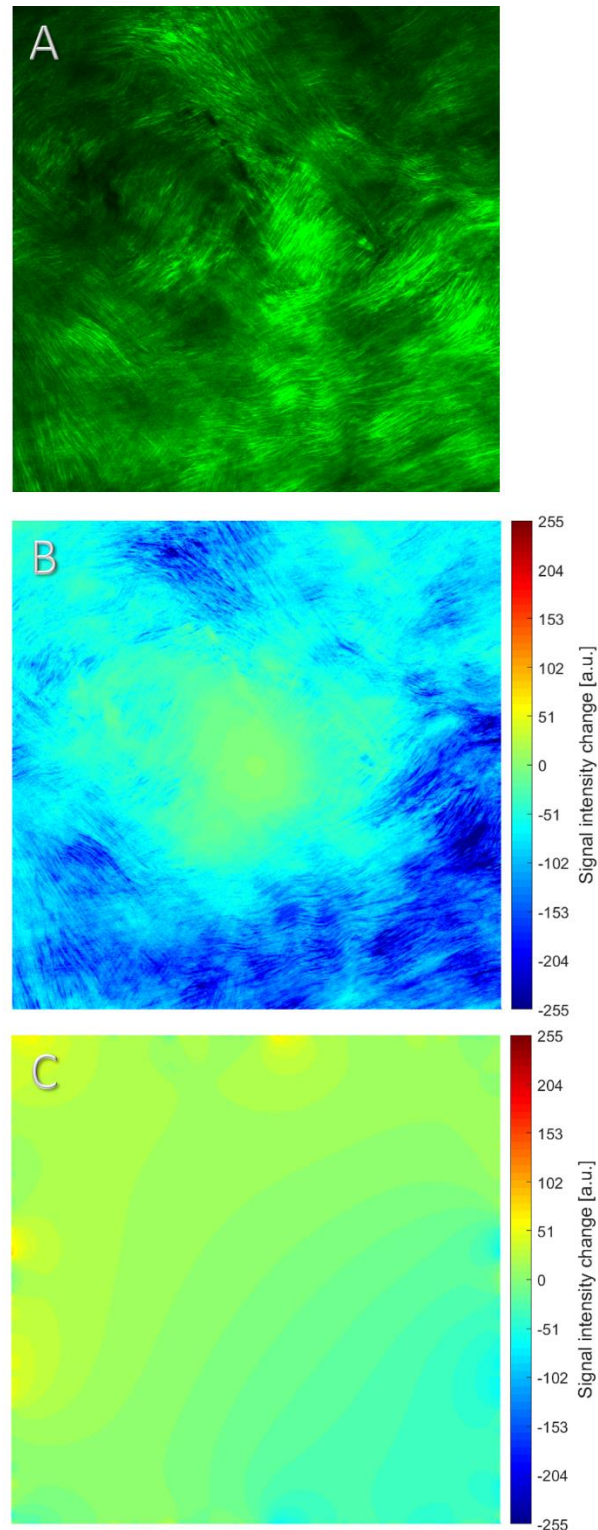


Figure 2.08 –Signal intensity alterations after applying apodization and P+SID. Colder colours are indicative of loss of signal intensity, warmer colours of increase in intensity, whilst green is no change (0). (A) 512x512 pixel resolution SHG image of interwoven collagen fibres within bovine PPS tissue; (B) Corresponding signal intensity changes to A after utilising a Hann windowing function; (C) Corresponding signal intensity changes to A after utilising the periodic component of P+SID.

### 2.4.3 Fibre orientation distribution analysis

The signal intensity within the frequency power spectrum is then integrated radially and the numerical values are placed into angular bins at every  $0.5^\circ$ . Extracting the signal amplitudes in the frequency domain permits an improved fibre recognition, whilst at the same time excluding frequencies from other structures (Ayres et al., 2006; Sander and Barocas, 2009; Kartasalo et al., 2015). Following analogous procedural steps to the WAXS analysis method (Section 2.2.3), the power spectrum amplitudes for each tile were plotted (Figure 2.09), shifted by  $90^\circ$ , from which a polar vector plot, representative of the fibrillar orientation and distribution, could be created (Figure 2.10). The angular signal distribution of the SHG image of a bovine PPS region (Figure 2.08A), with and without edge artefact corrections, were compared (Figure 2.09). The cross pattern artefact in the original image was manifested as an erroneous sharp peak observed at  $0^\circ$  and  $180^\circ$ , along with the less pronounced ones at  $90^\circ$  and  $270^\circ$ . Edge correction via apodization introduced a false signal increase, around  $150^\circ$  and  $330^\circ$ , with a greater amplitude than either the input or P+SID image, which closely resembled the former, apart from the Gibbs phenomenon peaks. Furthermore, when the absolute signal intensities were compared, the multiplication with a Hann function resulted in an overall decrease in amplitude, whilst the P+SID periodic component very closely followed the raw image signal (Figure 2.09B) and still effectively removed the cross artefact peaks.

The signal amplitudes were represented in polar coordinates as polygon vector plots (Figure 2.10). As the angle of the longest vector is indicative of the primary direction of preferred fibrillar orientation, it was calculated for the three different modalities. The main angle for the input image polar vector plot, excluding the peaks from the cross pattern artefact, was  $18.5^\circ$ ,  $56^\circ$  for the apodized one and again  $18.5^\circ$  for the P+SID one. This further reinforces the necessity for accurate handling of the inherent FFT Gibbs phenomenon, hence P+SID was adopted in the subsequent bovine PPS SHG image analysis (Chapter IV).

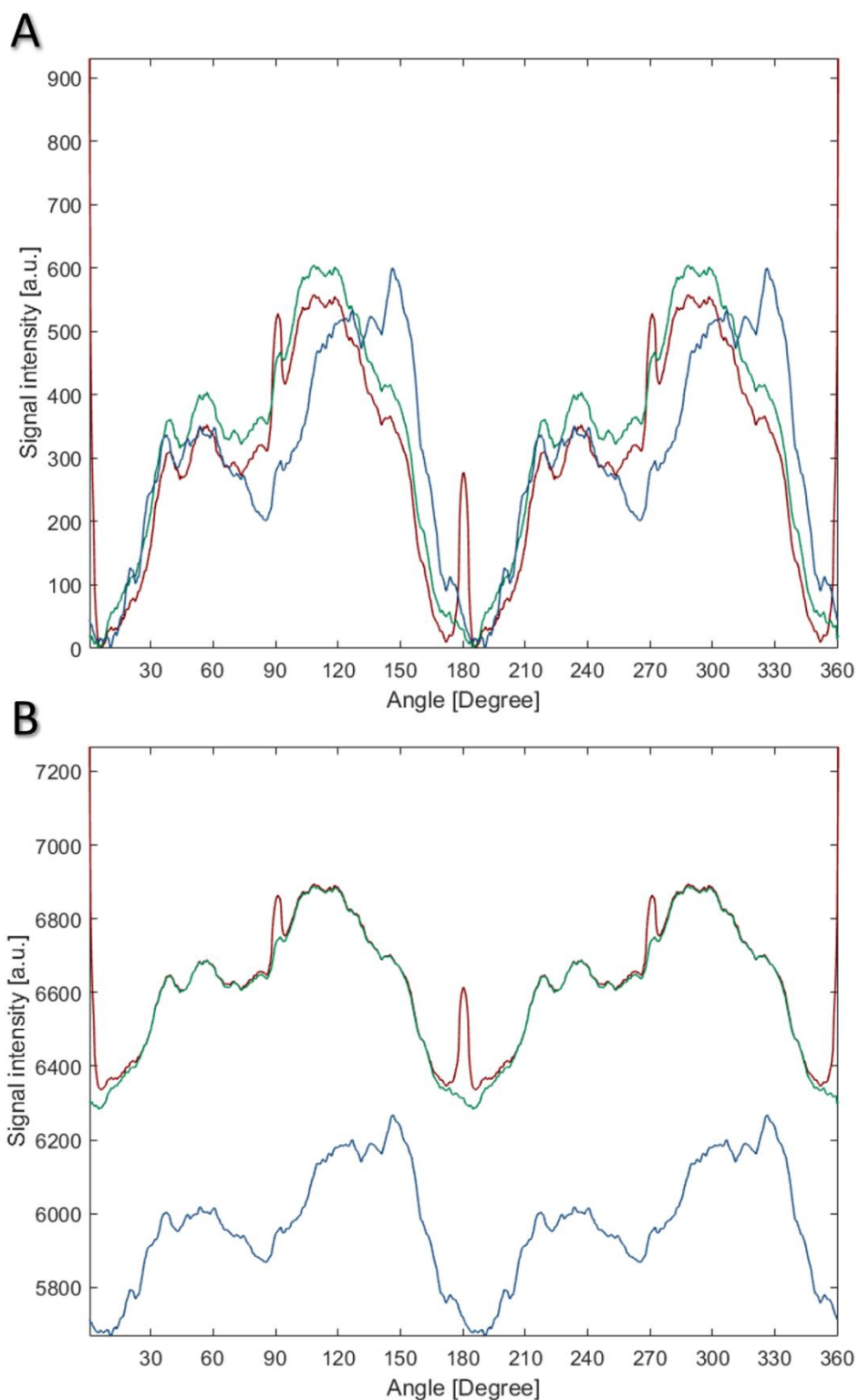


Figure 2.09 –Angular signal distribution amplitudes for the same image with no correction (red), apodization (blue) and P+SID periodic component (green), with implemented background subtraction (A) or overall intensity (B). Applying a Hann function caused an overall amplitude decrease, as well as changes in the peak distribution shape. Concurrently, the periodic component was closely reminiscent of the original angular distribution, apart from the targeted removal of the cross pattern artificial peaks.

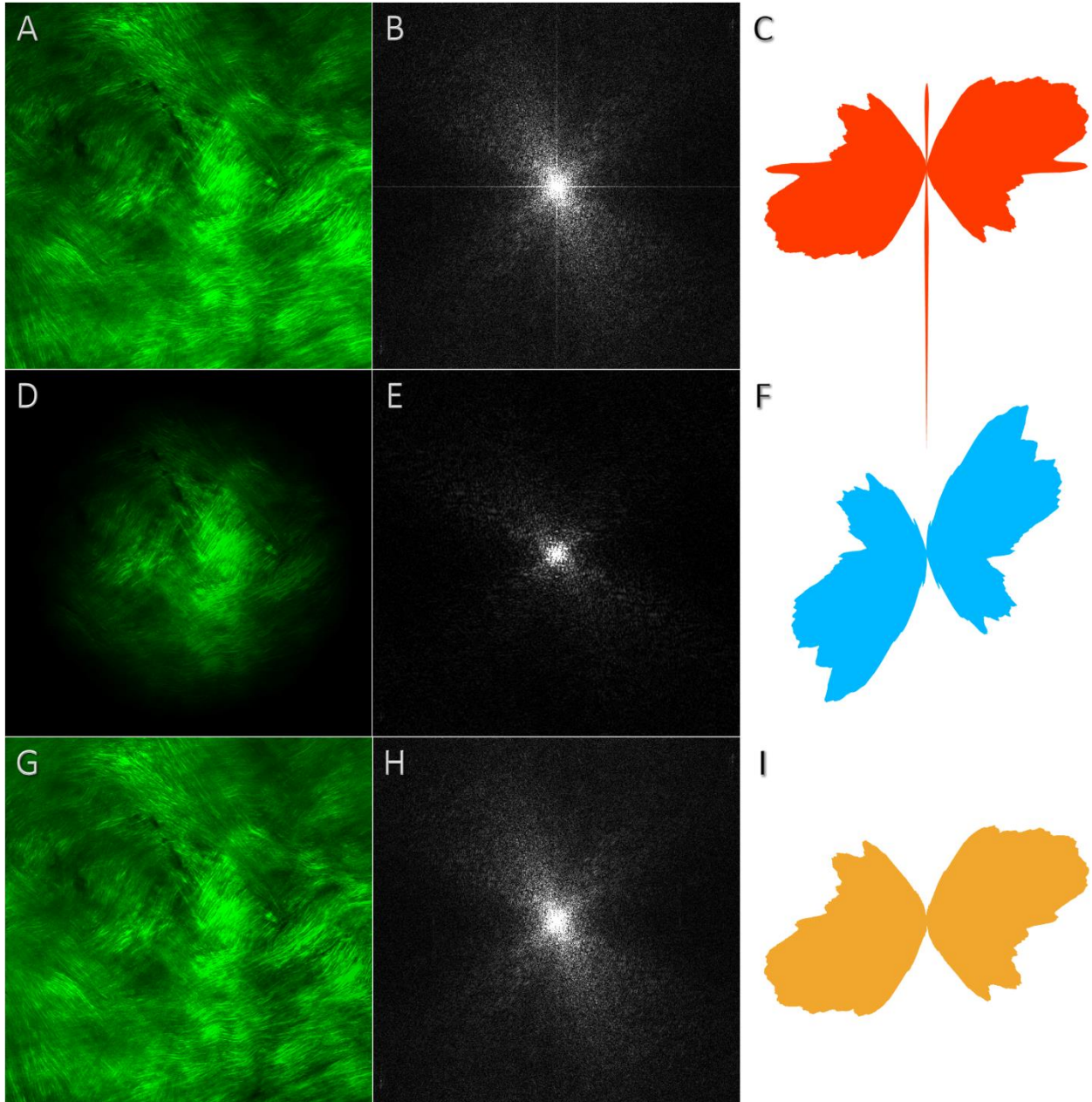


Figure 2.10 –Input, apodized and P+SID periodic component images before (A, D, G) and after 2D FFT (B, E, F), with corresponding polar vector plots (C, F, I). No applied correction (A) results in a cross pattern artefact in the frequency power spectrum (B), which is carried over as erroneous sharp peaks in the polar vector plot (C). Application of a Hann window function causes a loss of peripheral signal (D) and removes the cross artefact in the frequency power spectrum (E), whilst also changing the intensity distribution, as evidenced in the alteration to the polar vector plot lobe shapes (F). The P+SID periodic component has a more evenly distributed signal intensity (G), no cross pattern artefact in the frequency power spectrum (H) and produces a polar vector plot identical to the input one in C, apart from the targeted removal of the cross pattern artificial peaks (I). Hotter colours of the polar vector plots correlate to greater alignment, with the one after P+SID (I) being much closer in terms of anisotropy to the original (C) than the apodized one (F).

### 2.4.4 Polar vector plot mapping

As a final step, the individual polar vector plots were montaged together into two-dimensional maps, reminiscent of the WAXS analysis. The polar vector polygons from each partitioned tile can be shown overlaid onto the input SHG images, confirming visually the degree of alignment (Figure 2.11). Colour coding of the polar vector plots denotes the scaling of the intensity values. It should be noted that for SHG microscopy images, the signal intensity corresponds to the fibrillar collagen content, whilst with confocal microscopy the signal intensity cannot be considered absolute. Fluorescent microscopy images are affected by several parameters, most notably the microscope setup and the strength of antibody binding reactions, thus making it inaccurate to compare individual images. In this respect, the use of SHG is advantageous for quantitative fibre orientation analysis.

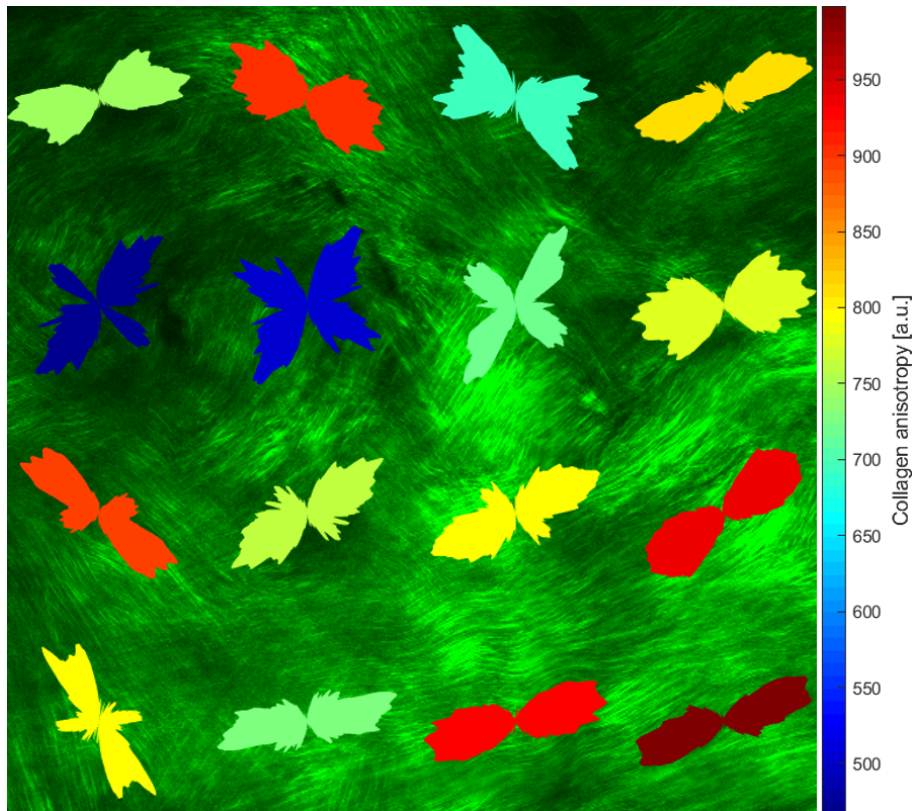


Figure 2.11 – 512x512 pixel resolution SHG image of interwoven collagen fibres within bovine PPS tissue with overlaid 16 polar vector plots, representative of corresponding underlying 128x128 pixel partition tiles. The orientation of the polar plots illustrates the average collagen fibre directional spread for the underlying tile, whilst the colouring is indicative of the level of anisotropy, with hotter colours correlating to greater alignment. The employed Gibbs phenomenon correction method was P+SID.

The Filum Trace method was also demonstrated to provide accurate, representative results for fibre orientation in other collagenous tissues, including rat tail tendon and chick cornea (Pijanka et al., 2019). Furthermore, it can also be used in measurement of F-actin cytoskeleton anisotropy in cultured fibroblasts, with future tests on vimentin intermediate filaments and microtubules also envisioned (Pijanka et al., 2019). Whilst for the purposes of the current work only the angular distribution was utilised, the bespoke method can also calculate the degree of fibre recruitment, the anisotropic proportion and total signal per tile (Pijanka et al., 2019). A potential future implementation is generation of angular histograms of primary polar vector plot directionalities.

## 2.5 Image data analysis

### 2.5.1 ImageJ and FibrilTool

ImageJ is a free-to-use software package for image processing and analysis, with the Fiji distribution focusing on biological images (Schindelin et al., 2012; Jensen, 2013). The plugin FibrilTool allows the quantitative assessment of the anisotropy of fibre arrays at their average orientation by using the average local nematic tensors over an area (Boudaoud et al., 2014). Isotropically distributed fibres yield anisotropy values close to 0, whilst uniaxially arranged ones should equal 1. Another benefit is that this plugin is less sensitive to noise in fluorescent images and thus does not require smoothing or other pre-processing. Furthermore, FibrilTool does not use the pixel intensity to discriminate between filaments and their surroundings, which also reduces the number of biases. As this plugin has been validated in a number of studies for a range of fibrillar structures, including F-actin, microtubules and collagen, it was the preferred tool for quantifying alignment (Boudaoud et al., 2014; Vergara et al., 2015; Ayala et al., 2017; Deepak et al., 2017; Harman et al., 2017; Daghma et al., 2018; Raquel et al., 2018). One of the prerequisites in using FibrilTool is creation of a region of interest (ROI) that encompasses only the structures to be analysed, for example, a single cell. Apart from the fibre anisotropy and mean orientation, the ROI can be used to assess the total area of the encompassed cell. Based on the shape of the ROI a measure of cell eccentricity can be calculated as the ratio between the second-longest (cellular width) and the longest axis (cellular length), which are perpendicular to each other. It must be noted that the eccentricity value is the inverse of the standard way of representing the aspect ratio,

which was performed to have the eccentricity between 0 and 1, with values closer to 0 signifying a more elongated shape.

### 2.5.2 OrientationJ

Another tensor-based ImageJ plugin is OrientationJ, which similarly to FibrilTool can provide a numerical assessment of the filament distribution as percentage coherency, as well as a directional angle (Rezakhaniha et al., 2012). Unlike the FibrilTool sum of all fibrillary orientations, OrientationJ determines the dominant direction by constructing a structure tensor based on the partial first derivatives of all pixels in an ROI. The plugin also provides a colour survey, where all of the degrees are colour coded, from  $-90^\circ$  to  $+90^\circ$ , which makes it easy to visually evaluate the angular distribution and variation. OrientationJ has also been applied to a range of studies, including ones on collagen and F-actin orientation (Perry et al., 2013; Palmieri et al., 2015; Clemons et al., 2018).

### 2.5.3 CT-FIRE and CurveAlign

CT-FIRE is part of the same distribution as CurveAlign, with both of them being standalone MATLAB-executables (Bredfeldt et al., 2014; Liu et al., 2017). The package uses the curvelet transform (CT) denoising and fibre extraction (FIRE) algorithms to identify and automatically extract fibres and associated parameters (Starck et al., 2002). Similar to the FFT in Filum Trace, the CT-FIRE curvelet transform calculates the orientation based on the entire ROI and not on individual pixels. The traced fibres can be represented as coloured overlays and their length and width can be assessed. Thus, parameter interpretation should be carried out carefully, as the absolute value will be dependent on the pixel element size and might not be representative of the actual filament size. However, comparison between groups is a viable approach. CT-FIRE produces fast and reproducible results and can handle and segment a large number of fibres in the same image. Furthermore, CT-FIRE was initially created for evaluating collagen fibres from SHG images (Bredfeldt et al., 2014; Hanley et al., 2015; Drifka et al., 2016; Hutson et al., 2016; Daghma et al., 2018; Kiss et al., 2018). The CurveAlign module can be performed in batch mode like

CT-FIRE, however, in contrast does not provide individual fibre segmentation. It produces an evaluation for the total fibre alignment, with values ranging from 0 to 1, reminiscent of the FibrilTool ones.

### 2.5.4 CytoSpectre

CytoSpectre is an automated tool that allows batch image spectral analysis, developed in MATLAB (Kartasalo et al., 2015). The algorithm includes an FFT, followed by extraction of the detailed component in the power spectrum, representative of more defined features, such as fibrillar structures. This selection allows the exclusion of low-resolution objects and windowing artefacts, thus circumventing the necessity for corrections of the Gibbs phenomenon. Following the previously listed software packages, CytoSpectre does not require any pre- and/or post-processing steps and has been validated against FibrilTool (Kartasalo et al., 2015). As the relevant data is extracted in the frequency domain this allows the package to handle images with low signal-to-noise ratio, such as with high fluorescent background. For assessment of alignment, it provides the circular variance, a measurement of the angle distribution, with value spread opposite to the established parameters, with 0 being anisotropic and 1 isotropic. An alternative is the angular standard deviation, bounded in the interval from 0 to  $1.41 (\sqrt{2})$ . In addition, CytoSpectre provides image polar histograms, comparable to the Filum Trace polar vector plots (Hyysalo et al., 2017; Skogberg et al., 2017; Rajan et al., 2018).

### 2.5.5 Chromatin condensation parameter

Gene expression is dependent on the level of compaction of chromatin in either the condensed heterochromatin or active euchromatin, which are organised in high-structured domains (Albiez et al., 2006). As mechanical loading can affect the condensation of chromatin, an image analysis approach based on the Sobel edge detection was applied (Sobel, 1978; Irianto et al., 2014). Image edges represent greater extrema in the image intensity, with the contrast in nuclei being indicative for different level of chromatin structure. This method was first proposed by Chen and colleagues and fully described and refined by Irianto et al. (Chen et al., 2012a; Irianto et al., 2014). Based on

the Sobel edge detection, an objective parametric assessment of chromatin compaction is produced, referred to as the chromatin condensation parameter (CCP). As the parameter calculates a ratio between the registered edges in pixels against the total pixel area, it can be compared between differently sized nuclei.

## 2.6 Cell mechanical loading procedures

### 2.6.1 Bovine scleral fibroblast experiments

#### 2.6.1.1 Bovine scleral fibroblast isolation: explant crawl-out

Scleral fibroblasts were obtained from six bovine eyes collected from a local abattoir and cleaned of external remaining tissue as previously described (Section 2.2.1.2). An incision was made with a scalpel and a circle with a diameter of around 25mm was cut from the sclera, encompassing the ONH and the surrounding PPS. Sterile 6mm diameter biopsy punches (Selles Medical, Hull, UK) were used to cut six pieces of each PPS, approximately 6mm away from the optic nerve. The explants were first disinfected by dipping them for 10-20s in 3.3% (v/v) betadine (povidone-iodine; IDS Manufacturing Limited, Pathumthani, Thailand), diluted from a 10% stock with Hank's balanced salt solution (HBSS; Invitrogen, Paisley, UK). Afterwards, explants were immersed in 1xPBS for 30-60s and washed four times in high strength antibiotics (HBSS containing 400µg/ml penicillin and 400U/ml streptomycin (Invitrogen, Paisley, UK)), followed by one final wash (HBSS containing 100µg/ml penicillin and 100U/ml streptomycin). The explants were further cut into three finer strips, each roughly 2mm in width, and transferred into individual wells of 6-well culture plates (Greiner Bio-One International GmbH, Kremsmünster, Austria), filled with 4ml of Dulbecco's Modified Eagle's Medium (DMEM)/Hams F12 with Glutamax™ (Invitrogen, Paisley, UK) containing 20% (v/v) foetal calf serum (FCS; Invitrogen, Paisley, UK) and 100µg/ml penicillin and 100U/ml streptomycin. Explants were incubated at 37°C, 5% (v/v) CO<sub>2</sub> with a humidified atmosphere in a Water-Jacketed, US Autoflow Automatic CO<sub>2</sub> Incubator NU-4950E (Nuaire, Caerphilly, UK). Media was changed the next day followed by media renewal once every three days thereafter.

### 2.6.1.2 Bovine scleral fibroblast cultivation

After reaching over 80% confluence, scleral explants and media were discarded and 0.25% (v/v) trypsin-ethylenediaminetetraacetic acid (EDTA; Invitrogen, Paisley, UK) was added to each well. Fibroblasts were gently agitated at 37°C for 15min, and cell suspensions pelleted by centrifugation at 157g for 5min on a benchtop IEC Centra CL2 centrifuge (Fisher Scientific, Loughborough, UK). The cell pellets were then resuspended in 30ml of fresh media, with 15ml of the solution being transferred to 175cm<sup>2</sup> Corning™ cell culture flasks (Sigma-Aldrich, Poole, UK), along with 20ml of media and 50µg/ml ascorbate-2-phosphate (Sigma-Aldrich, Poole, UK) to promote collagen synthesis (Murad et al., 1981). To maintain the rate of cell proliferation, the amount of FCS was reduced to 10% (v/v) and used for all subsequent media renewals. Cell suspensions from the third passage were seeded at a density of 4x10<sup>5</sup> fibroblasts per well of a BioFlex™ 6-well culture plate coated with type I collagen (Dunn Labortechnik, Asbach, Germany) for 24h before loading experiments.

### 2.6.1.3 Bovine scleral fibroblast mechanical loading

To assign proper loading conditions, the average bovine eye intraocular pressure (IOP) was assigned as 27mmHg (3.6kPa), whilst 60mmHg (8kPa) depicted the onset of acute glaucoma (Gum et al., 1998; Boyce et al., 2008). Based on measurements conducted in a collaboration with the Biomechanical Engineering Group (University of Liverpool) it was determined that the average thickness of the bovine globe was 1.6mm (Section 2.7.2 and 6.2.1.2), with a radius of 16.2mm. The Young-Laplace equation was utilised to determine the IOP-induced hoop stress after approximating the shape of the eye to a sphere (Figure 2.12).

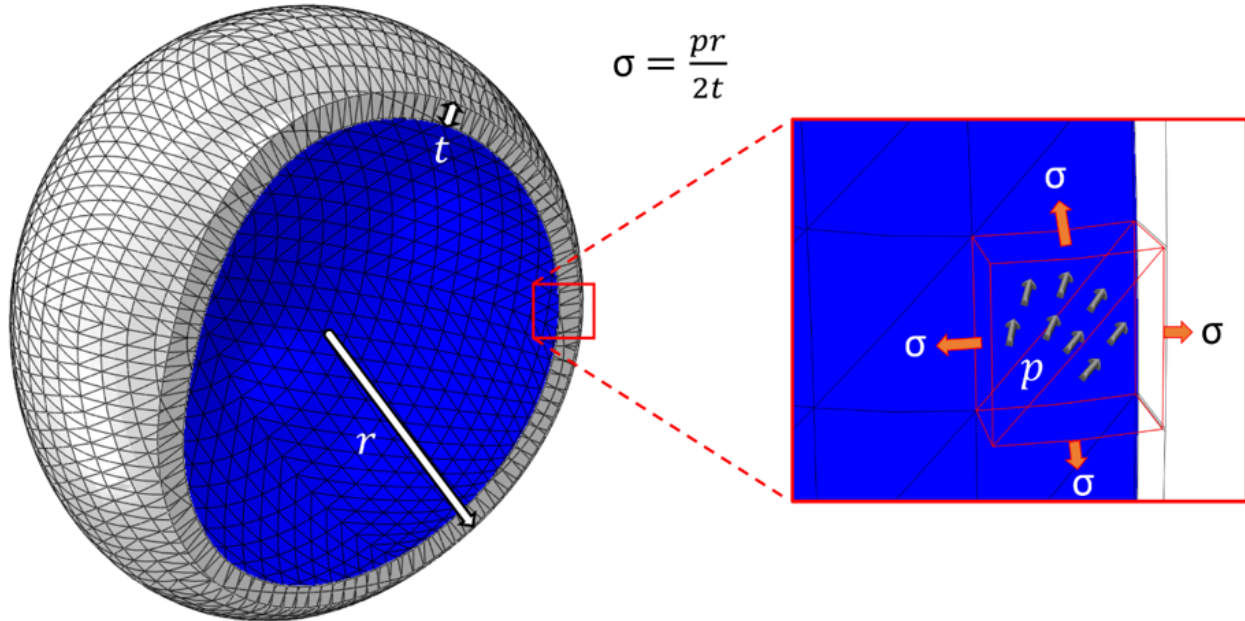


Figure 2.12 – Calculating the in-wall hoop stress in bovine ocular globes utilising the Young-Laplace law. The shape of the eye was approximated to an idealised sphere, resulting in most of the IOP stress to be hoop stress within the eye tunic.  $\sigma$  = in-wall stress;  $p$  = IOP;  $r$  = eye radius;  $t$  = eye tunic thickness.

Young's modulus for bovine eye globes varies between 1 and 7MPa (Litwiller et al., 2010). As strain is the ratio of stress divided by Young's modulus, the physiological tensile strain was between 0.26% and 1.8%, whilst the pathological strain was calculated in the range of 0.6-4% (Markov et al., 2019).

The BioFlex™ 6-well culture plates were divided into three categories depending on the cyclic tensile strain (CTS) regime utilised – unloaded group (not subjected to tensile strain), physiological load (0.26-1.8% strain) and pathological load (0.6%-4% strain), with  $n=3$  wells per plate. Three plates were attached at the same time ( $N=3$ ) to an FX3000 system (Flexcell International, Burlington, USA), with Teflon indents forming a vacuum to the bottom side of the well, providing uniform equibiaxial strain across the entire membrane surface (Figure 2.13). Each loading regime was applied for 1h with a 1Hz frequency, representative of the physiological IOP pulse frequency, in a CO27 incubator (New Brunswick Scientific, St Albans, UK) with 5% (v/v) CO<sub>2</sub>, humidified atmosphere at 37°C (Langham et al., 1989). Due to the loading system's specifics, there were some small variabilities in relation to the applied strain. For the physiological regime the minimal strain percentage reached 0.19-0.21%, with a maximum of 1.55-1.92%, whilst for the pathological

regime it was 0.49-0.55% and 4.27-4.55%, respectively. Therefore, the specified small strains will not be exact but will be referred through this work with the original intended values for greater consistency.

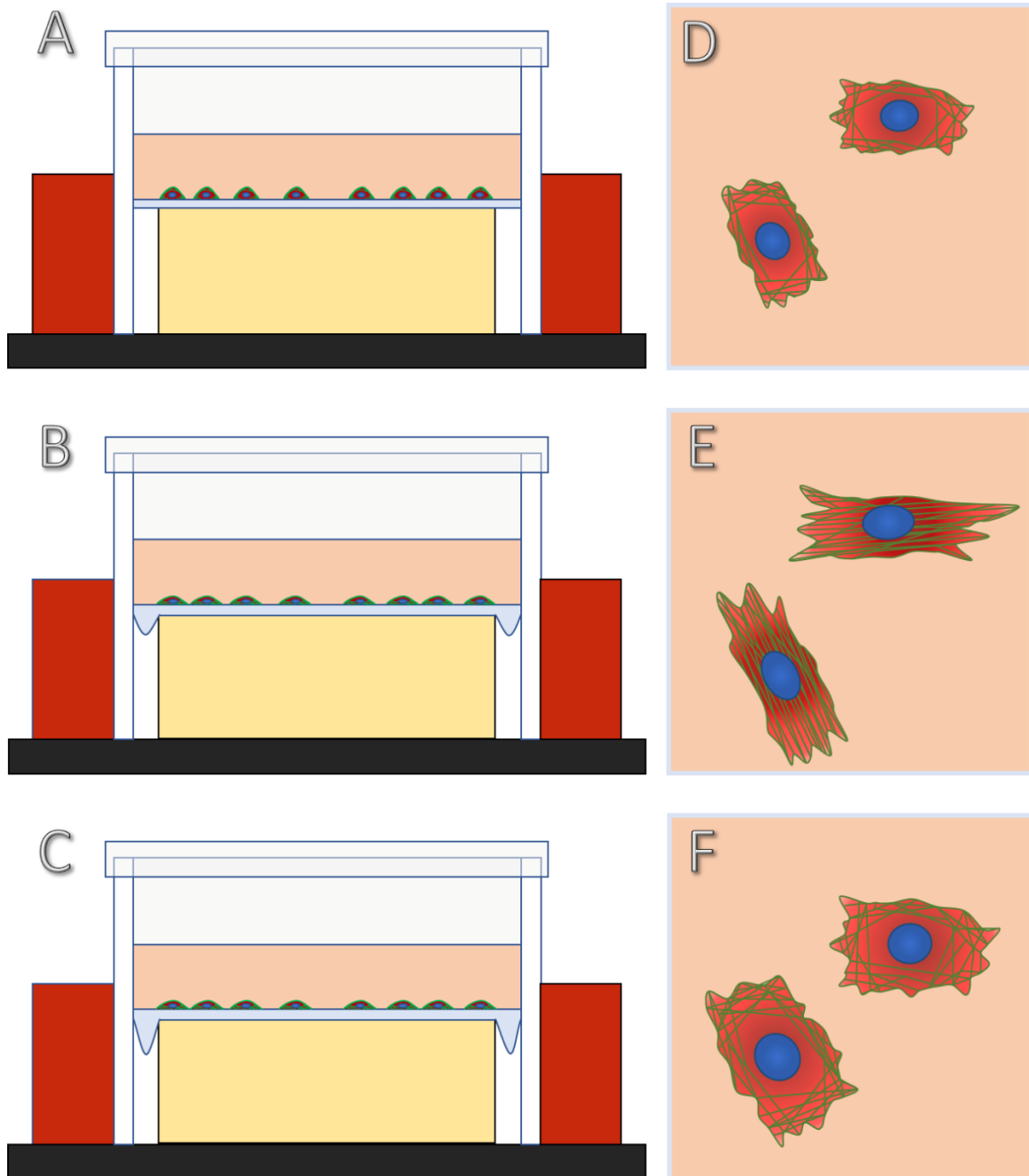


Figure 2.13 – Application of equibiaxial strain using an FX3000 tension system on a well from a BioFlex™ culture plate. (A) Side view of the setup with no applied strain; (B) Side view of the setup with applied physiological strain (0.26-1.8%, 1Hz for 1h); (C) Side view of the setup with applied pathological strain (0.6-4%, 1Hz for 1h); (D) Magnified top view of cells from A; (E) Magnified top view of cells from B; (F) Magnified top view of cells from C. Note: For D, E and F the cortical F-actin and stress fibres are indicated in green, whilst the nuclei in blue.

After completion of the loading regime, the plates from each group were further divided into subgroups, based on the time of fixation of the fibroblast monolayer – 1h, 6h and 24h after CTS ceased. For each time point, the samples were fixed with 2% (w/v) PFA for 15min, washed for 1min with 1xPBS and subsequently every membrane was cut into nine smaller pieces and immunochemically labelled.

### 2.6.2 Cytoskeletal visualisation using confocal microscopy

BioFlex™ type I collagen membrane pieces were first immersed in 1xPBS for 15min, followed by cell permeabilization with 0.5% (v/v) Triton-X-100 (Sigma-Aldrich, Poole, UK) for 30min. Sections designated for vimentin or  $\beta$ -tubulin visualisation were blocked with 2% (v/v) goat serum (Sigma-Aldrich, Poole, UK) for 1h to prevent non-specific binding. Primary mouse anti-vimentin V9 antibody (1:100 dilution; Sigma-Aldrich, Poole, UK) or primary mouse anti-tubulin E7 antibody (1:500 dilution; Developmental Studies Hybridoma Bank, Iowa City, USA) were added to different sets of membranes, after being washed twice with PBS-Tween™ (0.1% (v/v); Sigma-Aldrich, Poole, UK) for 5min. All membranes were incubated for 2h in the dark, in a humidified chamber. Following six washes with PBS-Tween™ for 5min each, a goat anti-mouse immunoglobulin G conjugated with Alexa-594™ secondary antibody (1:400 dilution; Invitrogen, Paisley, UK), was added for 1.5h in the dark. F-actin stress fibres were directly stained with Alexa-488™ phalloidin (1:40 dilution; Invitrogen, Paisley, UK), co-labelling the sections designated for vimentin visualisation. All sections were washed extensively in PBS-Tween™ and mounted in Vectashield™ antifade medium with 1.5 $\mu$ g/ml 4',6-diamidino-2-phenylindole (DAPI; Vector Laboratories, Burlingame, USA). Individual membranes were transferred to Surgipath™ adhesive glass slides (Leica Biosystems, Newcastle, UK), with the borosilicate glass coverslips sealed with nail varnish and stored with no direct exposure to light.

The cytoskeletal structures were observed using a Zeiss LSM 880 upright confocal microscope with Airyscan detection (Carl Zeiss Ltd, Jena, Germany) in FastAiryScan mode utilising ZEN Lite software package at the Bioimaging Hub (Cardiff University). Image acquisition was performed using sequential scanning for detection of multiple fluorophores, with a Plan-Apochromat 63x/1.4 Oil DIC M27 oil immersion objective lens and the listed channels and excitation/emission spectra:

(I) DAPI channel – for visualising nuclei. DAPI excitation wavelength was 405nm and emission at 461nm; (II) Fluorescein isothiocyanate (FITC) channel – for visualising F-actin stress fibres. Alexa-488™ phalloidin excitation wavelength was 488nm and emission at 518nm; (III) dsRed channel – for visualising vimentin intermediate filaments and  $\beta$ -tubulin microtubules. Alexa-594™ secondary antibody excitation wavelength was 561nm and emission at 617nm.

The microscope scan area was 134.95x134.95 $\mu$ m, with a pixel grid element size of 0.0706x0.0706 $\mu$ m (1,912x1,912 pixels) and pixel dwell time of 0.55 $\mu$ s. The 8-bit images were collected in line sequential scan mode, with a motorized x-y stage and one line averaging and recorded as CZI file format. The scanning parameters were optimised and on average 32 optical sections, every 0.14 $\mu$ m, were obtained to produce each Z-stack of confocal images. The number of cells from representative fields of view for each loading condition and time points are listed in Table 2.3.

Table 2.3 – Number of cells and confocal Z-stack images collected on a Zeiss LSM 880 confocal microscope with Airyscan laser in FastAiryScan mode (Carl Zeiss Ltd, Jena Germany). Images are further categorised in terms of the applied CTS and hours post-cessation of load. Note: as the same sections were labelled for F-actin and vimentin the number of cells and confocal images from those two groups are identical.

Load	Time	F-Actin		Vimentin		$\beta$ -Tubulin	
		Cells	Images	Cells	Images	Cells	Images
Phys	1h	129	41	129	41	130	47
	6h	111	28	111	28	122	30
	24h	145	33	145	33	141	26
Path	1h	136	36	136	36	101	24
	6h	103	29	103	29	119	32
	24h	144	27	144	27	150	29
Unl	1h	135	33	135	33	114	24
	6h	113	35	113	35	127	37
	24h	136	26	136	26	154	27

## 2.7 Specimen specific surface reconstruction

Acquisition of bovine eye geometry (Section 2.7.1) and thickness (Section 2.7.2) were conducted at the Biomechanical Engineering Group (University of Liverpool) laboratory using custom-built devices.

### 2.7.1 Recording eye globe topology

Frozen bovine eye globes from an abattoir were thawed immediately prior to careful removal of the external connective and muscle tissues (Section 2.2.1.2). Using a syringe with a 2x50mm hypodermic needle the vitreous and ciliary body were removed through the posterior pole of a left bovine eye. The needle was then left inside the remaining eye tunic and cyanoacrylate glue was applied around the edges to create an airtight seal. The eye was filled with 1xPBS until it returned to approximately natural curvature. The ocular globe, along with the needle, was then inserted into a specially designed chamber, immersed in 1xPBS to limit tissue swelling. The transparent borosilicate chamber provided tight control of hydration and temperature (Whitford et al., 2016). A pressure transducer (FDW 060-K262-01; RDP Electronics, Wolverhampton, USA) was fixed at the same elevation as the centre of the eye which measured the applied pressure with 0.1mmHg resolution. The eye was submerged in 1xPBS and was assumed that there was negligible pressure exerted on it. Photographs were collected by three of six high-resolution digital cameras (550D; Canon, Tokyo, Japan) with 100mm (fixed-focal-length) macro lenses (Figure 2.14). The cameras were mounted on a support frame for stability, pointing in the direction of the equator of the eye globe, with two cameras positioned together and separated from the adjacent group by 120°.

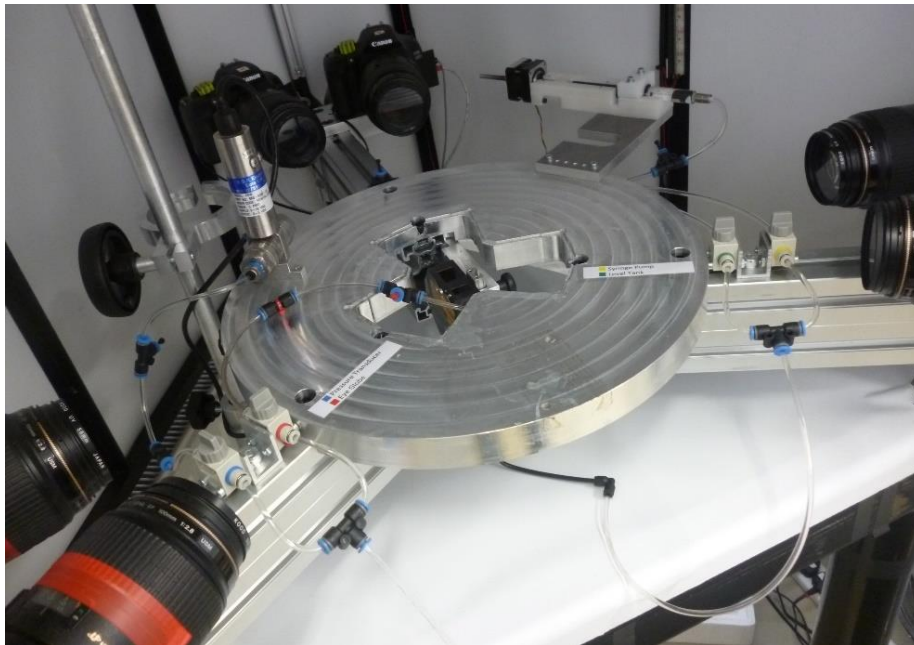


Figure 2.14 – Steel support frame of the eye globe topology imaging setup. Six high-resolution digital cameras were positioned around the central point where the borosilicate chamber, with a submerged eye in 1xPBS, was placed.

### 2.7.2 Measurements of eye tunic thickness

The eye tunic thickness was measured on an apparatus consisting of two main parts: (I) a spherically shaped ruby ( $\text{Al}_2\text{O}_3:\text{Cr}$ ), on which the ocular tissue samples were placed to retain natural curvature; (II) a probe head, positioned 3cm from the ruby, which moved in a downward direction until contact with the tissue surface was established (Figure 2.15). The travelled distance of the probe was then used to determine the thickness of the tissue, with an accuracy of  $\pm 3\mu\text{m}$  (Boote et al., 2016). Three bovine ocular tunics were assessed, with between four and five repeat measurements each for five different regions: central cornea, peripheral cornea, limbus, scleral equator, posterior pole.

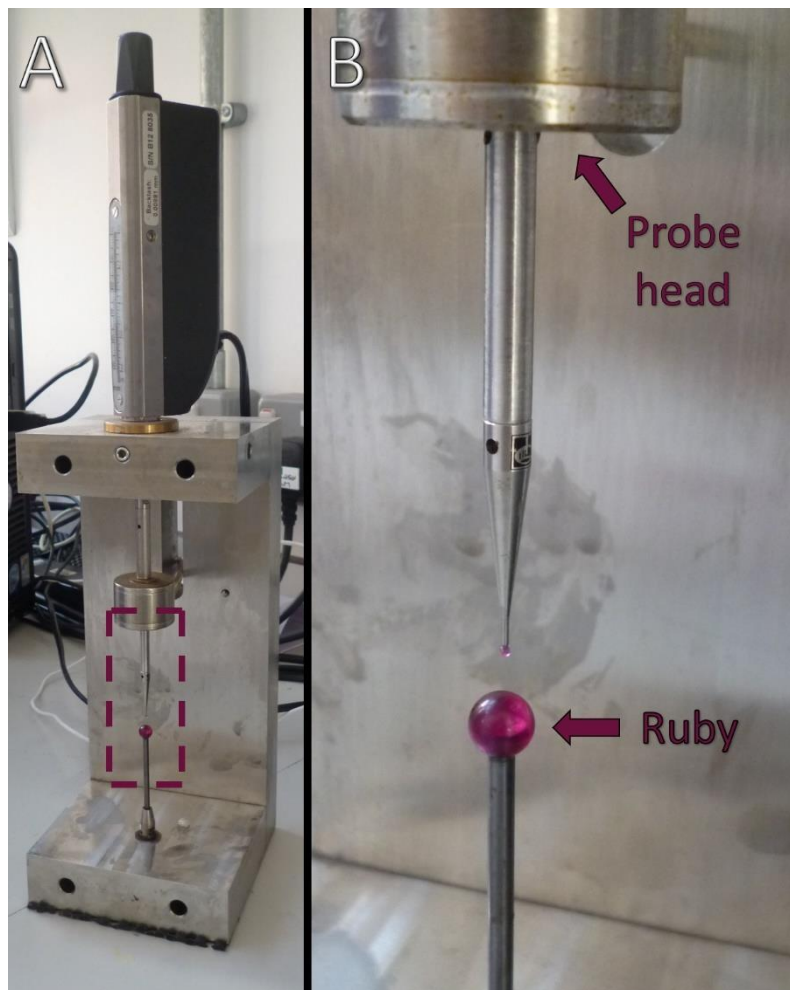


Figure 2.15 – (A) Custom measurement device for determining eye tunic thickness; (B) Magnified view of the indicated region in A. Ocular shells can be positioned on top of the spherical ruby to retain proper curvature, whilst the probe head descends until contact with the tissue is established.

---

### 2.7.3 Finite element and isosurface reconstructions

A bespoke MATLAB script was used to render a finite element (FE) model of the bovine eye geometry based on the acquired topology images. The FE model also incorporated the collected ocular tunic measurements and consisted of 4,800 C3D15H prism continuum shell elements (Figure 2.16C).

Bovine scleral fibroblast confocal microscopy Z-stack images (Section 2.6.2) were reconstructed into three-dimensional isosurfaces using Imaris 9.2 (Bitplane, Zurich, Switzerland), or as filaments by the Imaris plugin FilamentTracer, at the Bioimaging Hub (Cardiff University). The hollow surfaces consisted of CPS3 triangular elements (Figure 2.16A), whilst volume was created separately from C3D4 tetrahedral elements (Figure 2.16B).

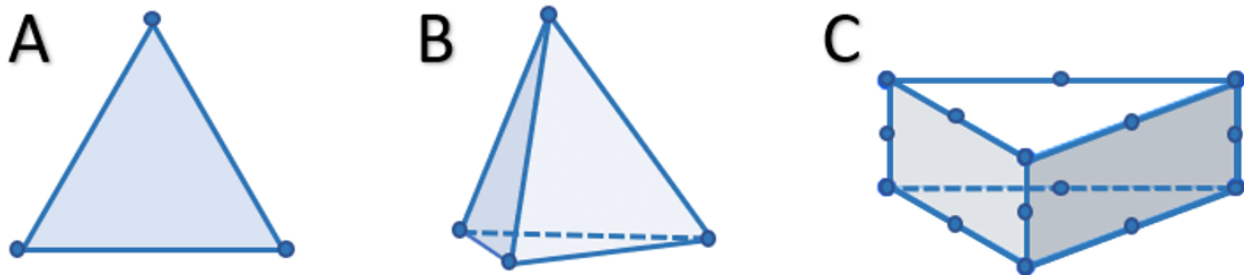


Figure 2.16 – Finite elements used for representation of cell component surface (A), volume (B) and eye tunic (C).  
(A) CPS3 3-node linear plane stress triangle; (B) C3D4 4-node linear tetrahedron;  
(C) C3D15H 15-node quadratic triangular prism.

For the subsequent remeshing and optimisation procedures (Chapter VI) the following free and commercial software packages were used: (I) MeshLab (23/12/2016 built; (Cignoni et al., 2008)); (II) Instant Meshes (Jakob et al., 2015); (III) Netfabb 7.4 (Netfabb GmbH, Parsberg, Germany); (IV) Gmsh 4.3.0 (Geuzaine and Remacle, 2009); (V) ABAQUS 6.14/CAE (Dassault Systèmes Simulia Corp., Rhode Island, USA).

## 2.8 Statistical analysis

All data were tested for normality (Anderson-Darling test) and equal distribution (Bartlett's two-sample F-test) prior to a one-way analysis of variance (ANOVA; Tukey's *post-hoc* test) in MATLAB 9.6 (MathWorks, Natick, USA). Non-parametric equivalent tests used were Mann-Whitney U-test for distribution and Kruskal-Wallis instead of the one-way ANOVA. Box plots represented the median and the 25<sup>th</sup> and 75<sup>th</sup> percentile for the edges, whilst the whiskers were the minimum and maximum excluding outlier values. Difference was considered significant at  $p < 0.05$  (\*: $p < 0.05$ , \*\*: $p < 0.01$ , \*\*\*: $p < 0.001$ ), with indication in figures through a bespoke MATLAB script (Campbell, 2019).

For the Chapter III statistical evaluation of differences between the three highly myopic and seven control specimens (Table 2.1), the collagen anisotropic proportion and main fibre alignment direction were compared through a linear mixed-model analysis for repeated measures in SPSS 24.0 (IBM Corporation, Armonk, USA) in collaboration with Dr Hla Myint Htoon (Department of Statistics, Singapore Eye Research Institute) (Markov et al., 2018). Each specimen was represented by 64 unique WAXS measurements in the PPS (Section 2.2.3.1), with control specimens N1 and N2 averaged point-for-point, as they were a pair from the same donor. The linear mixed-model approach allowed for marginal estimation through the increase in observations in the cluster variable, which maximised the statistical power of the analysis. A compound symmetry variance and covariance structure was selected, based on Hurvich and Tsai's criterion for small sample sizes, with the other compared structures being first-order autoregressive and diagonal (Hurvich and Tsai, 1989).

## **Chapter III**

### **Collagen microstructure in human normal and highly myopic sclera**

### 3.1 Introduction

Myopia is the most common type of visual impairment, with global prevalence constantly increasing (Holden et al., 2014; Dolgin, 2015; Holden et al., 2016). As the ocular globe elongates the visual image is registered in front of the retina, restricting the ability to see at greater distances. This axial lengthening involves remodelling of the sclera, the eye's main loading-bearing tissue, which comprises about 85% of the eye tunic in humans (Watson and Young, 2004; Boote et al., 2019). As a result, the sclera has been observed to become notably thinner, specifically in the posterior pole, where the optic nerve is located. This is of clinical importance, as the optic nerve head (ONH), where the fenestrated *lamina cribrosa* (LC) is located, can be considered a 'weak-spot' in the scleral tissue, allowing for accumulation of deformation forces (Girard et al., 2009a; Pijanka et al., 2012). The LC supports the axons of the retinal ganglion cells (RGC) which form the optic nerve and has been noted to be the primary damage site for the ocular pathology glaucoma, making the region of key biomechanical interest (Sigal et al., 2011; Strouthidis and Girard, 2013). Research studies have evidenced glaucomatous connective tissue changes in the adjacent peripapillary sclera (PPS), with less information being available for myopia (Pijanka et al., 2012). The occurring myopic alterations mainly affect the sclera's extracellular matrix (ECM) architecture of densely woven collagen fibrils, which provide the tissue's mechanical rigidity (Watson and Young, 2004; Tan et al., 2006). Unlike the highly organised cornea, scleral collagen fibres tend to be more disorganised with a high degree of regional variability in their bulk orientation (Hogan et al., 1971; Pijanka et al., 2013; Zhou et al., 2019b). The collagen fibril organisation in the PPS has a major role in governing the transmitted deformations to the ONH as a result of changes in the intraocular pressure (IOP), cerebrospinal fluid pressure (CSFP) and eye movements (Boote et al., 2019).

High myopia refers to clinical cases with  $>6D$  of refractive error, which are at greater risk of developing further ocular complications, such as glaucoma, staphyloma, macular degeneration and retinal detachment (Saw et al., 2005; Wong et al., 2014). The associated axial elongation of highly myopic eyes has been noted to lead to thinning of the sclera, as well as other tissues, such as the LC and choroid (Flores-Moreno et al., 2013; McBrien, 2013; Jonas and Xu, 2014). Furthermore, the diameter of the collagen fibrils also decreases, specifically near the posterior pole (McBrien et

al., 2001). Even though previous research studies confirmed alterations in the collagen fibril organisation in myopic sclera, until recently it remained unknown the extent of these changes in terms of the bulk collagen orientation, which is a key determinant of its direction-dependent biomechanical properties (McBrien et al., 2001; McBrien et al., 2009; Harper and Summers, 2015; Markov et al., 2018).

This Chapter provides an assessment of the bulk changes in the collagen fibril architecture in human high myopia posterior sclera using wide-angle X-ray scattering (WAXS).

## 3.2 Results and Discussion

### 3.2.1 Non-myopic control group

WAXS was performed on seven non-myopic human posterior sclerae (Table 2.1). Figure 3.01 presents a WAXS polar vector plot map of collagen fibril orientations of a non-myopic left human eye (specimen N3; Appendix A.1.1.3), overlaid on top of a photograph of the tissue before the X-ray scanning procedures. The recorded patterns exhibited characteristic and well-conserved structural features in accordance with previous WAXS studies, including the circumferential orientation of collagen fibre bundles around the optic nerve (Pijanka et al., 2012; Pijanka et al., 2013). This annulus of aligned collagen fibrils also displayed the highest observed collagen anisotropy, with the values being on average several times greater than those in the mid-posterior sclera. In addition, a recent study utilising the same eye tunic specimens confirmed through numerical simulations that the posterior pole and PPS has the greatest total collagen density in the eye (Zhou et al., 2019b). Another consistently reproduced feature was two linear fibre bands that originate in the inferior part of the PPS and radiate tangentially from the ring of aligned collagen outward (Coudrillier et al., 2015a). These bands were also orthogonal with each other, with one of them always parallel to the region of tendon insertions of the inferior oblique muscle in the mid-posterior sclera. It is possible that these linear fibre bands are in actuality part of a subpopulation of long collagen bundles oriented tangentially to the scleral canal edge, which were recently envisaged to contribute to the support of the optic nerve canal, based on polarised light microscopy studies (Voorhees et al., 2018; Boote et al., 2019). All of the listed features can be observed in the WAXS polar vector plots of non-myopic human specimens in this Chapter and in the Appendix.

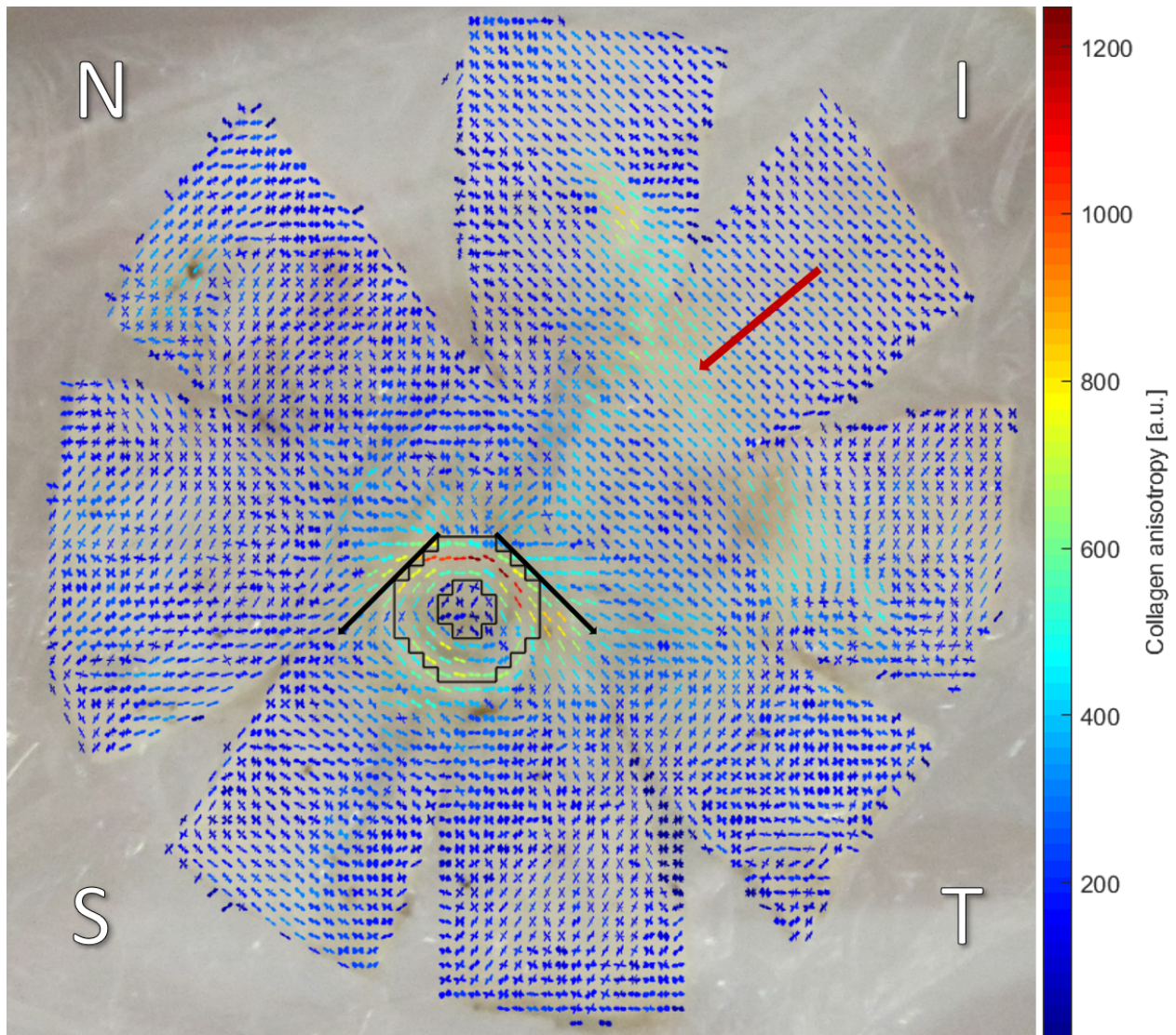


Figure 3.01 – Wide-angle X-ray scattering (WAXS) polar vector plot map of non-myopic human posterior sclera N3 overlaid on top of a photograph of the tissue before scanning. Polar vector plots are colour-coded according to the provided colour bar, with warmer colours indicating higher collagen anisotropy. The highly aligned annulus of collagen fibres in the peripapillary sclera (PPS) is bounded by black lines, with two tangential fibre bands being orthogonal (black arrows). The red arrow designates the insertion region of the inferior oblique extraocular muscle, with the superior (S), nasal (N), inferior (I) and temporal (T) directions indicated.

As noted, total collagen content in the posterior sclera was highest in the peripapillary region (Zhou et al., 2019b). To ascertain differences between non-myopic and highly myopic specimens, an average of the total collagen PPS values from seven non-myopic posterior sclerae was compared. The PPS was subdivided into four quadrants (superior nasal (SN), superior temporal (ST), inferior temporal (IT) and inferior nasal (IN)), with mean percentage presented (Table 3.1). The highest quadrant mean total collagen was taken as 100.00%, with the other three quadrants represented as

percentages of it. For non-myopic eyes, the collagen content was consistently highest in the inferior and lowest in the superior direction, whilst the three highly myopic eyes did not follow this pattern: (I) highly myopic case 1 (HM1) exhibited an opposing collagen distribution, with highest in the superior and lowest in the inferior direction, which in the IN quadrant was only 2/3 of the diagonally opposite ST; (II) the total collagen scatter from highly myopic specimen 2 (HM2) was homogenously distributed between the four quadrants, with lowest in the IT region ( $92.82 \pm 9.60\%$ ); (III) whilst high myopia 3 (HM3) showed most collagen content in the IN quadrant, comparable to the averaged control, the total collagen was lower in the IT region.

Table 3.1 – Comparison of total collagen scatter in the PPS per quadrant. An average of the non-myopic specimens ( $n=7$ ) was created, grouped by quadrant: superior nasal (SN), superior temporal (ST), inferior temporal (IT), inferior nasal (IN). The highly myopic specimens are listed individually due to their variability. Total collagen content per quadrant is presented as a percentage of the highest mean value per quadrant.

<b>Peripapillary scleral quadrant</b>	<b>SN</b>	<b>ST</b>	<b>IT</b>	<b>IN</b>
<b>Averaged control</b>	80.95% ±18.09%	81.48% ±18.80%	91.48% ±22.28%	100.00% ±25.05%
<b>High Myopia 1</b>	99.12% ±15.40%	100.00% ±11.72%	78.96% ±15.12%	66.63% ±7.38%
<b>High Myopia 2</b>	100.00% ±32.67%	98.77% ±18.76%	92.82% ±9.60%	99.58% ±27.43%
<b>High Myopia 3</b>	79.42% ±15.47%	85.80% ±13.20%	80.14% ±28.61%	100.00% ±20.66%

Although all highly myopic specimens were confirmed to possess a refractive error of  $>6D$ , the axial length was not determined before conducting the X-ray scattering experiments. To represent the scleral lengthening with high myopia, the distance between the WAXS polar vector plots of the edge of the optic nerve canal to the insertions of the inferior oblique muscle (ONH-IO) was measured for all specimens (Figure 3.02 and Table 2.1). The ONH-IO distance was highly consistent for the non-myopic controls, with a marked increase for the highly myopic sclera. The ONH-IO distance of myopic specimen HM1 could not be calculated accurately, due to the widespread structural deformations precluding the use of the extraocular muscle insertions.

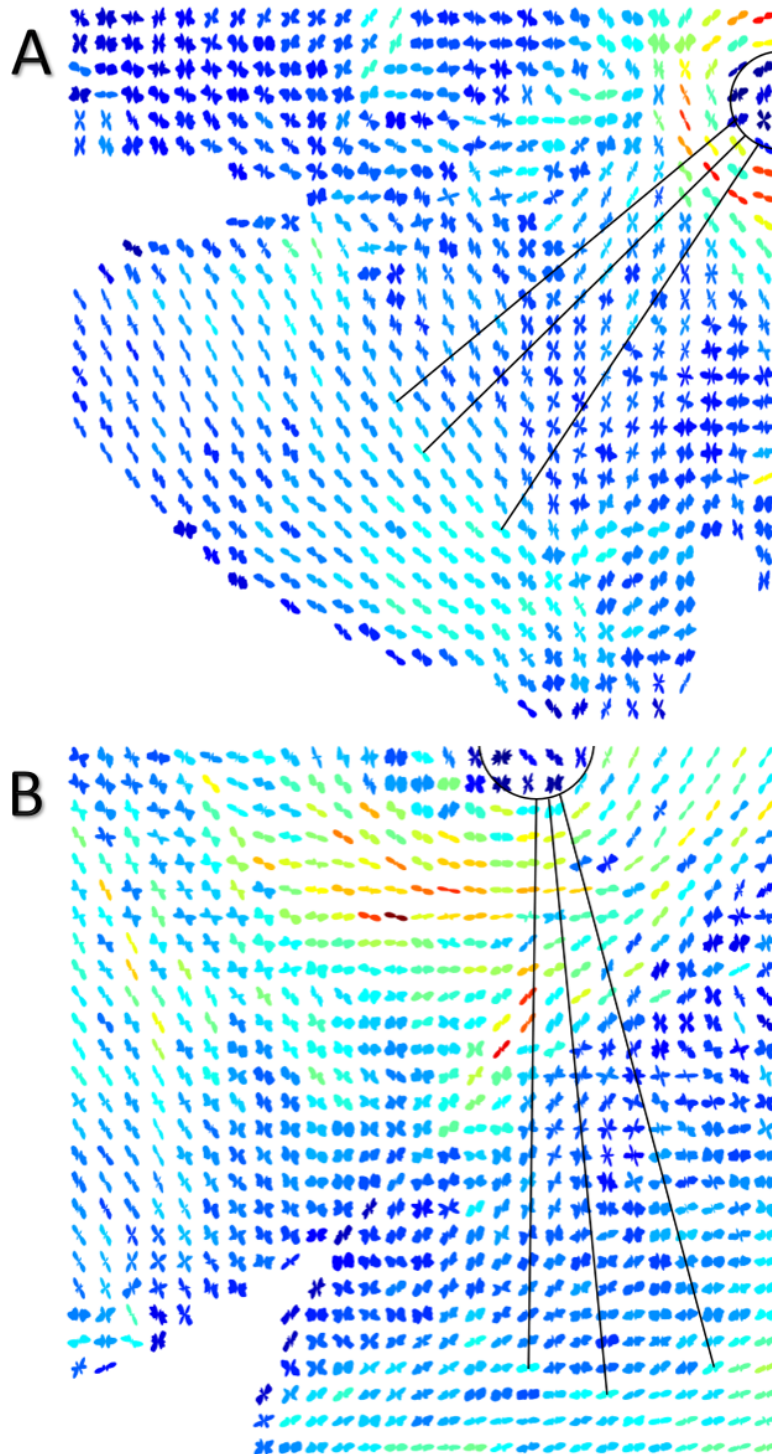


Figure 3.02 – Measurement of the distance between the optic nerve canal edge (curved line) and the muscle insertions of the inferior oblique muscle (ONH-IO) using WAXS polar vector plot maps. The optic nerve was surrounded by an annulus of circumferential collagen fibrils, whilst the muscle insertions were uniaxially aligned in the same direction. Three individual measurements (line length) were performed per sample, with the mean taken as representative. The centres of the vector plots were positioned at every 0.5mm and their size and spacing were accounted for in the calculations. (A) Magnified view (27x27 data points) of non-myopic human posterior sclera N7; (B) Magnified view (27x27 data points) of highly myopic human posterior sclera HM2.

The posterior sclera of specimen N4 (Figure 3.03), as well as in the rest of the non-myopic control group (Appendix A.1.1), had a disruption in the circumferential collagen fibril orientation that was localised in the SN quadrant of the PPS. The composing polar vector plots were more disorganised, with several well-defined peaks, representative of collagen fibril directionalities (Figure 3.03B). In addition, the collagen anisotropy was also lower, making them reminiscent of the vector plots in the mid-posterior sclera. This characteristic is in agreement with previous findings, where the weakest annular alignment was consistently observed in the SN region (Pijanka et al., 2012; Pijanka et al., 2013).

Figure 3.04 is analogous to Figure 3.03 by having the polar vector plots substituted by colour-coded representations of the value of the ratio of the aligned to total collagen signal, referred to as the collagen anisotropic proportion. Whilst the PPS anisotropic proportion has been noted to be on average one-third higher than the mid-posterior sclera in normal eyes, such an evaluation was not carried out due to the presence of relaxation incisions in the mid-posterior and difficult to define boundaries (Pijanka et al., 2012). In addition, there was a tendency in the mid-posterior sclera to exhibit higher anisotropic proportions in the superior and inferior directions, likely corresponding to the tendon insertion regions of the superior and inferior oblique extraocular muscles (Figure 3.04A). The anisotropic proportion values of the PPS of the seven non-myopic posterior sclerae were combined into an average control, similar to Table 3.1, and further categorised in four quadrants (Section 3.2.5). This pooling of data was justified due to the highly conserved collagen fibril annulus in the PPS of non-diseased eyes (Pijanka et al., 2012; Coudrillier et al., 2013; Pijanka et al., 2013; Coudrillier et al., 2015a).

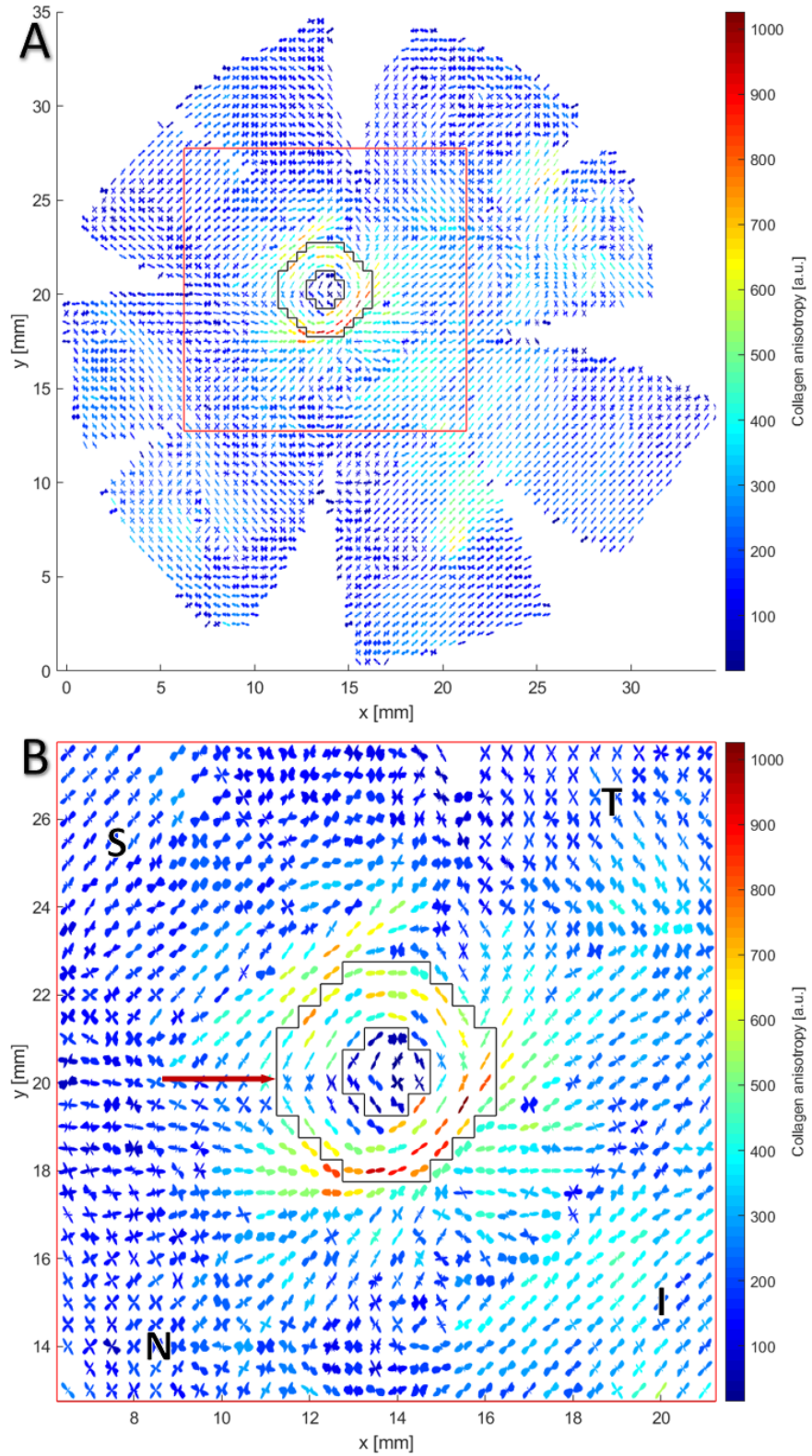


Figure 3.03 – WAXS polar vector plot map of human non-myopic specimen N4 (A) with a red square designating a 30x30 vector plot magnification expanded in (B). The PPS is bounded by black lines, whilst the red arrow denotes localised discontinuation in the circumferential collagen orientation in the SN region, with the superior (S), nasal (N), inferior (I) and temporal (T) directions indicated on B.

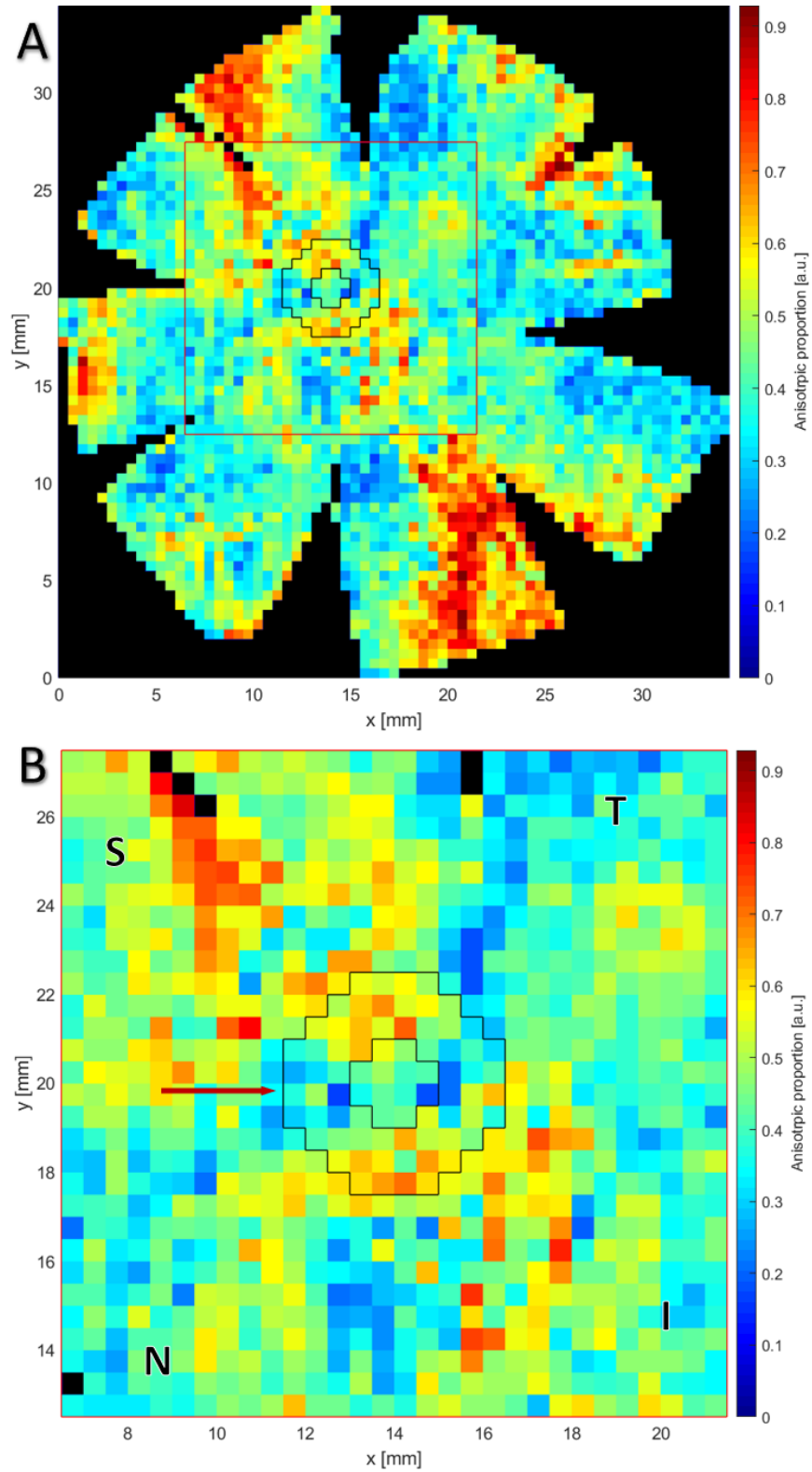


Figure 3.04 – WAXS collagen anisotropic proportion contour map of human non-myopic specimen N4 (A) with a red square designating a 30x30 data point magnification shown expanded in (B). The PPS is bounded by black lines, whilst the red arrow denotes localised discontinuation in the circumferential collagen orientation in SN region, with the superior (S), nasal (N), inferior (I) and temporal (T) directions indicated on B.

### 3.2.2 High myopia case 1

Highly myopic specimen HM1 showed several marked differences in the bulk collagen orientation (Figure 3.05) when compared with a typical non-myopic scleral polar vector plot map (Figure 3.03). The most noticeable change was the presence of two disruptions in the circumferential collagen alignment, neither being in the SN region (Figure 3.05B). Instead, the two breaks in PPS circumferential alignment were observed in the ST and IN quadrants. Furthermore, the optic nerve canal appeared to be stretched in the ST-IN direction, seemingly being more oval-shaped, with the polygon plots displaying wider angular distributions compared to the control group. When assessing the total collagen content per PPS quadrant, the highest mean signal was measured in the ST region, whilst the amount in the IN was two-thirds of the ST signal (Table 3.1). This could indicate that the disruptions in the annular collagen structure of the PPS might be due in part to reduced collagen content in those PPS regions, as previous studies have noted a decrease in collagen in the posterior pole in highly myopic eyes (Norton and Rada, 1995). This was further reflected as the two circumferential disruptions had lower anisotropic proportions than the rest of the PPS (Figure 3.06). These myopic observations are reminiscent of the glaucomatous changes reported by Pijanka et al., which showed significantly reduced fibre anisotropy in the ST and IN quadrants (Pijanka et al., 2012).

The mid-posterior sclera also appeared to be much more disorganised than the non-myopic control group, with large areas of realignment in the tissue. As a consequence, it was difficult to assess if the two characteristic linear fibre bands around the PPS were present. In accordance with Voorhees' proposed model on tangential collagen fibres providing further mechanical support, this could be indicative of increased strain to the optic nerve, perhaps contributing to the observed elongation and secondary disruption in the annular collagen structure (Voorhees et al., 2018).

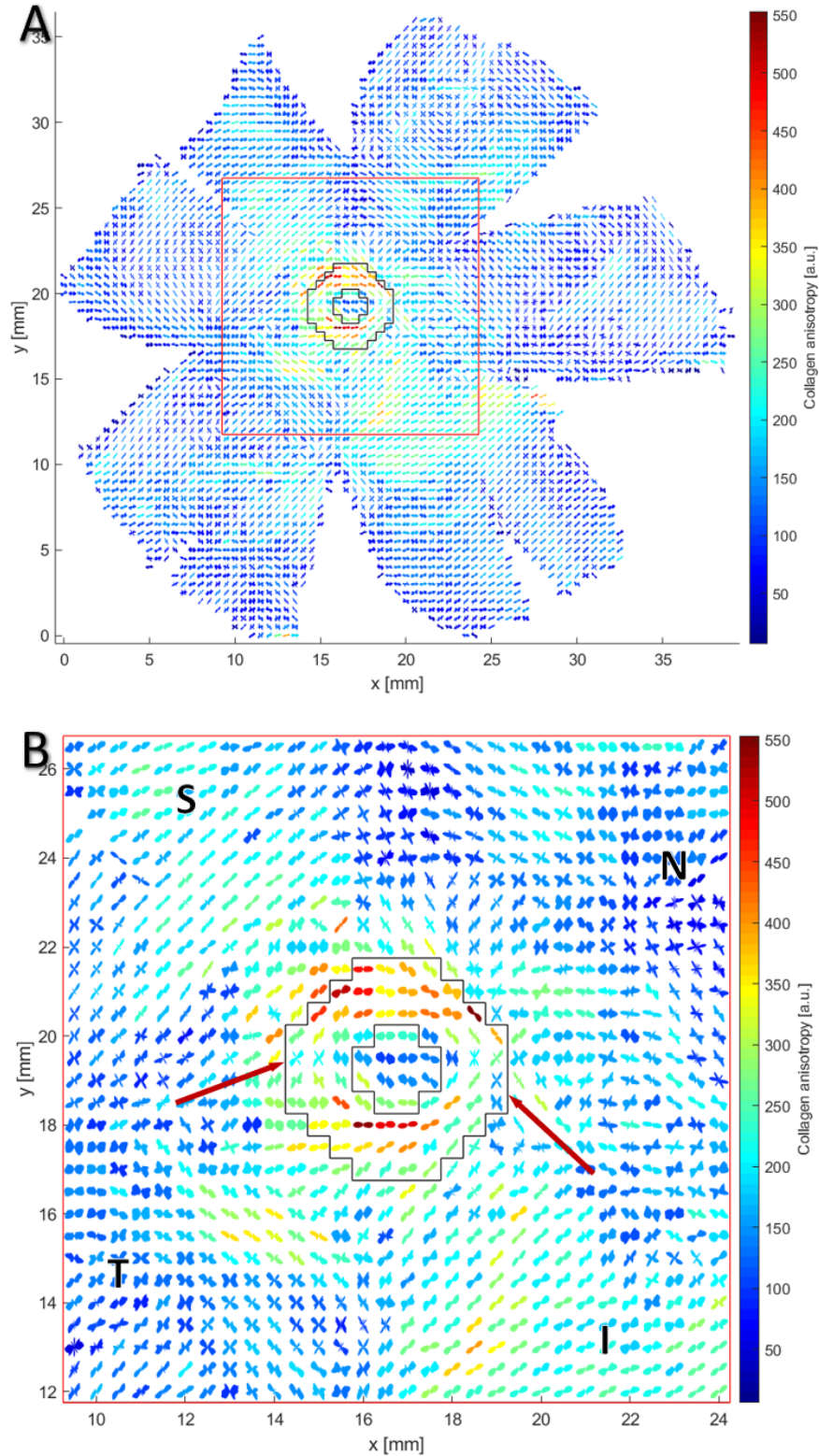


Figure 3.05 – WAXS polar vector plot map of human highly myopic specimen HM1 (A) with a red square designating a 30x30 vector plot magnification shown expanded in (B). The PPS is bounded by black lines, whilst the red arrow denotes localised discontinuation in the circumferential collagen orientation in the ST and IN regions, with the superior (S), nasal (N), inferior (I) and temporal (T) directions indicated on B.

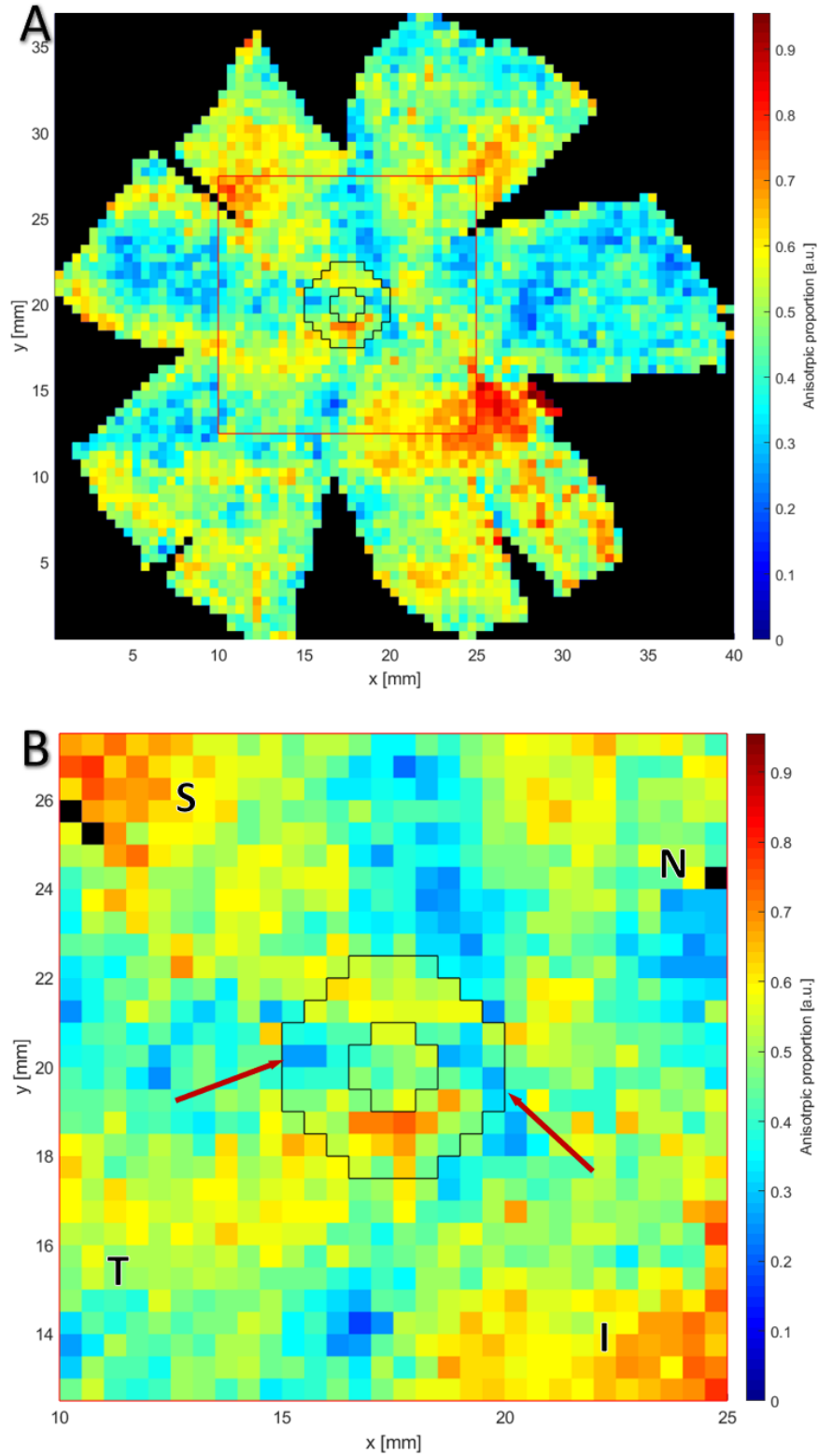


Figure 3.06 – WAXS collagen anisotropic proportion contour map of human highly myopic specimen HM1 (A) with a red square designating a 30x30 data point magnification shown expanded in (B). The PPS is bounded by black lines, whilst the red arrow denotes localised discontinuation in the circumferential collagen orientation in the ST and IN regions, with the superior (S), nasal (N), inferior (I) and temporal (T) directions indicated on B.

### 3.2.3 High myopia case 2

Myopic specimen HM2 (Figure 3.07) exhibited more widespread differences in the WAXS polar vector plot map. Compared to the normal controls, the optic nerve canal was wider, with the surrounding annulus of collagen being spread over a larger radial distance, extending well into the mid-posterior scleral tissue (Figure 3.07B), whilst showing reduced levels of anisotropy in the region immediately adjacent to the canal edge. Furthermore, the normally observed interruption in circumferential alignment in the SN quadrant was much more pronounced, with the polygon plots being comparable to those of the mid-posterior in both anisotropy values and fibrillar orientation. The collagen anisotropy was lower in the 64 data point region of the PPS, with the highest registered values located in the nasal part of the mid-posterior sclera. Due to the level of rearrangement, it was difficult to assess if those polar vector plots belonged to the annulus of collagen fibres or one of the tangential fibre bands, which were noted to be less linear and more curved. In addition, the fibre band traversing in the temporal direction was not directly tangential to the PPS, with a narrow region of less organised fibrils present between them.

The anisotropic proportion in the PPS of specimen HM2 exhibited the highest values on average than the controls or HM1 (Figure 3.08). This observation is initially at odds with the WAXS polar vector map (Figure 3.07), which indicated overall lower collagen anisotropy around the ONH. These two findings can, however, be reconciled if it is considered that the vector plot collagen anisotropy scales proportionally with tissue thickness and by extension the total collagen scatter, whereas the anisotropic proportion scales inversely with thickness, being a ratio of the aligned and total collagen signal (Section 2.2.3). Thus, it is likely that excessive scleral thinning around the posterior pole would have manifested in lower total collagen scatter, which was also nearly equally distributed (Table 3.1), leading to a higher anisotropic proportion; the absolute number of fibrils in a preferential direction, which defines the collagen anisotropy, would be small. This would also be consistent with the IO-ONH distance (Table 2.1), with HM2 showing the largest amount of axial scleral lengthening. In addition, the observed extensive scleral remodelling is probably associated with the ocular axial elongation (Tan et al., 2006; Vurgese et al., 2012). In the mid-posterior region, the collagen anisotropy values were also markedly higher, possibly further indicating an overall tissue thinning (Figure 3.08B).

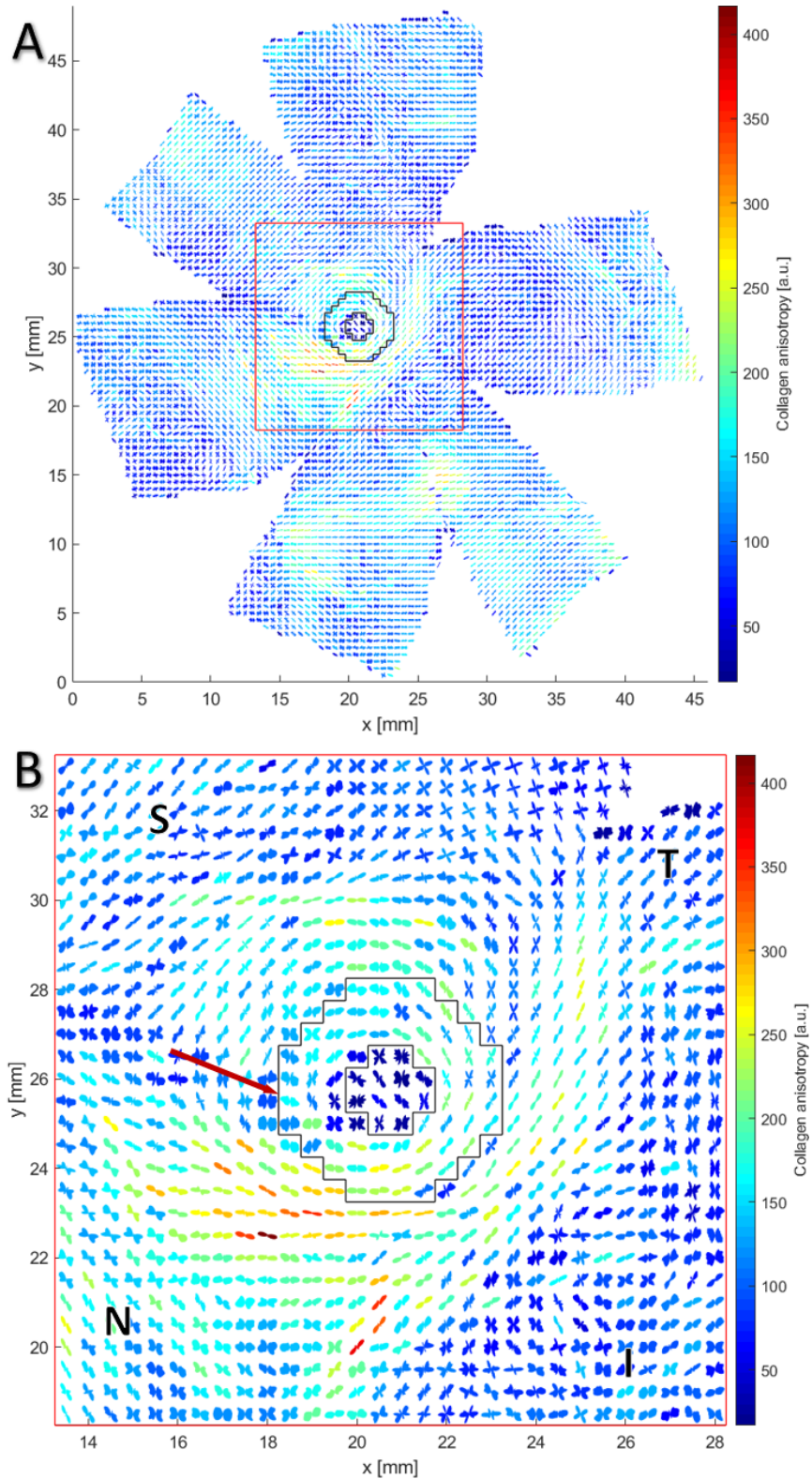


Figure 3.07 – WAXS polar vector plot map of human highly myopic specimen HM2 (A) with a red square designating a 30x30 vector plot magnification shown expanded in (B). The PPS is bounded by black lines, whilst the red arrow denotes localised discontinuation in the circumferential collagen orientation in the SN region, with the superior (S), nasal (N), inferior (I) and temporal (T) directions indicated on B.

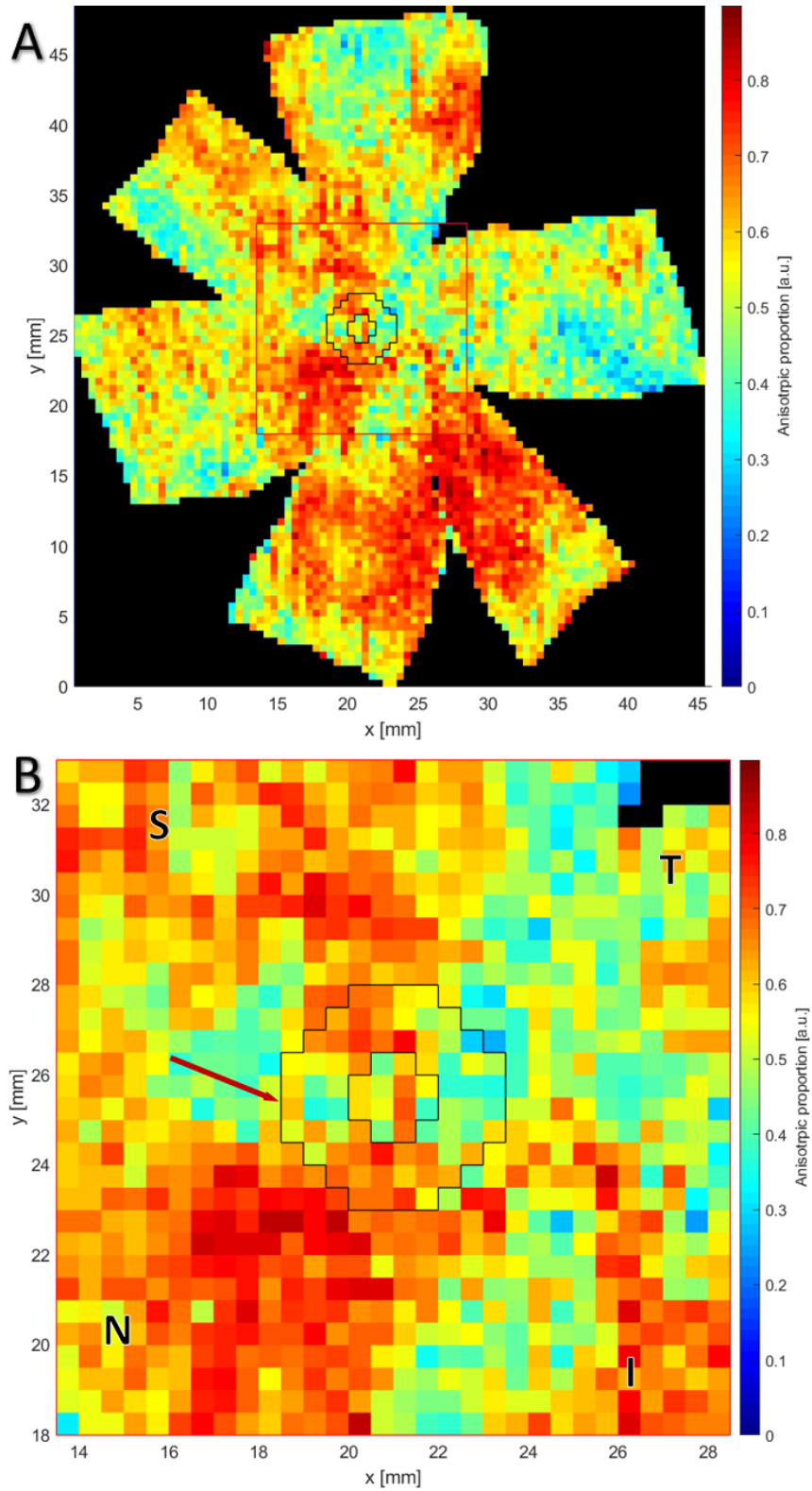


Figure 3.08 – WAXS collagen anisotropic proportion contour map of human highly myopic specimen HM2 (A) with a red square designating a 30x30 data point magnification shown expanded in (B). The PPS is bounded by black lines, whilst the red arrow denotes localised discontinuation in the circumferential collagen orientation in the SN region, with the superior (S), nasal (N), inferior (I) and temporal (T) directions indicated on B.

The observed enlarged scleral canal and disorganisation of the circumferential collagen fibrils in the PPS with high myopia were also in agreement with previous research. Jonas et al. described these optic discs as ‘secondary acquired macrodiscs’, which are accompanied by larger PPS atrophic regions (Jonas et al., 1988). Saw added to the list of abnormalities a tilt to the optic disc, as well as a thinner LC, whilst Bellezza and colleagues concluded that a larger disc is more susceptible to IOP-related glaucomatous damage, which could link the pathological changes to the scleral architecture of specimen HM2 (Bellezza et al., 2000; Saw et al., 2005). From a biomechanical aspect, for a given IOP a decreased PPS thickness may be expected to lead to accumulation of large shear strains in the LC, predictive of radial displacement of the optic nerve canal and axonal damage (Edwards et al., 2001; Norman et al., 2011; Ma et al., 2019).

### 3.2.4 High myopia case 3

Figure 3.09 presents a 30x30 data point magnified view of highly myopic specimen HM3, as only a 16x16mm square region centred on the ONH was available for the study. The polar vector plot map featured a larger disruption in the SN quadrant as compared to the normal circumferential collagen structure, along with a notable splitting of the fibre alignment into two subpopulations over large regions of the PPS (Figure 3.09A). This specimen was also characterised by further collagen realignment in the mid-posterior sclera which did not appear to be part of the tangential fibre bands, with only one being distinguishable on the temporal side of the PPS. The measured collagen anisotropy was the highest of all specimens, specifically in the PPS IT quadrant. The total collagen scatter on average was largest for the IN region of the PPS, similarly to non-myopic specimens, with the total collagen signal of IT quadrant being  $80.14 \pm 28.61\%$  of the IN (Table 3.1). The anisotropic proportion was greatest in the IT scleral region (Figure 3.09B), possibly the result of further highly myopic remodelling of the posterior sclera.

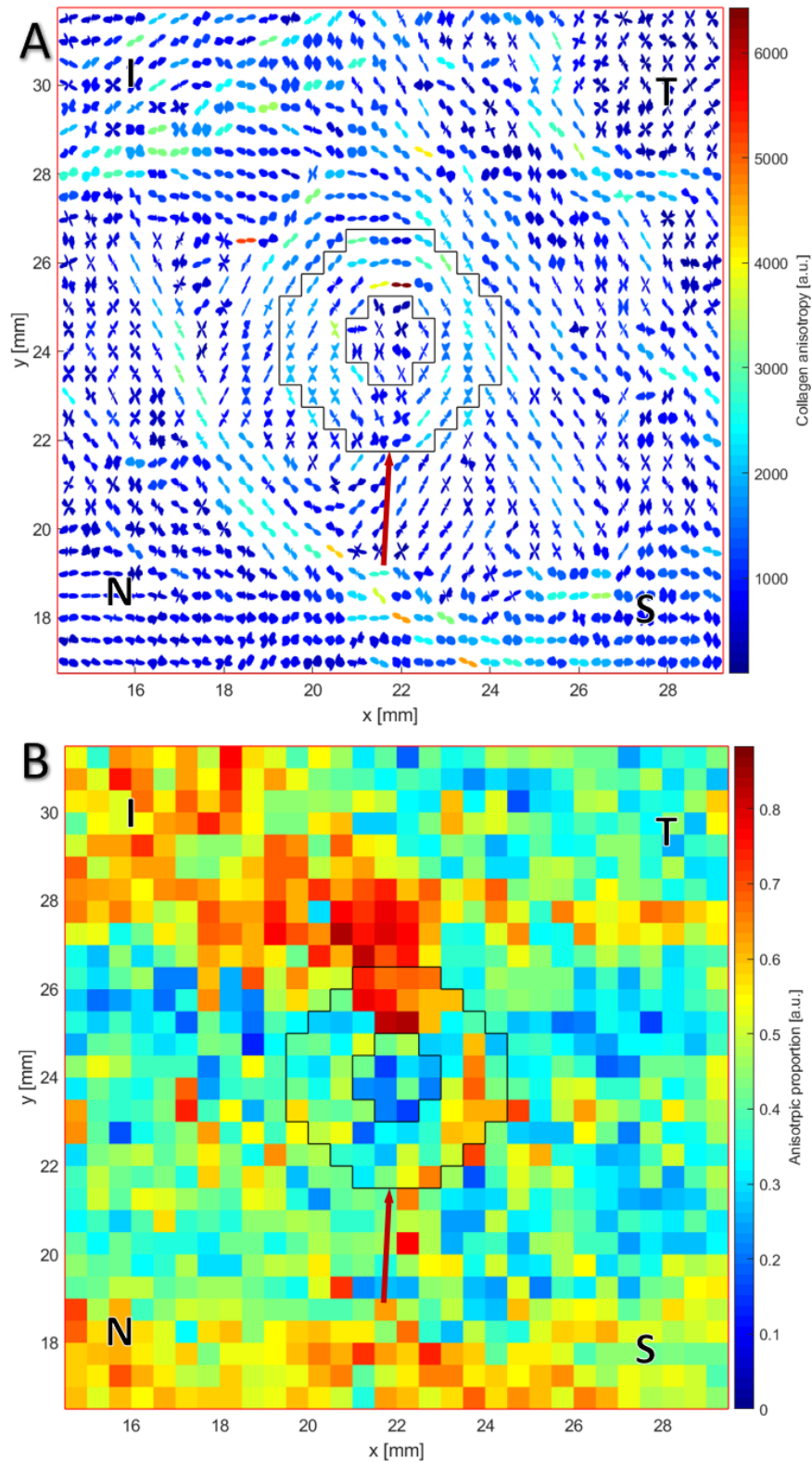


Figure 3.09 – Magnified WAXS polar vector plot map (A) and WAXS collagen anisotropic proportion contour map (B), consisting of 30x30 data points, of human highly myopic specimen HM3. The PPS is bounded by black lines, whilst the red arrow denotes localised discontinuation in the circumferential collagen orientation in the SN region, with the superior (S), nasal (N), inferior (I) and temporal (T) directions indicated.

### 3.2.5 Regional differences in anisotropy between normal and myopic eyes

An averaged control of PPS regional quantification of collagen anisotropic proportion was composed of the seven non-myopic specimens after proper reorientation of the 64 data points of the PPS region, which were further subdivided into four 16 measurement quadrants, representing the SN, ST, IT and IN regions (Figure 3.10). Minimum anisotropic proportion values for each posterior sclera were consistently observed in the SN quadrant, whilst the maximum values were in the IN. In addition, differences in the distributions were observed, with the anisotropic proportion in the ST and IN being significantly higher than both the SN and IT quadrants. These conserved patterns were not exhibited in the highly myopic specimens: (I) the minimum value for HM1 was located in the ST quadrant and highest in the IT; (II) HM2 showed the opposite pattern, with lowest anisotropy in the IT and maximum in ST; (III) HM3 displayed a maximum anisotropic proportion in the IT quadrant, comparable to HM1. HM3 was also the only instance of all three highly myopic eyes to have both a disruption in the collagen fibril circumferential alignment (Figure 3.5), as well as a collagen anisotropic proportion minimum in the same region, which was in the SN quadrant. The atypical PPS fibril alignment in the myopic sclerae are quantified in Section 3.2.6.

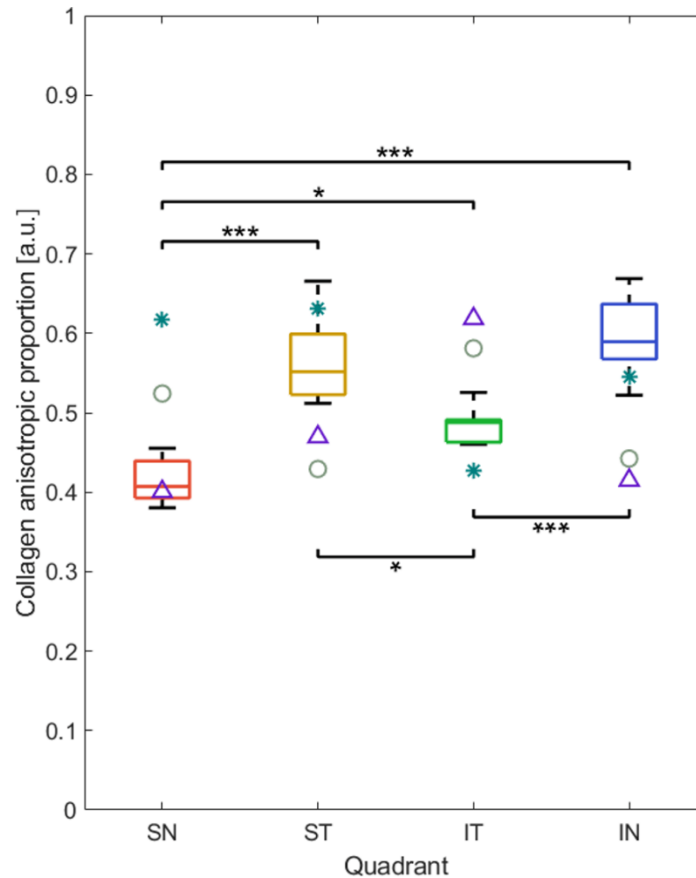


Figure 3.10 – Box plot of mean collagen anisotropic proportion in the PPS per quadrant. The non-myopic specimens (n=7) are grouped by quadrant: SN (red), ST (gold), IT (green), IN (blue). The highly myopic specimens are indicated as follows: HM1 (grey circle); HM2 (teal asterisk); HM3 (purple triangle), with the majority of them positioned outside of the non-myopic range. Data are presented as median  $\pm$  standard deviation (SD); \*:p<0.05; \*\*\*:p<0.001.

### 3.2.6 Peripapillary scleral fibre angle displacement in high myopia

Additional structural differences between the non-myopic control group and the three highly myopic eyes were revealed after a comparison of the angular displacement of the collagen polar vector plots from an idealised circumferential distribution (Figure 2.04). The orientation of the right eye was selected as the default, with mirror images of the polygon plot vector maps taken for the left eyes. Heat maps of main angle difference between the idealised polar vector plot distribution and the averaged control (Figure 3.11A) and with the three highly myopic specimens (Figure 3.11B, C and D) were generated, with displacements ranging from 0° to 90°, as indicated on a colour bar. The results confirmed that the non-myopic structure follows the idealised annular

orientation around the ONH (Figure 3.11A). HM1 mimicked the pattern to a lesser degree, with hot-spots of over  $50^\circ$  deviation in the IN, IT and ST quadrants, with the latter diverging markedly from the idealised distribution with a maximum deviation of  $74^\circ$  (Figure 3.11B). This is in agreement with the corresponding WAXS polar vector plot map, where the most obvious disruptions in PPS circumferential fibril orientation of HM1 were in the ST and IN regions (Figure 3.05B). For HM2, the differences were most pronounced in the outer parts of the peripapillary region in the SN quadrant, with a maximum measured deviation of  $83^\circ$  (Figure 3.11C). HM3 followed a similar pattern, with the largest changes again occurring in the SN quadrant, with highest angular displacement of  $79^\circ$ , corresponding to a notably large break in the circumferential polar vector plot alignment (Figure 3.09A).

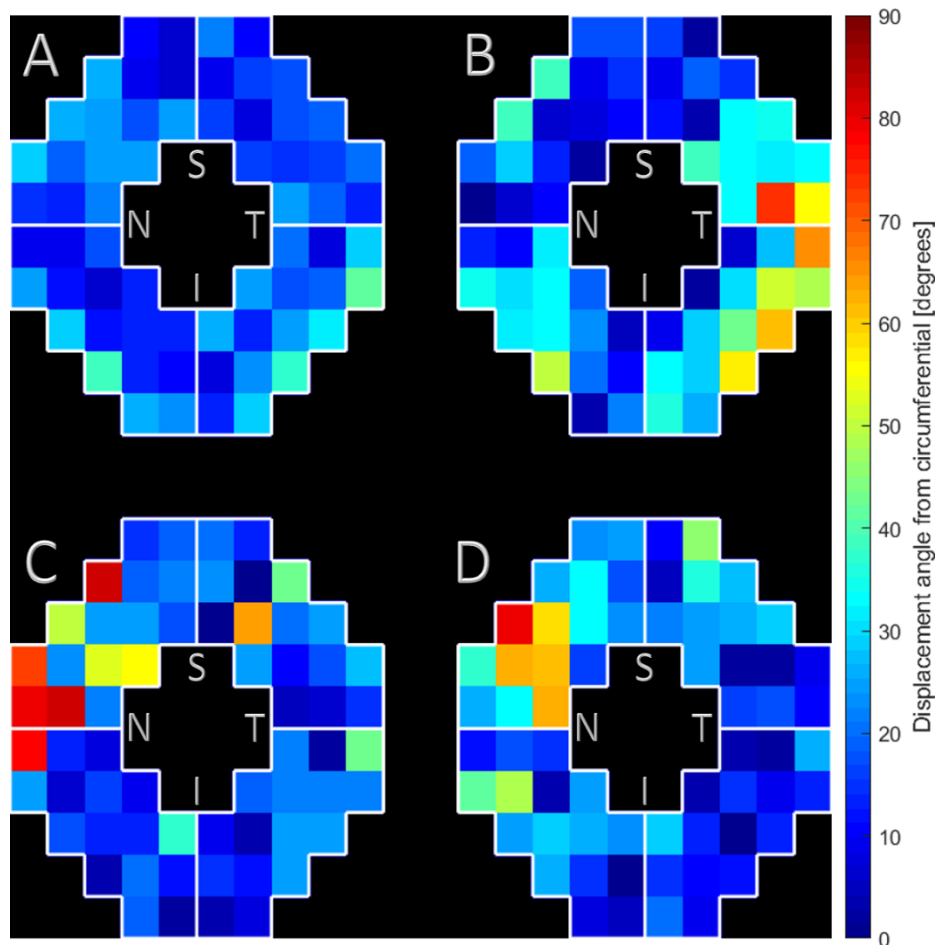


Figure 3.11 – Heat map of collagen fibril displacement angle from idealised circumferential orientation in the PPS based on WAXS polar vector plots. Superior (S), nasal (N), inferior (I) and temporal (T) directions are indicated where the optic nerve is positioned. (A) Averaged non-myopic control group (n=7); (B) Highly myopic specimen HM1; (C) Highly myopic specimen HM2; (D) Highly myopic specimen HM3.

Large deviations from circumferential alignment are exhibited in all myopic cases.

These angular displacement differences are further highlighted as quadrant-averaged box plots where the majority of the highly myopic data are again outliers to the control group (Figure 3.12). The combined non-myopic specimen group displayed the smallest overall displacement in the ST quadrant followed by the IN region, which also had the largest collagen anisotropic proportions (Figure 3.10). No such correlation was exhibited by the highly myopic specimens. Rather, the following observations were noted: (I) the maximum quadrant displacement for HM1 was in the IT, where the anisotropic proportion was also highest (Figure 3.10), with minimum displacement in the SN, likely due to the lack of disruption in the annular fibril arrangement; (II) for HM2 the maximum angular displacement was in the SN and the minimum was in the IT; (III) the highest and lowest deviations for HM3 were also in the SN and IT PPS quadrants, respectively.

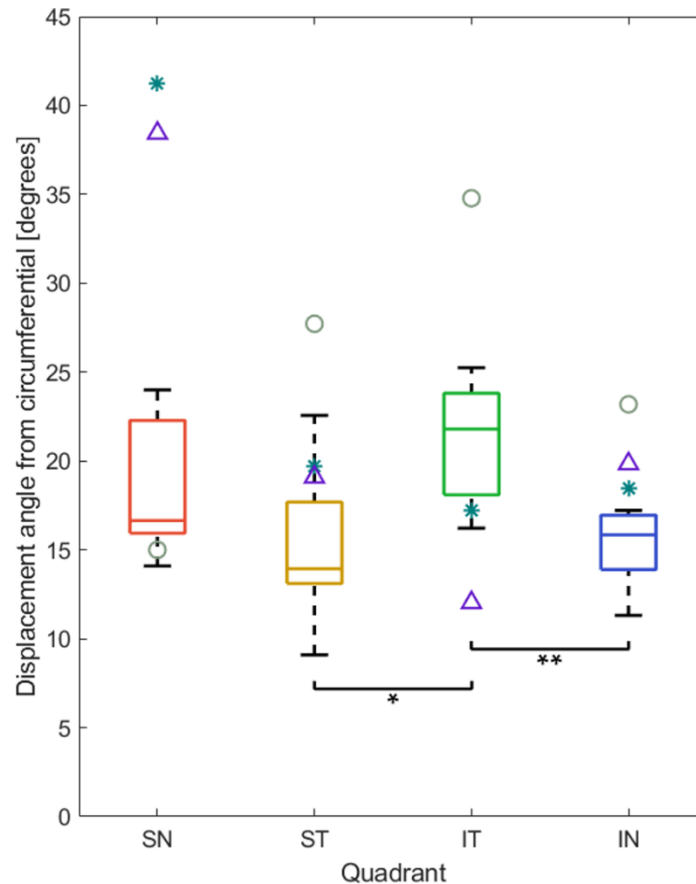


Figure 3.12 – Box plot of mean collagen fibril displacement angle from idealised circumferential orientation in the PPS per quadrant. The non-myopic specimens (n=7) are grouped by quadrant: SN (red), ST (gold), IT (green), IN (blue). The highly myopic specimens are indicated as follows: HM1 (grey circle); HM2 (teal asterisk); HM3 (purple triangle), with the majority of them positioned outside of the non-myopic range.

Data are presented as median  $\pm$  SD; \*:p<0.05; \*\*: p<0.01.

To assess the overall difference between the non-myopic controls and highly myopic specimens, they were grouped (n=6 and n=3, respectively; specimens N1 and N2 were averaged point-for-point, as they were a left/right pair). Linear mixed-model analysis (Section 2.8) was used to statistically compare the difference in the mean collagen anisotropic proportion in the whole PPS, which did not pass the  $p < 0.05$  statistical significance threshold (Figure 3.13A). This was most likely due to a cancelling effect in the highly myopic group, as some PPS quadrants showed an increase, whilst others displayed a decrease in the anisotropic proportion (Figure 3.10). The limited numbers of highly myopic specimens available precluded their statistical comparison with each other or the non-myopic control group, or a PPS quadrant-wise evaluation. The averaged displacement angle from circumferential orientation, however, was statistically different ( $p < 0.05$ ) between the non-myopic control ( $17.7 \pm 12.0^\circ$ ) and the highly myopic groups ( $23.9 \pm 18.2^\circ$ ; Figure 3.13B).

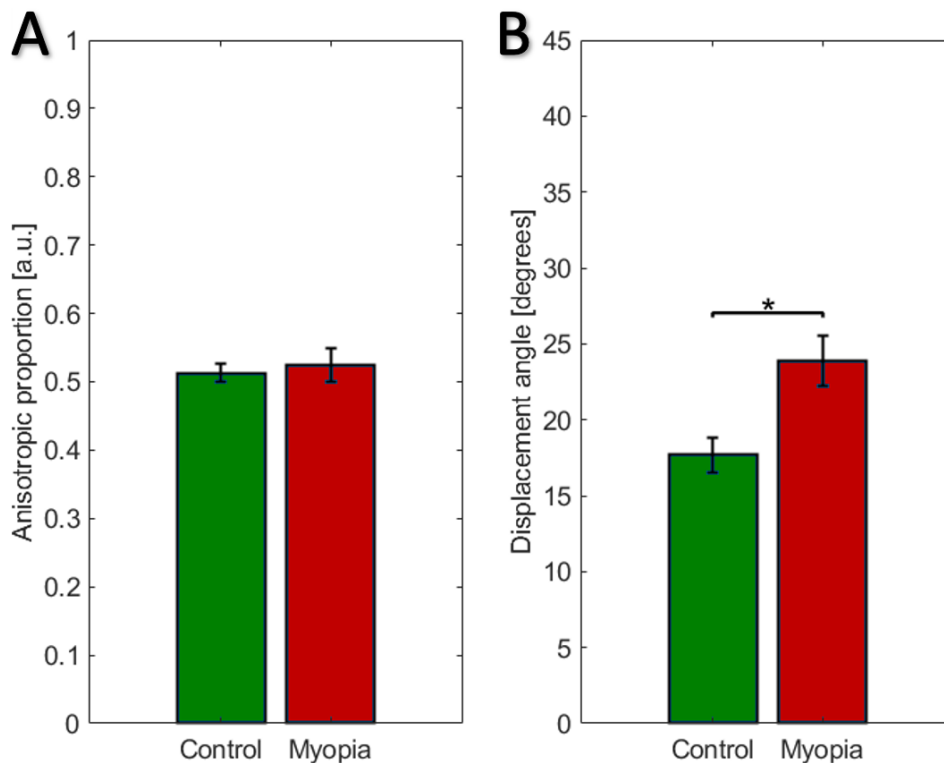


Figure 3.13 – Bar chart statistical comparison of the mean collagen anisotropic proportion (A) and the collagen fibril displacement angle from idealised circumferential orientation (B) in the whole PPS using linear mixed-model analysis; n(Control)=6, n(Myopia)=3; \*:  $p < 0.05$ .

### 3.2.7 Observations and limitations

The results presented in this Chapter evidence that highly myopic human posterior sclerae do not follow the normal collagen fibrillar organisation, with all three myopic specimens exhibiting notable alterations in the PPS. Specifically, the high myopia group had a significantly larger angular displacement of the collagen fibrils away from the typical circumferential arrangement, with more radially orientated fibres in the PPS overall (Figure 3.13B). As noted (Section 1.3), the annular structure of collagen fibril bundles provides mechanical stability to the ONH as they limit the IOP-related expansion of the optic nerve canal and reduce the in-plane tensile strains with the LC (Girard et al., 2009a; Girard et al., 2009b; Grytz et al., 2011; Sigal et al., 2011; Coudrillier et al., 2013). All of the highly myopic specimens presented in this Chapter displayed noticeable disruptions in the preferential orientation of collagen fibrils around the ONH, with HM2 and HM3 having enlarged breaks in the SN quadrant organisation (Figure 3.07B and 3.09A), whilst HM1 had two alternative ones in the ST and IN regions (Figure 3.05B). It is plausible that remodelling of the scleral ECM has occurred as a result of myopia, affecting the mechanical environment of the ONH and its physical response to IOP and CSFP fluctuations (Campbell et al., 2014; Grytz et al., 2014; Muñoz-Sarmiento et al., 2019). Therefore, alterations to the bulk peripapillary collagen architecture in myopia may be linked to an increased ONH susceptibility to glaucomatous damage (Pijanka et al., 2012; Coudrillier et al., 2015c; Jones et al., 2015). This would be in accordance with previous largescale studies that have linked a higher prevalence of glaucoma with patients with high myopia (Leske et al., 1994; Mitchell et al., 1999; Xu et al., 2007). Taken together, these findings suggest that a greater risk of developing glaucomatous damage could be associated with structural changes occurring with high myopia, such as the ones exemplified in this Chapter.

Whilst the structural changes of the three highly myopic specimens could be a consequence of scleral remodelling during axial lengthening, a further possibility is that they may represent a biomechanical adaption to increased scleral stresses in an enlarged and thinned tissue, if the Young-Laplace equation is applied to spherical pressure vessels (Section 2.6.1.3). Thus, alterations in the bulk collagen fibre orientation in myopic eyes could potentially be to loads other than the IOP and CSFP. For example, during horizontal ocular motions, the optic nerve can exert a traction force on the eye globe to shear and deform the tissues of the ONH (Jonas et al., 2016; Wang et al.,

2017). In high myopia, this optic nerve traction force could be considerably increased due to the axial elongation of the ocular globe, thus yielding a higher amount of optic nerve straightening for the ONH to travel the same distance, like that in an emmetropic eye. It has also been shown that in highly myopic eyes with staphyloma the optic nerve traction force can reach such proportions as to even retract the eye within its orbit (Demer, 2016). Should such a traction force increase with high myopia, then the contribution of the bulk collagen remodelling might become more important than that of the IOP or CSFP, with the collagen fibres probably orientating along the direction of higher stresses. This is further supported by a number of studies, which indicated that horizontal ocular motions considerably deform the ONH and may directly relate to the enlarged and disorganised optic nerve canal presented by the highly myopic specimens in the current study, in particular HM2 (Figure 3.07B) (Wang et al., 2016a; Wang et al., 2016b; Chang et al., 2017). During eye adduction, the *dura mater*, the largest of the three neuro-protective meningeal layers, transmits higher stress in the temporal direction of the PPS, which could plausibly result in a radial realignment of the collagen fibres. Highly myopic specimen HM1 exhibited optic nerve canal stretching in the ST-IN direction (Figure 3.05), which also coincides with areas of reduced collagen fibre anisotropy in glaucomatous specimens (Pijanka et al., 2012). Other highly myopic alterations, such as stretching and tilting of the ONH and atrophy in the  $\Gamma$  (area between Bruch's membrane and the ONH) and  $\Delta$  (central part of  $\Gamma$  absent of small blood vessels) zones of the PPS, could also affect the stress distribution within the PPS and thus other remodelling scenarios should not be excluded and warrant further investigation (Jonas et al., 2012; Jonas et al., 2016; Jonas et al., 2018). The levels of stress can also be high in the nasal part of the sclera due to abduction, which could possibly be linked to the disruption in circumferential fibril orientation in the SN quadrant of the PPS (Wang et al., 2017).

Although the structure of the three highly myopic eyes deviated noticeably from the seven non-myopic specimens, the structural features in the control group were highly reproducible between specimens (Appendix A.1.1). The number of analysed highly myopic specimens was small due to the universally limited availability of suitable posterior sclerae from patients with known myopic status, as well as the general low volition for eye donation (Lawlor et al., 2010; Lawlor and Kerridge, 2014). It also remained unknown when in their lifetime the donors developed myopia, with some of the specimens missing details of sex and ethnicity. Whilst to the best of the author's

knowledge there is no available data on a connection between sex and scleral microstructure, there is some evidence that the collagen fibre arrangement and stiffness of the posterior sclera may vary between ethnic groups (Section 1.4.2) (Yan et al., 2011; Fazio et al., 2014).

WAXS yields thickness-averaged measurement and cannot provide clarity on the structural composition throughout the tissue depth. Pijanka and colleagues previously showed that the circumferential collagen alignment does not persist through the entire PPS depth, but rather is concentrated in the outer two-thirds of the stroma (Pijanka et al., 2015). Thus, further experiments are required to assess if the myopic changes persist through the entire depth of the scleral tissue. A suitable approach would be the use of second harmonic generation (SHG) microscopy to assess depth-dependent alterations (Pijanka et al., 2019). Therefore, WAXS and SHG collection analysis of more highly myopic specimens will be part of future work. A detailed, mechanistic understanding of myopic changes to scleral structure and biomechanics would necessitate longitudinal data outside the scope of the cross-sectional investigations presented here and require the use of animal models. Chapter IV provides clarity on the posterior scleral arrangement of several mammalian species that will be an important step in establishing a suitable human analogue for studying myopia and other scleral disorders involving biomechanical influences.

### 3.3 Summary, conclusions and future work

In this Chapter, WAXS was used to map the bulk posterior scleral collagen architecture in three highly myopic human eyes. In comparison to non-myopic specimens, all highly myopic sclerae displayed disruptions in the characteristic circumferential collagen fibril organisation in the PPS and in the tangential linear fibre bands around it, as well as alterations in the typically well conserved regional pattern of anisotropic proportion. Summaries of the changes to the three highly myopic specimens are provided below (Table 3.2).

Table 3.2 – Alterations in collagen anisotropic proportion and angular displacement from circumferential orientation in the PPS for highly myopic specimens HM1, HM2 and HM3 in comparison to an averaged control group of seven non-myopic eyes. The changes are grouped by quadrant: SN, ST, IT and IN. The number of arrows indicates the level of parameter alteration.

Specimen	High Myopia 1			
Peripapillary scleral quadrant	SN	ST	IT	IN
Anisotropic proportion	↑	↓	↑	↓ ↓
Displacement from circumferential	—	↑ ↑	↑ ↑ ↑	↑
Specimen	High Myopia 2			
Peripapillary scleral quadrant	SN	ST	IT	IN
Anisotropic proportion	↑ ↑	—	↓	—
Displacement from circumferential	↑ ↑ ↑	—	—	↑
Specimen	High Myopia 3			
Peripapillary scleral quadrant	SN	ST	IT	IN
Anisotropic proportion	—	↓	↑ ↑	↓ ↓
Displacement from circumferential	↑ ↑ ↑	—	↓	↑

Legend: Increase ↑ ; Decrease ↓ ; No change —

The results presented here support the idea that pathological structural remodelling takes place with myopia that accompanies the axial lengthening of the eye and the mechanical alteration of the scleral tissue (Siegwart Jr and Norton, 1999; Grytz and Siegwart, 2015). Disruptions in the PPS may also link to the increased susceptibility of myopic eyes to glaucoma development. Therefore, the data presented here will enhance future modelling studies of ocular biomechanics in myopia

and in glaucoma, as well as inform emerging myopic treatments such as scleral cross-linking (Su et al., 2010; Campbell et al., 2017).

As mentioned, further investigation is necessary to ascertain whether the structural changes reported herein are a direct consequence of posterior scleral remodelling during ocular elongation or alternatively a mechanical adaptation to tissue stresses induced by fluid pressure or ocular movements that could be exacerbated in enlarged eyes. As highly myopic eyes are noted to be more susceptible to developing glaucoma, future research is envisioned to compare the posterior scleral architecture of myopic and glaucomatous specimens. For a more holistic evaluation, a combination of both WAXS and SHG techniques is warranted (Pijanka et al., 2019). The results of such an investigation could help clarify the question of why some individuals have glaucoma at normal IOP levels (Section 1.4.3) and further elucidate the connection of myopic status to glaucomatous disease progression. The cellular contribution to the myopic changes should also be investigated. In addition, it would be prudent to consider a quadrant-wise PPS study of the scleral fibroblasts, as a study by Oglesby and colleagues in murine glaucomatous sclerae noted that the mean fibroblast density in the nasal region was on average 25% lower than in the other three quadrants, which could possibly be related to local variations in the collagen fibril density and anisotropy (Oglesby et al., 2016).

## **Chapter IV**

### **Collagen microstructure in mammalian sclera**

## 4.1 Introduction

In general, there are several restrictions in carrying out scientific research on human tissue. Those include acquisition of appropriate and sufficiently numerous tissue samples from donors, which is a notable challenge for ocular tissues, and the necessity for rigorous ethical permission approvals (Lawlor et al., 2010; Lawlor and Kerridge, 2014). One major issue relevant to this project is that most of the available ocular globes come from elderly individuals, with research showing age-related changes to the sclera, including greater susceptibility to glaucoma (Section 1.4.2). Whilst the annular collagen fibril structure in the peripapillary sclera (PPS) was shown to remain fairly consistent with age, the same cannot be said about the scleral cells and their physiology, variations in which could preclude accurate investigations (Chapter III; (Coudrillier et al., 2015a,b; Markov et al., 2018)). Thus, it is preferable to perform experimental procedures with tissue obtained from individuals that are around the same age and are young adults. Where this is not practical for human studies, suitable animal models are often utilised.

Different animal species have been used as models for ocular pathologies involving the sclera, the most common of which are mice, tree shrews, chickens, monkeys, pigs and cattle (Albon et al., 2007; Girard et al., 2008; Girard et al., 2009c; Myers et al., 2010; Pijanka et al., 2014; Nguyen et al., 2017). Recently Gogola and colleagues used polarised light microscopy to show that the circumferential collagen fibril alignment in the PPS is present in several domestic animal species (Gogola et al., 2018b). However, it still remains uncertain which species is the closest to humans for this structure, given that appreciable variations were observed between the studied animals (Gogola et al., 2018b). Therefore, this study aimed to determine a suitable human analogue for future posterior scleral investigations. A species was sought that matched two essential criteria: (I) the circumferentially aligned annulus of collagen fibres in the PPS must be in similar proportion to that present in humans; (II) there needs to be ready access to new ocular material from age-matched individuals. Whilst poultry eyes have been widely used previously in scleral ECM studies of myopia, they are both genetically and physiologically distinct from humans and, in particular, the sclera has been noted to have a cartilaginous component not present in humans, which also contains fewer myofibroblasts in general (McBrien et al., 2009). Thus, only mammalian species were investigated in this study.

The Chapter presents a wide-angle X-ray scattering (WAXS) analysis and comparison of the posterior sclera from 11 mammalian species. This was performed to both select a suitable human analogue for further experimental work but also to determine specifics in the scleral collagen architecture as a function of eye size. In addition, PPS sections from the chosen species were later sectioned and imaged using second harmonic generation (SHG) laser microscopy to assess the depth-dependent organisation of the annular structure of collagen fibres around the optic nerve head (ONH).

## 4.2 Results and Discussion

### 4.2.1 Wide-angle X-ray scattering analysis

WAXS experiments were conducted on posterior sclera from 11 mammalian species (Table 2.2, Section 2.2.1.2). Information on the precise ocular globe size for all animals was not available, which is why the specimens are listed in terms of increase of body size, from smallest (mouse; Section 4.2.1.1) to largest (cattle; Section 4.2.1.11). For the purpose of comparison and reproducibility, the collected WAXS polar vector plot and contour maps are presented as octagons which, in relative terms, covered approximately the same representative area around the ONH. The size of these regions was dependent on the scanned tissue surface and encompassed the PPS and part of the mid-posterior sclera. The sampling interval for each animal was chosen according to their body size, in order to be relatively consistent across species. A size-accurate comparison of the sclerae is presented (Section 4.2.1.12).

#### 4.2.1.1 Laboratory mouse

The mouse (*Mus musculus*) is perhaps the most standard vertebrate model. In terms of ocular pathologies, it has been used to study glaucoma at both an extracellular matrix (ECM) and cellular level (Pijanka et al., 2014; Oglesby et al., 2016; Nguyen et al., 2017). A WAXS polar vector plot map of a posterior sclera of an albino mouse (Figure 4.01A) demonstrated that the lobes of the polygon plots were broad, indicating a larger spread of collagen fibrils, with the lowest measured collagen anisotropy of all the studied species. The collagen fibril annulus was not well-defined, specifically when compared to those in humans (Chapter III), with only partial circumferential orientation around the ONH, mostly on its left and right side (Figure 4.01A). The bounded region of the *lamina cribrosa* (LC) was also represented by polar vector plots with a more spread distribution and until recently it remained uncertain if the murine LC was even load-bearing, given that it is predominantly cellular in nature with relatively little ECM (Nguyen et al., 2017). The anisotropic proportion of the specimen was low, with no clear distinguishable patterns or features, indicating a mostly homogenous fibrillar distribution. Together, these observations could suggest that, unlike humans, the circumferential collagen structure in the PPS might not be primarily for resisting IOP-generated scleral stress in the mouse (Boote et al., 2019). Due to its small size, the murine eye was the only specimen to require relaxational incisions to flatten it for scanning (Figure 4.01), whilst for all other specimens a circular part of the posterior sclera was scanned in its natural curvature (Pijanka et al., 2014). However, the incisions ended outside the PPS, so as not to risk disruption of the fibrillar collagen architecture. Moreover, previous WAXS studies in human tissue has shown that mid-posterior scleral incisions have minimal effect on PPS structure (Pijanka et al., 2012; Pijanka et al., 2013).

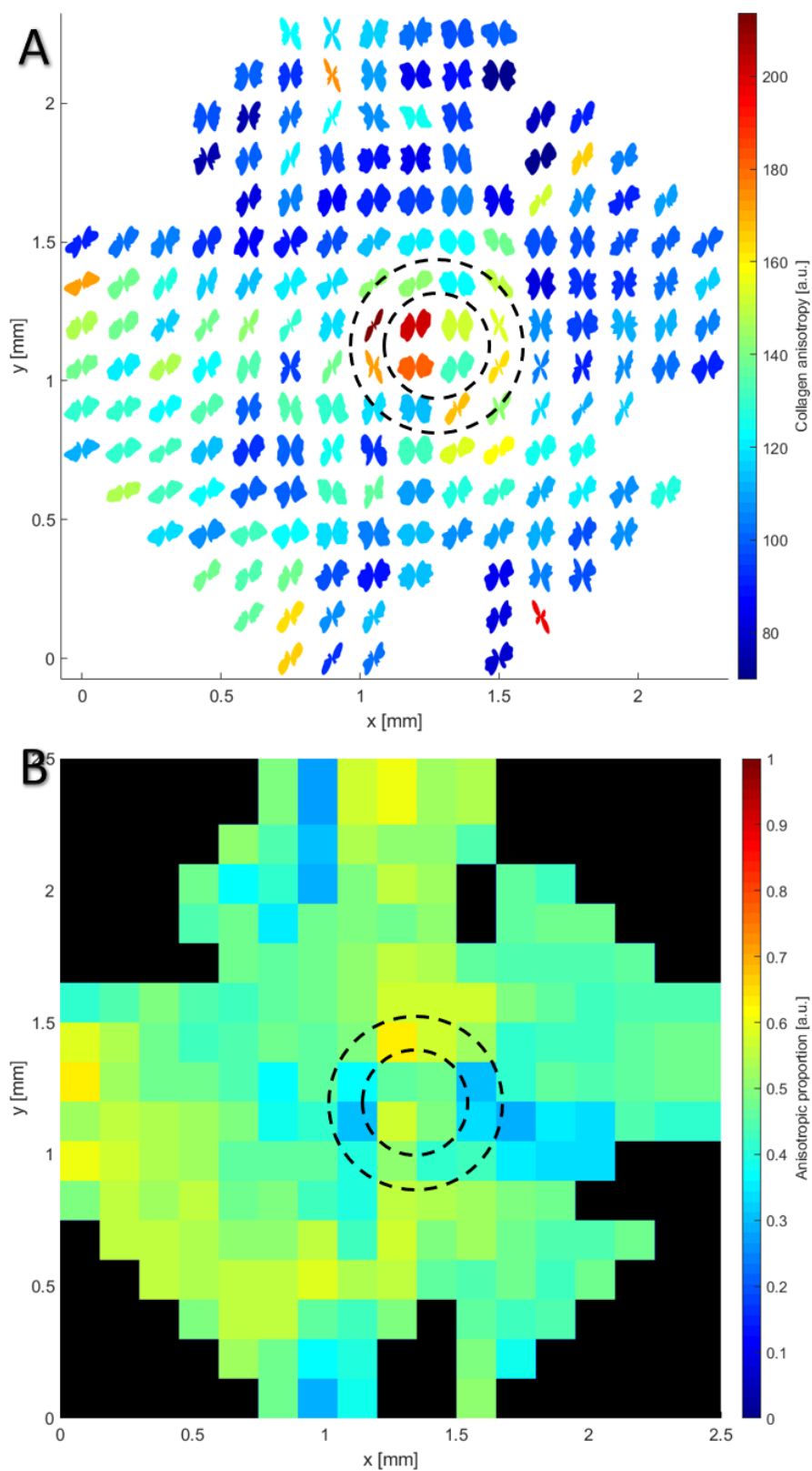


Figure 4.01 – Wide-angle X-ray scattering (WAXS) polar vector plot map (A) and collagen anisotropic proportion contour map (B) of a murine posterior sclera. The weakly aligned annulus of collagen fibres in the peripapillary sclera (PPS) is bounded by dashed lines. Data points were recorded at every 0.15mm.

4.2.1.2 Northern tree shrew

Northern tree shrews (*Tupaia belangeri*) have been used as ophthalmic animal models due to their close phylogenetic relationship with primitive primates, as well as for their well-developed sense of vision (Campbell, 1966). Many previous studies have also used the tree shrew eye to investigate myopia (Guggenheim and McBrien, 1996; Phillips and McBrien, 2004; Siegwart and Strang, 2007; Grytz and Siegwart, 2015). In comparison to the mouse (Figure 4.01A), the tree shrew has a wider optic nerve, but with a relatively narrow annular collagen fibril structure around it (Figure 4.02A). Albon and colleagues previously noted that the tree shrew optic nerve and LC resemble those of humans, with the WAXS polar vector plot map presented here confirming a more organised LC than in mice (Albon et al., 2007). Highest anisotropic proportion values were also registered in the area representative of the ONH (Figure 4.02B). As Boote and colleagues recently noted, accounting for IOP and scleral wall thickness, the in-wall hoop stress for the tree shrew sclera should be about twice as large as that of humans (Boote et al., 2019). In this respect, the relatively narrow circumferential PPS structure was unexpected given its generally purported role in protecting the LC from IOP-induced stress, suggesting other biomechanically relevant factors, such as eye movements and fluid pressures other than IOP, might be important in determining the scleral ECM architecture in tree shrews (Boote et al., 2019).

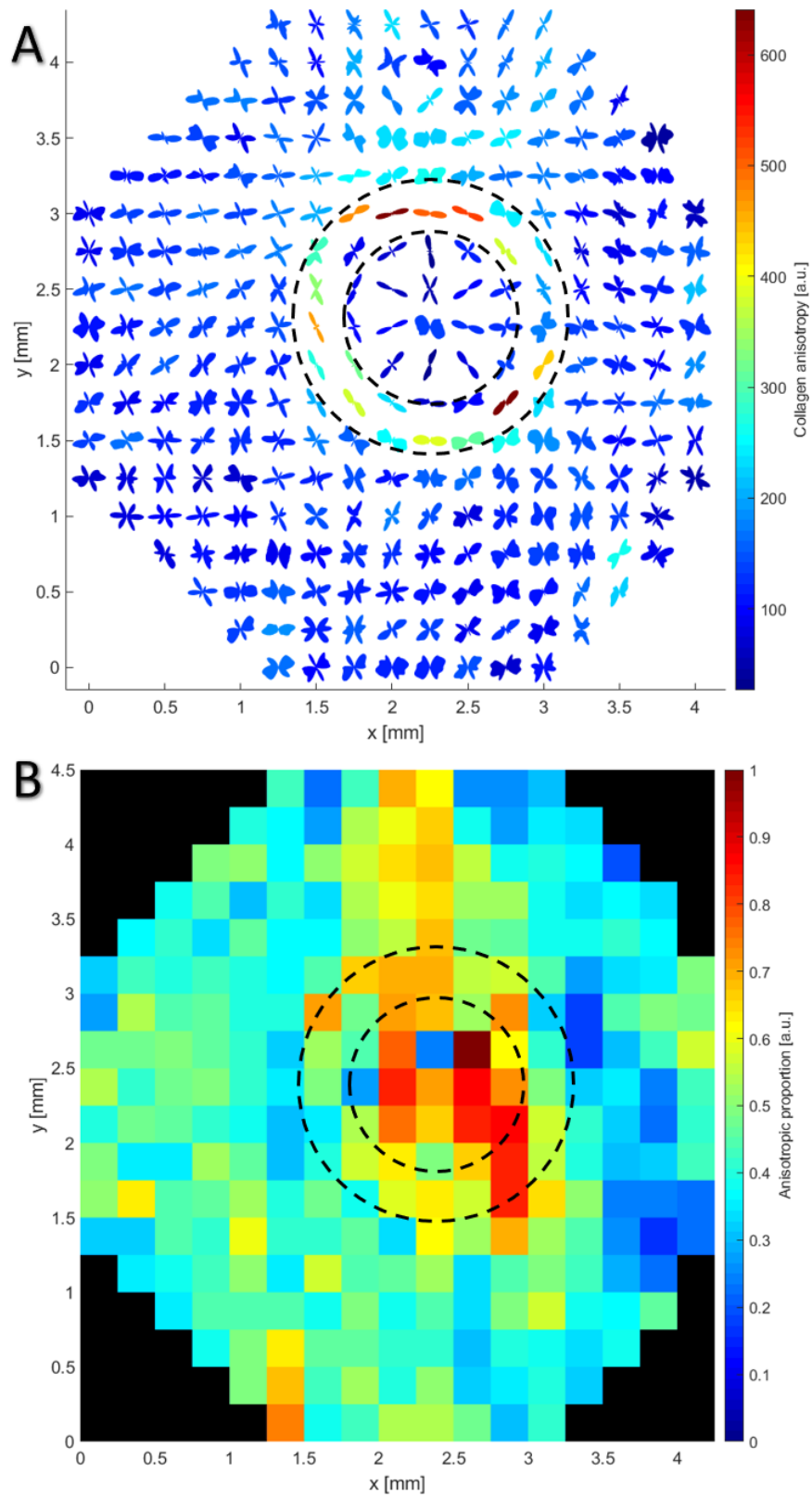


Figure 4.02 – WAXS polar vector plot map (A) and collagen anisotropic proportion contour map (B) of a northern tree shrew posterior sclera. The aligned annulus of collagen fibres in the PPS is bounded by dashed lines.

Data points were recorded at every 0.25mm.

#### 4.2.1.3 Guinea pig

The WAXS polar vector map of a guinea pig (*Cavia porcellus*) posterior sclera demonstrated that it was markedly different from the previous mammalian ones (Figure 4.03A). The scleral canal had an oval shape, with the circumferentially aligned collagen fibrils following closely this elliptical form. In addition, around the horizontal axis the collagen annulus appeared to be disrupted on both sides of the optic nerve, as seen by both the fibril orientation around the lateral sides of the ONH, but also in terms of the lower collagen anisotropy values. This observation was further supported by smaller anisotropic proportions in the corresponding regions (Figure 4.03B).

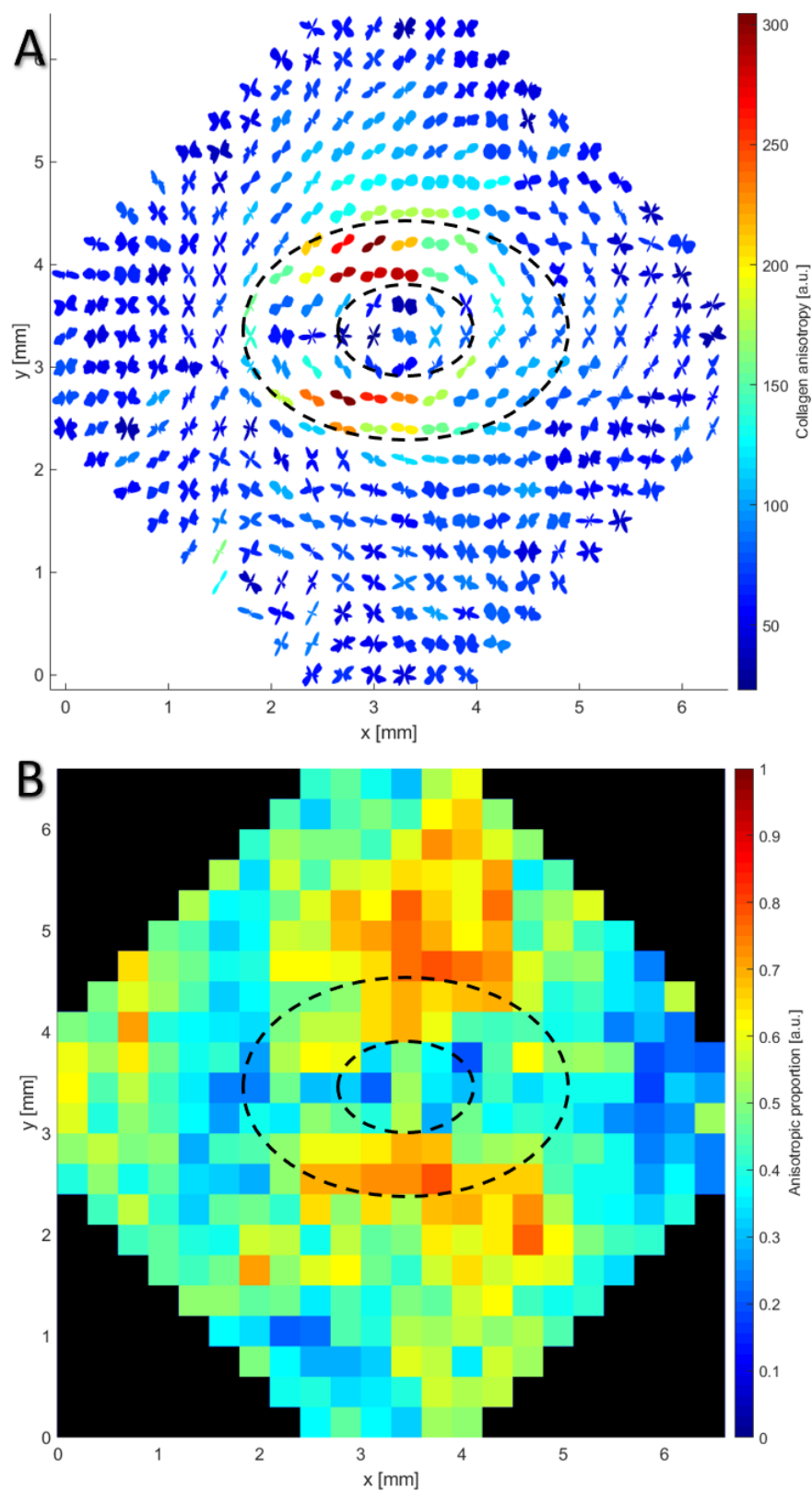


Figure 4.03 – WAXS polar vector plot map (A) and collagen anisotropic proportion contour map (B) of a guinea pig posterior sclera. The aligned annulus of collagen fibres in the PPS is bounded by dashed lines.

Data points were recorded at every 0.3mm.

#### 4.2.1.4 Black lion tamarin

Out of all the presented mammalian species in this Chapter, the black lion tamarin (*Leontopithecus chrysopygus*) was the closest one to humans genetically, as both species belong to the Primate order. The species is endemic to the Atlantic Forest in Southern Brazil (Garbino et al., 2016). As seen in Figure 4.04A, the PPS structure was more organised than the previous three species, but at the same time lacked the distinct tangential fibre bands and the characteristic break in circumferential alignment present in human posterior sclerae (Chapter III and Appendix A.1.1). However, similar to humans, the collagen anisotropic proportion values were highest in the PPS, with more clearly defined regions in the mid-posterior sclera as well (Figure 4.04B).

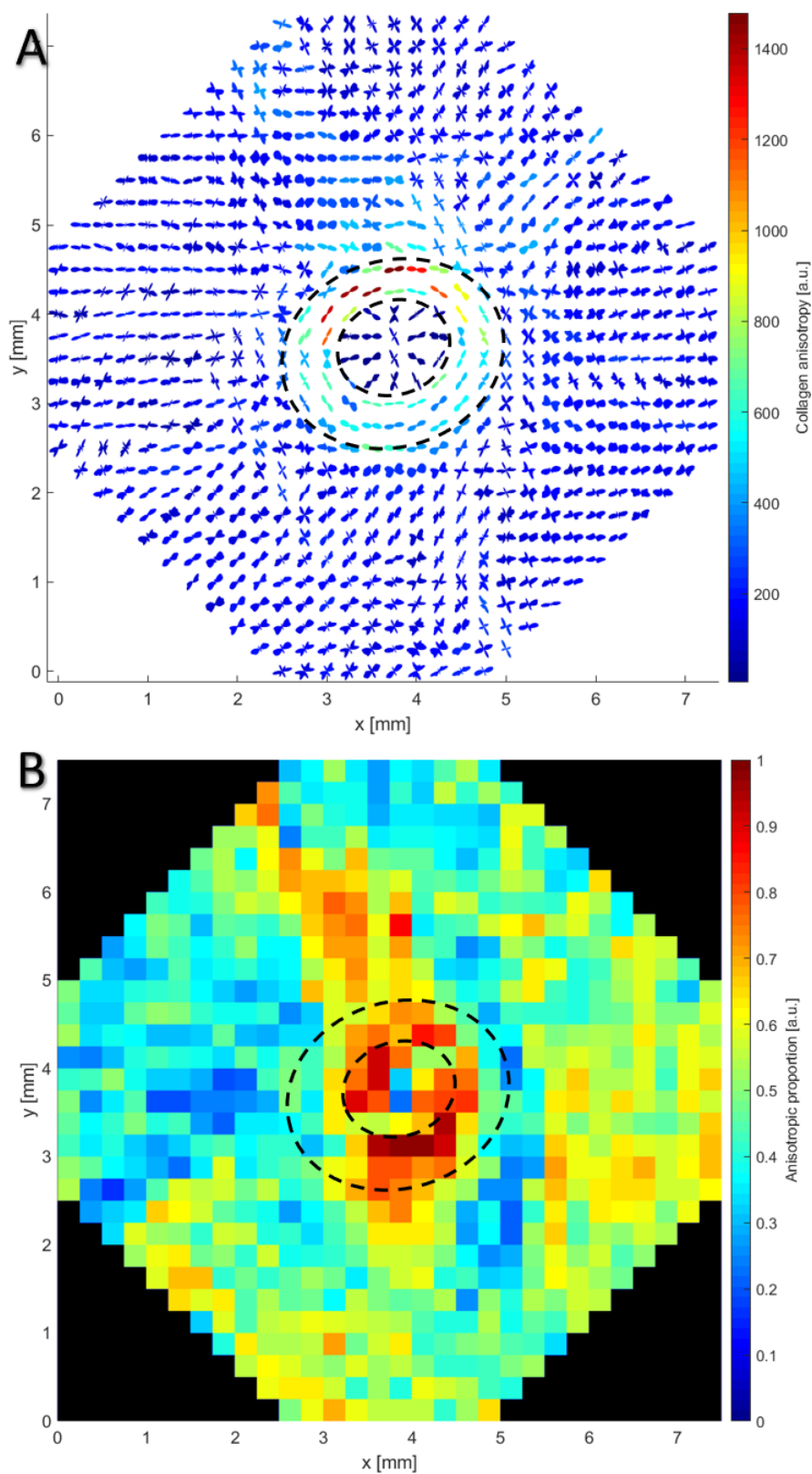


Figure 4.04 – WAXS polar vector plot map (A) and collagen anisotropic proportion contour map (B) of a black lion tamarin posterior sclera. The highly aligned annulus of collagen fibres in the PPS is bounded by dashed lines. Data points were recorded at every 0.25mm.

#### 4.2.1.5 Azara's agouti

Azara's agouti (*Dasyprocta azarae*) are South American rodents, with ocular globe axial length of  $14.02 \pm 0.01$  mm and IOP of  $11.61 \pm 0.44$  mmHg, (Tavares-Somma et al., 2017). Based on WAXS there appeared to be more circumferentially aligned polygon plots in the PPS (Figure 4.05A), along with more evidence of tangential fibre bands, similar to humans, than any of the other mammals presented so far. The anisotropic proportion contour map showed a crescent distribution of higher values around the ONH and lower to the right of it (Figure 4.05B). The corresponding polygon plots on the lateral sides of the scleral canal, however, did not appear different in terms of collagen anisotropy values or fibrillar distribution (Figure 4.05A).

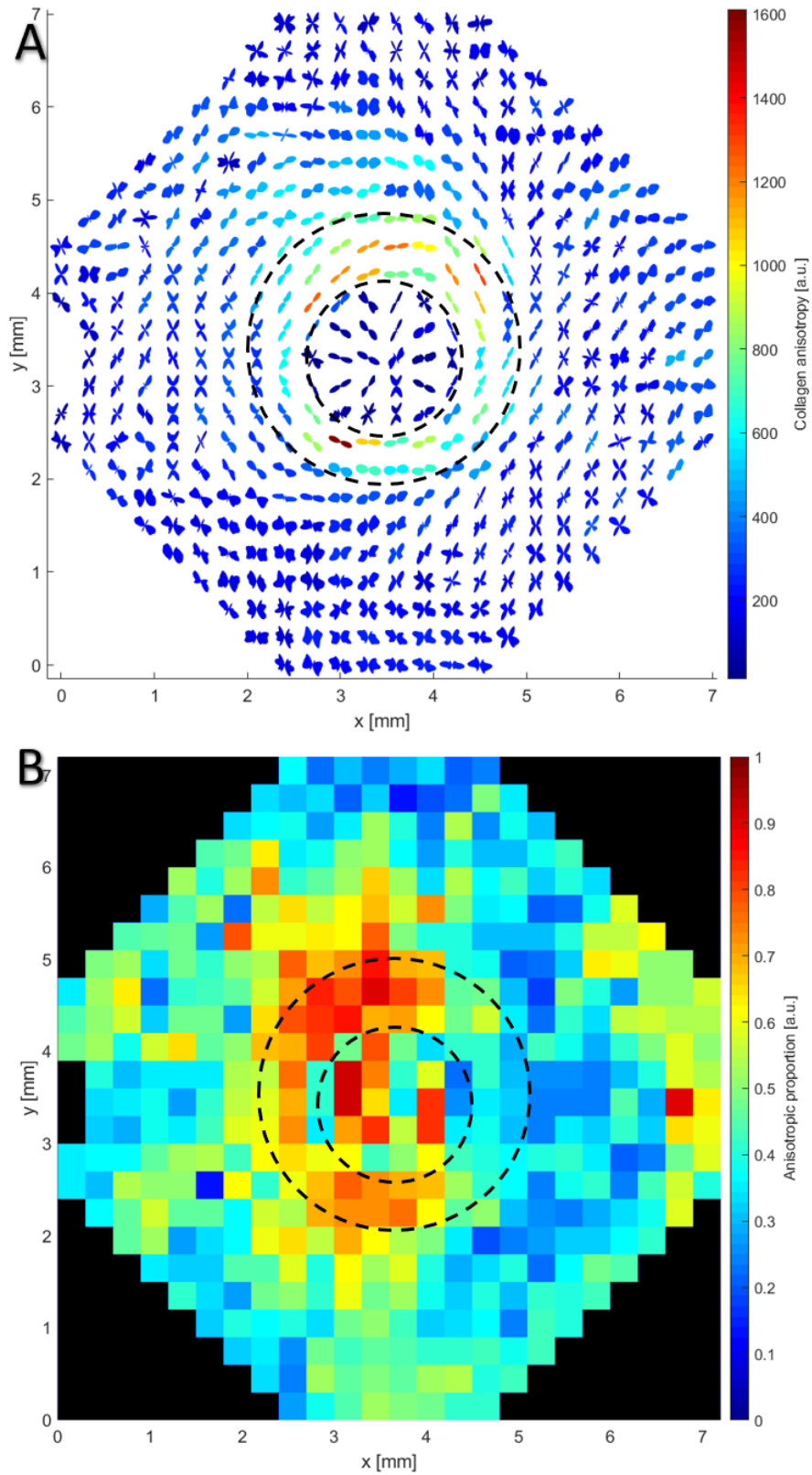


Figure 4.05 – WAXS polar vector plot map (A) and collagen anisotropic proportion contour map (B) of an Azara's agouti posterior sclera. The aligned annulus of collagen fibres in the PPS is bounded by dashed lines.

Data points were recorded at every 0.3mm.

#### 4.2.1.6 Lesser mouse-deer

The WAXS polar vector plot map of a lesser mouse-deer (*Tragulus javanicus*) posterior sclera had an atypically large elliptical scleral canal (Figure 4.06A). In addition, the collagen fibril annular ring appeared to be more circular and disproportionally narrow on the left side of the ONH, with a more disrupted feature. The anisotropic proportion contour map (Figure 4.06B) further supported these observations, with higher value distribution around the top and bottom of the optic nerve.

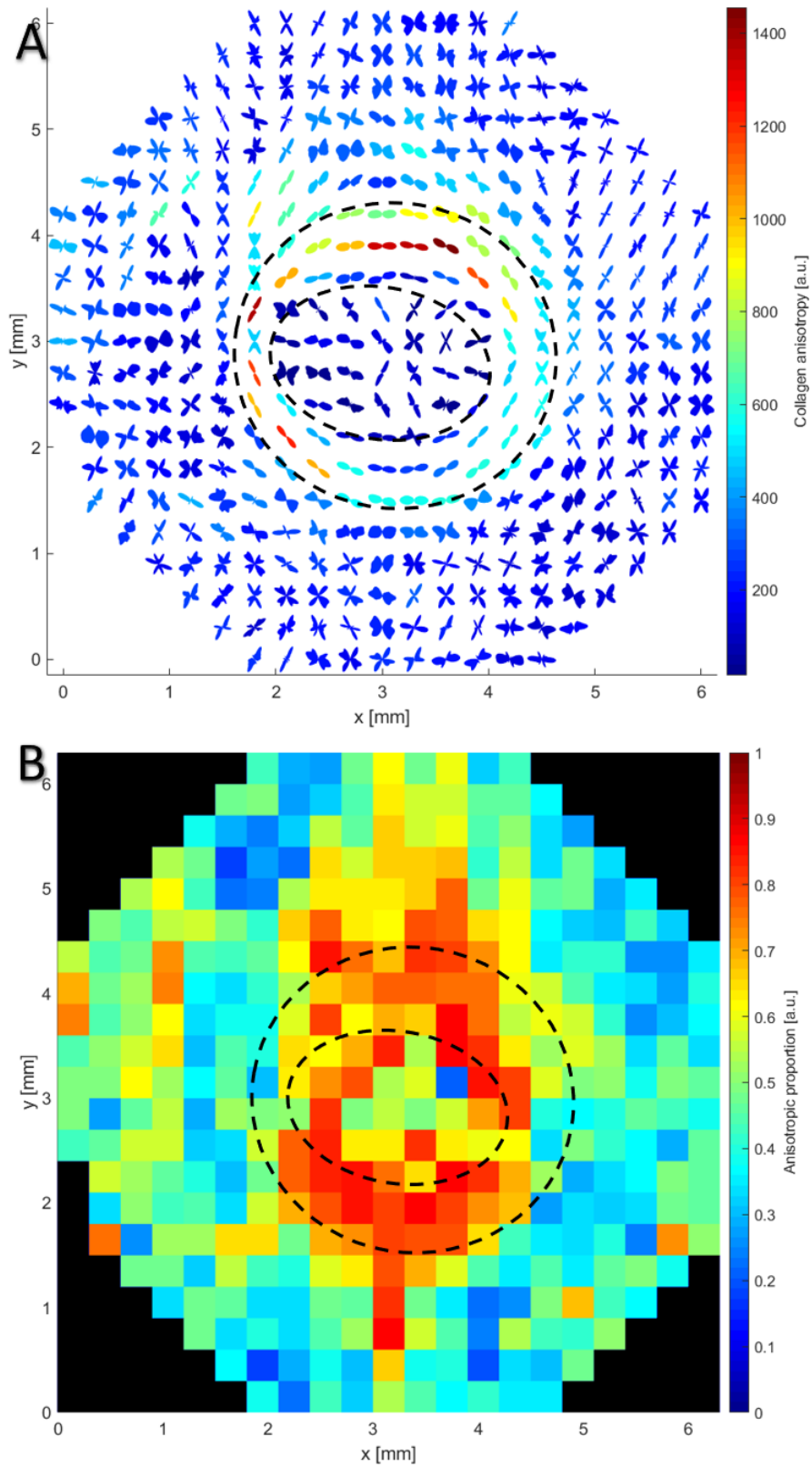


Figure 4.06 – WAXS polar vector plot map (A) and collagen anisotropic proportion contour map (B) of a lesser mouse-deer posterior sclera. The aligned annulus of collagen fibres in the PPS is bounded by dashed lines. Data points were recorded at every 0.3mm.

#### 4.2.1.7 Red panda

The red panda (*Ailurus fulgens*) also exhibited an interruption in the circumferential alignment of the collagen fibrils in the PPS similarly to the guinea pig (Figure 4.03A), but unlike it, the collagen formed a nearly perfect ring (Figure 4.07A). The mid-posterior sclera also showed regions of further structure, with most of the polar vector plots below the PPS being mostly parallel to it, possibly corresponding to muscle insertions similar to those observed in humans. There were also two notable diagonal fibre bands running from the top left and stopping in the mid-posterior before reaching the scleral canal. The anisotropic proportions were, on average, lower in the PPS than most of the other species, but still reflected the higher alignment on the top and bottom sides of the ONH.

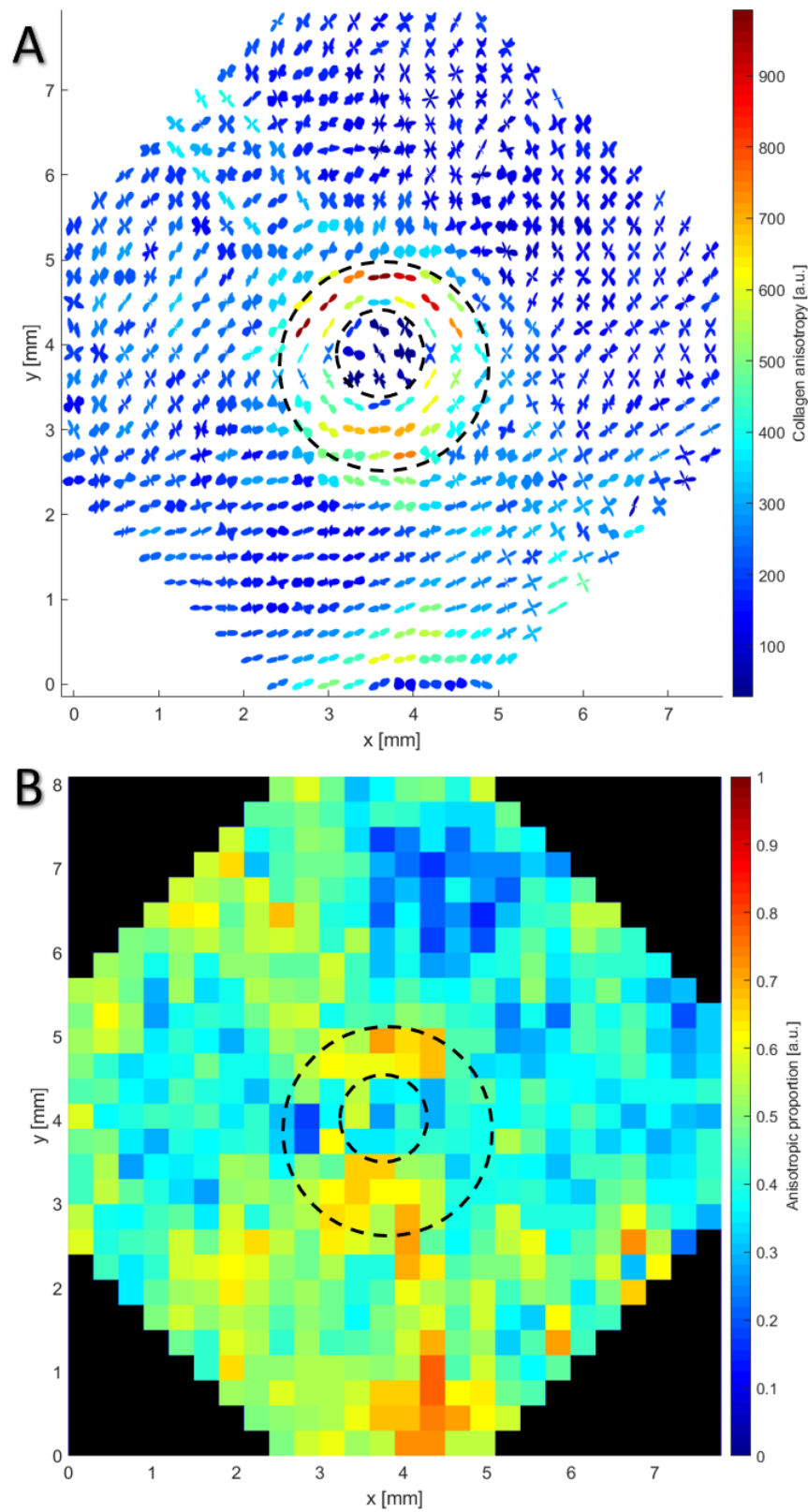


Figure 4.07 – WAXS polar vector plot map (A) and collagen anisotropic proportion contour map (B) of a red panda posterior sclera. The highly aligned annulus of collagen fibres in the PPS is bounded by dashed lines.

Data points were recorded at every 0.3mm.

### 4.2.1.8 North American river otter

The North American river otter (*Lontra canadensis*) had an extended collagen fibril annulus with several further aligned regions in the mid-posterior sclera (Figure 4.08A). The characteristic break in circumferential orientation in humans was observed in the otter PPS on the left side of the scleral canal, whilst on the top right in the mid-posterior there was a long tangential fibre band. In close proximity there were also two vector plots with lower collagen anisotropy and several other aligned polar plots around them, probably corresponding to blood vessels. Both the blood vessel lumen and the disruption in circumferential orientation were reflected in the anisotropic proportion contour map (Figure 4.08B). A possible explanation for the pronounced characteristics could be the result of lifestyle of certain animals that led to the migration of the eyes to the front of their faces, with binocular vision being optimal in more cluttered environments (Changizi and Shimojo, 2008). This shift in field of vision might have led to rearrangement in the position of the optic nerve in the posterior sclera and hence its supporting structures. It should be noted, that the river otter, along with the tamarin monkey (Section 4.2.1.4) and red panda (Section 4.2.1.7), have their eyes at the front of their faces and had highly aligned collagen fibril annuluses.

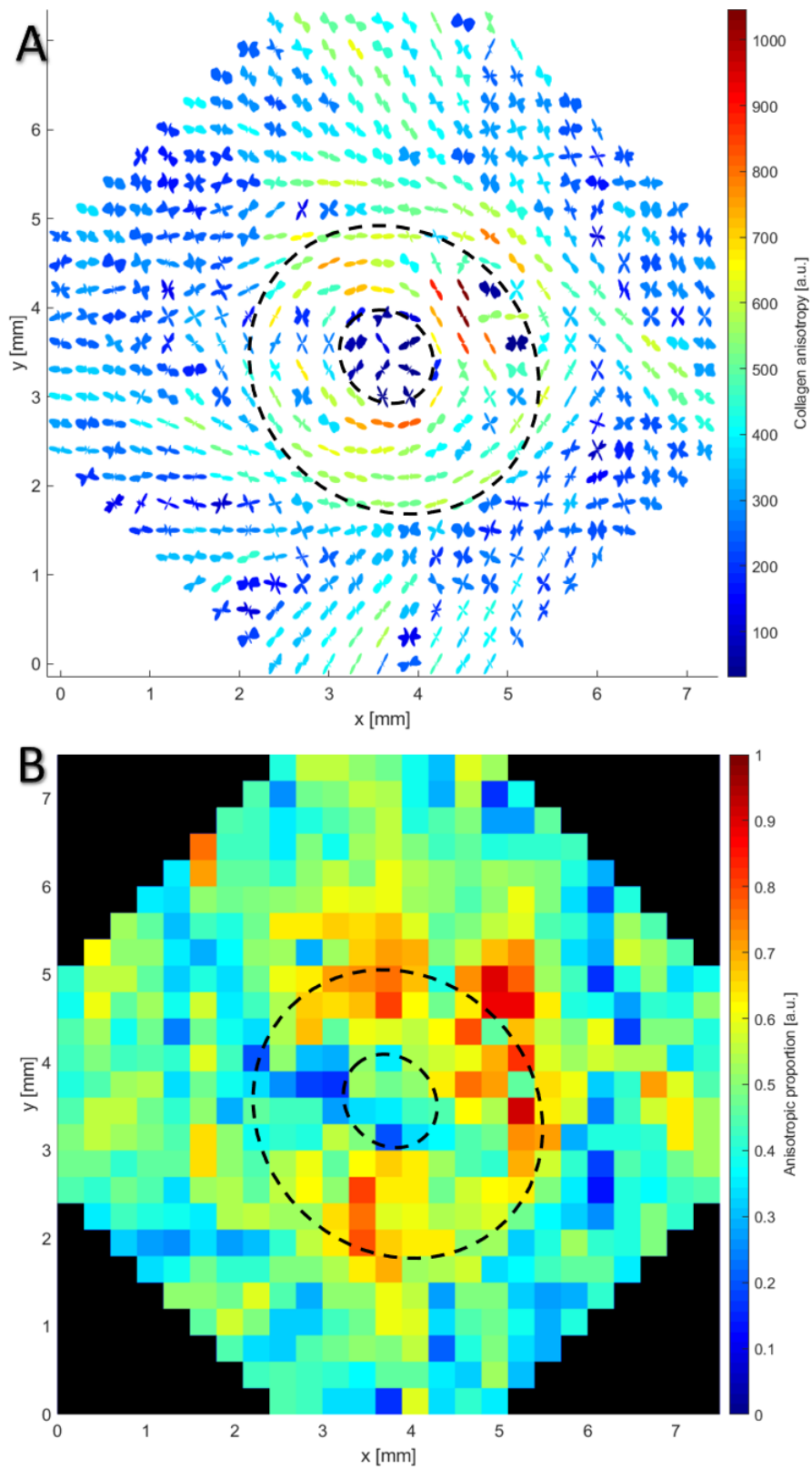


Figure 4.08 – WAXS polar vector plot map (A) and collagen anisotropic proportion contour map (B) of a North American river otter posterior sclera. The highly aligned annulus of collagen fibres in the PPS is bounded by dashed lines. Data points were recorded at every 0.3mm.

### 4.2.1.9 Domestic pig

Domestic pig (*Sus scrofa domesticus*) eyes have been commonly used as model substitutes to human eyes, due to their similar size ( $23.90\pm 0.08\text{mm}$ ) and shape, as well as IOP ( $15.2\pm 1.8\text{mmHg}$ ) (Ruiz-Ederra et al., 2005; Middleton, 2010; Sanchez et al., 2011). However, the ONH was oval with a wider and more spread ring of circumferentially aligned collagen fibrils compared to humans (Figure 4.09A). Equatorially, the annulus appeared to be thinner on the left side of the scleral canal, similarly to the lesser mouse-deer (Figure 4.06A), whilst having less aligned fibrils on the right side. The WAXS polar vector plot map indicated further structural regions in the mid-posterior sclera, with parallel fibres below the scleral canal, reminiscent of the red panda (Figure 4.07A), as well as defined cross patterns of collagen fibril distribution in the top right (Figure 4.09A). The primary structural difference between human and porcine eyes is the existence of an optic nerve ventral groove in the latter (Section 4.2.1.12.1). The groove can be identified in the top right part of the ONH as more highly aligned polar vector plots. Brooks and colleagues were the first to identify this structure in porcine and to note that it can be used to orientate the posterior sclera (Brooks et al., 1998). The anisotropic proportion contour map (Figure 4.09B) closely followed the collagen anisotropy, with lower values in the break in circumferential alignment and higher around the top and bottom side of the scleral canal.

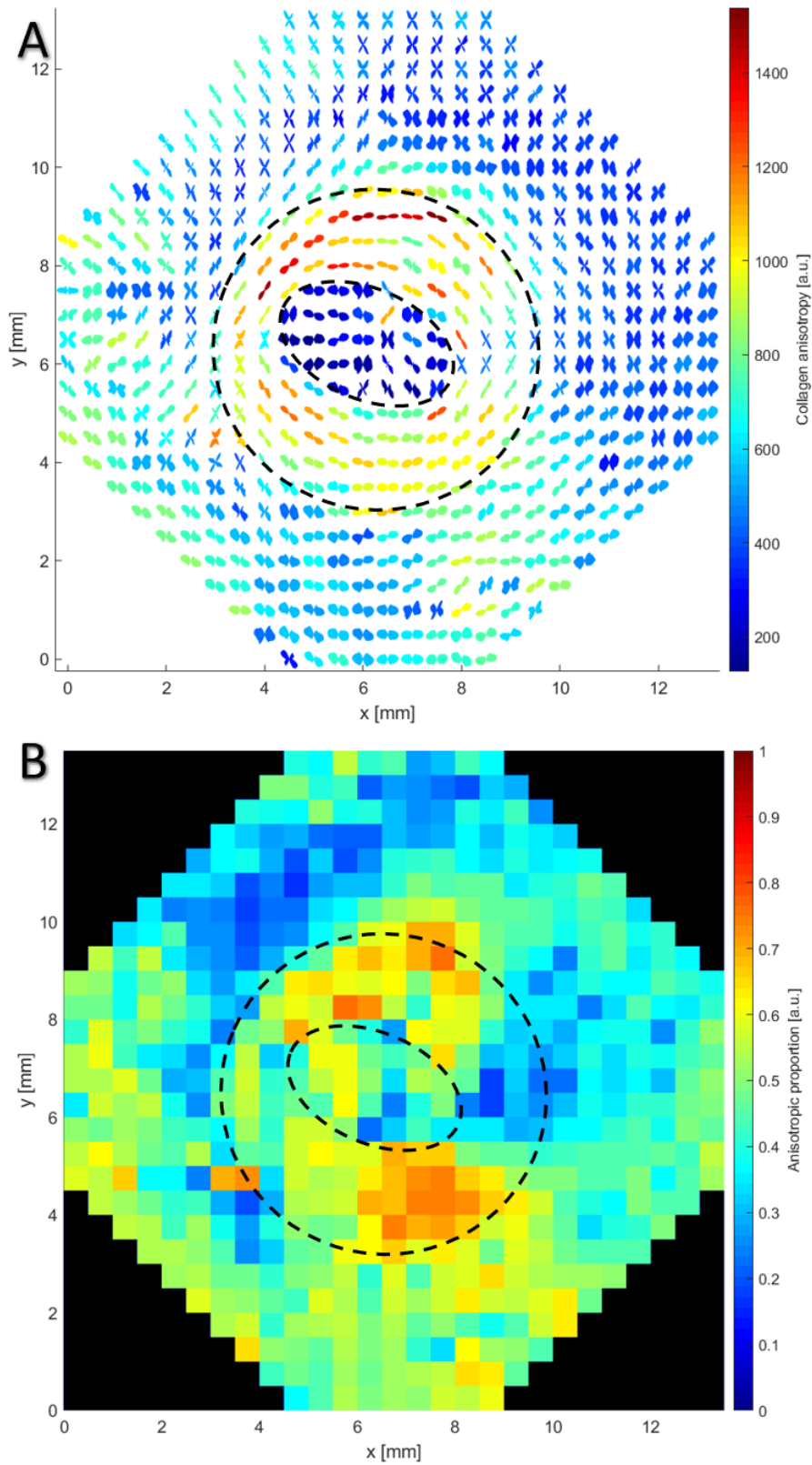


Figure 4.09 – WAXS polar vector plot map (A) and collagen anisotropic proportion contour map (B) of a porcine posterior sclera. The highly aligned annulus of collagen fibres in the PPS is bounded by dashed lines.

Data points were recorded at every 0.5mm.

4.2.1.10 Brazilian tapir

The Brazilian tapir (*Tapirus terrestris*) is the largest herbivore in South America, with small eyes in relation to its overall body size (Ruiz-García et al., 2016). Whilst larger than the domestic pig, the tapir has a notably narrower and more circular ONH and PPS circumferential structure in comparison (Figure 4.10A). Additionally, the posterior sclera appeared to have two narrow tangential fibre bands around the top and bottom of the collagen fibril annulus, which were also reflected by higher anisotropic proportion values (Figure 4.10B). The tapir did not possess a ventral groove in the optic nerve canal, but did, however, have similar polar vector plot cross patterns in the mid-posterior sclera, on the bottom side (Figure 4.10A). As both pigs and tapirs have their eyes positioned on the side of their heads, to provide larger field of vision for predators, this would probably exclude the ventral groove as a formation related to the ocular motions.

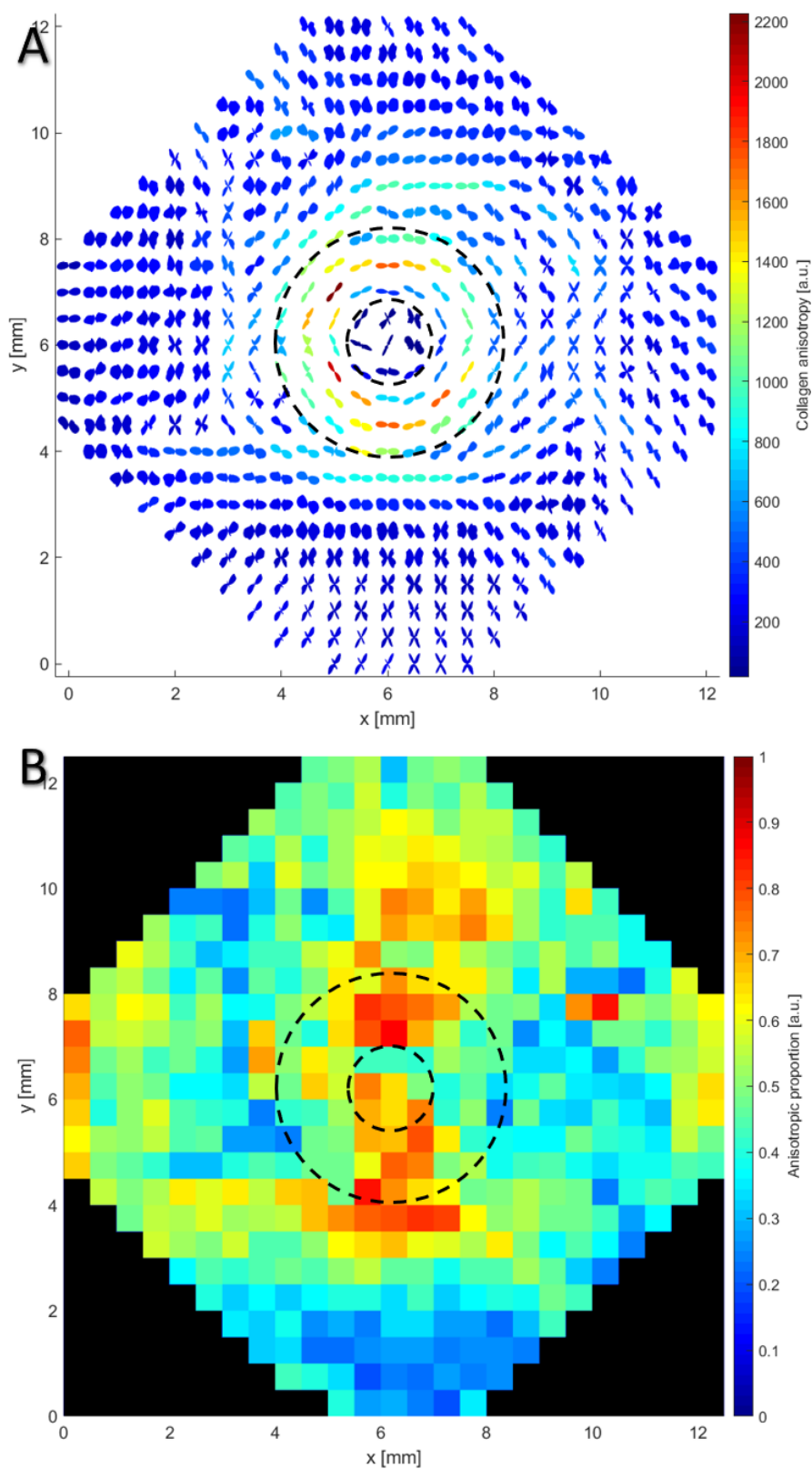


Figure 4.10 – WAXS polar vector plot map (A) and collagen anisotropic proportion contour map (B) of a Brazilian tapir posterior sclera. The highly aligned annulus of collagen fibres in the PPS is bounded by dashed lines. Data points were recorded at every 0.5mm.

4.2.1.11 Domestic cattle

The largest of the 11 compared animal species, domestic cattle (*Bos taurus domesticus*) have an elliptical optic nerve and a pronounced circular PPS collagen fibril structure (Figure 4.11A). In addition, similarly to porcine, bovine also possess a ventral groove, seen on the bottom right side of the scleral canal (Figure 4.11A). Markedly radial LC beam orientation was also evident, with data points on the opposite side of the groove having large anisotropic proportion values (Figure 4.11B). Structural organisation was evident in the mid-posterior sclera as well, with a tangential fibre band on the top right side of the circumferentially aligned collagen fibrils and cross pattern fibrillar organisation below the ONH.

Data acquisition was performed at every 0.5mm (Figure 4.11) or 0.25mm (Figure 4.12), with the latter revealing consistent structural patterns, but at 4x greater resolution than the former. A clearer structure of the LC was observed (Figure 4.12A), with a ‘stalk’ starting from the ventral groove and progressing uniaxially, possibly indicating a similar ‘hourglass’ shape of the LC as in humans (Quigley, 1999). Given the very similar characteristics of the two bovine eyes (Figure 4.11 and 4.12), B1 and B2, respectively, it appears that both were either left or right eyes and had comparable posterior scleral orientation. This is particularly evident in the respective high anisotropic proportion distributions (Figure 4.11B and 4.12B). In addition, precise ocular globe orientation was performed for the SHG microscopy analysis and revealed that the nerve ventral groove is facing the inferior/inferior temporal (IT) direction. Therefore, the area of circumferentially aligned polar vector plots with lower collagen anisotropy (Figure 4.12A), which were positioned on the opposite side of the groove, would be located in the superior/superior nasal (SN) PPS region. As discussed in Chapter III, the disruption in circumferential alignment in the human PPS is also in the SN direction and exhibits similarly lower collagen anisotropy values than the surrounding areas. Bovine eyes have also been used in ophthalmic studies for decades, with key studies determining the composition, elasticity and shear of the sclera, as well as the inflation behaviour of both the sclera and cornea (Smolek, 1988; Gum et al., 1998; Boyce et al., 2008; Myers et al., 2010; Argento et al., 2014). However, the cellular component has been less closely investigated (Markov et al., 2019).

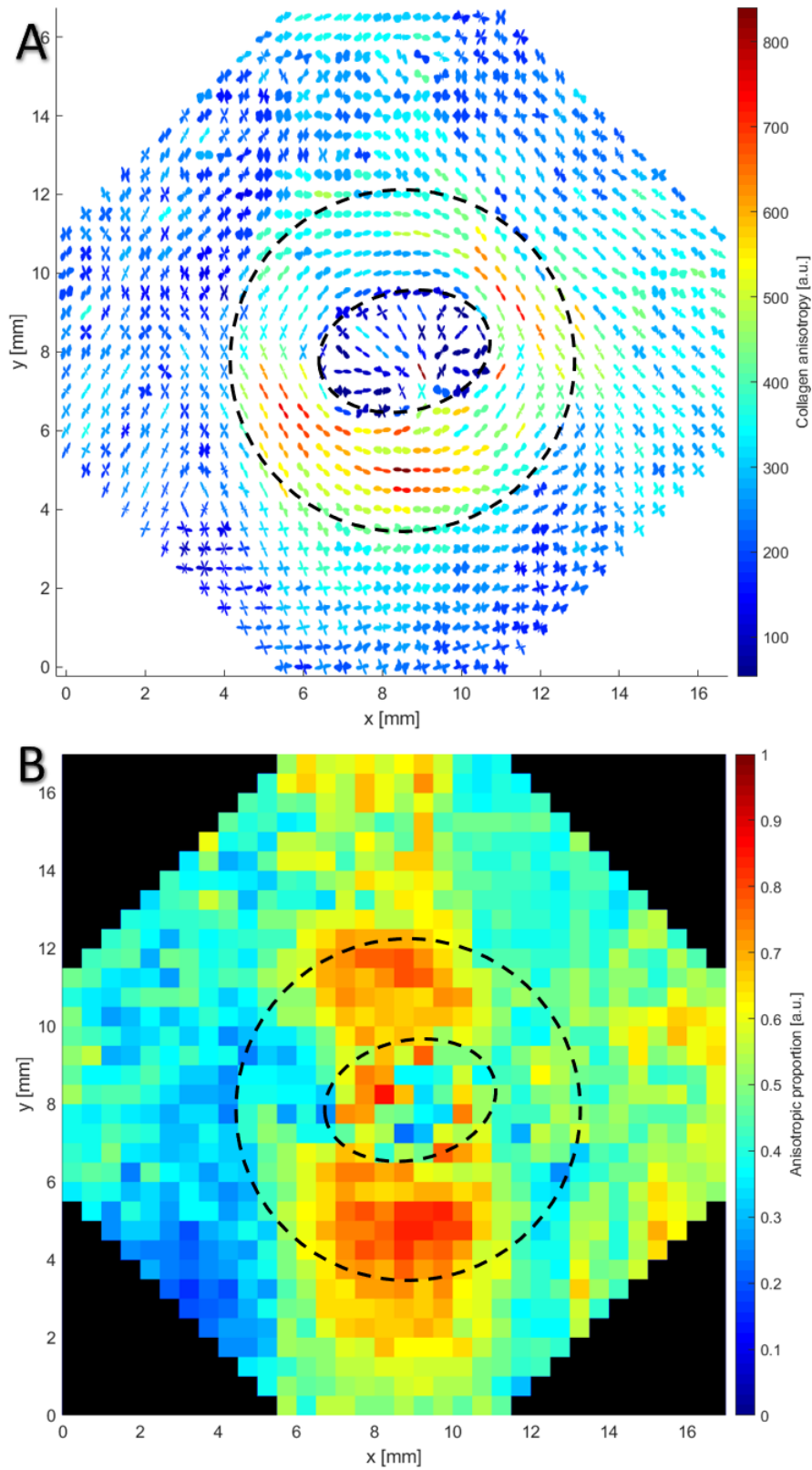


Figure 4.11 – WAXS polar vector plot map (A) and collagen anisotropic proportion contour map (B) of bovine posterior sclera B1. The highly aligned annulus of collagen fibres in the PPS is bounded by dashed lines.

Data points were recorded at every 0.5mm.

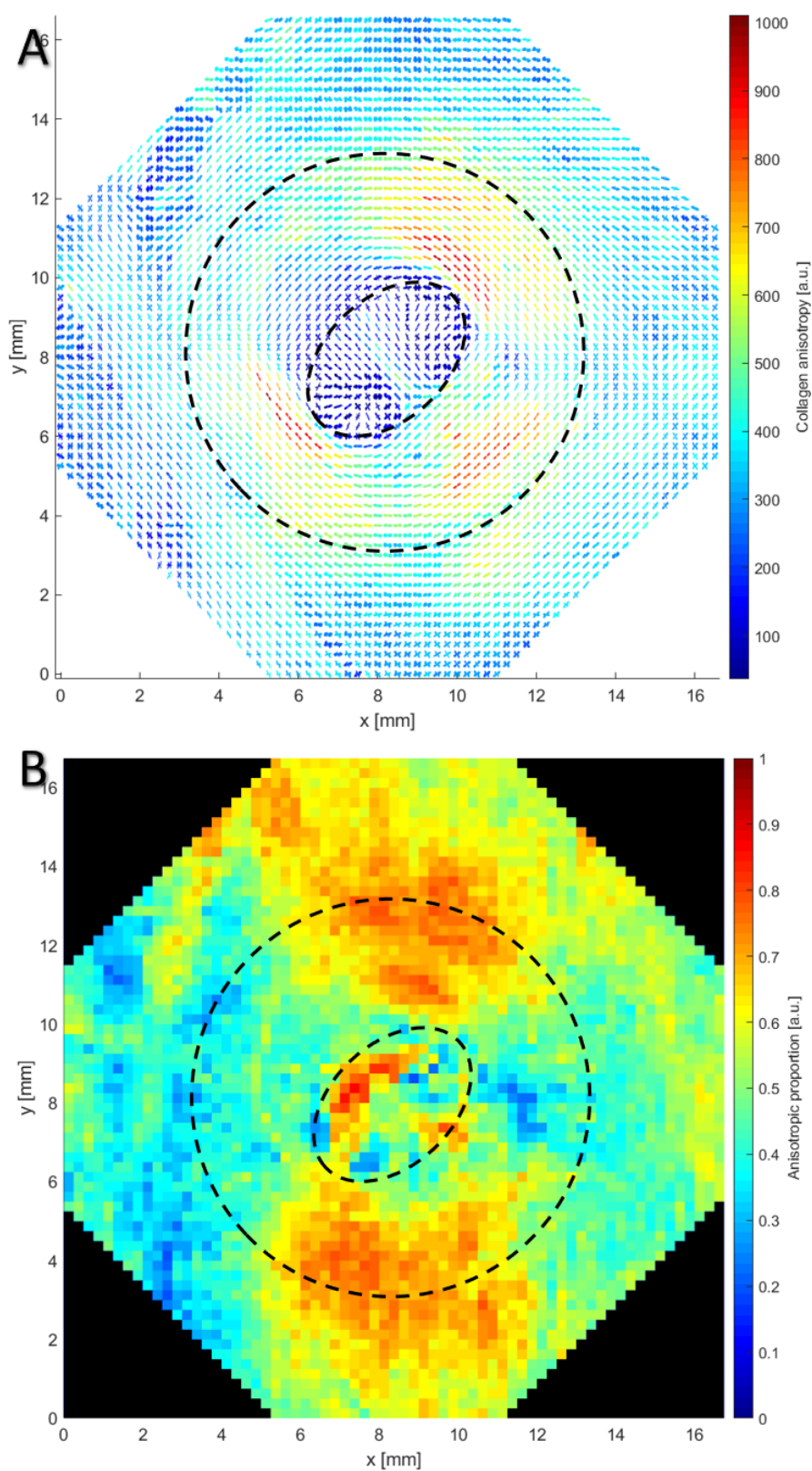


Figure 4.12 – WAXS polar vector plot map (A) and collagen anisotropic proportion contour map (B) of a bovine posterior sclera B2. The highly aligned annulus of collagen fibres in the PPS is bounded by dashed lines.

Data points were recorded at every 0.25mm.

4.2.1.12 Mammalian posterior scleral comparison

This study provides the widest comparison of posterior scleral fibre architecture in mammalian species. To the best of the author's knowledge, the only other non-human species for which the PPS was investigated with WAXS was the canine sclera from the beagle (Boote et al., 2016). In beagle dogs, the collagen fibril annulus appeared to have larger collagen anisotropy values than the surrounding mid-posterior, consistent with the observed animals of intermediate size presented here (Figure 4.07A and 4.08A). Some of the listed species here have also had their PPS investigated using polarised light microscopy (Gogola et al., 2018b). As seen from the previous Sections, all 11 mammalian species possessed a circumferential collagen structure in the PPS, which in general appeared less developed for smaller animals and gradually became more defined. WAXS polar vector plot maps of the 11 animal species were compared against an analogue polygon plot map from a human (Figure 4.13K; specimen N4, Chapter III). Additionally, all of the posterior scleral maps were scaled to accurate proportions and presented from smallest body size (mouse, Figure 4.13A) to largest (cattle, Figure 4.13L). Due to the small dimensions of the annular structure, for better visualisation and comparability, the polar vector plots comprising the ONH were removed, leaving the PPS and surrounding mid-posterior sclera. As the collagen anisotropy is affected by the total collagen scatter, and in turn by the tissue thickness, it can be expected that larger eyes would also exhibit larger anisotropy magnitudes overall. However, inter-species variations in the width of the annulus, in particular the markedly limited structure in the tree shrew (Figure 4.02), suggest that biomechanical factors other than IOP-induced scleral hoop stress may play a part in determining scleral microstructure in some animals (Boote et al., 2019). To identify a human analogue model species of the PPS, all of the WAXS vector plot maps were scaled to a maximum of 2,000a.u. for the collagen anisotropy, as the anisotropic differences between the PPS and mid-posterior were presented in the individual species sections.

As previously discussed, smaller mammals tend to have a less defined ring of circumferential collagen fibrils proportionally to the size of the ONH. This precludes them from being a suitable human model of the PPS architecture. Species with eyes positioned at the front, such as the tamarin monkey (Figure 4.13D) and the red panda (Figure 4.13G), whilst genetically closer or having similar characteristics in the PPS organisation, respectively, were endangered, automatically

excluding them. Meanwhile, the Brazilian tapir (Figure 4.13J) notably showed close structural homology with the posterior human eye, but, whilst not endangered, has been categorised as a vulnerable to extinction species.

Figure 4.14 is complementary to Figure 4.13, with all of the polar vector plot maps being substituted with anisotropic proportion contour values. As the collagen anisotropic proportion is the ratio of the aligned and total collagen scatter, the values are always between 0 and 1 and did not require specific scaling for the comparison. Numerous animals (Figure 4.13C, D, E, F, I, J, L) exhibited high anisotropic proportion on opposing sides of the ONH, potentially related to local collagen fibril organisation as a result of eye movements.

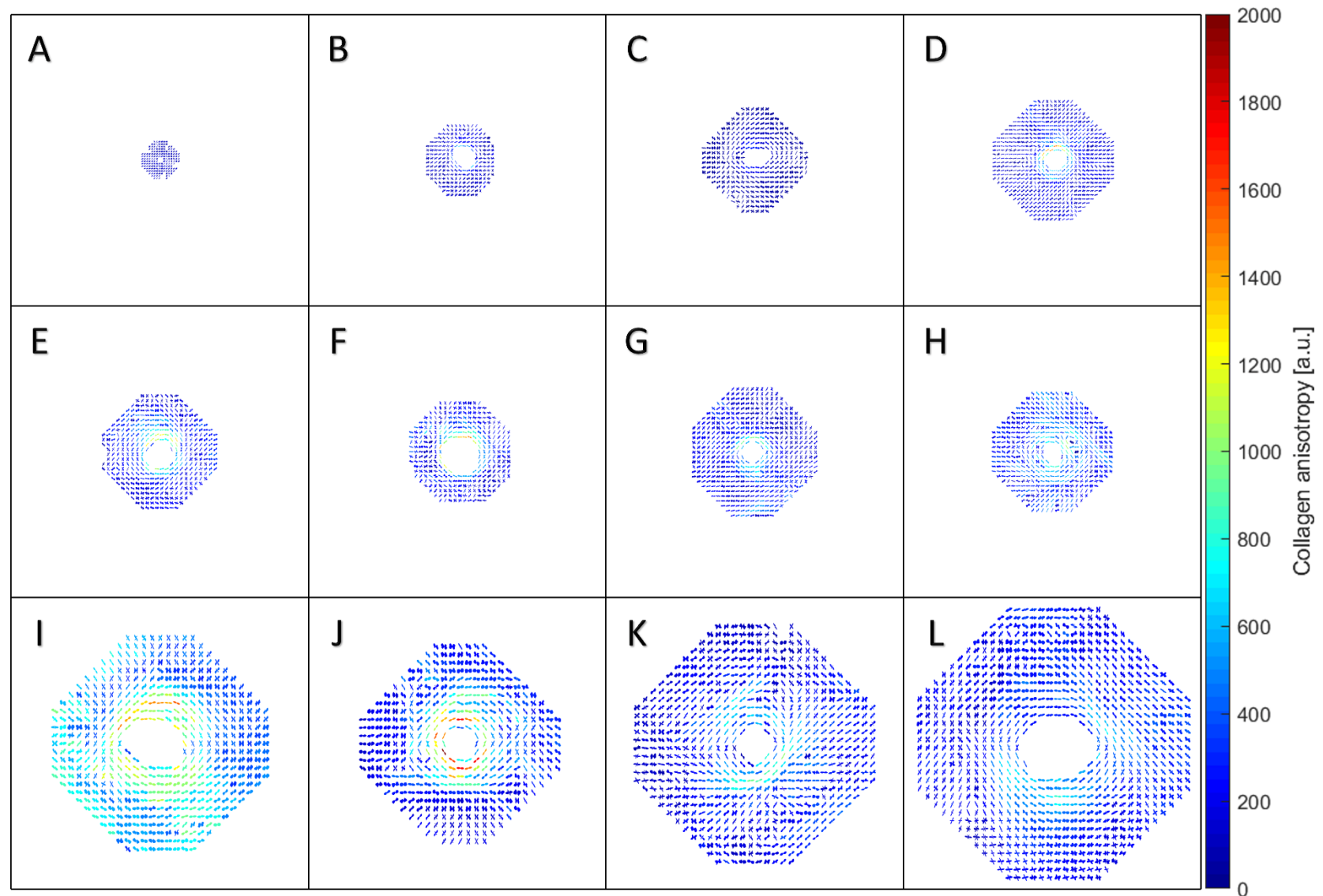


Figure 4.13 – Scaled WAXS polar vector plot map comparison between posterior sclera from 12 mammalian species. Data points composing the optic nerve head (ONH) have been excluded. (A) Laboratory mouse; (B) Northern tree shrew; (C) Guinea pig; (D) Black lion tamarin; (E) Azara’s agouti; (F) Lesser mouse-deer; (G) Red panda; (H) North American river otter; (I) Domestic pig; (J) Brazilian tapir; (K) Human; (L) Domestic cattle.

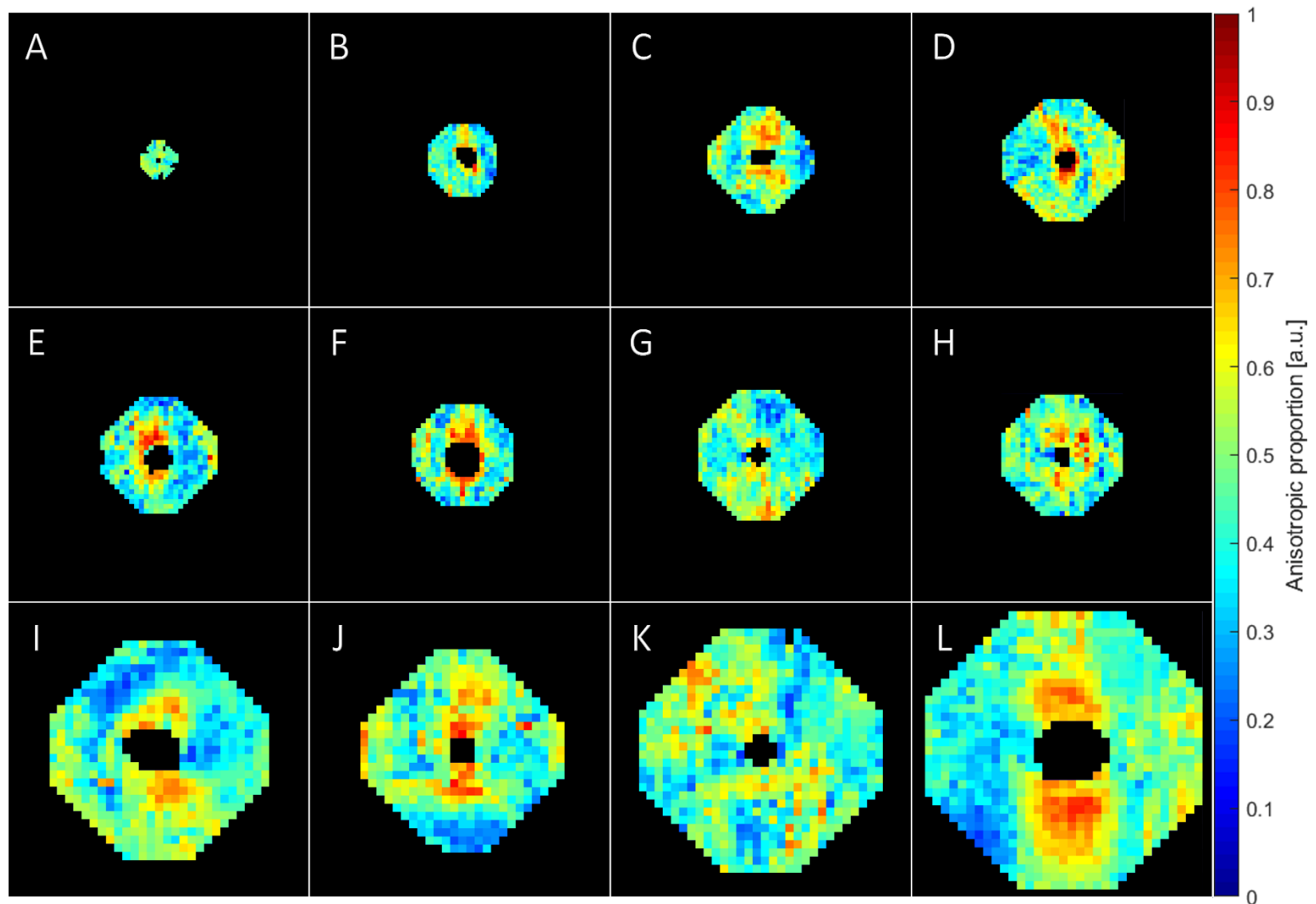


Figure 4.14 – Scaled WAXS collagen anisotropic proportion contour map comparison between posterior sclera from 12 mammalian species. Data points composing the ONH have been excluded. (A) Laboratory mouse; (B) Northern tree shrew; (C) Guinea pig; (D) Black lion tamarin; (E) Azara's agouti; (F) Lesser mouse-deer; (G) Red panda; (H) North American river otter; (I) Domestic pig; (J) Brazilian tapir; (K) Human; (L) Domestic cattle.

Whilst the porcine eye is close in terms of size to humans, the circumferentially aligned polar vector plots were more spread out into the mid-posterior sclera, with higher collagen anisotropy values (Figure 4.09A). The collagen fibril annulus structure and anisotropy distribution of the bovine sclera are more proportionally closer to humans (Figure 4.15). In general, all bovine eyes come from abattoirs, which fulfils the other prerequisite for a model species, which was the ease of access to new tissue. Furthermore, all of the animals have been reared under similar environmental and lighting conditions, as well as being young adults of the same age at slaughter (Section 2.2.1.2), making comparison between them much more representable. New eye tissue can easily be acquired, which along with the size of the globe make cattle eyes one of the most popular choices for research on scleral biomechanics. Hence bovine was selected as the animal model of choice in the rest of the investigations in this thesis.

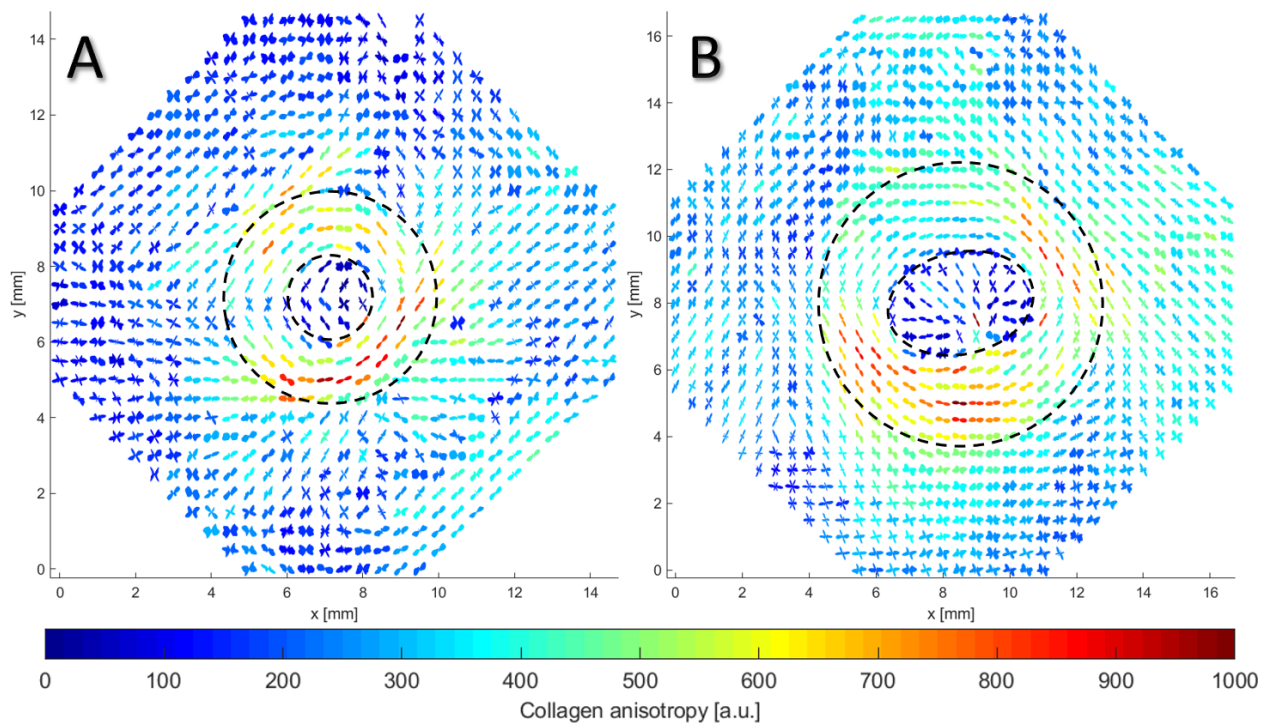


Figure 4.15 – Comparison of human N4 (A) and cattle B1 (B) WAXS polar vector plot maps. The collagen anisotropy was scaled to 1,000a.u. for both specimens. The highly aligned annulus of collagen fibres in the PPS is bounded by dashed lines. Data points were recorded at every 0.5mm. The general similarity in microstructure in the PPS region between human (A) and bovine (B) marked the latter as a suitable animal model for the remaining studies in this thesis.

### 4.2.1.12.1 Ventral groove

From the presented WAXS vector plot maps, only the porcine (Figure 4.09A) and bovine ones had a ventral groove in the ONH (Figure 4.11A and 4.12A; Appendix A1.2). Jan and colleagues showed that other domestic mammals, such as sheep, also have a groove in the LC (Jan et al., 2018). However, other large animals, like the tapir, did not have this structure, indicating a phylogenetic relationship (Figure 4.10A). Brooks proposed that the ventral groove has an embryonic origin, possibly a vestige of the embryonic optic fissure, whilst Feola showed that this region is where the retinal blood vessels enter the optic nerve (Brooks et al., 1998; Feola et al., 2017). In addition to providing a useful means of determining the orientation and position of the eye globe in untagged specimens, the presence of the groove in bovine and porcine eyes could affect the ONH environment. However, the effect of the ventral groove in bovine LC will have limited consequences for the current work, which focusses on the PPS region.

### 4.2.2 Second harmonic generation microscopy analysis

#### 4.2.2.1 Regional polar vector plots

It is known that depth variations exist in the fibrillar collagen orientation and architecture of the human PPS. In normal eyes, the circumferentially aligned collagen fibres are most prominent in the outer two-thirds of the scleral stroma, most likely as further support to the LC (Pijanka et al., 2015). The presented WAXS analysis provides representative quantitative measurements of the bulk fibre anisotropy by yielding thickness averaged data and, as such, no depth-dependent information could be acquired from this method. Thus, the optical slicing capability of SHG microscopy was utilised to investigate features in the collagen fibril microarchitecture in bovine PPS through the depth of the tissue.

Figure 4.16 presents three SHG images of different depth levels of the same left bovine PPS. The sections were properly orientated, with the superior region being uppermost, whilst the nasal side is on the left. The annular structure of circumferentially aligned collagen was subdivided into the eight cardinal and intercardinal directions, from each of which a representative 1,024x1,024 pixel

---

region was selected and Fourier transform-assessed using the bespoke image analysis software Filum Trace (Section 2.4; (Pijanka et al., 2019)). The selected regions formed a ring rather than an ellipse, since whilst the bovine scleral canal is more oval, the PPS collagen structure was indeed circular (Figure 4.11A and 4.12A). The generated polar vector plots were analogous to the corresponding plots from the WAXS analysis, with each polygon plot overlaid on top of the underlying area, denoted by a red square. The PPS sections were also scanned at the same microscopy settings, permitting a direct comparison of their signal.

Figure 4.16A illustrates the third inner section, corresponding to a depth from 2,080 to 2,240 $\mu\text{m}$ . The SHG collagen signal was strongest in the inferior region, with the representative polar vector plot having a main orientation angle of 151.5°, instead of the expected 180°. On the opposite side, the intensity was lower, with numerous darker patches, likely due to absence of collagen fibrils. This is reflected in the vector plot, which is cross-shaped, also indicating that the interweaving collagen fibres are more spatially distributed. The collagen anisotropy of these two regions had similar values, 324a.u. for the superior and 332a.u. for the inferior. Overall the anisotropy was low, with the highest one being 572a.u. at the IT, adjacent to where the ventral groove will be positioned. It should also be noted, that as the inner sections are closer to the choroid, some of the collagen fibril orientations are probably affected as well, with a more radial distribution possibly expected, likely associated with the predominant vessel orientation, as envisaged in humans (Pijanka et al., 2015). As this section corresponds to the prelamina, the LC was also not observed in the images. It is around this depth that the collagen fibrils start becoming more circumferential around the ONH.

A mid-stromal scleral section, depth from 1,280 to 1,440 $\mu\text{m}$ , is presented (Figure 4.16B). Compared to Figure 4.16A there was a more clearly defined ring of collagen fibres around the optic nerve, which is also evidently represented in the circular orientation of the eight polar polygon plots. The SHG signal was also more uniformly distributed, with the highest collagen anisotropy at the two lateral sides of the scleral canal: 874a.u. at the temporal and 809a.u. at the nasal. This observation agreed with the higher collagen anisotropy for the WAXS polar vector plots (Figure 4.11A and 4.12A). Furthermore, the PPS in the superior and SN directions appeared to be ‘indented’ (Figure 4.16B), which corresponded to the notable WAXS transition zone in the

same directions around the scleral canal (Figure 4.12A). In addition, the SHG polar vector plot of the superior region (Figure 4.16B) also had the lowest anisotropy (423a.u.). These observations further reinforce the high comparability between the WAXS and SHG techniques (Pijanka et al., 2019).

Figure 4.16C shows the outermost (16<sup>th</sup>) PPS section, with a depth of 0 to 160 $\mu$ m. The structural organisation was markedly different to the mid-stroma (Figure 4.16B), with the annulus of collagen fibrils being inter-connected with the *pia mater*, the first of the three meningeal layers, and the *subarachnoid* space, the cavernous tissue observed on the nasal side of the ONH. The *pia mater* was also directly connected to some of the beams of the LC, most notably at the ‘stalk’ at the ventral groove in the inferior/IT region, which was in agreement with observations in humans (Sigal et al., 2010). Blood vessel lumen were also present, which could accommodate the nearly vertical (77 $^{\circ}$ ) orientation of the polar vector plot in the superior region. As previously shown, the meninges in the outermost sclera were positioned along with the circumferential collagen fibrils (Pijanka et al., 2015). It should be noted that the SHG signal (813a.u.) and collagen anisotropy was highest on the temporal side for the well-aligned (87.5 $^{\circ}$ ) polar plot. The PPS organisation also appeared different from the rest of the section, with no exhibited subarachnoid space or blood vessels, as well as a thin *pia mater*. Possible explanations for these observations could be that the meningeal layers ‘insert’ into the bovine PPS at an inclination or that there is regional variability in their thickness. More experimental validation is required as part of future work to assess if this is a consistent feature and what significance it may hold for scleral biomechanics.

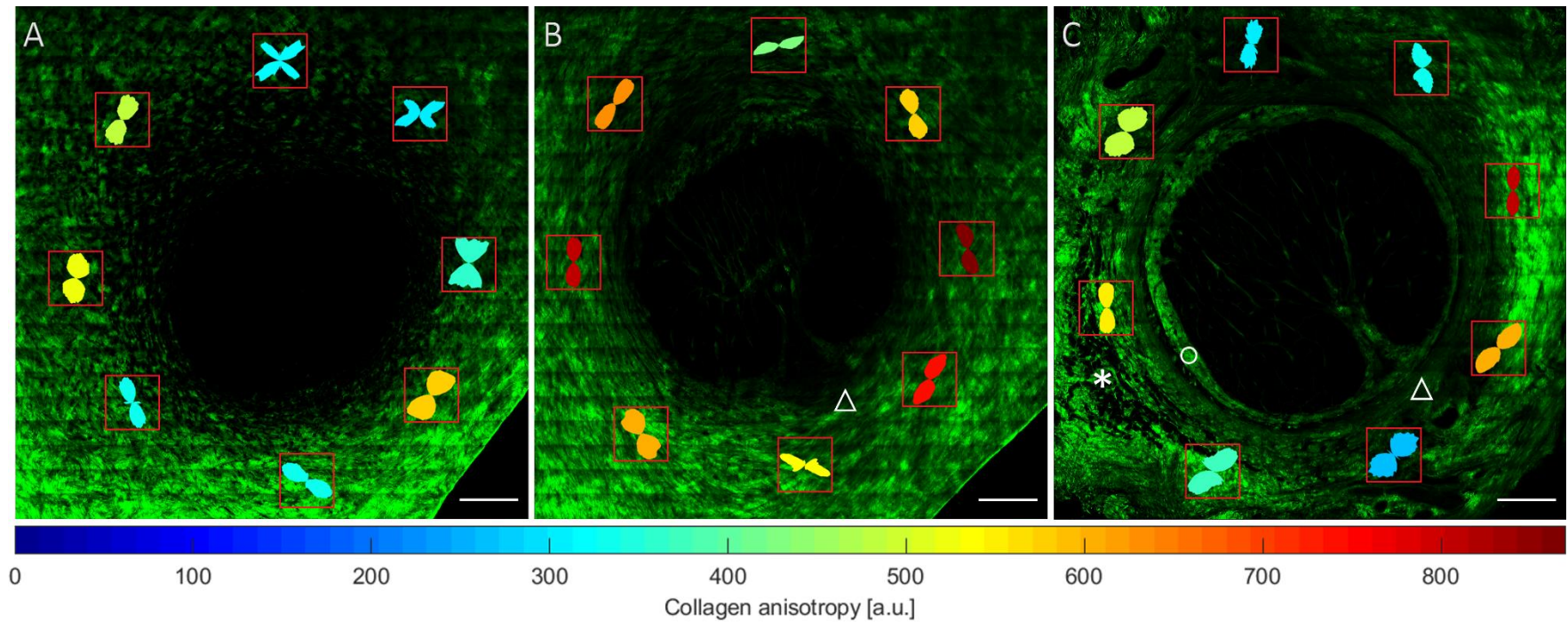


Figure 4.16 – Second harmonic generation (SHG) microscopy images of three 160 $\mu$ m thick sections from the inner (A), mid-stromal (B) and outermost PPS (C). For each section eight representative 1,024x1,024 pixel regions were selected, indicated by a red border, for which Filum Trace polar vector plots were calculated and overlaid on top. The orientation of the polar plots illustrates the average collagen fibre directional spread, whilst the colouring is indicative of the level of anisotropy, with hotter colours correlating to greater alignment. Triangles in B and C are representative of the region of the PPS closest to the ventral groove in the LC of the corresponding images. In C, the *pia mater* is denoted by a circle and the *subarachnoid* space by an asterisk. Scale bar = 1mm.

The Filum Trace polar vector plots from all 16 sections were compiled (Figure 4.17). The first row (Ex) is analogous of the idealised mathematical distribution (Figure 2.04) utilised in Chapter III, but only applied for the eight selected representative regions, with main angle difference between adjacent polar vector plots of  $\pi/4$ . Therefore, the closer sectional polygon plots are to the Ex plot of the same region, the more the PPS is circumferentially aligned around the ONH. Through the entire depth, the most consistently aligned, and with the highest collagen anisotropy values, were the nasal and temporal regions. This was also in agreement with both the SHG PPS sections (Figure 4.16) and with the WAXS vector plot maps (Figure 4.11A and 4.12A). The fibrillar orientation in the superior direction for the first two sections appeared vertical, instead of the expected horizontal distribution, which was tilted for most of the stromal sections and became radial in the outer sections. Similar consistent tilt was also observed in the inferior regions, which also exhibited more cross patterns, most likely due to a larger amount of orthogonally interweaving collagen fibres, further reflected by the SHG signal below the scleral canal (Figure 4.16A and 4.16B).

16 depth sections from a right bovine PPS were also imaged using SHG microscopy, to validate the observation from the first eye and to determine if there were any notable differences between the posterior sclera in right and left bovine eyes (Figure 4.18 and 4.17, respectively). Polar vector plots were similarly distributed and followed a mostly circumferential orientation. In addition, the collagen anisotropy of the polygon plots was scaled to the same maximum value (1,050a.u.), permitting direct visual comparison of the regions and sections (Figure 4.17 and 4.18). The collagen anisotropy was also consistently highest in the nasal region, with high values observed for the inferior nasal (IN) in the outer sections. The superior and inferior regions deviated again the most from the expected alignment, with a notable tilt in the distribution in the outer sections, most likely due to the presence of the meningeal layers and blood vessel lumen. To further assess the PPS collagen fibril structure, image analysis with several other software packages was conducted.

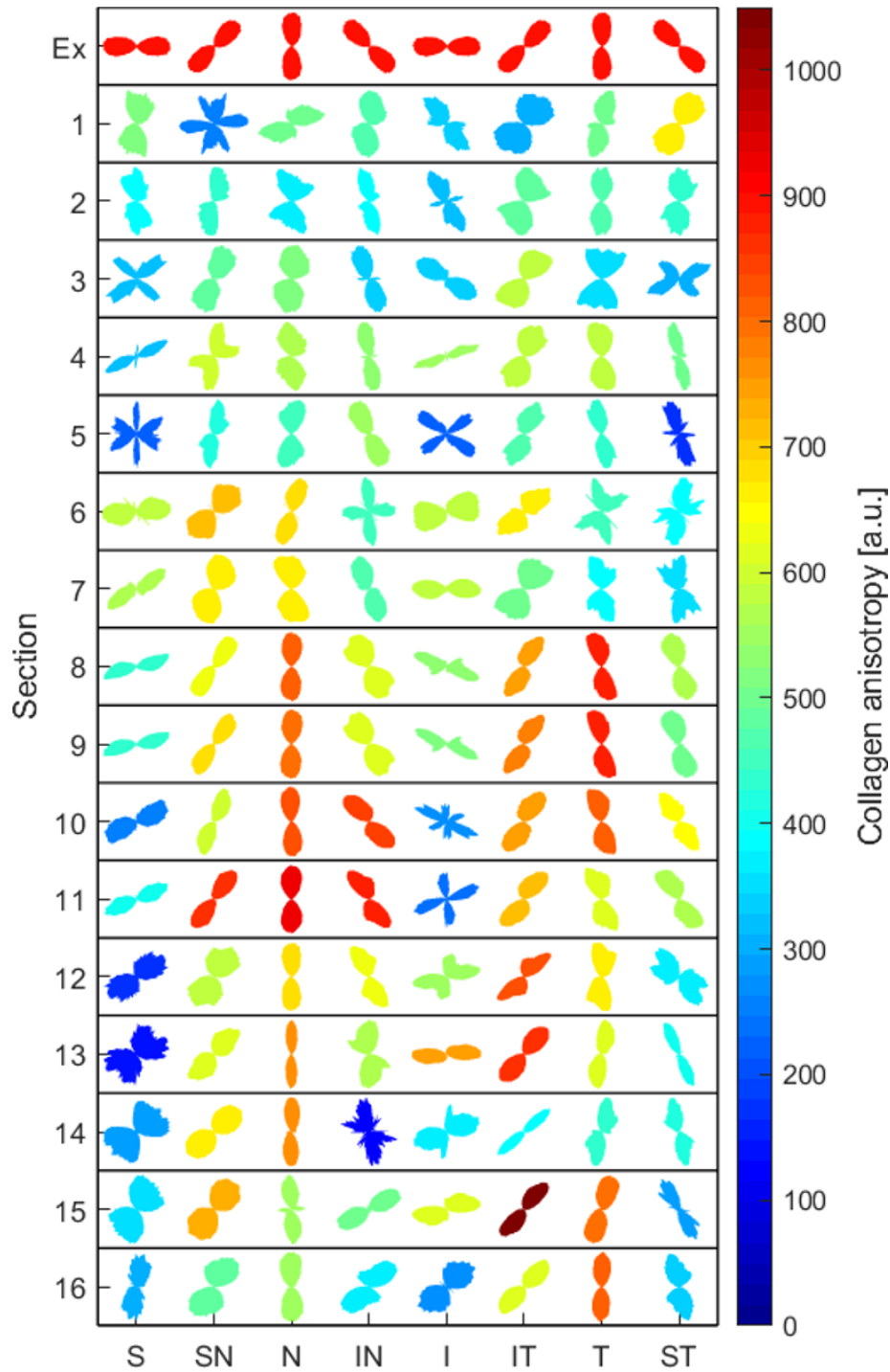


Figure 4.17 – Depth-dependent collagen fibre orientation in a left bovine PPS. Filum Trace polar vector plots representative of corresponding underlying 1,024x1,024 pixel partition tiles from eight selected regions per SHG image of 16 consecutive sections, listed from inner (1) to outermost (16). The orientation of the polar plots illustrates the average collagen fibre directional spread, whilst the colouring is indicative of the level of anisotropy, with hotter colours correlating to greater alignment. The regions are indicated counter-clockwise: S (superior); SN (superior nasal); N (nasal); IN (inferior nasal); I (inferior); IT (inferior temporal); T (temporal); ST (superior temporal).

The first row (Ex) presents an idealised polar vector plot distribution and anisotropy that corresponds to perfect circumferential orientation.

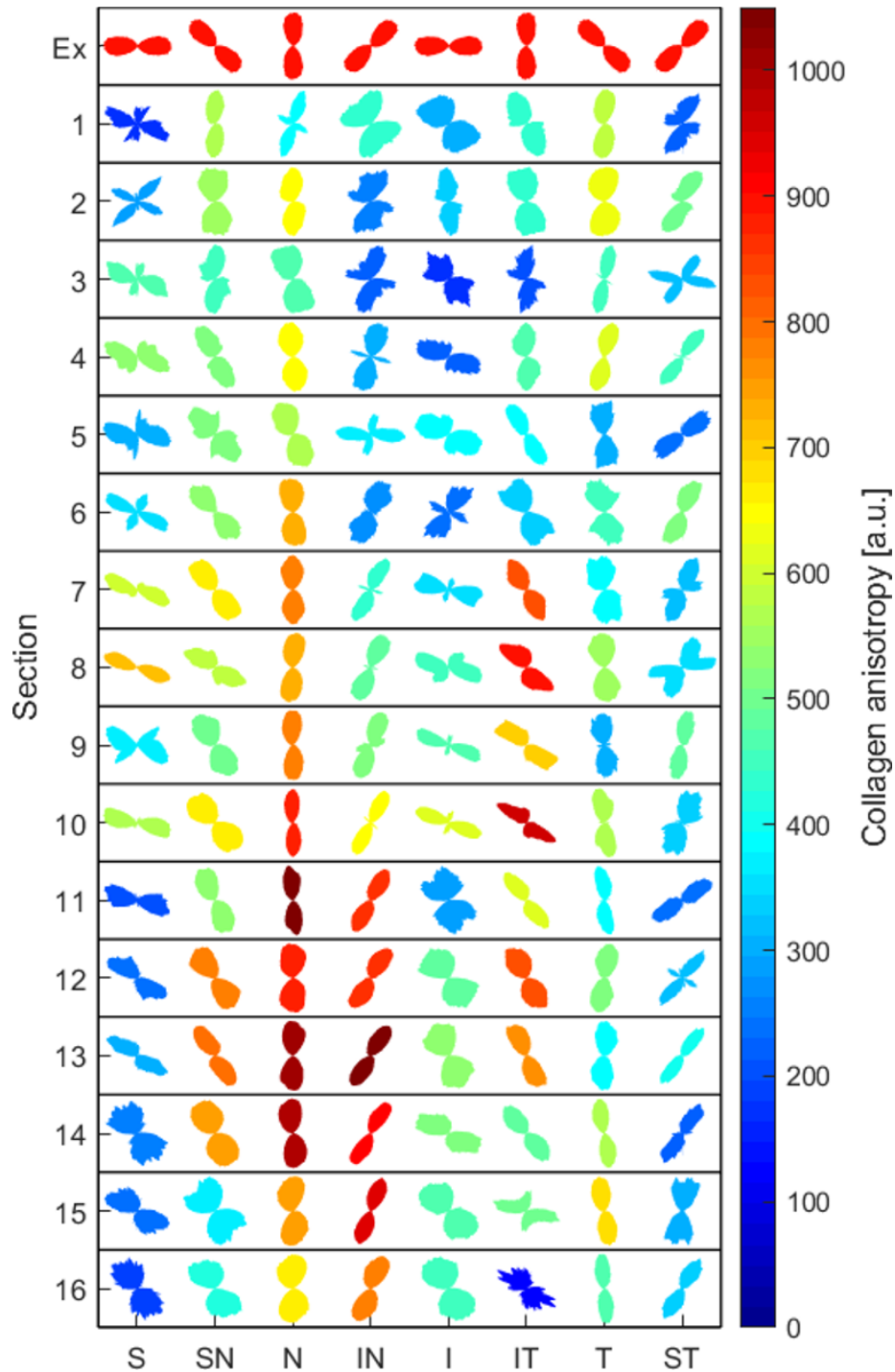


Figure 4.18 – Depth-dependent collagen fibre orientation in a right bovine PPS. Filum Trace polar vector plots representative of corresponding underlying 1,024x1,024 pixel partition tiles from eight selected regions per SHG image of 16 consecutive sections, listed from inner (1) to outermost (16). The orientation of the polar plots illustrates the average collagen fibre directional spread, whilst the colouring is indicative of the level of anisotropy, with hotter colours correlating to greater alignment. The regions are indicated clockwise: S (superior); SN; N (nasal); IN; I (inferior); IT; T (temporal); ST. The first row (Ex) presents an idealised polar vector plot distribution and anisotropy that corresponds to perfect circumferential orientation.

#### 4.2.2.2 Peripapillary scleral fibre angular displacement from circumferential

Figure 4.19 presents a visual representation of the output of six image analysis packages, applied to the same 1,024x1,024 pixel region. FibrilTool (Figure 4.19A) and OrientationJ (Figure 4.19B) are ImageJ plugins, which are based on structural tensors, whilst both Filum Trace (Figure 4.19C) and CytoSpectre (Figure 4.19D) were developed in MATLAB and utilise fast Fourier transform (FFT) (Rezakhaniha et al., 2012; Boudaoud et al., 2014; Kartasalo et al., 2015; Pijanka et al., 2019). CurveAlign (Figure 4.19E) and CT-FIRE (Figure 4.19F) are part of the same MATLAB distribution and unlike the other packages, trace multiple fibres through the use of the curvelet transform theory, with an average of all individual angles used for the purpose of this study (Starck et al., 2002; Bredfeldt et al., 2014; Liu et al., 2017). All of the listed software packages were used to produce the angular orientation of each of the representative regions, from which the displacement angle from circumferential alignment was calculated, using the same eight region idealised distribution (Figure 4.17 and 4.18).

The results are presented as heat maps of the angular deviations and are grouped by mean sectional (Figure 4.20) and regional displacement (Figure 4.21). Whilst it is possible that some tilting of the sections might have occurred prior to the imaging, which could have affected the non-linear collagen emission signal, it would have been minimal as seen by the representative images (Figure 4.16). In addition, as discussed, the image analysis packages used in this study (Section 2.5) are based on different mathematical approaches in their evaluations and as all of their results are illustrated, this should mitigate any signal intensity-associated local variations.

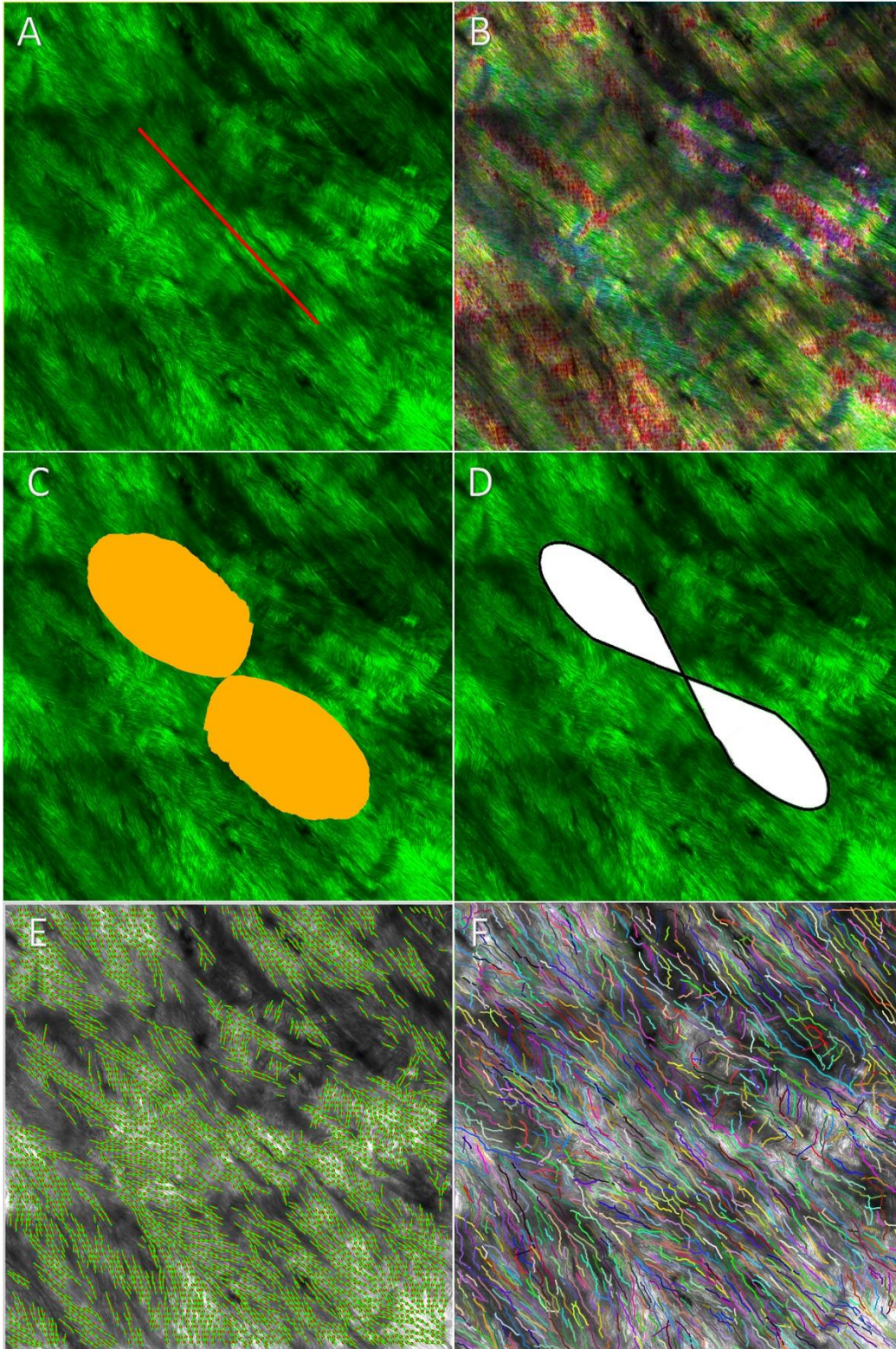


Figure 4.19 – Image analysis software package output comparison for a 1,024x1,024 pixel partition tile of an SHG image of a bovine PPS. The principal collagen fibre angular orientation was measured using FibrilTool (A), OrientationJ (B), Filum Trace (C) and CytoSpectre (D), whilst the average angle of all fibres was calculated for CurveAlign (E) and CT-FIRE (F).

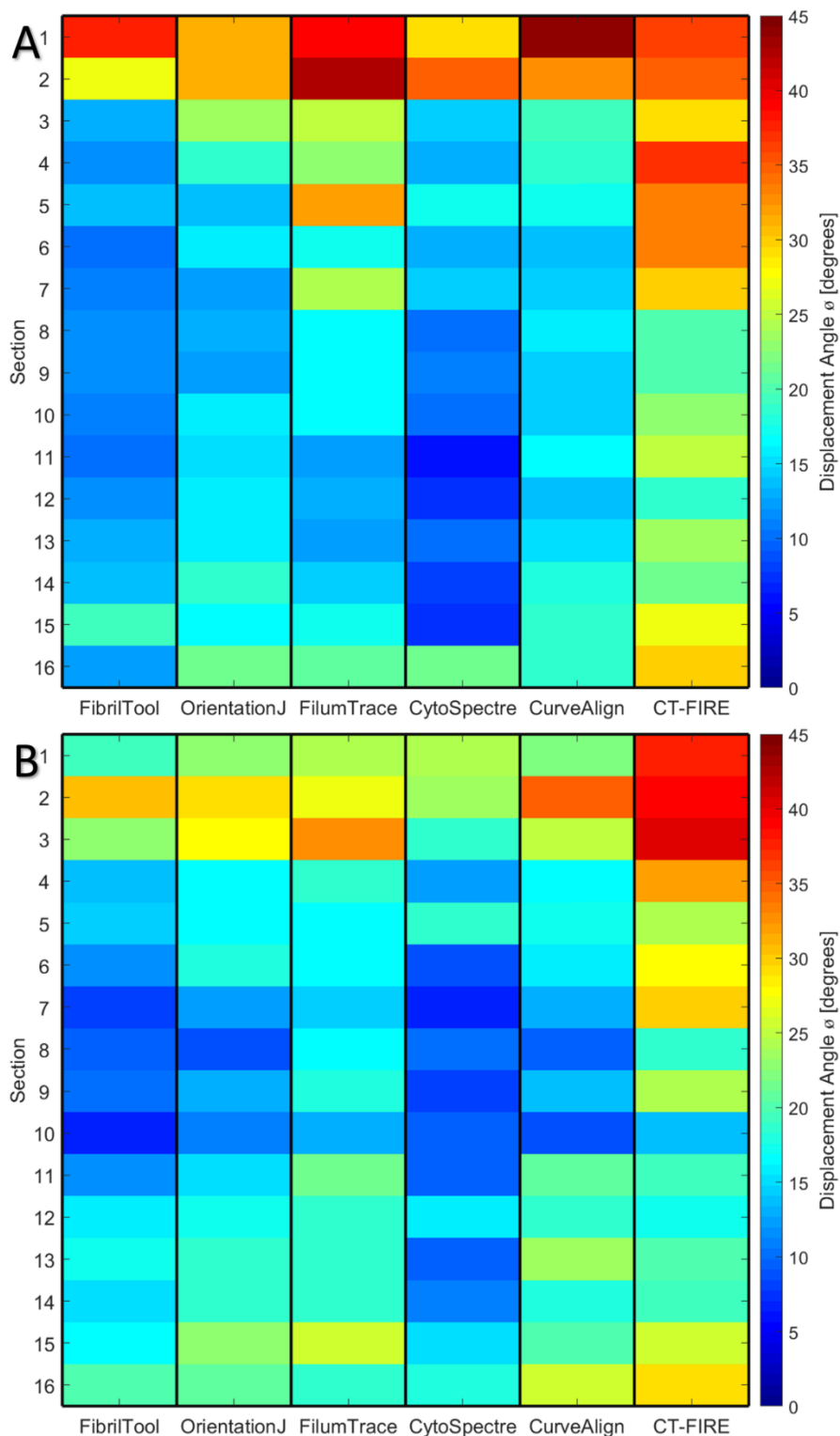


Figure 4.20 – Heat map of collagen fibril displacement angle from idealised circumferential orientation in the PPS based on results of six image analysis software packages (FibrilTool, OrientationJ, Filum Trace, CytoSpectre, CurveAlign, CT-FIRE) on 1,024x1,024 pixel partition tiles from eight selected regions per SHG image of 16 consecutive sections for a left (A) and a right (B) bovine PPS. The mean angular displacements are grouped by section, listed from inner (1) to outermost (16).

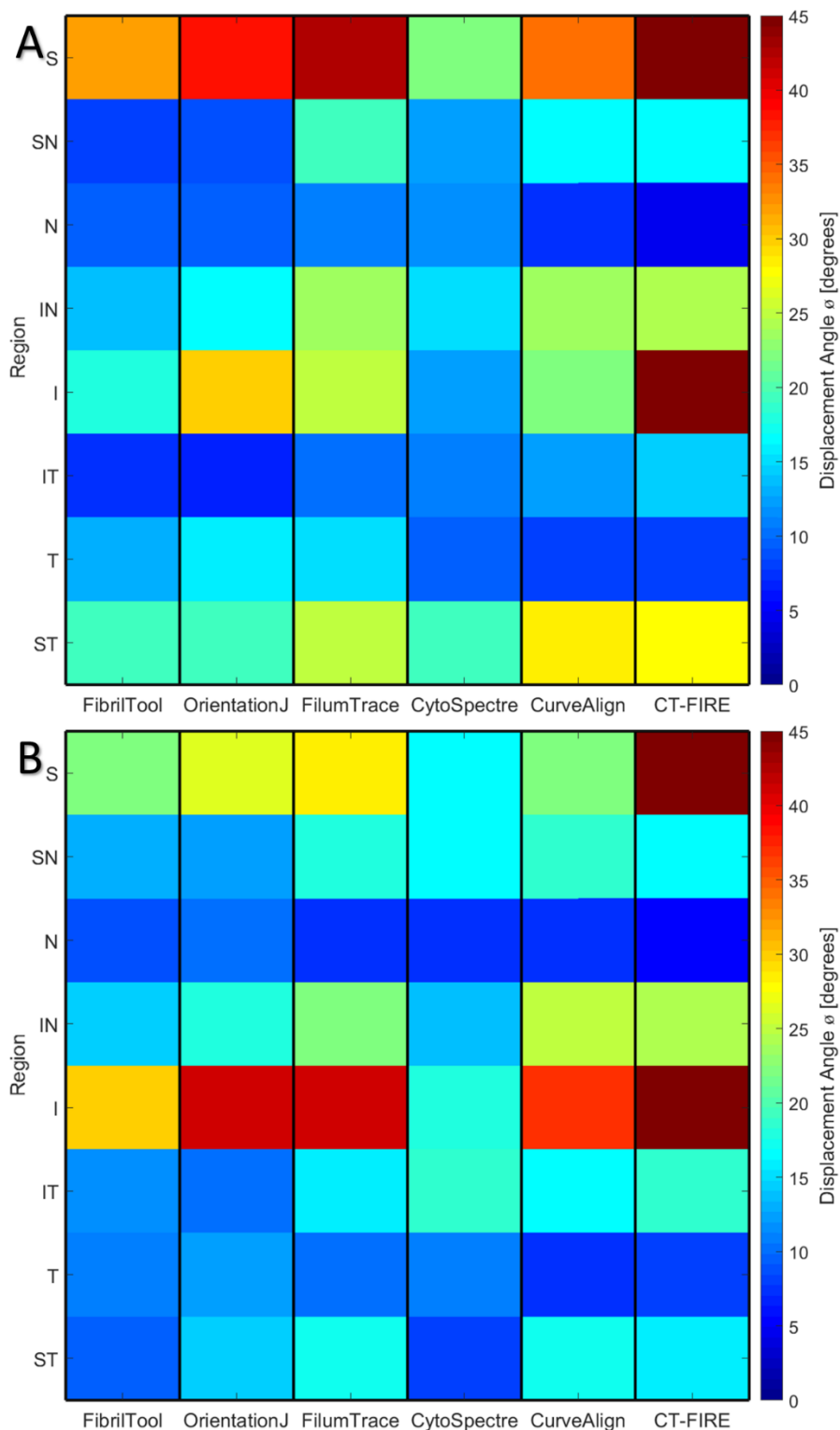


Figure 4.21 – Heat map of collagen fibril displacement angle from idealised circumferential orientation in the PPS based on results of six image analysis software packages (FibrilTool, OrientationJ, Filum Trace, CytoSpectre, CurveAlign, CT-FIRE) on 1,024x1,024 pixel partition tiles from eight selected regions per SHG image of 16 consecutive sections for a left (A) and a right (B) bovine PPS. The mean angular displacements are grouped by region with indexing as follows: S (superior); SN; N (nasal); IN; I (inferior); IT; T (temporal); ST.

The greatest deviation from circumferential for both posterior sclerae was in the innermost depth sections (Figure 4.20; 1-3). For the left bovine PPS (Figure 4.20A), there was no significance between the displacement from circumferential calculated from the six software packages, of the first two sections. However, section 2 and 3 showed a difference in most software, the most notable exclusion being CT-FIRE, which indicated a consistent deviation from circumferential up to section 7, which was not supported by the other packages. The right eye (Figure 4.20B) exhibited similar trends to the left, with the main differences appearing between section 3 and 4. CT-FIRE again showed more constant displacement, which continued to the middle sections. It is possible that this is due to the result being the average of the deviations of multiple traced fibres, with initial sections having a more widespread distribution of fibres. Along with the SHG images, these observations would indicate that the collagen fibrils become circumferentially aligned around the ONH around section 3 to 4, which corresponds to a depth of somewhere between 1,920 and 2,240 $\mu\text{m}$ . Furthermore, the collagen fibril annulus would have persisted until the outermost sections, as exemplified by the smaller angular displacements in the latter sections. Overall, the bovine sclera was similar to the human in that the outer ~four-fifths of the tissue depth was largely circumferentially aligned, with a pronounced deviation in the remaining inner layers proximal to the choroid (Pijanka et al., 2015).

In terms of regional consistency (Figure 4.21), in both the left and right eye, the superior and inferior regions deviated most from circumferential fibrillar orientation. Whilst CT-FIRE continued to indicate the largest displacements out of all the analysis packages, CytoSpectre had the lowest, with the deviations appearing similar to the other regions calculated by the same software. As previously noted, in the superior direction there were more spatially distributed fibres in some of the sections, as well as in general nearly orthogonally interweaving fibres. Therefore, as the WAXS signal is an average of the incident beam traversed tissue, the observations for the superior region will be reflected in the overall lower collagen anisotropy and more cross-shaped polar vector plots in the PPS directly above the ONH (Figure 4.11A and 4.12A). Furthermore, the perpendicularly interweaving fibres in the inferior were also in close proximity to the ventral groove, which could provide an alternative explanation for the displacement from circumferential, as there were local realignments around it (Figure 4.12A).

For both of the sectioned bovine PPS, the nasal region exhibited the smallest deviation from the idealised angular distribution in all six analysis software packages. Similarly, the displacement on the opposite side of the scleral canal was low as well, with the angular deviation for the temporal region not exceeding  $15^\circ$  in all instances. This was once more in agreement with the polar vector plot orientation and collagen anisotropy in the corresponding WAXS maps (Figure 4.11A and 4.12A). Furthermore, whilst it remained undetermined if the two bovine posterior sclerae used for WAXS were both left or right, the large regions of high collagen anisotropic proportion would coincide with the nasal and temporal directions of the specimens, should they be left. Furthermore, an independent study using small-angle light scattering also detected greater collagen alignment on the lateral side of the optic nerve (Girard et al., 2011). A plausible explanation for these features would be increased collagen fibrillar anisotropy and alignment on the two lateral sides of the ONH, which could better resist the in-tissue stress and shear arising from horizontal eye movements in cattle. Additionally, both the IT and SN regions were also close to circumferential alignment, with their positions being adjacent to or opposite of the optic nerve ventral groove, respectively. As the retinal blood vessels enter the eye at the groove, the greater circumferential orientations in these two regions could further support the blood supply to the ocular tissue (Section 4.2.1.12.1). Whilst there were variations in fibril distribution in the superior and inferior regions (Figure 4.16), the collagen fibres of the PPS closely circumscribed the optic nerve canal. This is further evidenced by the WAXS tissue averaged polar vector plots (Figure 4.15), which also showed a great resemblance of the bulk collagen microstructure between bovine and human.

### 4.3 Summary, conclusions and future work

WAXS polar vector plot maps revealed that the ring of circumferentially aligned collagen fibrils increases with the size of the eye, becoming more structurally defined. The bovine PPS was selected as an analogue to the human one, with SHG microscopy indicating that the collagen annulus encompasses the outer four-fifths of the scleral thickness.

WAXS analysis was performed for the first time on the posterior scleral tissue from several mammalian species. The conducted comparisons suggest that the collagen fibre annulus is related to the size of the eye and does not appear to be genetically associated with how close the species

is to humans. The collagen fibrils were much less aligned in smaller animals, with a higher degree of anisotropy occurring with the increase in eye size. The bovine PPS was selected as a model analogue to the human one for future ECM studies due to its structural similarity to humans and the availability of suitable, age-matched tissue.

SHG microscopy was used to determine the prominence and distribution of the PPS collagen structure throughout the tissue depth. The observations could be interpreted as the existence of two subpopulations of collagen fibres on either side of the scleral canal, which encompass it laterally and cross and interweave above and below the ONH. The PPS circumferential structure forms around 1,920-2,240 $\mu\text{m}$  and continues through the rest of the scleral thickness. That would indicate that the protective ring of circumferential fibres persist for four-fifths of the outer sclera in bovine, which when compared to the two-thirds in humans further supports the conclusion that the structure is related to ocular size rather than evolutionary development in mammals (Pijanka et al., 2015; Boote et al., 2019). The aligned fibrillar annulus in cattle was, similarly to humans, not a complete cylinder, as around 320-480 $\mu\text{m}$  (section 14) the meningeal layers ‘insert’ themselves between the optic nerve and the PPS collagen structure (Pijanka et al., 2015).

Future experiments envision SHG microscopy imaging of more bovine PPS specimens to further investigate the described features. The utilised image analysis software packages permit the calculation of a large assortment of parameters, most notably alignment, which will also be evaluated regionally and for different sections. Given the importance of the LC in scleral biomechanics, it would prove beneficial to ascertain if the shape and size change through the tissue depth, as well as that of the composing laminar beams and their architecture. Gogola et al. suggested that there are three different types of collagen fibre organisation in the sclera, which would necessitate elucidation of their depth-dependent organisation as well (Gogola et al., 2018b). These studies could also be combined with labelling the nuclei of the resident cells, to better comprehend their spatial distribution in young adult animals and to create accurate volume reconstructions of the PPS (Winkler et al., 2010).

# **Chapter V**

## **Effects of mechanical loading on bovine scleral fibroblasts**

## 5.1 Introduction

The biomechanical theory of glaucoma states that the high intraocular pressure (IOP) in the eye can deform the connective tissues of the optic nerve head (ONH) – the peripapillary sclera (PPS) and *lamina cribrosa* (LC). This, in turn, influences the glaucomatous damage on the optic nerve and retina, most notably by the death of retinal ganglion cells (RGC) (Strouthidis and Girard, 2013). Despite numerous research studies conducted on the extracellular matrix (ECM) component of the scleral biomechanics, there persists a need for further investigation into the cellular aspect (Boote et al., 2019). Cells are dynamically connected to their surrounding ECM environment through the cytoskeleton, with signalling by the process of mechanotransduction (Jansen et al., 2017). As detailed in Chapter I, the PPS has a key role in protecting the optic nerve during increased IOP, by resisting the exerted mechanical forces, specifically tensile strain. Thus, it is inevitable that the IOP would affect the resident cells of the PPS, the sporadically distributed scleral fibroblasts.

Within the relatively flat fibroblasts, the F-actin stress fibres and microtubules tend to be organised in a single plane, whilst the vimentin filaments create a cage-like structure surrounding the nucleus. The orientation of the actin cytoskeleton is dependent on the applied strain, which in turn influences the deformation mechanism of the filaments (Chaudhuri et al., 2007). The actin microfilaments form a stress fibre network (Section 1.2.3.1), contributing to the stiffness of the cell and providing a greater shear modulus than the vimentin intermediate filaments or the microtubules (Janmey et al., 1991; Wang et al., 1993). The ability to study cellular and cytoskeletal deformations in response to applied loading is fundamental for understanding how deformations may damage cells and tissues and contribute to cell-driven tissue growth and remodelling.

This Chapter describes reorganisation of the bovine scleral fibroblast cytoskeleton after applying physiologically normal and pathologically high cyclic tensile strains (CTS). Measurements of changes to the overall cell surface and nuclei are also presented.

## 5.2 Results and Discussion

Monolayers of bovine scleral fibroblasts were cultured on BioFlex™ 6-well plates and subjected to mechanical strain for 1h mimicking physiological IOP (0.26-1.8% strain), pathological glaucoma-like IOP (0.6-4.0% strain) or remained unloaded, acting as controls (Section 2.6.1.3). The cells from each condition were then analysed 1, 6 and 24h after cessation of CTS, to determine the extent of cytoskeletal network remodelling in response to load.

### 5.2.1 Scleral fibroblast shape response to physiological and pathological strain

Measurements were performed in ImageJ, based on cell-specific region of interest (ROI) created manually for each individual cell around the F-actin cytoskeletal boundaries, as cortical actin and stress fibres were situated around the fibroblast perimeter.

#### 5.2.1.1 Fibroblast area

The cell area of scleral fibroblasts exposed to CTS was significantly higher in both loading conditions, over all time points, in comparison to the unloaded cells (Figure 5.01). 1h after physiological load, the fibroblast area was on average approximately 200% that of the unloaded cells (Figure 5.01A;  $4,431 \pm 1,149 \mu\text{m}^2$  and  $2,264 \pm 830 \mu\text{m}^2$ , respectively). These values were in accordance with another study that utilised equibiaxial cyclic stretch (10%, 0.25Hz for 0-30min) on rat arteriole vascular smooth muscles cells (Na et al., 2007). They also reported a significantly greater vinculin signal in cells stretched for 2min, suggesting a rapid increase in focal adhesions, which could also explain the larger fibroblast area and numerous aligned stress fibres. At 6h post-physiological CTS (Figure 5.01B) the mean cell area was not significantly smaller than that observed after 1h ( $4,190 \pm 1,911 \mu\text{m}^2$ ;  $p=0.610$ ) or between the 6h and 24h time points ( $3,440 \pm 1,773 \mu\text{m}^2$ ;  $p=0.237$ ; Figure 5.01C). In terms of the pathologically loaded cells, their area was also not different over time post-load cessation ( $p(1\text{h} \rightarrow 6\text{h})=0.641$ ;  $p(6\text{h} \rightarrow 24\text{h})=0.664$ ). The surface area of the unloaded scleral fibroblasts remained consistently smallest with no differences as time went on ( $p(1\text{h} \rightarrow 6\text{h})=0.776$ ;  $p(6\text{h} \rightarrow 24\text{h})=0.825$ ).

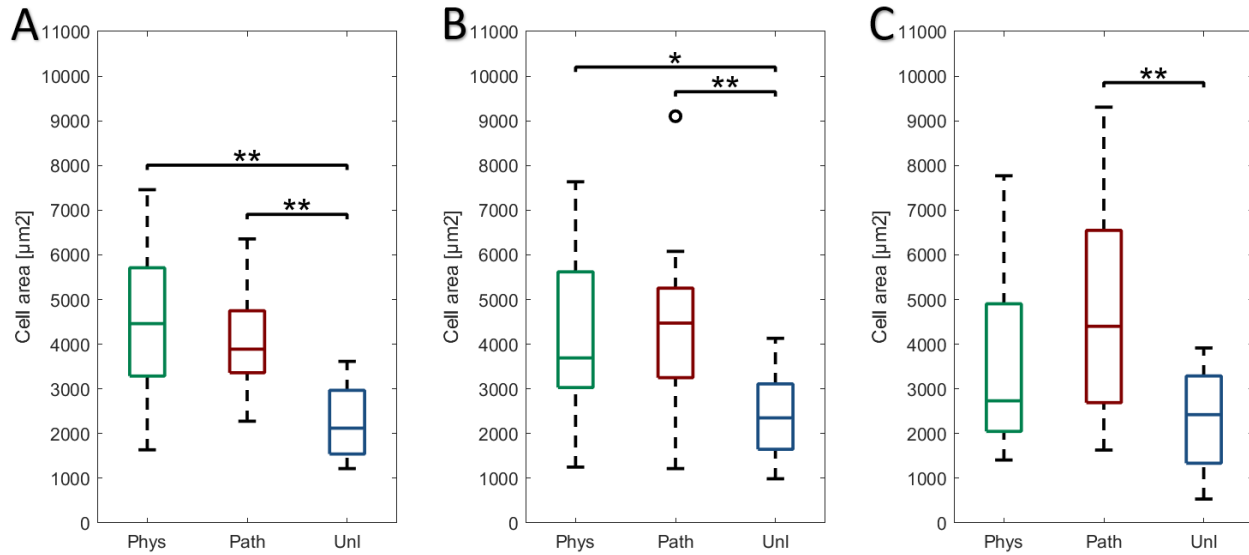


Figure 5.01 – Comparison of the cell area of bovine scleral fibroblasts between three relaxation time points 1h (A), 6h (B) and 24h (C) post-CTS (n=3 wells, N=3 plates). Data were calculated by region of interest (ROI)-based ImageJ analysis based on maximum intensity projections and grouped by applied CTS and relaxation time, presented as median  $\pm$  SD. (A) n=129-136 cells; (B) n=103-113 cells; (C) n=136-145 cells; \*:p<0.05; \*\*:p<0.01.

### 5.2.1.2 Fibroblast length

Given the significant increase in cell area, scleral fibroblasts elongated in the main axial direction with applied CTS (Figure 5.02). At 1h post-strain cessation, cells exposed to physiological ( $108.4 \pm 19.3 \mu\text{m}$ ) and pathological loads ( $93.7 \pm 17.6 \mu\text{m}$ ) were not significantly different from each other ( $p=0.076$ ; Figure 5.02A). As time progressed, cell length did not significantly alter in the fibroblasts exposed to physiological or pathological load (Figure 5.02B and C). Furthermore, the unloaded group remained constant through the observed time frame ( $p(1\text{h} \rightarrow 6\text{h})=0.306$ ;  $p(6\text{h} \rightarrow 24\text{h})=0.248$ ).

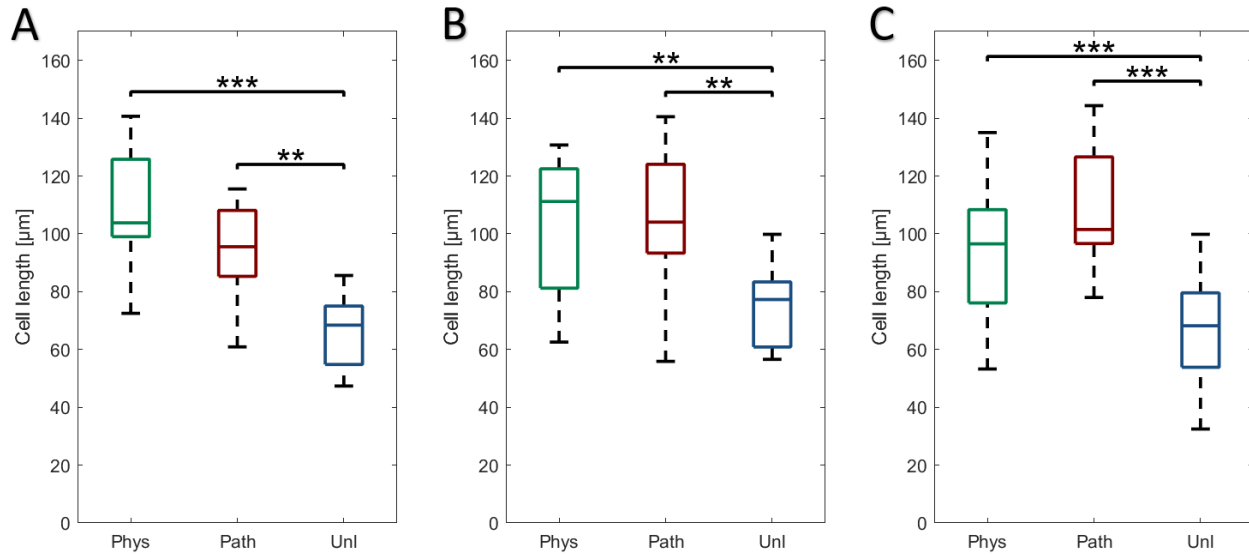


Figure 5.02 – Comparison of the cell length of bovine scleral fibroblasts between three relaxation time points 1h (A), 6h (B) and 24h (C) post-CTS (n=3 wells, N=3 plates). Data were calculated by ROI-based ImageJ analysis based on maximum intensity projections and grouped by applied CTS and relaxation time, presented as median  $\pm$  SD.

(A) n=129-136 cells; (B) n=103-113 cells; (C) n=136-145 cells; \*\*:p<0.01; \*\*\*:p<0.001.

### 5.2.1.3 Fibroblast width

No significant differences were observed in the scleral fibroblast width in response to physiological and pathological CTS or post-load at specific durations.

### 5.2.1.4 Fibroblast eccentricity

Instead of the standard aspect ratio (AR), for this study, the cell eccentricity was used as a parameter illustrating cell elongation and stretching. Eccentricity was selected for convenience in visualisation, as it was the ratio of the cell width divided by length, thus resulting in values between 0 and 1, corresponding to elongated or rounded cells, respectively. 1h post-CTS there was a significant decrease in eccentricity in physiologically loaded fibroblasts, compared to unloaded cells, as illustrated by the stretched shape (Figure 5.03). There were also differences in eccentricity between the two loading magnitudes as well (Figure 5.03A), which is of particular interest, as it further illustrates a global cell reshaping as a result of the different applied strain. As cell width for physiologically loaded fibroblasts does not significantly alter from the initial unloaded state, this

data indicates that elongation is the cause of greater cell area and smaller eccentricity. At 24h post-physiological CTS cell eccentricity was increased ( $p=0.040$ ), as reflected by the less elongated shape. The pathologically loaded fibroblasts did not present statistically significant changes in eccentricity with time ( $p(1h \rightarrow 6h)=0.778$ ;  $p(6h \rightarrow 24h)=0.191$ ) and had the smallest average value at 24h post-CTS ( $0.494 \pm 0.165$ ; Figure 5.03C). In general, scleral fibroblasts with no CTS applied had the highest eccentricity and by extension were the least structurally elongated, which was in accordance with the other presented parameters.

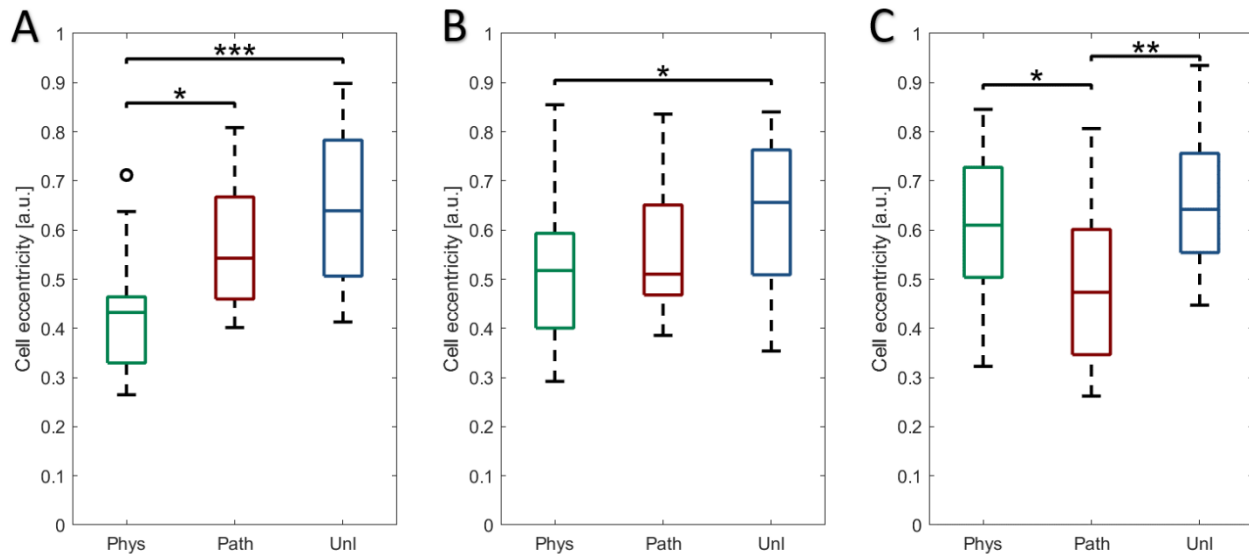


Figure 5.03 – Comparison of the cell eccentricity of bovine scleral fibroblasts between three relaxation time points 1h (A), 6h (B) and 24h (C) post-CTS ( $n=3$  wells,  $N=3$  plates). Data were calculated by ROI-based ImageJ analysis based on maximum intensity projections and grouped by applied CTS and relaxation time, presented as median  $\pm$  SD. (A)  $n=129$ -136 cells; (B)  $n=103$ -113 cells; (C)  $n=136$ -145 cells; \*:  $p < 0.05$ ; \*\*:  $p < 0.01$ ; \*\*\*:  $p < 0.001$ .

### 5.2.1.5 Summary of tensile strain-induced effects on scleral fibroblast shape

Overall, the results from the measurements support each other, illustrating in all instances an enlargement of fibroblast area and changes in cell shape as a result of applying CTS. This is most likely a compensatory mechanism to spread the tensile strain over a larger surface, along with elongation and formation of actin stress fibres. The cellular eccentricity (Figure 5.03) and the anisotropy of the F-actin cytoskeleton (Figure 5.07) were inversely proportional in their alterations with the loading conditions and relaxation time. This observation supports previous research,

which confirmed a strong correlation between the stress fibre anisotropy and cell shape, most notably that parallel fibres follow the major axis in elongated cells (Peeters et al., 2004; Deshpande et al., 2006; Goffin et al., 2006; Reynolds et al., 2014; Gavara and Chadwick, 2016).

## 5.2.2 F-Actin stress fibre response to physiological and pathological strain

### 5.2.2.1 Differential effect of strain on F-actin stress fibre rearrangement

Post-physiological CTS, the microfilament cytoskeleton remodelled to become more aligned and elongated (Figure 5.04A and D), when compared to the unloaded group (Figure 5.04C and F). The actin microfilaments exposed to mechanical loading had formed bundles of between 10 and 30 filaments, referred to as actin stress fibres (Lazarides and Burridge, 1975; Cramer et al., 1997; Na et al., 2007). Whilst cells in suspension do not develop a proper F-actin network, those on ECM substrates, such as the type I collagen coated wells, form a structured F-actin cytoskeleton (Reynolds et al., 2014). Furthermore, formation of stress fibres is independent of the dimensionality of the matrix (2D or 3D), but rather depends upon the presence of an isometric tension (Burridge and Wittchen, 2013). In response to physiological strain, the fibroblast area had increased on average by  $95.68 \pm 65.79\%$  (Section 5.2.1.1), in conjunction with the number of detected stress fibres, with many of them being parallel and orientated in the dominant cell axis direction (Tomasek et al., 1992). This could be due to the tensile forces increasing F-actin turnover (Figure 1.07), which results in the formation of more stress fibres as a protective mechanism to adapt the fibroblast contractility against the equibiaxial strain. Whilst the pathologically loaded group (Figure 5.04B and E) also exhibited an increase in cell area, the fibre distribution remains largely isotropic, with a mostly rounded shape, reminiscent of the unloaded group (Figure 5.04C and F). Based on the confocal images it appeared that during the first hour after cessation of CTS, cells exposed to pathological load do not exhibit the same cytoskeletal reorganisation as the physiological group. Furthermore, the morphology of the high strain fibroblasts was much more reminiscent of those not exposed to mechanical loading at all.

Following 6h post-CTS cessation, the actin stress fibre network retained heightened alignment in the physiological group, although to a lower extent than at 1h post-CTS (Figure 5.05A and D).

Furthermore, the fibroblasts were less elongated and the overall area was reduced. In contrast, the pathological group displayed a larger fibre anisotropy than that observed at 1h, however, the greater alignment was not different from that of the unloaded cells (Figure 5.05B and E). Unloaded scleral fibroblasts did not display any noticeable changes from those exhibited at 1h (Figure 5.05C and F).

At 24h after CTS (Figure 5.06), the morphology of the fibroblasts exposed to physiological strain was comparable to the unloaded cells, with low fibre anisotropy and high eccentricity (Figure 5.06A and D). However, the area of the fibroblasts did remain larger than the unloaded cells (Figure 5.06C and F). The remodelled cytoskeletal architecture of the pathologically loaded fibroblasts changed significantly and was similar to the F-actin organisation observed in cells 1h after exposure to physiological strain, with a dense network of fibre bundles (Figure 5.06B and E). In addition, the cell area was at its largest of all experimental groups (Figure 5.01C). This would suggest a delayed reaction, or high strain inhibition, from the pathological CTS cells, as the exhibited morphology was reminiscent of the 1h physiological strain response.

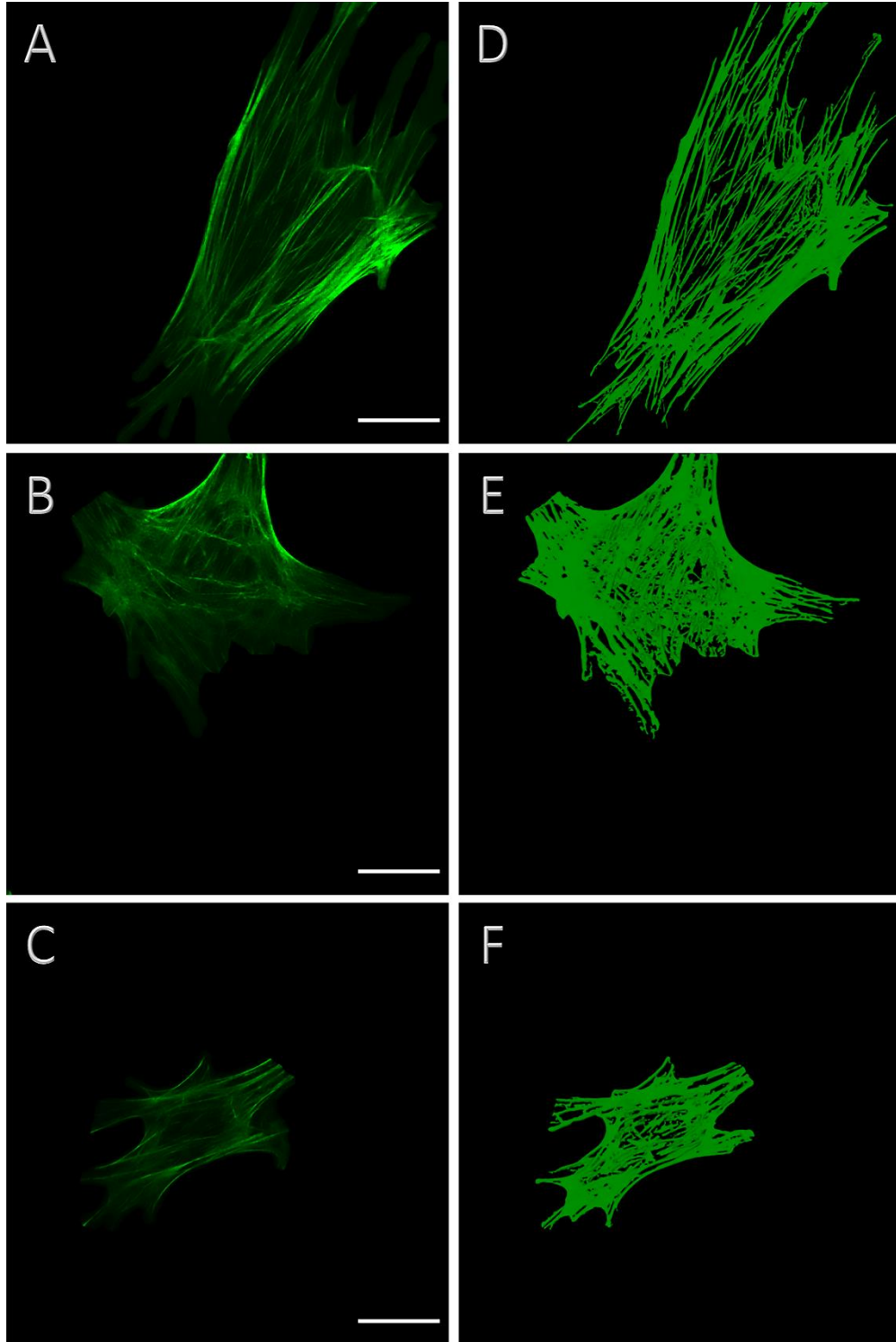


Figure 5.04 – Representative F-actin stress fibres in bovine scleral fibroblasts 1h after cyclic tensile strain (CTS), labelled with Alexa-488™ phalloidin (n=3 wells, N=3 plates). Maximum intensity projection of confocal images taken at 63x magnification and resolution of 1,912x1,912 pixels with Z-stack surface reconstructions in Imaris 9.2.

(A) Physiological CTS (0.26-1.8%, 1Hz for 1h) group; (B) Pathological CTS (0.6-4%, 1Hz for 1h) group; (C) Unloaded group; (D) Surface reconstruction of A; (E) Surface reconstruction of B; (F) Surface reconstruction of C. Scale bar = 25 $\mu$ m.

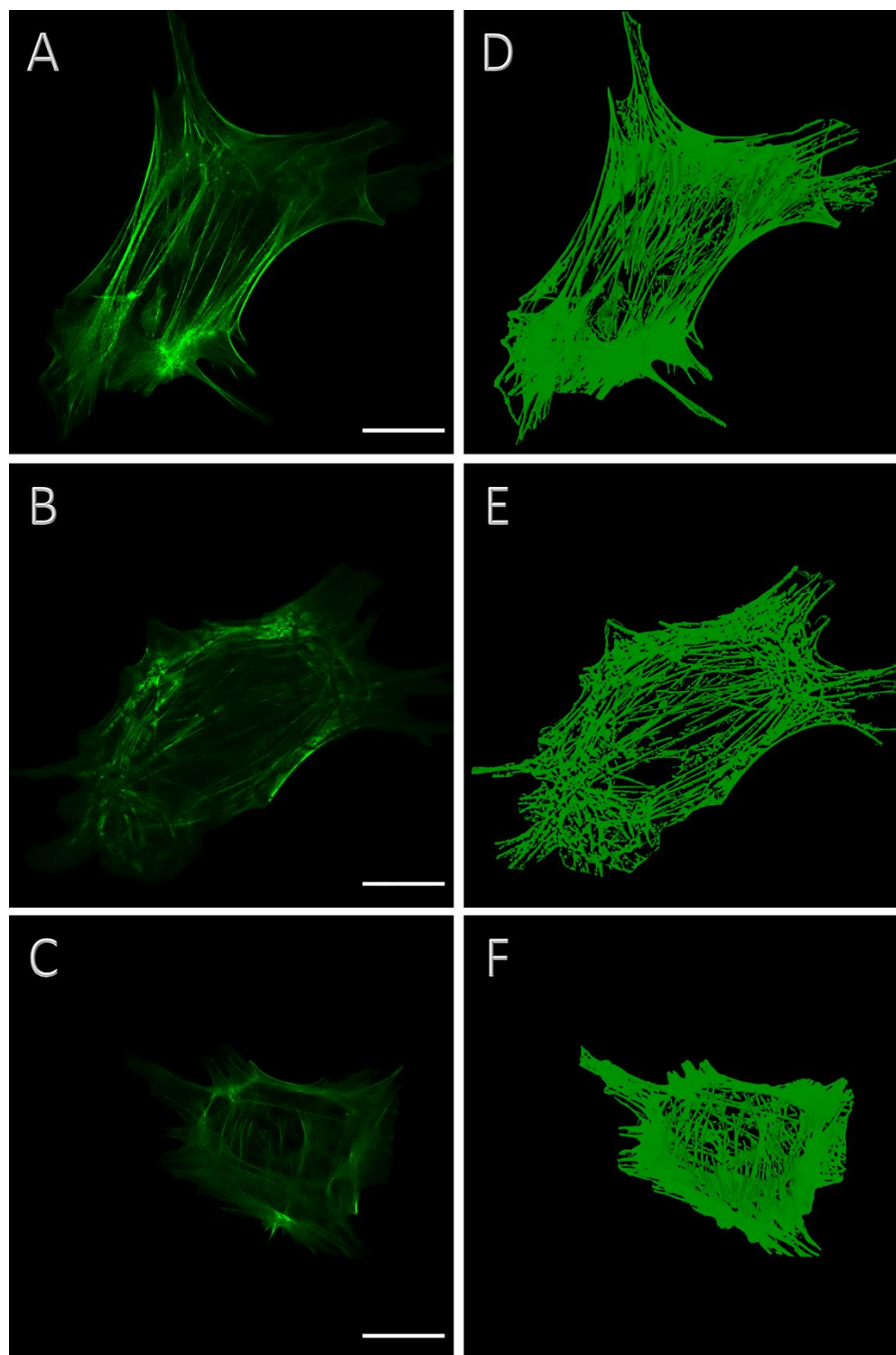


Figure 5.05 – Representative F-actin stress fibers in bovine scleral fibroblasts 6h after cyclic tensile strain (CTS), labelled with Alexa-488™ phalloidin (n=3 wells, N=3 plates). Maximum intensity projection of confocal images taken at 63x magnification and resolution of 1,912x1,912 pixels with Z-stack surface reconstructions in Imaris 9.2.

(A) Physiological CTS (0.26-1.8%, 1Hz for 1h) group; (B) Pathological CTS (0.6-4%, 1Hz for 1h) group; (C) Unloaded group; (D) Surface reconstruction of A; (E) Surface reconstruction of B; (F) Surface reconstruction of C. Scale bar = 25 $\mu$ m.

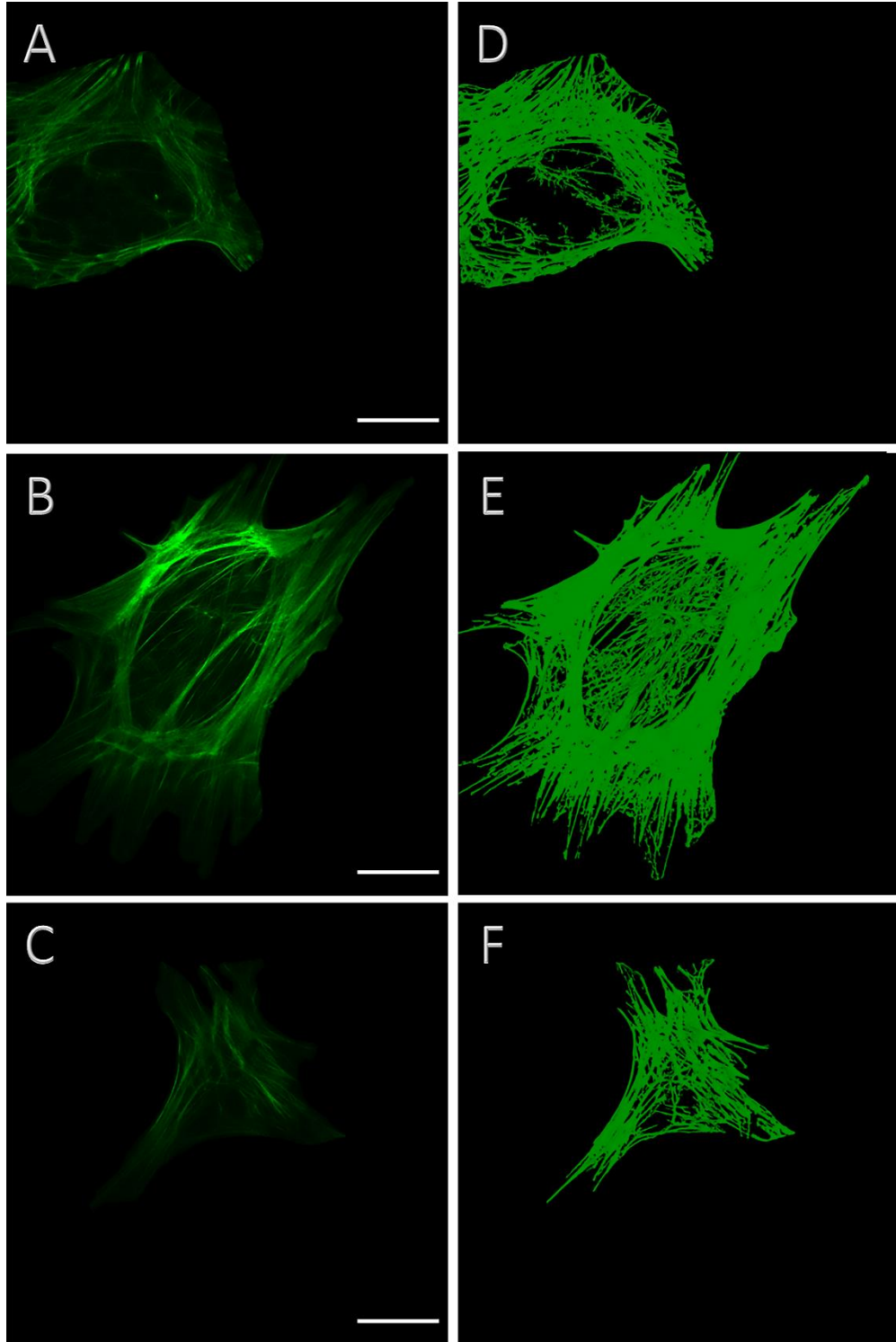


Figure 5.06 – Representative F-actin stress fibres in bovine scleral fibroblasts 24h after cyclic tensile strain (CTS), labelled with Alexa-488™ phalloidin (n=3 wells, N=3 plates). Maximum intensity projection of confocal images taken at 63x magnification and resolution of 1,912x1,912 pixels with Z-stack surface reconstructions in Imaris 9.2.

(A) Physiological CTS (0.26-1.8%, 1Hz for 1h) group; (B) Pathological CTS (0.6-4%, 1Hz for 1h) group; (C) Unloaded group; (D) Surface reconstruction of A; (E) Surface reconstruction of B; (F) Surface reconstruction of C. Scale bar = 25µm.

### 5.2.2.2 ImageJ analysis

The image analysis results are presented as box plot comparison between the three loading conditions at the same time point. For better visibility in the figures, the physiological group has been shortened to 'Phys', pathological to 'Path' and the unloaded cells to 'Unl'.

#### 5.2.2.2.1 Anisotropy

There was a significantly greater F-actin fibre anisotropy in fibroblasts 1h after exposure to physiological strain compared to both the unloaded and pathologically loaded cells (Figure 5.07A). The anisotropy, as calculated by FibrilTool, varies between 0 and 1, with higher values indicating a greater fibre alignment, whilst lower values are closer to a completely random distribution. 6h post-CTS F-actin anisotropy in physiologically loaded cells had decreased ( $p(1h \rightarrow 6h) = 0.011$ ), but retained a noticeable significance relative to the two other groups (Figure 5.07B). The mean anisotropy value for the pathologically loaded cells did not increase significantly ( $0.142 \pm 0.037$  at 1h and  $0.165 \pm 0.053$  at 6h post-CTS) and there was no difference with the unloaded group, which remained constant. At 24h F-actin anisotropy in fibroblasts exposed to physiological strain had reverted to an organisation comparable to the unloaded state, whilst the pathologically loaded cells had increased anisotropy (Figure 5.07C;  $p(6h \rightarrow 24h) = 0.006$ ).

Based on these data it can be inferred that there is a time-dependent delay in the orientation of the F-actin stress fibres in response to pathological strain, which become more structurally organised with time following application of CTS. In contrast, the physiologically loaded cells exhibited a decrease in anisotropy as time progressed (Figure 5.07), confirming the confocal observations (Figures 5.04 to 5.06).

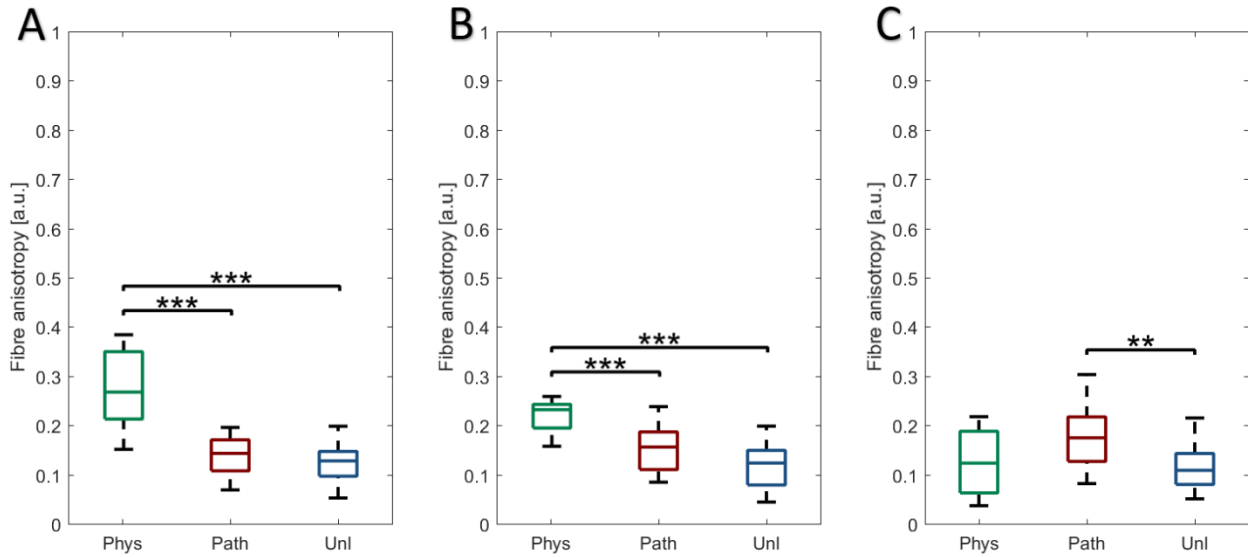


Figure 5.07 – Comparison of F-actin stress fibre anisotropy between three relaxation time points 1h (A), 6h (B) and 24h (C) post-CTS (n=3 wells, N=3 plates). Data were calculated by FibrilTool based on maximum intensity projections and grouped by applied CTS and relaxation time, presented as median  $\pm$  standard deviation (SD).

(A) n=129-136 cells; (B) n=103-113 cells; (C) n=136-145 cells; \*\*:p<0.01; \*\*\*:p<0.001.

#### 5.2.2.2.2 Coherency

OrientationJ fibre coherency analysis validated the trends observed using FibrilTool (Figure 5.08). Physiologically loaded cells had the greatest coherency in stress fibre alignment at 1h which gradually decreased, returning to the unloaded baseline at 24h after loading. In contrast, pathologically loaded cells displayed a time delay in F-actin reorganisation, reaching a more organised state at 24h after cessation of tensile strain. Coherency values at 24h post-CTS for the physiologically loaded scleral fibroblasts were not different from the unloaded cells ( $p=0.052$ ); no changes were observed in the unloaded cells as a function of time ( $p(1h \rightarrow 6h)=0.891$ ;  $p(6h \rightarrow 24h)=0.962$ ).

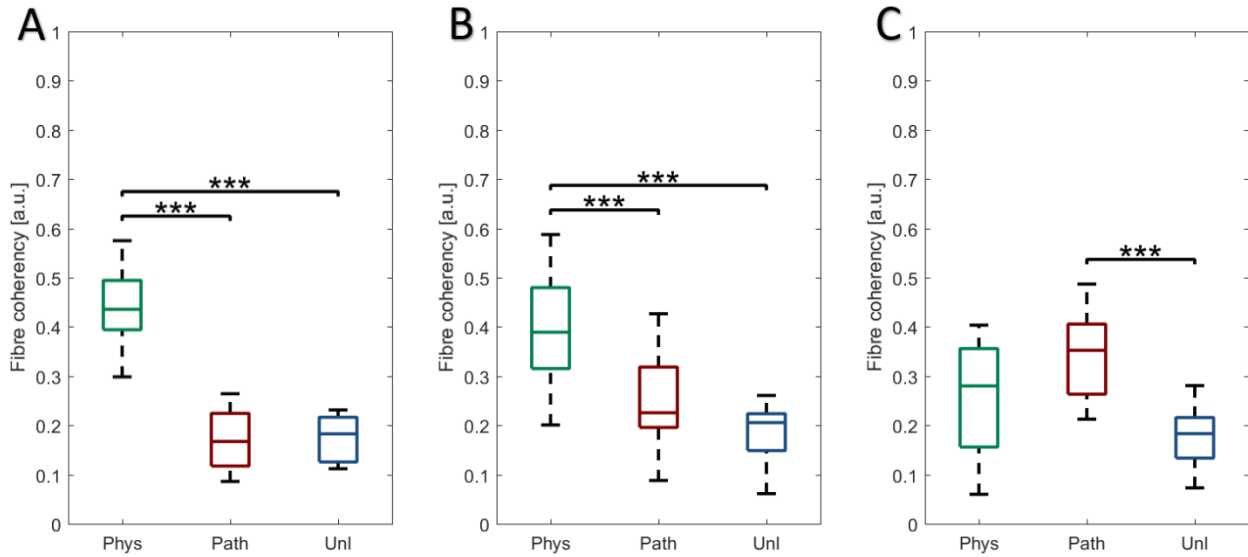


Figure 5.08 – Comparison of F-actin stress fibre coherency between three relaxation time points 1h (A), 6h (B) and 24h (C) post-CTS (n=3 wells, N=3 plates). Data were calculated by OrientationJ based on maximum intensity projections and grouped by applied CTS and relaxation time, presented as median  $\pm$  SD. (A) n=129-136 cells; (B) n=103-113 cells; (C) n=136-145 cells; \*\*\*:p<0.001.

### 5.2.2.3 Summary of tensile strain-induced effects on F-actin stress fibres

The assembly of F-actin microfilaments with myosin forms the highly aligned and elongated actin stress fibres (Section 1.2.3.1), with their organisation in bovine scleral fibroblasts being strain- and time-dependent. When applying a physiologically relevant mechanical load to the cells, the microarchitecture of the stress fibre network is highly aligned with parallel fibres spanning most of the cell length (Figure 5.04A and D). The experimental observations were in accordance with numerical simulations, which predicted that to achieve a better distribution of strain and stresses, the fibres need to be organised in the same general direction, with increased length and that the applied tensile strain needs to be relatively low (Sabuncuoglu et al., 2013). The greater anisotropy of the network would also make it stiffer; research on a murine embryonic fibroblast cell line (NIH3T3) suggested no significant contribution from the myosin organisation, but a notable dependence on the presence of thick aligned stress fibres (Gavara and Chadwick, 2016). As the 1h post-physiological load was designed to reflect the *in situ* conditions that fibroblasts are exposed to in the PPS, more research is required to further confirm these observations.

Fibre anisotropy and coherency (Figure 5.07 and 5.08, respectively) were calculated to reflect the overall F-actin organisation in a cell. Both parameters confirmed aligned fibres at 1h after physiological CTS and at 24h post-pathological strain. Furthermore, other software packages show similar trends (Appendix A.2). The FibrilTool anisotropy data for the unloaded fibroblasts was also in accordance with recorded values for NIH3T3 murine embryonic fibroblasts (Ayala et al., 2017). As noted (Section 1.2.3), the actin cytoskeleton is a dynamic structure with constant assembly and disassembly of G-actin into F-actin. Based on the presented data, the applied physiological tensile forces could have led to upregulation of actin turnover, resulting in the formation of stress fibres to adapt to the external stimulus. Following removal of the CTS, the stress fibres progressively disassemble to return to the unloaded state.

In contrast, pathological levels of strain appear to initially delay remodelling of the F-actin cytoskeleton, suggesting that high tensile forces prevent stress fibre reorganisation as that observed in physiologically loaded cells. Following removal of the pathological strain, and over a 24h period, F-actin organisation began to resemble the architecture that was initially observed in response to physiological strain – a phenomenon subsequently referred to as ‘inhibition delay’ (Section 5.2.6).

### 5.2.3 Vimentin intermediate filament response to physiological and pathological strain

#### 5.2.3.1 Differential effect of strain on vimentin intermediate filament rearrangement

Alterations in the arrangement of the vimentin intermediate filament cytoskeleton were observed 1h after CTS (Figure 5.09). Whilst vimentin does not form fibre bundles, rather being structured in a highly connected filamentous network, the physiologically loaded cells did seem to exhibit filament orientation corresponding to the primary cell axial direction (Figure 5.09A and D). This was not observed in the other two groups, which appeared to be mostly isotropic (Figure 5.09B and E; Figure 5.09C and F). It is probable that the reorientation was a result of the fibroblast elongation (Section 5.2.1.2) and/or connections with the highly aligned F-actin stress fibres, thus pulling the intermediate filament network in the same direction. This was supported by the observations 6h after loading (Figure 5.10A and D), where the physiologically loaded cells were more spread. Similarly, vimentin organisation in the 6h post-pathologically loaded fibroblasts appeared to be more orientated (Figure 5.10B and E), whilst after 24h they were composed of a large network of connected filaments (Figure 5.11B and E).

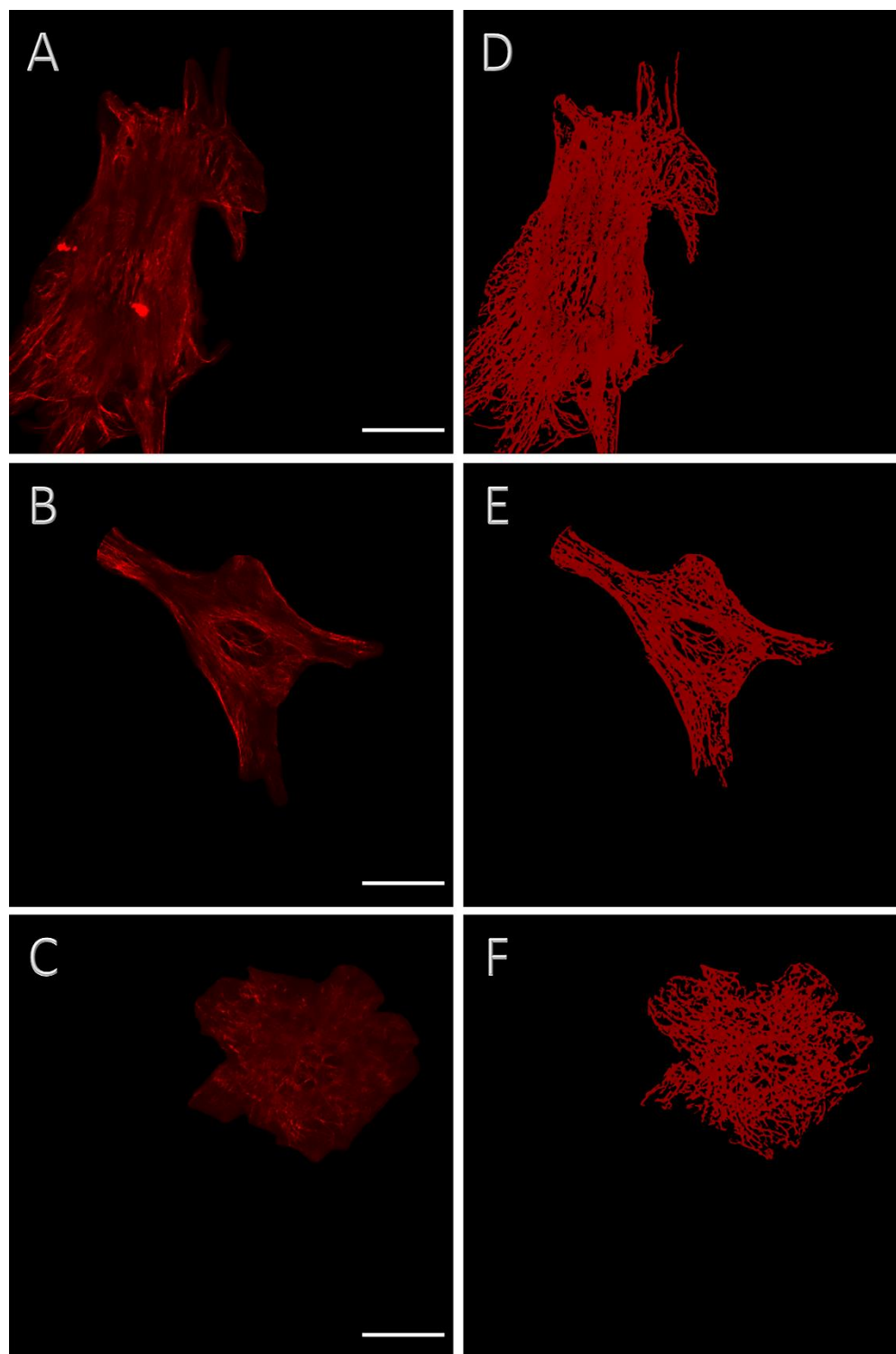


Figure 5.09 – Representative vimentin intermediate filaments in bovine scleral fibroblasts 1h after CTS, labelled with V9 primary and Alexa-594™ secondary antibody (n=3 wells, N=3 plates). Maximum intensity projection of confocal images taken at 63x magnification and resolution of 1,912x1,912 pixels with Z-stack surface reconstructions in Imaris 9.2. (A) Physiological CTS (0.26-1.8%, 1Hz for 1h) group; (B) Pathological CTS (0.6-4%, 1Hz for 1h) group; (C) Unloaded group; (D) Surface reconstruction of A; (E) Surface reconstruction of B; (F) Surface reconstruction of C. Scale bar = 25µm.

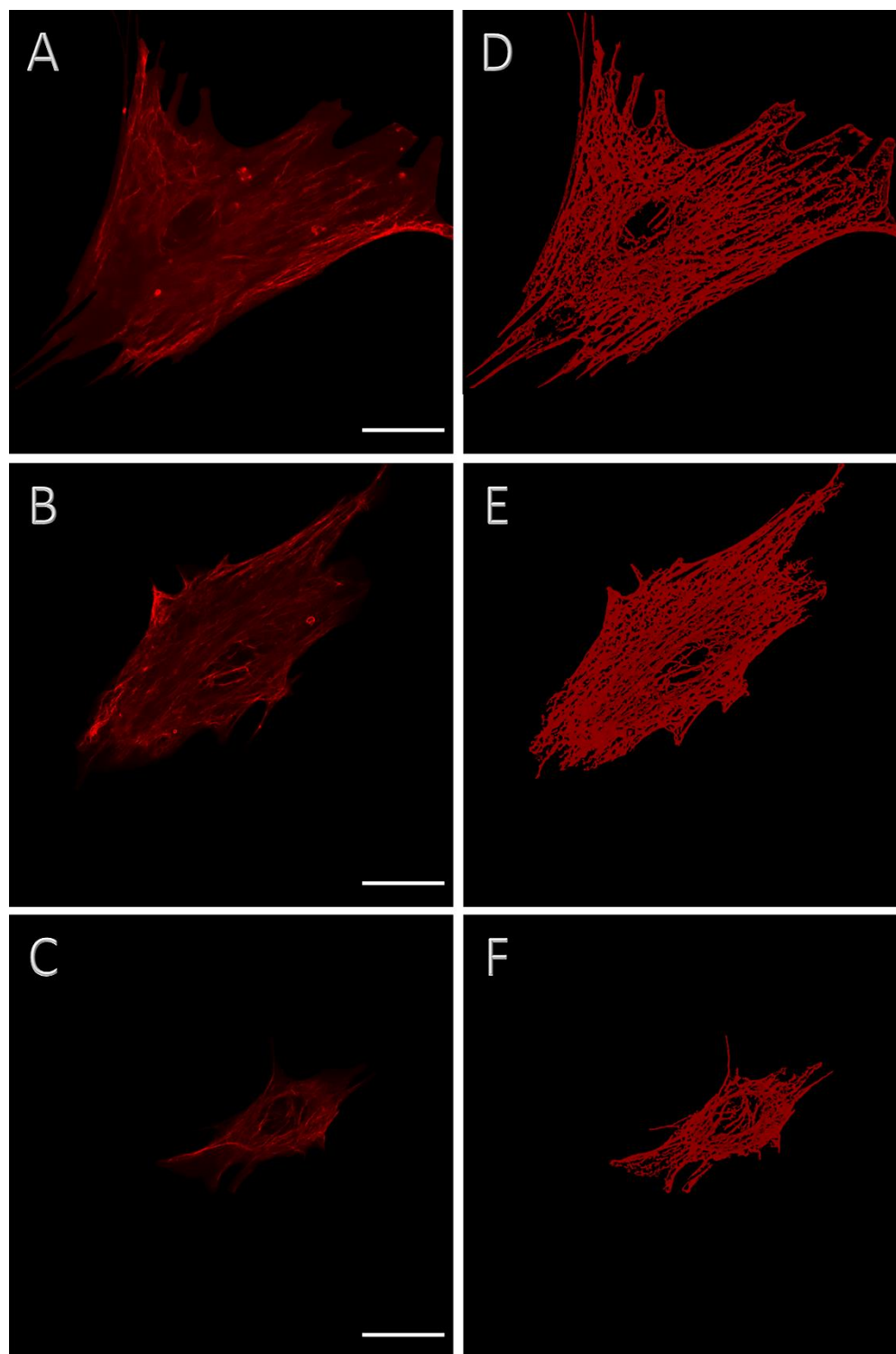


Figure 5.10 – Representative vimentin intermediate filaments in bovine scleral fibroblasts 6h after CTS, labelled with V9 primary and Alexa-594™ secondary antibody (n=3 wells, N=3 plates). Maximum intensity projection of confocal images taken at 63x magnification and resolution of 1,912x1,912 pixels with Z-stack surface reconstructions in Imaris 9.2. (A) Physiological CTS (0.26-1.8%, 1Hz for 1h) group; (B) Pathological CTS (0.6-4%, 1Hz for 1h) group; (C) Unloaded group; (D) Surface reconstruction of A; (E) Surface reconstruction of B; (F) Surface reconstruction of C. Scale bar = 25µm.

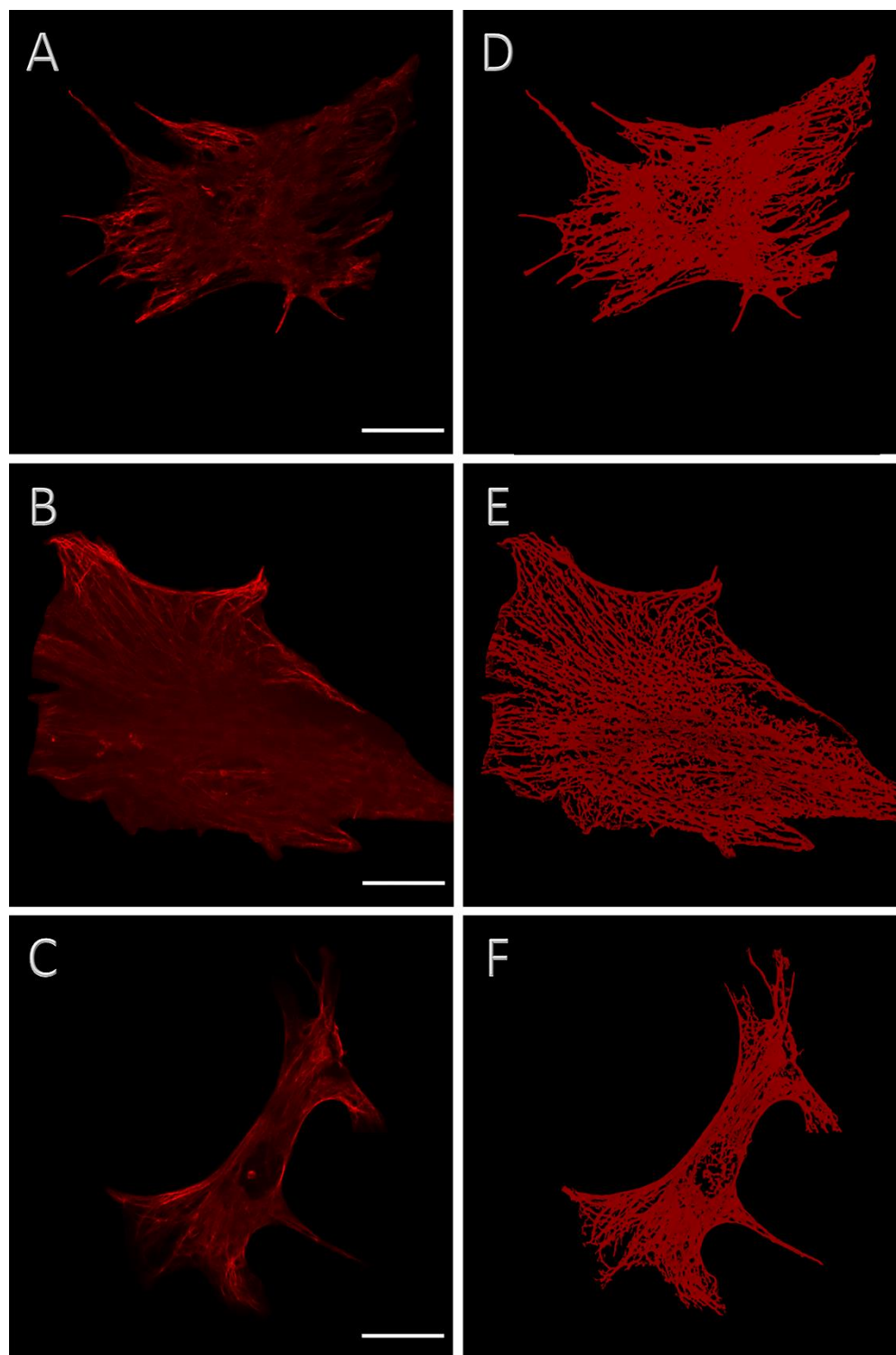


Figure 5.11 – Representative vimentin intermediate filaments in bovine scleral fibroblasts 24h after CTS, labelled with V9 primary and Alexa-594™ secondary antibody (n=3 wells, N=3 plates). Maximum intensity projection of confocal images taken at 63x magnification and resolution of 1,912x1,912 pixels with Z-stack surface reconstructions in Imaris 9.2. (A) Physiological CTS (0.26-1.8%, 1Hz for 1h) group; (B) Pathological CTS (0.6-4%, 1Hz for 1h) group; (C) Unloaded group; (D) Surface reconstruction of A; (E) Surface reconstruction of B; (F) Surface reconstruction of C. Scale bar = 25µm.

## 5.2.3.2 ImageJ analysis

## 5.2.3.2.1 Anisotropy

As with the F-actin stress fibres, the vimentin network was most anisotropic 1h after physiological load ( $0.104 \pm 0.046$ ), but remained consistently low over time ( $p(1h \rightarrow 6h) = 0.747$ ;  $p(6h \rightarrow 24h) = 0.376$ ) (Figure 5.12). The vimentin architecture was more disorganised 1h after applying the pathological CTS ( $0.062 \pm 0.028$ ) when compared to either the physiologically loaded or unloaded counterparts (Figure 5.12A). No significant changes were observed for the remainder of the times points; at 24h post-CTS  $p(\text{Path\_Phys}) = 0.070$  and  $p(\text{Path\_Unl}) = 0.083$ .

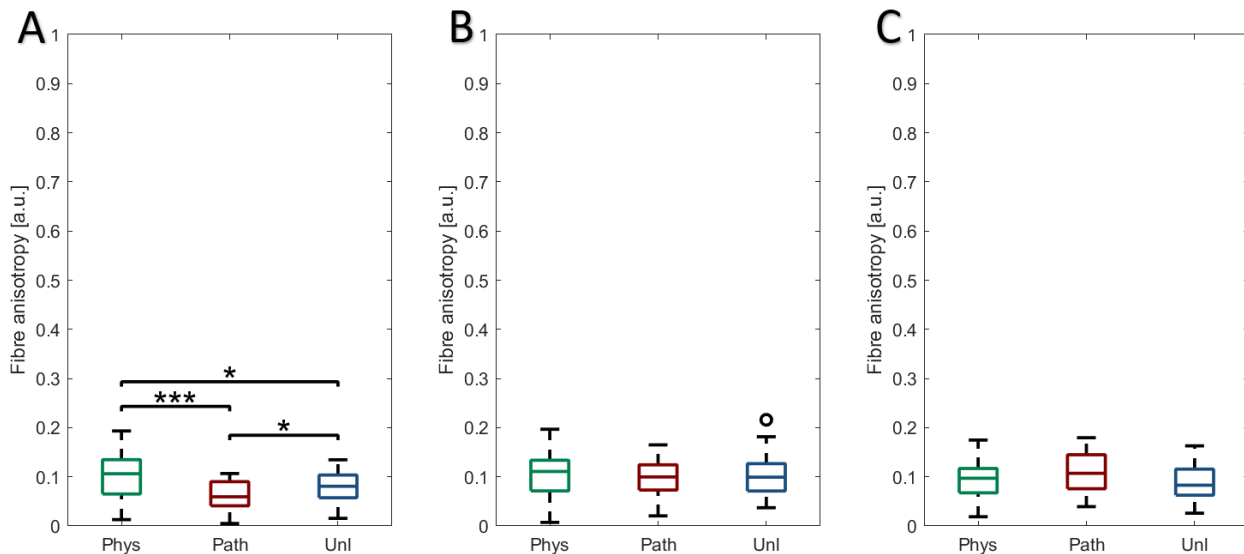


Figure 5.12 – Comparison of vimentin intermediate filament anisotropy between three relaxation time points 1h (A), 6h (B) and 24h (C) post-CTS ( $n=3$  wells,  $N=3$  plates). Data were calculated by FibrilTool based on maximum intensity projections and grouped by applied CTS and relaxation time, presented as median  $\pm$  SD.

(A)  $n=129-136$  cells; (B)  $n=103-113$  cells; (C)  $n=136-145$  cells; \*:  $p < 0.05$ ; \*\*\*:  $p < 0.001$ .

## 5.2.3.2.2 Coherency

The low filament anisotropy observed for the pathologically loaded cells (Figure 5.12A) was not reflected in the coherency values calculated by OrientationJ (Figure 5.13A). Whilst in general OrientationJ provides the same trends for the vimentin fibre orientation as FibrilTool, there was no significant difference between the pathological and unloaded cells ( $0.114 \pm 0.059$  and  $0.111 \pm 0.067$ ,

respectively;  $p=0.918$ ). However, at 6h post-CTS ( $p(\text{Phys\_Unl})=0.069$ ;  $p(\text{Path\_Unl})=0.053$ ; Figure 5.13B), the coherency values seemed to more closely follow the vimentin filament anisotropy. At the 24h time point (Figure 5.13C) the coherency for the pathologically loaded cells was larger than the unloaded ones ( $0.181\pm 0.076$  and  $0.130\pm 0.057$ , respectively;  $p=0.011$ ), but not with the physiologically loaded cells ( $p=0.073$ ). Overall, both physiological and pathological strains led to smaller alterations in vimentin organisation compared to the effects observed with the actin stress fibres, with significant difference for both parameters observed only for the physiological strain 1h after CTS.

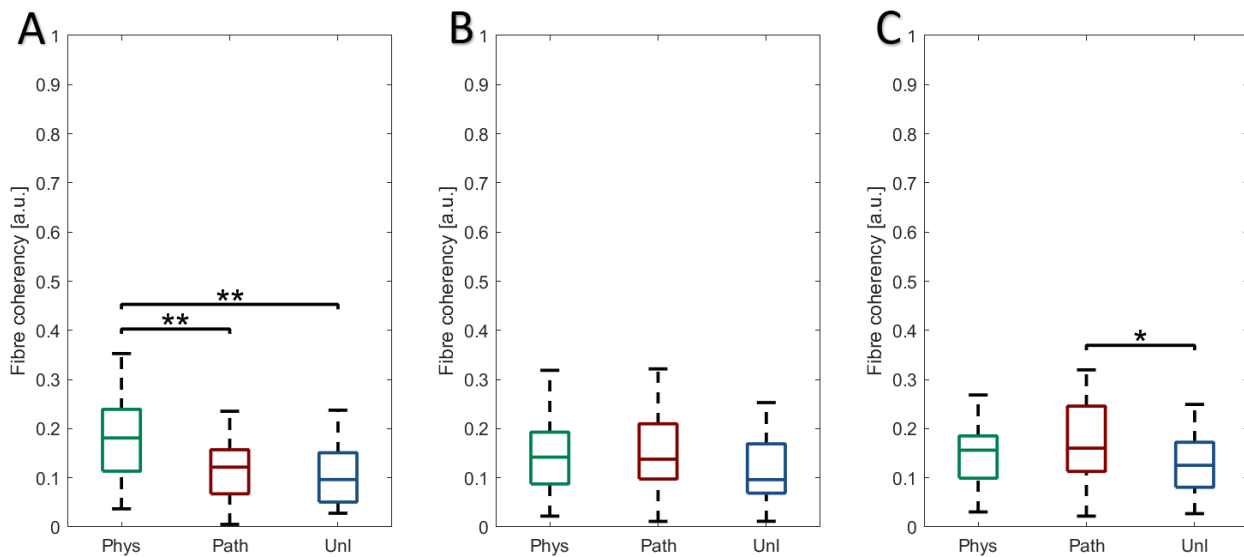


Figure 5.13 – Comparison of vimentin intermediate filament coherency between relaxation time points 1h (A), 6h (B) and 24h (C) post-CTS ( $n=3$  wells,  $N=3$  plates). Data were calculated by OrientationJ based on maximum intensity projections and grouped by applied CTS and relaxation time, presented as median  $\pm$  SD.

(A)  $n=129-136$  cells; (B)  $n=103-113$  cells; (C)  $n=136-145$  cells; \*:  $p<0.05$ ; \*\*:  $p<0.01$ .

### 5.2.3.3 Summary of tensile strain-induced effects on vimentin intermediate filaments

Scleral fibroblasts contain the intermediate filament vimentin; these filaments surround and attach to the nucleus from the top, with the organisation providing loadbearing characteristics and resistance to compression (Cui et al., 2008). As vimentin intermediate filaments are connected to the F-actin cytoskeleton and have been noted to align with the primary directional axis, alterations to the actin stress fibres could also result in a rearrangement of the vimentin network (Shah et al.,

1998; Costigliola et al., 2017). This could provide clarity for the changes in vimentin architecture observed 1h after physiological tensile strain when the actin cytoskeleton rearranged the most as well. Furthermore, only the coherency of the vimentin filaments (Section 5.2.3.2.2) was significantly greater than the corresponding unloaded cells, unlike the actin stress fibres where most of the measured parameters were higher (Section 5.2.1). It is possible that these observations are due to differences in recovery rates between F-actin fibres and vimentin filaments following removal of the CTS, with the former being noted to reorganise and reach equilibrium within 90s of applying static pressure in bovine chondrocytes (Pravincumar et al., 2012). To the best of the author's knowledge no literature is available on the time-frame dynamics of intermediate filament remodelling.

Unlike the actin and microtubule cytoskeleton, the vimentin network was not mostly situated in a single plane but surrounded the nucleus from the top and sides. The resulting approximation of the vimentin cytoskeleton to a layer was acceptable for several reasons: (I) the filaments were only positioned over the nucleus and not underneath it, thus there was no overlap of filaments; (II) the bovine scleral fibroblasts were flat in all experimental conditions, adhering to the underlying type I collagen substrate; (III) there are no available substitutes that accurately represent the cytoskeleton that would allow measurement of the presented parameters; (IV) utilisation of the maximum intensity projection has been previously performed for image-analysis based research on the vimentin cytoskeleton (Costigliola et al., 2017).

Calculating the precise cellular height remains a limitation of this work. As the fibroblasts were plated on a collagen substrate, with the BioFlex™ membrane pieces placed on glass slides, the confocal microscopy optical slices had the cells not always on the exact same visualisation level. The distance between the optical sections was kept consistent at 0.14µm, but the cell positioning and intensity of the detected signal necessitated adjustment for the number of slices for each collected confocal Z-stack. Whilst some height profile anisotropy might have occurred, research suggests that it will be negligible to the fibre orientation changes in the main plane of the cell (Gavara and Chadwick, 2016).

## 5.2.4 $\beta$ -Tubulin microtubule response to physiological and pathological strain

### 5.2.4.1 Differential effect of strain on $\beta$ -tubulin microtubule rearrangement

The microtubules are the largest of the cytoskeletal elements and in bovine scleral fibroblasts tended to be arranged in predominately a single plane. Following 1h post-physiological CTS, the microtubules were extensively spread within the elongated cell area (Figure 5.14A and D). In contrast, the microtubules did not appear to align in the direction of pathological strain (Figure 5.14B and E), instead resembling the organisation observed in the unloaded cells (Figure 5.14C and F). At 6h post-physiological CTS the microtubular network was still extensively organised but was less densely packed and did not align as obviously as at 1h (Figure 5.15A and D) and by 24h of recovery the microtubules appeared to have a random organisation comparable to the unloaded cells (Figure 5.16A and D and Figure 5.16C and F, respectively). However, in contrast, the tubulin network appeared more orientated 24h following cessation of pathological strain (Figure 5.16B and E). A notable high-intensity signal was frequently observed near the nucleus, most probably stemming from the microtubule organising centre (MTOC) (Section 1.2.5).

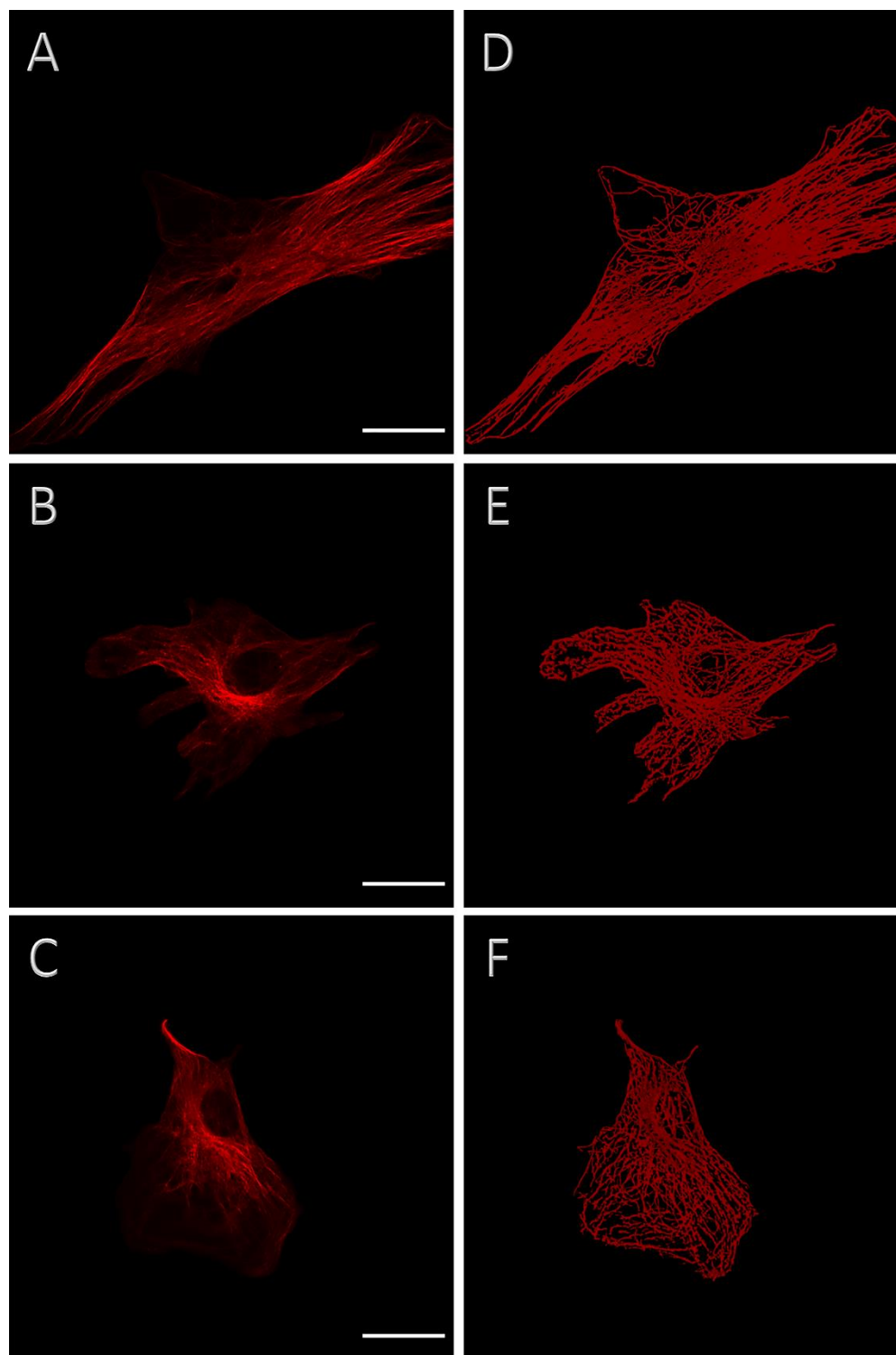


Figure 5.14 – Representative  $\beta$ -tubulin microtubules in bovine scleral fibroblasts 1h after CTS, labelled with E7 primary and Alexa-594™ secondary antibody (n=3 wells, N=3 plates). Maximum intensity projection of confocal images taken at 63x magnification and resolution of 1,912x1,912 pixels with Z-stack surface reconstructions in Imaris 9.2. (A) Physiological CTS (0.26-1.8%, 1Hz for 1h) group; (B) Pathological CTS (0.6-4%, 1Hz for 1h) group; (C) Unloaded group; (D) Surface reconstruction of A; (E) Surface reconstruction of B; (F) Surface reconstruction of C. Scale bar = 25 $\mu$ m.

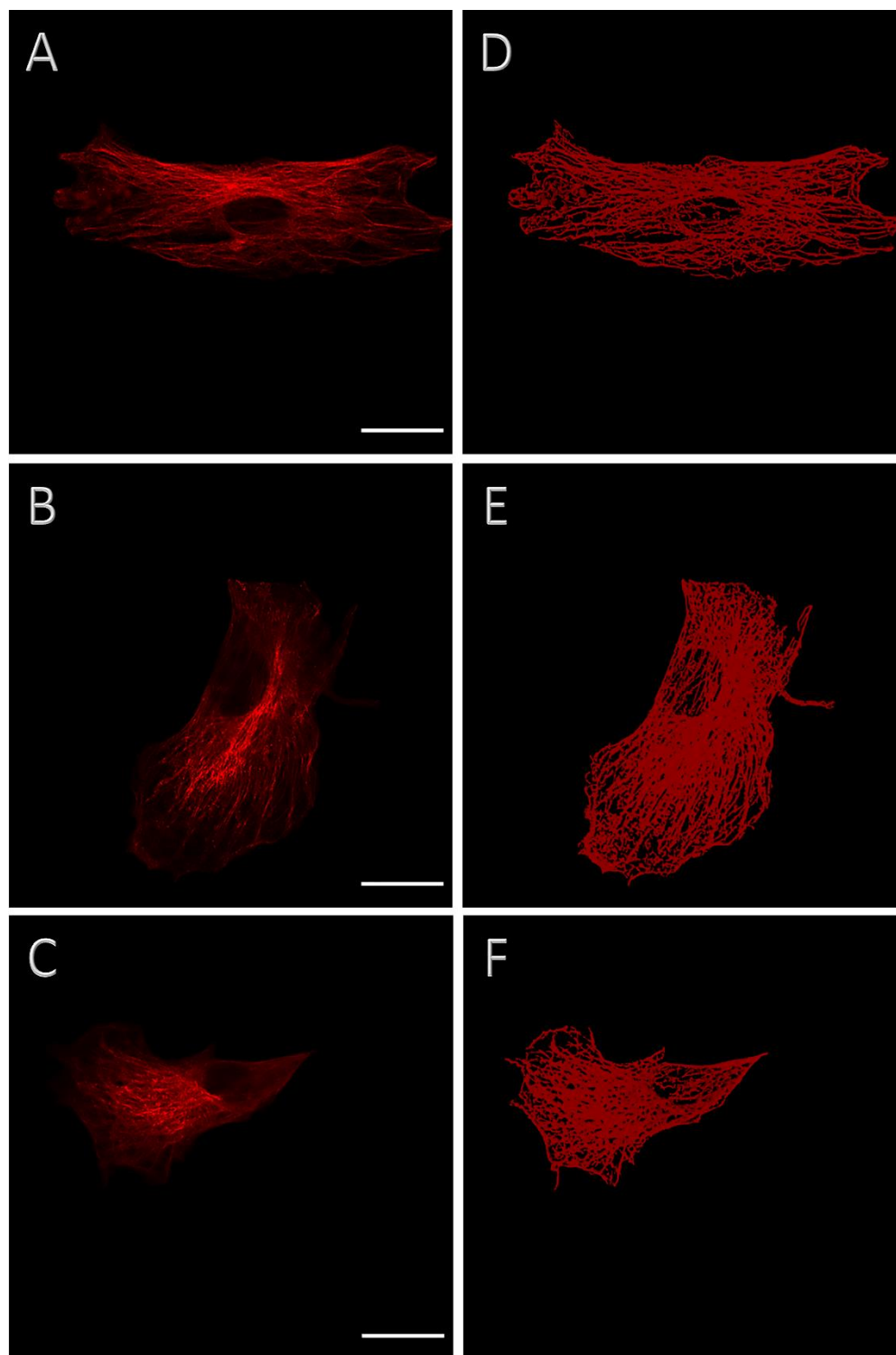


Figure 5.15 – Representative  $\beta$ -tubulin microtubules in bovine scleral fibroblasts 6h after CTS, labelled with E7 primary and Alexa-594™ secondary antibody (n=3 wells, N=3 plates). Maximum intensity projection of confocal images taken at 63x magnification and resolution of 1,912x1,912 pixels with Z-stack surface reconstructions in Imaris 9.2. (A) Physiological CTS (0.26-1.8%, 1Hz for 1h) group; (B) Pathological CTS (0.6-4%, 1Hz for 1h) group; (C) Unloaded group; (D) Surface reconstruction of A; (E) Surface reconstruction of B; (F) Surface reconstruction of C. Scale bar = 25 $\mu$ m.

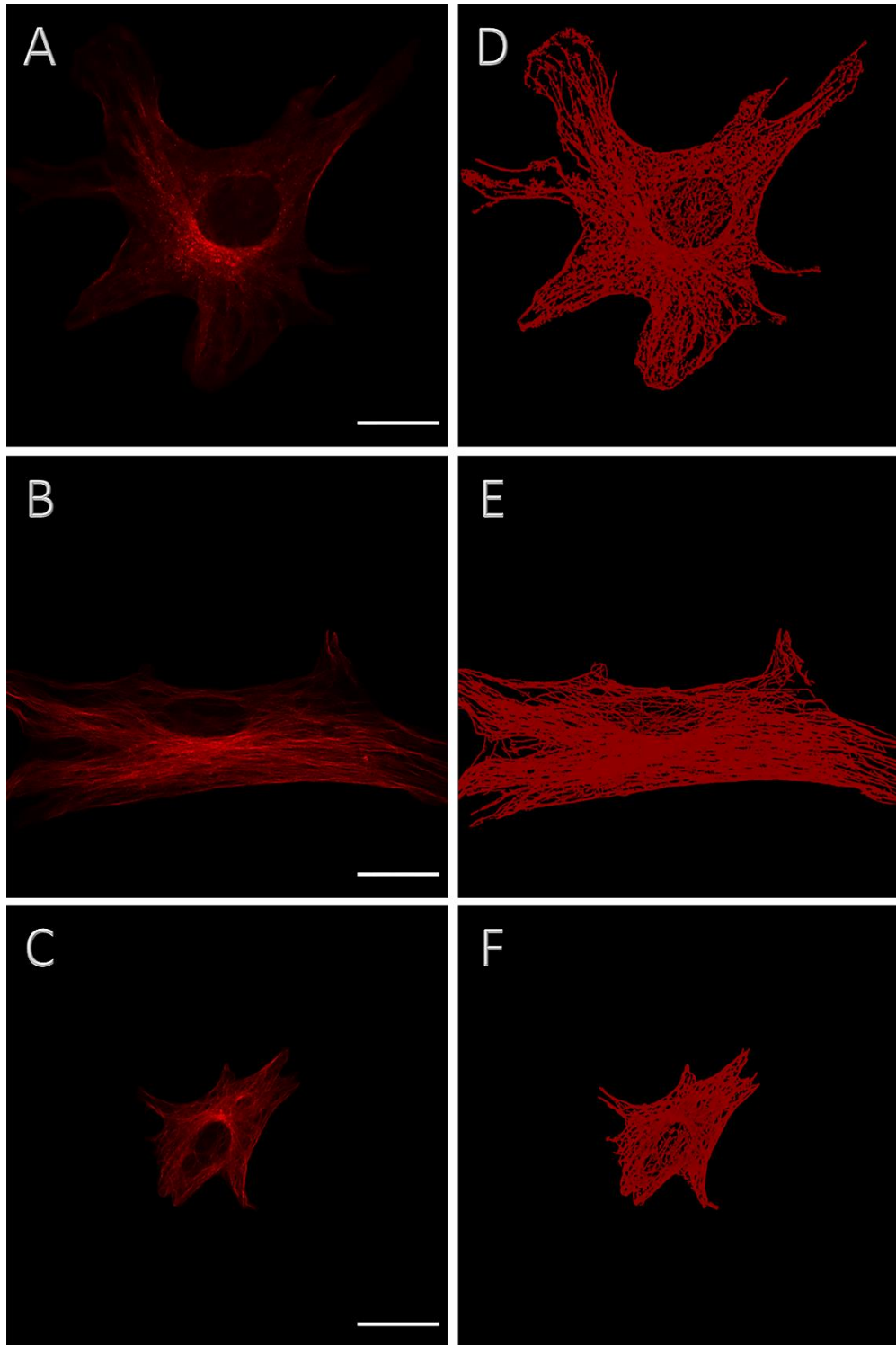


Figure 5.16 – Representative  $\beta$ -tubulin microtubules in bovine scleral fibroblasts 24h after CTS, labelled with E7 primary and Alexa-594™ secondary antibody (n=3 wells, N=3 plates). Maximum intensity projection of confocal images taken at 63x magnification and resolution of 1,912x1,912 pixels with Z-stack surface reconstructions in Imaris 9.2. (A) Physiological CTS (0.26-1.8%, 1Hz for 1h) group; (B) Pathological CTS (0.6-4%, 1Hz for 1h) group; (C) Unloaded group; (D) Surface reconstruction of A; (E) Surface reconstruction of B; (F) Surface reconstruction of C. Scale bar = 25 $\mu$ m.

## 5.2.4.2 ImageJ analysis

## 5.2.4.2.1 Anisotropy

Unlike both the actin and vimentin cytoskeleton, there were minimal changes to microtubule anisotropy (Figure 5.17). 1h post-CTS the microtubule anisotropy for the physiologically loaded cells was greater than the unloaded cells (Figure 5.17A;  $p=0.022$ ), with no other differences detected ( $p(\text{Path\_Unl})=0.063$ ). 6h post-cessation of load there were no statistical significances between the groups. Following a 24h recovery period, there was no effect on microtubule anisotropy in pathologically loaded cells ( $p(\text{Path\_Unl})=0.092$ ; Figure 5.17C).

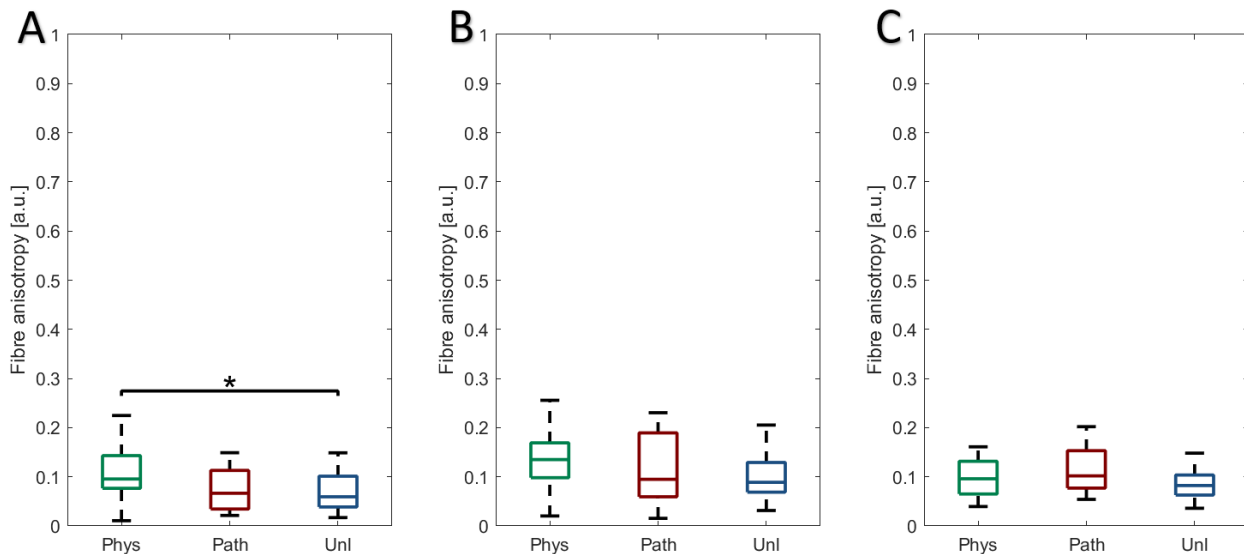


Figure 5.17 – Comparison of  $\beta$ -tubulin microtubule anisotropy between three relaxation time points 1h (A), 6h (B) and 24h (C) post-CTS ( $n=3$  wells,  $N=3$  plates). Data were calculated by FibrilTool based on maximum intensity projections and grouped by applied CTS and relaxation time, presented as median  $\pm$  SD.

(A)  $n=101-130$  cells; (B)  $n=119-127$  cells; (C)  $n=141-154$  cells; \*:  $p<0.05$ .

## 5.2.4.2.2 Coherency

The measured microtubule coherency further confirmed the FibrilTool calculations (Figure 5.18). The only detected change was an increased coherency between the 1h physiologically loaded and the unloaded cells (Figure 5.18A) Similar to the anisotropy, there was no difference in microtubule

coherency at 24h ( $p(\text{Path\_Unl})=0.063$ ; Figure 5.18C). The small anisotropy and coherency values are most likely a reflection of the low tensile strain sensitivity of the microtubules.

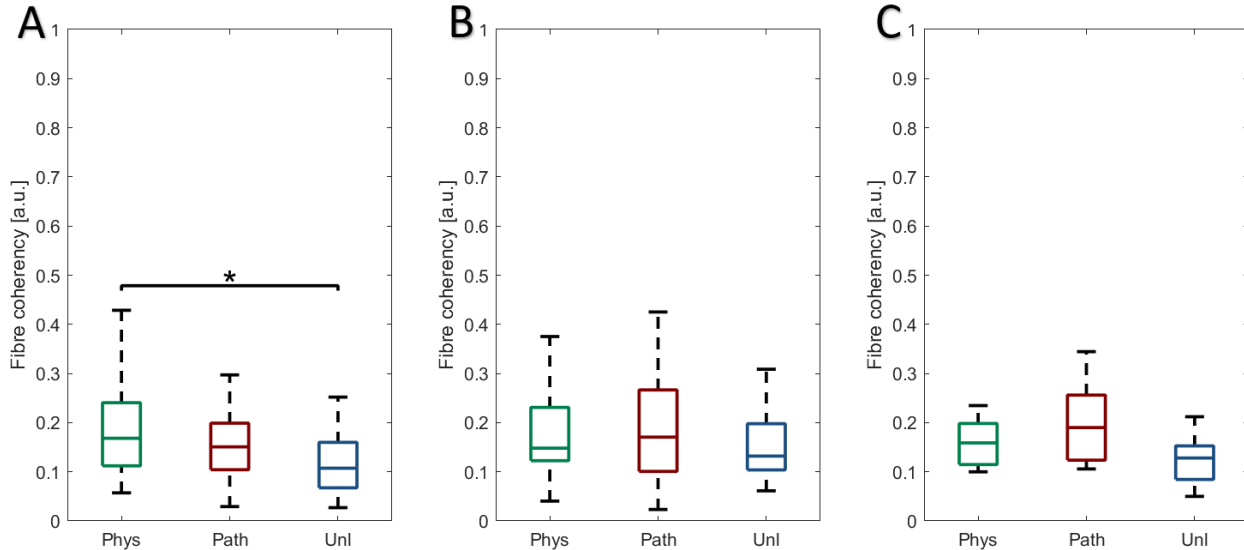


Figure 5.18 – Comparison of  $\beta$ -tubulin microtubule coherency between three relaxation time points 1h (A), 6h (B) and 24h (C) post-CTS ( $n=3$  wells,  $N=3$  plates). Data were calculated by OrientationJ based on maximum intensity projections and grouped by applied CTS and relaxation time, presented as median  $\pm$  SD.

(A)  $n=101-130$  cells; (B)  $n=119-127$  cells; (C)  $n=141-154$  cells; \*:  $p<0.05$ .

#### 5.2.4.3 Summary of tensile strain-induced effects on $\beta$ -tubulin microtubules

As indicated throughout this Section, microtubules appeared to be the least sensitive to tensile strain out of the cytoskeletal elements. This observation was in agreement with other work which point to the microtubules not being part of the CTS cell alignment mechanism (Sears and Kaunas, 2016). In addition, in rat gingival and embryonic chick heart fibroblasts, microtubule-depolymerisation drugs tend to stimulate stress fibre formation and vice-versa (Danowski, 1989). Furthermore, Kaverina et al. showed that exposing murine melanoma cells to tensile strain (constant pressure of 2-4kPa) induces growth of microtubules, along with focal adhesions at the periphery, which could contribute to the lower tubule alignment (Kaverina et al., 2002). Therefore, it can be assumed that the microtubules are not specifically affected by cyclic strain and all detectable alterations are the indirect result of actin stress fibre remodelling and whole-cell

reorientation. Additional alignment image analysis by the CurveAlign and CytoSpectre software packages are included in the Appendix (A.2).

## 5.2.5 Nuclear response to physiological and pathological strain

### 5.2.5.1 Differential effect of strain on nuclear rearrangement

Figure 5.19 to 5.21 illustrate changes to the shape of the fibroblast nuclei as a result of mechanical loading over all three time points. The nuclei ROI were traced manually each time; as some of the scleral fibroblasts had undergone division this resulted in more nuclei than cells being confocally imaged. The nuclei were represented as a maximum intensity projection of the confocal Z-stack, a surface reconstruction in Imaris and chromatin condensation parameter (CCP) image output (Irianto et al., 2014). All recorded scleral fibroblast nuclei appeared to be in interphase, as confirmed by confocal images of 4',6-diamidino-2-phenylindole (DAPI)-labelled nuclear phases in HeLa cells (Chuang et al., 2008). This agreed with estimates of bovine scleral fibroblast doubling time being of around five days, thus excluding any stimulated proliferation in the recorded time frame. Following the cellular and cytoskeletal behaviour, the nuclei 1h post-physiological CTS were also elongated (Figure 5.19A). At the same time, pathologically loaded cells also exhibited larger nuclear areas and appeared more circular (Figure 5.19B). This observation was consistent for the 6h and 24h time points as well (Figure 5.20B and 5.21B). In all instances, there was visible chromatin condensation above 0, including in the unloaded fibroblasts, which remained the smallest detected nuclei (Figure 5.19C, 5.20C and 5.21C). The pathologically loaded fibroblasts also had the highest CCP, with many detected edges for the 1h and 6h time points (Figure 5.19B and 5.20B, respectively).

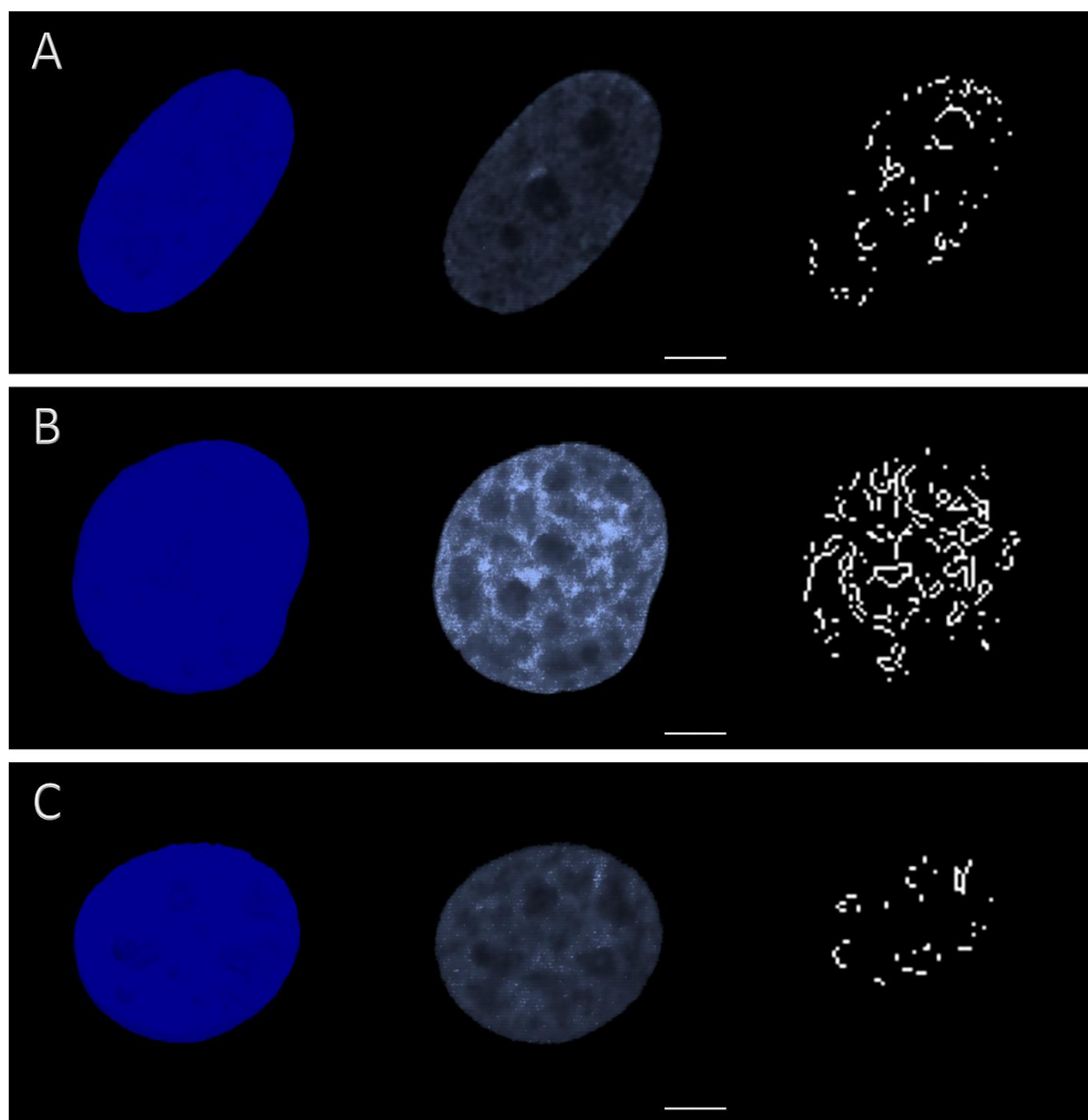


Figure 5.19 – Magnified view of representative nuclei in bovine scleral fibroblasts 1h after CTS, labelled with 4',6-diamidino-2-phenylindole (DAPI) (n=3 wells, N=3 plates). Maximum intensity projection of confocal images taken at 63x magnification and original resolution of 1,912x1,912 pixels (Centre) with Z-stack surface reconstructions in Imaris 9.2 (Left) and corresponding Sobel edge detection algorithm chromatin condensation (Right).

(A) Physiological CTS (0.26-1.8%, 1Hz for 1h) group; (B) Pathological CTS (0.6-4%, 1Hz for 1h) group; (C) Unloaded group. Scale bar = 10 $\mu$ m.

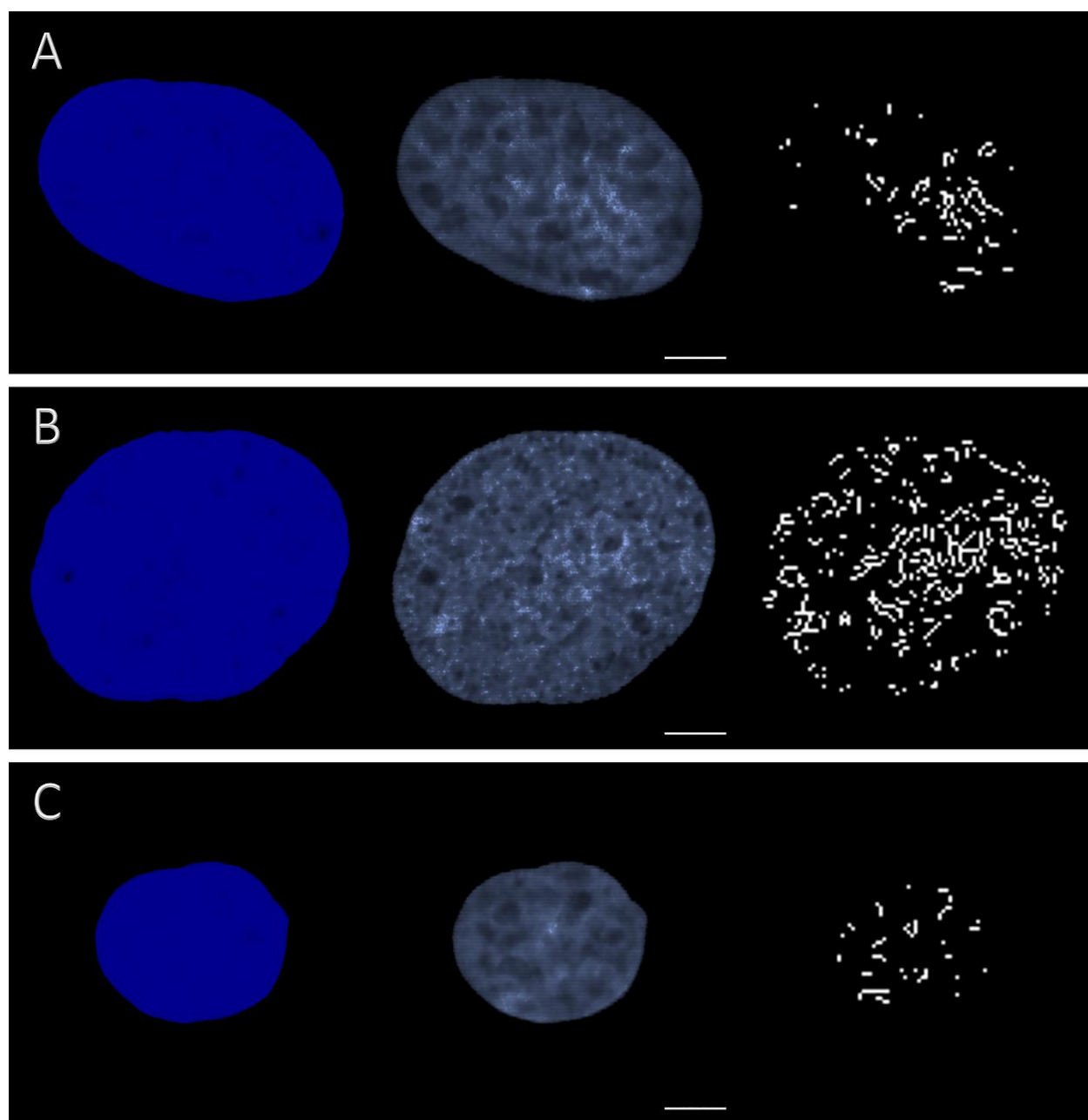


Figure 5.20 – Magnified view of representative nuclei in bovine scleral fibroblasts 6h after CTS, labelled with 4',6-diamidino-2-phenylindole (DAPI) (n=3 wells, N=3 plates). Maximum intensity projection of confocal images taken at 63x magnification and original resolution of 1,912x1,912 pixels (Centre) with Z-stack surface reconstructions in Imaris 9.2 (Left) and corresponding Sobel edge detection algorithm chromatin condensation (Right).

(A) Physiological CTS (0.26-1.8%, 1Hz for 1h) group; (B) Pathological CTS (0.6-4%, 1Hz for 1h) group; (C) Unloaded group. Scale bar = 10 $\mu$ m.

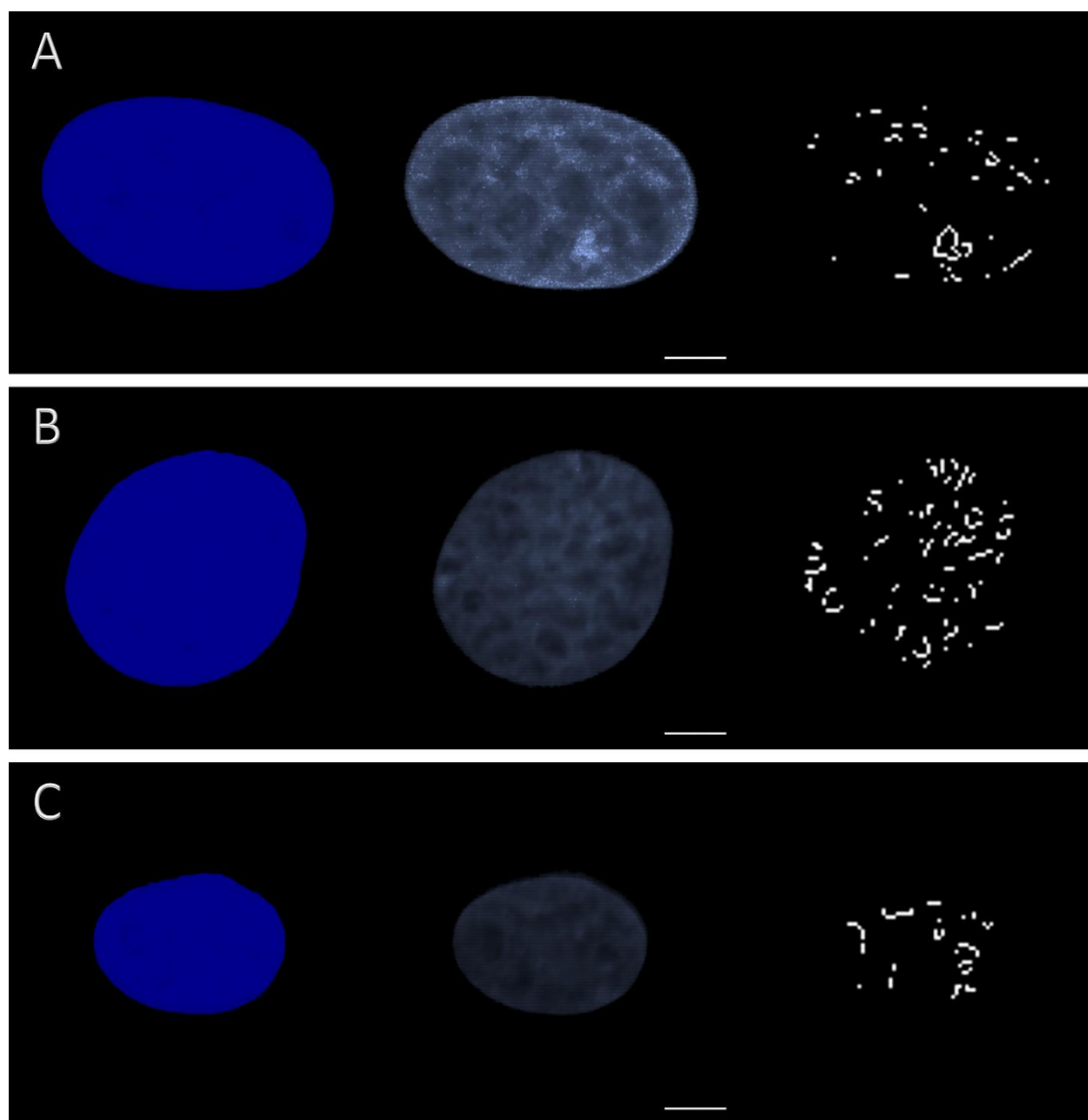


Figure 5.21 – Magnified view of representative nuclei in bovine scleral fibroblasts 24h after CTS, labelled with 4',6-diamidino-2-phenylindole (DAPI) (n=3 wells, N=3 plates). Maximum intensity projection of confocal images taken at 63x magnification and original resolution of 1,912x1,912 pixels (Centre) with Z-stack surface reconstructions in Imaris 9.2 (Left) and corresponding Sobel edge detection algorithm chromatin condensation (Right).

(A) Physiological CTS (0.26-1.8%, 1Hz for 1h) group; (B) Pathological CTS (0.6-4%, 1Hz for 1h) group; (C) Unloaded group. Scale bar = 10 $\mu$ m.

## 5.2.5.2 Nuclear area

Nuclear area was significantly larger in scleral fibroblasts at 1h following application of pathological and physiological strains when compared to unloaded cells (Figure 5.22A). At 6h the nuclear size in the pathologically loaded group was on average  $270.4 \pm 67.4 \mu\text{m}^2$  (Figure 5.22B) and reached a plateau, which was retained at 24h ( $272.2 \pm 86.8 \mu\text{m}^2$ ; Figure 5.22C). The nuclear area of the physiologically loaded fibroblasts ( $220.9 \pm 47.0 \mu\text{m}^2$ ) became lower than the pathological ones ( $272.3 \pm 86.7 \mu\text{m}^2$ ) at 24h post-CTS (Figure 5.22C). The area of both loaded cell populations remained larger than the unloaded, similarly to the overall cell area observed (Figure 5.01).

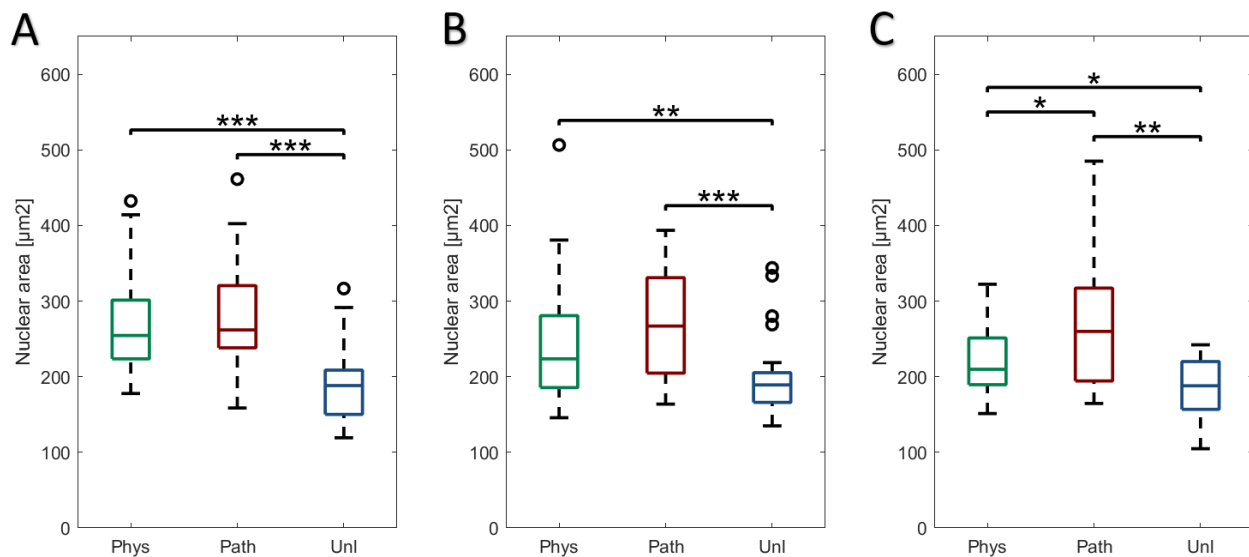


Figure 5.22 – Comparison of nuclear area between three relaxation time points 1h (A), 6h (B) and 24h (C) post-CTS (n=3 wells, N=3 plates). Data were calculated by ROI-based ImageJ analysis based on maximum intensity projections and grouped by applied CTS and relaxation time, presented as median  $\pm$  SD. (A) n=236-291 nuclei; (B) n=227-299 nuclei; (C) n=243-296 nuclei; \*:p<0.05; \*\*:p<0.01; \*\*\*:p<0.001.

## 5.2.5.3 Nuclear roundness

Nuclear morphology was evaluated based on the ROIs utilised for area determination (Figure 5.23). Roundness was calculated as  $4 * area / (\pi * length^2)$ , with a perfect circle having a roundness of 1. The lower nuclear roundness (greater elongation) in fibroblasts 1h after application of physiological load was in agreement with the observed cytoskeletal and cellular

stretching (Figure 5.23A). The nuclear roundness increased at the subsequent time point and then remained constant ( $p(1h \rightarrow 6h)=0.022$ ;  $p(6h \rightarrow 24h)=0.222$ ). Whilst initially predicting that the pathologically loaded fibroblasts would follow the reverse trend, in accordance with the cell parameter data, unexpectedly their nuclei were significantly more elongated 1h after tensile strain (Figure 5.23A). Furthermore, the 24h post-pathological CTS nuclei were not different from either the unloaded or physiologically loaded cell nuclei (Figure 5.23C).

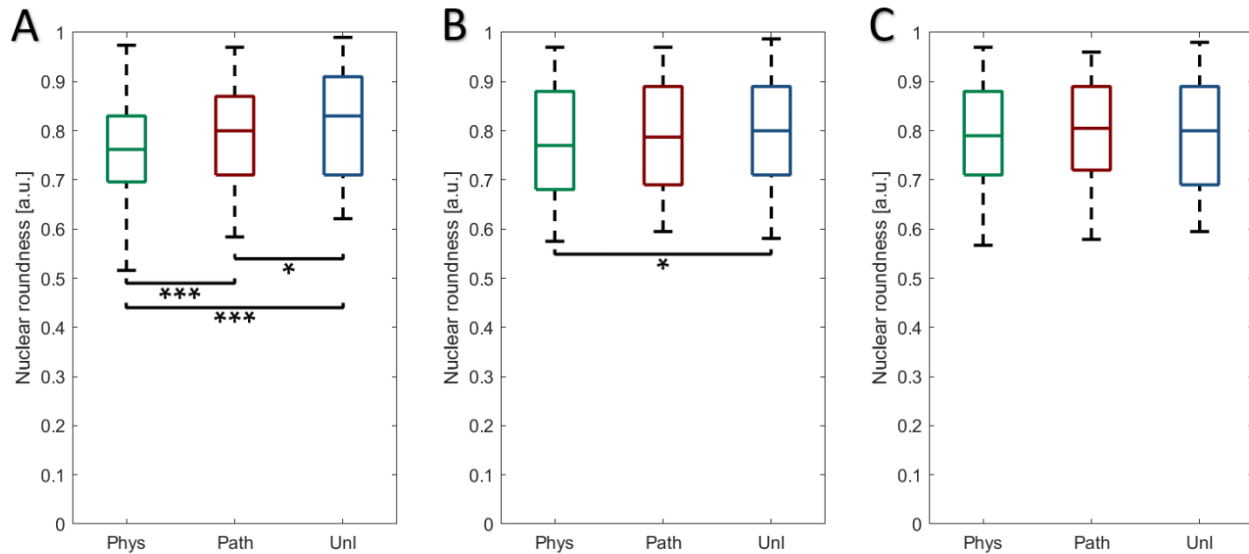


Figure 5.23 – Comparison of nuclear roundness between three relaxation time points 1h (A), 6h (B) and 24h (C) post-CTS ( $n=3$  wells,  $N=3$  plates). Data were calculated by ROI-based ImageJ analysis based on maximum intensity projections and grouped by applied CTS and relaxation time, presented as median  $\pm$  SD. (A)  $n=236-291$  nuclei; (B)  $n=227-299$  nuclei; (C)  $n=243-296$  nuclei; \*:  $p<0.05$ ; \*\*\*:  $p<0.001$ .

#### 5.2.5.4 Chromatin condensation

CCP was calculated through a bespoke MATLAB script with the authors' suggested default parameters (Irianto et al., 2014). The most notable difference was the high CCP values for the pathologically loaded cells at the 1h time point, with an average of  $7.22 \pm 2.36\%$  (Figure 5.24A). As higher CCP corresponds to more heterochromatin, this feature of the pathologically loaded cells could be indicative of gene silencing as a result of the application of high tensile strain. In addition, the mean CCP of the physiologically loaded cells had also increased in comparison to the unloaded fibroblasts ( $2.82 \pm 1.29\%$  and  $2.33 \pm 1.11\%$ , respectively;  $p<0.001$ ). At 6h after CTS, the CCP of

physiologically loaded fibroblasts had decreased and was not different from the unloaded, whilst the CCP of pathologically loaded cells had marginally decreased ( $6.94 \pm 2.31\%$ ; Figure 5.24B); however, it remained higher than the other two groups of nuclei even at 24h post-CTS ( $2.83 \pm 1.18\%$ ; Figure 5.24C). It should be noted that at all time points the CCP value distribution for the post-pathologically strained fibroblasts was skewed, with an elongated tail towards higher chromatin condensation. Combined with the exhibited cytoskeletal rearrangements, the data indicate that physiological levels of CTS caused rapid remodelling of cytoskeletal and chromatin organisation, which had disappeared by 24h post-load, whilst pathological tensile strain had a prolonged and continuous effect even 24h after mechanical loading had ceased.

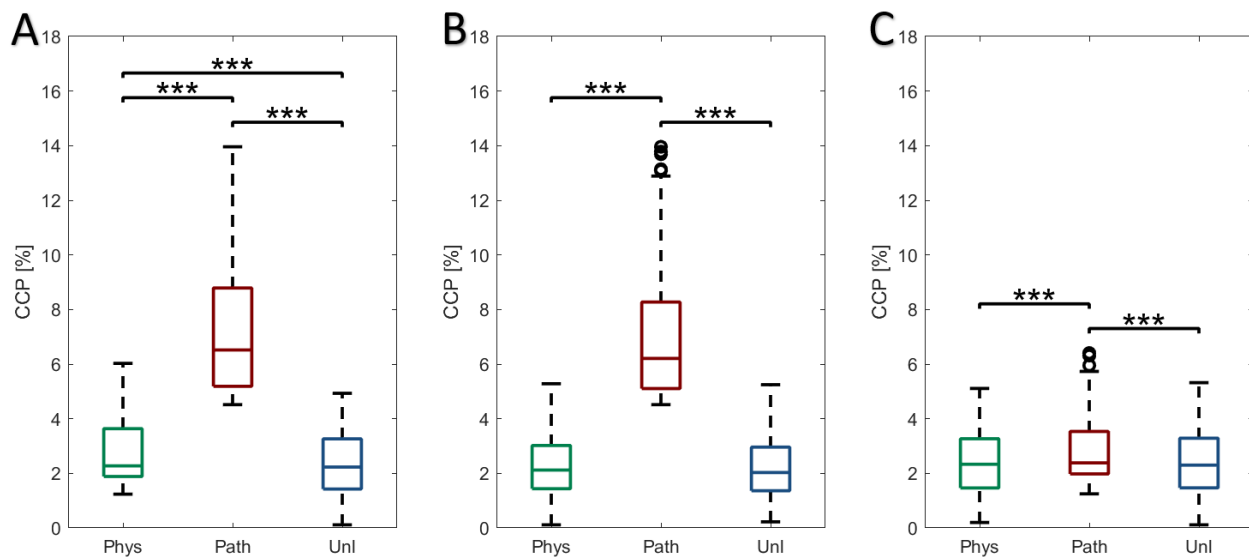


Figure 5.24 – Comparison of chromatin condensation parameter (CCP) between three relaxation time points 1h (A), 6h (B) and 24h (C) post-CTS ( $n=3$  wells,  $N=3$  plates). Data were calculated by a bespoke MATLAB script based on maximum intensity projections and grouped by applied CTS and relaxation time, presented as median  $\pm$  SD (Irianto et al., 2014). (A)  $n=236-291$  nuclei; (B)  $n=227-299$  nuclei; (C)  $n=243-296$  nuclei; \*\*\*: $p < 0.001$ .

CCP-based evaluation of chromatin condensation has been utilised in several studies, with the work by Heo et al. also applying tensile strain, albeit to bovine mesenchymal stems cells (Chen et al., 2012a; Irianto et al., 2013; Heo et al., 2016; Di et al., 2017). They proposed that the increase in chromatin condensation by dynamic tensile loading is through signalling pathways mediated by ATP, the release of which requires actomyosin contractions. This could provide a comprehensive explanation for the high chromatin condensation and isotropic cytoskeletal orientation in the 1h

post-pathological strained fibroblasts. Furthermore, mechanical loading in bovine chondrocytes also releases ATP via hemichannels (Garcia and Knight, 2010). Most likely the GTPase RhoA and Rho-associate kinase (ROCK) pathway has been affected, as research has identified its key role in remodelling of the actin cytoskeleton (Maekawa et al., 1999; Katoh et al., 2001; Amano et al., 2010; Tanner et al., 2010; Huang et al., 2012). CTS of murine embryonic NIH3T3 fibroblasts (10%, 0.3Hz for 1h) was shown to increase RhoA activity within 5min, in conjunction with reorganisation of actin stress fibres; inhibiting ROCK caused alterations in the *in situ* cytoskeletal stress formation and distribution in human tracheal smooth muscle cells and in murine lung fibroblasts (Hu et al., 2003; Chiquet et al., 2009; Liu et al., 2010). More in-depth research into alterations in gene expression between the loading conditions and time points is required before a precise evaluation can be provided. It should be acknowledged that for each CCP assessment, the background around the ROI was removed as to not interfere with the calculations.

#### 5.2.5.5 Summary of tensile strain-induced effects on nuclei

CTS increased nuclear area and elongation, as well as chromatin condensation, 1h after application of both loading regimens. The CCP percentage remained high for the pathologically loaded scleral fibroblasts and they also became rounder with time which occurred at a faster rate than the nuclei of cells post-physiological strain. It was not possible to measure both cell apoptosis and proliferation objectively based on confocal images. A study on human PPS fibroblasts did show that applied CTS (10%, 0.5Hz for 24h) did not cause alteration to either proliferation or apoptosis, but did induce cell division and reduce programmed cell death in peripheral scleral fibroblasts (Qiu et al., 2018). Furthermore, the 24h time frame was shorter than the fibroblast doubling time (~five days), thus excluding detection of induced alterations to the cell number. In addition, human PPS fibroblast proliferation was shown to be suppressed by ROCK inhibition (Pitha et al., 2018). As chromatin condensation can be linked to apoptosis, performing labelling for the phospholipid-binding protein annexin V to exclude apoptosis would be a useful follow-on experiment (Vermees et al., 1995).

### 5.2.6 Pathological strain inhibits proper cytoskeletal orientation in scleral fibroblasts

Under *in vivo* conditions, the scleral fibroblasts are exposed to pulsatile IOP, mimicked by the applied physiological CTS (0.26-1.8% strain, 1Hz). In contrast, high tension glaucoma was represented by the elevated pathological CTS (0.6-4% strain, 1hz), with both experimental CTS regimens never reaching a complete relaxation of 0% strain. Of the three recorded time points, the 1h after CTS was expected to be the most accurate in illustrating alterations in the physiological and pathological phenotype. Therefore, a too high or low strain would disrupt the proper functioning and performance of the scleral fibroblasts (Figure 5.25). This normal or physiological level of loading also dictates the cell's typical shape and cytoskeletal fibre architecture, which seems to fit with Ingber's proposed model on cell 'tensegrity' and biomechanical prestress (Ingber, 2008; Ingber et al., 2014). After removal of the physiological CTS, the fibroblasts progressively lost their high fibre anisotropy, becoming more isotropic, with a smaller, less elongated shape. In the events of a high IOP, or pathological CTS, it overwhelmed the cells, exhibited by their close resemblance to their previous unloaded state, including the disorganised stress fibres. Thus, the high load phenotype could be interpreted as a compensatory protective mechanism for preservation of cell integrity, along with 'inhibition delay' of the *in situ* cytoskeletal reorganisation. Cessation of the CTS resulted in a gradual realignment of the cell's architecture to their native physiological state, as observed in the 24h time points. Both mechanical loading phenotypes were the result of fast dynamic reactions to preserve the cell and continue functioning in the altered environment, governed actively by the actin cytoskeleton (Ralphs et al., 2002).

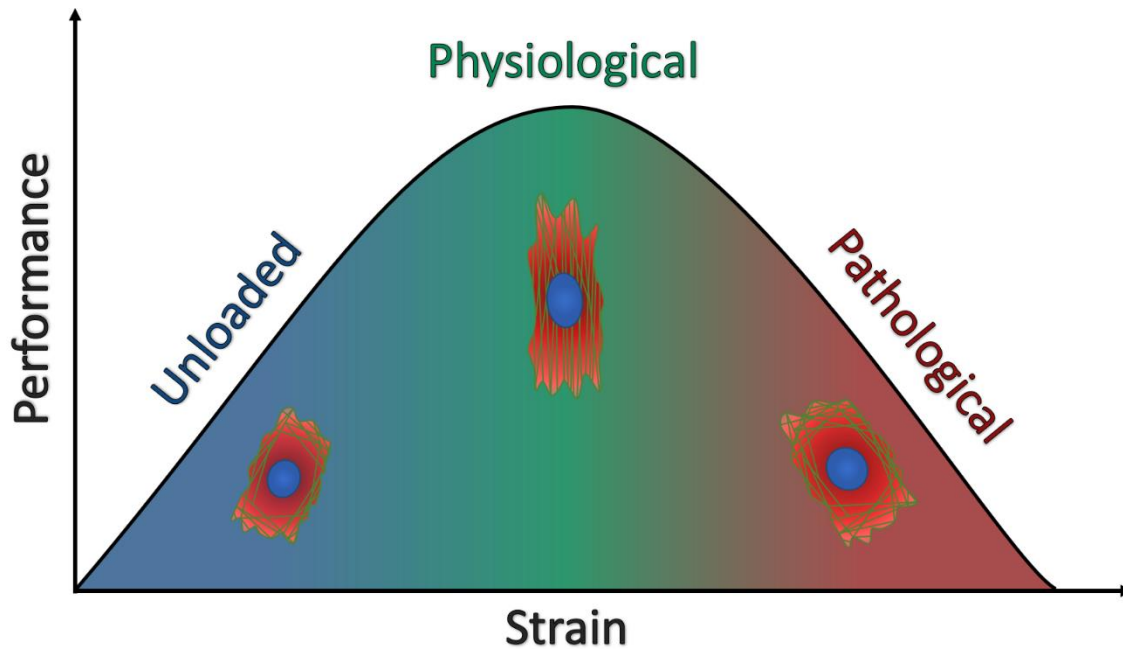


Figure 5.25 – Proposed scleral fibroblast performance as a function of applied strain.

The observed strain-related behaviour of the stress fibres is in agreement with experimental and computational research, specifically when taking into consideration that the collagen ECM has been shown to strengthen and become stiffer with CTS (Saez et al., 2007; Obbink-Huizer et al., 2014; Susilo et al., 2016). At lower substrate stiffness, stress fibres aligned with the primary stiffness direction, whilst when the ECM stiffness was too high there was an absence of preferential orientation. In addition, a study on compressed cells indicated that their return to a steady-state, after removal of external forces, was due to a time-dependent rearrangement of the F-actin stress fibre cytoskeleton (Ronan et al., 2012). The exhibited alterations in the stress fibres are also part of mechanisms for retention of tensional homeostasis (Paszek et al., 2005; Na et al., 2007; Kassianidou and Kumar, 2015). It should not be excluded that the cytoskeletal reorganisation post-CTS could follow a hysteresis (Fletcher and Mullins, 2010). Thus, further and intermediate time points are necessary to fully illustrate the relaxation behaviour post-loading.

The statistically significant differences between the pathologically loaded and unloaded fibroblasts at the initial 1h time point were: (I) larger overall area (Figure 5.01A), due to the cells being longer (Figure 5.02) but not wider; (II) lower vimentin intermediate filament cytoskeleton anisotropy (Figure 5.12A); (III) larger nuclear area (Figure 5.22A) and more elongated nuclei (Figure 5.23A); (IV) notable increase in chromatin condensation (Figure 5.24A). The last difference signifies a

potential alteration in gene expression, with chromatin condensation persisting for at least 24h after pathological CTS cessation. The larger cell area should also correlate to more adhesive connections to the underlying collagen ECM, thus preventing the stress fibres from dissociating from it. Furthermore, the more isotropic arrangement of the vimentin cytoskeleton is likely also to contribute to preserving integrity.

A certain level of contraction of the actin stress fibres should also not be excluded as a contribution to the pathological phenotype (Dowling et al., 2013). The alterations to the cellular and nuclear shape, cytoskeletal and chromatin organisation persisted for at least 24h after exposure to high CTS for 1h. No further points after 24h were recorded and it is suggested for future work to investigate if, at later time points, the pathologically loaded cells return to basal levels at the same rate as the fibroblasts exposed to physiological strain. Furthermore, application of CTS for longer periods should also be considered, to determine if simulating chronically high IOP would differ from the current setup mimicking acute reactions. This study was of importance to also showcase that scleral fibroblast organisation quickly alters without exposure to equibiaxial stretching from IOP. *Ex vivo* experiments utilising enucleated eyes should take these observations into consideration for the evaluation of their assessments.

### 5.2.7 Advantages and limitations of experimental system

The bovine scleral fibroblasts were plated as monolayers on two-dimensional type I collagen coated BioFlex™ membranes. Whilst the fibroblasts are situated in the three-dimensional environment of the PPS, the tensile system applies equibiaxial strain only to the bottom of the membrane, mitigating the CTS effect when implemented to a 3D scaffolding. Furthermore, research indicates that inside three-dimensional collagen matrices, the fibroblasts are more spindle-like and very narrow, with the conformation being a deviation from their native phenotype, making the 2D system in this Chapter a more suitable choice in this respect (Hakkinen et al., 2010). Most often cells are cultured on stiff surfaces, such as glass or plastic (Figure 1.05), which can alter the morphology of the cells (Fletcher and Mullins, 2010). This can skew the general perception for how these cells look when it needs to be remembered that an *in vivo* cellular environment can be highly variable and in principle less stiff than the common cell culture plates (Kumar et al., 2006).

Kuboki et al. provide a clear illustration for the spread and reorganisation of the three primary components of the cytoskeleton, in human mesenchymal stem cells, on different substrates (Kuboki et al., 2012). As the collagen fibrils are circumferentially organised around the optic nerve in the PPS (Section 1.3), it is suggested for future work to investigate the effect of uniaxial tensile strain, instead of cyclic, in representing the alterations of cells attached to the highly anisotropic collagen ECM. This could be implemented through the use of an Arctangle™ loading station (Flexcell International, Burlington, USA) with scleral fibroblasts cultured on type I collagen coated UniFlex™ (Dunn Labortechnik, Asbach, Germany) culture plates.

Whilst all three cytoskeletal components contributed to the cellular rearrangement, the F-actin stress fibres exhibited the largest changes. This follows previous research on bovine chondrocytes, with little contribution of both the vimentin and microtubule networks to the mechanical response (Dowling et al., 2012). As the vimentin intermediate filaments have been noted to directly interact with F-actin, fast reorganisation of the vimentin cytoskeleton into a more interwoven network could have resulted in the lower calculated anisotropy (Shah et al., 1998). In addition, the cytoskeletal components could have become entangled, thus stiffening to resist any further deformations (Storm et al., 2005). Along with the observations in Section 5.2.1 to 5.2.4, this seems to indicate that the high CTS does not just delay the *in situ* reorientation of the cytoskeleton from the initial unloaded state, but that rather the fibroblasts are undergoing processes to protect cell integrity against the external forces. As the immunochemical signal intensity is not directly proportional to the amount of labelled component, unlike other techniques such as second harmonic generation (SHG), it was not feasible to compare intensity differences in the confocal image Z-stacks as a result of mechanical loading or time. A solution could be the use of Western blot or enzyme-linked immunosorbent assay (ELISA) to assess changes in the amount of cytoskeletal proteins post-CTS (Mahmood and Yang, 2012; Gan and Patel, 2013). For consistency, all three cytoskeletal components were analysed with identical parameters of the image processing software. This, however, might have resulted in some inaccuracies, as best exemplified by the very similar and high detected fibre widths, due to the number of detected pixels per fibre, which necessitated the use of relative width. Nonetheless, this does not reduce the credibility of the analysis, as significant differences were still able to be recognised.

### 5.3 Summary, conclusion and future work

This Chapter illustrated that representative physiological and pathological mechanical loads cause a difference in the orientation and remodelling of scleral fibroblast cytoskeleton. This work has several key strengths: (I) the application of specifically calculated relevant strain levels; (II) several time point observations over a 24h time frame; (III) the implementation of multiple approved image analysis packages; (IV) the high number of repeated measurements per group.

Applied physiological CTS resulted in a highly ordered alignment of the cytoskeleton in bovine scleral fibroblasts, most significantly to the F-actin stress fibres. The fibre organisation returned to an unloaded-like state at 24h post-cessation of load, whilst the cell length remained enlarged. Pathologically high CTS had an inhibitory influence on the *in situ* cytoskeletal architecture. Following 24h after tensile strain had been applied, the cytoskeletal fibres reorganised to a state closely reminiscent of the initial physiological morphology. Whilst it has been extensively documented that high pressure disrupts the typical ECM organisation, these findings indicate that *in vitro* high CTS/IOP has an adverse effect on the scleral cell population. From these findings, it can be speculated that the higher IOP inhibits the *in situ* scleral fibroblasts' architecture and behaviour and can contribute to the glaucomatous pathology. Summaries of the observed alterations are presented below (Table 5.1-5.3).

Table 5.1 – Shape alterations of bovine scleral fibroblasts as a function of applied physiological or pathological CTS, 1, 6 and 24h post-loading, in comparison to unloaded cells. The number of arrows indicates the level of parameter alteration.

Fibroblast shape	Post-Physiological Load			Post-Pathological Load		
	1h	6h	24h	1h	6h	24h
Area	↑ ↑	↑	↑	↑	↑ ↑	↑ ↑
Length	↑ ↑ ↑	↑ ↑	↑ ↑	↑ ↑	↑ ↑	↑ ↑ ↑
Eccentricity	↓ ↓ ↓	↓	—	—	—	↓ ↓

Legend: Increase ↑ ; Decrease ↓ ; No change —

Table 5.2 – Rearrangement of the bovine scleral fibroblast cytoskeleton as a function of applied physiological or pathological CTS, 1, 6 and 24h post-loading, in comparison to unloaded cells. The number of arrows indicates the level of parameter alteration.

F-Actin stress fibres	Post-Physiological Load			Post-Pathological Load		
	1h	6h	24h	1h	6h	24h
Anisotropy	↑ ↑ ↑	↑ ↑ ↑	—	—	—	↑ ↑
Coherency	↑ ↑ ↑	↑ ↑ ↑	—	—	—	↑ ↑ ↑
Width	↑ ↑ ↑	↑ ↑	—	—	↑	↑ ↑
Vimentin intermediate filaments	Post-Physiological Load			Post-Pathological Load		
	1h	6h	24h	1h	6h	24h
Anisotropy	↑	—	—	↓	—	—
Coherency	↑ ↑	—	—	—	—	↑
Width	↑	↓	—	—	—	—
β-Tubulin microtubules	Post-Physiological Load			Post-Pathological Load		
	1h	6h	24h	1h	6h	24h
Anisotropy	↑	—	—	—	—	—
Coherency	↑	—	—	—	—	—
Width	↑	—	—	—	↑	↑ ↑

Legend: Increase ↑ ; Decrease ↓ ; No change —

Table 5.3 – Nuclear changes in bovine scleral fibroblasts as a function of applied physiological or pathological CTS, 1, 6 and 24h post-loading, in comparison to unloaded cells. The number of arrows indicates the level of parameter alteration.

Nucleus shape	Post-Physiological Load			Post-Pathological Load		
	1h	6h	24h	1h	6h	24h
Area	↑ ↑	↑ ↑	↑	↑ ↑	↑ ↑	↑ ↑
Roundness	↓ ↓	↓	▬	↓	▬	▬
CCP	↑	▬	▬	↑ ↑ ↑	↑ ↑ ↑	↑

Legend: Increase ↑ ; Decrease ↓ ; No change ▬

The work by Cui and colleagues illustrated that linear strain (4% for 24h) has an effect on human scleral fibroblast transcription, with 308 genes having altered expression (Cui et al., 2004). Whilst the changes to the chromatin condensation may also indicate alterations in gene expression, they remain inconclusive on their own and future work is suggested to provide better clarity by including RNA-seq or real-time polymerase chain reaction (qPCR) experiments (Navarro et al., 2015). As noted earlier, repeating the experimental procedures with extended loading and more time points could provide greater clarity for the cellular behaviour, specifically the pathologically loaded cells. The experimental setup did not allow for live-cell imaging, which would be ideal for observing cytoskeletal remodelling in the same cell (Rápalo et al., 2015). Labelling for stress fibre associated proteins, such as myosin or  $\alpha$ -actinin, could contribute in further investigating the cytoskeletal reorganisation, as well as for adhesion proteins, such as vinculin and n-cadherin, which have increased production with CTS in chick tendon (Ralphs et al., 2002). As mechanical loading also stimulates synthesis of new ECM, comparison of both composition and structure of the collagen network after CTS could help in determining to what extent the different loading conditions alter normal fibroblast function (Chiquet et al., 2009). Finally, it would be beneficial to perform ELISA tests to colourimetrically evaluate cell proliferation, along with terminal deoxynucleotidyl transferase-mediated dUTP nick end labelling (TUNEL) assay for apoptosis, to determine how CTS relates to changes in the cell volume fraction (Darzynkiewicz et al., 2008; Gan and Patel, 2013).

# **Chapter VI**

## **Finite element reconstruction of eye globe and cellular components**

## 6.1 Introduction

Whilst experimental observations provide valuable insight into the anatomy and physiology of organisms there are instances where they prove to be insufficient on their own. Over the past several decades, computational models have been utilised to study objects and their reactions to conditions which cannot be replicated experimentally. Modelling is based on the conscious simplification of real systems by selectively investigating the most important characteristics of the system. In combination with experimental results and scientific theories, far greater precision can be achieved in both describing and predicting the behaviour of the object of study.

The finite element (FE) method is a modelling approach which approximates and subdivides a system into discrete regions referred to as ‘finite elements’. It has application in both scientific research and medicine, with a widespread approach that utilises digital images of, for example, specific organs, tumours, bones and reconstructs them as patient-specific models (Burkhart et al., 2013; Wittek et al., 2016). This mitigates the inherent error in FE analysis, which stems from the simplifications and approximations of the system, allowing for more accurate models which can handle the complex biological geometries. Numerous studies of ocular biomechanics have relied on numerical simulations of the eye’s geometry, tissue architecture and biomechanical properties (Sigal, 2009; Grytz et al., 2011; Coudrillier et al., 2015a; Jin et al., 2018). Whilst most studies have moved away from portraying the eye as a sphere, few perform their numerical simulations on models based on actual globes. One technique utilising digital image correlation (DIC) was used by Whitford et al. to represent the outer surface topology of intact, internally pressurized human and porcine eyes under simulated *in vivo* conditions (Whitford et al., 2016).

The FE method can also handle non-linear complex analysis of nonhomogeneous materials, such as viscoelastic cells and the surrounding extracellular matrix (ECM). To assess the mechanical behaviour of cells it is crucial to have the cytoskeleton represented accurately. The complexity and dynamics of the cytoskeleton have proven to be the main hurdle in developing numerical models, with myriad oversimplifications and exclusion of key components being common. Furthermore, representing the cytoskeleton as individual fibres, rather than a network of components, in computational simulations could lead to false conclusions (Fletcher and Mullins, 2010; Barreto et

al., 2013; Barreto et al., 2014). A potential solution would be to follow the approach used for medical application; by collecting digital image information of cellular components and then reconstructing the geometries for FE modelling. The image analysis software Imaris provides surface segmentation tools to generate isosurface triangular meshes based on the Marching Cubes algorithm (Lorensen and Cline, 1987). This results in an oversampled wireframe of millions of vertices, which requires further steps to make it suitable for modelling (Cebal and Löhner, 2001; Jakob et al., 2015).

This Chapter provides methodologies for creating representations of two different types of biological structures: (I) construction of eye-specific geometry with accurate globe size and shell thickness; (II) generation of validated, rendered fibroblast cytoskeleton and nuclei meshes.

## 6.2 Results and Discussion

### 6.2.1 Eye globe reconstruction

#### 6.2.1.1 Ocular globe geometric modelling

Utilising the facilities and proprietary MATLAB script of the Biomechanical Engineering Group (University of Liverpool), a specimen-specific model of bovine eye geometry was created (Whitford et al., 2016). The custom-built experimental inflation rig allows for testing of whole ocular globes, with software control of the PBS-mediated internal eye pressure, mimicking intraocular pressure (IOP). The external topography was created from consecutive images taken by six high-resolution cameras (Section 2.7.1). Image data points following the eye curvature were further manually selected as part of the MATLAB procedure. The internal topography was based on the external one, with regional thickness variations of the eye tunic implemented (Whitford et al., 2016). The internal and external three-dimensional topography were interpolated based on the relative spherical coordinates between the discrete points of measurement.

The model geometry was imported as an orphan mesh in ABAQUS 6.14/CAE. As the mesh information was separated, or orphaned, it contained coordinates only for the vertices, elements and surfaces, but not the geometry of the object. In addition, the FE model was free from

restrictions of rotational symmetry. Figure 6.01 represents a progressive superimposing of the FE geometry over one of the camera photographs, closely following the contours of the eye and excluding any residual fat and muscle tissue. The model accurately recreates the captured topography, including different regions such as the limbus. Due to the size of the bovine eye globe exceeding the camera's field of view, part of the posterior pole could not be recorded and the missing data points were extrapolated using Zernike polynomials as part of the MATLAB mesh generation (Cook, 1976).

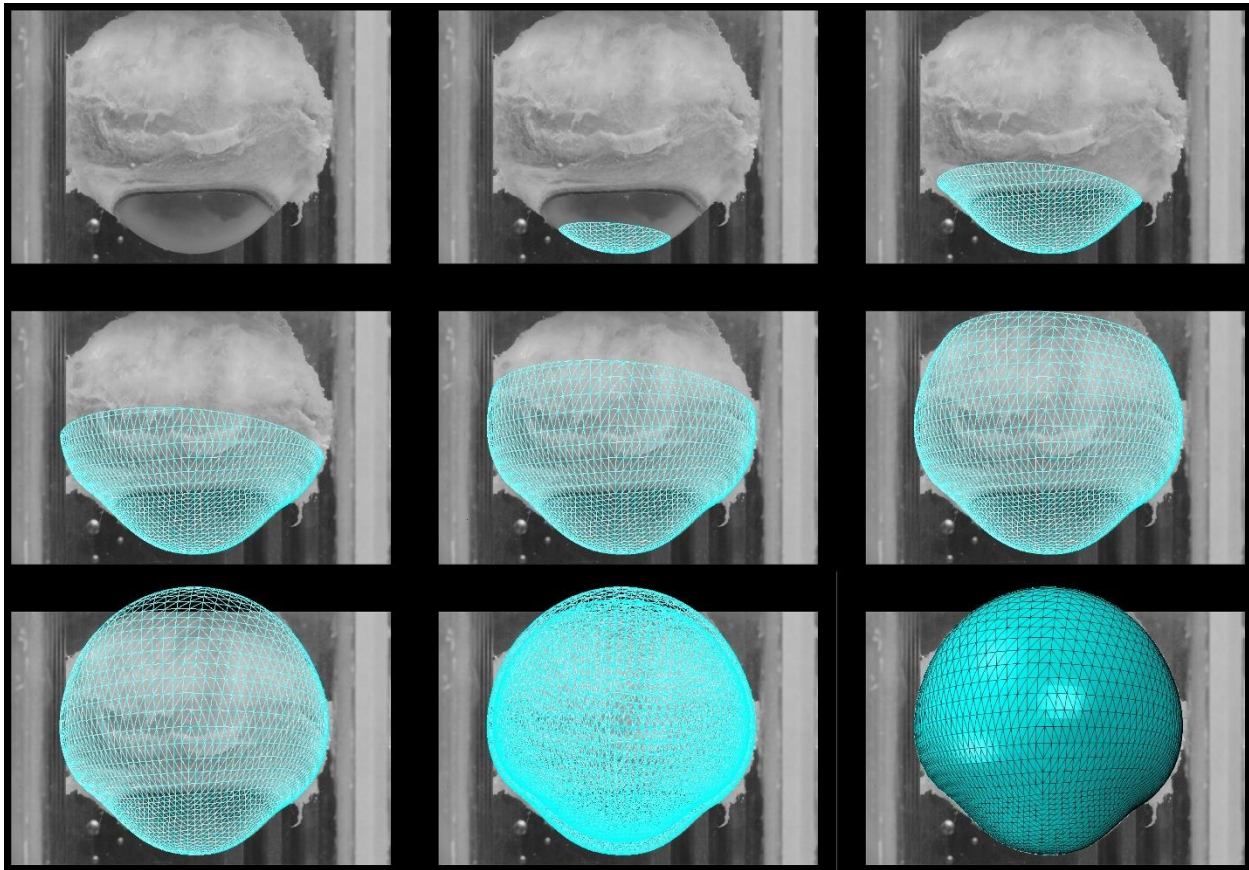


Figure 6.01 – Superimposed match between imaged and modelled topology of a bovine eye globe. Reconstruction was performed through a bespoke MATLAB script (Biomechanical Engineering Group) and manual surface point selection, with Zernike polynomials used to extrapolate the posterior sclera.

The reconstructed mesh contained 4,800 C3D15H first-order solid wedge elements, which are composed of 15 vertices each (Whitford et al., 2016; Zhou et al., 2019a). Although quadratic elements are more stable and preferred in general, they are a poor choice for curved or oval structures, such as an eyeball. Thus, an FE mesh composed of triangle prisms is much more precise

in terms of smooth geometrical representation of the eye, whilst retaining accuracy and keeping the processing time at a reasonable computational level. The elements were arranged in 40 circumferential rings, with 16 representing the cornea, one the limbus and 23 for the sclera, further grouped by the six meridian profiles of the collected photographs (Figure 6.02).

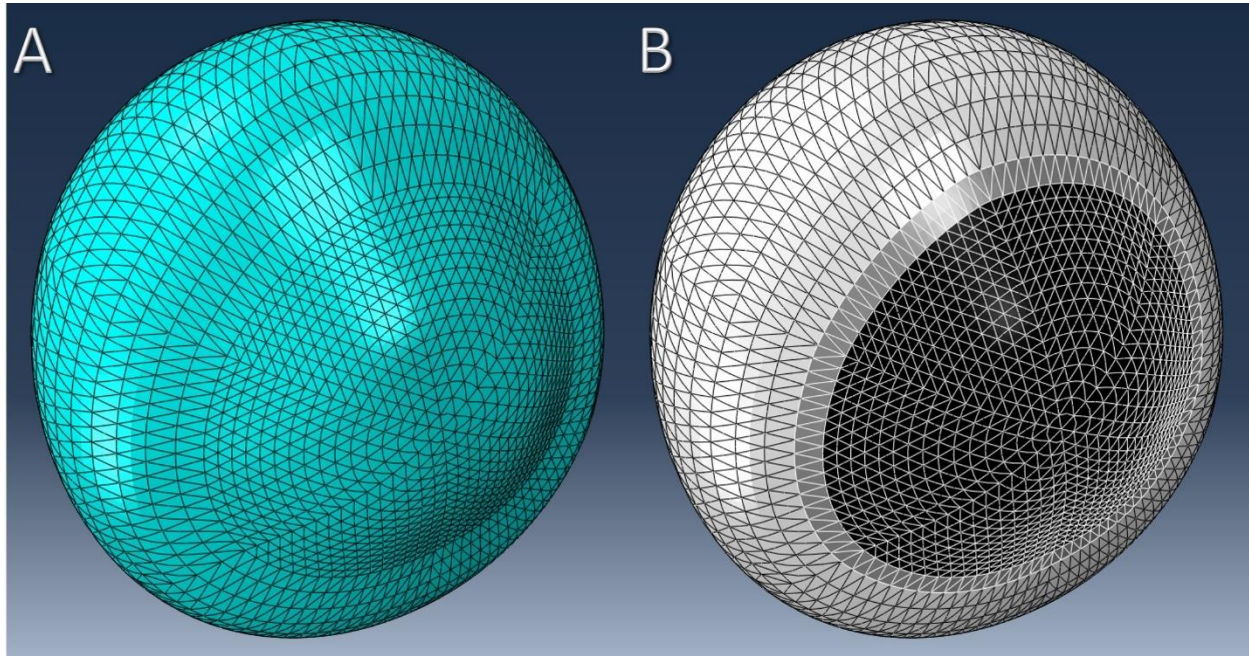


Figure 6.02 – Surface triangulation of a left bovine eye composed of 4,800 C3D15H prism elements representing the cornea, limbus and sclera. (A) Original ocular globe reconstruction; (B) Corresponding reconstruction of A with coloured elements by region: cornea (black), limbus (grey), sclera (white).

#### 6.2.1.2 Ocular globe tunic thickness assessment

To account for the regional variability in corneal and scleral thickness, the size of the prism elements needed to reflect these differences. Data on the eye tunic was collected from three bovine eyes (Section 2.7.2), with measurements for the cornea consisting of both the centre and periphery, the limbal region and for the sclera – the equatorial scleral region and posterior pole (Figure 6.03). A notable feature is the significant progressive decrease in thickness from the central cornea in the direction of the lateral sides of the eye, with the thinnest segment being the equatorial sclera. This is followed by a drastic increase in the peripapillary sclera (PPS), where the region of circumferentially aligned collagen is situated. Whilst the human eye is thickest in the posterior sclera as well, it exhibits a thinner cornea, specifically in the centre (Meek and Knupp, 2015).

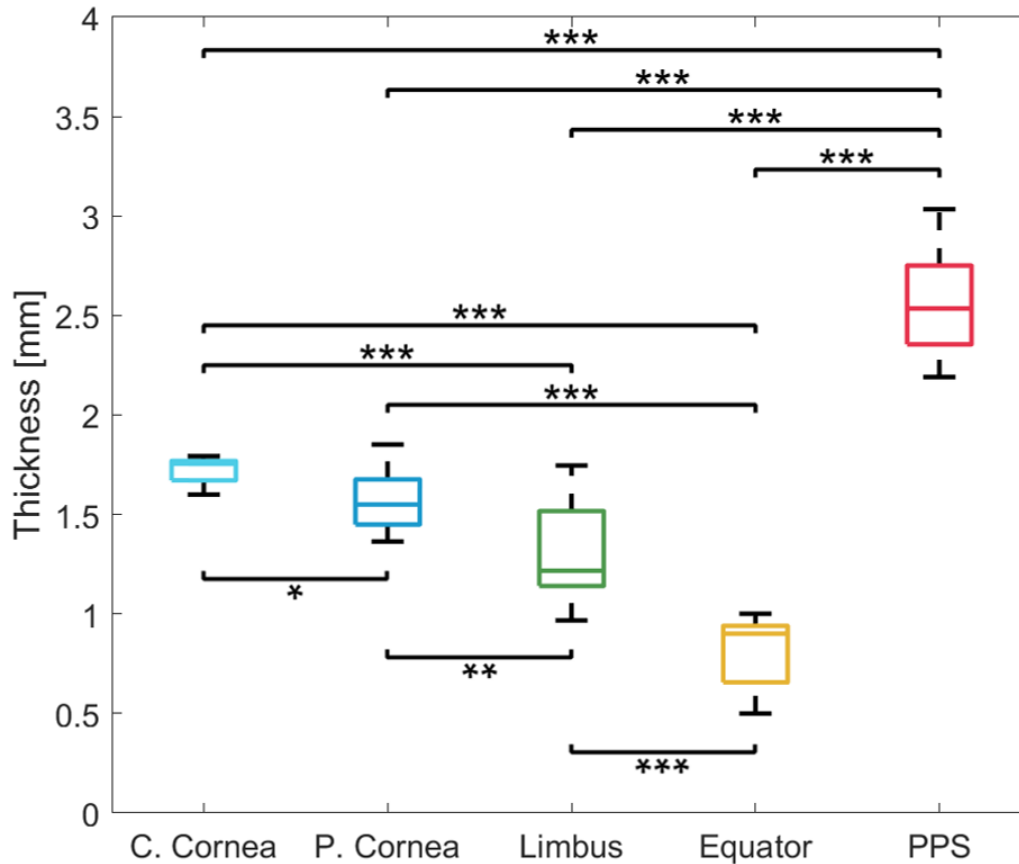


Figure 6.03 – Regional variation in the bovine eye tunic thickness. Regions are listed from top to bottom with indicated mean and standard deviation (SD): Central corneal thickness (aqua):  $1.727 \pm 0.062$  mm (n=10); Peripheral corneal thickness (blue):  $1.587 \pm 0.145$  mm (n=13); Limbal thickness (green):  $1.317 \pm 0.236$  mm (n=13); Equatorial scleral thickness (gold):  $0.818 \pm 0.159$  mm (n=12); Peripapillary sclera (PPS) thickness (red):  $2.548 \pm 0.244$  mm (n=12). Box plot data are presented as median  $\pm$  SD; \*:  $p < 0.05$ ; \*\*:  $p < 0.01$ ; \*\*\*:  $p < 0.001$ .

The results were successfully incorporated into the FE model as 13 different thickness regions; four for the corneal material properties, one for the limbus and eight for the sclera. The integrated element thickness is visualised in a transversal cross-section of the mesh with indicated mean values (Figure 6.04). The presented model closely follows the physiological topology and thickness of the bovine eye globe and is envisioned to be used in future FE analysis.

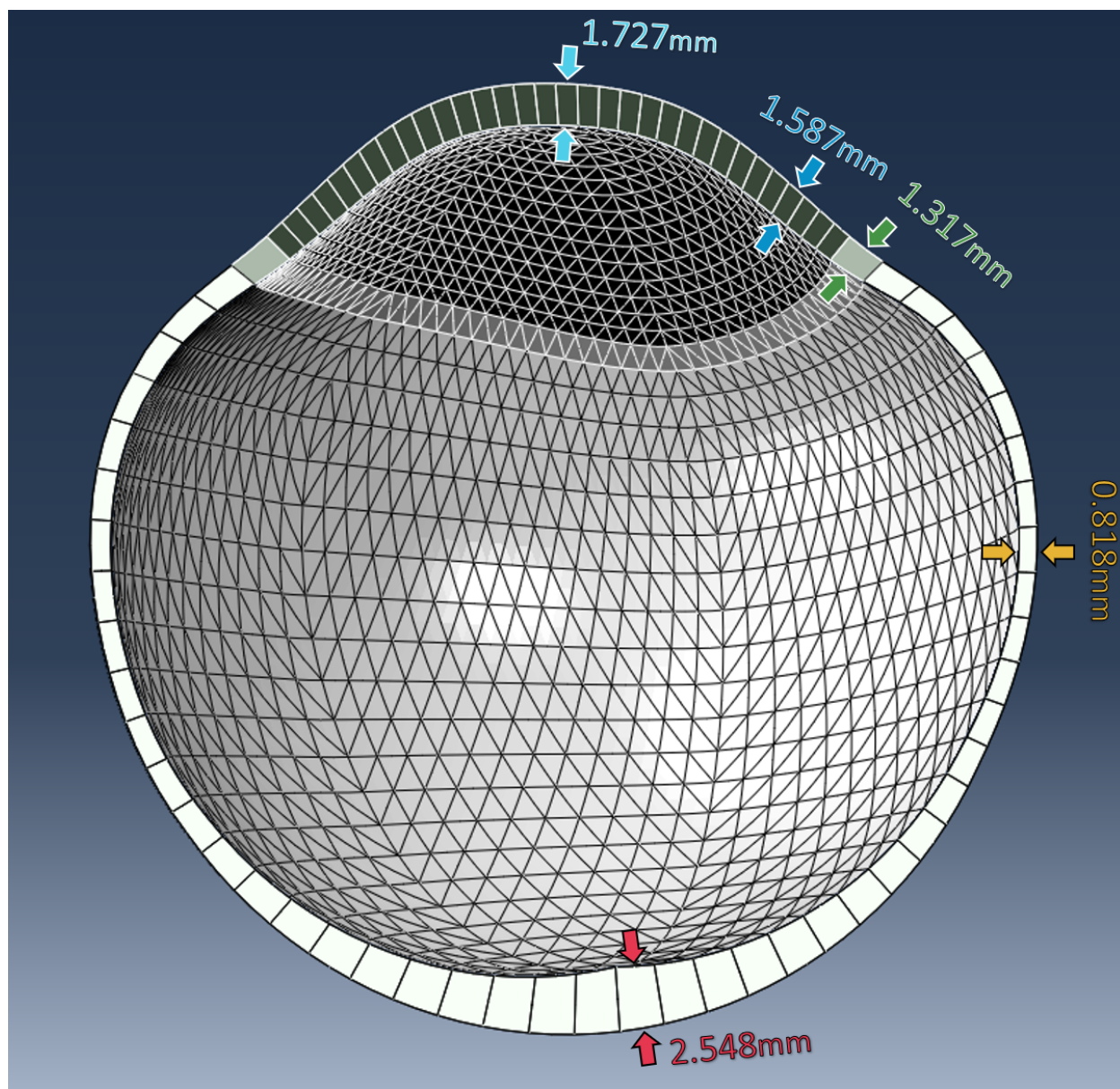


Figure 6.04 – Transversal cross-section of the bovine eye globe reconstruction. The model accommodates the different thickness of the eye tunic. Region averages are listed. Central corneal thickness (aqua); Peripheral corneal thickness (blue); Limbal thickness (green); Equatorial scleral thickness (gold); PPS (red).

### 6.2.1.3 Advantages and limitations of the experimental system

A sample-specific FE geometry of a bovine eye was created in collaboration with the Biomechanical Engineering Group (University of Liverpool). Unlike previous sample-specific models which utilise corneal or scleral regions, the presented FE model is based on an intact globe (Pandolfi and Holzapfel, 2008; Jiaa et al., 2016). To mimic the IOP that the eye is exposed to *in vivo*, to maintain proper shape and curvature, the globe was filled with 1xPBS and immersed in it, resulting in a stress-free geometry. Initial experimental procedures envisioned as a subsequent step increasing the pressure inside the eye to recreate elevated IOP. This would have been combined with DIC to study inflation deformation of bovine eyes, representing the high IOP conditions of glaucoma. The instrumental setup was constructed with the purposes of assessing the size and deformations of human eyeballs (Whitford et al., 2016). Whilst the cattle eye could fit inside the borosilicate chamber, the globe exceeded the maximum camera field of view, resulting in part of the posterior sclera not being imaged (Figure 6.01). As the PPS is the main site of change and damage as a result of elevated pressure, not being able to collect visual information on it was a limitation and it was decided to prioritise rendering of the FE model, with the missing data points successfully extrapolated and reconstructed.

A main advantage of this model is the inclusion of regional variations to the cornea and sclera, along with being one of the few models to incorporate the limbus as a separate structure, accurately accommodating the different thickness of the eye tunic. It must be noted that in humans the cornea is thinner than the limbus, whilst the opposite was observed in cattle (Meek and Knupp, 2015). Although corneal swelling may explain this observation, both the inside and outside of the eye tunic were surrounded with 1xPBS, which should limit any swelling. Furthermore, the same instrumental setup was used in assessing the regional thickness in human eyes (Zhou et al., 2019a). The values Zhou and colleagues present are in agreement with such accepted for humans, thus confirming that the higher value for central corneal thickness in bovine eyes is not due to an instrumental error. A thinner limbus in comparison to the central cornea is observed in other mammalian species as well, such as mice (Henriksson et al., 2009). A study by Myers et al. reported mean thickness values for the cattle posterior scleral pole as  $2.15 \pm 0.39$ mm and  $1.10 \pm 0.34$ mm for the equatorial sclera, which are within the deviations reported in this Chapter

(Myers et al., 2010). Cui and colleagues constructed an FE model of the bovine eye based on micro-computed tomography scans and whilst they listed thinner PPS, between 1.55mm and 1.86mm, it must be noted that they carried out their measurements on tissue strips and not intact eye tunics (Cui et al., 2015).

### 6.2.2 Cellular component reconstruction

Modern-day microscopy systems allow production and recording of extensive volume image data sets though non-destructive optical sectioning, with laser scanning confocal microscopy as a pioneering approach. In combination with proprietary software packages, the captured information can be reconstructed in three-dimensional space and further exported and refined. The following procedures detail an approach for accurate generation of cell-specific cytoskeletal components and nuclei, which can be successfully imported into FE solvers for numerical modelling (Figure 6.05).

The proposed workflow relies on the commercial software packages Imaris and ABAQUS for the initial and final steps, respectively, with all other software being freeware (Figure 6.06). Open-source alternatives are also discussed (Table 6.4). Whilst specific programmes have been utilised, it must be noted the importance of the principles behind their application, such as simplification and smoothing (Cebal and Löhner, 2001). Thus, depending on data and software availability, this workflow can be compatible and applicable to a variety of scientific studies.

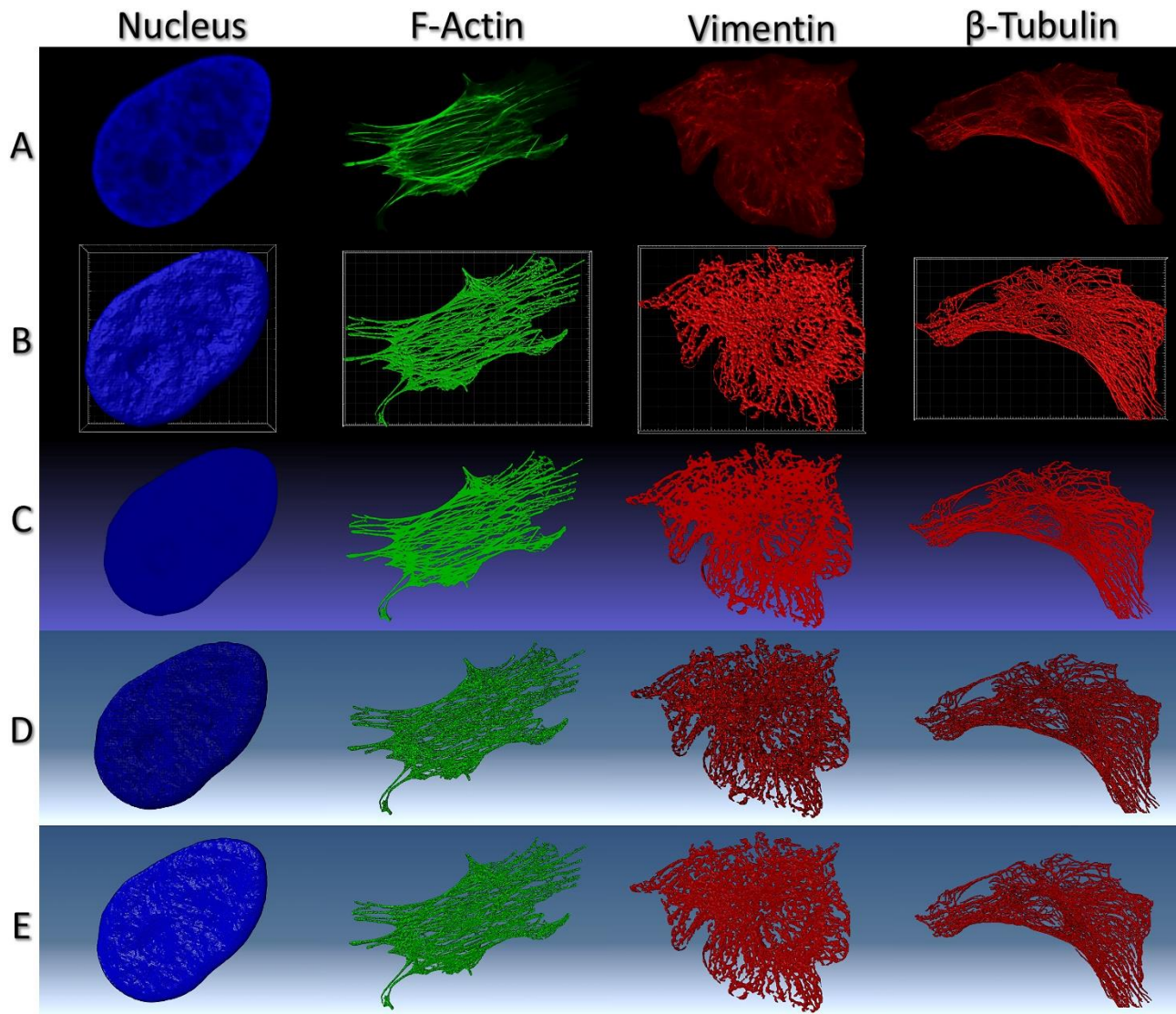


Figure 6.05 – Representative images of a nucleus, F-actin, vimentin and  $\beta$ -tubulin cytoskeleton at different procedural steps. (A) Maximum intensity projection of confocal image Z-stacks taken at 63x magnification and resolution of 1,912x1,912 pixels; (B) Surface triangulation in Imaris 9.2; (C) Rendering in MeshLab; (D) Initial mesh in ABAQUS 6.14/CAE; (E) Simplified and uniform mesh in ABAQUS 6.14/CAE.

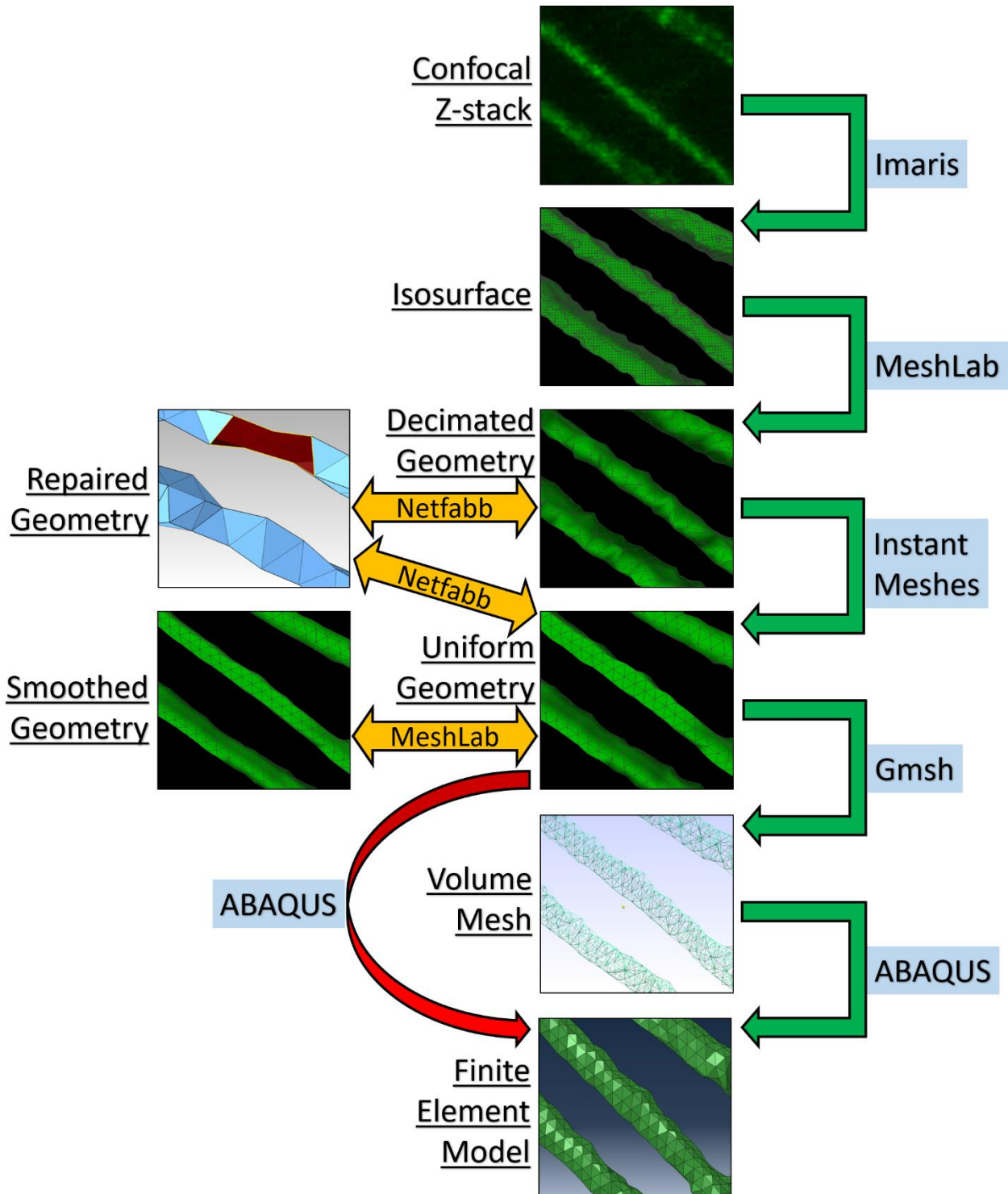


Figure 6.06 – Workflow schematic for the generation of finite element (FE) triangular geometries from image volume dataset. Software packages are highlighted by blue rectangles, whilst model steps are underlined. Green arrows indicate the main standard procedure pipeline, with the yellow arrows suggesting optional steps for optimising geometry quality. Red arrow represents an ABAQUS plugin dependent step.

### 6.2.2.1 Imaris

Imaris is a microscopy image analysis software, which can extract surface detail from input digital image Z-stacks and on the basis of the absolute intensity thresholding and smoothing can reconstruct a discrete isosurface (Figure 6.05B). This is achieved through the Marching Cubes algorithm which computes a surface triangulation from a three-dimensional matrix, which is the Z-stack voxel intensity, making it widely used in visualisation of medical scan images (Lorensen and Cline, 1987). As this study aimed to keep the procedures as automated as possible, few changes were applied to the recommended reconstruction parameters. The most notable alteration was the inclusion of background subtraction, which increased the precision and speed of the reconstruction. Manual tracing is also available but was not enlisted due to decreased accuracy of the isosurfaces and time constraints.

The importance of proper initial parameter selection is illustrated (Figure 6.07). Using a maximum intensity projection of a confocal stack of scleral fibroblast  $\beta$ -tubulin cytoskeleton images as an example (Figure 6.07A), a steep threshold can result in a discontinuous surface (Figure 6.07B), whilst a small threshold will include low-intensity voxels and overestimate the structure (Figure 6.07C). As the background was not excluded from the imported Z-stack, many of the fibres were recognised as being part of the same structure, merging clusters of fibres into an inaccurately large continuous surface. An alternative is the use of the Imaris commercial plugin FilamentTracer, which contains tools for detection of filamentous structures (Figure 6.07D). Similar to the core package, FilamentTracer uses imaging data intensity to trace the structure as connected filaments. To accomplish this in higher intensity regions, seed points are created which serve as origin points to trace the rest of the network and simultaneously hold it together.

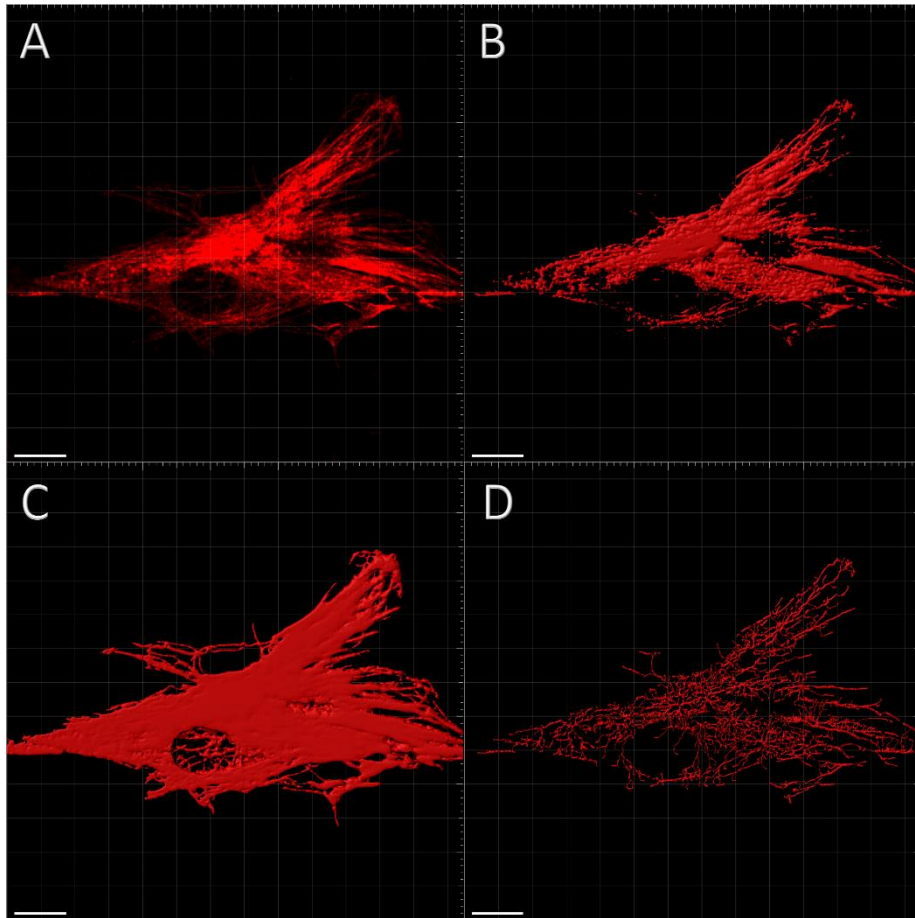


Figure 6.07 – Imaris-based reconstruction of a confocal Z-stack of scleral fibroblast  $\beta$ -tubulin cytoskeleton. (A) Maximum intensity projection of  $\beta$ -tubulin microtubules (anti-tubulin antibody conjugated to Alexa-594<sup>TM</sup> secondary antibody); (B) Imaris 9.2 reconstructed isosurface with high threshold (C); Imaris 9.2 reconstructed isosurface with low threshold; (D) FilamentTracer reconstructed filaments. Scale bar = 15 $\mu$ m.

Data sets with recorded individual signal channels can be rendered together, including both isosurfaces and traced filaments (Figure 6.08). As the green channel contained image intensity information of F-actin stress fibres they were properly represented as having a greater width than the vimentin intermediate filaments. The traced fibres also depicted the complex intertwined cytoskeletal arrangement. However, as the two networks were created individually, it did not allow for interweaving fibres, which is a restriction of the modalities. Furthermore, the vimentin network surrounds the nucleus in a cage-like configuration, which due to low threshold for the nucleus reconstruction can lead to a larger nucleus than the confocally recorded one (Figure 6.08). Finally, as the seed points were required for the proper filament connective they were reconstructed as part of the filament network which is an unwanted artefact for subsequent modelling (Figure 6.08B).

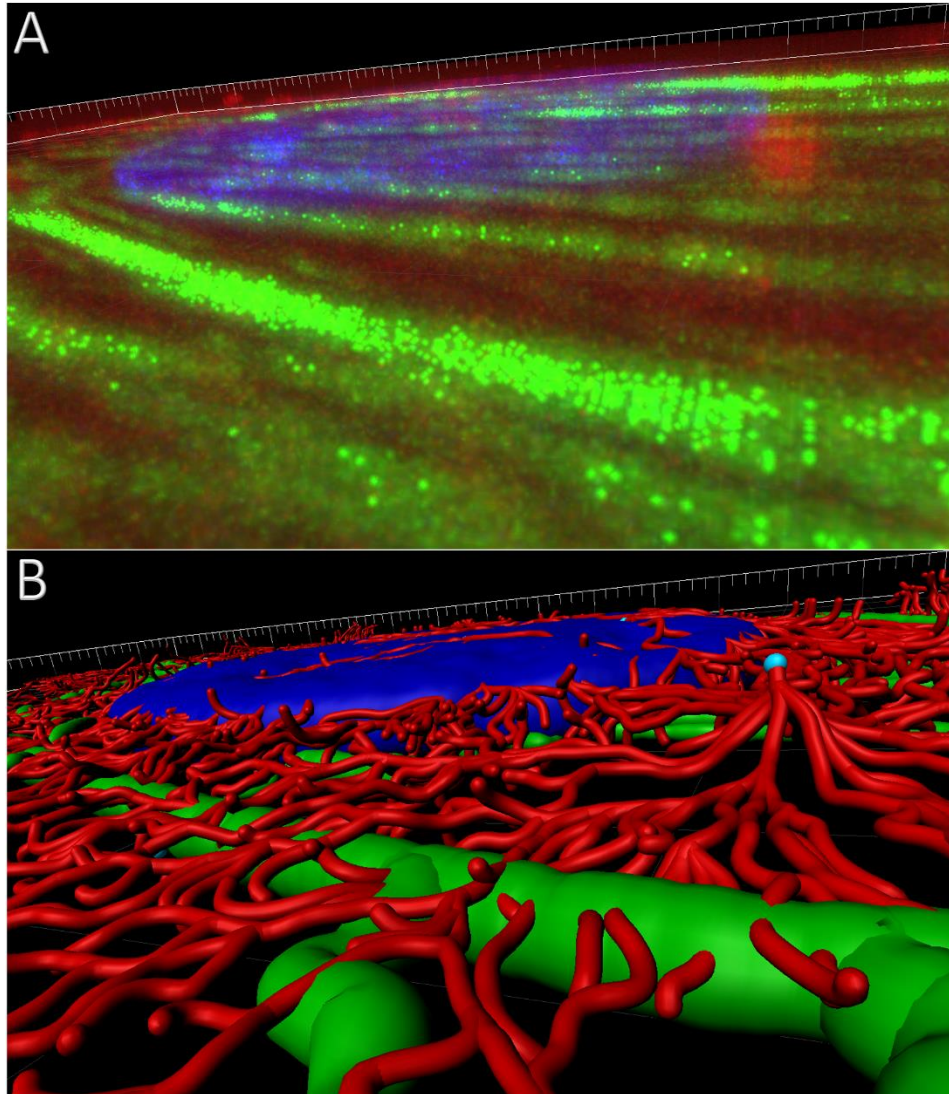


Figure 6.08 – Comparison between original signal and reconstruction of intracellular structures in Imaris 9.2. (A) Blue (4',6-diamidino-2-phenylindole (DAPI)-stained nucleus), green (Alexa 488™ phalloidin stained F-actin stress fibres) and red (anti-vimentin antibody conjugated to Alexa-594™ for visualisation of vimentin intermediate filaments) channel signals; (B) Surface (nucleus) and FilamentTracer (actin stress fibres and vimentin cytoskeleton) reconstruction in Imaris. Vimentin cytoskeleton seed point represented in aqua.

Both individual and several surfaces can be recorded in the same file, which was the standard WRL/VRML2 (Virtual reality modelling language 2) format for this study. This permits accurate positioning and further handling of several objects which are components of the same system. For example, a nucleus and F-actin cytoskeletal fibres from the same imaged cell, recorded in different channels, can be exported together. For the subsequent procedures only properly reconstructed isosurfaces were utilised. FilamentTracer does not permit direct export of the traced filaments, which necessitates their transformation to a signal channel, which can then be reconstructed as an

isosurface. Furthermore, the resulting surface triangulations contain a large number of vertices ( $10^{8+}$ ); these are mostly a result of the software preserving the smooth traced topology of the curved fibres, but can lead to processing issues further down the pipeline.

The above issues can impede the implementation of FilamentTracer for reconstructing complex tissue structures, such as the densely interwoven collagen fibres in the PPS (Figure 6.09). Whilst the traced structure (Figure 6.09B) appeared to have followed the original contours (Figure 6.09A) accurately, a side view (Figure 6.09C) revealed many filaments were protruding in the vertical direction, whereas in the input Z-stack collagen fibres were positioned in lamellae.

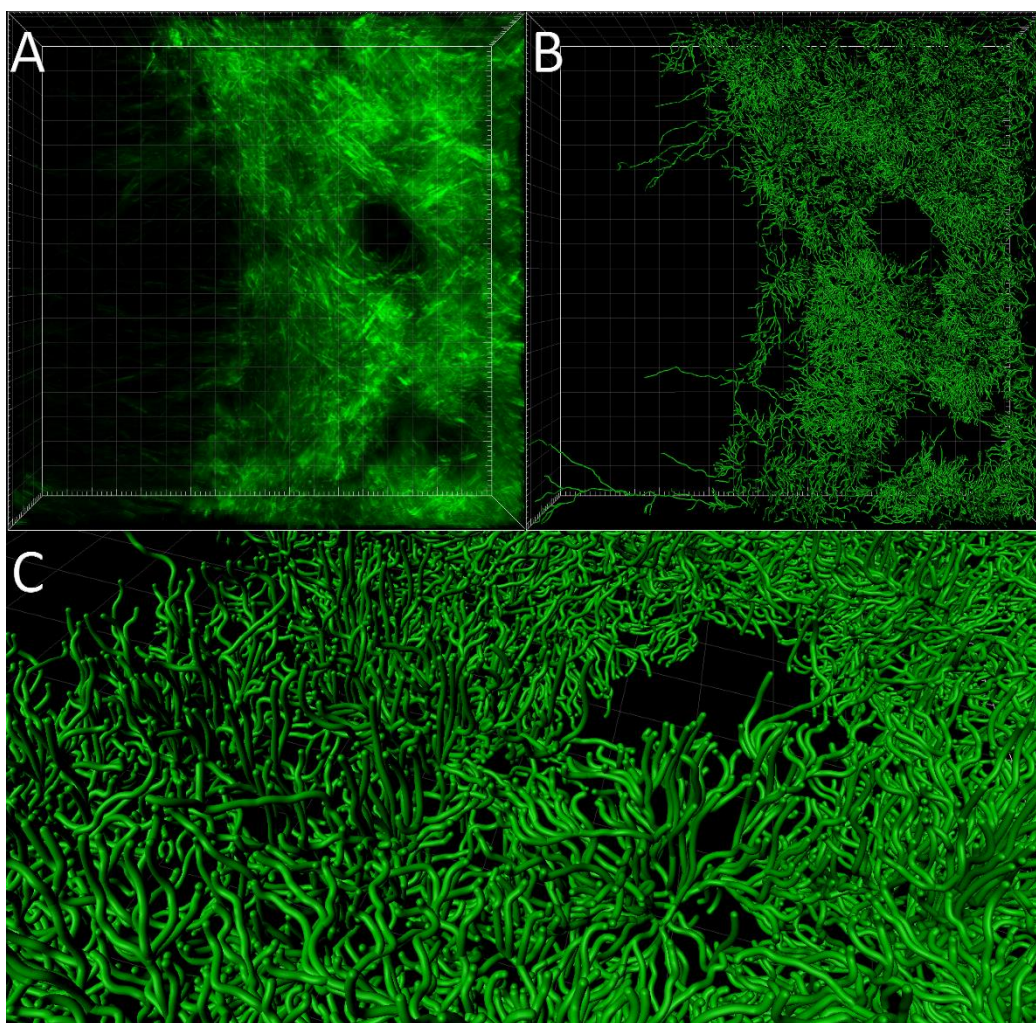


Figure 6.09 – FilamentTracer reconstructed collagen fibres from a section of a human PPS second harmonic generation (SHG) Z-stack in Imaris 9.2. The dark region on the left side is part of the *lamina cribrosa* (LC), whilst the central ones are blood vessel lumen. (A) SHG Z-stack of interwoven collagen fibres; (B) Corresponding traced fibres; (C) Side-view of B. Original Z-stack data was provided by Dr Craig Boote and Dr Jacek Pijanka.

## 6.2.2.2 MeshLab

Initial geometrical data obtained from Imaris is oversampled and contains low-quality triangular elements with sharp angles. As the performance of the FE analysis is dependent on the quality of the input mesh, the initial geometry is unsuitable in this state and requires simplification procedures. This can be achieved through MeshLab, an open-source processing software for handling meshes (Cignoni et al., 2008). The exported Imaris WRL files can be opened in MeshLab, where the tessellation of the isosurface can be viewed, as it was hidden in the Imaris interface. The large selection of tools can easily merge duplicate vertices or remove such with quality lower than a specified threshold. Manual manipulations are permitted, with selective removal of vertices or elements. However, these clean-up procedures are insufficient when the geometry contains millions of elements and controlled surface triangulation reduction is required.

Mesh decimation is a class of algorithms that reduce complexity by transforming a polygonal mesh into another with fewer faces, edges, and vertices. The simplification process is usually controlled by a set of user-defined quality criteria that can preserve specific properties of the original mesh as much as possible, such as the geometric distance between the vertices and visual appearance of the entire mesh. Quadric edge collapse decimation (QECD) is a variation of the edge collapse algorithm based on quadric error metric by Garland and Heckbert (Garland and Heckbert, 1998). Unlike other simplification procedures, such as vertex clustering, QECD provides explicit control for retention of mesh topology with penalising parameters (Figure 6.05C). In rapid iterations, retention of each vertex is determined based on the input parameters, whilst simultaneously the quality of the mesh is assessed before and after vertex removal. Thus, each remaining vertex after QECD is in the position of minimizing quadric error.

A quick way of visualising the mesh topology and any inconsistencies after decimation is to colour code the surface triangulation according to the shape and aspect ratio (AR) of the triangular elements. The AR is computed as the longest side of the element divided by the shortest, with equilateral triangles having an AR of 1, whilst right-angled ones with identical catheti of 1.41 ( $\sqrt{2}$ ). In MeshLab, elements with low AR are visualised in cold colours, with hotter colours indicating more irregular triangles with a higher AR. An F-actin stress fibre traced with FilamentTracer has

been compared with three different levels of decimation for mesh quality (50%, 25% and 10% number of elements of the input; Figure 6.10). As QECD has been set to preserve the topology, the remaining vertices are repositioned to fill the vacancies, which can result in elongated triangular elements. This is most notably seen at the last fibre where only 10% of the input elements remained.

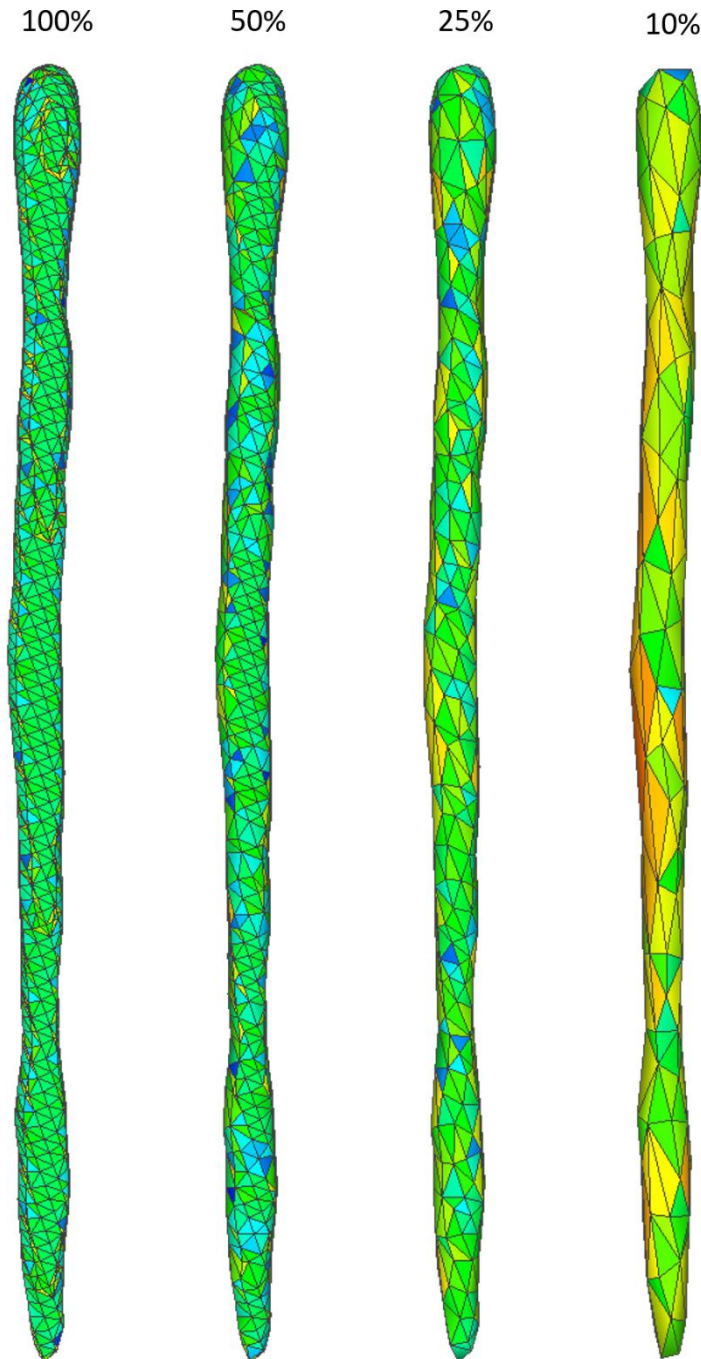


Figure 6.10 – FilamentTracer reconstructed F-actin stress fibre with different levels of element retention after quadric edge collapse decimation (QECD) in MeshLab. 100%: 1,498 vertices, 2,992 elements; 50%: 750 vertices, 1,496 elements; 25%: 357 vertices, 748 elements; 10%: 151 vertices, 298 elements.

The above raises the question of how many elements must be preserved after decimation. Whilst a smaller number of elements is preferable, too great a reduction will result in loss of structural composition. 73 WRL files were imported into MeshLab from Imaris, of which 22 were nuclei, 20 F-actin, 17 vimentin and 14  $\beta$ -tubulin cytoskeleton isosurface geometries. The polygon reduction for nuclei (to be referred to as ‘simple geometries’) was set to 10% of the original number of elements, whilst for cytoskeletal networks (to be referred to as ‘complex geometries’) – to 5%. Computational testing with other percentages confirmed that the selected reduction levels provide a more manageable element number whilst retaining initial structure precision (Figure 6.11 and 6.12). Figure 6.11 illustrates one of each of the four different rendered structures in Imaris with coloured initial surface triangulation based on the AR. The magnified regions provide a better view of the topology and number of elements. Corresponding structures and close-up regions are shown for the isosurfaces after QECD (Figure 6.12). In all instances, the number of composing elements had been highly reduced, whilst the structure quality had been maintained. Furthermore, based on the colour maps, post-QECD there were more triangular elements in blue, indicating the preferred equilateral triangles.

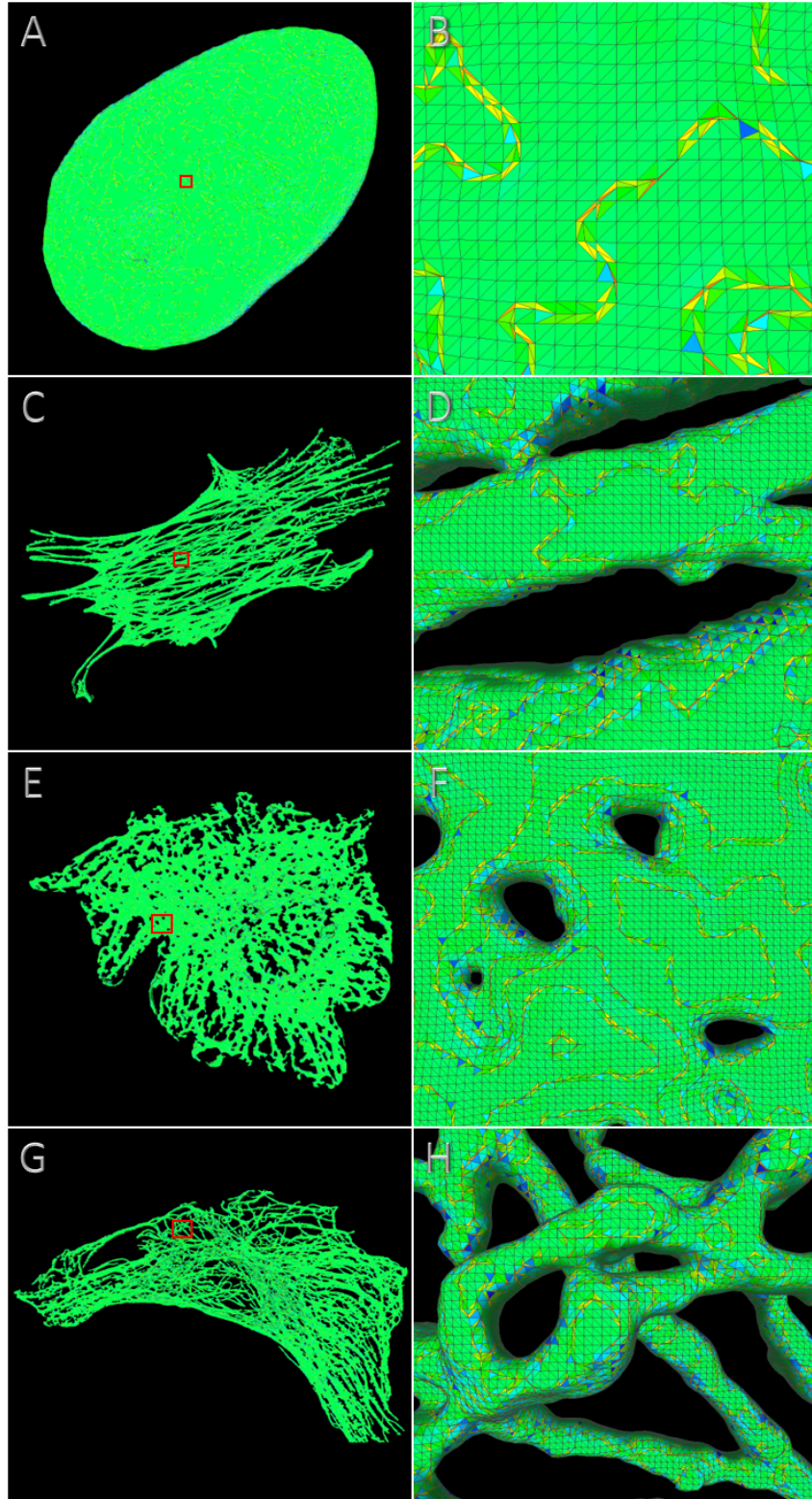


Figure 6.11 – Imaris generated triangular surfaces of a nucleus (A), actin stress fibre (C), vimentin (E) and  $\beta$ -tubulin cytoskeleton (G) visualised in MeshLab. B, D, F and H represent a magnified region indicated by the red square in A, C, E, G, respectively. The colour scheme denotes the element shape: equilateral (blue), right-angled (green), highly distorted triangular elements (yellow, orange).

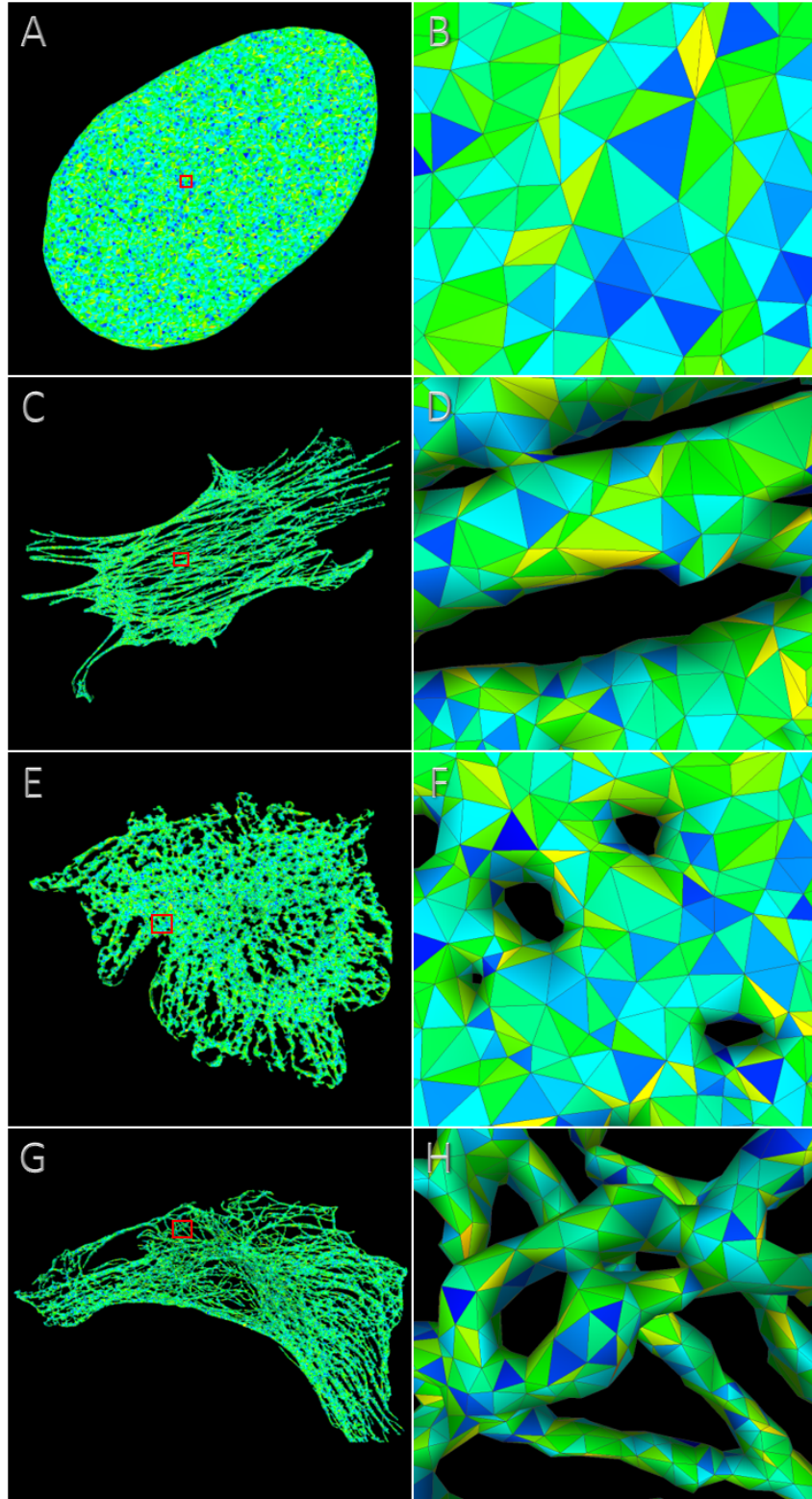


Figure 6.12 – MeshLab QECD decimated triangular surfaces of a nucleus (A), actin stress fibre (C), vimentin (E) and  $\beta$ -tubulin cytoskeleton (G) visualised in MeshLab. B, D, F and H represent a magnified region indicated by the red square in A, C, E, G, respectively. The colour scheme denotes the element shape: equilateral (blue), right-angled (green), highly distorted triangular elements (yellow, orange).

Another advantage of QECD is that it can be applied to a specified region and not the entire geometry. This provides a selective method for controlling mesh density in areas of key interest, with further options for refinement. However, poor element shape (high AR) can affect the convergence of the mesh, causing significant error in numerical simulations (Marchandise et al., 2010). It is then preferable for the triangulation to be composed of identical equilateral triangles. To uniform the geometry, a retopology, or remeshing, needs to be conducted.

### 6.2.2.3 Instant Meshes

Jakob and colleagues presented Instant Meshes as a precise tool for remeshing and producing an isotropic mesh of triangular or quadratic elements (Jakob et al., 2015). The package is not computationally demanding and can handle meshes comprised of millions of elements in seconds as the algorithm performs on the level of a vertex and its close neighbours, with option for parallelisation. Unlike MeshLab, which supports a large variety of file formats, Instant Meshes is more restricted, as the decimated geometry was imported as a Wavefront OBJ file, a common 3D image format.

Instant Meshes provides a list of options for the retopology, including a choice of element shape. It was decided to continue representing the geometry with triangular elements for several reasons. The initial isosurface generated in Imaris was triangulated, with quadratic elements being split into two composing right-angled triangular elements further in the pipeline. Furthermore, quadratic elements are less suitable for representing the curved topology of fibres, unlike triangles. User manual input allows for control over the alignment of the elements as well. Remeshing includes a step for assignment of target vertex count, which is regulated by a slider with suggested values. This is due to the uniformity of the new mesh allowing for only a certain number of final vertices. The performance of Instant Meshes was very accurate, with almost the entire surface of the nucleus being composed of identical equilateral triangle elements (Figure 6.13A and B). The only exclusions are in topologically uneven regions, where for the complex geometries there were some different elements; this is an inevitable compromise, given that these geometries were composed of ~5% of the original isosurface (Figure 6.20), yet retained a high level of precision. Furthermore, different element shapes are necessary to accommodate for the curvatures of the cytoskeleton.

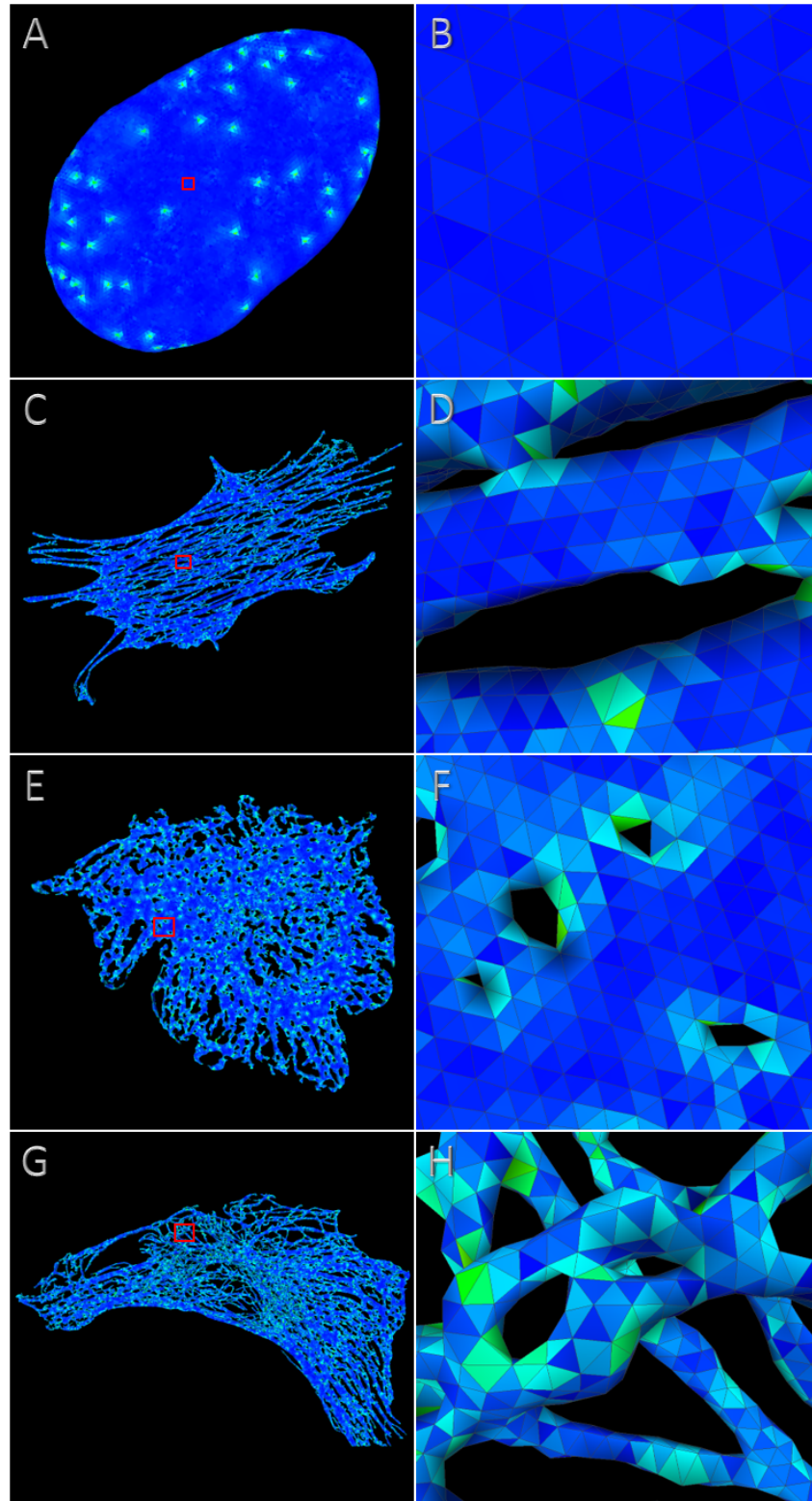


Figure 6.13 – Instant Meshes uniform triangular surfaces of a nucleus (A), actin stress fibre (C), vimentin (E) and  $\beta$ -tubulin cytoskeleton (G) visualised in MeshLab. B, D, F and H represent a magnified region indicated by the red square in A, C, E, G, respectively. The colour scheme denotes the element shape: equilateral (blue), right-angled triangular elements (green).

---

#### 6.2.2.4 Geometry repair and smoothing

##### 6.2.2.4.1 Netfabb geometry repair

During simplification, topology inaccuracies may result in holes or semi-detached regions, which could render the mesh to not be intact or watertight. In those events, Netfabb provides tools of automatic patching of topology discontinuities (Figure 6.14).

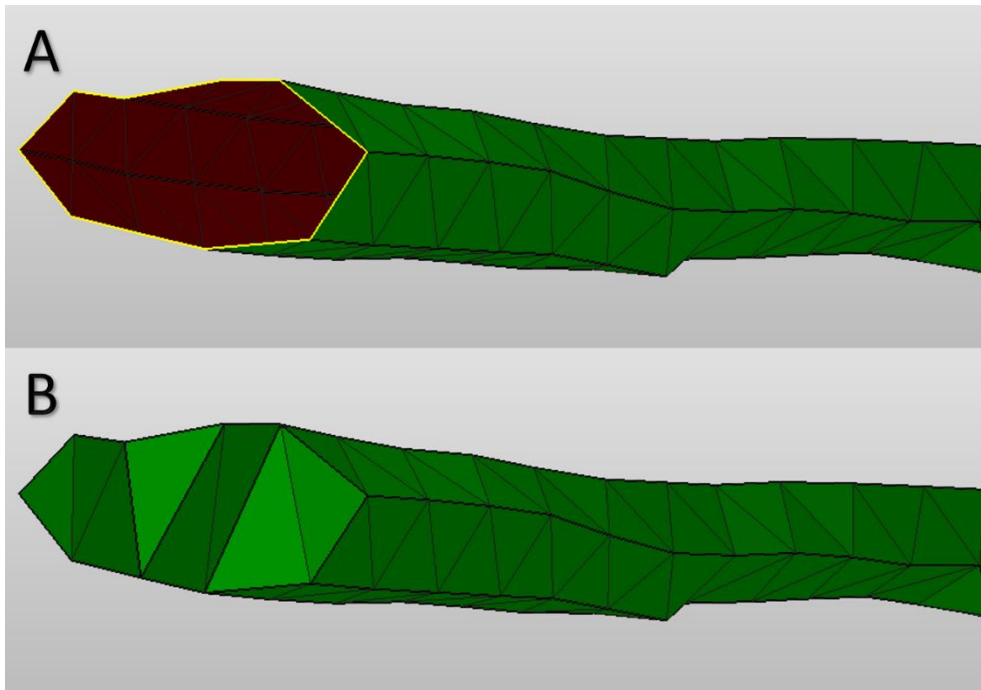


Figure 6.14 – Surface discontinuity of a reconstructed F-actin stress fibre (A) and repaired section (B) in Netfabb.

##### 6.2.2.4.2 MeshLab post-simplification

Importing meshes back into MeshLab can be useful for assessing if any other post-simplification procedures need to be applied. As voxel signal intensity can contain information from several signal channels, this may lead to overlapping of the cytoskeletal surface reconstructions, as each one is recreated separately. Three different geometries from the same cell were imported and fitted together (Figure 6.15) and although the vimentin intermediate filaments were positioned around the nucleus as expected (Figure 6.15D), there were some intersecting F-actin stress fibres within it (Figure 6.15E). Furthermore, when all of the intracellular components were combined it was illustrated how some of the geometries occupy the same three-dimensional space (Figure 6.15F).

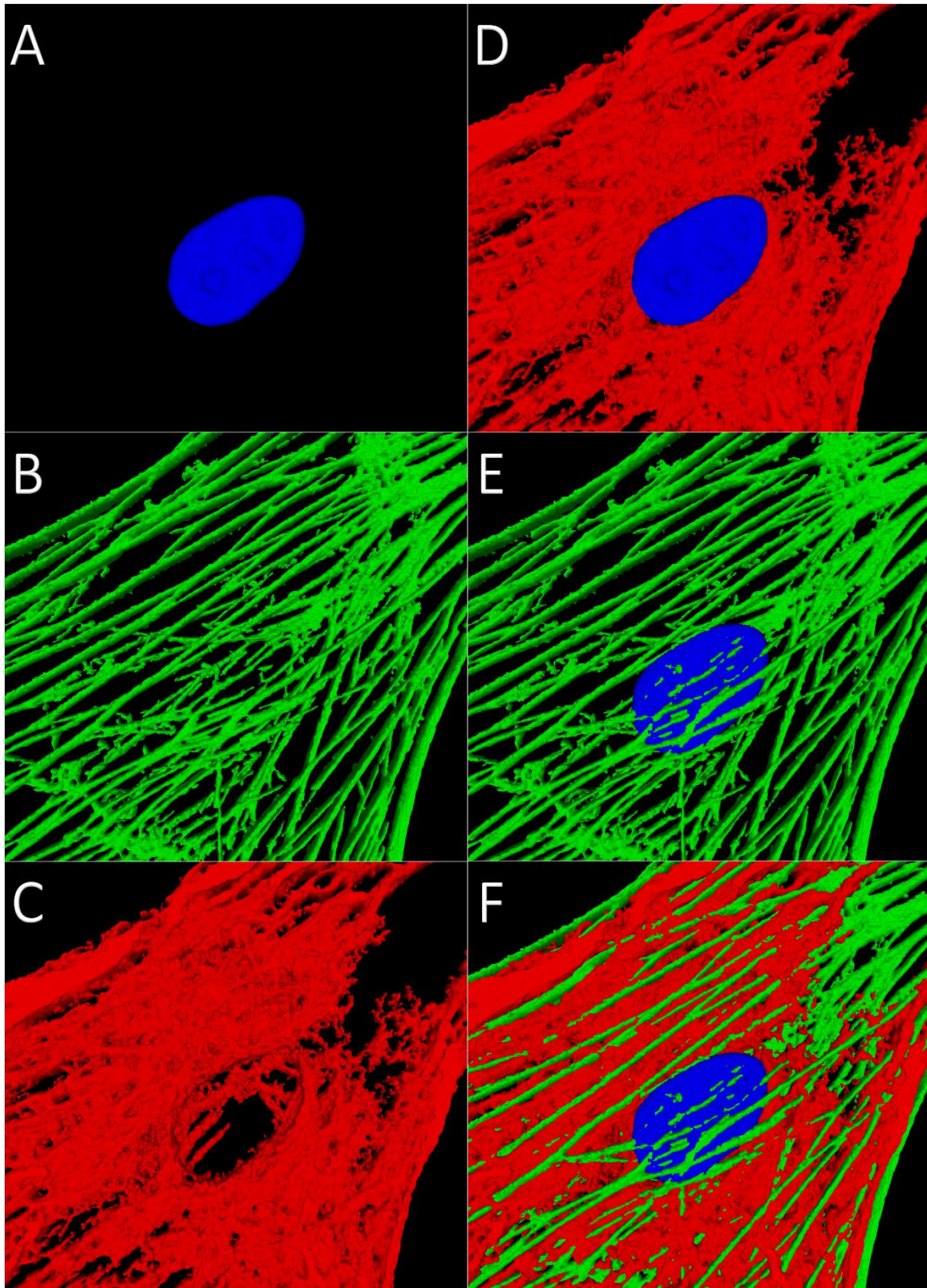


Figure 6.15 – Uniform geometries visualised in MeshLab. (A) Nucleus; (B) F-actin stress fibres; (C) Vimentin intermediate filaments; (D) Combined visualisation of A and C; (E) Combined visualisation of A and B; (F) Combined visualisation of A, B and C.

Whilst this could be remedied by recreating the surfaces in Imaris, as noted, MeshLab contains a variety of post-processing utilities. Mesh smoothing takes an existing mesh and iteratively deforms the positions (but not connectivity) of the vertices, reducing noise and improving overall mesh quality. The smoothing applied in this study was an HC Laplacian (Vollmer et al., 1999). Each vertex was moved in the average position of the neighbouring vertices, creating a ‘tighter’ mesh. The repositioning does not change the number of composing vertices or elements as no new connections are established between them.

For simple geometries, which were mostly smooth before the procedure, there was minimal effect, with small reduction in grooves in the nuclear topology (Figure 6.16A and B). Alterations were more prevalent for the complex geometries (Figure 6.16C-H). Although other fibres (Figure 6.16D and F) retained good uniformity of the surface elements, the thin  $\beta$ -tubulin fibres were further reduced in width (Figure 6.16H), deforming to an extent some of the composing elements to retain the shape. If performed, smoothing is recommended to be executed as a last geometry processing step, as at earlier stages, the repositioning and thinning of fibres could cause discontinuities and unevenly deform the geometry.

Another simplification procedure that can be performed in MeshLab is the screened Poisson surface reconstruction (Kazhdan and Hoppe, 2013). As the geometries can be described as ‘clouds’ of vertices with information on their connections, implementing it could reduce the number of vertices by having them better spread in relation to their original positions. Afterwards, the vertices can be reconnected to form a simplified version of the input geometry. As several simplification and refinement steps have already been implemented, this approach is acknowledged as a potential alternative to test as part of future research.

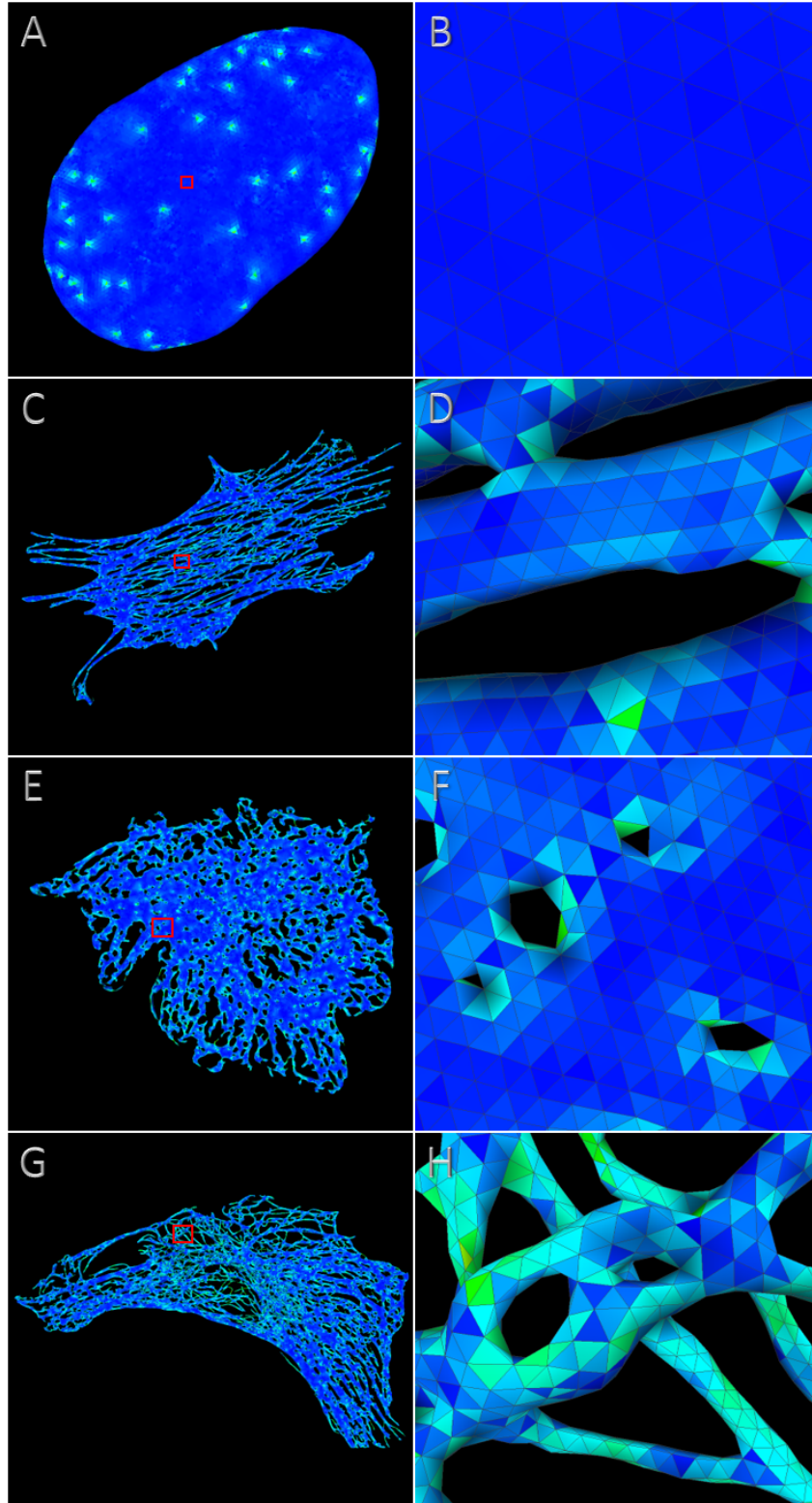


Figure 6.16 – MeshLab HC Laplacian smoothed triangular surfaces of a nucleus (A), actin stress fibre (C), vimentin (E) and  $\beta$ -tubulin cytoskeleton (G) visualised in MeshLab. B, D, F and H represent a magnified region indicated by the red square in A, C, E, G, respectively. The colour scheme denotes the element shape: equilateral (blue), right-angled triangular elements (green).

---

### 6.2.2.5 Gmsh

To import the tessellated surfaces into FE analysis solvers, they need to be in recognisable computer-aided design (CAD) file formats, which can be performed through Gmsh (Geuzaine and Remacle, 2009). Gmsh has fast performance, supporting many different types of files and allows for easy step recording to create reproducible scripts for automatization. From MeshLab the triangular geometries can be exported to Gmsh as stereolithography (STL) files, which are amongst the most common CAD-associated files for storing geometry. The STL is then converted to an INP file, a primary model-associate format of the FE software ABAQUS. At this stage the triangular geometries contain only surface information and no volume, which is required for actual numerical simulations.

#### 6.2.2.5.1 Volume construction

After the surface triangulation has been properly remeshed and refined, Gmsh can add a volume to the geometry and create a three-dimensional mesh out of it (Figure 6.17). The produced continuum (solid) elements are C3D4 tetrahedrons, composed of four vertices forming four triangles between them. They are first-order, with linear connections between the vertices, unlike second-order elements which utilise parabolic interpolations. As the tetrahedrons adjacent to the surface contain the surface vertices and triangular elements, large and uneven meshes will result in many distorted tetrahedral elements, reinforcing the necessity of the previous simplification steps.

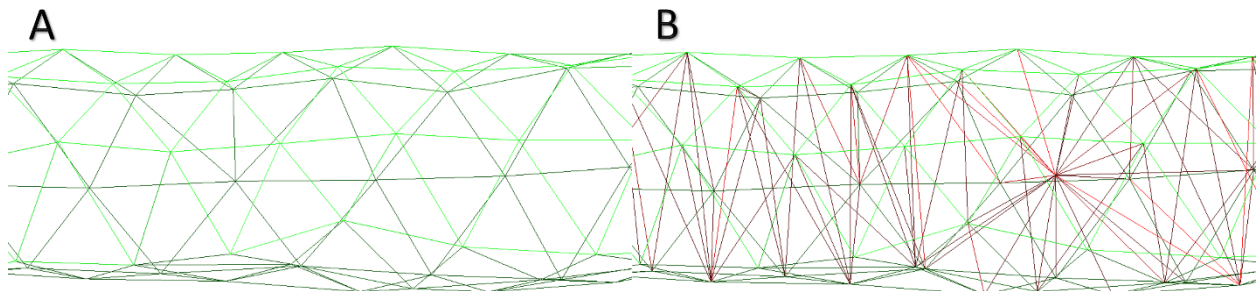


Figure 6.17 – Volume rendering of triangular geometry of an F-actin stress fibre in Gmsh 4.3.0. (A) Input surface of CPS3 triangular elements (Green); (B) Output mesh composed of a surface of CPS3 triangular elements (Green) with internal C3D4 tetrahedron elements (Red).

## 6.2.2.5.2 Quality assessment

Gmsh also provides tools for assessing mesh quality, which can be applied to both the surface and volume meshes. Instead of the element's AR, Gmsh utilises the ratio between the inscribed and circumscribed radius, referred to as Gamma (Figure 6.18). It varies from 0 to 1, with higher values indicating a more uniform mesh with better quality.

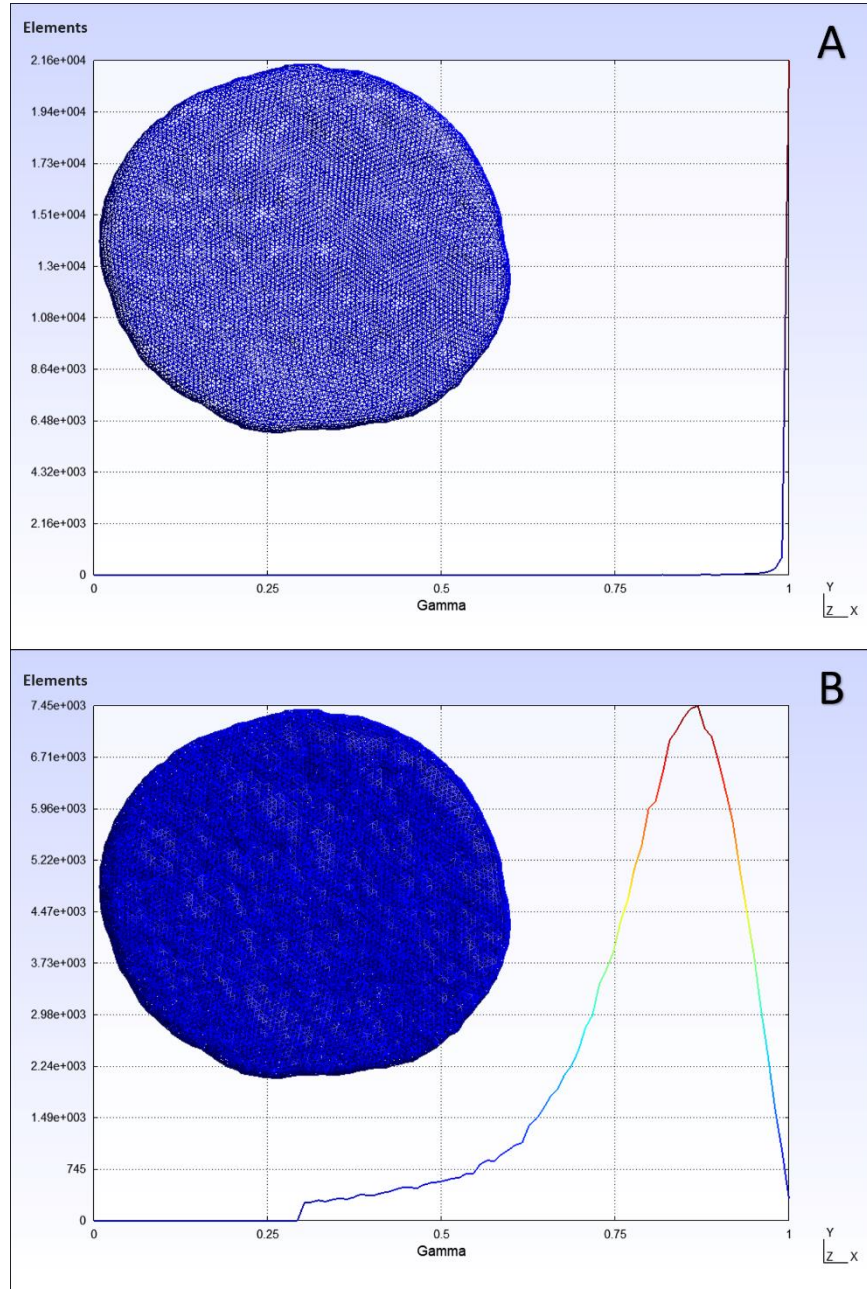


Figure 6.18 – Gamma value plot, with corresponding 3D reconstruction, of a uniform nucleus geometry before (A) and after volume construction (B) in Gmsh 4.3.0.

#### 6.2.2.6 ABAQUS

The final step of the workflow is importing the uniform geometry volume meshes into the FE solver ABAQUS as INP files. Confocal image data of bovine scleral fibroblasts under different strain levels (Chapter V) were successfully processed through the proposed pipeline (Figure 6.05), with initial image input and mesh output presented (Figure 6.19). Even complex topologies, such as the cytoskeletal networks, retain the proper contours with high level of accuracy, demonstrating the validity of this approach in generating cell-specific internal structures for numerical simulations.

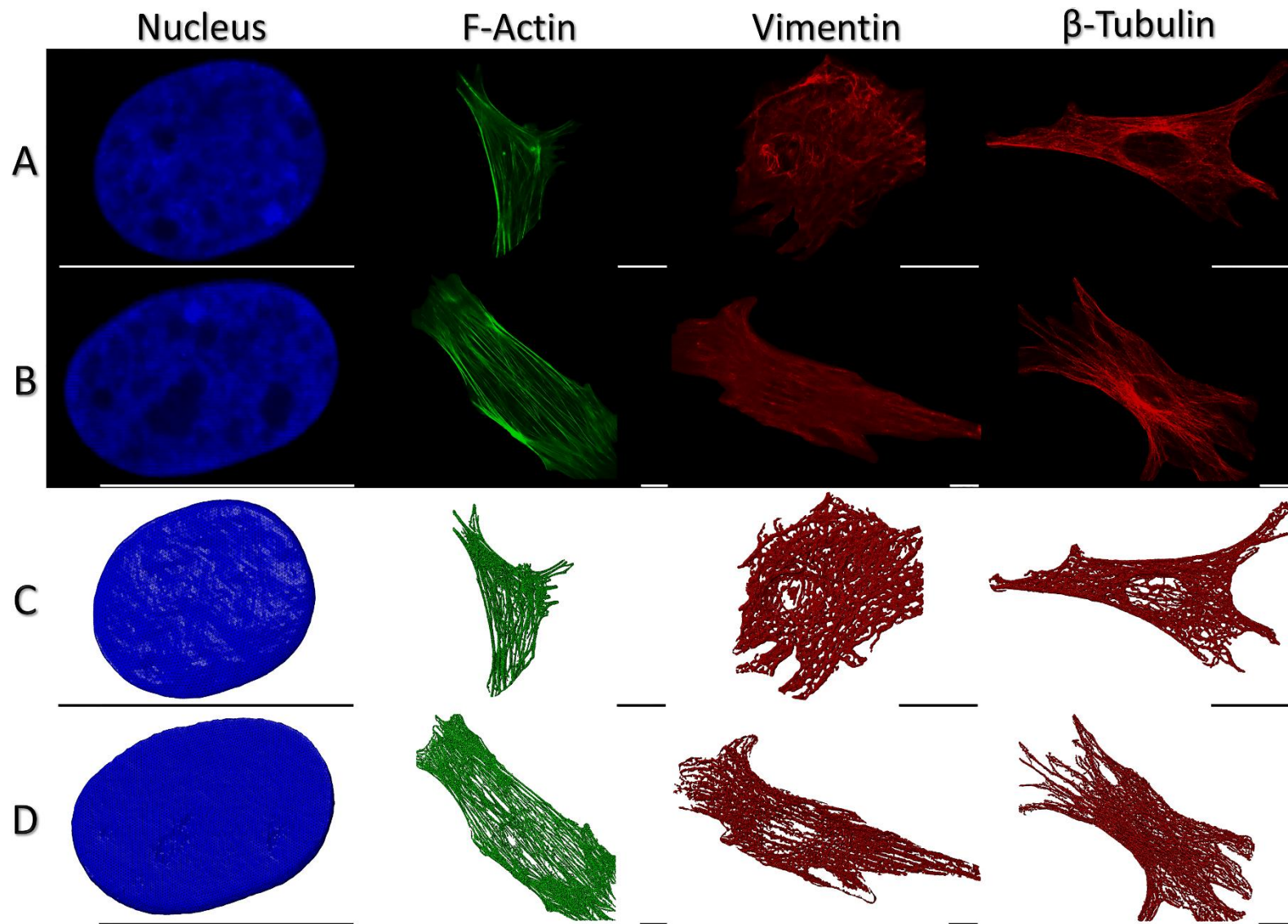


Figure 6.19 – Confocal microscopy image data of a nucleus, F-actin, vimentin and  $\beta$ -tubulin cytoskeleton (A, B) and corresponding reconstructed meshes (C, D) in ABAQUS 6.14/CAE. (A) Confocal images with no applied mechanical load; (B) Confocal images 1h after cessation of mechanical load (0.26-1.8% strain, 1Hz for 1h); (C) Corresponding reconstructed meshes to A; (D) Corresponding reconstructed meshes to B. Scale bar = 20 $\mu$ m.

Before proceeding with simulation, the quality of the meshes requires validation to determine if they are suitable for the subsequent FE analysis procedures. ABAQUS provides tools for this assessment, with information on the number of vertices and elements, their types and shapes. AR details are also included, with the mean AR, worst AR and percentage of mesh elements with AR over 10 calculated (Section 6.2.2.7.3). The worst AR helps to identify regions of local element inconsistencies, for which ABAQUS toolsets can be used to, for example, combine small surface elements with adjacent edges. For proper performance and low discretization error, the element AR needs to be small, preferably under a ratio of 10 as suggested by the ABAQUS documentation.

An alternative to creating a volume mesh in Gmsh is to directly load the uniform STL file into ABAQUS and generate the mesh in it. This procedure is dependent on the 3D Mesh to Geometry ABAQUS plugin. The STL is converted to a geometry model which can go through further refinement and remeshing. Unlike Gmsh, which only permits creation of C3D4 tetrahedral elements, the internal ABAQUS mesh generation supports a wide list of options, including the aforementioned tetrahedrons, but also hexahedrons and wedge elements similar to the ones utilised in the reconstruction of the bovine eye globe (Figure 6.02), providing greater flexibility when creating internal mesh volume. For proper evaluation, further testing and optimisation of this approach will be a part of future work. However, the previous workflow is still required for the creation of high-quality STL files, with the Gmsh Gamma values being a quick way to assess the geometries.

#### 6.2.2.7 Mesh quality comparison

As noted, mesh quality is essential for proper FE simulations. To assess the necessity of the procedural workflow of generating high-quality cell-specific meshes, the geometries at four different steps were compared for several parameters. The geometry exported from Imaris was referred to as ‘Initial’, the geometry after QECD as ‘Decimated’, the geometry after making the tessellation isotropic as ‘Uniform’ and the optional procedural step of applying an HC Laplacian smoothing in MeshLab as ‘Smooth’ geometry. The Initial Imaris output geometry contains in some instances  $10^7$  triangular elements, which are reduced further down the pipeline, necessitating evaluation of element and vertex number decrease. MeshLab also allows the calculation of a

geometry's area and volume (in  $\mu\text{m}^2$  and  $\mu\text{m}^3$ , respectively). Finally, the Gmsh Gamma and ABAQUS AR parameters provide assessment for the shape of the elements.

The 73 different meshes were split into two groups – 22 representing simple geometries (nuclei) and 51 for complex geometries (cytoskeletal components). The division was performed to evaluate how the utilised software packages handle the two fundamentally different groups of structures. Furthermore, the quality of volume meshes was only assessed for the simple geometries; the complexity and number of comprising elements for the Initial geometries of the cytoskeletal structures caused Gmsh to malfunction and crash when mesh volume construction was initiated. Thus, for statistical analysis, only the volume meshes of the nuclei were compared, whilst the surface triangulation was assessed for both the simple and complex structures. To exclude individual variations, each Initial geometry was represented as being 100% of itself, with the following simplifications illustrated as percentages of the parameter of the corresponding geometry.

#### 6.2.2.7.1 Vertices and elements

The target element reduction for QECD was set to 5% for complex geometries, with expectation for the number of vertices to scale down as well. Decimation was confirmed as successful, with the initial elements count reduced to  $5.00 \pm 0.00\%$  (Figure 6.20B). The number of vertices was slightly lower ( $4.91 \pm 0.03\%$ ) due to triangular element merging and establishing new connections (Figure 6.20A). This trend was continued in both the Uniform and Smooth geometries. As the HC Laplacian smoothing only repositions the vertices, their number (and for the elements) was identical to the Uniform ones. Due to Instant Meshes creating an isotropic triangulation with a set number of elements, there was a significant decrease in both elements and vertices, with larger variability in the distribution due to the range and sizes of structures.

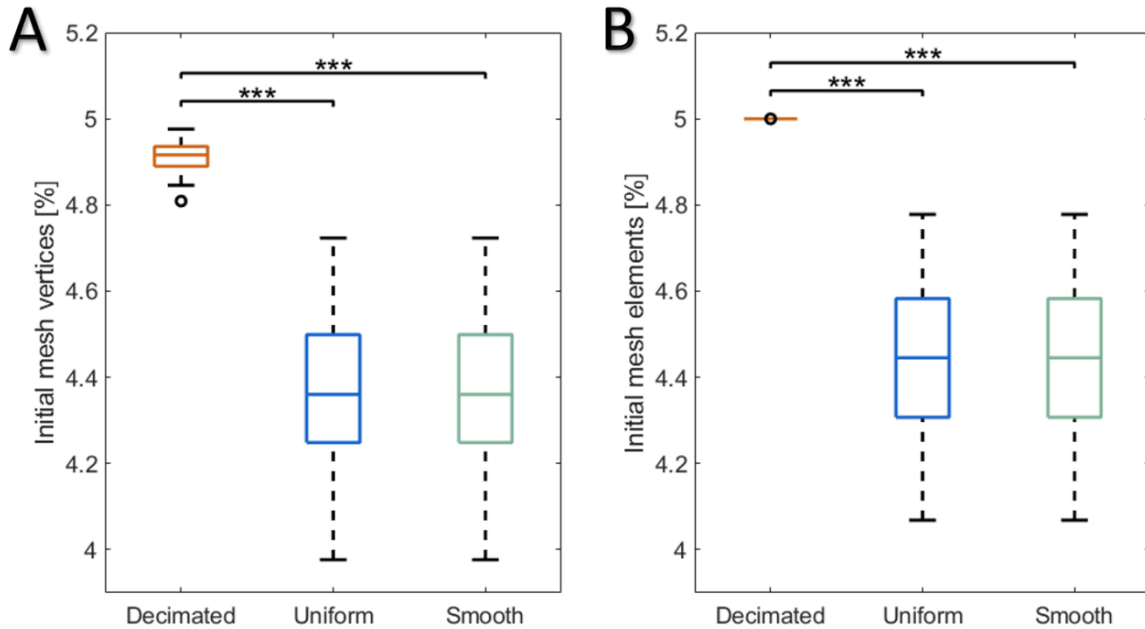


Figure 6.20 – Complex geometries comparison of number of vertices (A) and elements (B) to the Initial geometry. Data are presented as median  $\pm$  SD (n=51); \*\*\*: p<0.001.

Following expectations, the QECD produced simple geometries with  $10.00 \pm 0.00\%$  elements of the initial input (Figure 6.21B). As the nuclear topology is not a 3D network and more round, fewer vertices required further removal during QECD in comparison to the cytoskeletal structures, resulting in Decimated nuclear vertices to be at  $10.00 \pm 0.00\%$  (Figure 6.21A). For comparison, volume was added in Gmsh to the Initial geometries. After constructing volume for the Decimated geometries, the number of vertices increased more than twice, with a mean of  $21.20 \pm 2.18\%$ , instead of the expected 10% (Figure 6.21C). This value includes the total number of vertices before (Figure 6.21A) and after the volume was added. The Decimated geometries contain a heterogeneous distribution of triangular elements, with those possessing a higher AR (Section 6.2.2.7.3) needing to be accommodated by a larger number of vertices. Properly isotropic triangulations, such as the Uniform and Smooth ones, consisted of  $8.03 \pm 0.31\%$  and  $8.19 \pm 0.33\%$  on average, respectively, of the number of vertices the Initial mesh had. Accurate positioning of the vertices would have created a larger number of tetrahedral elements than for the Decimated geometry (Figure 6.21D). It must be noted that whilst for the surface geometries the number of elements was identical between the Uniform and Smooth, as the vertices have different coordinates after creating tetrahedral elements, they were significantly larger for the Smooth group. Only the number of tetrahedral elements was

compared (Figure 6.21D), as the triangular elements composing the surface of the geometry also formed part of the tetrahedral ones. The Decimated group were composed of differently sized tetrahedrons to fill the volume, which could explain their lower relative number.

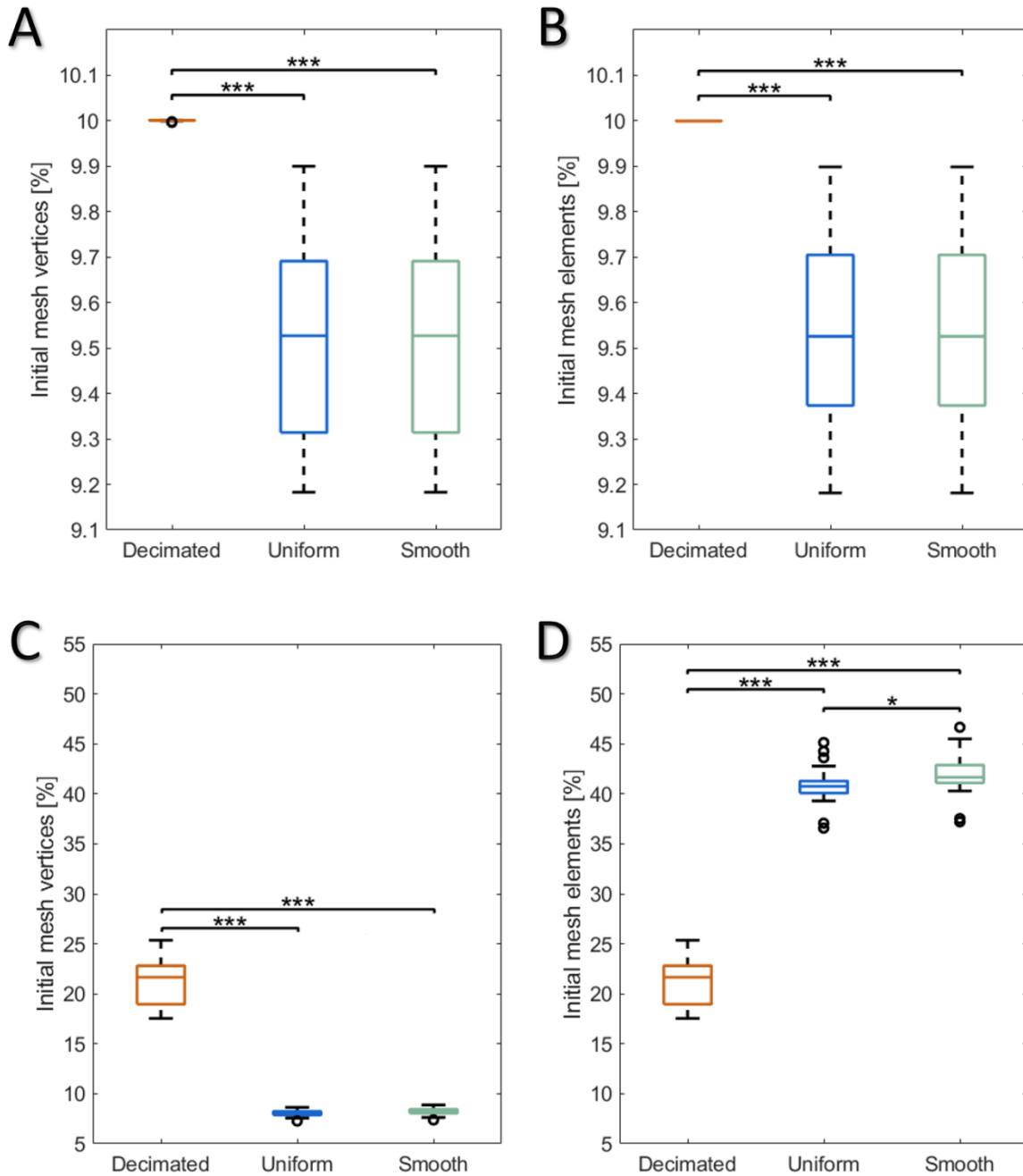


Figure 6.21 – Simple geometries comparison of number of vertices (A) and elements (B) to the Initial geometry. Comparison of the total number of vertices after volume construction (C) and the number of tetrahedral elements (D) with the Initial geometry with volume. Data are presented as median  $\pm$  SD (n=22); \*: p<0.05; \*\*\*: p<0.001.

## 6.2.2.7.2 Area and volume

For the complex geometries, apart from the Decimated group, the surface area decreased at each step of simplification (Figure 6.22A). The topology volume was also reduced at each workflow step (Figure 6.22B). As the complex meshes are fibrillar networks, the overall area was also larger, which caused smoothing to decrease both the area and volume the most. The higher area average for the surface Decimated group ( $100.34 \pm 0.93\%$ ) could be an effect of the vertex repositioning during QECD whilst trying to preserve the topology shape. 16 of the 51 Decimated geometries did, however, have areas smaller than their corresponding Initial ones.

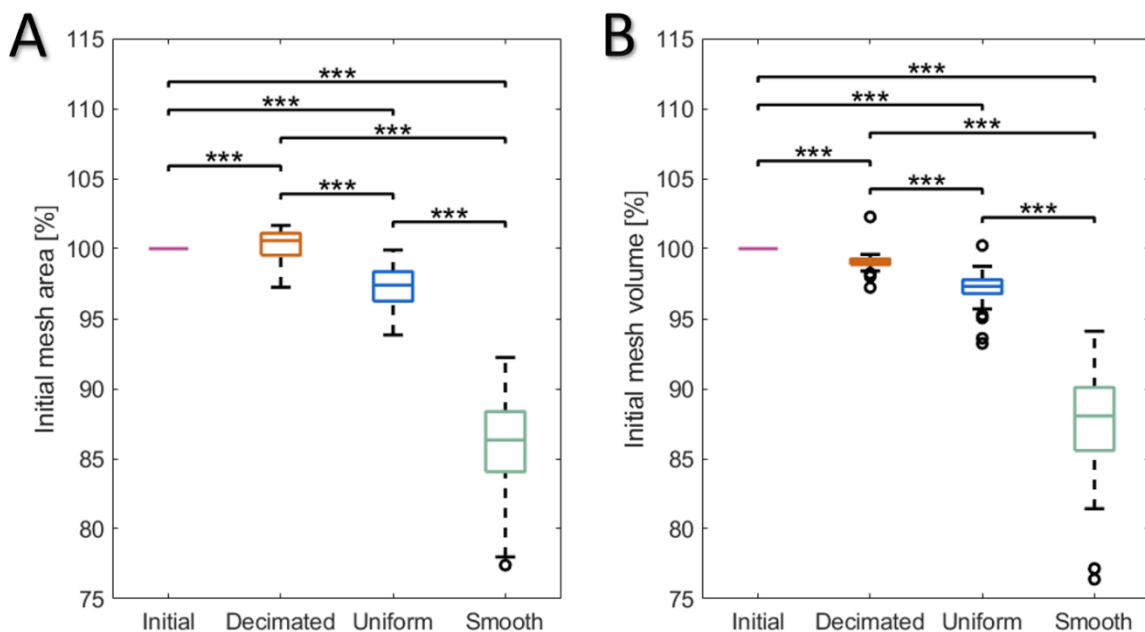


Figure 6.22 – Complex geometries comparison of area (A) and volume (B) to the Initial geometry. Data are presented as median  $\pm$  SD (n=51); \*\*\*: p<0.001.

Simple geometries experienced smaller decreases in area and volume than the complex group (Figure 6.23). The mean area of the Initial and Decimated group were not different ( $p=0.169$ ), whilst their volumes were ( $p<0.001$ ). The Smooth geometries had the smallest area and volume as well, consistent with the observations for the cytoskeletal components, but with not so large relative reduction.

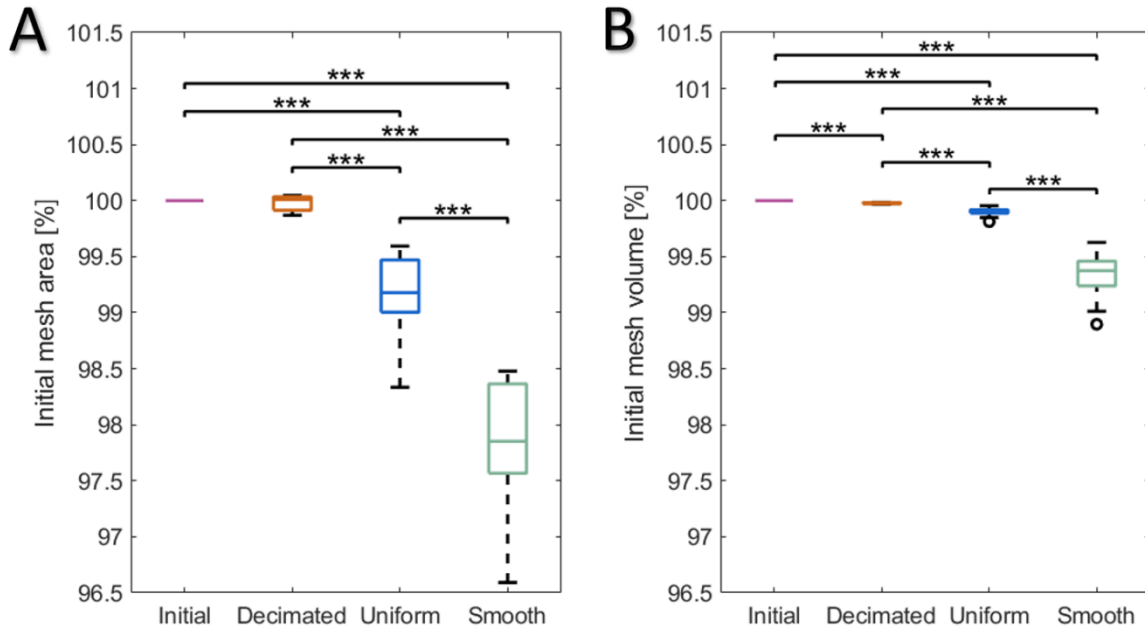


Figure 6.23 – Simple geometries comparison of area (A) and volume (B) to the Initial geometry. Data are presented as median  $\pm$  SD (n=22); \*\*\*: p<0.001.

Measuring the size of the triangular and tetrahedral elements was not carried out, as it will change to accommodate the surface and volume meshes. This is best illustrated during QECD where the area and volume of the topology are very close to the Initial whilst having 95% or 90% less composing elements (Figure 6.12).

### 6.2.2.7.3 Aspect ratio

As all of the elements were first-order, the Jacobian ratio, which assesses mesh quality of second-order elements, was not calculated. ‘Fibre Triangle’ refers to the complex triangulated geometries, ‘Nucleus Triangle’ for the simple triangulated geometries and ‘Nucleus Tetrahedron’ for simple tetrahedrite meshes, with only the tetrahedral element quality evaluated. All AR data were presented as mean  $\pm$  standard deviation (SD), with lower AR values ( $\sim$ 1) indicating highly isotropic meshes.

In all instances, no significant differences were observed between the Uniform and Smooth groups, confirming that on average smoothing does not decrease element composition quality (Table 6.1).

Simplification procedures consistently reduced the elements' AR, with the Instant Meshes step bringing the AR for the surface triangulations close to 1. Following previous cases, the nuclei had an overall better mesh quality than the cytoskeletal components, which was within expectations, given their simpler shape and smaller number of comprising elements. The tetrahedral elements in the Initial group had a lower AR than the corresponding triangular elements, which could be due to the proximity of the tetrahedral elements allowing for fewer deformations on average. However, deformed triangular elements will only produce highly irregular tetrahedral ones.

Table 6.1 – Mean element AR at different stages of simplification. AR values ~1 indicate a proper isotropic mesh. Uniform and Smooth meshes were not significantly different. n(Fibre Triangle)=51; n(Nucleus Triangle)=22; n(Nucleus Tetrahedron)=22. Data are presented as mean  $\pm$  SD.

Geometry	Initial	Decimated	Uniform	Smooth
<b>Fibre Triangle</b>	6.153 $\pm 0.434$	1.709 $\pm 0.049$	1.170 $\pm 0.059$	1.174 $\pm 0.053$
<b>Nucleus Triangle</b>	4.583 $\pm 0.510$	1.677 $\pm 0.033$	1.051 $\pm 0.004$	1.045 $\pm 0.005$
<b>Nucleus Tetrahedron</b>	2.778 $\pm 0.253$	2.082 $\pm 0.152$	1.549 $\pm 0.008$	1.544 $\pm 0.009$

Each of the isosurfaces exported from Imaris contained several highly irregular triangular elements (Table 6.2). Whilst the average worst AR value was higher for the simple geometries, they also had much higher variability than the complex ones, which was carried over to the tetrahedral elements in the nuclei. Such distorted elements will induce significant errors in any computation, making the meshes unusable. Decimation decreased the average worst AR nearly 2,000 times for the cytoskeletal components and about 3,300 times for the nuclear triangulations, further underlying the importance of reducing the number of initial elements. Making the geometries uniform additionally improved the quality, bringing the AR in all instances below 5. As noted, the HC Laplacian smoothing creates a tighter surface, which displaces vertices, and whilst the mean AR was not different between the Uniform and Smooth group, the worst AR for the smoothed triangulations was higher. In contrast, the smoothing procedure further decreased the worst AR for the simple topologies, signifying the need for caution when deciding on implementing any modifications after creation of an isotropic mesh.

Table 6.2 – Worst element AR at different stages of simplification. High AR values, such as the Initial meshes, make them unusable. Uniform and Smooth meshes had  $AR < 5$ .  $n(\text{Fibre Triangle})=51$ ;  $n(\text{Nucleus Triangle})=22$ ;  $n(\text{Nucleus Tetrahedron})=22$ . Data are presented as mean  $\pm$  SD.

Geometry	Initial	Decimated	Uniform	Smooth
<b>Fibre Triangle</b>	36,922.000 $\pm 9,102.500$	18.707 $\pm 15.907$	3.916 $\pm 0.668$	4.604 $\pm 0.934$
<b>Nucleus Triangle</b>	39,966.000 $\pm 19,520.000$	12.123 $\pm 23.018$	2.848 $\pm 0.141$	2.136 $\pm 0.290$
<b>Nucleus Tetrahedron</b>	70,769.000 $\pm 35,028.000$	11.311 $\pm 3.279$	4.496 $\pm 0.415$	3.357 $\pm 0.419$

As most of the Initial meshes contain millions of elements, specifically the complex, having several percent of elements with an AR over 10 equates to several thousand distorted elements (Table 6.3). Decimation reduced the overall element AR as previously observed (Table 6.2). Furthermore, all of the Uniform and Smooth meshes did not have any AR values above 10, which makes them much more preferable for numerical analysis.

Table 6.3 – Percentages of element AR greater than 10 at different stages of simplification. Uniform and Smooth meshes do not have any  $AR > 10$ .  $n(\text{Fibre Triangle})=51$ ;  $n(\text{Nucleus Triangle})=22$ ;  $n(\text{Nucleus Tetrahedron})=22$ . Data are presented as mean  $\pm$  SD.

Geometry	Initial	Decimated	Uniform	Smooth
<b>Fibre Triangle</b>	5.323 $\pm 0.408$	0.002 $\pm 0.002$	0.000 $\pm 0.000$	0.000 $\pm 0.000$
<b>Nucleus Triangle</b>	3.448 $\pm 0.488$	0.001 $\pm 0.002$	0.000 $\pm 0.000$	0.000 $\pm 0.000$
<b>Nucleus Tetrahedron</b>	1.338 $\pm 0.369$	0.003 $\pm 0.004$	0.000 $\pm 0.000$	0.000 $\pm 0.000$

### 6.2.2.7.4 Gamma

As the Gmsh value Gamma is calculated differently from AR, higher values closer to 1 indicate a better overall element distribution. Gamma is related to the entire mesh, which would include both triangular and tetrahedral elements together for the nuclei volume meshes (Figure 6.24C). Initial complex and simple geometries had the lowest value of Gamma, progressively increasing in the Decimated and Uniform groups, which was in accordance with the mesh quality observations for the AR (Figure 6.24A and B). Whilst not identical, the Uniform and Smooth groups were not significantly different when compared and had the same variance. Contrary to expectations, after volume meshing the value for the Decimated group was lower than for the Initial, on average  $0.693 \pm 0.027$  and  $0.747 \pm 0.016$ , respectively (Figure 6.24C). As Gamma is a ratio between radii it could indicate that after QECD the volume of each individual element was more distorted than it was in the Initial step. Making the mesh uniform does resolve the issue, although the Gamma values are lower than for the corresponding surface (Figure 6.24B). Overall, the simple structures returned greater Gamma values than the complex ones, which still had very high values, specifically  $0.971 \pm 0.009$  for the Uniform cytoskeletal group (Figure 6.24A).

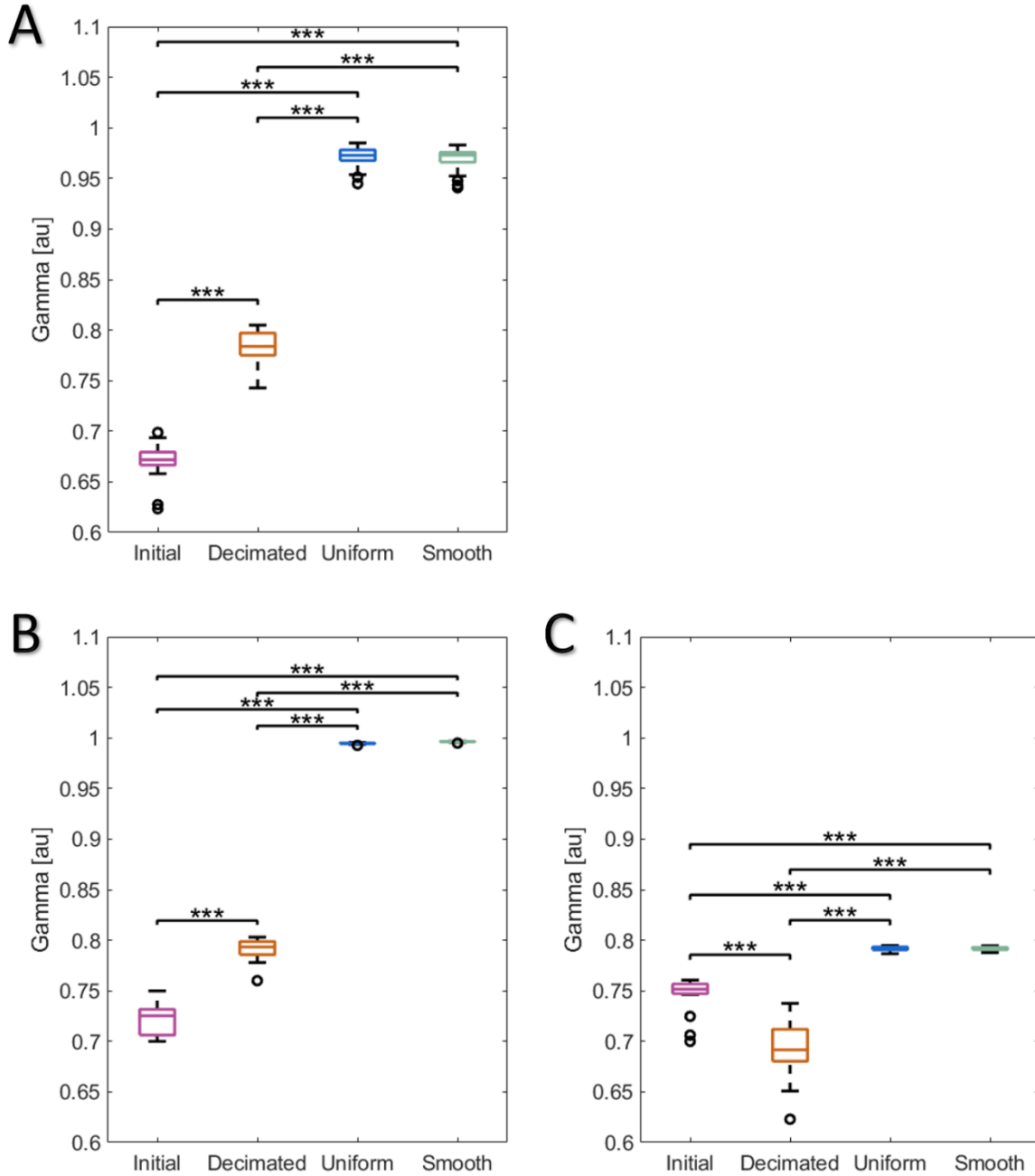


Figure 6.24 – Gamma value comparison of complex surface (A; n=51), simple surface (B; n=22) and volume (C; n=22) mesh. Data are presented as median  $\pm$  SD; \*\*\*:  $p < 0.001$ .

The mesh quality assessment validated the order of procedures and their necessity for simultaneous reduction of the number of composing elements with increasing surface mesh isotropy.

### 6.2.2.8 ImageJ

An alternative to Imaris would be the implementation of the ImageJ plugin 3D Viewer (Schmid et al., 2010). Apart from volume and surface visualisation, the toolset allows for construction of a triangular isosurface based on the Marching Cubes algorithm, similarly to Imaris (Lorensen and Cline, 1987). The visualisation is heavily dependent on the initial parameters, notably the applied threshold to the input Z-stack of images and the resampling factor. The surface can then be exported as an STL and processed via the listed optimisation procedures.

Whilst Imaris permits a greater level of automatization this is not feasible with 3D Viewer. Each volume dataset requires careful assignment of appropriate parameters, as empirical testing of the algorithm showed it to be more sensitive to irregularities and dips in signal intensity than Imaris. This can generate significantly uneven surfaces, which require resampling to decrease the triangular element composition, similar to the QECD function in MeshLab. Unlike MeshLab, however, there is no option to retain the original boundaries. Each resampling reduces the number of vertices and elements by about 50%, with higher iterations producing a smoother surface. Spherical structures benefit from this approach, as it reduces the number of surface elements (Figure 6.26A-D). Thicker fibrillar networks retain most of their form, whilst thinner ones are reduced to disassembled remnants (Figure 6.25E-H).

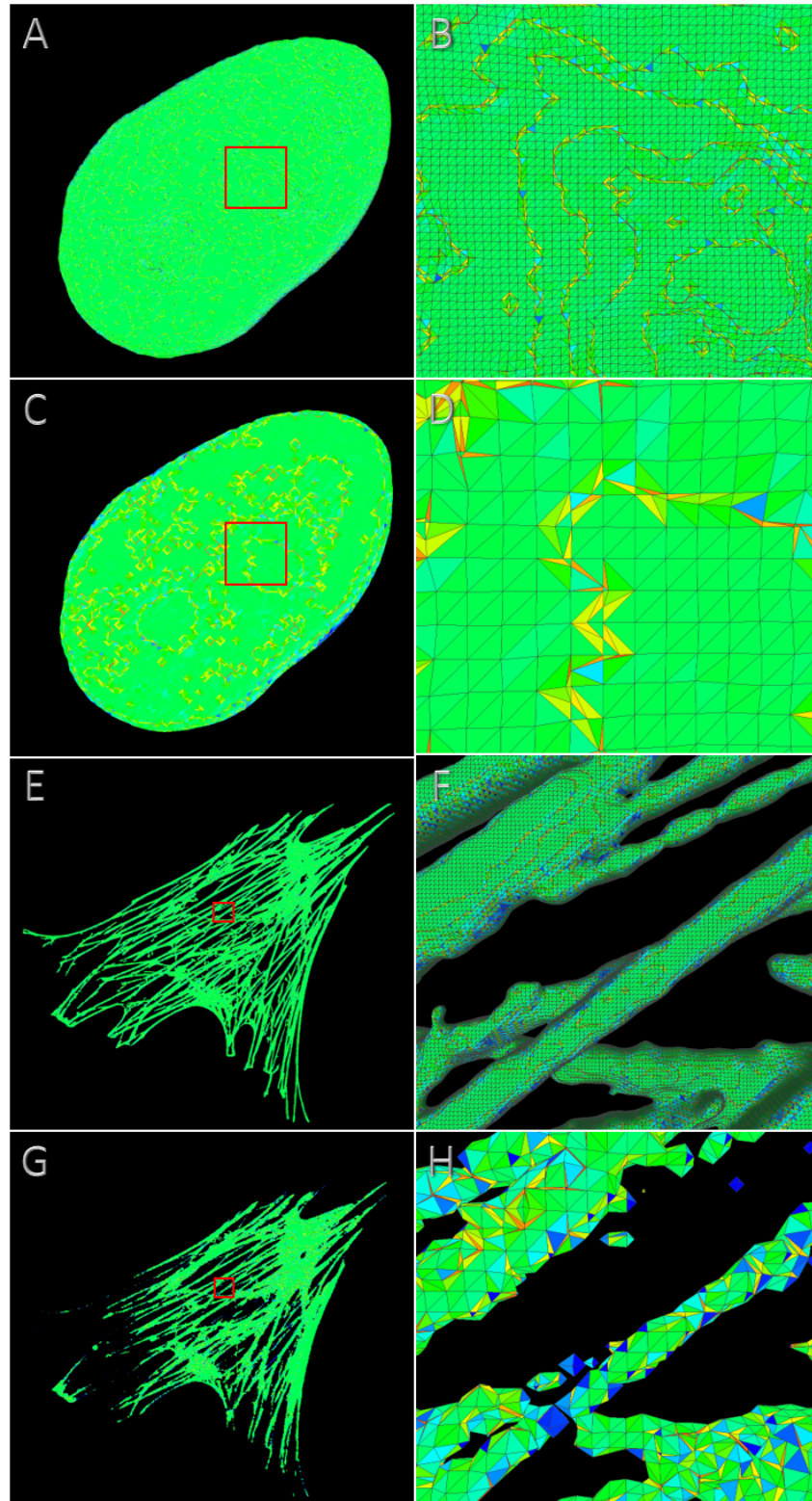


Figure 6.25 – Imaris generated triangular surfaces of a nucleus (A) and actin stress fibre cytoskeleton (E) with corresponding structures from the ImageJ 3D Viewer (C and G) visualised in MeshLab. B, D, F and H represent a magnified region from the indicated red square in A, C, E, G, respectively. The colour scheme denotes the element shape: equilateral (blue), right-angle (green), highly distorted triangular elements (yellow, orange).

### 6.2.2.9 Advantages and limitations of the reconstruction procedures

The presented approach permits incorporation of complex cytoskeletal protein architecture into the commercial FE solver ABAQUS for greater physiological relevancy. The workflow can be applied to any imaging technique that produces volume data sets, with laser confocal microscopy selected for this study. Confocal microscopy was chosen on the basis of the high-resolution optical sectioning that can be achieved to create volume image stacks without physical re-sectioning of the specimens. As the data was reconstructed in Imaris, on the basis of voxel intensity projection, it needs to be acknowledged that this can skew the spatial relationship between data points in some instances. However, to the best of the author's knowledge, no superior alternatives are available. Furthermore, Imaris' Marching Cubes algorithm is widely acknowledged and utilized for surface reconstruction (Reif et al., 2015; Craver et al., 2016; Osaki et al., 2017; Homan et al., 2019).

Current cell FE models make a variety of oversimplifications, from depicting the cell as an ellipsoid to containing only random fibres (Ronan et al., 2012; Dowling et al., 2013; Barreto et al., 2014). The meshes proposed in this Chapter provide greater accuracy in representing the cytoskeleton and nucleus, as they are constructed from experimental results rather than approximating and idealising components. The triangulated geometries closely follow the contours and dimensions of the fibre network, with reconstruction precision dependent on the fibre density and specified rendering and meshing parameters. Cytoskeletal mesh precision will be of key value for FE modelling, as the cytoskeleton is integral for the cell's organisation, structure and biomechanical responses (Fletcher and Mullins, 2010). Whilst several earlier publications have utilised cell-specific meshes for FE analysis, they, however, did not accommodate the proper cytoskeletal orientation (Slomka and Gefen, 2010; Or-Tzadikario and Gefen, 2011; Slomka et al., 2011; Yao et al., 2016). Furthermore, this is the first work to create cell-specific digital reconstructions of the vimentin intermediate filaments and  $\beta$ -tubulin microtubular networks. Whilst Yao et al. imaged actin stress fibres, they were represented as linear connections between several vertices, with a reported number of 22 fibres (Yao et al., 2016).

The advantage of the approach presented in this Chapter lies in combining the high-resolution digital image Z-stacks obtained using confocal microscopy (Chapter V) with accurate Imaris

surface triangulation and refinement. This allowed proper visualisation and rendering of individual fibres, as well as fibre bundles, which have not been previously included in models. Fibre density varies by both type and cell region, with particularly dense regions represented as continuous surfaces. The microtubule organising centre (MTOC), where new microtubules form, was recorded in most  $\beta$ -tubulin volume data sets and can also be reconstructed as a surface, which can be further refined with more detailed elements.

As the cytoskeleton is reconstructed as a single object, individual fibres are merged at their base. This makes it difficult to assess if the fibres were originally connected or positioned above each other, which may be the result of the voxel intensity reconstruction. However, as detailed in Chapter V, the imaged bovine scleral fibroblasts were thin flat cells, with most of the fibres situated in the same plane, with the exception of vimentin intermediate filaments, which surround the nucleus from the top and sides. Staining for specific cytoskeletal accessory molecules, such as the actin-binding proteins  $\alpha$ -actinin and filamin, can be part of future cellular experiments to determine in denser fibre regions their connectivity and positioning. The cytoskeleton persists in a state of dynamic equilibrium, with numerical simulations indicating a necessity to include actin stress fibre contractility and reshaping to produce realistic biomechanical responses (Ronan et al., 2012; Reynolds et al., 2014). At least a partial solution could be accomplished by utilising cytoskeletal meshes from different time points and mechanical loading conditions as references for the dynamic changes in the cytoskeleton (Figure 6.19).

### 6.2.2.9.1 Procedural steps

The workflow surface triangulation reduction and optimisation were carried out to improve the overall quality, whilst making the meshes more suitable for numerical calculations. Large complex structures, such as the cytoskeletal geometries, contained at the Initial step on average more than  $10^6$  elements. This was also in part due to the Marching Cubes, which prioritises render accuracy without trying to minimise the number of produced vertices. Proper specification of the reconstruction parameters in Imaris determines the level of detail and smoothing of the resultant isosurface. Parameters that require special attention include: (I) the threshold and background subtraction to select appropriate voxel signal intensity for the reconstruction; (II) the surface detail,

which at high values began to connect fibres inaccurately; (III) the render quality, which is responsible for the triangulation.

Imaris isosurfaces follow accurately the input data sets, however, there are instances where unnecessary signal has been recognised and rendered as well. Instead of reconstructing the surface anew, MeshLab provides a toolset for manual removal of selected vertices and elements, which can also be assigned to any discontinued elements. As QECD is a primary step of the simplification pipeline, such small clean-up procedures are suggested to be performed after decimation, as some of the inconsistencies may be resolved through the reduction of composing elements. Potential larger decimations of the Initial triangulation, than the ones presented in this Chapter, are possible and will depend on the initial number of elements and complexity of the geometry. For the nuclei, decimation to 5% removed most of the topological specifics, making the surface mostly even. Thus, for better visualisation of the reconstructions, the QECD was increased to 10%. Overall, decimation beneath the recommended 5% caused issues around curves and holes, as they had to be represented by linear triangles.

As part of the Instant Meshes step includes selection of an approximate number of vertices for uniforming the geometry, then decimation could be excluded. The quality comparison in Section 6.2.2.7 revealed that although the Decimated geometry is preferable to the Initial, the Uniform one was most suitable overall, showing that performing QECD is insufficient alone in producing proper final triangulated surfaces. However, the MeshLab decimation allows for retention of the original shape, with penalising parameters, which is absent from Instant Meshes. This makes reducing the triangulation before making it isotropic a safer option for preserving accuracy, specifically when dealing with complex structures. If final element number is not a concern, or a very fine mesh is required, then the Initial geometry can be handled in Instant Meshes, after the Imaris WRL output file is converted to an Instant Meshes OBJ format in MeshLab. Furthermore, as the Instant Meshes' output OBJ cannot be opened in Gmsh it requires conversion again through MeshLab to STL file format.

Uniforming the geometry is arguably the most important retopology step as large meshes will be computationally heavy but can produce more physiologically accurate results if the mesh is of high

quality. This was exemplified in this Chapter, where whilst the Decimated and Uniform triangulations had a relatively close number of elements and vertices (Figure 6.21), after volume creation the Decimated had on average  $46.29 \pm 24.04\%$  less tetrahedral elements and  $164.11 \pm 27.13\%$  more vertices than the Uniform. The importance of properly formed elements is further reinforced where the overall tetrahedral mesh quality of the Decimated ones was lower than the Initial (Section 6.2.2.7). Instant Meshes has two main limitations for the purposes of this approach. First, it is applied for the entire geometry and cannot be localised like QECD. Second, in instances of the aforementioned highly complex geometries with full or partial discontinuities, the algorithm will try to make them isotropic. The resulting displacement may be shifted causing the mesh to not be watertight, having discontinuities or severely uneven parts, thus making it impossible to create an internal volume if not remedied. Holes can quickly be fixed in Netfabb and exported again to Instant Meshes for a second iteration to uniform the patched region.

Smoothing and other post-simplification procedures are optional and need to be carefully considered on what advantages they provide. HC Laplacian smoothing was selected as a representative example as it noticeably altered the topology without discontinuing thin fibres and losing detail. The most important effect was surface compression, reducing both the area and volume (Section 6.2.2.7.2), as well as decreasing the worst AR value (Table 6.2) for triangular and tetrahedral simple meshes. This confirms that stopping the geometrical refinement after making it isotropic in Instant Meshes is sufficient, specifically for cytoskeletal reconstructions where the average worst AR increased with smoothing. Smoothed geometries are more suitable for visualisation and 3D printing, as smoothing is a noise filtering procedure, providing a more even topology (Perry et al., 2017).

As both MeshLab and Instant Meshes handle surface geometries it is not possible to import the INP tetrahedral volume meshes from Gmsh. Thus, any errors or inconsistencies will have to be resolved in ABAQUS or another FE solver with appropriate remeshing toolsets. Gmsh also produces only a single type of tetrahedral elements, which is the C3D4, unlike the larger selection in ABAQUS. The alternative pathway is to import an STL file directly into ABAQUS, through the 3D Mesh to Geometry plugin, which will be recognised as an orphan mesh – an FE mesh composed of vertices and elements that exist without an associated geometry. A comparison of the Gmsh and

ABAQUS generated volume meshes will be part of future work. The evaluation can be conducted only in ABAQUS as similarly to the Gmsh INP files the ABAQUS files cannot be transferred and optimised in any of the previous software packages, Gmsh included, as it can export INP files but not import them. Thus, any user-induced errors need to be resolved in ABAQUS. The primary future target is the utilisation of the cell-specific models for FE analysis in ABAQUS, which allows merging and handling of several parts, such as the cytoskeletal components in the same model. Whilst the approach of generating cell-specific components was conducted with a list of specific software, other free-to-use and commercial packages can also be utilised (Table 6.4).

Table 6.4 – Suggestions for possible procedural step software alternatives with listed applications, advantages and disadvantages.

Software	Application	Advantages	Disadvantages
Amira	Surface/Volume rendering	Suitable for tissues; Export directly for FE	Difficult to use; Commercial
FEBio	FE analysis	Tailored for biomechanics; Free	Less wide-spread
FreeCAD	Volume rendering	Free	Slow import into ABAQUS
ImageJ 3D Viewer	Surface Rendering	Free	Less accurate than Imaris
MATLAB	Simplification	Versatility	Requires coding skills; Commercial

### 6.3 Summary, conclusion and future work

Numerical simulations, and FE analysis in particular, are becoming an integral part of biomedical research. In this Chapter, various geometrical modelling software and techniques were implemented to create semi-automatic approaches for producing sample-specific geometrical models of eye globes and cellular components.

A sample-specific bovine eye model with accurate variable thickness was created. Whilst sample-specific FE meshes have been used for years in the ocular biomechanics field, the few cell-specific

models do not take advantage of the capabilities of proper surface triangulation tools, such as Imaris. The work performed and described in this Chapter is the first instance of cell-specific cytoskeletal models with a detailed refinement workflow. Initial geometries are controllably reduced to a specific number of elements and then made isotropic, with further options for smoothing. Summaries of the alterations of the Initial geometry at different simplification steps are provided below (Table 6.5-6.7).

Table 6.5 – Quality assessment of the surface triangulation of complex geometries at different simplification steps in comparison to the Initial geometry. The number of arrows indicates the degree of parameter alteration.

<b>Fibre Triangle</b>	<b>Decimated</b>	<b>Uniform</b>	<b>Smooth</b>
<b>Vertices</b>	↓	↓ ↓	↓ ↓
<b>Elements</b>	▬	↓ ↓	↓ ↓
<b>Area</b>	↑	↓ ↓	↓ ↓ ↓
<b>Volume</b>	↓	↓ ↓	↓ ↓ ↓
<b>Mean AR</b>	↓ ↓	↓ ↓ ↓	↓ ↓ ↓
<b>Worst AR</b>	↓ ↓ ↓	↓ ↓ ↓	↓ ↓ ↓
<b>Gamma</b>	↑	↑ ↑ ↑	↑ ↑ ↑

Legend: Increase ↑ ; Decrease ↓ ; No change ▬

Table 6.6 – Quality assessment of the surface triangulation of simple geometries at different simplification steps in comparison to the Initial geometry. The number of arrows indicates the degree of parameter alteration.

<b>Nucleus Triangle</b>	<b>Decimated</b>	<b>Uniform</b>	<b>Smooth</b>
<b>Vertices</b>			
<b>Elements</b>			
<b>Area</b>			 
<b>Volume</b>			 
<b>Mean AR</b>	 	  	  
<b>Worst AR</b>	  	  	  
<b>Gamma</b>		  	  

Legend: Increase  ; Decrease  ; No change 

Table 6.7 – Quality assessment of the volume mesh of simple geometries at different simplification steps in comparison to the Initial geometry. The number of arrows indicates the degree of parameter alteration.

<b>Nucleus Tetrahedron</b>	<b>Decimated</b>	<b>Uniform</b>	<b>Smooth</b>
<b>Vertices</b>	 		
<b>Elements</b>	 	  	  
<b>Mean AR</b>		 	 
<b>Worst AR</b>	  	  	  
<b>Gamma</b>			

Legend: Increase  ; Decrease  ; No change 

The primary goal of subsequent work will be to build a multiscale model of the eye, by combining the bovine eye geometry model with the cell-specific meshes of bovine scleral fibroblasts and surrounding collagen ECM network. This will be the first model of the eye to unite ECM and cellular biomechanics in numerical analysis. Furthermore, as both the tissue and cell meshes are reconstructions of raw experimental data, this should increase the model’s clinical validity.

Future work also envisions including wide-angle X-ray scattering (WAXS) data of the collagen microarchitecture of bovine sclera as tissue-level layers in the multiscale biomechanical model (Chapter IV) using published methodologies (Zhou et al., 2019a; Zhou et al., 2019b). In addition, the collected WAXS data contains information on total collagen content per recorded point which can then be utilised to represent regions with higher or lower collagen density. This inclusion is of importance for conditions such as myopia, which have indicated a reduction in collagen content in the affected regions.

As the scleral fibroblast deformation to two distinct levels of mechanical load have been collected (Chapter V) and reconstructed as volume meshes they could potentially be used in inverse FE analysis to assess the cell's mechanical properties (Boote et al., 2019). Such physiologically relevant biomechanical models should be better suited for the study of ocular disease with biomechanical aspects, such as glaucoma. Application to other branches of the biomedical field are also open, with the possibility of creating models for both physiological and pathological conditions to identify disease progression (Barreto et al., 2014).

Other potential future work includes splitting the complex geometries into individual fibres, utilising MeshLab, which can then be reconnected in ABAQUS. Another avenue is the use of ImageJ's 3D Viewer (Section 6.2.2.8) and specifying a low initial threshold and a higher resampling factor to an F-actin Z-stack, to render the outer boundaries of the cortical actin network, which should correspond to a representation of the cell's plasma membrane.

# **Chapter VII**

## **General discussion**

Over 1.78 billion people worldwide are affected by vision disorders, which if left unsupervised can escalate and cause permanently diminished sight and blindness (Holden et al., 2016). As vision is the primary human sense, impairing it increases the risk of depression, loss of independence, mobility and social capital, along with incurring a great economic burden globally (Köberlein et al., 2013; Rahman et al., 2013; Choi et al., 2018; Pezzullo et al., 2018). Amongst ocular pathologies, myopia has the most common occurrence, whilst glaucoma is the leading cause of irreversible blindness, with both conditions being associated with alterations in the peripapillary sclera (PPS) extracellular matrix (ECM) microarchitecture (Pijanka et al., 2012; Coudrillier et al., 2015c; Markov et al., 2018).

This work was:

1. The first study to compare the posterior scleral bulk collagen organisation between human normal and highly myopic sclera.
2. The first study to investigate the posterior scleral collagen architecture around the optic nerve in 11 mammalian species and to determine a suitable human analogue for further scleral biomechanical experiments.
3. Able to produce an accurate software tool for analysing fibrillar image data to ascertain depth changes in the bovine PPS collagen microarchitecture.
4. The first study to characterise the behaviour of scleral fibroblasts to different loading conditions and investigate all three main components of the cytoskeleton.
5. The first study to create cell component specific 3D reconstructions with a detailed methodology on their generation and optimisation.

Wide-angle X-ray scattering (WAXS) measurements were conducted to determine the bulk collagen microstructure in seven non-myopic and three highly myopic human posterior sclerae. The WAXS polar vector plots represented the fibrillar collagen distribution, corroborating consistent similarities between non-myopic sclerae. The connective tissue aligned circumferentially around the optic nerve canal, limiting the expansion and in-plane tensile strains in cases of elevated intraocular pressure (IOP) (Girard et al., 2009a; Winkler et al., 2010; Grytz et al., 2011; Pijanka et al., 2012). Lowest anisotropy was exhibited in the superior nasal (SN)

quadrant of the PPS, consistent with previous studies (Pijanka et al., 2012; Coudrillier et al., 2013; Coudrillier et al., 2015b). The highly myopic specimens, however, did not follow this pattern, with a variety of alterations to the collagen fibril architecture observed, including lower anisotropy and an overall more disorganised fibrillar distribution. Thus, it is possible that these structural changes, along with the myopic thinning of the sclera, could contribute to the greater predisposition amongst high myopes for glaucomatous damage to occur at both normal and elevated IOP levels. Whilst the sample size was relatively low, due to limited human sclera availability and allocated Beamline time at the Diamond Light Source, the applied linear mixed-modelling and angular displacement measurements reaffirmed the significance of the myopic sclera differences. A potential avenue for myopic treatment is scleral collagen cross-linking, aiming to reduce the strain experienced by the sclera (Danilov et al., 2008; Campbell et al., 2017; Yuan et al., 2018). As discussed, the cellular component of scleral biomechanics has remained less explored, making it prudent to investigate how the scleral fibroblasts are affected in myopia and high myopia. This would be of key importance, as previous research has shown that the myopic phenotype is underpinned by increased synthesis of collagenases and decreased production of type I collagen (Jones et al., 1996; Gentle et al., 2003; McBrien et al., 2009). Furthermore, *in vitro* experiments outlined in this thesis, mimicking high IOP glaucoma-like *in situ* conditions, revealed changes to cytoskeletal protein organisation in scleral fibroblasts, particularly to F-actin stress fibres, encouraging more investigations into the myopic phenotype (Markov et al., 2019).

WAXS was also enlisted to map the PPS collagen structure of 11 mammalian species in the search of a suitable PPS human analogue to conduct further investigations on. Smaller animals had a less structurally organised collagen fibril arrangement around the optic nerve, making them a suboptimal choice for this kind of biomechanical study (Boote et al., 2019). Bovine PPS were selected based on the close proportional resemblance to the human PPS and affordable access to new tissue samples. Second harmonic generation (SHG) microscopy revealed that the collagen fibril annulus encompasses four-fifths of the stromal depth, whilst in humans it is two-thirds (Pijanka et al., 2015). In addition, the collagen fibrils were most strongly circumferentially orientated in the lateral sides of the optic nerve head (ONH) and least strongly in the superior and inferior regions. As cattle are a commonly used ocular model, this study also provides greater clarity in terms of the scleral collagen microstructure. Elastin content in young individuals is low

and not possible to register using two-photon-excited fluorescence (TPEF). Whilst older animals would have more elastin in the PPS, it needs to be reminded that the eyes were collected from an abattoir, making it unviable to acquire aged tissue samples. However, future experiments could apply SHG and TPEF microscopy to non-myopic and myopic human eyes, specifically in relation to the decreased annular organisation in the SN and other affected regions. Both techniques can also be useful in determining changes to the fibrillar crimp angles, which perhaps increase with the myopic globe axial elongation. Larger amounts of straight fibres might also result in an incapability of the sclera to resist tensile strain at high IOP levels associated with glaucoma. For further assessment of the bulk collagen structural organisation in both human and cattle posterior sclerae, image processing modalities for evaluating fibre density and crimp angle could also be developed and implemented.

In most types of glaucoma, elevated IOP generates tensile force in the scleral wall, affecting both the ECM and the resident cells. The influenced cellular mechanotransduction pathways might lead to a myriad of changes, possibly including even stiffening of the sclera (Kirwan et al., 2004; Strouthidis and Girard, 2013). *In vitro* modelling of the bovine scleral fibroblast response to acute physiological (0.26-1.8%, 1Hz for 1h) and pathological (0.6-4%, 1Hz for 1h) levels of cyclic tensile strain (CTS) showed marked differences. Cells exposed to the physiological regime became elongated and had highly aligned F-actin stress fibres immediately after load, progressively reversing to the unloaded phenotype over a 24h time period. In response to the higher load, however, fibroblasts exhibited an ‘inhibition delay’ in cytoskeletal organisation and at 24h post-CTS were reminiscent of the initial phenotype of the physiologically loaded fibroblasts. In addition, they also had a consistently greater percentage of condensed chromatin in the nuclei. Together, these observations would suggest that normal IOP levels could have an integral role in mechanically regulating the tensional homeostasis and cytoskeletal architecture of the scleral cells. It is possible that under elevated IOP conditions the resulting tensile strain prevents scleral fibroblasts from assuming their *in situ* cytoskeletal organisation, ultimately preventing normal cellular function, as well as synthesis and remodelling of the collagen ECM. This study was also the first to compare scleral fibroblasts at different magnitudes of strain, showing alterations to the three primary components of the cytoskeleton. Microtubules were relatively unresponsive to CTS, with the observed changes being likely a passive response to the whole-cell remodelling.

Mimicking progressive and chronic IOP elevation on scleral fibroblasts can be part of future work, as long as appropriate measures are undertaken to provide nutrition and aeration for a prolonged period of time. If accessible, atomic force microscopy could also be combined with green fluorescent protein labelling to record cytoskeletal remodelling along with stiffness changes in live cells (Kidoaki et al., 2006).

Differentiation into a myofibroblast phenotype in response to applied load may also have occurred but was not measured in the current work. *In vitro* experiments on human scleral fibroblasts previously confirmed that greater exposure to CTS (4%, 5Hz for 24h) induces transition to myofibroblasts (Qu et al., 2015). *In vivo* research on murine experimental glaucoma provided further evidence, along with indication of stimulated cell proliferation (Oglesby et al., 2016). Myofibroblasts were detected in animal myopic models as well, with suggested involvement in reducing the axial length of tree shrew eyes (Phillips and McBrien, 2004). Additionally, the tension generated in the F-actin stress fibres after the pathological CTS could have activated transforming growth factor  $\beta$ 1 (TGF $\beta$ 1), the second essential factor in myofibroblast progression along with mechanical stress (Wipff et al., 2007). Future work could further investigate scleral fibroblast transdifferentiation by assessing the amount of latent and active TGF $\beta$ 1 released from cells exposed to different strain magnitudes by enzyme-linked immunosorbent assay (ELISA). Rearrangements in the underlying type I collagen ECM could also promote differentiation, as stiffer ECM in murine lung fibrosis was noted to induce mechanotransduction pathways that caused reorganisation of the actin cytoskeleton and transition to myofibroblasts (Huang et al., 2012). It is possible that the myofibroblast phenotype is part of the *in situ* scleral cell population and might be necessary for resisting deformational change in high tension glaucoma due to their high contractility. In addition, as the cellular physiology slows down and changes with older age, that could prove to be detrimental in myofibroblast formation, increasing the susceptibility to glaucomatous damage. The noted increase in chromatin condensation for fibroblasts exposed to high strain could also be regulated by TGF $\beta$ 1 signalling (Heo et al., 2016). Furthermore, inhibition of Rho-associated kinase (ROCK) abrogates the TGF $\beta$ 1 myofibroblast differentiation of human PPS fibroblasts (Pitha et al., 2018). Therefore, further research into the role of myofibroblasts in normal and high IOP conditions is encouraged.

This thesis also provides methodological approaches for creating representative and more physiologically accurate finite element (FE) models of intracellular structures. Confocal microscopy recorded scleral fibroblast cytoskeleton and nuclei were 3D reconstructed in Imaris. This was followed by both a reduction in the number of composing elements and a notable step towards uniformity of the mesh. In addition, as the meshes were rendered from experimental imaging data, this makes them possess fewer approximations than current cellular models (Ortizadikario and Gefen, 2011; Ronan et al., 2012; Dowling et al., 2013; Yao et al., 2016). In collaboration with the Biomechanical Engineering Group (University of Liverpool), digital image correlation (DIC) was employed to reconstruct a bovine ocular shell. In future, it is envisaged that the resultant shell model will be combined with the cellular geometries into a multilayer FE model, becoming the first ocular model to take into account both the ECM and cells of the eye. Additional work conceives the implementation of the WAXS and SHG bovine scleral data to represent the regional collagen density, along with possibly the fibrillar angular distribution (Zhou et al., 2019a; Zhou et al., 2019b). Furthermore, as the individual components are based on experimentally collected geometries, this will increase the credibility of the computational results in studying the complex ocular biomechanics. Continuing development and optimisation of these FE models will inform our knowledge of ocular biomechanics and could positively impact the search for future treatments for diseases such as myopia and glaucoma.

The proposed methodology can be applied to other biological structures as well, opening an avenue of potential applications that rely on more physiologically accurate, instead of generic, models. Whilst Imaris admirably reconstructed isolated cellular components, for tissue samples other alternatives, such as Amira, might provide better results. This could be of use in representing the complex architecture of the *lamina cribrosa* (LC) where the high IOP-related glaucomatous damage is concentrated. In addition, Amira also allows for simplification and direct export of stereolithography (STL) and computer-aided design (CAD) files, which can then be imported into ABAQUS or another FE analysis package. Potentially, programming languages and environments, such as Python and MATLAB, could also be utilised in regulating mesh complexity. Furthermore, it would be of use to define boundary conditions, along with size and composition of representative volume elements (RVE), through them. RVE could be generated for both cell and tissue level organisation, to simplify the overall complexity and reduce computational time. However,

inclusion of randomly distributed beam elements is ill-advised for numerous reasons: (I) as illustrated by SHG, collagen fibres in bovine posterior sclerae tend to be organised in closely packed bundles through the whole tissue depth; (II) the bundles complexly interweave with other groups of collagen fibres; (III) collagen crimp is an important factor for scleral biomechanics; (IV) there are variations in the collagen density in different regions of the ocular tunic; (V) the length of the collagen bundles can span a large portion of the ocular tunic (Boote et al., 2019). Thus, the proposed, experimentally-based geometries are a more suitable choice.

As the fibroblast reconstructions are at several time points, it would be beneficial for them to potentially be used as references which can be extrapolated to represent time-dependent cellular rearrangement. Afterwards, inverse FE analysis could be employed to assess the mechanical properties of the different components. Furthermore, as the cytoskeleton is a dynamic structure this modelling of the system could be beneficial in depicting the continuous reorganisation. For standard FE analysis, or confirmations of the inverse one, a list of suggested initial cellular and scleral material properties are provided by previous studies (Smolek, 1988; Gum et al., 1998; Boyce et al., 2008; Litwiller et al., 2010; Myers et al., 2010; Slomka and Gefen, 2010; Slomka et al., 2011; Barreto et al., 2013; Argento et al., 2014; Reynolds and McGarry, 2015). Additionally, it should be noted that most components will need to be modelled as viscoelastic, as otherwise erroneous conclusions about the biomechanical behaviour may be reached (Battaglioli and Kamm, 1984; Kumar et al., 2006; Lu et al., 2008; Boote et al., 2019). This would also necessitate the inclusion of the cytoplasm as mechanical forces are also transferred through it, with, in general, negligible friction with the cytoskeleton (Hu et al., 2003; Kassianidou and Kumar, 2015).

The overall aims of this interdisciplinary thesis were achieved, with the presented work contributing to the greater understanding of scleral biomechanics, along with proposing a fast and more accurate way of creating computational representations of microstructures. Reduction of IOP is not always the most suitable course of action for managing glaucoma, as there are numerous instances of normal-tension glaucoma, with a proportion of high-tension glaucoma patients also not responding to IOP-lowering. Therefore, prospective alternative treatments could first be tested through FE modelling, with the work in this thesis serving as a foundation for future scleral-target studies on glaucoma and myopia.

# **Bibliography**

- Abhilash A, Baker BM, Trappmann B, Chen CS, Shenoy VB (2014) Remodeling of fibrous extracellular matrices by contractile cells: predictions from discrete fiber network simulations. *Biophys J* **107**(8): 1829-1840.
- Albiez H, Cremer M, Tiberi C, Vecchio L, Schermelleh L, Dittrich S, Küpper K, Joffe B, Thormeyer T, von Hase J (2006) Chromatin domains and the interchromatin compartment form structurally defined and functionally interacting nuclear networks. *Chromosome Res* **14**(7): 707-733.
- Albon J, Farrant S, Akhtar S, Young R, Boulton ME, Smith G, Taylor M, Guggenheim J, Morgan JE (2007) Connective tissue structure of the tree shrew optic nerve and associated ageing changes. *Invest Ophthalmol Vis Sci* **48**(5): 2134-2144.
- Albon J, Purslow PP, Karwatowski WS, Easty DL (2000) Age related compliance of the lamina cribrosa in human eyes. *Br J Ophthalmol* **84**(3): 318-323.
- Alenghat FJ, Ingber DE (2002) Mechanotransduction: all signals point to cytoskeleton, matrix, and integrins. *Sci Signal* **2002**(119): 1-4.
- Amano M, Nakayama M, Kaibuchi K (2010) Rho- kinase/ROCK: a key regulator of the cytoskeleton and cell polarity. *Cytoskeleton* **67**(9): 545-554.
- Argento A, Kim W, Rozsa FW, DeBolt KL, Zikanova S, Richards JR (2014) Shear behavior of bovine scleral tissue. *J Biomech Eng-T Asme* **136**(7): 1-12.
- Asenjo AB, Chatterjee C, Tan D, DePaoli V, Rice WJ, Diaz-Avalos R, Silvestry M, Sosa H (2013) Structural model for tubulin recognition and deformation by kinesin-13 microtubule depolymerases. *Cell Rep* **3**(3): 759-768.
- Ayala YA, Pontes B, Hissa B, Monteiro ACM, Farina M, Moura-Neto V, Viana NB, Nussenzveig HM (2017) Effects of cytoskeletal drugs on actin cortex elasticity. *Exp Cell Res* **351**(2): 173-181.
- Ayres C, Bowlin GL, Henderson SC, Taylor L, Shultz J, Alexander J, Telemeco TA, Simpson DG (2006) Modulation of anisotropy in electrospun tissue-engineering scaffolds: Analysis of fiber alignment by the fast Fourier transform. *Biomaterials* **27**(32): 5524-5534.
- Barreto S, Clausen CH, Perrault CM, Fletcher DA, Lacroix D (2013) A multi-structural single cell model of force-induced interactions of cytoskeletal components. *Biomaterials* **34**(26): 6119-6126.

- Barreto S, Perrault CM, Lacroix D (2014) Structural finite element analysis to explain cell mechanics variability. *J Mech Behav Biomed Mater* **38**(1): 219-231.
- Battaglioli J, Kamm R (1984) Measurements of the compressive properties of scleral tissue. *Invest Ophthalmol Vis Sci* **25**(1): 59-65.
- Bees M, Hill N (1997) Wavelengths of bioconvection patterns. *J Exp Bio* **200**(10): 1515-1526.
- Bellezza AJ, Hart RT, Burgoyne CF (2000) The optic nerve head as a biomechanical structure: Initial finite element modeling. *Invest Ophthalmol Vis Sci* **41**(10): 2991-3000.
- Bilderback DH, Elleaume P, Weckert E (2005) Review of third and next generation synchrotron light sources. *J Phys B* **38**(9): 773-797.
- Blain EJ (2009) Involvement of the cytoskeletal elements in articular cartilage homeostasis and pathology. *Int J Exp Pathol* **90**(1): 1-15.
- Boland MV, Ervin A-M, Friedman DS, Jampel HD, Hawkins BS, Vollenweider D, Chelladurai Y, Ward D, Suarez-Cuervo C, Robinson KA (2013) Comparative effectiveness of treatments for open-angle glaucoma: a systematic review for the US Preventive Services Task Force. *Ann Intern Med* **158**(4): 271-279.
- Boote C, Dennis S, Huang Y, Quantock AJ, Meek KM (2005) Lamellar orientation in human cornea in relation to mechanical properties. *J Struct Biol* **149**(1): 1-6.
- Boote C, Palko JR, Sorensen T, Mohammadvali A, Elsheikh A, Komaromy AM, Pan XL, Liu J (2016) Changes in posterior scleral collagen microstructure in canine eyes with an ADAMTS10 mutation. *Mol Vis* **22**(1): 503-517.
- Boote C, Sigal IA, Grytz R, Hua Y, Nguyen TD, Girard MJ (2019) Scleral structure and biomechanics. *Prog Retin Eye Res* **74**: 100773.
- Boudaoud A, Burian A, Borowska-Wykret D, Uyttewaal M, Wrzalik R, Kwiatkowska D, Hamant O (2014) FibrilTool, an ImageJ plug-in to quantify fibrillar structures in raw microscopy images. *Nat Protoc* **9**(2): 457-463.
- Bourne RR, Flaxman SR, Braithwaite T, Cicinelli MV, Das A, Jonas JB, Keeffe J, Kempen JH, Leasher J, Limburg H (2017) Magnitude, temporal trends, and projections of the global prevalence of blindness and distance and near vision impairment: a systematic review and meta-analysis. *Lancet Glob Health* **5**(9): 888-897.
- Boyce BL, Grazier JM, Jones RE, Nguyen TD (2008) Full-field deformation of bovine cornea under constrained inflation conditions. *Biomaterials* **29**(28): 3896-3904.

- Bredfeldt JS, Liu Y, Pehlke CA, Conklin MW, Szulczewski JM, Inman DR, Keely PJ, Nowak RD, Mackie TR, Eliceiri KW (2014) Computational segmentation of collagen fibers from second-harmonic generation images of breast cancer. *J Biomed Opt* **19**(1): 1-11.
- Brisard S, Davy CA, Michot L, Troadec D, Levitz P (2019) Mesoscale pore structure of a high-performance concrete by coupling focused ion beam/scanning electron microscopy and small angle X- ray scattering. *J Am Ceram Soc* **102**(5): 2905-2923.
- Brisseau M (1709) *Traite de la cataracte et du glaucome*. Paris, France: 42-43.
- Brooks DE, Arellano E, Kubilis PS, Komaromy AM (1998) Histomorphometry of the porcine scleral lamina cribrosa surface. *Vet Ophthalmol* **1**(2- 3): 129-135.
- Buehler MJ (2006) Nature designs tough collagen: explaining the nanostructure of collagen fibrils. *Proc Natl Acad Sci USA* **103**(33): 12285-12290.
- Burger W, Burge MJ (2016) *Digital image processing: an algorithmic introduction using Java*. Springer.
- Burgoyne CF, Downs JC (2008) Premise and prediction - how optic nerve head biomechanics underlies the susceptibility and clinical behavior of the aged optic nerve head. *J Glaucoma* **17**(4): 318-328.
- Burkhart TA, Andrews DM, Dunning CE (2013) Finite element modeling mesh quality, energy balance and validation methods: A review with recommendations associated with the modeling of bone tissue. *J Biomech* **46**(9): 1477-1488.
- Burridge K, Wittchen ES (2013) The tension mounts: stress fibers as force-generating mechanotransducers. *J Cell Biol* **200**(1): 9-19.
- Campbell C (1966) Taxonomic status of tree shrews. *Science* **153**(3734): 436-436.
- Campbell IC, Coudrillier B, Mensah J, Abel RL, Ethier CR (2015) Automated segmentation of the lamina cribrosa using Frangi's filter: a novel approach for rapid identification of tissue volume fraction and beam orientation in a trabeculated structure in the eye. *J Royal Soc Interface* **12**(104): 1-9.
- Campbell IC, Coudrillier B, Ross Ethier C (2014) Biomechanics of the posterior eye: a critical role in health and disease. *J Biomech Eng* **136**(2): 1-19.
- Campbell IC, Hannon BG, Read AT, Sherwood JM, Schwaner SA, Ethier CR (2017) Quantification of the efficacy of collagen cross-linking agents to induce stiffening of rat sclera. *J R Soc Interface* **14**(129): 1-9.

- Campbell JJ, Blain EJ, Chowdhury TT, Knight MM (2007) Loading alters actin dynamics and up-regulates cofilin gene expression in chondrocytes. *Biochem Biophys Res Commun* **361**(2): 329-334.
- Campbell R. 2019. raacampbell/sigstar. <https://www.github.com/raacampbell/sigstar>, GitHub.
- Casson RJ, Chidlow G, Wood JPM, Crowston JG, Goldberg I (2012) Definition of glaucoma: clinical and experimental concepts. *Clin Exp Ophthalmol* **40**(4): 341-349.
- Casson RJ, Han G, Ebnetter A, Chidlow G, Glihotra J, Newland H, Wood JP (2014) Glucose-induced temporary visual recovery in primary open-angle glaucoma: a double-blind, randomized study. *Ophthalmology* **121**(6): 1203-1211.
- Cebral JR, Löhner R (2001) From medical images to anatomically accurate finite element grids. *Int J Numer Meth Eng* **51**(8): 985-1008.
- Chang MY, Shin A, Park J, Nagiel A, Lalane RA, Schwartz SD, Demer JL (2017) Deformation of optic nerve head and peripapillary tissues by horizontal duction. *Am J Ophthalmol* **174**: 85-94.
- Changizi MA, Shimojo S (2008) “X-ray vision” and the evolution of forward-facing eyes. *J Theor Biol* **254**(4): 756-767.
- Chansangpetch S, Panpruk R, Manassakorn A, Tantisevi V, Rojanapongpun P, Hurst CP, Lin SC (2017) Impact of myopia on corneal biomechanics in glaucoma and nonglaucoma patients. *Invest Ophthalmol Vis Sci* **58**(12): 4990-4996.
- Chaudhuri O, Parekh SH, Fletcher DA (2007) Reversible stress softening of actin networks. *Nature* **445**(7125): 295-298.
- Chen AC-H, McNeilly C, Liu AP-Y, Flaim CJ, Cuttle L, Kendall M, Kimble RM, Shimizu H, McMillan JR (2011) Second harmonic generation and multiphoton microscopic detection of collagen without the need for species specific antibodies. *Burns* **37**(6): 1001-1009.
- Chen J, Irianto J, Inamdar S, Pravincumar P, Lee D, Bader DL, Knight M (2012a) Cell mechanics, structure, and function are regulated by the stiffness of the three-dimensional microenvironment. *Biophys J* **103**(6): 1188-1197.
- Chen J, Yan W, Setton LA (2004) Static compression induces zonal-specific changes in gene expression for extracellular matrix and cytoskeletal proteins in intervertebral disc cells in vitro. *Matrix Biol* **22**(7): 573-583.

- Chen X, Nadiarynkh O, Plotnikov S, Campagnola PJ (2012b) Second harmonic generation microscopy for quantitative analysis of collagen fibrillar structure. *Nat Protoc* **7**(4): 654-669.
- Chernyatina AA, Nicolet S, Aebi U, Herrmann H, Strelkov SV (2012) Atomic structure of the vimentin central  $\alpha$ -helical domain and its implications for intermediate filament assembly. *Proc Natl Acad Sci U S A* **109**(34): 13620-13625.
- Chinthalapudi K, Heissler SM, Preller M, Sellers JR, Manstein DJ (2017) Mechanistic insights into the active site and allosteric communication pathways in human nonmuscle myosin-2C. *Elife* **6**(1): 1-40.
- Chiquet M, Gelman L, Lutz R, Maier S (2009) From mechanotransduction to extracellular matrix gene expression in fibroblasts. *BBA-Mol Cell Res* **1793**(5): 911-920.
- Choi HG, Lee MJ, Lee S-M (2018) Visual impairment and risk of depression: A longitudinal follow-up study using a national sample cohort. *Sci Rep* **8**(2083): 1-8.
- Chuang J-Y, Wang Y-T, Yeh S-H, Liu Y-W, Chang W-C, Hung J-J (2008) Phosphorylation by c-Jun NH2-terminal kinase 1 regulates the stability of transcription factor Sp1 during mitosis. *Mol Biol Cell* **19**(3): 1139-1151.
- Cicchi R, Kapsokalyvas D, De Giorgi V, Maio V, Van Wiechen A, Massi D, Lotti T, Pavone FS (2010) Scoring of collagen organization in healthy and diseased human dermis by multiphoton microscopy. *J Biophotonics* **3**(1): 34-43.
- Cignoni P, Callieri M, Corsini M, Dellepiane M, Ganovelli F, Ranzuglia G (2008) Meshlab: an open-source mesh processing tool. *Eurographics Italian chapter conference*. 129-136.
- Clemons TD, Bradshaw M, Toshniwal P, Chaudhari N, Stevenson AW, Lynch J, Fear MW, Wood FM, Iyer KS (2018) Coherency image analysis to quantify collagen architecture: implications in scar assessment. *RSC Adv* **8**(18): 9661-9669.
- Conchello J-A, Lichtman JW (2005) Optical sectioning microscopy. *Nat Methods* **2**(12): 920-931.
- Cook J (1976) The Zernike polynomials. *J Mod Opt* **23**(8): 679-680.
- Costigliola N, Ding L, Burckhardt CJ, Han SJ, Gutierrez E, Mota A, Groisman A, Mitchison TJ, Danuser G (2017) Vimentin fibers orient traction stress. *Proc Natl Acad Sci USA* **114**(20): 5195-5200.

- Coudrillier B, Boote C, Quigley HA, Nguyen TD (2013) Scleral anisotropy and its effects on the mechanical response of the optic nerve head. *Biomech Model Mechanobiol* **12**(5): 941-963.
- Coudrillier B, Pijanka J, Jefferys J, Sorensen T, Quigley HA, Boote C, Nguyen TD (2015a) Collagen structure and mechanical properties of the human sclera: Analysis for the effects of age. *J Biomech Eng-T Asme* **137**(4): 1-14.
- Coudrillier B, Pijanka J, Jefferys J, Sorensen T, Quigley HA, Boote C, Nguyen TD (2015b) Effects of age and diabetes on scleral stiffness. *J Biomech Eng-T Asme* **137**(7): 1-10.
- Coudrillier B, Pijanka JK, Jefferys JL, Goel A, Quigley HA, Boote C, Nguyen TD (2015c) Glaucoma-related changes in the mechanical properties and collagen micro-architecture of the human sclera. *Plos One* **10**(7): 1-21.
- Coudrillier B, Tian J, Alexander S, Myers KM, Quigley HA, Nguyen TD (2012) Biomechanics of the human posterior sclera: Age- and glaucoma-related changes measured using inflation testing. *Invest Ophthalmol Vis Sci* **53**(4): 1714-1728.
- Cramer LP, Siebert M, Mitchison TJ (1997) Identification of novel graded polarity actin filament bundles in locomoting heart fibroblasts: implications for the generation of motile force. *J Cell Biol* **136**(6): 1287-1305.
- Craver BM, Acharya MM, Allen BD, Benke SN, Hultgren NW, Baulch JE, Limoli CL (2016) 3D surface analysis of hippocampal microvasculature in the irradiated brain. *Environ Mol Mutagen* **57**(5): 341-349.
- Cui D, Trier K, Chen X, Zeng J, Yang X, Hu J, Ge J (2008) Distribution of adenosine receptors in human sclera fibroblasts. *Mol Vis* **14**(1): 523.
- Cui W, Bryant MR, Sweet PM, McDonnell PJ (2004) Changes in gene expression in response to mechanical strain in human scleral fibroblasts. *Exp Eye Res* **78**(2): 275-284.
- Cui YH, Huang JF, Cheng SY, Wei W, Shang L, Li N, Xiong K (2015) Study on establishment and mechanics application of finite element model of bovine eye. *Bmc Ophthalmol* **15**: 1-16.
- Curtin BJ, Iwamoto T, Renaldo DP (1979) Normal and staphylomatous sclera of high myopia: an electron microscopic study. *Arch Ophthalmol* **97**(5): 912-915.

- Daghma DES, Malhan D, Simon P, Stötzel S, Kern S, Hassan F, Lips KS, Heiss C, El Khassawna T (2018) Computational segmentation of collagen fibers in bone matrix indicates bone quality in ovariectomized rat spine. *J Bone Miner Metab* **36**(3): 297-306.
- Dailey HL, Ricles LM, Yalcin HC, Ghadiali SN (2009) Image-based finite element modeling of alveolar epithelial cell injury during airway reopening. *J Appl Physiol* **106**(1): 221-232.
- Danford FL, Yan DM, Dreier RA, Cahir TM, Girkin CA, Vande Geest JP (2013) Differences in the region- and depth-dependent microstructural organization in normal versus glaucomatous human posterior sclerae. *Invest Ophthalmol Vis Sci* **54**(13): 7922-7932.
- Danilov NA, Ignatieva NY, Iomdina EN, Semenova SA, Rudenskaya GN, Grokhovskaya TE, Lunin VV (2008) Stabilization of scleral collagen by glycerol aldehyde cross-linking. *Biochim Biophys Acta* **1780**(5): 764-772.
- Danowski BA (1989) Fibroblast contractility and actin organization are stimulated by microtubule inhibitors. *J Cell Sci* **93**(2): 255-266.
- Darzynkiewicz Z, Galkowski D, Zhao H (2008) Analysis of apoptosis by cytometry using TUNEL assay. *methods* **44**(3): 250-254.
- Deepak V, Kayastha P, McNamara LM (2017) Estrogen deficiency attenuates fluid flow–induced  $[Ca^{2+}]_i$  oscillations and mechanoresponsiveness of MLO-Y4 osteocytes. *FASEB J* **31**(7): 3027-3039.
- Deguchi S, Ohashi T, Sato M (2006) Tensile properties of single stress fibers isolated from cultured vascular smooth muscle cells. *J Biomech* **39**(14): 2603-2610.
- deLuise VP, Anderson DR (1983) Primary infantile glaucoma (congenital glaucoma). *Surv Ophthalmol* **28**(1): 1-19.
- Demer JL (2016) Optic nerve sheath as a novel mechanical load on the globe in ocular ductation. *Invest Ophthalmol Vis Sci* **57**(4): 1826-1838.
- Deshpande VS, McMeeking RM, Evans AG (2006) A bio-chemo-mechanical model for cell contractility. *Proc Natl Acad Sci USA* **103**(38): 14015-14020.
- Di Y, Li M-Y, Qiao T, Lu N (2017) Edge detection and mathematic fitting for corneal surface with Matlab software. *Int J Ophthalmol* **10**(3): 336.
- Dolgin E (2015) The myopia boom. *Nature* **519**(7543): 276-278.

- Dombeck DA, Kasischke KA, Vishwasrao HD, Ingelsson M, Hyman BT, Webb WW (2003) Uniform polarity microtubule assemblies imaged in native brain tissue by second-harmonic generation microscopy. *Proc Natl Acad Sci U S A* **100**(12): 7081-7086.
- Dowling EP, Ronan W, McGarry JP (2013) Computational investigation of in situ chondrocyte deformation and actin cytoskeleton remodelling under physiological loading. *Acta Biomater* **9**(4): 5943-5955.
- Dowling EP, Ronan W, Ofek G, Deshpande VS, McMeeking RM, Athanasiou KA, McGarry JP (2012) The effect of remodelling and contractility of the actin cytoskeleton on the shear resistance of single cells: a computational and experimental investigation. *J Royal Soc Interface* **9**(77): 3469-3479.
- Downs JC, Burgoyne CF, Seigfreid WP, Reynaud JF, Strouthidis NG, Sallee V (2011) 24-hour IOP telemetry in the nonhuman primate: Implant system performance and initial characterization of IOP at multiple timescales. *Invest Ophthalmol Vis Sci* **52**(10): 7365-7375.
- Downs JC, Roberts MD, Burgoyne CF (2008) The mechanical environment of the optic nerve head in glaucoma. *Optom Vis Sci* **85**(6): 425-435.
- Drews RC (2006) Green cataract. *Arch Ophthalmol* **124**(4): 579-586.
- Drifka CR, Loeffler AG, Mathewson K, Mehta G, Keikhosravi A, Liu Y, Lemancik S, Ricke WA, Weber SM, Kao WJ (2016) Comparison of picosirius red staining with second harmonic generation imaging for the quantification of clinically relevant collagen fiber features in histopathology samples. *J Histochem Cytochem* **64**(9): 519-529.
- Edwards ME, Wang SSS, Good TA (2001) Role of viscoelastic properties of differentiated SH-SY5Y human neuroblastoma cells in cyclic shear stress injury. *Biotechnol Prog* **17**(4): 760-767.
- Erickson HP, O'Brien ET (1992) Microtubule dynamic instability and GTP hydrolysis. *Annu Rev Biophys Biomol Struct* **21**(1): 145-166.
- Fazio MA, Grytz R, Morris JS, Bruno L, Gardiner SK, Girkin CA, Downs JC (2014) Age-related changes in human peripapillary scleral strain. *Biomech Model Mechanobiol* **13**(3): 551-563.

- Feola AJ, Coudrillier B, Mulvihill J, Geraldles DM, Vo NT, Albon J, Abel RL, Samuels BC, Ethier CR (2017) Deformation of the lamina cribrosa and optic nerve due to changes in cerebrospinal fluid pressure. *Invest Ophthalmol Vis Sci* **58**(4): 2070-2078.
- Fletcher DA, Mullins RD (2010) Cell mechanics and the cytoskeleton. *Nature* **463**(7280): 485-492.
- Flores-Moreno I, Lugo F, Duker JS, Ruiz-Moreno JM (2013) The relationship between axial length and choroidal thickness in eyes with high myopia. *Am J Ophthalmol* **155**(2): 314-319.
- Fuchs E, Cleveland DW (1998) A structural scaffolding of intermediate filaments in health and disease. *Science* **279**(5350): 514-519.
- Fujiwara T, Imamura Y, Margolis R, Slakter JS, Spaide RF (2009) Enhanced depth imaging optical coherence tomography of the choroid in highly myopic eyes. *Am J Ophthalmol* **148**(3): 445-450.
- Gan SD, Patel KR (2013) Enzyme immunoassay and enzyme-linked immunosorbent assay. *J Invest Dermatol* **133**(9): 1-3.
- Garbino GST, Rezende GC, Valladares-Padua C (2016) Pelage variation and distribution of the black lion tamarin, *Leontopithecus chrysopygus*. *Folia Primatol* **87**(4): 244-261.
- Garcia M, Knight MM (2010) Cyclic loading opens hemichannels to release ATP as part of a chondrocyte mechanotransduction pathway. *J Orthop Res* **28**(4): 510-515.
- Garland M, Heckbert PS (1998) Simplifying surfaces with color and texture using quadric error metrics. *Proceedings Visualization'98 (Cat. No. 98CB36276)*. IEEE: 263-269.
- Gavara N, Chadwick RS (2016) Relationship between cell stiffness and stress fiber amount, assessed by simultaneous atomic force microscopy and live-cell fluorescence imaging. *Biomech Model Mechanobiol* **15**(3): 511-523.
- Gentle A, Liu Y, Martin JE, Conti GL, McBrien NA (2003) Collagen gene expression and the altered accumulation of scleral collagen during the development of high myopia. *J Biomech Eng* **278**(19): 16587-16594.
- Geraghty B, Jones SW, Rama P, Akhtar R, Elsheikh A (2012) Age-related variations in the biomechanical properties of human sclera. *J Mech Behav Biomed Mater* **16**(1): 181-191.
- Geroski DH, Edelhauser HF (2001) Transscleral drug delivery for posterior segment disease. *Adv Drug Deliver Rev* **52**(1): 37-48.

- Geuzaine C, Remacle JF (2009) Gmsh: A 3-D finite element mesh generator with built- in pre- and post- processing facilities. *Int J Numer Methods Eng* **79**(11): 1309-1331.
- Girard M, Suh J-KF, Hart RT, Burgoyne CF, Downs JC (2007) Effects of storage time on the mechanical properties of rabbit peripapillary sclera after enucleation. *Curr Eye Res* **32**(5): 465-470.
- Girard MJA, Dahlmann-Noor A, Rayapureddi S, Bechara JA, Bertin BME, Jones H, Albon J, Khaw PT, Ethier CR (2011) Quantitative mapping of scleral fiber orientation in normal rat eyes. *Invest Ophthalmol Vis Sci* **52**(13): 9684-9693.
- Girard MJA, Downs JC, Bottlang M, Burgoyne CF, Suh JKF (2009a) Peripapillary and posterior scleral mechanics-Part II: Experimental and inverse finite element characterization. *J Biomech Eng-T Asme* **131**(5): 1-10.
- Girard MJA, Downs JC, Burgoyne CF, Suh JKF (2008) Experimental surface strain mapping of porcine peripapillary sclera due to elevations of intraocular pressure. *J Biomech Eng-T Asme* **130**(4): 1-6.
- Girard MJA, Downs JC, Burgoyne CF, Suh JKF (2009b) Peripapillary and posterior scleral mechanics-Part I: Development of an anisotropic hyperelastic constitutive model. *J Biomech Eng-T Asme* **131**(5): 1-9.
- Girard MJA, Suh JKF, Bottlang M, Burgoyne CF, Downs JC (2009c) Scleral biomechanics in the aging monkey eye. *Invest Ophthalmol Vis Sci* **50**(11): 5226-5237.
- Goffin JM, Pittet P, Csucs G, Lussi JW, Meister J-J, Hinz B (2006) Focal adhesion size controls tension-dependent recruitment of  $\alpha$ -smooth muscle actin to stress fibers. *J Cell Biol* **172**(2): 259-268.
- Gogola A, Jan N-J, Brazile B, Lam P, Lathrop KL, Chan KC, Sigal IA (2018a) Spatial patterns and age-related changes of the collagen crimp in the human cornea and sclera. *Invest Ophthalmol Vis Sci* **59**(7): 2987-2998.
- Gogola A, Jan N-J, Lathrop KL, Sigal IA (2018b) Radial and circumferential collagen fibers are a feature of the peripapillary sclera of human, monkey, pig, cow, goat, and sheep. *Invest Ophthalmol Vis Sci* **59**(12): 4763-4774.
- Goldschmidt E, Jacobsen N (2014) Genetic and environmental effects on myopia development and progression. *Eye* **28**(2): 126-133.

- Gore S, García ES, Hendrickx PM, Gutmanas A, Westbrook JD, Yang H, Feng Z, Baskaran K, Berrisford JM, Hudson BP (2017) Validation of structures in the Protein Data Bank. *Structure* **25**(12): 1916-1927.
- Gottlieb D, Shu C-W (1997) On the Gibbs phenomenon and its resolution. *SIAM Rev* **39**(4): 644-668.
- Grytz R, Fazio MA, Libertiaux V, Bruno L, Gardiner S, Girkin CA, Downs JC (2014) Age- and race-related differences in human scleral material properties. *Invest Ophthalmol Vis Sci* **55**(12): 8163-8172.
- Grytz R, Meschke G, Jonas JB (2011) The collagen fibril architecture in the lamina cribrosa and peripapillary sclera predicted by a computational remodeling approach. *Biomech Model Mechanobiol* **10**(3): 371-382.
- Grytz R, Siegwart JT (2015) Changing material properties of the tree shrew sclera during minus lens compensation and recovery. *Invest Ophthalmol Vis Sci* **56**(3): 2065-2078.
- Grytz R, Sigal IA, Ruberti JW, Meschke G, Downs JC (2012) Lamina cribrosa thickening in early glaucoma predicted by a microstructure motivated growth and remodeling approach. *Mech Mater* **44**: 99-109.
- Guérette D, Khan PA, Savard PE, Vincent M (2007) Molecular evolution of type VI intermediate filament proteins. *BMC Evol Biol* **7**(164): 1-10.
- Guggenheim JA, McBrien NA (1996) Form-deprivation myopia induces activation of scleral matrix metalloproteinase-2 in tree shrew. *Invest Ophthalmol Vis Sci* **37**(7): 1380-1395.
- Gum G, Gelatt K, Miller D, Mackay E (1998) Intraocular pressure in normal dairy cattle. *Vet Ophthalmol* **1**(2- 3): 159-161.
- Hakkinen KM, Harunaga JS, Doyle AD, Yamada KM (2010) Direct comparisons of the morphology, migration, cell adhesions, and actin cytoskeleton of fibroblasts in four different three-dimensional extracellular matrices. *Tissue Eng Part A* **17**(5-6): 713-724.
- Han M, Giese G, Bille JF (2005) Second harmonic generation imaging of collagen fibrils in cornea and sclera. *Opt Express* **13**(15): 5791-5797.
- Hanley CJ, Noble F, Ward M, Bullock M, Drifka C, Mellone M, Manousopoulou A, Johnston HE, Hayden A, Thirdborough S, Liu Y, Smith DM, Mellows T, Kao WJ, Garbis SD, Mirnezami A, Underwood TJ, Eliceiri KW, Thomas GJ (2015) A subset of

- myofibroblastic cancer-associated fibroblasts regulate collagen fiber elongation, which is prognostic in multiple cancers. *Oncotarget* **7**(5): 6159-6174.
- Hardy É, Levy A, Métris G, Rodrigues M, Touboul P (2013) Determination of the equivalence principle violation signal for the microscope space mission: Optimization of the signal processing. *Space Sci Rev* **180**(1-4): 177-191.
- Harman RM, Bihun IV, Van de Walle GR (2017) Secreted factors from equine mesenchymal stromal cells diminish the effects of TGF- $\beta$ 1 on equine dermal fibroblasts and alter the phenotype of dermal fibroblasts isolated from cutaneous fibroproliferative wounds. *Wound Repair Regen* **25**(2): 234-247.
- Harper AR, Summers JA (2015) The dynamic sclera: Extracellular matrix remodeling in normal ocular growth and myopia development. *Exp Eye Res* **133**(1): 100-111.
- Hayreh SS (2001) Blood flow in the optic nerve head and factors that may influence it. *Prog Retin Eye Res* **20**(5): 595-624.
- Hayward C, Brock DJ (1997) Fibrillin- 1 mutations in Marfan syndrome and other type- 1 fibrillinopathies. *Hum Mutat* **10**(6): 415-423.
- Henriksson JT, McDermott AM, Bergmanson JPG (2009) Dimensions and morphology of the cornea in three strains of mice. *Invest Ophthalmol Vis Sci* **50**(8): 3648-3654.
- Henson FMD, Vincent TA (2008) Alterations in the vimentin cytoskeleton in response to single impact load in an in vitro model of cartilage damage in the rat. *Bmc Musculoskelet Disord* **9**(1): 1-10.
- Heo S-J, Han WM, Szczesny SE, Cosgrove BD, Elliott DM, Lee DA, Duncan RL, Mauck RL (2016) Mechanically induced chromatin condensation requires cellular contractility in mesenchymal stem cells. *Biophys J* **111**(4): 864-874.
- Herrmann H, Aebi U (2000) Intermediate filaments and their associates: multi-talented structural elements specifying cytoarchitecture and cytodynamics. *Curr Opin Cell Biol* **12**(1): 79-90.
- Hesse M, Magin TM, Weber K (2001) Genes for intermediate filament proteins and the draft sequence of the human genome: novel keratin genes and a surprisingly high number of pseudogenes related to keratin genes 8 and 18. *J Cell Sci* **114**(14): 2569-2575.

- Hinz B, Dugina V, Ballestrem C, Wehrle-Haller B, Chaponnier C (2003) Alpha-smooth muscle actin is crucial for focal adhesion maturation in myofibroblasts. *Mol Biol Cell* **14**(6): 2508-2519.
- Hinz B, Phan SH, Thannickal VJ, Galli A, Bochaton-Piallat M-L, Gabbiani G (2007) The myofibroblast: one function, multiple origins. *Am J Pathol* **170**(6): 1807-1816.
- Hogan M, JA A, JE W (1971) Histology of the human eye. Philadelphia: WB Saunders.
- Holden B, Sankaridurg P, Smith E, Aller T, Jong M, He M (2014) Myopia, an underrated global challenge to vision: where the current data takes us on myopia control. *Eye* **28**(2): 142-146.
- Holden BA, Fricke TR, Wilson DA, Jong M, Naidoo KS, Sankaridurg P, Wong TY, Naduvilath TJ, Resnikoff S (2016) Global prevalence of myopia and high myopia and temporal trends from 2000 through 2050. *Ophthalmology* **123**(5): 1036-1042.
- Homan KA, Gupta N, Kroll KT, Kolesky DB, Skylar-Scott M, Miyoshi T, Mau D, Valerius MT, Ferrante T, Bonventre JV (2019) Flow-enhanced vascularization and maturation of kidney organoids in vitro. *Nat Methods* **16**(3): 255-262.
- Hovden R, Jiang Y, Xin HL, Kourkoutis LF (2015) Periodic artifact reduction in fourier transforms of full field atomic resolution images. *Microsc Microanal* **21**(2): 436-441.
- Hu S, Chen J, Fabry B, Numaguchi Y, Gouldstone A, Ingber DE, Fredberg JJ, Butler JP, Wang N (2003) Intracellular stress tomography reveals stress focusing and structural anisotropy in cytoskeleton of living cells. *Am J Physiol-Cell Ph* **285**(5): 1082-1090.
- Huang X, Yang N, Fiore VF, Barker TH, Sun Y, Morris SW, Ding Q, Thannickal VJ, Zhou Y (2012) Matrix stiffness-induced myofibroblast differentiation is mediated by intrinsic mechanotransduction. *Am J Respir Cell Mol Biol* **47**(3): 340-348.
- Hurvich CM, Tsai C-L (1989) Regression and time series model selection in small samples. *Biometrika* **76**(2): 297-307.
- Hutson HN, Marohl T, Anderson M, Eliceiri K, Campagnola P, Masters KS (2016) Calcific aortic valve disease is associated with layer-specific alterations in collagen architecture. *Plos One* **11**(9): 1-18.
- Hyysalo A, Ristola M, Joki T, Honkanen M, Vippola M, Narkilahti S (2017) Aligned poly( $\epsilon$ -caprolactone) nanofibers guide the orientation and migration of human pluripotent stem

- cell-derived neurons, astrocytes, and oligodendrocyte precursor cells in vitro. *Macromol Biosci* **17**(7): 1-8.
- Idowu BD, Knight MM, Bader DL, Lee DA (2000) Confocal analysis of cytoskeletal organisation within isolated chondrocyte sub-populations cultured in agarose. *Histochem J* **32**(3): 165-174.
- Ingber DE (2008) Tensegrity-based mechanosensing from macro to micro. *Prog Biophys Mol Biol* **97**(2): 163-179.
- Ingber DE, Wang N, Stamenović D (2014) Tensegrity, cellular biophysics, and the mechanics of living systems. *Rep Prog Phys* **77**(4): 1-42.
- Irianto J, Lee DA, Knight MM (2014) Quantification of chromatin condensation level by image processing. *Med Eng Phys* **36**(3): 412-417.
- Irianto J, Swift J, Martins RP, McPhail GD, Knight MM, Discher DE, Lee DA (2013) Osmotic challenge drives rapid and reversible chromatin condensation in chondrocytes. *Biophys J* **104**(4): 759-769.
- Jaalouk DE, Lammerding J (2009) Mechanotransduction gone awry. *Nat Rev Mol Cell Biol* **10**(1): 63-73.
- Jackson WM, Jaasma MJ, Tang RY, Keaveny TM (2008) Mechanical loading by fluid shear is sufficient to alter the cytoskeletal composition of osteoblastic cells. *Am J Physiol-Cell Ph* **295**(4): 1007-1015.
- Jakob W, Tarini M, Panozzo D, Sorkine-Hornung O (2015) Instant field-aligned meshes. *ACM Trans Graph* **34**(6): 189:181-189:115.
- Jan N-J, Brazile BL, Hu D, Grube G, Wallace J, Gogola A, Sigal IA (2018) Crimp around the globe; patterns of collagen crimp across the corneoscleral shell. *Exp Eye Res* **172**(1): 159-170.
- Jan N-J, Lathrop K, Sigal IA (2017) Collagen architecture of the posterior pole: High-resolution wide field of view visualization and analysis using polarized light microscopy posterior pole collagen architecture. *Invest Ophthalmol Vis Sci* **58**(2): 735-744.
- Janmey PA, Euteneuer U, Traub P, Schliwa M (1991) Viscoelastic properties of vimentin compared with other filamentous biopolymer networks. *J Cell Biol* **113**(1): 155-160.
- Jansen K, Atherton P, Ballestrem C (2017) Mechanotransduction at the cell-matrix interface. *Semin Cell Dev Biol*. Elsevier: 75-83.

- Jensen EC (2013) Quantitative analysis of histological staining and fluorescence using ImageJ. *Anat Rec* **296**(3): 378-381.
- Jia X, Yu J, Liao S-H, Duan X-C (2016) Biomechanics of the sclera and effects on intraocular pressure. *Int J Ophthalmol* **9**(12): 1824-1831.
- Jiaa X, Liaob S, Duana X, Zhengb W, Zoub B, Duan X (2016) Anisotropic finite element modeling based on a harmonic field for patient-specific sclera. *BioMed Res Int*:
- Jin Y, Wang X, Zhang L, Jonas JB, Aung T, Schmetterer L, Girard MJ (2018) Modeling the origin of the ocular pulse and its impact on the optic nerve head. *Invest Ophthalmol Vis Sci* **59**(10): 3997-4010.
- Jiu Y, Peränen J, Schaible N, Cheng F, Eriksson JE, Krishnan R, Lappalainen P (2017) Vimentin intermediate filaments control actin stress fiber assembly through GEF-H1 and RhoA. *J Cell Sci* **130**(5): 892-902.
- Johnson J, Young T, Rada J (2006) Small leucine rich repeat proteoglycans (SLRPs) in the human sclera: Identification of abundant levels of PRELP. *Mol Vis* **12**(119-21): 1057-1066.
- Jonas JB, Dai Y, Panda-Jonas S (2016) Peripapillary suprachoroidal cavitation, parapapillary gamma zone and optic disc rotation due to the biomechanics of the optic nerve dura mater. *Invest Ophthalmol Vis Sci* **57**(10): 4373-4373.
- Jonas JB, Fang Y, Weber P, Ohno-Matsui K (2018) Parapapillary gamma and delta zones in high myopia. *Retina* **38**(5): 931-938.
- Jonas JB, Gusek GC, Naumann GO (1988) Optic disk morphometry in high myopia. *Graefes Arch Clin Exp Ophthalmol* **226**(6): 587-590.
- Jonas JB, Holbach L, Panda-Jonas S (2013) Peripapillary arterial circle of Zinn-Haller: Location and spatial relationships with myopia. *Plos One* **8**(11): 1-8.
- Jonas JB, Jonas SB, Jonas RA, Holbach L, Dai Y, Sun X, Panda-Jonas S (2012) Parapapillary atrophy: histological gamma zone and delta zone. *Plos One* **7**(10): 1-7.
- Jonas JB, Xu L (2014) Histological changes of high axial myopia. *Eye* **28**(2): 113-117.
- Jones BE, Thompson EW, Hodos W, Waldbillig R, Chader GJ (1996) Scleral matrix metalloproteinases, serine proteinase activity and hydrational capacity are increased in myopia induced by retinal image degradation. *Exp Eye Res* **63**(4): 369-381.

- Jones H, Girard M, White N, Fautsch MP, Morgan J, Ethier C, Albon J (2015) Quantitative analysis of three-dimensional fibrillar collagen microstructure within the normal, aged and glaucomatous human optic nerve head. *J R Soc Interface* **12**(106): 1-12.
- Kartasalo K, Pölönen R-P, Ojala M, Rasku J, Lekkala J, Aalto-Setälä K, Kallio P (2015) CytoSpectre: a tool for spectral analysis of oriented structures on cellular and subcellular levels. *BMC bioinformatics* **16**(344): 1-23.
- Kassianidou E, Kumar S (2015) A biomechanical perspective on stress fiber structure and function. *Biochim Biophys Acta Mol Cell Res* **1853**(11): 3065-3074.
- Kato H, Kano Y, Amano M, Kaibuchi K, Fujiwara K (2001) Stress fiber organization regulated by MLCK and Rho-kinase in cultured human fibroblasts. *Am J Physiol Cell Physiol* **280**(6): 1669-1679.
- Kaverina I, Krylyshkina O, Beningo K, Anderson K, Wang Y-L, Small JV (2002) Tensile stress stimulates microtubule outgrowth in living cells. *J Cell Sci* **115**(11): 2283-2291.
- Kazhdan M, Hoppe H (2013) Screened poisson surface reconstruction. *ACM Trans Graph* **32**(3): 29-41.
- Keeley FW, Morin JD, Vesely S (1984) Characterization of collagen from normal human sclera. *Exp Eye Res* **39**(5): 533-542.
- Kidoaki S, Matsuda T, Yoshikawa K (2006) Relationship between apical membrane elasticity and stress fiber organization in fibroblasts analyzed by fluorescence and atomic force microscopy. *Biomech Model Mechanobiol* **5**(4): 263-272.
- Kim J-A, Kim T-W, Weinreb RN, Lee EJ, Girard MJ, Mari JM (2018) Lamina cribrosa morphology predicts progressive retinal nerve fiber layer loss in eyes with suspected glaucoma. *Sci Rep* **8**(1): 1-10.
- Kirwan RP, Crean JK, Fenerty CH, Clark AF, O'Brien CJ (2004) Effect of cyclical mechanical stretch and exogenous transforming growth factor- $\beta$ 1 on matrix metalloproteinase-2 activity in lamina cribrosa cells from the human optic nerve head. *J Glaucoma* **13**(4): 327-334.
- Kiss N, Haluszka D, Lőrincz K, Gyöngyösi N, Bozsányi S, Bánvölgyi A, Szipöcs R, Wikonkál N (2018) Quantitative analysis on ex vivo nonlinear microscopy images of basal cell carcinoma samples in comparison to healthy skin. *Pathol Oncol Res* **6**(1): 1-7.

- Klein B, Klein R, Linton K (1992) Intraocular pressure in an American community. The Beaver Dam Eye Study. *Invest Ophthalmol Vis Sci* **33**(7): 2224-2228.
- Köberlein J, Beifus K, Schaffert C, Finger RP (2013) The economic burden of visual impairment and blindness: a systematic review. *BMJ open* **3**(11): 1-14.
- Komai Y, Ushiki T (1991) The three-dimensional organization of collagen fibrils in the human cornea and sclera. *Invest Ophthalmol Vis Sci* **32**(8): 2244-2258.
- Kramer RZ, Bella J, Mayville P, Brodsky B, Berman HM (1999) Sequence dependent conformational variations of collagen triple-helical structure. *Nat Struct Mol Biol* **6**(5): 454-457.
- Kuboki T, Kantawong F, Burchmore R, Dalby MJ, Kidoaki S (2012) 2D-DIGE proteomic analysis of mesenchymal stem cell cultured on the elasticity-tunable hydrogels. *Cell Struct Funct* **37**(2): 127-139.
- Kumar S, Maxwell IZ, Heisterkamp A, Polte TR, Lele TP, Salanga M, Mazur E, Ingber DE (2006) Viscoelastic retraction of single living stress fibers and its impact on cell shape, cytoskeletal organization, and extracellular matrix mechanics. *Biophys J* **90**(10): 3762-3773.
- Laios K, Moschos MM, Androustos G (2016) Glaucoma and the origins of its name. *J Glaucoma* **25**(5): 507-508.
- Langham ME, Farrell RA, O'Brien V, Silver DM, Schilder P (1989) Blood flow in the human eye. *Acta Ophthalmol* **67**(191): 9-13.
- Lawlor M, Kerridge I (2014) Understanding selective refusal of eye donation. *J Bioethical Inq* **11**(1): 57-64.
- Lawlor M, Kerridge I, Ankeny R, Dobbins T, Billson F (2010) Specific unwillingness to donate eyes: the impact of disfigurement, knowledge and procurement on corneal donation. *Am J Transplant* **10**(3): 657-663.
- Lazarides E, Burridge K (1975)  $\alpha$ -Actinin: immunofluorescent localization of a muscle structural protein in nonmuscle cells. *Cell* **6**(3): 289-298.
- Leske MC, Connell A, Schachat AP, Hyman L (1994) The Barbados Eye Study: prevalence of open angle glaucoma. *Arch Ophthalmol* **112**(6): 821-829.

- Lewis PN, Pinali C, Young RD, Meek KM, Quantock AJ, Knupp C (2010) Structural interactions between collagen and proteoglycans are elucidated by three-dimensional electron tomography of bovine cornea. *Structure* **18**(2): 239-245.
- Li S, Jia X, Duance VC, Blain EJ (2011) The effects of cyclic tensile strain on the organisation and expression of cytoskeletal elements in bovine intervertebral disc cells: an in vitro study. *Eur Cell Mater* **21**(1): 508-522.
- Lichtman JW, Conchello J-A (2005) Fluorescence microscopy. *Nat Methods* **2**(12): 910-919.
- Ling YTT, Shi R, Midgett DE, Jefferys JL, Quigley HA, Nguyen TD (2019) Characterizing the collagen network structure and pressure-induced strains of the human lamina cribrosa. *Invest Ophthalmol Vis Sci* **60**(7): 2406-2422.
- Litwiller DV, Lee SJ, Kolipaka A, Mariappan YK, Glaser KJ, Pulido JS, Ehman RL (2010) MR elastography of the ex vivo bovine globe. *J Magn Reson Imaging* **32**(1): 44-51.
- Liu F, Mih JD, Shea BS, Kho AT, Sharif AS, Tager AM, Tschumperlin DJ (2010) Feedback amplification of fibrosis through matrix stiffening and COX-2 suppression. *J Cell Biol* **190**(4): 693-706.
- Liu Y, Keikhosravi A, Mehta GS, Drifka CR, Eliceiri KW. 2017. Methods for quantifying fibrillar collagen alignment. In: Rittié, L. ed. *Fibrosis: Methods and Protocols*. Springer New York, 429-451.
- Lorensen WE, Cline HE (1987) Marching cubes: A high resolution 3D surface construction algorithm. *ACM SIGGRAPH Computer Graphics*. ACM: 163-169.
- Lowery J, Kuczmarski ER, Herrmann H, Goldman RD (2015) Intermediate filaments play a pivotal role in regulating cell architecture and function. *J Biol Chem* **290**(28): 17145-17153.
- Lu L, Oswald SJ, Ngu H, Yin FC-P (2008) Mechanical properties of actin stress fibers in living cells. *Biophys J* **95**(12): 6060-6071.
- Ma Y, Pavlatos E, Clayson K, Pan X, Kwok S, Sandwisch T, Liu J (2019) Mechanical deformation of human optic nerve head and peripapillary tissue in response to acute IOP elevation. *Invest Ophthalmol Vis Sci* **60**(4): 913-920.
- Maekawa M, Ishizaki T, Boku S, Watanabe N, Fujita A, Iwamatsu A, Obinata T, Ohashi K, Mizuno K, Narumiya S (1999) Signaling from Rho to the actin cytoskeleton through protein kinases ROCK and LIM-kinase. *Science* **285**(5429): 895-898.

- Mahmood T, Yang P-C (2012) Western blot: technique, theory, and trouble shooting. *N Am J Med Sci* **4**(9): 429-434.
- Malone AMD, Batra NN, Shivaram G, Kwon RY, You LD, Kim CH, Rodriguez J, Jair K, Jacobs CR (2007) The role of actin cytoskeleton in oscillatory fluid flow-induced signaling in MC3T3-E1 osteoblasts. *Am J Physiol-Cell Ph* **292**(5): 1830-1836.
- Marchandise E, Compère G, Willemet M, Bricteux G, Geuzaine C, Remacle JF (2010) Quality meshing based on STL triangulations for biomedical simulations. *Int J Numer Method Biomed Eng* **26**(7): 876-889.
- Markov P, Boote C, Zhu H, Blain E (2019) Effects of mechanical load on cytoskeletal protein arrangement in scleral fibroblasts. *Invest Ophthalmol Vis Sci* **60**(9): 6175.
- Markov PP, Eliasy A, Pijanka JK, Htoon HM, Paterson NG, Sorensen T, Elsheikh A, Girard MJ, Boote C (2018) Bulk changes in posterior scleral collagen microstructure in human high myopia. *Mol Vis* **24**(1): 818-833.
- Matteini P, Ratto F, Rossi F, Cicchi R, Stringari C, Kapsokalyvas D, Pavone FS, Pini R (2009) Photothermally-induced disordered patterns of corneal collagen revealed by SHG imaging. *Opt Express* **17**(6): 4868-4878.
- Maumenee IH (1981) The eye in the Marfan syndrome. *Trans Am Ophthalmol Soc* **79**: 684-733.
- McBrien NA (2013) Regulation of scleral metabolism in myopia and the role of transforming growth factor-beta. *Exp Eye Res* **114**(1): 128-140.
- McBrien NA, Cornell LM, Gentle A (2001) Structural and ultrastructural changes to the sclera in a mammalian model of high myopia. *Invest Ophthalmol Vis Sci* **42**(10): 2179-2187.
- McBrien NA, Jobling AI, Gentle A (2009) Biomechanics of the sclera in myopia: extracellular and cellular factors. *Optom Vis Sci* **86**(1): 23-30.
- McBrien NA, Metlapally R, Jobling AI, Gentle A (2006) Expression of collagen-binding integrin receptors in the mammalian sclera and their regulation during the development of myopia. *Invest Ophthalmol Vis Sci* **47**(11): 4674-4682.
- Meek KM, Boote C (2009) The use of X-ray scattering techniques to quantify the orientation and distribution of collagen in the corneal stroma. *Prog Retin Eye Res* **28**(5): 369-392.
- Meek KM, Knupp C (2015) Corneal structure and transparency. *Prog Retin Eye Res* **49**: 1-16.
- Meek KM, Quantock AJ (2001) The use of X-ray scattering techniques to determine corneal ultrastructure. *Prog Retin Eye Res* **20**(1): 95-137.

- Mercatelli R, Ratto F, Rossi F, Tatini F, Menabuoni L, Malandrini A, Nicoletti R, Pini R, Pavone FS, Cicchi R (2017) Three- dimensional mapping of the orientation of collagen corneal lamellae in healthy and keratoconic human corneas using SHG microscopy. *J Biophotonics* **10**(1): 75-83.
- Middleton S (2010) Porcine ophthalmology. *Vet Clin N Am-Food A* **26**(3): 557-572.
- Midgett DE, Pease ME, Jefferys JL, Patel M, Franck C, Quigley HA, Nguyen TD (2017) The pressure-induced deformation response of the human lamina cribrosa: Analysis of regional variations. *Acta Biomater* **53**(1): 123-139.
- Mitchell P, Hourihan F, Sandbach J, Jin Wang J (1999) The relationship between glaucoma and myopia: The Blue Mountains eye study. *Ophthalmology* **106**(10): 2010-2015.
- Moisan L (2011) Periodic plus smooth image decomposition. *J Math Imaging Vision* **39**(2): 161-179.
- Morris HJ, Tang J, Cruz Perez B, Pan X, Hart RT, Weber PA, Liu J (2013) Correlation between biomechanical responses of posterior sclera and IOP elevations during micro intraocular volume change. *Invest Ophthalmol Vis Sci* **54**(12): 7215-7222.
- Muñoz-Sarmiento DM, Rodríguez-Montaña ÓL, Alarcón-Castiblanco JD, Gamboa-Márquez MA, Corredor-Gómez JP, Cortés-Rodríguez CJ (2019) A finite element study of posterior eye biomechanics: The influence of intraocular and cerebrospinal pressure on the optic nerve head, peripapillary region, subarachnoid space and meninges. *Inform Med Unlocked* **1**(1): 1-16.
- Murad S, Grove D, Lindberg KA, Reynolds G, Sivarajah A, Pinnell SR (1981) Regulation of collagen synthesis by ascorbic acid. *Proc Natl Acad Sci USA* **78**(5): 2879-2882.
- Murienne BJ, Jefferys JL, Quigley HA, Nguyen TD (2015) The effects of glycosaminoglycan degradation on the mechanical behavior of the posterior porcine sclera. *Acta Biomater* **12**(1): 195-206.
- Myers KM, Coudrillier B, Boyce BL, Nguyen TD (2010) The inflation response of the posterior bovine sclera. *Acta Biomater* **6**(11): 4327-4335.
- Na S, Meininger G, Humphrey J (2007) A theoretical model for F-actin remodeling in vascular smooth muscle cells subjected to cyclic stretch. *J Theor Biol* **246**(1): 87-99.
- Navarro E, Serrano-Heras G, Castaño M, Solera J (2015) Real-time PCR detection chemistry. *Clin Chim Acta* **439**(1): 231-250.
-

- Nemet AY, Assia EI, Apple DJ, Barequet IS (2006) Current concepts of ocular manifestations in Marfan syndrome. *Surv Ophthalmol* **51**(6): 561-575.
- Nguyen C, Midgett D, Kimball EC, Steinhart MR, Nguyen TD, Pease ME, Oglesby EN, Jefferys JL, Quigley HA (2017) Measuring deformation in the mouse optic nerve head and peripapillary sclera. *Invest Ophthalmol Vis Sci* **58**(2): 721-733.
- Nickels S, Hopf S, Pfeiffer N, Schuster AK (2019) Myopia is associated with education: Results from NHANES 1999-2008. *Plos One* **14**(1): 1-15.
- Nogales E, Wolf SG, Downing KH (1998) Structure of the  $\alpha\beta$  tubulin dimer by electron crystallography. *Nature* **391**(6663): 199-203.
- Norman RE, Flanagan JG, Sigal IA, Rausch SMK, Tertinegg I, Ethier CR (2011) Finite element modeling of the human sclera: Influence on optic nerve head biomechanics and connections with glaucoma. *Exp Eye Res* **93**(1): 4-12.
- Norton TT, Rada JA (1995) Reduced extracellular matrix in mammalian sclera with induced myopia. *Vision Res* **35**(9): 1271-1281.
- Obbink-Huizer C, Oomens CW, Loerakker S, Foolen J, Bouten CV, Baaijens FP (2014) Computational model predicts cell orientation in response to a range of mechanical stimuli. *Biomech Model Mechanobiol* **13**(1): 227-236.
- Oglesby EN, Tezel G, Cone-Kimball E, Steinhart MR, Jefferys J, Pease ME, Quigley HA (2016) Scleral fibroblast response to experimental glaucoma in mice. *Mol Vis* **22**(1): 82-99.
- Or-Tzadikario S, Gefen A (2011) Confocal-based cell-specific finite element modeling extended to study variable cell shapes and intracellular structures: the example of the adipocyte. *J Biomech* **44**(3): 567-573.
- Osaki T, Kageyama T, Shimazu Y, Mysnikova D, Takahashi S, Takimoto S, Fukuda J (2017) Flatbed epi relief-contrast cellular monitoring system for stable cell culture. *Sci Rep* **7**(1): 1-11.
- Otterbein LR, Graceffa P, Dominguez R (2001) The crystal structure of uncomplexed actin in the ADP state. *Science* **293**(5530): 708-711.
- Paddock SW (1999) Confocal laser scanning microscopy. *Biotechniques* **27**(5): 992-1004.
- Palmieri V, Lucchetti D, Maiorana A, Papi M, Maulucci G, Calapà F, Ciasca G, Giordano R, Sgambato A, De Spirito M (2015) Mechanical and structural comparison between

- primary tumor and lymph node metastasis cells in colorectal cancer. *Soft Matter* **11**(28): 5719-5726.
- Pan CW, Ramamurthy D, Saw SM (2012) Worldwide prevalence and risk factors for myopia. *Ophthalmic Physiol Opt* **32**(1): 3-16.
- Pandolfi A, Holzapfel GA (2008) Three-dimensional modeling and computational analysis of the human cornea considering distributed collagen fibril orientations. *J Biomech Eng-T Asme* **130**(6): 1-12.
- Paszek MJ, Zahir N, Johnson KR, Lakins JN, Rozenberg GI, Gefen A, Reinhart-King CA, Margulies SS, Dembo M, Boettiger D (2005) Tensional homeostasis and the malignant phenotype. *Cancer cell* **8**(3): 241-254.
- Pavlatos E, Perez BC, Morris HJ, Chen H, Palko JR, Pan XL, Weber PA, Hart RT, Liu J (2016) Three-dimensional strains in human posterior sclera using ultrasound speckle tracking. *J Biomech Eng-T Asme* **138**(2): 1-9.
- Peeters EA, Bouten CV, Oomens CW, Bader DL, Snoeckx LH, Baaijens FP (2004) Anisotropic, three-dimensional deformation of single attached cells under compression. *Ann Biomed Eng* **32**(10): 1443-1452.
- Pellegrin S, Mellor H (2007) Actin stress fibres. *J Cell Sci* **120**(20): 3491-3499.
- Perry I, Szeto J-Y, Isaccs M, Gearly E, Rose R, Scofield S, Watson P, Hayes A (2017) Production of 3D printed scale models from microscope volume datasets for use in STEM education. *EMSESJ* **1**(1): 1-11.
- Perry SW, Schueckler JM, Burke K, Arcuri GL, Brown EB (2013) Stromal matrix metalloprotease-13 knockout alters Collagen I structure at the tumor-host interface and increases lung metastasis of C57BL/6 syngeneic E0771 mammary tumor cells. *BMC Cancer* **13**(1): 411.
- Peterson LJ, Rajfur Z, Maddox AS, Freel CD, Chen Y, Edlund M, Otey C, Burridge K (2004) Simultaneous stretching and contraction of stress fibers in vivo. *Mol Biol Cell* **15**(7): 3497-3508.
- Pettersen EF, Goddard TD, Huang CC, Couch GS, Greenblatt DM, Meng EC, Ferrin TE (2004) UCSF Chimera—a visualization system for exploratory research and analysis. *J Comput Chem* **25**(13): 1605-1612.

- Pezzullo L, Streatfeild J, Simkiss P, Shickle D (2018) The economic impact of sight loss and blindness in the UK adult population. *BMC Health Serv Res* **18**(63): 1-13.
- Phillips JR, McBrien NA (2004) Pressure-induced changes in axial eye length of chick and tree shrew: significance of myofibroblasts in the sclera. *Invest Ophthalmol Vis Sci* **45**(3): 758-763.
- Piez KA, Miller A (1974) The structure of collagen fibrils. *J Supramol Struct* **2**(1): 121-137.
- Pijanka JK, Abass A, Sorensen T, Elsheikh A, Boote C (2013) A wide-angle X-ray fibre diffraction method for quantifying collagen orientation across large tissue areas: application to the human eyeball coat. *J Appl Crystallogr* **46**: 1481-1489.
- Pijanka JK, Coudrillier B, Ziegler K, Sorensen T, Meek KM, Nguyen TD, Quigley HA, Boote C (2012) Quantitative mapping of collagen fiber orientation in non-glaucoma and glaucoma posterior human sclerae. *Invest Ophthalmol Vis Sci* **53**(9): 5258-5270.
- Pijanka JK, Kimball EC, Pease ME, Abass A, Sorensen T, Nguyen TD, Quigley HA, Boote C (2014) Changes in scleral collagen organization in murine chronic experimental glaucoma. *Invest Ophthalmol Vis Sci* **55**(10): 6554-6564.
- Pijanka JK, Markov PP, Midgett D, Paterson NG, White N, Blain EJ, Nguyen TD, Quigley HA, Boote C (2019) Quantification of collagen fiber structure using second harmonic generation imaging and 2D discrete fourier transform analysis: Application to the human optic nerve head. *J Biophotonics* **12**(5): 1-19.
- Pijanka JK, Spang MT, Sorensen T, Liu J, Nguyen TD, Quigley HA, Boote C (2015) Depth-dependent changes in collagen organization in the human peripapillary sclera. *Plos One* **10**(2): 1-17.
- Pitha I, Oglesby E, Chow A, Kimball E, Pease ME, Schaub J, Quigley H (2018) Rho-kinase inhibition reduces myofibroblast differentiation and proliferation of scleral fibroblasts induced by transforming growth factor  $\beta$  and experimental glaucoma. *Transl Vis Sci Technol* **7**(6): 1-12.
- Pollard TD, Cooper JA (2009) Actin, a central player in cell shape and movement. *Science* **326**(5957): 1208-1212.
- Poukens V, Glasgow BJ, Demer JL (1998) Nonvascular contractile cells in sclera and choroid of humans and monkeys. *Invest Ophthalmol Vis Sci* **39**(10): 1765-1774.

- Pravincumar P, Bader DL, Knight MM (2012) Viscoelastic cell mechanics and actin remodelling are dependent on the rate of applied pressure. *Plos One* **7**(9): 1-10.
- Prockop DJ, Kivirikko KI (1995) Collagens - molecular-biology, diseases, and potentials for therapy. *Annu Rev Biochem* **64**(1): 403-434.
- Qiu C, Chen M, Yao J, Sun X, Xu J, Zhang R, Wang X, Li G, Qian S (2018) Mechanical strain induces distinct human scleral fibroblast lineages: Differential roles in cell proliferation, apoptosis, migration, and differentiation. *Invest Ophthalmol Vis Sci* **59**(6): 2401-2410.
- Qu J, Chen H, Zhu L, Ambalavanan N, Girkin CA, Murphy-Ullrich JE, Downs JC, Zhou Y (2015) High-magnitude and/or high-frequency mechanical strain promotes peripapillary scleral myofibroblast differentiation. *Invest Ophthalmol Vis Sci* **56**(13): 7821-7830.
- Quaranta L, Riva I, Gerardi C, Oddone F, Floriano I, Konstas AG (2016) Quality of life in glaucoma: a review of the literature. *Adv Ther* **33**(6): 959-981.
- Quigley HA (1999) Neuronal death in glaucoma. *Prog Retin Eye Res* **18**(1): 39-57.
- Quigley HA (2011) Glaucoma. *Lancet* **377**(9774): 1367-1377.
- Quigley HA, Broman AT (2006) The number of people with glaucoma worldwide in 2010 and 2020. *Brit J Ophthalmol* **90**(3): 262-267.
- Rada JA, Achen VR, Penugonda S, Schmidt RW, Mount BA (2000a) Proteoglycan composition in the human sclera during growth and aging. *Invest Ophthalmol Vis Sci* **41**(7): 1639-1648.
- Rada JA, Nickla DL, Troilo D (2000b) Decreased proteoglycan synthesis associated with form deprivation myopia in mature primate eyes. *Invest Ophthalmol Vis Sci* **41**(8): 2050-2058.
- Rahman M, Beard S, Discombe R, Sharma R, Montgomery D (2013) Direct healthcare costs of glaucoma treatment. *Br J Ophthalmol* **97**(6): 720-724.
- Rajan DK, Kreutzer J, Välimäki H, Pekkanen-Mattila M, Ahola A, Skogberg A, Aalto-Setälä K, Ihalainen H, Kallio P, Lekkala J (2018) A portable live-cell imaging system with an invert-upright-convertible architecture and a mini-bioreactor for long-term simultaneous cell imaging, chemical sensing, and electrophysiological recording. *IEEE Access* **6**(1): 11063-11075.
- Ralphs J, Waggett A, Benjamin M (2002) Actin stress fibres and cell-cell adhesion molecules in tendons: organisation in vivo and response to mechanical loading of tendon cells in vitro. *Matrix Biol* **21**(1): 67-74.

- Rápalo G, Herwig JD, Hewitt R, Wilhelm KR, Waters CM, Roan E (2015) Live cell imaging during mechanical stretch. *J Vis Exp* **1**(102): 1-12.
- Raquel C-A, T.O. CD, J.S. FM, Tamagno P, Monica M, J.W.A. vLJ, L. GP, E. GM (2018) Continuous exposure to simulated hypergravity-induced changes in proliferation, morphology, and gene expression of human tendon cells. *Stem Cells Dev* **27**(12): 858-869.
- Reif R, Karlsson J, Günther G, Beattie L, Wrangborg D, Hammad S, Begher-Tibbe B, Vartak A, Melega S, Kaye PM (2015) Bile canalicular dynamics in hepatocyte sandwich cultures. *Arch Toxicol* **89**(10): 1861-1870.
- Reynolds N, McGarry J (2015) Single cell active force generation under dynamic loading—Part II: active modelling insights. *Acta Biomater* **27**(1): 251-263.
- Reynolds NH, Ronan W, Dowling EP, Owens P, McMeeking RM, McGarry JP (2014) On the role of the actin cytoskeleton and nucleus in the biomechanical response of spread cells. *Biomaterials* **35**(13): 4015-4025.
- Rezakhaniha R, Agianniotis A, Schrauwen JT, Griffa A, Sage D, Bouten CV, Van de Vosse F, Unser M, Stergiopoulos N (2012) Experimental investigation of collagen waviness and orientation in the arterial adventitia using confocal laser scanning microscopy. *Biomech Model Mechanobiol* **11**(3): 461-473.
- Ribeiro JEA, Pinotsis N, Ghisleni A, Salmazo A, Konarev PV, Kostan J, Sjoebloom B, Schreiner C, Polyansky AA, Gkougkoulia EA (2014) The structure and regulation of human muscle  $\alpha$ -actinin. *Cell* **159**(6): 1447-1460.
- Ricard-Blum S (2011) The collagen family. *Cold Spring Harb Perspect Biol* **3**(1): 1-19.
- Robert A, Hookway C, Gelfand VI (2016) Intermediate filament dynamics: What we can see now and why it matters. *BioEssays* **38**(3): 232-243.
- Roberts MD, Grau V, Grimm J, Reynaud J, Bellezza AJ, Burgoyne CF, Downs JC (2009) Remodeling of the connective tissue microarchitecture of the lamina cribrosa in early experimental glaucoma. *Invest Ophthalmol Vis Sci* **50**(2): 681-690.
- Ronan W, Deshpande VS, McMeeking RM, McGarry JP (2012) Numerical investigation of the active role of the actin cytoskeleton in the compression resistance of cells. *J Mech Behav Biomed Mater* **14**(1): 143-157.

- Ronan W, McMeeking RM, Chen CS, McGarry JP, Deshpande VS (2015) Cooperative contractility: The role of stress fibres in the regulation of cell-cell junctions. *J Biomech* **48**(3): 520-528.
- Rose AS, Bradley AR, Valasatava Y, Duarte JM, Prlić A, Rose PW (2018) NGL viewer: web-based molecular graphics for large complexes. *Bioinformatics* **34**(21): 3755-3758.
- Ruiz-Ederra J, Garcia M, Hernandez M, Urcola H, Hernandez-Barbachana E, Araiz J, Vecino E (2005) The pig eye as a novel model of glaucoma. *Exp Eye Res* **81**(5): 561-569.
- Ruiz-García M, Vásquez C, Sandoval S, Kaston F, Luengas-Villamil K, Shostell JM (2016) Phylogeography and spatial structure of the lowland tapir (*Tapirus terrestris*, Perissodactyla: Tapiridae) in South America. *Mitochondrial DNA A* **27**(4): 2334-2342.
- Sabuncuoglu B, Acar M, Silberschmidt VV (2013) Finite element modelling of fibrous networks: Analysis of strain distribution in fibres under tensile load. *Comput Mater Sci* **79**(1): 143-158.
- Saez A, Ghibaudo M, Buguin A, Silberzan P, Ladoux B (2007) Rigidity-driven growth and migration of epithelial cells on microstructured anisotropic substrates. *Proc Natl Acad Sci U S A* **104**(20): 8281-8286.
- Sanchez I, Martin R, Ussa F, Fernandez-Bueno I (2011) The parameters of the porcine eyeball. *Graefes Arch Clin Exp Ophthalmol* **249**(4): 475-482.
- Sander EA, Barocas VH (2009) Comparison of 2D fiber network orientation measurement methods. *J Biomed Mater Res A* **88**(2): 322-331.
- Sapir L, Tzlil S (2017) Talking over the extracellular matrix: How do cells communicate mechanically? *Semin Cell Dev Biol*. Elsevier: 99-105.
- Saw SM, Gazzard G, Shih- Yen EC, Chua WH (2005) Myopia and associated pathological complications. *Ophthalmic Physiol Opt* **25**(5): 381-391.
- Schindelin J, Arganda-Carreras I, Frise E, Kaynig V, Longair M, Pietzsch T, Preibisch S, Rueden C, Saalfeld S, Schmid B (2012) Fiji: an open-source platform for biological-image analysis. *Nat Methods* **9**(7): 676-682.
- Schippert R, Brand C, Schaeffel F, Feldkaemper MP (2006) Changes in scleral MMP-2, TIMP-2 and TGFβ-2 mRNA expression after imposed myopic and hyperopic defocus in chickens. *Exp Eye Res* **82**(4): 710-719.

- Schmid B, Schindelin J, Cardona A, Longair M, Heisenberg M (2010) A high-level 3D visualization API for Java and ImageJ. *BMC bioinformatics* **11**(274): 1-7.
- Sears C, Kaunas R (2016) The many ways adherent cells respond to applied stretch. *J Biomech* **49**(8): 1347-1354.
- Seetharaman S, Etienne-Manneville S (2019) Microtubules at focal adhesions—a double-edged sword. *J Cell Sci* **132**(19): 1-11.
- Shah JV, Wang LZ, Traub P, Janmey PA (1998) Interaction of vimentin with actin and phospholipids. *Biol Bull* **194**(3): 402-405.
- Shoulders MD, Raines RT. 2009. Collagen structure and stability. *Annu Rev Biochem*. Annual Reviews, 929-958.
- Siegrwart Jr JT, Norton TT (1999) Regulation of the mechanical properties of tree shrew sclera by the visual environment. *Vision Res* **39**(2): 387-407.
- Siegrwart JT, Strang CE (2007) Selective modulation of scleral proteoglycan mRNA levels during minus lens compensation and recovery. *Mol Vis* **13**(211-12): 1878-1886.
- Sigal IA (2009) Interactions between geometry and mechanical properties on the optic nerve head. *Invest Ophthalmol Vis Sci* **50**(6): 2785-2795.
- Sigal IA, Flanagan JG, Ethier CR (2005) Factors influencing optic nerve head biomechanics. *Invest Ophthalmol Vis Sci* **46**(11): 4189-4199.
- Sigal IA, Flanagan JG, Tertinegg I, Ethier CR (2010) 3D morphometry of the human optic nerve head. *Exp Eye Res* **90**(1): 70-80.
- Sigal IA, Yang H, Roberts MD, Burgoyne CF, Downs JC (2011) IOP-induced lamina cribrosa displacement and scleral canal expansion: an analysis of factor interactions using parameterized eye-specific models. *Invest Ophthalmol Vis Sci* **52**(3): 1896-1907.
- Skogberg A, Mäki A-J, Mettänen M, Lahtinen P, Kallio P (2017) Cellulose nanofiber alignment using evaporation-induced droplet-casting, and cell alignment on aligned nanocellulose surfaces. *Biomacromolecules* **18**(12): 3936-3953.
- Slomka N, Gefen A (2010) Confocal microscopy-based three-dimensional cell-specific modeling for large deformation analyses in cellular mechanics. *J Biomech* **43**(9): 1806-1816.
- Slomka N, Oomens CW, Gefen A (2011) Evaluating the effective shear modulus of the cytoplasm in cultured myoblasts subjected to compression using an inverse finite element method. *J Mech Behav Biomed Mater* **4**(7): 1559-1566.

- Smolek M (1988) Elasticity of the bovine sclera measured with real-time holographic-interferometry. *Am J Optom Physiol Opt* **65**(8): 653-660.
- Sobel I (1978) Neighborhood coding of binary images for fast contour following and general binary array processing. *Comput Graph Image Process* **8**(1): 127-135.
- Starck J-L, Candès EJ, Donoho DL (2002) The curvelet transform for image denoising. *IEEE Trans Image Process* **11**(6): 670-684.
- Steinert PM, Chou Y-H, Prahlaad V, Parry DA, Marekov LN, Wu KC, Jang S-I, Goldman RD (1999) A high molecular weight intermediate filament-associated protein in BHK-21 cells is nestin, a type VI intermediate filament protein limited co-assembly in vitro to form heteropolymers with type III vimentin and type IV  $\alpha$ -internexin. *Journal of Biological Chemistry* **274**(14): 9881-9890.
- Storm C, Pastore JJ, MacKintosh FC, Lubensky TC, Janmey PA (2005) Nonlinear elasticity in biological gels. *Nature* **435**(7039): 191-194.
- Stricker J, Falzone T, Gardel ML (2010) Mechanics of the F-actin cytoskeleton. *J Biomech* **43**(1): 9-14.
- Strouthidis NG, Girard MJA (2013) Altering the way the optic nerve head responds to intraocular pressure—a potential approach to glaucoma therapy. *Curr Opin Pharmacol* **13**(1): 83-89.
- Su J, Wall ST, Healy KE, Wildsoet CF (2010) Scleral reinforcement through host tissue integration with biomimetic enzymatically degradable semi-interpenetrating polymer network. *Tissue Eng Part A* **16**(3): 905-916.
- Sugita S, Matsumoto T (2017) Multiphoton microscopy observations of 3D elastin and collagen fiber microstructure changes during pressurization in aortic media. *Biomech Model Mechanobiol* **16**(3): 763-773.
- Summers Rada JA, Shelton S, Norton TT (2006) The sclera and myopia. *Exp Eye Res* **82**(2): 185-200.
- Susilo ME, Paten JA, Sander EA, Nguyen TD, Ruberti JW (2016) Collagen network strengthening following cyclic tensile loading. *Interface Focus* **6**(1): 1-11.
- Tan JCH, Kalapesi FB, Coroneo MT (2006) Mechanosensitivity and the eye: cells coping with the pressure. *Brit J Ophthalmol* **90**(3): 383-388.

- Tanner K, Boudreau A, Bissell MJ, Kumar S (2010) Dissecting regional variations in stress fiber mechanics in living cells with laser nanosurgery. *Biophys J* **99**(9): 2775-2783.
- Tavares-Somma A, Seabra N, Moore BA, Sato M, Lange RR, Montiani-Ferreira F (2017) The eye of the Azara's Agouti (*Dasyprocta Azarae*): morphological observations and selected ophthalmic diagnostic tests. *J Zoo Wildl Med* **48**(4): 1108-1119.
- Tham Y-C, Li X, Wong TY, Quigley HA, Aung T, Cheng C-Y (2014) Global prevalence of glaucoma and projections of glaucoma burden through 2040: A systematic review and meta-analysis. *Ophthalmology* **121**(11): 2081-2090.
- Tielsch JM, Sommer A, Katz J, Royall RM, Quigley HA, Javitt J (1991) Racial variations in the prevalence of primary open-angle glaucoma: the Baltimore eye survey. *Jama* **266**(3): 369-374.
- Tojkander S, Gateva G, Lappalainen P (2012) Actin stress fibers—assembly, dynamics and biological roles. *J Cell Sci* **125**(1): 1-10.
- Tomasek JJ, Gabbiani G, Hinz B, Chaponnier C, Brown RA (2002) Myofibroblasts and mechano-regulation of connective tissue remodelling. *Nat Rev Mol Cell Biol* **3**(5): 349-363.
- Tomasek JJ, Haaksma CJ, Eddy RJ, Vaughan MB (1992) Fibroblast contraction occurs on release of tension in attached collagen lattices: dependency on an organized actin cytoskeleton and serum. *Anat Rec* **232**(3): 359-368.
- Tsatsos M, Broadway D (2007) Controversies in the history of glaucoma: is it all a load of old Greek? *Br J Ophthalmol* **91**(11): 1561-1562.
- Tun TA, Wang X, Baskaran M, Nongpiur ME, Tham Y-C, Perera SA, Strouthidis NG, Aung T, Cheng C-Y, Girard MJ (2019) Variation of peripapillary scleral shape with age. *Invest Ophthalmol Vis Sci* **60**(10): 3275-3282.
- Vergara D, Ferraro MM, Cascione M, del Mercato LL, Leporatti S, Ferretta A, Tanzarella P, Pacelli C, Santino A, Maffia M, Cocco T, Rinaldi R, Gaballo A (2015) Cytoskeletal alterations and biomechanical properties of parkin-mutant human primary fibroblasts. *Cell Biochem Biophys* **71**(3): 1395-1404.
- Verkicharla PK, Ohno- Matsui K, Saw SM (2015) Current and predicted demographics of high myopia and an update of its associated pathological changes. *Ophthalmic Physiol Opt* **35**(5): 465-475.

- Vermes I, Haanen C, Steffens-Nakken H, Reutellingsperger C (1995) A novel assay for apoptosis flow cytometric detection of phosphatidylserine expression on early apoptotic cells using fluorescein labelled Annexin V. *J Immunol Methods* **184**(1): 39-51.
- Vikstrom KL, Lim S-S, Goldman RD, Borisy GG (1992) Steady state dynamics of intermediate filament networks. *J Cell Biol* **118**(1): 121-129.
- Vollmer J, Mencl R, Mueller H (1999) Improved laplacian smoothing of noisy surface meshes. *Computer graphics forum*. Wiley Online Library: 131-138.
- Voorhees AP, Jan N-J, Hua Y, Yang B, Sigal IA (2018) Peripapillary sclera architecture revisited: a tangential fiber model and its biomechanical implications. *Acta Biomater* **79**(1): 113-122.
- Vurgese S, Panda-Jonas S, Jonas JB (2012) Scleral thickness in human eyes. *Plos One* **7**(1): 1-9.
- Wang N, Butler JP, Ingber DE (1993) Mechanotransduction across the cell-surface and through the cytoskeleton. *Science* **260**(5111): 1124-1127.
- Wang X, Beotra MR, Tun TA, Baskaran M, Perera S, Aung T, Strouthidis NG, Milea D, Girard MJ (2016a) In vivo 3-dimensional strain mapping confirms large optic nerve head deformations following horizontal eye movements. *Invest Ophthalmol Vis Sci* **57**(13): 5825-5833.
- Wang X, Fisher LK, Milea D, Jonas JB, Girard MJ (2017) Predictions of optic nerve traction forces and peripapillary tissue stresses following horizontal eye movements. *Invest Ophthalmol Vis Sci* **58**(4): 2044-2053.
- Wang X, Rumpel H, Lim WEH, Baskaran M, Perera SA, Nongpiur ME, Aung T, Milea D, Girard MJ (2016b) Finite element analysis predicts large optic nerve head strains during horizontal eye movements. *Invest Ophthalmol Vis Sci* **57**(6): 2452-2462.
- Wang YX, Jiang R, Ren XL, Chen JD, Shi HL, Xu L, Wei WB, Jonas JB (2016c) Intraocular pressure elevation and choroidal thinning. *Br J Ophthalmol* **100**(12): 1676-1681.
- Watson PG, Young RD (2004) Scleral structure, organisation and disease. A review. *Exp Eye Res* **78**(3): 609-623.
- Weinreb RN, Aung T, Medeiros FA (2014) The pathophysiology and treatment of glaucoma: a review. *Jama* **311**(18): 1901-1911.

- Whitford C, Joda A, Jones S, Bao F, Rama P, Elsheikh A (2016) Ex vivo testing of intact eye globes under inflation conditions to determine regional variation of mechanical stiffness. *Eye and Vision* **3**(1): 1-21.
- Williams KM, Hammond CJ (2014) Prevalence of myopia and association with education in Europe. *Lancet* **383**(1): 109.
- Williams RM, Zipfel WR, Webb WW (2005) Interpreting second-harmonic generation images of collagen I fibrils. *Biophys J* **88**(2): 1377-1386.
- Winick H (1995) Synchrotron radiation sources: a primer. World Scientific.
- Winkler M, Jester B, Nien-Shy C, Massei S, Minckler DS, Jester JV, Brown DJ (2010) High resolution three-dimensional reconstruction of the collagenous matrix of the human optic nerve head. *Brain Res Bull* **81**(2-3): 339-348.
- Wipff P-J, Rifkin DB, Meister J-J, Hinz B (2007) Myofibroblast contraction activates latent TGF- $\beta$ 1 from the extracellular matrix. *J Cell Biol* **179**(6): 1311-1323.
- Wittek A, Grosland NM, Joldes GR, Magnotta V, Miller K (2016) From finite element meshes to clouds of points: A review of methods for generation of computational biomechanics models for patient-specific applications. *Ann Biomed Eng* **44**(1): 3-15.
- Wong TY, Ferreira A, Hughes R, Carter G, Mitchell P (2014) Epidemiology and disease burden of pathologic myopia and myopic choroidal neovascularization: an evidence-based systematic review. *Am J Ophthalmol* **157**(1): 9-25.
- Wu J, Akhmanova A (2017) Microtubule-organizing centers. *Annu Rev Cell Dev Biol* **33**(1): 51-75.
- Wu LJ, You QS, Duan JL, Luo YX, Liu LJ, Li X, Gao Q, Zhu HP, He Y, Xu L (2015) Prevalence and associated factors of myopia in high-school students in Beijing. *Plos One* **10**(3): 1-12.
- Xu L, Wang Y, Wang S, Wang Y, Jonas JB (2007) High myopia and glaucoma susceptibility: The Beijing eye study. *Ophthalmology* **114**(2): 216-220.
- Yamamoto S, Hashizume H, Hitomi J, Shigeno M, Sawaguchi S, ABE H, Ushiki T (2000) The subfibrillar arrangement of corneal and scleral collagen fibrils as revealed by scanning electron and atomic force microscopy. *Arch Histol Cytol* **63**(2): 127-135.
- Yamamoto S, Sawaguchi S, Iwase A, Yamamoto T, Abe H, Tomita G, Tomidokoro A, Araie M (2014) Primary open-angle glaucoma in a population associated with high prevalence of

- primary angle-closure glaucoma: the Kumejima Study. *Ophthalmology* **121**(8): 1558-1565.
- Yan D, McPheeters S, Johnson G, Utzinger U, Vande Geest JP (2011) Microstructural differences in the human posterior sclera as a function of age and race. *Invest Ophthalmol Vis Sci* **52**(2): 821-829.
- Yao Y, Lacroix D, Mak AF (2016) Effects of oxidative stress-induced changes in the actin cytoskeletal structure on myoblast damage under compressive stress: confocal-based cell-specific finite element analysis. *Biomech Model Mechanobiol* **15**(6): 1495-1508.
- Yuan Y, Li M, Chen Q, Me R, Yu Y, Gu Q, Shi G, Ke B (2018) Crosslinking enzyme lysyl oxidase modulates scleral remodeling in form-deprivation myopia. *Curr Eye Res* **43**(2): 200-207.
- Zhou D, Abass A, Eliasy A, Studer HP, Movchan A, Movchan N, Elsheikh A (2019a) Microstructure-based numerical simulation of the mechanical behaviour of ocular tissue. *J R Soc Interface* **16**(154): 1-10.
- Zhou D, Eliasy A, Abass A, Markov P, Whitford C, Boote C, Movchan A, Movchan N, Elsheikh A (2019b) Analysis of X-ray scattering microstructure data for implementation in numerical simulations of ocular biomechanical behaviour. *Plos One* **14**(4): 1-16.
- Zipfel WR, Williams RM, Webb WW (2003) Nonlinear magic: multiphoton microscopy in the biosciences. *Nat Biotechnol* **21**(11): 1369-1377.

# Appendix

## A.1 Wide-angle X-ray scattering analysis

## A.1.1 Human specimens

## A.1.1.1 N1

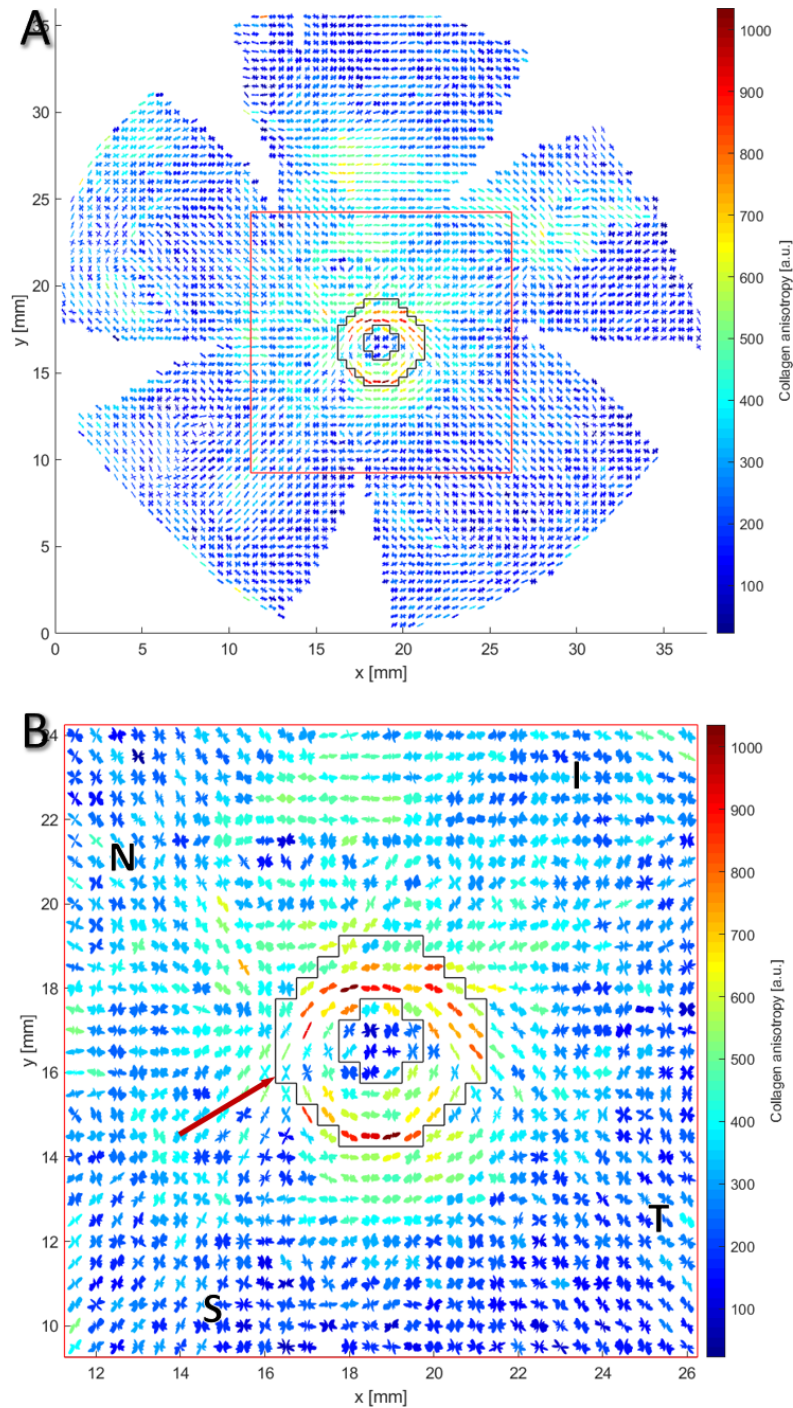


Figure A.01 – Wide-angle X-ray scattering (WAXS) polar vector plot map of human non-myopic specimen N1 (A) with a red square designating a 30x30 vector plot magnification (B). The peripapillary sclera (PPS) is bounded by black lines, whilst the red arrow denotes discontinuation in the circumferential collagen orientation in the superior nasal (SN) region, with the superior (S), nasal (N), inferior (I), temporal (T) directions indicated on B.

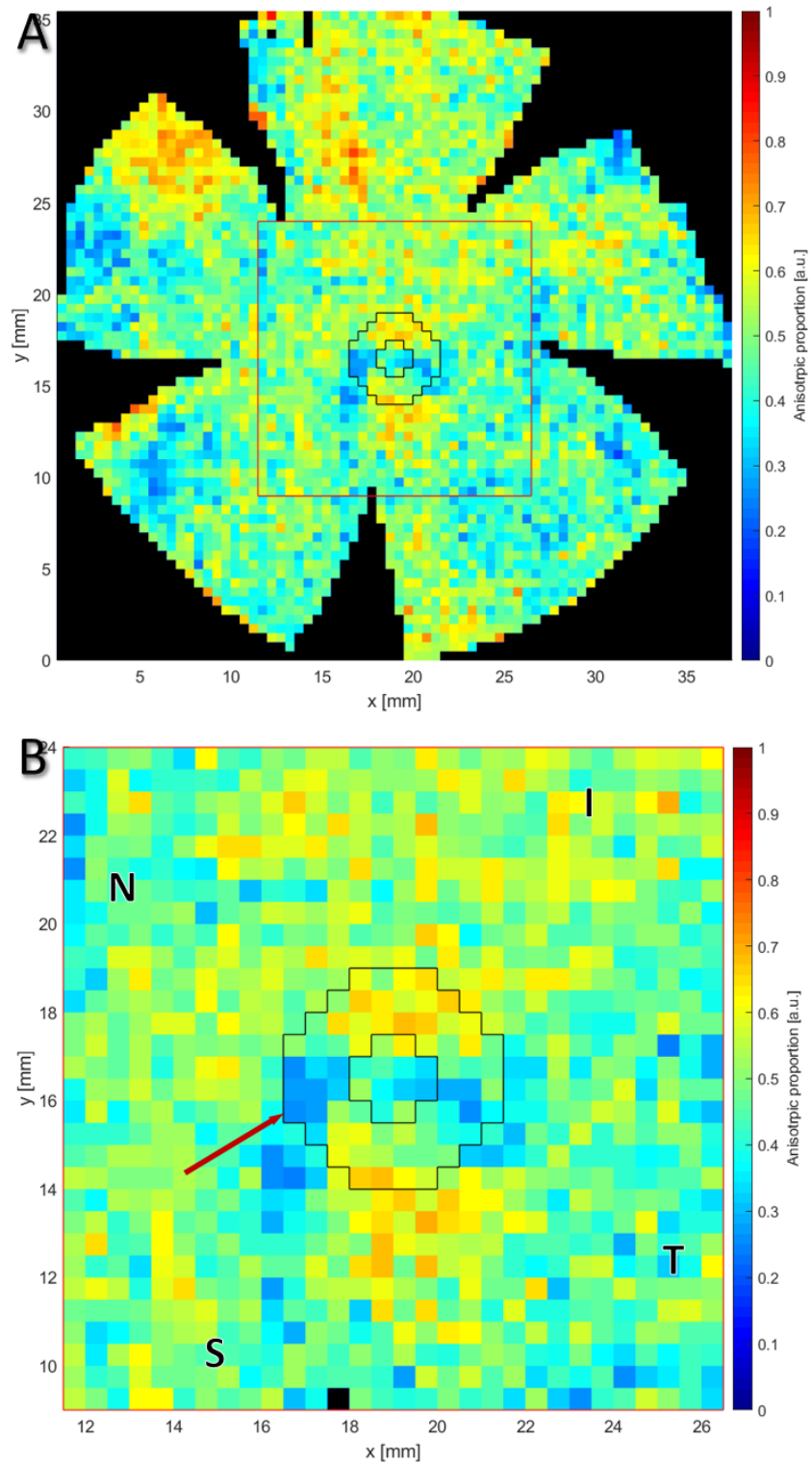


Figure A.02 – WAXS collagen anisotropic proportion contour map of human non-myopic specimen N1 (A) with a red square designating a 30x30 vector plot magnification (B). The PPS is bounded by black lines, whilst the red arrow denotes discontinuation in the circumferential collagen orientation in the SN region, with the superior (S), nasal (N), inferior (I), temporal (T) directions indicated on B.

## A.1.1.2 N2

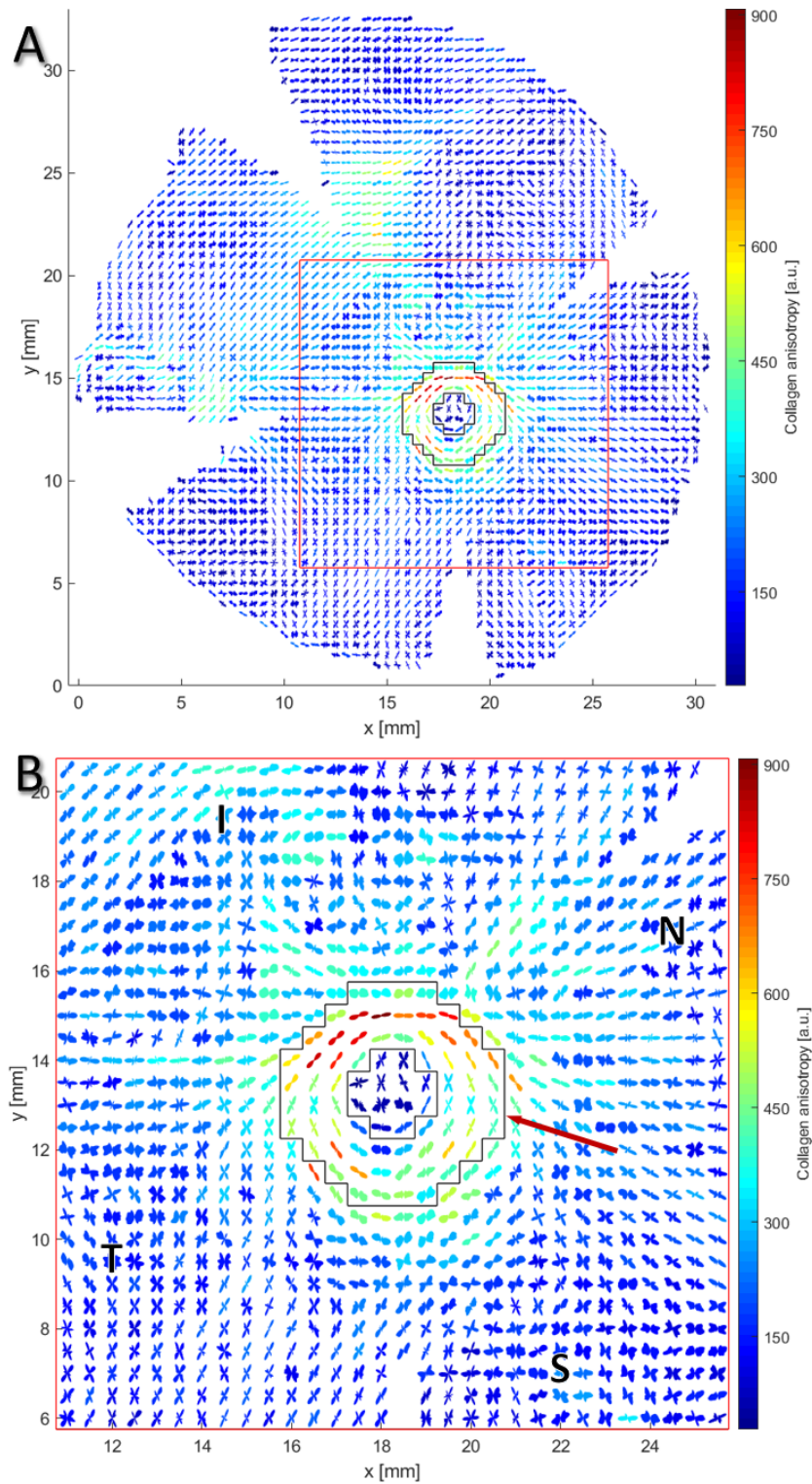


Figure A.03 – WAXS polar vector plot map of human non-myopic specimen N2 (A) with a red square designating a 30x30 vector plot magnification (B). The PPS is bounded by black lines, whilst the red arrow denotes discontinuation in the circumferential collagen orientation in the SN region, with the superior (S), nasal (N), inferior (I), temporal (T) directions indicated on B.

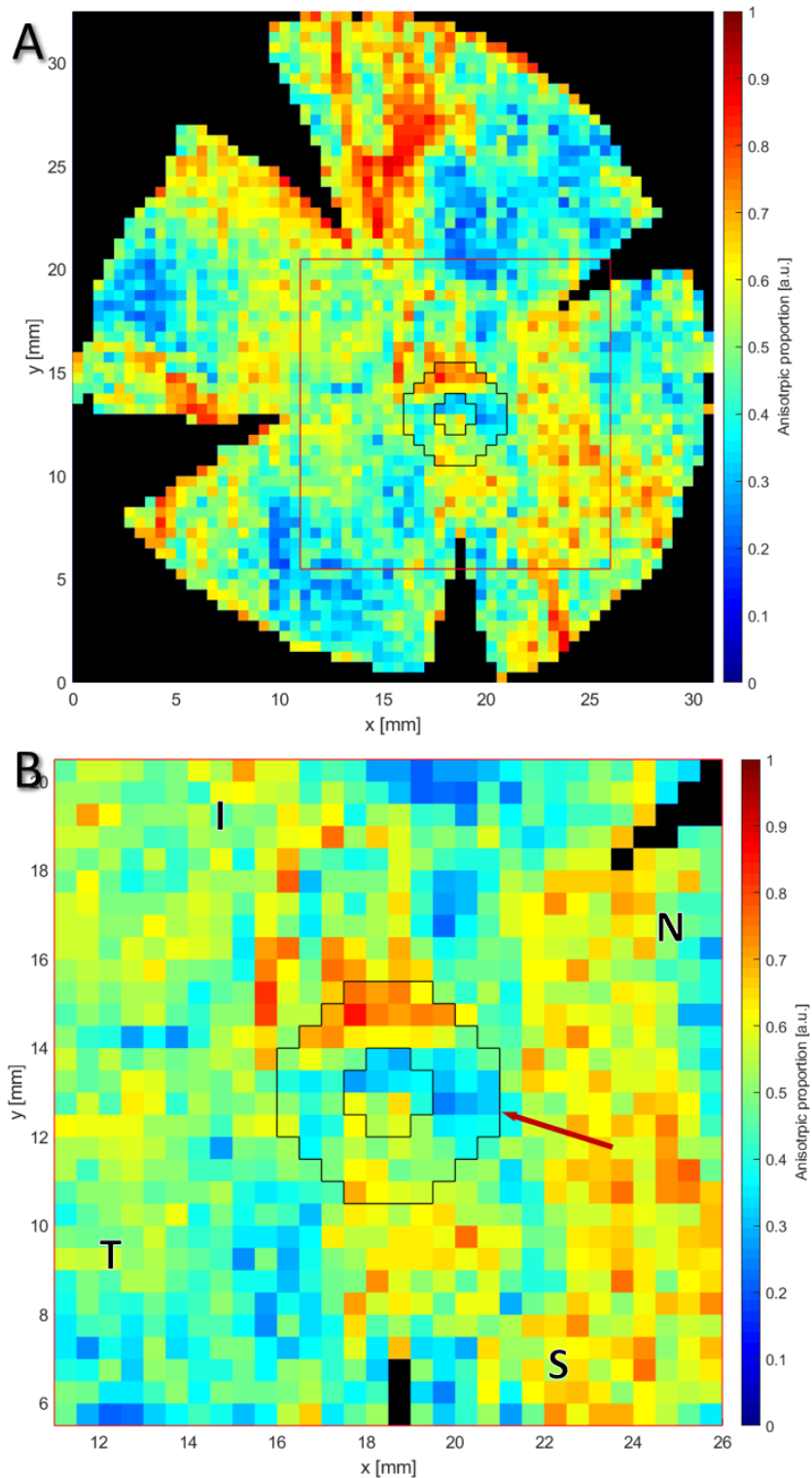


Figure A.04 – WAXS collagen anisotropic proportion contour map of human non-myopic specimen N2 (A) with a red square designating a 30x30 vector plot magnification (B). The PPS is bounded by black lines, whilst the red arrow denotes discontinuation in the circumferential collagen orientation in the SN region, with the superior (S), nasal (N), inferior (I), temporal (T) directions indicated on B.

A.1.1.3 N3

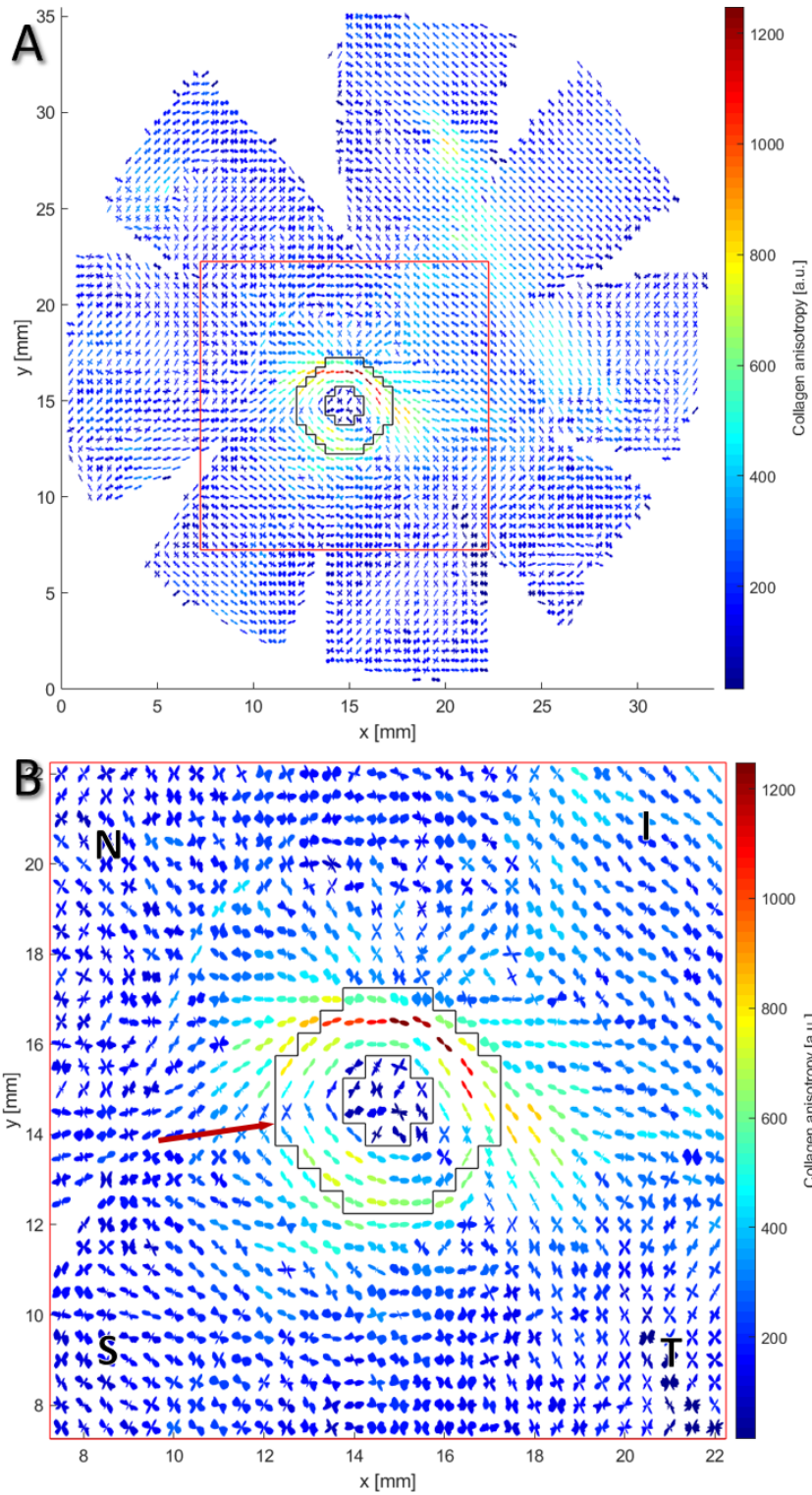


Figure A.05 – WAXS polar vector plot map of human non-myopic specimen N3 (A) with a red square designating a 30x30 vector plot magnification (B). The PPS is bounded by black lines, whilst the red arrow denotes discontinuation in the circumferential collagen orientation in the SN region, with the superior (S), nasal (N), inferior (I), temporal (T) directions indicated on B.

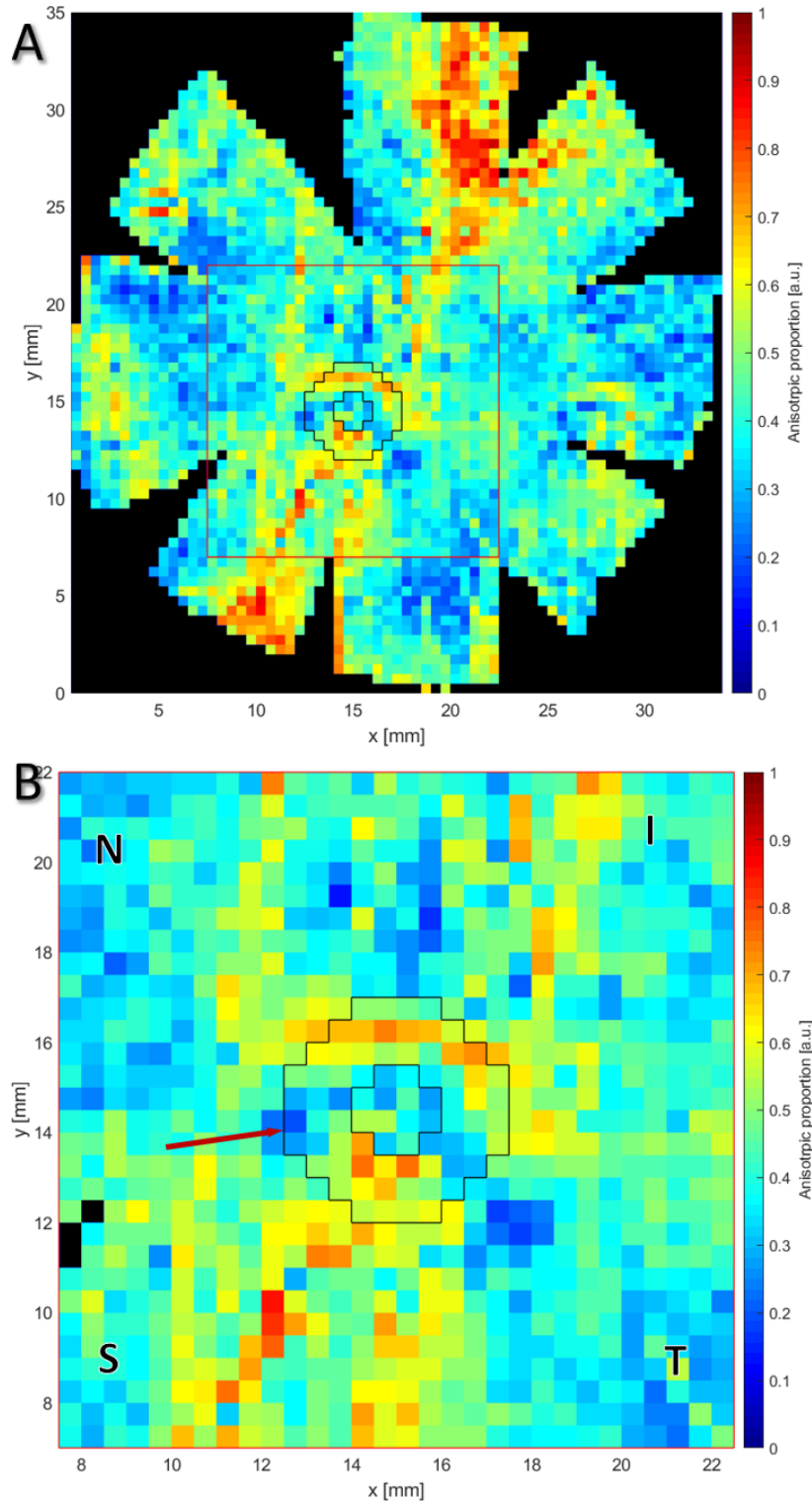


Figure A.06 – WAXS collagen anisotropic proportion contour map of human non-myopic specimen N3 (A) with a red square designating a 30x30 vector plot magnification (B). The PPS is bounded by black lines, whilst the red arrow denotes discontinuation in the circumferential collagen orientation in the SN region, with the superior (S), nasal (N), inferior (I), temporal (T) directions indicated on B.

A.1.1.4 N5

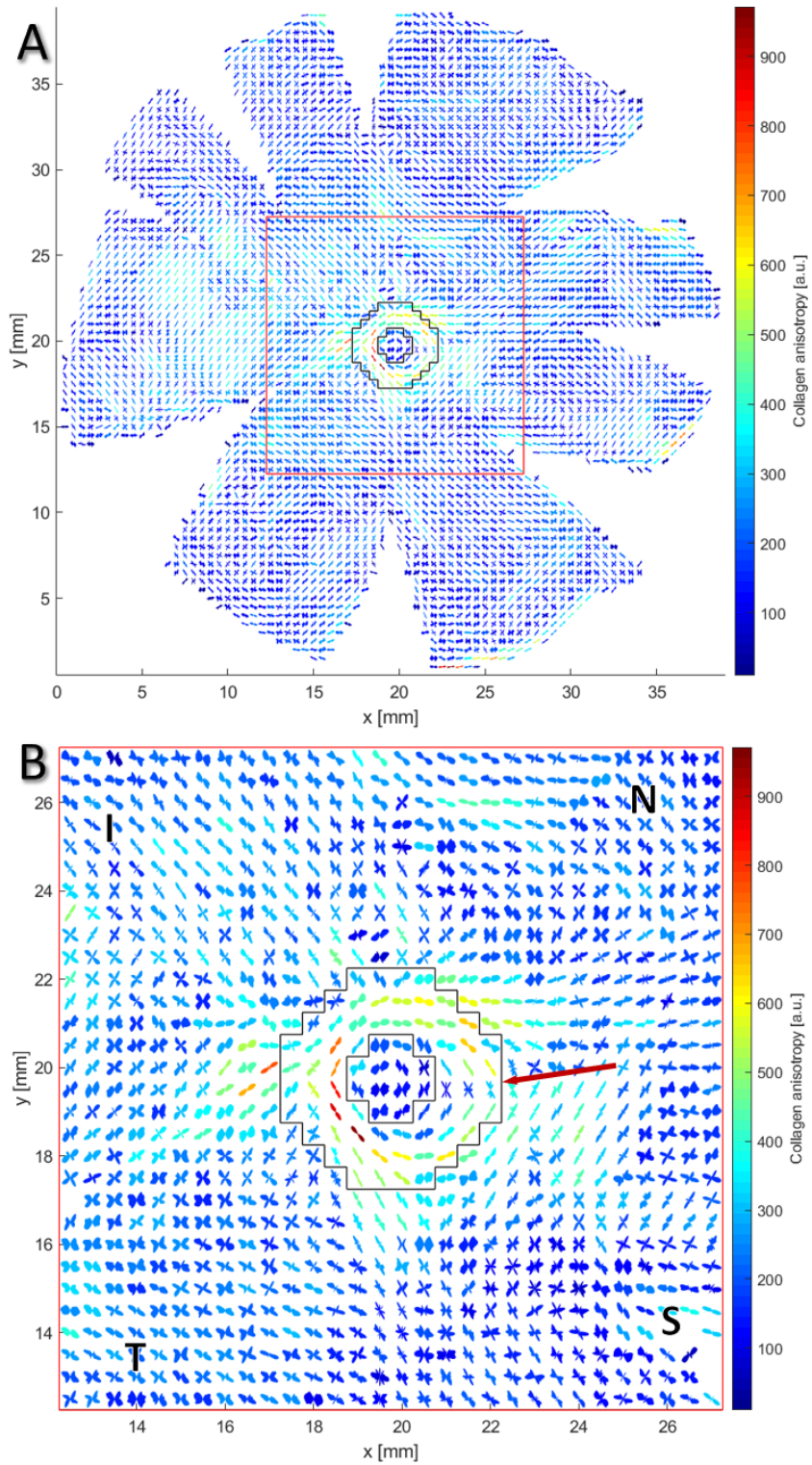


Figure A.07 – WAXS polar vector plot map of human non-myopic specimen N5 (A) with a red square designating a 30x30 vector plot magnification (B). The PPS is bounded by black lines, whilst the red arrow denotes discontinuation in the circumferential collagen orientation in the SN region, with the superior (S), nasal (N), inferior (I), temporal (T) directions indicated on B.

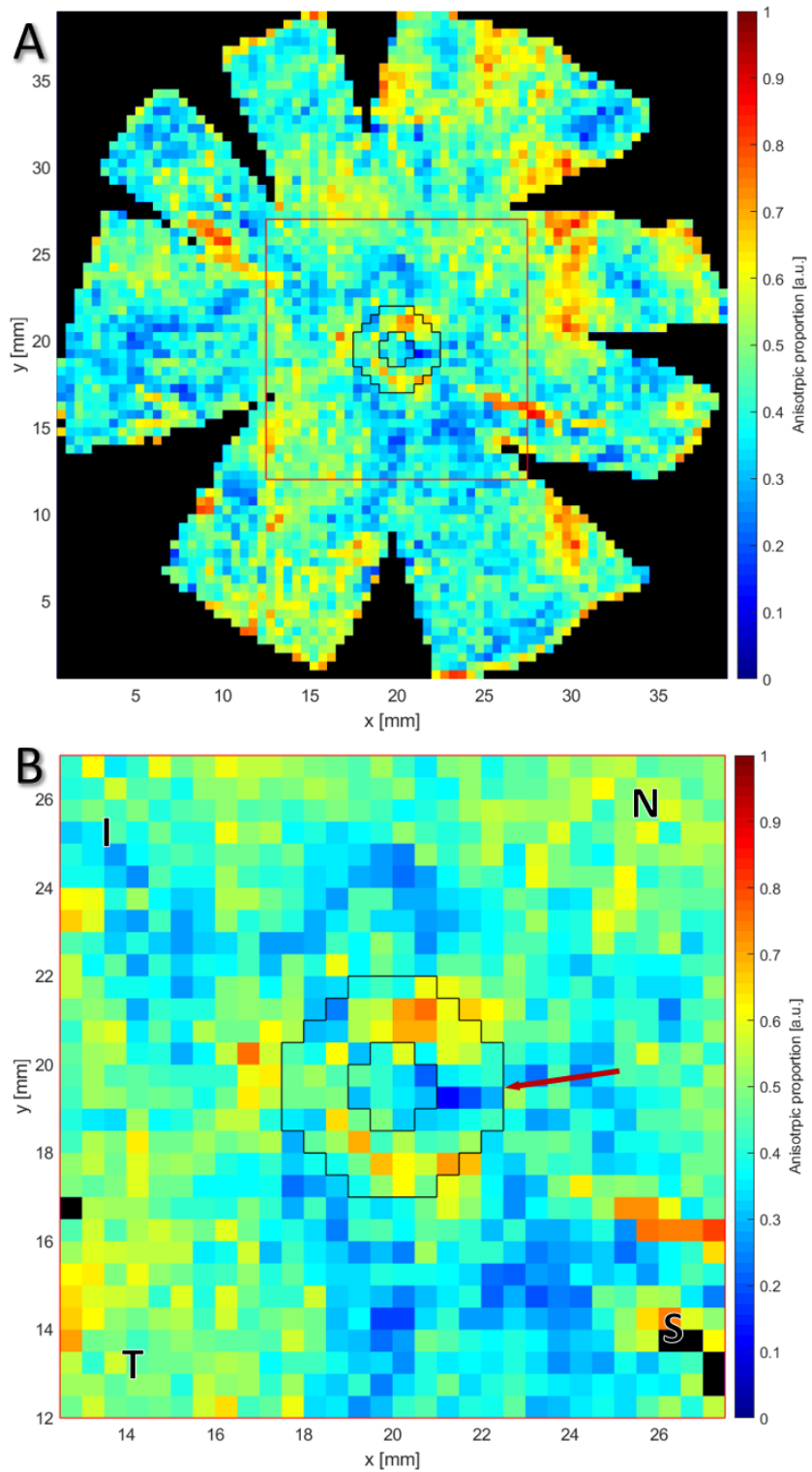


Figure A.08 – WAXS collagen anisotropic proportion contour map of human non-myopic specimen N5 (A) with a red square designating a 30x30 vector plot magnification (B). The PPS is bounded by black lines, whilst the red arrow denotes discontinuation in the circumferential collagen orientation in the SN region, with the superior (S), nasal (N), inferior (I), temporal (T) directions indicated on B.

A.1.1.5 N6

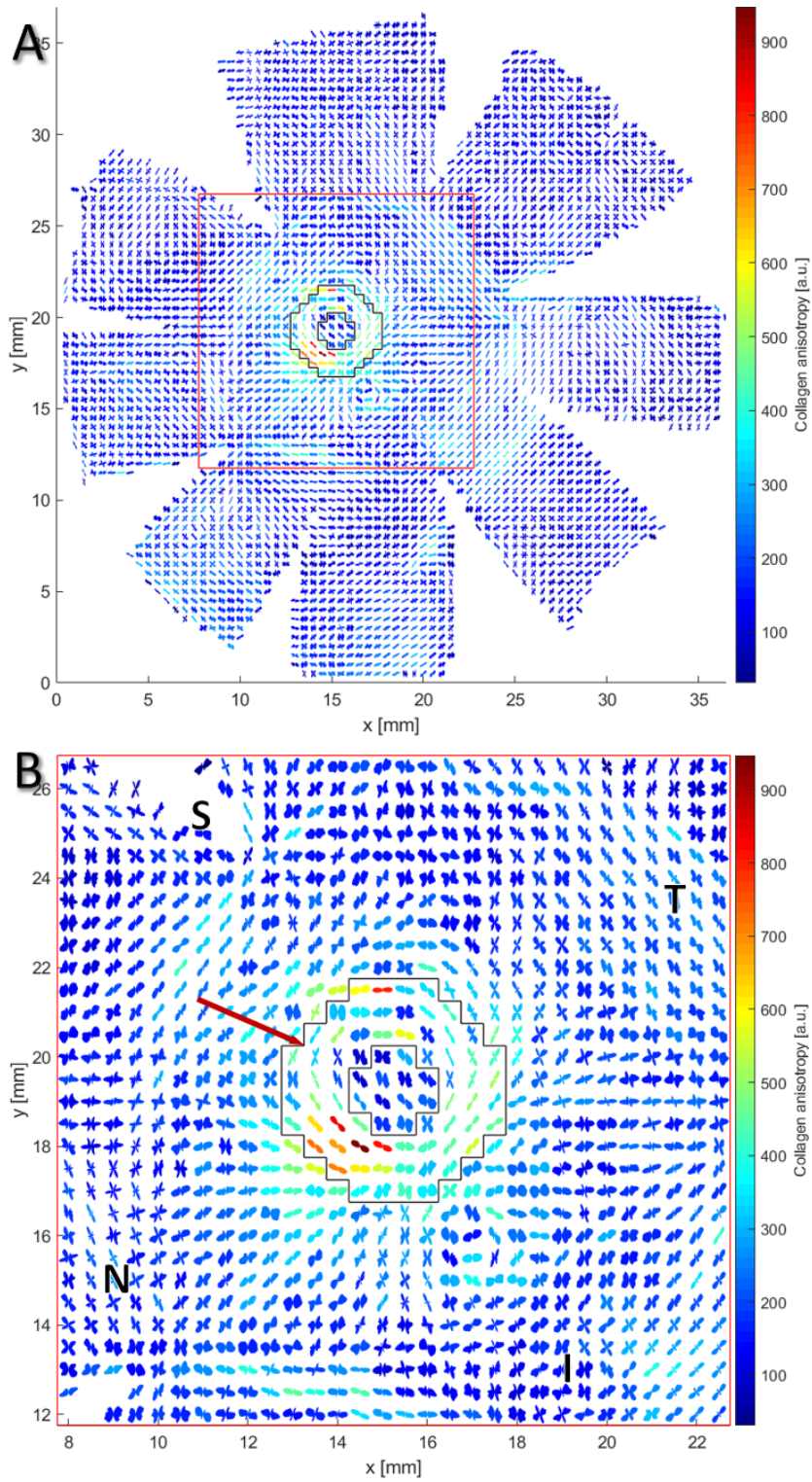


Figure A.09 – WAXS polar vector plot map of human non-myopic specimen N6 (A) with a red square designating a 30x30 vector plot magnification (B). The PPS is bounded by black lines, whilst the red arrow denotes discontinuation in the circumferential collagen orientation in the SN region, with the superior (S), nasal (N), inferior (I), temporal (T) directions indicated on B.

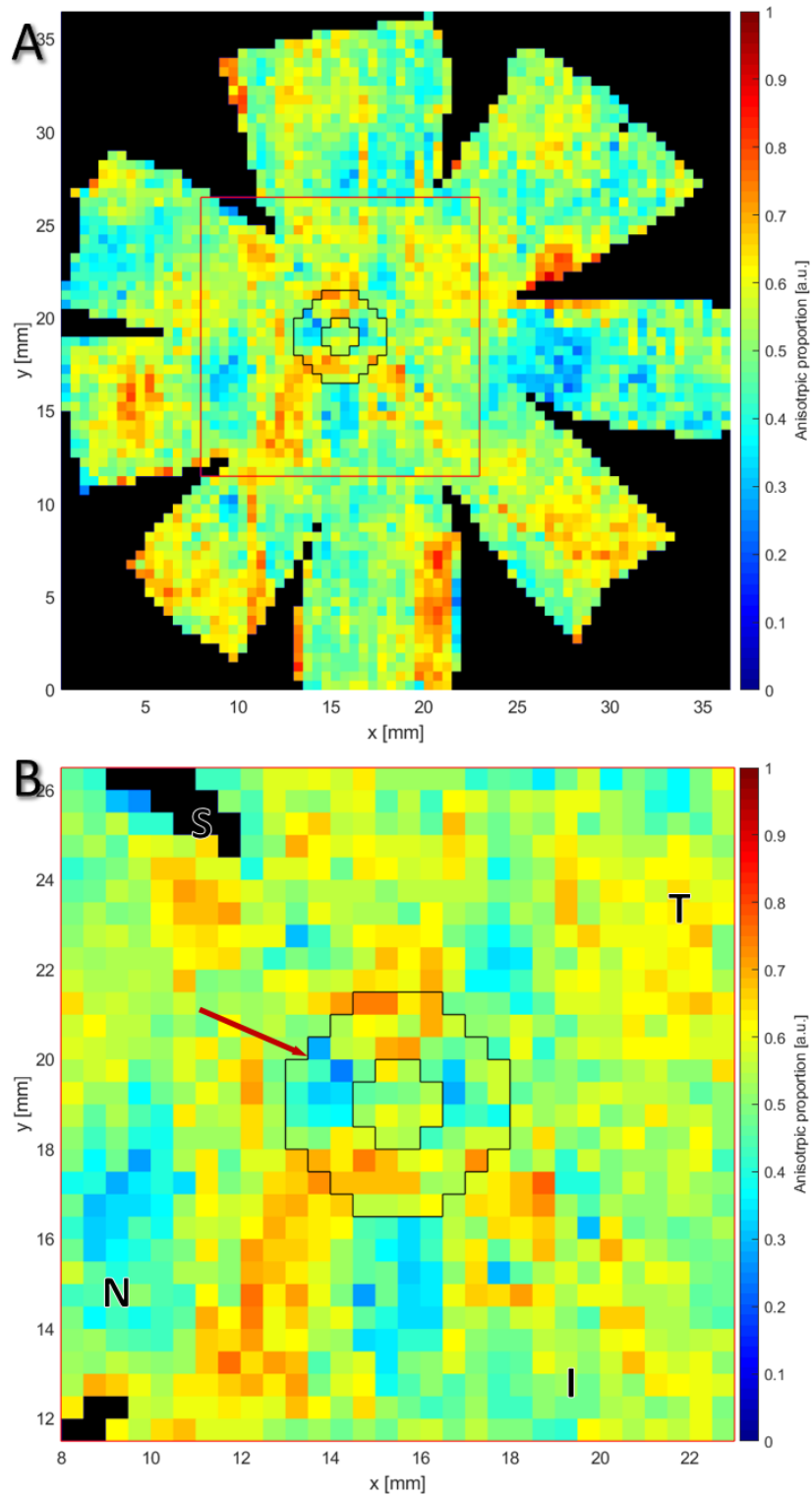


Figure A.10 – WAXS collagen anisotropic proportion contour map of human non-myopic specimen N6 (A) with a red square designating a 30x30 vector plot magnification (B). The PPS is bounded by black lines, whilst the red arrow denotes discontinuation in the circumferential collagen orientation in the SN region, with the superior (S), nasal (N), inferior (I), temporal (T) directions indicated on B.

## A.1.1.6 N7

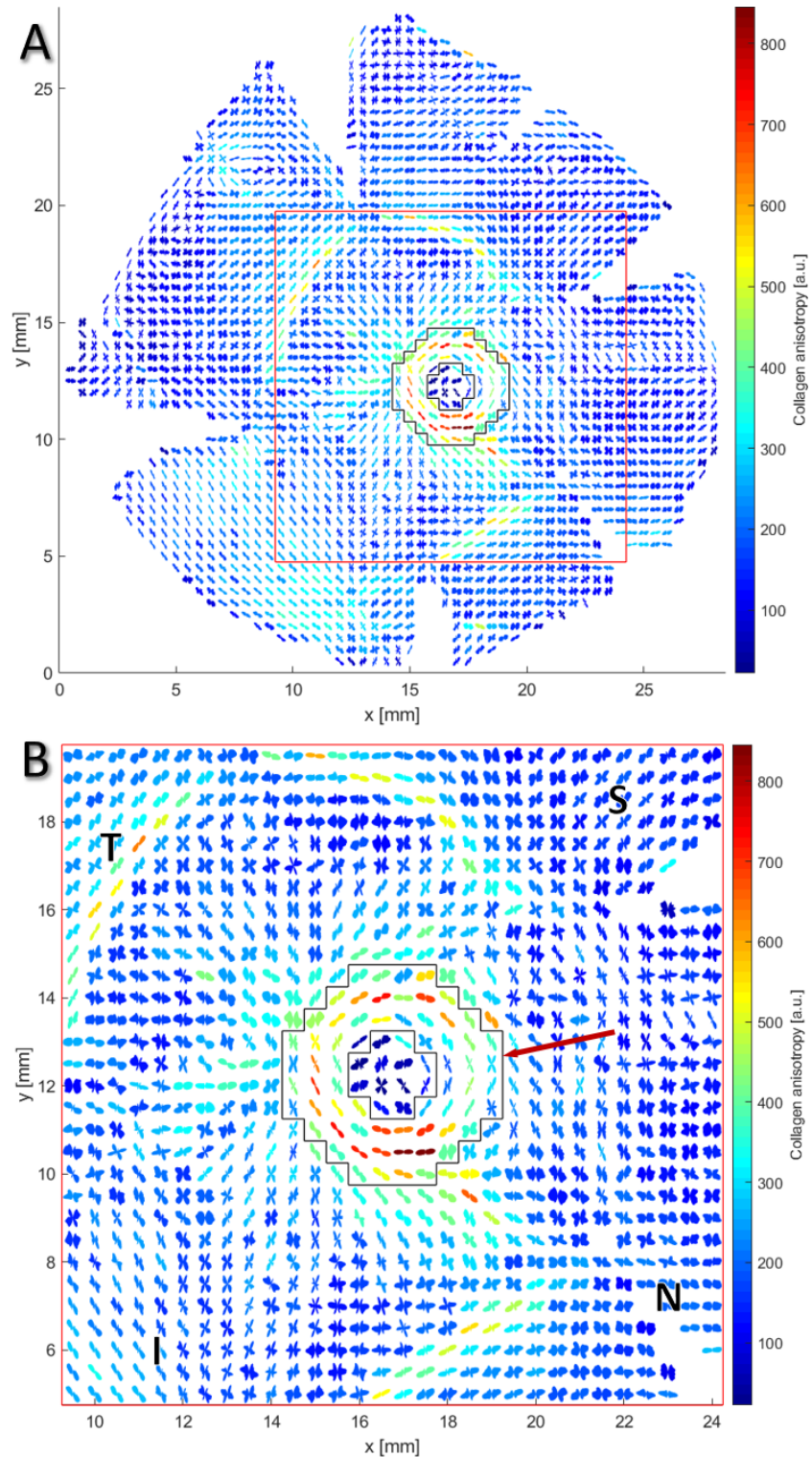


Figure A.11 – WAXS polar vector plot map of human non-myopic specimen N7 (A) with a red square designating a 30x30 vector plot magnification (B). The PPS is bounded by black lines, whilst the red arrow denotes discontinuation in the circumferential collagen orientation in the SN region, with the superior (S), nasal (N), inferior (I), temporal (T) directions indicated on B.

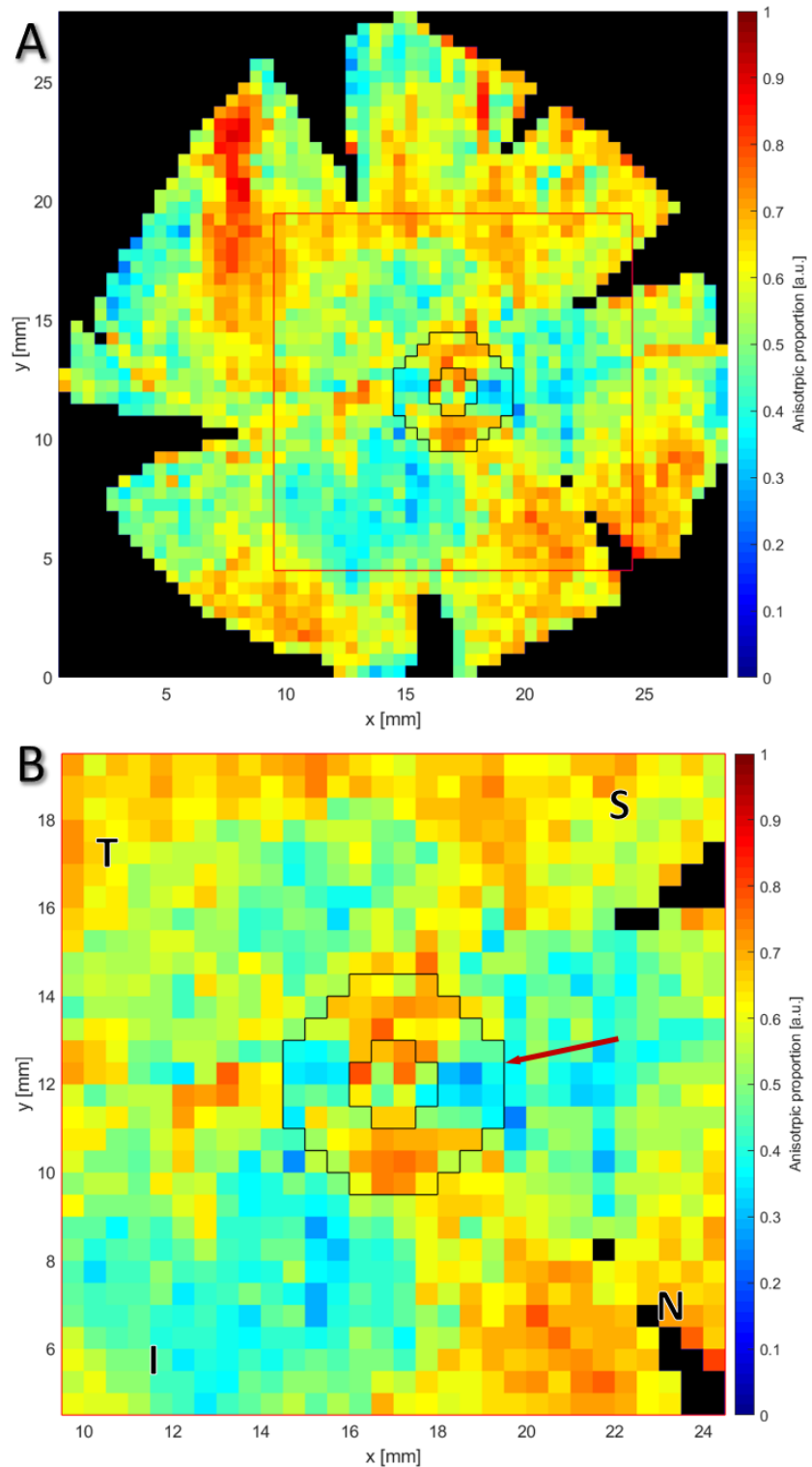


Figure A.12 – WAXS collagen anisotropic proportion contour map of human non-myopic specimen N7 (A) with a red square designating a 30x30 vector plot magnification (B). The PPS is bounded by black lines, whilst the red arrow denotes discontinuation in the circumferential collagen orientation in the SN region, with the superior (S), nasal (N), inferior (I), temporal (T) directions indicated on B.

## A.1.2 Bovine specimens

## A.1.2.1 B3

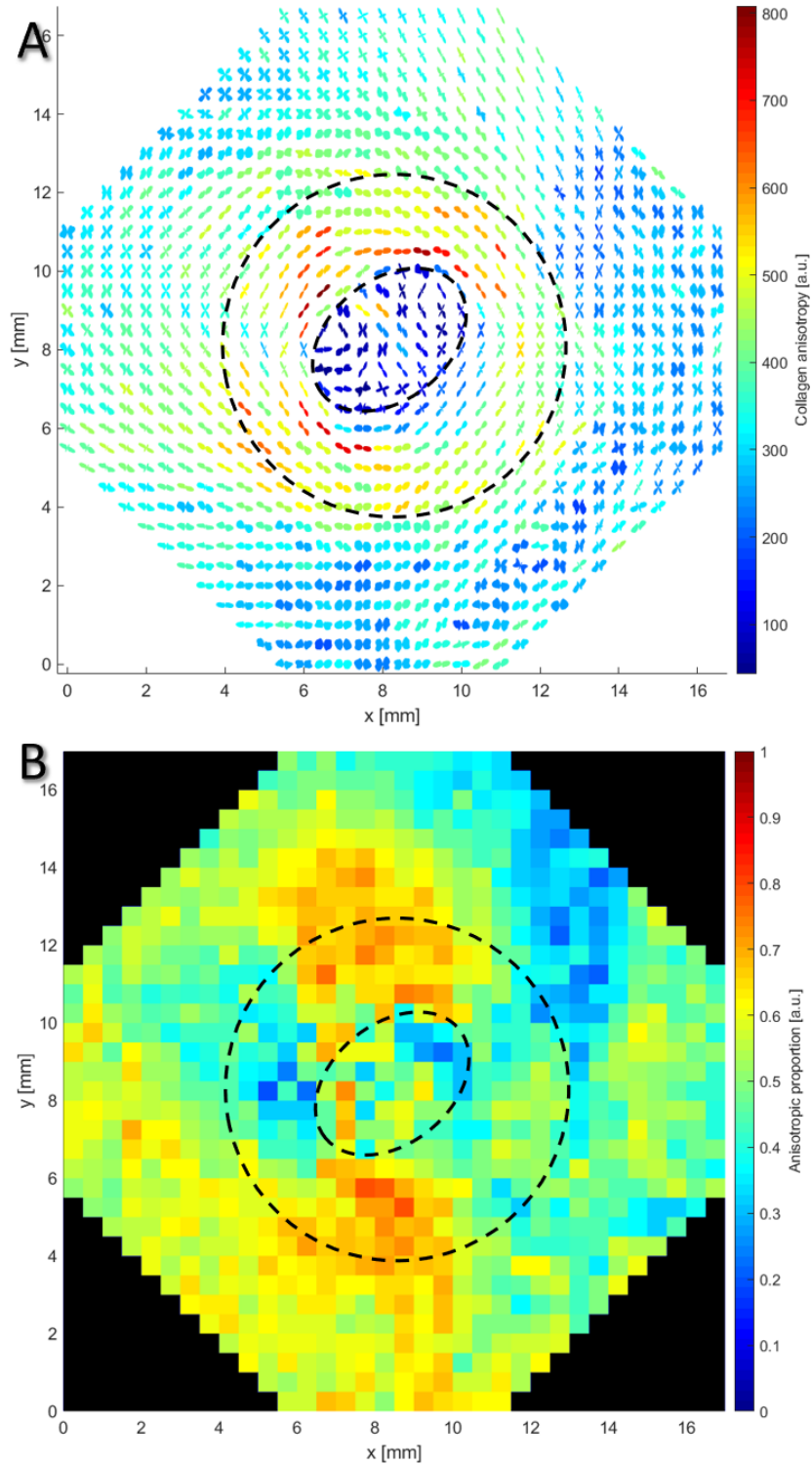


Figure A.13 – WAXS polar vector plot map (A) and collagen anisotropic proportion contour map (B) of bovine posterior sclera B3. The highly aligned annulus of collagen fibres in the PPS is bounded by dashed lines.

Data points were recorded at every 0.5mm.

A.1.2.2 B4

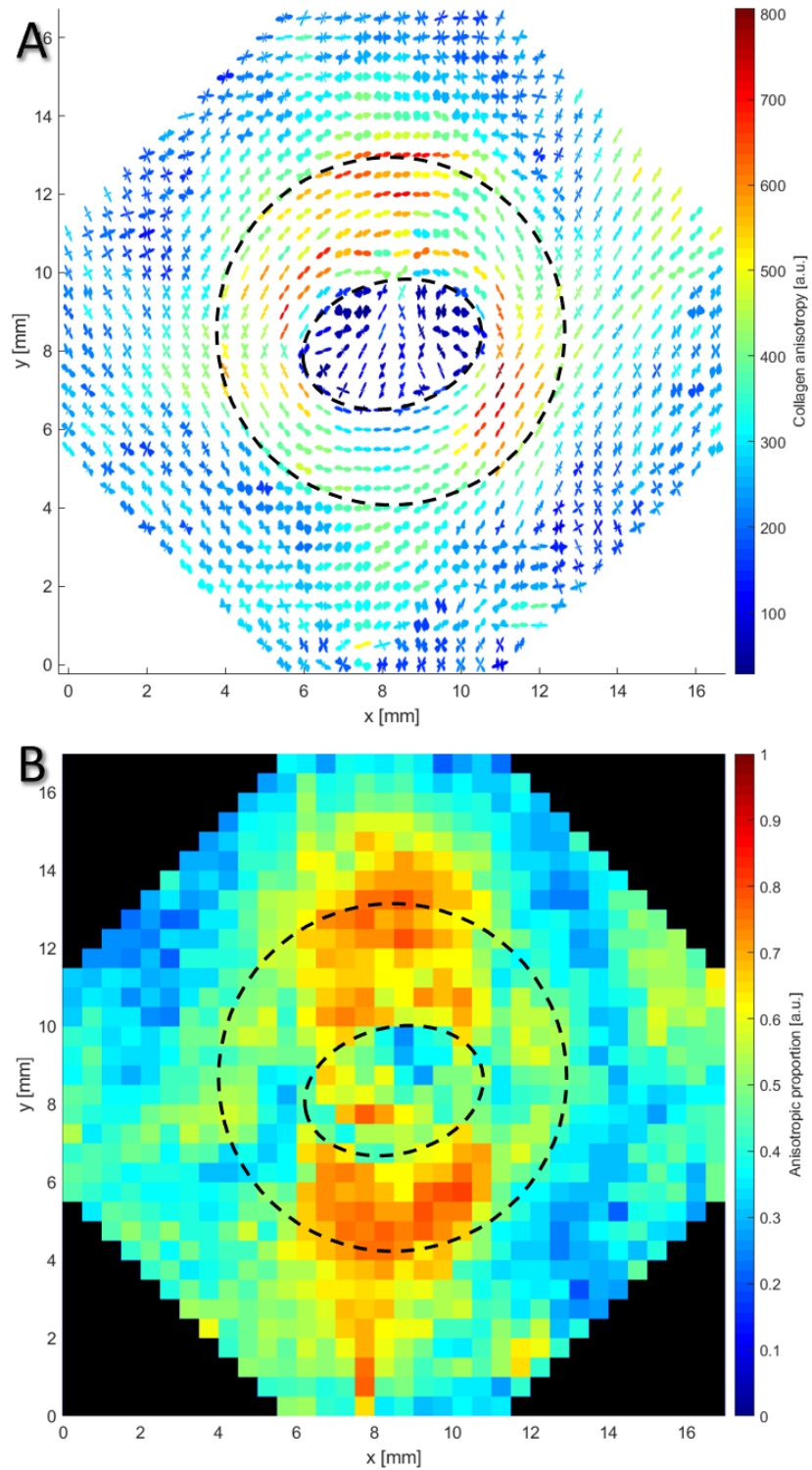


Figure A.14 – WAXS polar vector plot map (A) and collagen anisotropic proportion contour map (B) of bovine posterior sclera B4. The highly aligned annulus of collagen fibres in the PPS is bounded by dashed lines.

Data points were recorded at every 0.5mm.

## A.2 Confocal image analysis

## A.2.1 CurveAlign

## A.2.1.1 Alignment

## A.2.1.1.1 F-Actin stress fibres

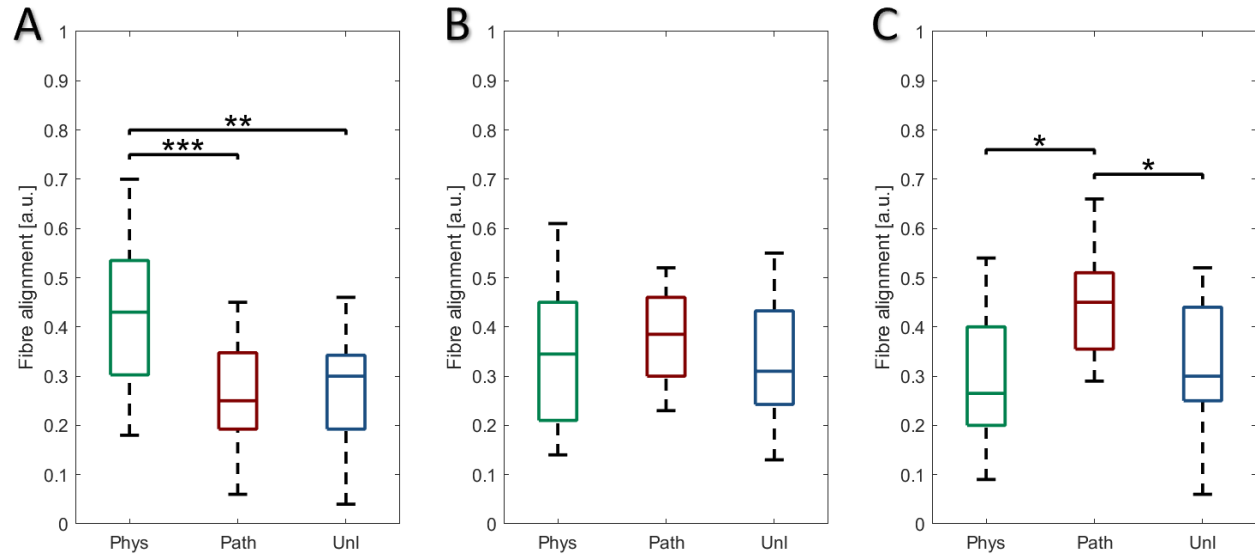


Figure A.15 – Comparison of F-actin stress fibre alignment between three relaxation time points 1h (A), 6h (B) and 24h (C) post-cyclic tensile strain (CTS) (n=3 wells, N=3 plates). Data were calculated by CurveAlign based on maximum intensity projections and grouped by applied CTS and relaxation time, presented as median  $\pm$  standard deviation (SD). (A) n=129-136 cells; (B) n=103-113 cells; (C) n=136-145 cells; \*:p<0.05; \*\*:p<0.01; \*\*\*:p<0.001.

A.2.1.1.2 Vimentin intermediate filaments

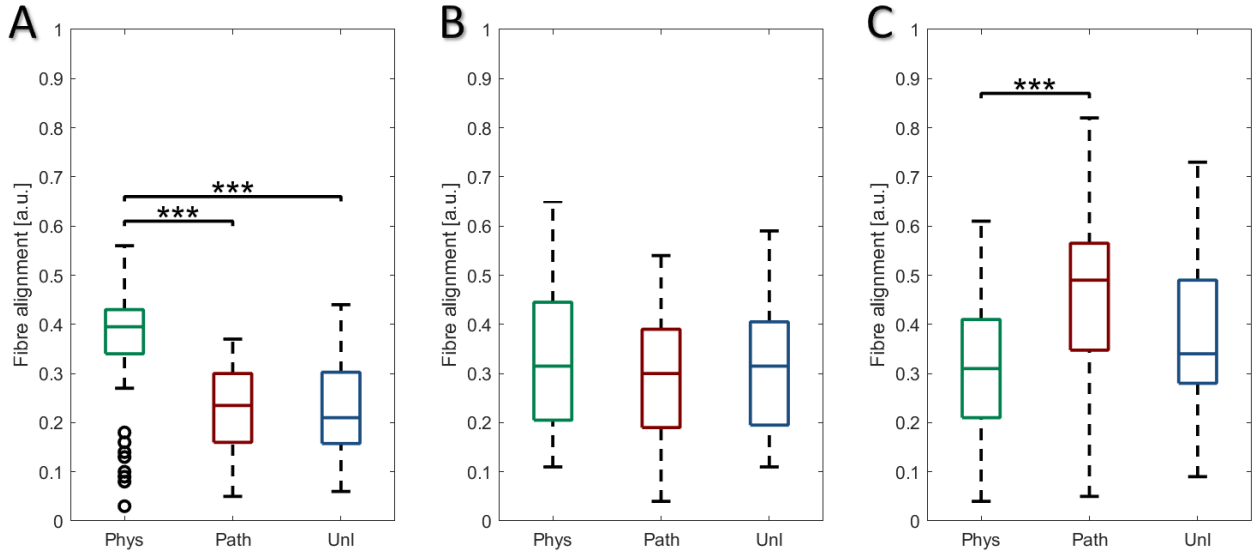


Figure A.16 – Comparison of vimentin intermediate filament alignment between three relaxation time points 1h (A), 6h (B) and 24h (C) post-CTS (n=3 wells, N=3 plates). Data were calculated by CurveAlign based on maximum intensity projections and grouped by applied CTS and relaxation time, presented as median  $\pm$  SD.

(A) n=129-136 cells; (B) n=103-113 cells; (C) n=136-145 cells; \*\*\*:p<0.001.

A.2.1.1.3  $\beta$ -Tubulin microtubules

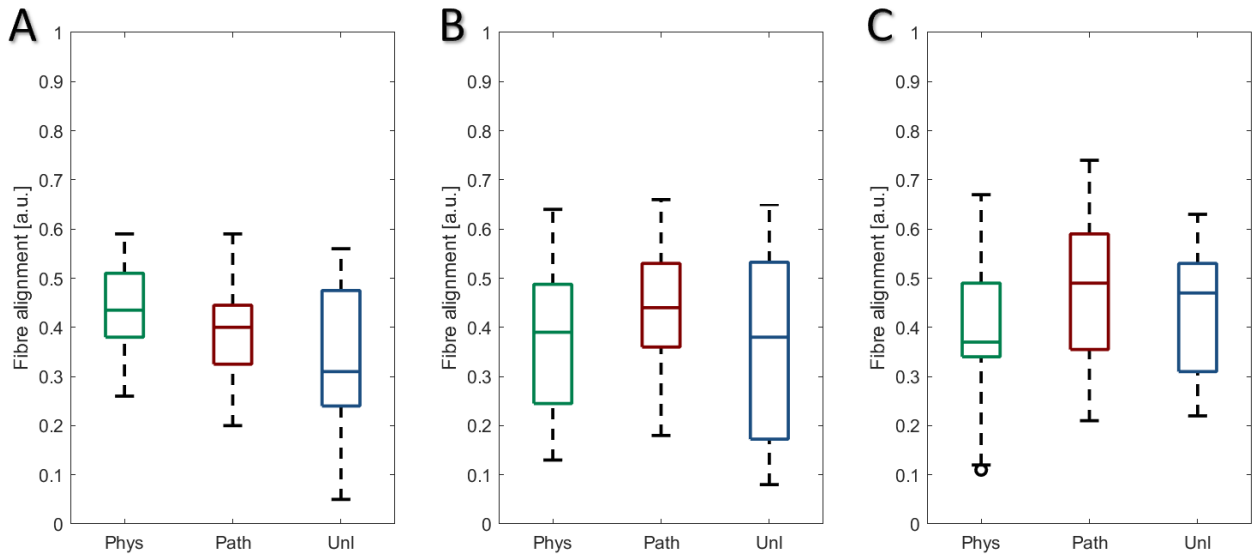


Figure A.17 – Comparison of  $\beta$ -tubulin microtubule alignment between three relaxation time points 1h (A), 6h (B) and 24h (C) post-CTS (n=3 wells, N=3 plates). Data were calculated by CurveAlign based on maximum intensity projections and grouped by applied CTS and relaxation time, presented as median  $\pm$  SD.

(A) n=101-130 cells; (B) n=119-127 cells; (C) n=141-154 cells.

A.2.2 CytoSpectre

A.2.2.1 Circular variance

A.2.2.1.1 F-Actin stress fibres

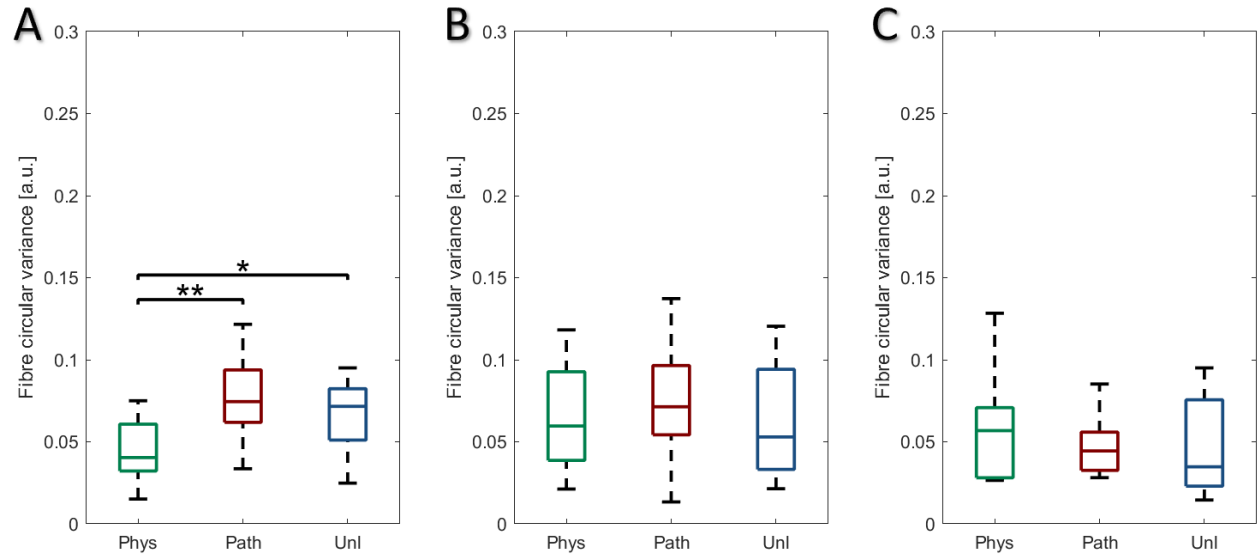


Figure A.18 – Comparison of F-actin stress fibre circular variance between three relaxation time points 1h (A), 6h (B) and 24h (C) post-CTS (n=3 wells, N=3 plates). Data were calculated by CytoSpectre based on maximum intensity projections and grouped by applied CTS and relaxation time, presented as median  $\pm$  SD.

(A) n=129-136 cells; (B) n=103-113 cells; (C) n=136-145 cells; \*:p<0.05; \*\*:p<0.01.

## A.2.2.1.2 Vimentin intermediate filaments

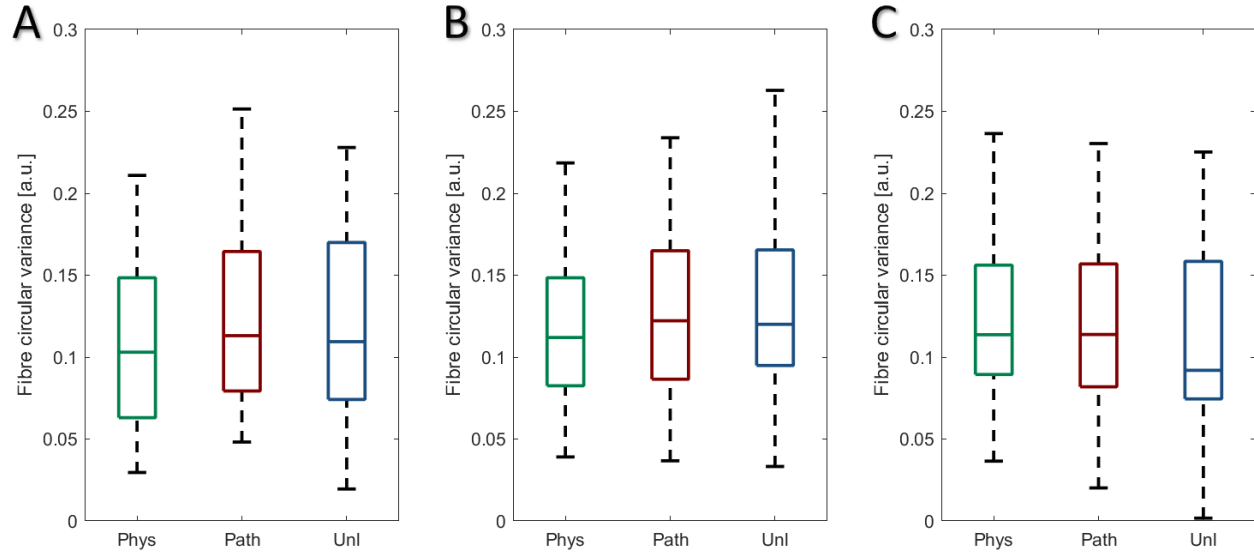


Figure A.19 – Comparison of vimentin intermediate filament circular variance between three relaxation time points 1h (A), 6h (B) and 24h (C) post-CTS ( $n=3$  wells,  $N=3$  plates). Data were calculated by CytoSpectre based on maximum intensity projections and grouped by applied CTS and relaxation time, presented as median  $\pm$  SD.

(A)  $n=129$ -136 cells; (B)  $n=103$ -113 cells; (C)  $n=136$ -145 cells.

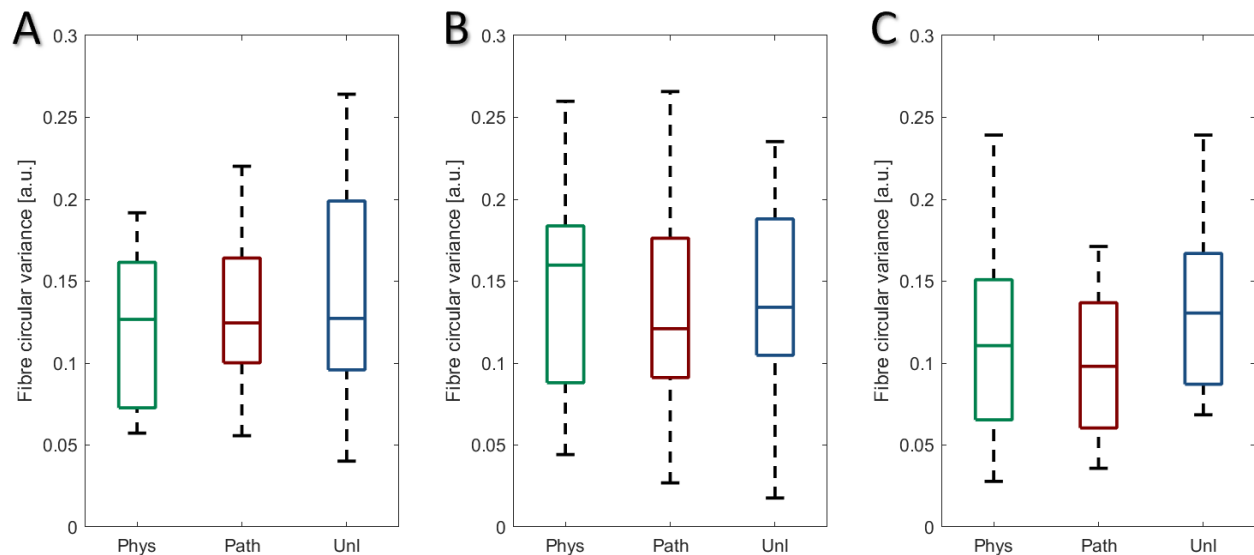
A.2.2.1.3  $\beta$ -Tubulin microtubules

Figure A.20 – Comparison of  $\beta$ -tubulin microtubule circular variance between three relaxation time points 1h (A), 6h (B) and 24h (C) post-CTS ( $n=3$  wells,  $N=3$  plates). Data were calculated by CytoSpectre based on maximum intensity projections and grouped by applied CTS and relaxation time, presented as median  $\pm$  SD.

(A)  $n=101$ -130 cells; (B)  $n=119$ -127 cells; (C)  $n=141$ -154 cells.

## A.2.2.2 Angular standard deviation

## A.2.2.2.1 F-Actin stress fibres

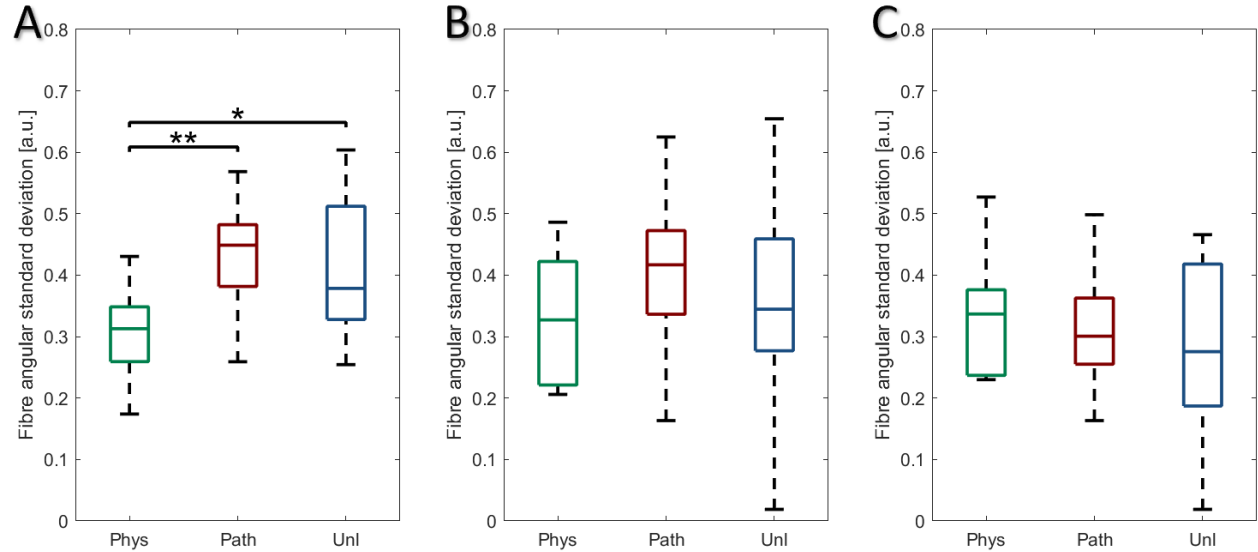


Figure A.21 – Comparison of F-actin stress fibre angular standard deviation between three relaxation time points 1h (A), 6h (B) and 24h (C) post-CTS (n=3 wells, N=3 plates). Data were calculated by CytoSpectre based on maximum intensity projections and grouped by applied CTS and relaxation time, presented as median  $\pm$  SD. (A) n=129-136 cells; (B) n=103-113 cells; (C) n=136-145 cells; \*:p<0.05; \*\*:p<0.01.

## A.2.2.2.2 Vimentin intermediate filaments

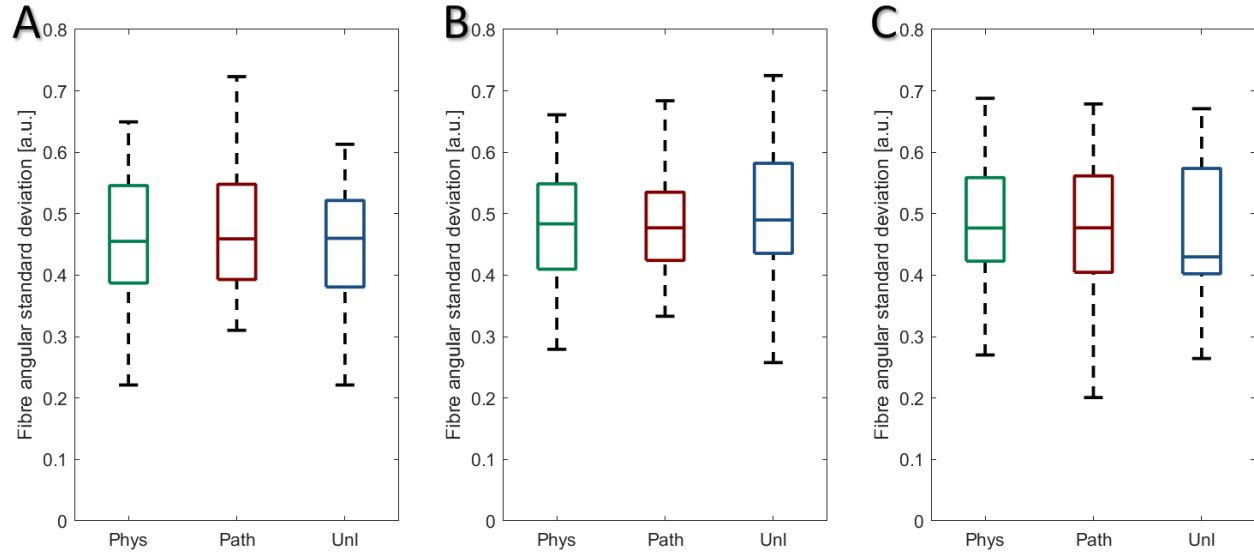


Figure A.22 – Comparison of vimentin intermediate filament angular standard deviation between three relaxation time points 1h (A), 6h (B) and 24h (C) post-CTS (n=3 wells, N=3 plates). Data were calculated by CytoSpectre based on maximum intensity projections and grouped by applied CTS and relaxation time, presented as median  $\pm$  SD. (A) n=129-136 cells; (B) n=103-113 cells; (C) n=136-145 cells.

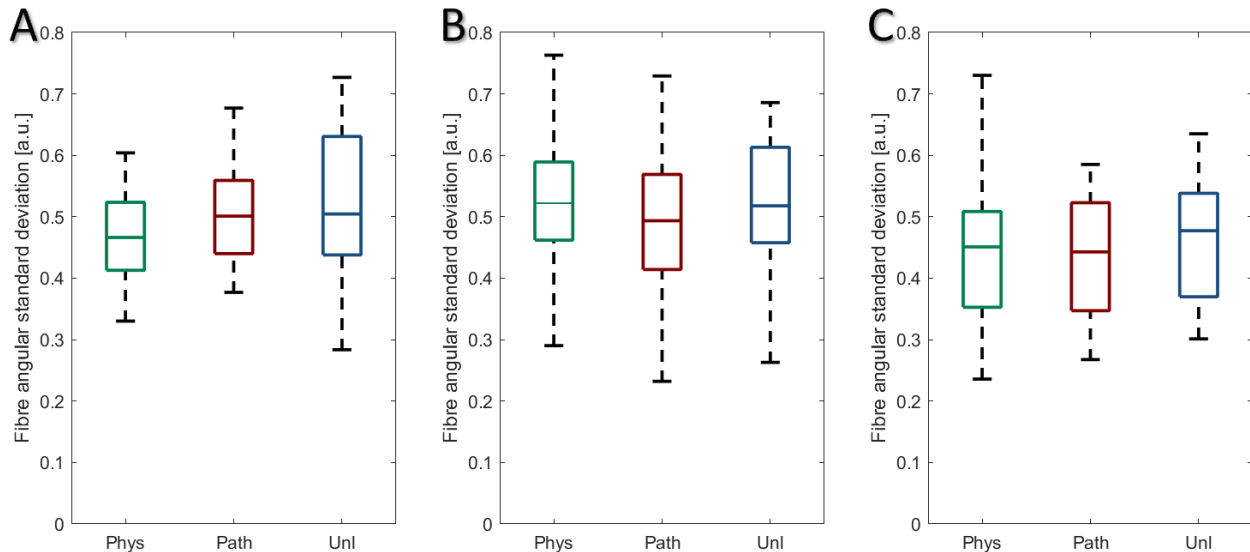
A.2.2.2.3  $\beta$ -Tubulin microtubules

Figure A.23 – Comparison of  $\beta$ -tubulin microtubule angular standard deviation between three relaxation time points 1h (A), 6h (B) and 24h (C) post-CTS (n=3 wells, N=3 plates). Data were calculated by CytoSpectre based on maximum intensity projections and grouped by applied CTS and relaxation time, presented as median  $\pm$  SD. (A) n=101-130 cells; (B) n=119-127 cells; (C) n=141-154 cells.

### A.3 Publications, conference presentations and achievements

#### A.3.1 Publications

- Markov P, Eliasy A, Pijanka JK, Htoon HM, Paterson NG, Sorensen T, Elsheikh A, Girard MJ, Boote C (2018) Bulk changes in posterior scleral collagen microstructure in human high myopia. *Mol Vis* **24**(1): 818-833.
- Pijanka JK, Markov P, Midgett D, Paterson NG, White N, Blain EJ, Nguyen TD, Quigley HA, Boote C (2019) Quantification of collagen fiber structure using second harmonic generation imaging and 2D discrete Fourier transform analysis: Application to the human optic nerve head. *J Biophotonics* **12**(5): 1-19. (π – Joint First Author)
- Zhou D, Eliasy A, Abass A, Markov P, Whitford C, Boote C, Movchan A, Movchan N, Elsheikh A (2019) Analysis of X-ray scattering microstructure data for implementation in numerical simulations of ocular biomechanical behaviour. *Plos One* **14**(4): 1-16.
- Markov P, Boote C, Zhu H, Blain E (2019) Effects of mechanical load on cytoskeletal protein arrangement in scleral fibroblasts. *Invest Ophthalmol Vis Sci* **60**(9): 6175.

#### A.3.2 Conference presentations

- Speaking of Science Interdisciplinary Conference 2017 – **Podium Presentation**; Cardiff, UK; 04/05/2017.
- Vision Researchers Colloquium 2017 – **Podium Presentation**; Bath, UK; 23/06/2017.
- 15<sup>th</sup> International Congress on Vision Science and Ophthalmology – **Podium Presentation; Student Ambassador**; London, UK; 11/08/2017.
- Cardiff Institute for Tissue Engineering and Repair (CITER) Network Showcase and Annual Scientific Meeting 2017 – **Podium Presentation**; Cardiff, UK; 18/09/2017.
- Speaking of Science Interdisciplinary Conference 2018 – **Poster Presentation; People's Choice Award for Best Poster**; Cardiff, UK; 03/05/2018.
- SenSyT Symposium 2018 – **Poster Presentation**; London, UK; 03/12/2018.
- Association for Research in Vision and Ophthalmology (ARVO) Annual Meeting 2019 – **Poster Presentation**; Vancouver, Canada; 02/05/2019.
- 25<sup>th</sup> Congress of the European Society of Biomechanics – **Podium Presentation**; Vienna, Austria; 08/07/2019.

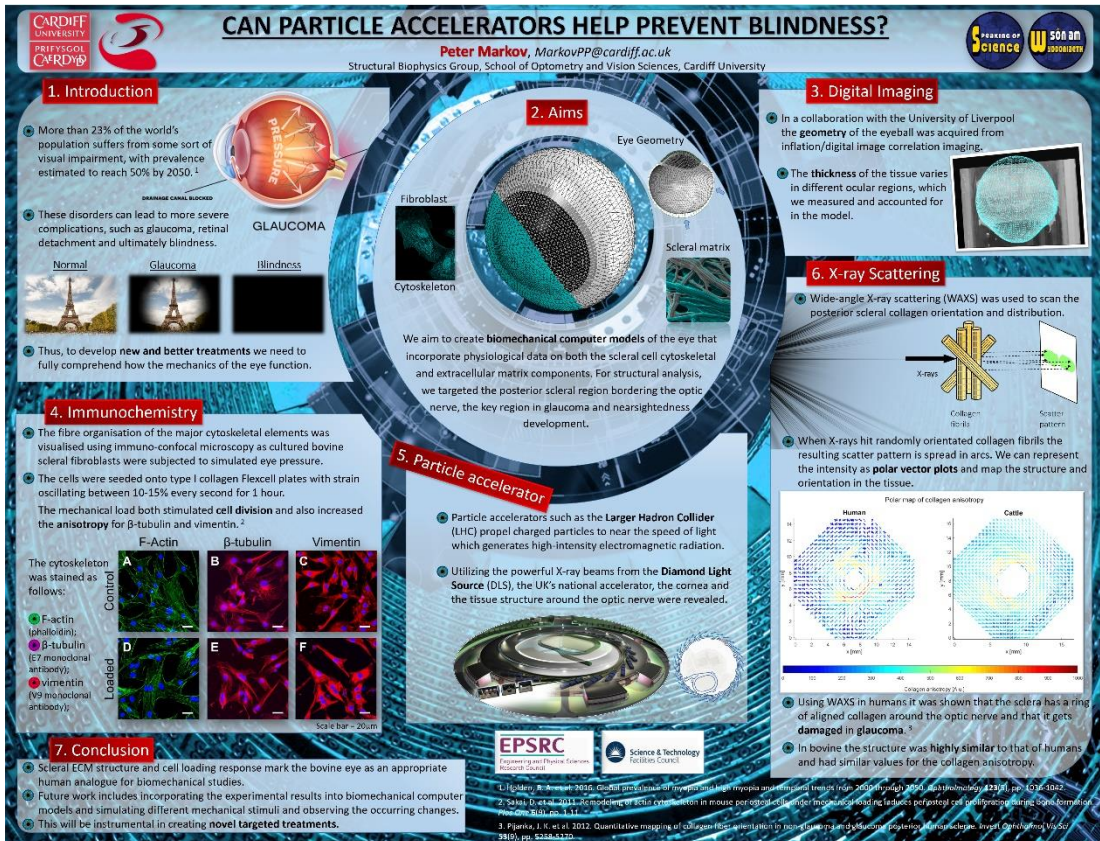


Figure A.24 – Poster for Speaking of Science 2018 (Cardiff, UK)

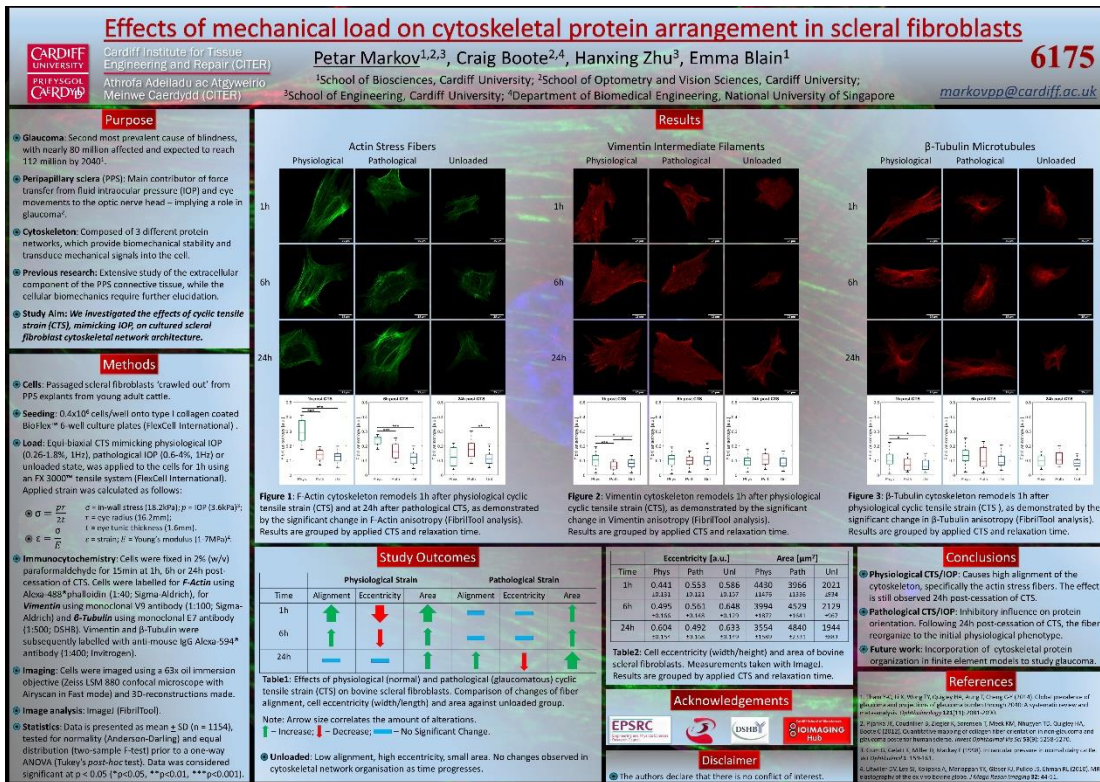


Figure A.25 – Poster for ARVO Annual Meeting 2019 (Vancouver, Canada)

A.3.3 Miscellaneous achievements

- **Laboratory Demonstrator** for ‘Cells to System’ and ‘Ocular Anatomy and Physiology’ First-year practical courses in Optometry; Cardiff University School of Optometry and Vision Sciences, Cardiff, UK; 01/2017-03/2020.
- **STEM Ambassador** for Wales since 20/04/2017.
- **Lead Volunteer** for ‘Safety Walk Scheme’ project; Cardiff University Students’ Union, Cardiff, UK; 2017/2018 Academic Year.
- **Team Leader** for Brain Games 2018 and 2019; National Museum Wales, Cardiff, UK; 18/03/2018 and 10/03/2019.
- **Group Category Winner** in the Wales Volunteer of the Year Awards for the ‘Safety Walk Scheme’; Wales Council for Voluntary Action, Cardiff, UK; 13/06/2018.
- **Lead Volunteer** for ‘Student Science Superheroes’ joint project with Cancer Research Wales; Cardiff University Students’ Union, Cardiff, UK; 2018/2019 Academic Year.
- **Vice-President/Secretary and Welfare/Wellbeing Officer** of the Cardiff University Fencing Club; Cardiff University, Cardiff, UK; 2018/2019 Academic Year.
- **Associate Fellow of the Higher Education Academy (AFHEA)** since 10/12/2018.
- **Conference Travel Bursary** (£778) to present at ARVO Annual Meeting; CITER, Cardiff, UK; 04/04/2019.
- **Diploma of Professional Development in Leadership (Distinction)** for volunteering 200 hours in a Leadership position; Cardiff University Students’ Union, Cardiff, UK; 25/04/2019.